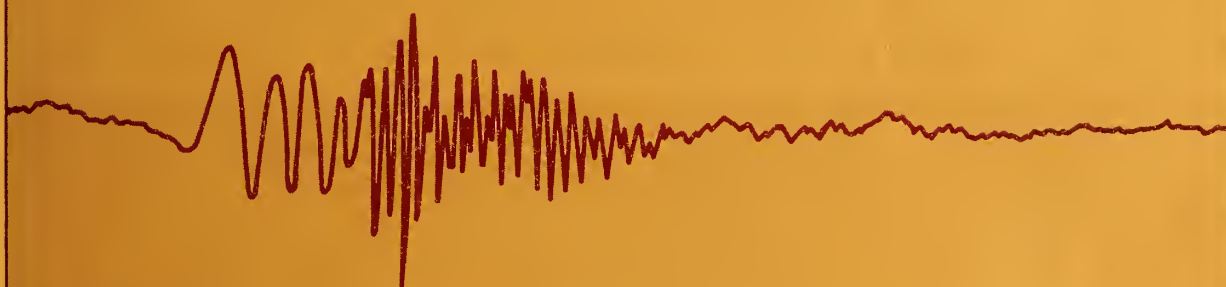


# acoustic-gravity waves in the atmosphere

symposium proceedings



sponsored by the  
department of commerce:  
environmental science services administration  
and the  
department of defense:  
advanced research projects agency

boulder, colorado  
15 - 17 july 1968



Digitized by the Internet Archive  
in 2013

<http://archive.org/details/acousticgravityw00essa>

# acoustic-gravity waves in the atmosphere

symposium proceedings

edited by t.m. georges

sponsored by the  
environmental science services administration  
and the  
advanced research projects agency

boulder, colorado  
15 - 17 july 1968

E S S A / A R P A    SYMPOSIUM ON ACOUSTIC-GRAVITY WAVES

General Chairman:                    A. Glenn Jean  
Technical Program Chairman:    James R. Wait  
Executive Secretary:                Mrs. Dee Belsher

Advisory Committee:

G. S. Benton	E. R. Benton
K. Davies	W. L. Flock
B. Haurwitz	C. O. Hines
R. W. Knecht	J. K. Lerohl
S. Lukasik	A. D. Pierce
G. C. Reid	R. J. Slutz
W. F. Utlaut	J. W. Warwick



## FOREWORD

The Symposium on Acoustic-Gravity Waves in the Atmosphere was held in Boulder, Colorado, from 15 through 17 July 1968, and was sponsored jointly by the Environmental Science Services Administration (ESSA) and the Advanced Research Projects Agency (ARPA) of the Department of Defense.

The aim of the Symposium was to draw together specialists from the several diverse disciplines that have come to be concerned with wave motions in the neutral atmosphere. Some 48 papers were presented by participants with backgrounds that covered the spectrum from meteorology and oceanography to atmospheric and ionospheric physics, radio physics and wave theory. Topics dealt with included the generation of atmospheric waves by natural and artificial sources, propagation in the terrestrial environment, and effects in the upper atmosphere and ionosphere.

As a collection of almost all the papers presented, this volume hopefully represents a valid cross section of current research and the present state of knowledge in this new and rapidly developing field. But perhaps more importantly, it also reveals the state of our ignorance, and will serve its purpose if it stimulates the interest of both theorist and experimentalist in the imposing array of unsolved theoretical and observational problems.

To expedite rapid publication, most of the papers were reproduced directly from manuscripts supplied by each author. Thanks are due my colleagues at ESSA who helped review the contributions, and to Mrs. Jane Ross, who typed several of the manuscripts.

T. M. Georges  
Boulder, Colorado  
October, 1968



## CONTENTS

Foreword		iii
Contents		v
I.   ATMOSPHERIC WAVES GENERATED BY ARTIFICIAL SOURCES		
Generation of acoustic-gravity waves by nuclear detonations - W. E. Knabe and S. L. Kahalas		1
Theoretical source models for the generation of acoustic gravity waves by nuclear explosions - Allan D. Pierce		9
Acoustic-gravity waves produced by energy release - J. D. Cole and C. Greifinger		25
Theoretical calculations of traveling ionospheric disturbances generated by low-altitude nuclear explosions - J. S. Greene and W. A. Whitaker		45
Note on compressible bores - Wallace D. Hayes		65
Propagation velocity of acoustic gravity waves due to a large nuclear explosion - Ryozauro Yamamoto		69
Acoustic waves in the ionosphere following nuclear explosions - Donald M. Baker		79
Propagating energy in the upper atmosphere including lower ionosphere generated by artificial sources - Uri Fehr		87
II.   NATURAL SOURCES OF ATMOSPHERIC WAVES - THEORY		
The launching of low frequency travelling disturbances by auroral currents - G. Chimonas		101
Mesoscale pressure fluctuations in the atmosphere - Ivan Tolstoy		107
Jet stream associated gravity waves and implications concerning jet stream stability - T. R. Madden and J. F. Claerbout		121
Electromagnetic effects of atmospheric gravity waves - J. F. Claerbout and T. R. Madden		135
III.   NATURAL SOURCES OF ATMOSPHERIC WAVES - OBSERVATIONS		
The auroral zone as a source of traveling ionospheric disturbances - W. L. Flock and R. D. Hunsucker		159
Short-period ionospheric oscillations associated with severe weather - T. M. Georges		171
Dispersion of acoustic-gravity waves in the atmosphere - N. K. Balachandran and William L. Donn		179
Infrasonic waves from natural and artificial sources - William L. Donn and Eric Posmentier		195

	Subsonic atmospheric oscillations - Richard K. Cook	209
	"Subsonic" waves and severe weather phenomena - Howard S. Bowman	215
IV.	ATMOSPHERIC WAVE PROPAGATION IN THE TERRESTRIAL ENVIRONMENT	
	Ducting of internal gravity waves in a temperature- and wind-stratified atmosphere - C. A. Reddy	225
	Some speculations on the roles of critical level interactions between internal gravity waves and mean flows - Richard S. Lindzen	231
	Gravity wave propagation with a time-dependent critical level - David D. Houghton and Walter L. Jones	241
	Ray tracing for internal gravity waves (summary) - Walter L. Jones	249
	Vertical energy flux in a wind and temperature stratified atmosphere - Robert F. MacKinnon	253
	Theoretical calculations of vertical mechanical wave energy flux in the atmosphere - F. W. G. Warren	263
	Vertically propagating waves in an atmosphere with Newtonian cooling inversely proportional to density (summary) - Richard S. Lindzen	277
	Full-wave calculations of coupled neutral air wave propagation through the thermosphere - H. E. Volland	281
	Excitation and dispersion of the atmosphere surface wave - David G. Harkrider and Frederick J. Wells	299
	An approach to the mode-conversion problem in non-uniform acoustic waveguides - James R. Wait	315
	The diurnal source and nature of gravity waves ducted in the lower atmosphere - A. F. Wickersham, Jr.	325
	Scatter propagation of infrasound - William C. Meecham	337
	Higher order approximations in the theory of acoustic-gravity waves - F. Einaudi	345
	Iterative series methods for finding exact solutions for a class of second order differential equations - Jack P. Friedman and Bruce W. Crawford	349
V.	ATMOSPHERIC-WAVE EFFECTS IN THE UPPER ATMOSPHERE AND IONOSPHERE	
	Measurements of gravity waves in the neutral air at thermospheric heights by Explorer 32 (summary) - G. P. Newton, D. T. Pelz and H. Volland	365
	The response of the F-region ionosphere to internal atmospheric gravity waves - William H. Hooke	367

On possible methods of determining the origin of E-region wind shear - William H. Hooke	373
Collisional interaction of atmospheric waves with the ionospheric F region - T. M. Georges	377
The effect of velocity bandwidth on the cross-spectra of wave recordings from spatially separated sites - Earl E. Gossard	381
A hydromagnetic coupling of acoustic-gravity waves and the ionized atmosphere - S. Kato, C. A. Reddy and S. Matsushita	397
Hydromagnetic waves with influence of gravity - H. Poeverlein	403
A ray-tracing study of direction-of-arrival variations through a traveling ionospheric disturbance - W. J. Surtees	411
CONCLUDING REMARKS - C. O. Hines	425
APPENDIX I - Abstracts of papers presented at the Symposium but not included in these Proceedings.	427
APPENDIX II - Program for the Symposium.	433



# I Atmospheric waves generated by artificial sources





## GENERATION OF GRAVITY-ACOUSTIC WAVES BY NUCLEAR DETONATIONS

W. E. Knabe and S. L. Kahalas  
Mt. Auburn Research Associates, Inc.  
Cambridge, Massachusetts 02139

Various generating mechanisms are considered as sources of acoustic and gravity waves, taking into consideration nuclear detonation outputs. Such mechanisms include: shock motion, violent heating of air, turbulence, and non-linear effects.

### Introduction

The generation of acoustic disturbances has been considered since the very first nuclear detonations. Since one of the most obvious consequences of a low altitude nuclear detonation is the blast wave produced, the question arose as to how much of the energy liberated by nuclear processes would appear in the shock wave. The generation of shock waves, and - in the linear case - of acoustic and gravity waves from the energy release has been treated and discussed to quite some extent. However, to our knowledge no general consideration has been given to the various ways in which a nuclear detonation may produce fluctuating fluid flows which lead to the generation of gravity and acoustic waves in the atmosphere. We will discuss some of these generating mechanisms and wish to emphasize that the propagation of these waves from the place of origination to the place of detection is not what we are here concerned with. Instead, we attempt to explore various possible source mechanisms which may produce acoustic and gravity waves.

Perhaps a word of explanation is necessary as to why the treatment of the blast wave is not a sufficient description of bomb-generated acoustic and gravity wave phenomena. This is most easily seen by considering a burst at high altitude, say above the E-layer, (e.g. 400 km) where the energy is not absorbed locally as it is for low altitude detonations. If there is an acoustic disturbance detected at ground level, then it must be due to acoustic signals generated by one or more of the primary bomb radiations interacting with the atmosphere over a distance. Generally, if a sufficient amount of energy is deposited, flow will be produced. These secondary flows may then radiate acoustic waves. And even at low altitude, the shock wave itself is not the whole story. A concentration of energy exists in the rising fireball and, again, acoustic or gravity wave disturbances may be generated. Also the flow field induced in the atmosphere by the shock motion, i.e., the flow behind the shock front, must be considered as a potential source of acoustic energy emission.

Thus, in general, we are concerned with the following questions: What are the primary bomb radiation outputs and how do these interact with the atmosphere at the altitudes under consideration? What sort of flows are induced by these interactions? Are they stable or unstable? And finally, how will they generate acoustic or gravity waves?

In this paper, we present some examples of flows produced by bomb outputs interacting with the atmosphere and give estimates of the possible magnitude of acoustic or gravity waves produced (in a specific region of the atmosphere) by these flows.

## Nuclear Detonation Phenomenology

Nuclear detonations have several general characteristics regardless of the altitude at which the detonation occurs. The initial release of energy into several different forms of radiation is similar, so that the observed properties of detonations at various altitudes will depend mainly on how the various output radiations interact with the earth's atmosphere, taking into account that the energy may be transformed from one form into another.

The various radiations are: neutrons, gamma rays, beta rays, X-rays, and debris which are the heavy particles in the weapon residues (Glasstone, 1962). The X-rays and debris contain between 80 and 90 percent of the total bomb energy output and they are primarily responsible for large-scale hydrodynamic effects leading to the generation of sound or gravity waves. X-rays by themselves, of course, are not described in terms of hydrodynamic phenomena, but they are absorbed in air which may be heated very strongly, and then expand. The debris expansion itself constitutes a hydrodynamic phenomenon, but its kinetic energy will be transformed into motion of the air, except at high altitude where the interaction between air and debris is weak. This suggests a classification into three altitude regimes in connection with the study of hydrodynamic motions:

1. Low-Altitude Regime (0 km - 30 km) (Glasstone, 1962).
2. Intermediate-Altitude Regime (30 km - 120 km)
3. High-Altitude Regime (greater than 120 km)

These regimes are characterized by the degree to which the atmosphere contains the radiations as follows: In the low-altitude regime, neither X-rays nor debris can escape from the immediate vicinity of the detonation. In the intermediate regime the X-rays can escape, partially or totally, from the immediate vicinity of the detonation. In the high-altitude regime even the debris is no longer wholly contained by the tenuous ambient atmosphere and magnetic effects become important, or even predominant. The altitudes of demarcation for these regimes, however, are actually not well definable.

## Some Specific Examples of Acoustic Generation

Turbulence may be induced by shock waves, debris motion, and intense energy deposition in the form of X-rays. Also the deposition of large X-ray energy densities at the level of the mesopause from explosions in the high-altitude range may result in considerable heating and ensuing expansion which is likely to be accompanied by instabilities leading to turbulence. In extreme cases, a shock wave will be generated as front edge of the expansion. The pressure fluctuations of such turbulent flow fields may be identified as sources for acoustic noise. For a rough estimate it is sufficient to consider the mean values of the pressure fluctuations in the turbulent region. The pressure fluctuation,  $\delta p$ , is of the order  $\delta p \sim \rho (\delta u)^2$ , where  $\delta u$  is the scale of the velocity fluctuation. An energy flux of  $\sim 100 \text{ erg cm}^{-2} \text{ sec}^{-1}$  is required at around the 80 km level to give an observable surface amplitude of the pressure wave of about  $1 \text{ dyne cm}^{-2}$  (Maeda and Watanabe, 1964).

The energy investment into turbulent motion from both shock wave motion and bomb X-ray deposition in the 80 km level may be estimated by dimensional arguments, and upper limits of acoustic power generation may be established. Such estimates, for these two cases, are given in the following.

1. Turbulence Induced by X-Ray Heating. In the case of high-altitude explosions at levels above the X-ray deposition layer ( $h > 80 \text{ km}$ ) a large amount of the bomb energy is deposited as heat over an extensive region, the thickness of which is a few scale heights and the lateral extent of which depends primarily upon the burst altitude. For sufficiently strong heating the resulting expansion will almost immediately grow unstable and lead to turbulent motion. The latter constitutes a potential source of

acoustic radiation (namely, quadrupole emission from a turbulent medium). To be more precise, immediately after the deposition of the X-rays from a nuclear explosion, the velocity field in the deposition region will retain its original structure for a short time (order of a second), before the motion caused by the instantaneous heating becomes predominant. The rate and degree of the modification of the original flow field depend primarily on the intensity of the heating, provided that no other gross effects from the explosion interfere, such as debris motion. It appears that any of the possible situations from insignificant modification to complete change of the natural condition through violent expansion and shock formation may become of practical interest. One may estimate, by a simplified analysis, the threshold of heating of the deposition layer at which significant vertical upward expansion of the instantaneously heated air layer occurs. We find that excess temperatures of several hundred degrees are required to give strong upward expansion. The formation of shock waves and supersonic conditions will occur in these and more extreme cases. For an instantaneously produced peak pressure of 4 times the normal value at 80 km, for example, an estimate of the time interval of shock formation gives a value  $\Delta t \sim 5$  sec. The stability of such flows has not been investigated in detail but it may be assumed, on the basis of a simple argument involving the Reynolds number, that turbulence is likely to occur. We suppose fully developed turbulence to prevail in the perturbed upper-atmospheric regions as a result of the X-ray deposition and estimate the rate of acoustic energy emission.

First, we make a crude assessment of the energy dissipation rate,  $\epsilon$ , and of the internal scale,  $\lambda_0$ , of the turbulence which one might expect from an X-ray energy deposition comparable to that of Star Fish. We wish to stress that certain ad hoc assumptions are made which are not based on any experimental or other evidence, and that, therefore, only tentative results can be expected.

We take an energy deposition of about  $1 \text{ erg/cm}^3$  at the 80 km level. For an atmospheric density of about  $10^{-8} \text{ g/cm}^3$  (corresponding to this level) the energy absorbed per unit mass is  $10^8 \text{ erg g}^{-1}$ . We assume that the heating produced gives rise to turbulence. As the scale of turbulence we take the scale height, i. e.,  $\ell \sim H (= 5 \times 10^5 \text{ cm})$ . We further assume that all of the deposited energy appears as turbulent energy at the internal scale  $\lambda_0$  where it is dissipated by viscous effects, and finally assume that the turbulent energy is dissipated gradually (in a quasi-stationary manner) in a time period of the order of  $10^3$  sec. Then the average dissipation rate of turbulent energy is  $\epsilon \sim \frac{10^8}{10^3} = 10^5 \text{ erg g}^{-1} \text{ sec}^{-1}$ , which is about three orders of magnitude greater than the corresponding value for natural turbulence. We have neglected here the effect of turbulent mixing with the ambient cold air, and assume the energy dissipation to occur at altitude levels which are not significantly different from the deposition levels (local dissipation). We have overestimated the value of  $\epsilon$ , but are primarily interested in an upper limit for  $\epsilon$ . Using the value of  $\nu \approx 10^4 \text{ cm}^2 \text{ sec}^{-1}$  for the kinematic viscosity, we obtain for the scale of turbulence  $\lambda_0 \sim (\nu^3/\epsilon)^{1/4} = 10^{7/4} \sim 10^2 \text{ cm} (= 1 \text{ m})$ . It is seen that  $\lambda_0$  is not very sensitive to variations of  $\epsilon$ . Therefore, even though the estimate for  $\epsilon$  may be very inaccurate, the above result for  $\lambda_0$  probably indicates the correct order of magnitude of the internal scale, i.e., the size of the smallest eddies for the turbulent state. The effective Reynolds number may be estimated as  $\text{Re} \sim \left\{ \frac{\ell}{\lambda_0} \right\}^{4/3} \sim 10^5$ . Isotropy probably may be assumed for scales  $\lambda \ll \ell$ . One would expect then that Kolmogoroff's law is obeyed over an appreciable range of the spectrum.

The emission of acoustic power from such a turbulent atmospheric layer may be found from Lighthill's theory of aerodynamic generation of sound which has been extended by others with inclusion of gravity. In the linearized form one obtains the wave equation for acoustic and internal gravity waves, with the separated non-linear terms of the flow representing the sources which, through their fluctuating components, act as force functions of oscillatory motion upon the stratified atmosphere. In particular, we employ the result of R. F. Stein (Stein, 1967) for acoustic emission by turbulence in a stratified atmosphere, according to which the acoustic energy production rate is



$$W_{ac} = 10^3 \rho_0 \epsilon M_t^5 \text{ erg cm}^{-3} \text{ sec}^{-1} \quad (1)$$

where  $\rho_0$  is the ambient density and  $M_t$  is the Mach number of the turbulence. From this expression, one has, with  $\rho_0 \sim 10^{-8} \text{ g/cm}^3$  and the above value for  $\epsilon$ ,

$$W_{ac} = M_t^5 \text{ erg cm}^{-3} \text{ sec}^{-1}$$

The Mach number of the turbulence is defined as  $M_t = \frac{\delta u}{c_s}$  where  $\delta u$  is the scale of the scale of the velocity variation, and  $c_s$  is the ambient sound speed.  $\delta u$  is estimated from  $\delta u \sim (\ell \epsilon)^{1/3}$ , and one finds a value about an order of magnitude smaller than that of the sound speed. Hence,  $M_t \sim 0.1$ . Thus, we finally obtain for the upper limit  $W_{ac} \sim 10^{-5} \text{ erg cm}^{-3} \text{ sec}^{-1}$ . This is a very small acoustic energy.

The corresponding scale of pressure fluctuation in the flow for the example of Star Fish is  $\delta p \sim \rho (\delta u)^2 \sim 10 \text{ dyne cm}^{-2}$ . For a case of higher X-ray energy deposition, the acoustic output might well be of practical interest. For the emission in the frequency range of internal gravity waves in the upward direction, Stein (Stein, 1967) derives a relation for the flux which may be expressed in terms of  $W_{ac}$  as

$$\phi_{ig} = 10^{-1} \left( \frac{\ell}{M_t H} \right)^5 W_{ac} \text{ erg cm}^{-3} \text{ sec}^{-1} \quad (2)$$

This expression is a sensitive function of  $\frac{\ell}{H}$ , and an order-of-magnitude estimate for this quantity is not sufficient in this case. A representative value of  $\frac{\ell}{H}$  is presumably somewhere in the range between 0.1 and 1. It is seen that in the presence of large eddies with  $\ell \approx H$  the emission of internal gravity waves is strongly favored in a stationary state. However, for more or less instantaneously generated turbulence, the larger eddies will not be present for long in comparison with the total decay time (dissipation at the internal scales) of the turbulence.

We have not considered yet the time dependence for bomb-induced turbulence in the atmosphere. Under conditions of strong convective motion, the generation of internal gravity waves inside the turbulent region is suppressed.

According to Lighthill's suggestion (Lighthill, 1967) it is, nevertheless, possible in the presence of convection for turbulence to generate internal gravity waves, namely at the interface between the convective region and an adjacent stratified stable region. The mechanism of the generation of internal gravity waves at the upper boundary of the convective layer is provided simply by the convective penetration (overshooting) of turbulent elements into the stable region. These elements lose energy which goes into generation of gravity waves. It is important, however, that the eddy frequencies are below the Väisälä-Brunt frequency. Lighthill (Lighthill, 1967) estimates that about 5% of the total turbulent energy might be extracted in this manner from the convective zone, and that this mechanism might be at least as efficient in the generation of internal gravity waves as the turbulent mechanism of acoustic energy emission in the bulk of the flow.

2. Shock-Induced Turbulence at Upper-Atmospheric Levels. Next we consider acoustic emission from shock-induced turbulence. For easier comparison with the results obtained for X-ray deposition, we consider the 100 km region.

The case for the generation of turbulence may be argued by considering the Reynolds number of the corresponding flow. We estimate the critical Mach number,  $M_{crit}$ , which might be expected to cause turbulence at this level.

As characteristic parameter we consider the Reynolds number  $Re = \frac{v \ell}{\nu}$ , where  $v$  is the shock-induced air speed (behind the shock front),  $\ell$  is taken to be equal to the

local scale height, and  $\nu$  is the kinematic viscosity ( $\nu \approx \frac{1}{3} \bar{v} \lambda_{\text{coll}}$ ;  $\bar{v}$  = mean molecular velocity,  $\lambda_{\text{coll}}$  = molecular mean-free path). With  $\bar{v} = 1.35 c_s$ , where  $c_s$  is the local sound speed, and the values (for 100 km),  $\lambda_{\text{coll}} = 16$  cm and  $l = 6 \times 10^5$  cm, we obtain  $R_e = \frac{3\nu l}{\bar{v} \lambda_{\text{coll}}} \approx 10^5 \frac{\bar{v}}{c_s}$ . This is approximately  $R_e \approx 10^5 M$  where  $M$  is the Mach number.

Thus, to order of magnitude, if  $10^5$  is the Reynolds number for turbulence, this occurs for Mach number about one. A more accurate analysis shows that, in the case of shock-induced motion in the upper atmosphere, shocks with Mach numbers slightly greater than unity are necessary to give rise to turbulence. But the acoustic power output must be practically nil for such weak shocks. By arguments similar to that of the preceding section, we now estimate the turbulent characteristics and the acoustic power output induced by strong shocks ( $M \geq 5$ ).

We have, in the strong-shock limit, for the flow speed induced behind the shock front

$$v \approx 0.8 M c_s$$

where  $c_s$  is the local sound speed (for the unshocked state). This corresponds to an input of kinetic energy of  $1/2 v^2 \sim 10^8 M^2$  ergs per unit mass. The density,  $\rho_2$ , of the shocked atmosphere is raised by a factor of about 6 over the original local value. Again we assume that this energy is fully invested into turbulence, and dissipated at the internal scale,  $\lambda_0$ , over a time period of  $10^3$  seconds. Then one finds for the dissipation rate  $\epsilon \sim \frac{10^8 M^2}{10^3} = 10^5 M^2 \text{ erg g}^{-1} \text{ sec}^{-1}$ .

According to Eq. (1) we have

$$W_{\text{ac}} = 10^3 \rho_2 \epsilon M_t^5 \text{ erg cm}^{-3} \text{ sec}^{-1}$$

Now,  $M_t \sim \frac{\delta u}{c_2}$ , where  $c_2$  is the sound speed of the shocked gas; and  $\delta u \sim (l \epsilon)^{1/3}$ . For the strong shock limit  $c_2 = \sqrt{\gamma \frac{p_2}{\rho_2}} \approx \frac{1}{2} M c_s$ . A value for  $\delta u$ , however, is not easily obtained in this case, because  $l$  is difficult to estimate. From a closer consideration of this question, it appears that  $\delta u \sim \alpha M$ , where  $\alpha \sim 10^3$ , may be an acceptable choice. This yields  $M_t \sim 10^{-1}$ .

Because of the uncertainty about the value of  $M_t$  and in view of the sensitivity of  $W_{\text{ac}}$  to the value of  $M_t$ , the estimate is necessarily extremely crude:

$$W_{\text{ac}} \sim 10^{-4} M^2 \text{ erg cm}^{-3} \text{ sec}^{-1}.$$

The pressure is  $\delta p \sim \rho (\delta u)^2 \sim 10^{-1} M^2 \text{ dyne cm}^{-2}$ . Hence, for  $M = 30$ ,  $\delta p \sim 100 \text{ dyne cm}^{-2}$ , at about 80 km altitude.

The estimate of the emission in the frequency range of internal gravity waves (on the basis of Eq. (2)) is completely analogous to the previous case.

3. Production of Gravity-Acoustic Waves by the Rising Fireball. The fireball will rise in altitude, and as it does so, will interact with the atmosphere so that a fluid motion will be imposed upon it. Gravity-acoustic waves may be excited especially if a fireball sets the atmosphere in motion in the vicinity of a sharp change in density or temperature. We do not attempt to make a precise estimate of this effect. Indeed, there are many problems associated with doing so. These include the fact that the fireball is a fluid in turbulent internal motion and is expanding and entraining ambient air as it rises. Also, when the fireball rises through the atmosphere, the fluid dynamic processes such as turbulence are non-linear and are not easily treated.

Finally, many different modes of gravity-acoustic waves can occur in the atmosphere. We shall not distinguish between them for the purposes of making this estimate.

It has been observed that the Teak (76 km, megaton range weapon) fireball (Glasstone, 1962) rose at a critical rate of about 2 km/sec. Thus it must have quickly risen through the region of temperature minimum at 80 km, at about the same velocity. This would very roughly impart a kinetic energy density to the air in that region of  $\frac{\rho v^2}{2}$  where  $\rho_0 = 10^{-8}$  gm/cm<sup>3</sup> (ambient density). Then  $\frac{\rho v^2}{2} \sim 200$  ergs/cm<sup>3</sup> and this would be the order of magnitude of the initial pressure pulse in the 80 km region (i.e.,  $p \sim 200$  dynes/cm<sup>2</sup>). The estimate assumes that energy transfer between the various forms is quite efficient.

#### Note Added After Presentation of Paper

After the presentation of this paper at the Acoustic-Gravity Symposium at Boulder, R. Scorer made some criticisms which we wish to rebut. He claims that Lighthill's mechanism of sound generation by turbulence requires vorticity to be present and that in our discussion of sound generation of X-rays deposited in the 80 km region, we did not show that the required turbulence would occur. Scorer is correct in this, since we assumed that turbulence would be generated by instabilities resulting from the large input of X-ray energy into the 80 km region. Since the purpose of the paper is to make order of magnitude estimates for various acoustic-gravity wave generating effects which have hitherto not been treated, it seemed reasonable to us not to attempt to treat the transition from ambient atmosphere to turbulent flow in this paper. The magnitude of the resulting effect would then be used to determine whether or not it would be worth further investigating processes such as this transition. However, with Scorer's comment, we wish to discuss in more detail the possibility of X-ray and also shock induced turbulence.

First, we do not believe that the question of whether turbulence occurs from X-ray deposited energy in a high altitude nuclear detonation has very much to do with the corresponding question of the onset of turbulence in the normal atmosphere. There has been a great deal of discussion on the latter point, centered around the Richardson number, whether it is a good criterion and under what conditions (Calder, 1949). However, we are considering situations in which the pressure and temperature due to the initial X-ray energy deposition are large perturbations compared to the ambient values. Under these conditions, consideration of the appearance of turbulence from criteria applicable in the case of normal atmospheric conditions does not seem proper.

It is not possible for us to prove that turbulence will occur after the deposition of X-ray energy. However, it can be shown that instabilities will occur. These should generate vorticity and lead to turbulence. As has been noted by Prandtl, "the unstable oscillations calculated by Tolmien which are of a very long-drawn-out form, still do not represent turbulence, which is a motion with a much shorter wavelength. In practice, however, it is found that the actual turbulence regularly sets in at a point only a short distance from where instability is predicted by calculation." (Prandtl, 1962).

The question as to which number should be large (or small) for turbulence to occur, whether it be the Reynolds number, the Rayleigh number, the Richardson number, etc. does not, therefore, appear to be appropriate to consider. Instead we shall consider the question of whether an instability will occur.

The X-ray energy deposited in the layer varies with the size of the detonation and its proximity to the layer. The energy deposition for Star Fish is of the order 1 erg/cm<sup>3</sup> corresponding at 80 km to 10<sup>8</sup> erg/gram. This is not sufficient to give strong heating in the 80 km region, since the ambient energy density is about a factor of 10 larger. If we assume that the energy deposition is about 100 times larger than for Star Fish, so that temperatures in the order of 1000°K will be produced by the



X-ray deposition, then the resulting motion will be an expansion of this high temperature, high pressure layer in all directions, but since the layer is long and narrow, principally in the upward and downward directions initially.

Thus we have a hot gas accelerating into a lighter fluid in the upward direction and into a denser fluid in the downward direction. The instability of an interface between a lighter and heavier fluid accelerated in the direction of the heavier fluid is the well-known Rayleigh-Taylor instability. The maximum growth rate of this instability  $\gamma_{\max}$  based upon viscosity is (Miles and Dienes, 1966)

$$\gamma_{\max} = \frac{1}{2} \left( \frac{a^2}{2\nu} \right)^{1/3}$$

where  $a$  is the acceleration of the interface and  $\nu$  is the kinematic viscosity. Now the acceleration of the strongly heated layer may be estimated from

$$a \sim \frac{\nabla p}{\rho} \sim \frac{p - p_0}{\rho h} \sim p / \rho_0 H_s$$

where  $p$  is the pressure in the layer,  $\rho$  is the density in the layer,  $h$  is the distance over which the pressure changes appreciably, and we have assumed  $p \gg p_0$ ,  $\rho \approx \rho_0$  and  $h \sim H_s$  (scale height). Then with pressure of the order of 100 times larger than ambient as previously assumed, we have  $a = 10^5$  cm/sec<sup>2</sup>. The kinematic viscosity  $\nu \sim 10^4 \frac{\text{cm}^2}{\text{sec}}$  so that

$$\gamma_{\max} \approx \frac{1}{2} \left( \frac{10^{10}}{2 \cdot 10^4} \right) \approx 40 \text{ sec}^{-1}$$

so that the fastest growing instabilities have periods of the order of .025 seconds. However, this has a wavelength of about 200 cm. Since this wavelength is small compared to the distance over which the ambient density changes (i.e., 5 km, a scale height) we cannot apply the simple model of Rayleigh-Taylor instability of two fluids of differing density and get a meaningful answer for the stratified atmosphere. In fact, we must ask what is the growth rate for instabilities whose wavelength is the order of a scale height. This is given as  $\gamma = \sqrt{ka}$  which, for our case, is approximately 1 second. Thus we conclude that instabilities will develop on times of the order of 1 second and lengths on the order of a scale height.

In addition, there are other mechanisms of instability which may become active. For instance, the Helmholtz instability is likely to play a role in the motion. Due to the fact that the distance of the horizontal expansion is much larger than that of the vertical downward motion after the motion has had time to develop, the situation of a horizontal motion of a lighter fluid over a heavier fluid is realized to some degree in a certain range about the X-ray deposition region. One would expect considerable vertical velocity gradients in the expansion flow. This could lead to instability and turbulence due to the effect of shear.

Moreover, shear forces will not only act in this transition layer, but will also be important in the bulk of the expansion flow. The leading edge of the expansion constitutes a shock front at which the Rankine-Hugoniot relations must be satisfied. This shock front expands into the stratified (i.e. non-homogeneous) ambient atmosphere and velocity gradients occur along directions parallel to the shock front in the flow behind it later. The Reynolds number of such flows, as a function of the Mach number, was estimated earlier in our considerations, for the simplified case of a plane shock wave, using the scale height as characteristic length. For sufficiently large Mach number, the velocity gradients perpendicular to the flow direction should be expected to render the flow unstable. We quote Goldstein, "...a motion which is isentropic and irrotational upstream of shock wave is, in general, neither isentropic nor

irrotational downstream, and is approximately so only if the shock wave is sufficiently weak." (Goldstein, 1960).

Our assumption that sufficiently strong shock waves will generate vorticity and induce turbulence seems reasonable in view of the various instabilities which may occur.

#### References

Calder, K. L., The criterion of turbulence in a fluid of variable density with particular reference to conditions in the atmosphere, Quart. J. Roy. Met. Soc. 75, 71 (1949).

Glasstone, S., The Effects of Nuclear Weapons, U. S. Government Printing Office, 1962.

Goldstein, S. Lectures on Fluid Mechanics, Interscience Publication, p. 170, 1960.

Lighthill, M. J., Predictions of the velocity field coming from acoustic noise and a generalized turbulence in a layer overlaying a convectively unstable atmospheric region, I. A. U. Symposium No. 28, p. 429 (1967), Academic Press, London (1967), edited by R. N. Thomas.

Maeda, K. and Watanabe, T., Pulsating aurorae and infrasonic waves in the polar atmosphere, J. Atmos. Sc. 21, 15 (1964).

Miles, J. W. and Dienes, J. K., Taylor Instability in a viscous liquid, Phys. Fluids 9, 2518 (1966).

Prandtl, L. Essentials of Fluid Dynamics (transl. of 1949 ed. of Führer durch die Stromungslehre) Hafner Publishing Co., p. 114, New York (1952).

Stein, R. E., Generation of acoustic and gravity waves by turbulence in an isothermal stratified atmosphere, Solar Phys. 2, 385 (1967).

THEORETICAL SOURCE MODELS FOR THE GENERATION  
OF ACOUSTIC-GRAVITY WAVES BY NUCLEAR EXPLOSIONS

Allan D. Pierce  
Department of Mechanical Engineering  
Massachusetts Institute of Technology  
Cambridge, Massachusetts 02139

A generally accepted source model (as regards hydrodynamic effects) for a nuclear explosion is that of an initially small high temperature sphere of total energy  $E$  and initially of ambient density. Since the early history of the blast wave involves highly nonlinear effects, this model cannot be incorporated directly into a linear theory for the interpretation of far field microbarograms. The usual practice is for one to assume a decoupling between nonlinear effects and the combined gravitational and atmospheric effects, by selecting a linear source model with reference to computations of blast waveforms in a homogeneous atmosphere without gravity. Possible methods for incorporating source models into a linear formulation are discussed. Mass and energy point source models are compared as to their far field predictions. The two types of sources are formally equivalent when the explosion is near the ground but differ markedly as regards excitation of incompressible guided modes for above ground explosions. The applicability of point source models is argued to be valid for the interpretation of acoustic arrivals. They may not be applicable in the interpretation of the gravity wave even when the characteristic number  $(E/p_0)^{1/3}g/c^2$  is small, as the computations neglecting gravity cannot be relied on to accurately predict the tail of the blast wave. A simple calculation indicates that as much energy as  $E/4$  may be associated with the rise of the bubble created by wave transport of mass from the center of detonation. Qualitative implications of this are explored by examination of the fully linear acoustic-gravity initial value problem. The results suggest that (insofar as the gravity wave is concerned) a linear model with a point impulsive energy source may suffice. If this is true, then the waveform amplitude should be proportional to  $E$  and the waveform shape should be independent of  $E$ .

Introduction

The best known sources of acoustic-gravity waves in the atmosphere from the standpoint of phenomenology are nuclear explosions [Donn and Shaw, 1967; Yamamoto, 1956, 1957; Carpenter et al., 1961; Donn and Ewing, 1962a, b; Wexler and Hass, 1962; Araskog and Wagner, 1962; Bhartendu and Currie, 1964; Dieminger and Kohl, 1962; Row, 1967; Kohl, 1964; Hines, 1967; Wickersham, 1966]. In contrast to the case for many naturally occurring wave disturbances, the source of the characteristic waveforms recorded following a nuclear test generally can be identified both as to its location and as to its gross physical properties. Because of this fact, the nuclear explosion generated waves admit a relatively high possibility of detailed theoretical interpretation.

The basic theoretical problem as regards the interpretation of nuclear explosion generated waves is as follows. Given the location, time of detonation, altitude, and energy yield of a nuclear explosion and given some knowledge of the atmosphere's properties, what is the nature of the acoustic disturbance at some remote point? (Of course, since the atmosphere's properties can never be specified in complete detail, a total agreement of theory with experiment can never be achieved. However, one may hope to quantitatively infer basic characteristic features of the waveforms which are relatively independent of small variations in atmospheric properties. Perhaps one could even give a probabilistic description of the disturbance, treating the entire problem as a stochastic process.)

In the consideration of the basic theoretical problem defined above, a subsidiary problem of a definitely nontrivial nature presents itself. This is that of adequately describing the source and yet retaining a mathematical model of sufficient simplicity that a detailed numerical prediction is within the scope of the present state of the art as regards analytical techniques and electronic computer capabilities.

The present status of acoustic-gravity wave theory is almost entirely confined to linear mathematical models. The restriction to a linear model appears almost mandatory as the simplest order of magnitude estimates of machine running times easily convince one that suitable numerical integration

stepwise in time of nonlinear partial differential equations would require execution times of the order of 10 years or greater [Forsythe and Wasow, 1960] on a large size digital computer to deduce waveforms at distances of several thousand kilometers. The linear equations, on the other hand, are amenable to Fourier transform techniques and asymptotic methods. One can therefore in principle proceed to compute far field waveforms at a given point without a detailed knowledge of the time history of the wave.

The chief obstacle to the adoption of a linear model is the rather obvious fact that nuclear explosions are certainly not governed by linear equations - particularly at close-in distances. The only method apparent for overcoming this obstacle is to define an effective source for use with the linear model. The criterion for selection of this effective source is that the resulting solution agree with those results in principle attainable from the corresponding completely nonlinear model appropriate to the problem.

To discuss this effective source problem, it is pertinent to first briefly review the linear equations of hydrodynamics which form the basis of acoustic gravity theory [Eckart, 1960; Tolstoy, 1963; Hines, 1965]. We denote ambient density, pressure, wind velocity, and sound speed by  $\rho_0$ ,  $p_0$ ,  $\vec{u}$  and  $c$ , respectively. It is assumed that these quantities depend only on the vertical coordinate  $z$  and that, moreover, the winds are horizontal. The hydrostatic equation  $dp_0/dz = -g\rho_0$  where  $g$  is the acceleration of gravity then relates the vertical variations of ambient pressure and density. The sound speed may be considered as defined by  $c^2 = \gamma p_0 / \rho_0$  where  $\gamma = 1.4$  is the specific heat ratio. The resulting equations for acoustic pressure  $p$ , acoustic density  $\rho$ , and acoustic fluid velocity  $\vec{u}$  are then [Weston and VanHulsteyn, 1962]

$$\rho_0 [D_t \vec{u} + (\vec{u} \cdot \nabla) \vec{u}] = -\nabla p - g\rho \vec{e}_z \quad (1a)$$

$$D_t \rho + \nabla \cdot (\rho_0 \vec{u}) = 0 \quad (1b)$$

$$(D_t p + \vec{u} \cdot \nabla p_0) = c^2 (D_t \rho + \vec{u} \cdot \nabla \rho_0) \quad (1c)$$

where  $D_t = (\partial/\partial t) + \vec{u} \cdot \nabla$  represents the time derivative following the ambient wind.

Equations (1) may be considered as equivalent to five scalar coupled partial differential equations for  $p$ ,  $\rho$ , and the three components of  $\vec{u}$ . In the absence of a source, their solution is presumed to be zero for all acoustic quantities. For simplicity, the ground at  $z = 0$  is presumed to be flat and rigid - such that  $u_z = 0$  at  $z = 0$ .

There are three basic methods of incorporating the presence of a source into the mathematical formulation:

1. The Initial Value Problem. In this type of formulation,  $p$ ,  $\rho$ , and  $\vec{u}$  are specified everywhere at some time  $t_0$ . Equation (1) is then understood to govern the variation of the disturbance for all later times.
2. The Boundary Value Problem. At every point on some hypothetical surface completely enclosing the true source, the complete time history of a sufficient number of acoustic variables is specified. Providing the problem is not overspecified, the problem can then be formally solved by Green's function techniques. Just what should be specified on the surface is a somewhat involved problem. The author's tentative conclusion, based on the case of a vertical cylindrical surface, is that only the surface pressure or normal component of fluid velocity need be specified (just as in ordinary acoustics). The Green's function dyadic (a 5-by-5 matrix for 5 coupled scalar equations) [see Morse and Feshbach, 1954] would have to satisfy somewhat complicated (although still homogeneous) boundary conditions on the surface. If two variables are independently specified and the Green's dyadic is chosen with the correspondingly admissible arbitrariness, one has no guarantee that the resulting formal solution will reduce to the prespecified values when the observer is on the surface.



3. The Source Term Formulation. Additional terms varying with both position and time are added to the right hand side of one or more of Eqs. (1). The resulting set of inhomogeneous equations can then be considered as governing the disturbance at every point and for all times.

In addition to the above basic formulations, one could also take combinations of the three (e.g., source terms outside a bounding surface, source terms plus specified initial values, etc.). Each formulation can be formally tackled by standard techniques appropriate to linear partial differential equations.

#### Point Source Formulations

The simplest method of incorporating a source into the model is the point source method. This method is either explicitly or implicitly used in the numerical computations of waveforms carried out by Hunt, Palmer, and Penney [1960], by Weston [1961, 1962] and by Harkrider [1964]. Examination of each of these three cited papers reveals that each source formulation was mathematically equivalent to adding a point mass source to the right hand side of Eq. (1b) such that the resulting conservation of mass equation took the form

$$D_t \rho + \nabla \cdot (\rho_0 \vec{u}) = 4\pi f_M(t) \delta(\vec{r} - \vec{r}_0) \quad (2)$$

Here the mass added per unit time at the source location is denoted by  $4\pi f_M(t)$ . The assumed form of  $f_M(t)$  was different in each of the three cited papers.

It should be noted that, even if one restricts his formulation to point source models and even if one allows considerable latitude in the selection of  $f_M(t)$ , that there is no a priori reason that Eq. (2) should represent the ideal formulation for the nuclear explosion problem. For example, instead of adopting a mass source model, one could adopt an energy source model instead, taking Eq. (1c) in the form

$$[D_t p + \vec{u} \cdot \nabla p_0] - c^2 [D_t \rho + \vec{u} \cdot \nabla \rho_0] = 4\pi c^2 f_E(t) \delta(\vec{r} - \vec{r}_0) \quad (3)$$

Here  $4\pi c^2 f_E(t)/(\gamma - 1)$  may be considered as representing the energy added per unit time to the atmosphere.

Before discussing the merits of the models represented by Eqs. (2) and (3), one may appropriately question whether or not there is a significant physical distinction between the predictions of the two formulations as regards far field wave disturbances. It turns out that, if gravity is neglected and  $f_E(t)$  is set equal to  $f_M(t)$ , the two models give identical predictions. Thus, any such distinction will be entirely a gravitational effect. To explore the nature of the distinction, we may formally solve the linear equations with the two types of sources, denoting the resulting solutions for acoustic pressure by  $p_M$  and  $p_E$ , respectively. Doing this, we find [using a method of derivation similar to that of Pierce, 1965]

$$p_{M,E} = \int_{-\infty}^{\infty} dk_x \int_{-\infty}^{\infty} dk_y e^{i\vec{k} \cdot (\vec{r} - \vec{r}_0)} \int_{-\infty + i\epsilon}^{\infty + i\epsilon} g_{M,E}(\omega) \psi_{M,E}(z) e^{-i\omega t} d\omega \quad (4)$$

where

$$f_{M,E}(t) = \int_{-\infty + i\epsilon}^{\infty + i\epsilon} g_{M,E}(\omega) e^{-i\omega t} d\omega \quad (5)$$

The functions  $\psi_M(z)$  and  $\psi_E(z)$  should be considered as also dependent on  $\omega$ ,  $k_x$ , and  $k_y$  and on the source height  $z_0$ . Their resulting forms are given by

$$\psi_{M,E} = [\rho_0(z_0)/\rho_0(z)]^{1/2} [i/(\pi\Omega)] Q_{M,E} / [Z_\ell(z_0) Y_u(z_0)] \quad (6)$$

where

$$Q_m = Z_u(z_0) Z_\ell(z) \quad z_0 > z \quad (7a)$$

$$= Z_u(z) Z_\ell(z_0) \quad z_0 < z \quad (7b)$$

$$Q_E = [Z_u(z_0) - g Y_u(z_0)] Z_\ell(z) \quad z_0 > z \quad (8a)$$

$$= [Z_\ell(z_0) - g Y_\ell(z_0)] Z_u(z) \quad z_0 < z \quad (8b)$$

Here the subscripts  $\ell$  and  $u$  refer to functions which satisfy the upper and lower boundary conditions, respectively. Each set,  $(Y_u, Z_u)$  and  $(Y_\ell, Z_\ell)$ , may be expressed in terms of the functions  $\phi_1$  and  $\phi_2$  which satisfy the equations [Piercé, 1966, 1967a, b]

$$\frac{d}{dz} \begin{bmatrix} \phi_1 \\ \phi_2 \end{bmatrix} = \begin{bmatrix} B_{11} & B_{12} \\ B_{21} & B_{22} \end{bmatrix} \begin{bmatrix} \phi_1 \\ \phi_2 \end{bmatrix} \quad (9)$$

by the relations

$$Z = (g/c)\phi_1 - c\phi_2 \quad (10a)$$

$$Y = (1/c)\phi_1 \quad (10b)$$

The coefficients  $B_{ij}$  in the residual equations are as given previously by the author

$$B_{11} = g(k^2/\Omega^2) - \gamma g/(2c^2) \quad (11a)$$

$$B_{12} = 1 - c^2 k^2 / \Omega^2 \quad (11b)$$

$$B_{21} = g^2 k^2 / (\Omega^2 c^2) - \Omega^2 / c^2 \quad (11c)$$

$$B_{22} = -B_{11} \quad (11d)$$

with  $k^2 = k_x^2 + k_y^2$  and  $\Omega = \omega - \vec{k} \cdot \vec{v}$ . The upper boundary condition on  $\phi_{1u}$  and  $\phi_{2u}$  is that both functions [Pierce, 1963] vanish for all  $\text{Im}(\omega) > 0$  as  $z \rightarrow \infty$ . The lower boundary condition on  $\phi_{1l}$  and  $\phi_{2l}$  is that  $\phi_{1l} = 0$  at  $z = 0$ .

The chief distinction between the two formal solutions is evident from the forms of Eqs. (2.6) and (2.7); extra terms represented by  $-gY_u(z_0)Z_u(z)$  or  $-gY_l(z_0)Z_l(z)$  are present in the energy source solution. The distinction vanishes only if the integrals over these terms should vanish. [The reader may wonder if the solution represented by Eqs. (4), (6), and (8) for the energy source formulation is continuous at  $z = z_0$ . It turns out that the total integral is continuous except at  $\vec{r} = \vec{r}_0$  even though (8) is not continuous at  $z = z_0$ .]

The distinction between the two solutions becomes more apparent when the guided mode approximation [Pierce, 1965] is employed to perform the  $k_x$  and  $k_y$  integrations in Eq. (4). Since the contributions in this approximation come from poles in the complex  $k$  plane where  $Y_u(0) = 0$ , the upper and lower boundary conditions are satisfied for the residues. The  $n$ -th residue for the two solutions will contain, respectively, the factors

$$Z_n(z_0) Z_n(z)$$

and

$$[Z_n(z_0) - gY_n(z_0)] Z_n(z)$$

where  $(Z_n, Y_n)$  denote an eigenfunction pair. Thus, the distinction between types of sources shows up as differences in excitation for the various modes. If the source is on the ground, then  $Y_n(z_0)$  must be zero and there will be no distinction. However, if the source is above the ground and at a point where  $Z_n(z_0)$  has a node while  $Y_n(z_0)$  does not, there will be a sizable distinction. One should note that, for an isothermal atmosphere [Pierce, 1965], the only mode has  $Y_n(z)$  identically zero. Thus there will be no distinction (at least in the guided wave approximation) for an isothermal atmosphere. One may note that  $Z_n(z)$  represents the height profile of  $p/\rho^{1/2}$  while  $Z_n(z_0) - gY_n(z_0)$  represents the height profile of  $\rho^{1/2} \nabla \cdot \vec{u} / \Omega$ . Since  $\nabla \cdot \vec{u} = 0$  for incompressible fluid motions, it follows that an energy source is a poor exciter of any modes for which the atmosphere behaves primarily as an incompressible medium.

To quantitatively assess the magnitude of the distinction for moderate altitude bursts in nonisothermal atmospheres would require an extensive numerical study - which is beyond the scope of the present paper. Of the two point source models, the author's preference is the point energy source for reasons discussed in the remainder of the article.

#### Nonlinear Models

It is appropriate at this point to review those nonlinear models generally considered as valid representations of nuclear explosions. To avoid complications of radiative transfer, radioactive decay, etc., we limit our discussions here to the generally accepted hydrodynamic model of an initially isothermal sphere. The sphere at the given initial time is assumed to have ambient density and fluid velocity, but also is assumed to have very high temperature and pressure. An



additional simplification is for one to consider the specific heat ratio as constant. Although this is not strictly true at the high temperatures inside a nuclear fireball, it seems a minor approximation compared to those which must inevitably be made in deriving a suitable source for the linear theory.

A distinction must be made between ground bursts and air bursts (where the fireball does not touch the ground). Since the isothermal sphere model strictly applies only to airbursts, ground bursts will be excluded from consideration here. (The extension of the discussion as regards far field acoustic effects to ground bursts is probably not difficult. However, due to the extreme complexity of the problem, it is advisable to first examine it in its least complex form, i.e., for air bursts.) The adoption of an isothermal sphere probably also excludes high altitude bursts (above 100,000 ft.) from the discussion. The reason for this is simply that the appropriate dimensions of the initial disturbance for moderate yields become comparable to a scale height above 100,000 ft. for energy yields of interest.

An upper limit for the radius of the initial isothermal sphere may be estimated as the fireball radius just before shock breakaway. A more precise estimate is complicated by the fact that it is difficult to assign a value to that time when hydrodynamic effects become dominant. What is normally defined as shock breakaway time is too large an estimate as it depends on the opacity of the air in the shock. A more likely estimate of the radius of the initial sphere is that which is the radius of the fireball at hydrodynamic separation. The hydrodynamic separation radius is defined as that fireball radius when shock front and radiation front coincide. Unfortunately, it is evidently a difficult quantity to measure. The Effects of Nuclear Weapons (henceforth referred to as ENW) [Glasstone, 1962], states that this hydrodynamic separation radius is roughly 40 feet for a 20 kiloton explosion near sea level. A more general relation is suggested by the statement that it occurs when the temperature of the isothermal sphere has fallen to about 300,000°C. Some general considerations of the distinction between radiative transfer and hydrodynamic shock propagation suggest that, as a rough approximation, this figure might be used regardless of the yield and height of burst. On this basis, the initial radius  $b$  could be estimated from the relation

$$E_{hy} = \rho_o \left( \frac{4}{3} \right) \pi b^3 c_v T \quad (12)$$

where  $E_{hy}$  represents the hydrodynamic energy of the explosion (roughly 0.5 of the total energy, according to ENW). This gives

$$b = .045 (E_{hy}/p_o)^{1/3} [c(z_o)/c(o)]^{2/3} \quad (13)$$

The ratio of the two sound speeds is for all intents close enough to 1 that  $b$  can be considered as roughly 5% of the length  $(E_{hy}/p_o)^{1/3}$ . The discrepancy between hydrodynamic and total energy is interpreted as the energy lost through thermal and nuclear radiation.

Given the value  $E_{hy}$ , the radius  $b$ , and the fact that the sphere is initially isothermal, the initially uniform excess pressure in the sphere is readily shown to be

$$p = \frac{(\gamma - 1) E_{hy}}{(4/3) \pi b^3} \quad (14)$$

Here use has been made of the well known expression for energy density in an ideal gas.

An additional simplification is to consider the parameter  $b$  as vanishingly small, but to take  $E_{hy}$  as fixed (point source approximation). The computed results for small  $b$  at moderate distances should be insensitive to small variations in  $b$ , providing  $b$  is sufficiently small. Thus the point source model should be a valid approximation to a small  $b$  model in many cases of interest. The first computations of blast waves generated by nuclear explosions were made by G. I. Taylor [1950]

who used the point source model.

A clearcut criterion for considering the point source model as a reasonable approximation to a given isothermal sphere model is that  $b$  be significantly less than the characteristic length  $\lambda_0 = (E_0/p_0)^{1/3}$ . The length  $\lambda_0$  is the only characteristic quantity with units of length associated with the mathematical formulation of a point source explosion in a uniform atmosphere with gravity neglected. Numerical computations [Brode, 1955] indicate that  $\lambda_0$  gives a fair order of magnitude estimate for almost any length associated with the blast wave. Brode's computations show, for example, that the blast positive phase length is  $0.35\lambda_0$  at moderate distances; the negative phase length is  $1.22\lambda_0$  for almost all distances; and the shock wave becomes virtually linear at distances of the order of  $0.3\lambda_0$ .

There seems little doubt that the point source requirement  $b \ll \lambda_0$  is adequately guaranteed by Eq. (13). This is amply substantiated by Brode's comparison of the point source solution with isothermal sphere cases where  $b = .036\lambda_0$  and  $b = .09\lambda_0$ . The agreement was excellent at larger distances. In view of such results the point source model seems amply justified insofar as the far field effects are concerned.

For an airburst in a real atmosphere there is at least one other characteristic length whose magnitude should be considered. This is the scale height  $H = c^2/(\gamma g)$  which is typically of the order of 8 km for altitudes below 100,000 ft. For many cases of interest,  $H$  is somewhat greater than  $\lambda_0$ . For 1 kiloton at sea level,  $\lambda_0$  is 350 meters; for 1 megaton, 3.50 km; for 25 megatons, 10 km. At 50,000 ft.,  $\lambda_0$  is only increased by a factor of 2.1 of its sea level values for the same yield, i.e.,  $\lambda_0$  is still only 7.3 km for a 1-megaton explosion. However, at 100,000 ft.,  $\lambda_0$  becomes magnified by a factor of 10. (It is 35 km. for a 1 megaton explosion). This suggests that the consideration of  $\lambda_0$  being less than or comparable to  $H$  specifically excludes megaton class explosions at high altitudes but almost certainly includes most imaginable explosions near the surface and probably most explosions below 50,000 feet.

The criterion for the neglect or non-neglect of gravity in the formulation of the near field nonlinear model is not completely clear. At very early times (shock pressures still above twice ambient) the shock radius does not extend beyond  $.5\lambda_0$ . During very early times, buoyancy forces appear to be negligible. The density behind the shock is never greater than  $(\gamma+1)/(\gamma-1) = 6$  times the ambient value. At later times the overdensity is just the shock overpressure multiplied by  $c^2$ . As the overpressure gets down towards ambient, the pressure gradients behind the shock are typically of the order of  $3 p_s / \lambda_0$  (estimated from Figure 4 in Brode's paper) where  $p_s$  is the shock overpressure. Thus the pressure gradients are sufficiently ample to dominate the buoyancy forces (at least in the vicinity of the shock front) if  $3 p_s / \lambda_0 > g$  or if

$$\frac{p_s}{p_0} > \frac{2\lambda_0}{H_s} \quad (15)$$

The above criterion is probably very conservative, but it does suggest that the calculations performed by Brode may be considered as being valid even for large explosions at sufficiently early times providing that the initial sphere radius  $b$  is substantially smaller than a scale height. The latter requirement would seem to be satisfied in almost all cases of interest if Eq. (13) is accepted for  $b$ . The only excluded cases would be megaton class explosions at high altitudes.

At later times than specified by Eq. (15), it is difficult to assess the effects of the neglect of gravity and atmospheric inhomogeneities. Although computations have been carried out by Whitaker et. al. [1966] using the particle-in-cell technique, the only examples presently available to the author are of lower yield nonnuclear explosions.

To a certain extent, the intermediate time gravity effects may be qualitatively deduced from Brode's [1955] computations. The positive phase portion of the blast wave will terminate at a pressure node which will spread out approximately in a circle with the speed of sound. The shock front, however, will be somewhat asymmetric due to the fact that the relative shock overpressure above the detonation will be higher. A necessary consequence of this is that the positive phase above the detonation will be longer than that below the detonation. Since the positive phase for most cases of interest is generally considerably shorter than 1/4 of Brunt's period [approximately 1/4 of 300 sec. or 75 sec.] it would seem that the ordinary laws of acoustics would probably govern the propagation of the positive phase to moderate horizontal distances of 100 km

or so with some correction for the accumulative nonlinear effect of positive phase length increasing with time. Locally, the propagation would be governed by the wave equation for  $p/p_0^{1/2}$  rather than  $p$ . A consequence of this would be that  $p/p_0$  should eventually increase with altitude above the explosion. A strong shock must eventually reform which vents into the vacuum at infinite height within a finite time [Hayes, 1968; Raizer, 1964; Kompaneets, 1960]. This latter phenomenon undoubtedly must have some substantial effects on ionospheric observations of acoustic-gravity disturbances but does not seem to have much relevance for ground based observations since the principal modes carrying energy close to the ground are not efficiently excited by ionosphere level disturbances [Pfeffer and Zarichny, 1963; Pierce, 1967b].

The portions of the early hydrodynamic disturbance which seem most likely to be significantly affected by gravity effects are the negative phase and the residual disturbance left by passage of the shock. In the latter respect, there is one extremely disturbing feature of Brode's computations. As the blast wave moves outward, it carries a finite amount of mass. Although the density is reduced in the negative phase, the net mass excess in the positive phase is somewhat greater than the mass defect in the negative phase. The result of this phenomenon in Brode's model is a hole of nearly zero density centered about the origin. A sketch of the resulting density profile at moderately late times is shown in Figure 1 (which is based on Brode's computation). It will be noted that the hole has a radius of the order of  $0.4 (E/p_0)^{1/3}$ , which is certainly a non-negligible quantity.

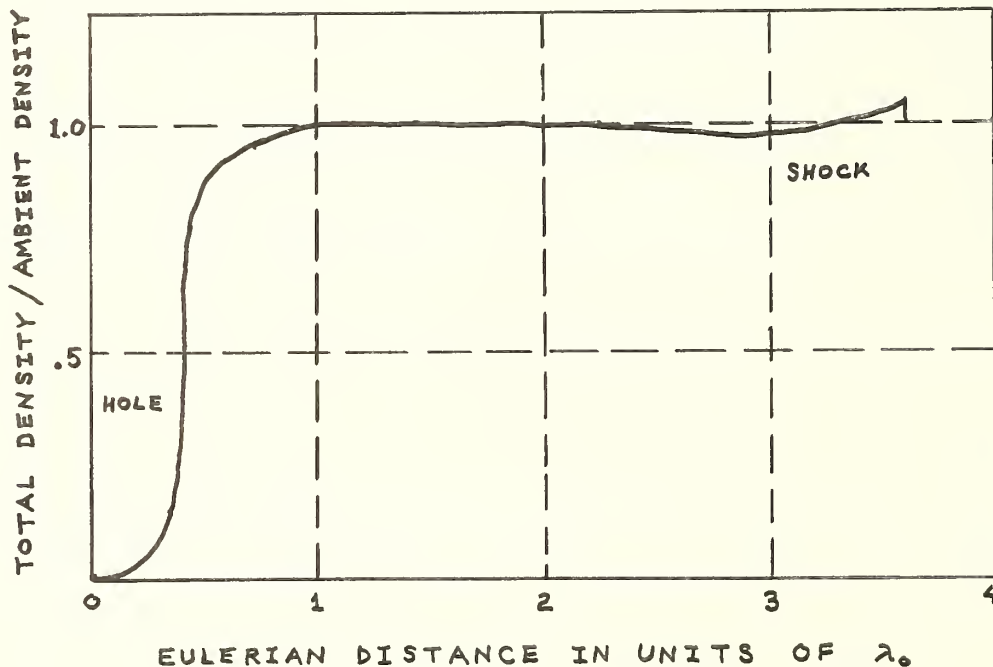


Figure 1. Plot of density ratio versus radial distance for a point explosion of energy  $E$  at time  $3\lambda_0/c$ . The plot is based on numerical computations of H. Brode [1955].



Since the hole is at substantially lower density than the surrounding air, it represents an extremely unstable situation when the effects of gravity are considered. On intuitive grounds one might expect the hole to rise just as a bubble of air in a liquid rises to the surface. However, it probably would be a vast oversimplification to consider the hole to rise as a unit. While the bubble rise may or may not be a significant source of acoustic-gravity waves, it cannot be discounted on the basis of energy considerations. One can consider the presence of the hole as representing a potential source of energy. The maximum amount of energy convertible into fluid motion through the process of buoyant rise may be estimated as the equivalent work necessary to create a hole of such a radius due to expansion against the ambient pressure  $p_0$ . This method of estimation gives the available energy as being equal to the product of  $p_0$  and the hole's volume  $(4/3)\pi(0.4)^3 E/p_0$ . Thus the energy turns out to be of the order of  $(1/4)E$ . By contrast, the energy in the positive phase at distances of the order of  $3\lambda_0$  may be estimated from Brode's computations and the relation

$$(4\pi/3)[p_s^2/(\rho_0 c^2)][L_{pp}]R_s^2$$

where  $p_s$  is the shock overpressure,  $L_{pp}$  is the length of the positive phase, and  $R_s$  is the shock radius. The factor of  $1/3$  comes from the fact that the pressure decreases nearly linearly behind the shock front. Taking numerical values from Fig. 4 in Brode's paper, one finds  $.045E$  as the energy in the positive phase. [Hunt, Palmer, and Penney (1960) give the value of  $.08E$  but do not indicate how this value was obtained.] These rather simple calculations strongly suggest that a significant portion of the energy available for atmospheric motion is not in the blast wave.

The question of whether or not the blast wave per se is the source of the observed far field radiation may be partly resolved insofar as the higher frequencies are concerned. Since the disturbance propagating to large distances are governed primarily by linear equations, only those aspects of the near field disturbance which have the prerequisite energy spectrum need be concerned. For frequencies well above Brunt's frequency (which is the order of 1 cycle in five minutes) the only realistic source is the blast wave. While the gravitational induced effects behind the blast may encompass a range of frequencies it is probable that this range would not include much beyond the natural resonance frequency. Thus, if one is interested in explaining the acoustic (higher frequency arrivals) it would seem appropriate to use either of the two point source models discussed in the previous section. The functions  $f_M(t)$  and  $f_E(t)$  could be selected such that the linear near field disturbance agrees with Brode's computations at intermediate distances.

Unfortunately, most of the published data gives microbarograph records which are predominantly comprised of lower frequencies. For the interpretation of such records, there is no clear cut evidence that the above described procedure is applicable.

#### Linear Initial Value Problems

To resolve the problem described in the previous section, one should properly examine the results of a number of numerical solutions of nonlinear initial value problems in gravitating atmospheres. In lieu of this, some insight may be gained from an examination of linear initial value problems. Although such problems cannot resolve the question of the significance of coupling between nonlinear effects and gravitational effects, they may give some suggestion as to whether or not the near field disturbance left by the passage of the blast wave is a significant source of far field radiation.

Since even the linear initial value problem for acoustic gravity waves is quite complicated, only the simplified problem of initial disturbances in an isothermal atmosphere with no winds is considered here. Furthermore, the presence of the ground is neglected.

A relatively simple initial value problem which gives some suggestive results is the hot sphere initial value problem where a sphere of some radius  $a$  is initially of ambient density, but of slightly higher than ambient pressure. The solution for the no-gravity case is well-known and evidently due to Poisson [Lamb, 1925]. The result is sketched in Fig. 2. The outgoing wave is of the form of an N wave with a "shock" overpressure  $(1/2)(a/r)P_0$  where  $P_0$  is the initial excess pressure in the sphere. The passage of the wave away from the initial sphere carries a finite amount of mass such that the density in the spherical region is depleted by an amount  $-- P_0/c^2$ . The amount of the depletion is easily derived from the requirement that the sphere be at ambient pressure at late times but have the same entropy density that it did at the initial time.

Figure 2 should be compared with Figure 1 which is based on Brode's nonlinear computation. The qualitative resemblance does indicate that some insight into the effects of gravity on the nonlinear blast problem might be attained by solution of the acoustic-gravity wave version of the acoustic problem depicted by Fig. 2.

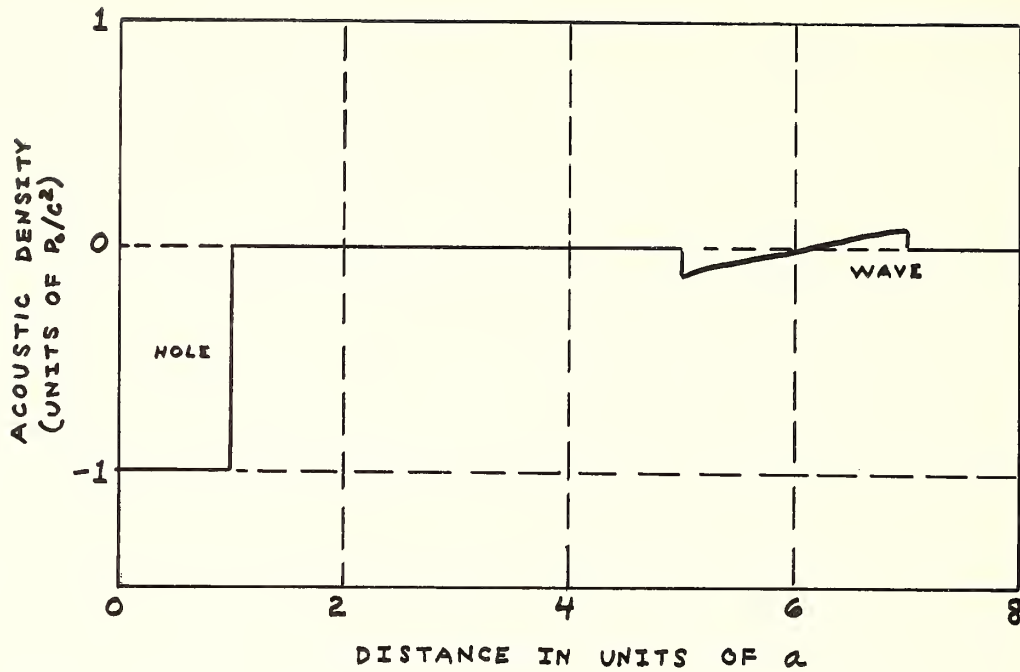


Figure 2. Plot of acoustic density versus radial distance for a time of  $6a/c$ , representing solution to acoustic hot sphere initial value problem. The sphere at time 0 had overdensity  $P_0$  and was of radius  $a$ .

To solve the initial value problem one proceeds from the fourth order partial differential equation [Pierce, 1963]

$$\{(D_t^2 + \omega_B^2)\nabla_2^2 + D_t^2[\partial^2/\partial z^2] - c^{-2}(D_t^2 + \omega_A^2)\}P = 0 \quad (16)$$

where  $D_t = (\partial/\partial t)$ ,  $P = p/\sqrt{\rho_0}$ , and the quantities  $\omega_B$ ,  $\omega_A$ , and  $c$  represent Brunt's frequency  $(\gamma-1)^{1/2}g/c$ , the acoustic cutoff frequency  $(\gamma/2)g/c$ , and the sound speed. The operator  $\nabla_2^2$  represents the horizontal part of the gradient operator.

The appropriate initial values for  $P$  and its time derivatives are, for  $t = 0$

$$P = F(\vec{r}) \quad (17a)$$

$$D_t P = 0 \quad (17b)$$

$$D_t^2 P = [c^2 \nabla^2 - g(\partial/\partial z) + (\gamma/2)(1 - [\gamma/2])g^2/c^2]F(\vec{r}) \quad (17c)$$

$$D_t^3 P = 0 \quad (17d)$$

where  $F(\vec{r})$  is the initial value of  $P$ . The last three conditions can be deduced from Eqs. (1) and the fact that  $\vec{u}$  and  $\rho$  are initially zero. For simplicity, we consider  $F(\vec{r}) = 0$  for  $r > 0$ ;  $F(\vec{r}) = P_0$  for  $r < 0$ . The delta function\* resulting in Eq. (17c) can be handled formally and lead to no singularities in the final solution.

The solution to the initial value problem presented by Eqs. (11) and (17) can be formally obtained by the Green's function technique. Although the analysis is a straightforward generalization of that used in ordinary acoustics [Morse and Feshbach, 1954], the derivation is somewhat lengthy. Thus, only the result is quoted here:

$$P(\vec{r}, t) = -(P_0/c^2) [D_t^2 - g(\partial/\partial z) + (\gamma/2)g^2/c^2] D_t \iiint G dV_0 \quad (18)$$

The Green's function  $G(\vec{r} - \vec{r}_0)$  is given by

$$G = \frac{1}{8\pi^2} \int_{-\infty}^{\infty} \frac{e^{-i\omega t} e^{i(v\zeta/\mu c)R}}{\mu\zeta R} d\omega \quad (19)$$

where  $R = |\vec{r} - \vec{r}_0|$ ,  $\mu = (\omega^2 - \omega_B^2)^{1/2}$ ,  $v = (\omega^2 - \omega_A^2)^{1/2}$ ,  $\zeta = (\omega^2 - \omega_c^2)^{1/2}$ ;  $\omega_c = [(z - z_0)/R]\omega_B$ . The integration in Eq. (18) extends over the volume of the sphere while the contour as well as phases and branchlines in Eq. (19) are chosen from causality considerations. Unfortunately (19) can be evaluated only in the case when  $|z - z_0| = R$ . However, some useful approximate results can be given [Row, 1966].

Our chief concern here will be comparing Eq. (18) with the result for the equivalent point source. For the point energy source, one has

$$P = -\{4\pi/[\rho_0(0)]^{1/2}\} D_t [D_t^2 - g(\partial/\partial z) + (\gamma/2)g^2/c^2] Q_E \quad (20)$$

while for the point mass source, one has

$$P = -\{4\pi/[\rho_0(0)]^{1/2}\} D_t [D_t^2 + \omega_B^2] Q_M \quad (21)$$

where

$$Q_{M,E} = \int_{-\infty}^{\infty} G(\vec{r}, t - t_0) f_{M,E}(t_0) dt_0 \quad (22)$$

The common operator factors in Eqs. (18) and (20) should be particularly noted. This suggests that we concentrate on comparing these two expressions.

Since we are at liberty to choose  $f_E$  in any manner we please, let us take  $f_E$  to be such that Eqs. (18) and (22) agree exactly in the limit of  $g = 0$ . Doing this gives

$$f_E(t) = 0 \quad |t| > a/c \quad (23a)$$

$$= (P_0/4) [\rho_0(0)]^{1/2} c[(a/c)^2 - t^2] \quad |t| < a/c \quad (23b)$$

To compare the two results, we first simplify the volume integral in Eq. (18). The variation of  $\omega_c$  over the sphere is negligible for moderate distances from the source. Thus one sets  $\omega_c = \omega_B z/r$  as what could appear to be a reasonable approximation. In this event, the angular integrations are trivially performed and one finds

$$\begin{aligned} \iiint G dV_o &= (\pi/r) \int_{r-a}^{r+a} G(R,t) R [a^2 - (R-r)^2] dR \\ &= [(4/3)\pi a^3] \{\Phi(La)\} G(r,t) \end{aligned} \quad (24)$$

where  $\{\Phi\}$  is the operator

$$\{\Phi(La)\} = 3[(La)^{-3} \sin(La) - (La)^{-2} \cos(La)] \quad (25)$$

with  $L = v\zeta/\mu c$ . [strictly speaking, Eq. (24) should be interpreted as a Fourier transform.] In a similar manner, one can write

$$\rho_E = P_o [\rho_o(0)]^{1/2} / 3 (a^3/c^2) \{\Phi(\omega a/c)\} G(r,t) \quad (26)$$

The resulting expressions (18) and (20) would then exactly agree if  $\{\Phi(La)\}G(r,t)$  were equal to  $\{\Phi(\omega a/c)\}G(r,t)$ . Although this is certainly not the case, there is a considerable realm of agreement. At high frequencies  $L \sim \omega/c$  and the two results agree. Near  $\omega = \omega_A$ , if  $\omega_A a/c$  is small, both  $\Phi(La)$  and  $\Phi(\omega a/c)$  are virtually equal to 1. The situation is analogous near  $\omega = \omega_c$  and holds down to  $\omega = 0$ . The only troublesome point is near  $\omega = \omega_B$ , where  $\Phi(La)$  has an essential singularity. However, the remaining factors in the integrand include a  $\exp[iLr]$  which also has an essential singularity and which may be expected to dominate for  $r \gg a$ . Thus the singular behavior of  $\Phi(La)$  may be expected to create no new difficulties in so far as the evaluation of the term  $\Phi(La)G$  is concerned. Furthermore, it is well-known that the group velocity [Pierce, 1963] vanishes at  $\omega_B$ . Thus one would not expect the narrow band discrepancy between  $\Phi(La)$  and  $\Phi(\omega a/c)$  centered about  $\omega_B$  to have much effect on far field waveforms.

In Fig. 3, a sketch of  $\Phi(La)$  and  $\Phi(\omega a/c)$  versus frequency for  $\omega_A a/c = .2$  and  $\omega_c = (1/2)\omega_B$  is given.



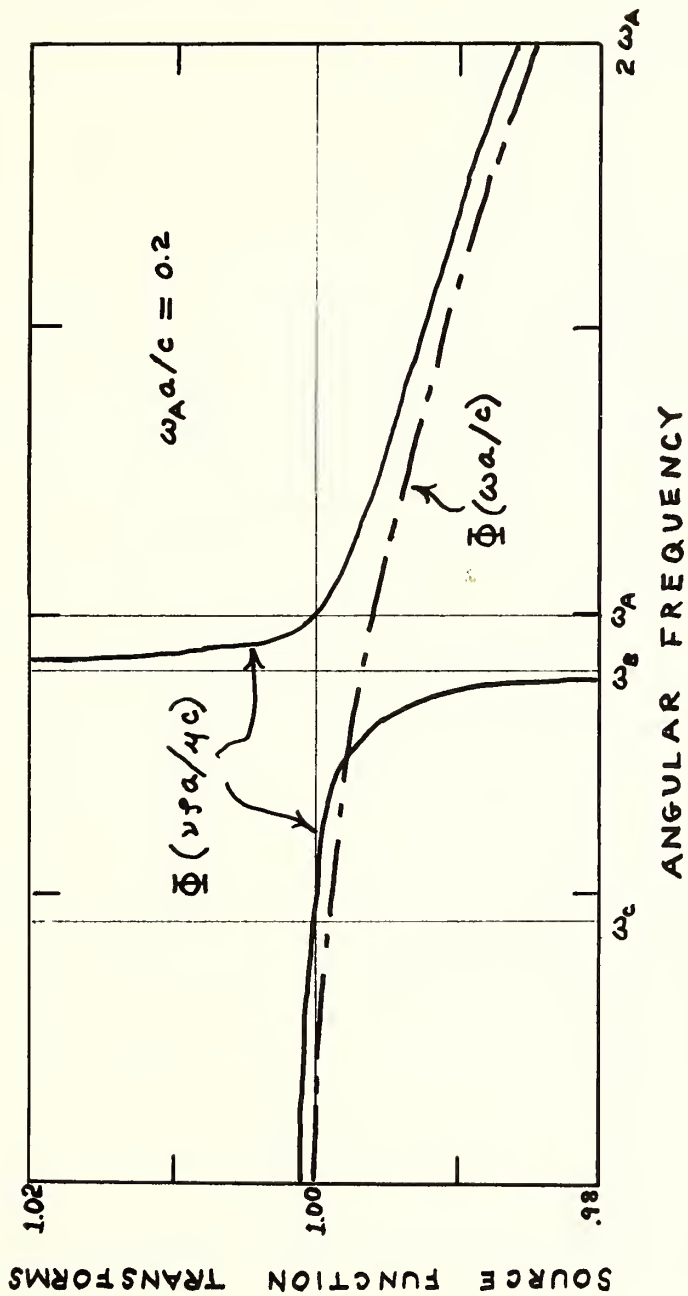


Fig. 3. Comparison of source functions  $\Phi(\omega a/c)$  and  $\Phi(La)$  for point energy source problem and hot sphere acoustic-gravity initial value problem. The two functions represent corresponding factors in the Fourier transforms of the far field disturbances.

### Concluding Remarks

While the question of an adequate source formulation still remains open, the example treated in the previous section does give some basis for the belief that a linear point energy source model with source time dependence selected from results of nonlinear calculation neglecting gravity may give a fair representation of far field energy waveforms. With reference to Brode's computations, one would take the function  $f_E(t)$  in Eq. (3) to be of the form

$$f_E(t) = (\lambda_o^2/c_s) p_{os} \int_{-\infty}^{\lambda_o^1 c_s t} F(X) dX \quad (27)$$

where  $F(X)$  represents the asymptotic form (distances of 3 to 6  $\lambda_o$ ) of the blast pressure waveform (with time in units of  $\lambda_o/c_s$ ) multiplied by observer distance in units of  $\lambda_o$ . The pressure would be in units of  $p_{os}$ . Thus  $F(X)$  would represent a universal function applicable to any yield and height of burst. The time origin can conveniently be chosen such that  $F(X)$  is zero for  $X < 0$ . A sketch of  $F(X)$  is given in Fig. 4 derived from Brode's computations. The results in the previous section suggest that the described model may be applicable as long as  $\omega \lambda_o/c_s$  is somewhat smaller than 1. For a 30 MT sea-level explosion, for example, this ratio is about 0.6. Thus the model could be applicable up to relatively high yields.

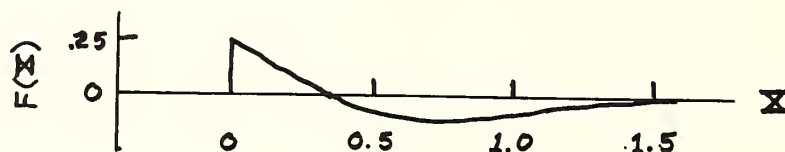


Fig. 4. Characteristic source function independent of yield and burst altitude, derived from computations of H. Brode (1955).

A striking aspect of the far field data, particularly as given by Donn and Shaw [1967], is that the dominant periods are significantly greater than what would be expected on the basis of the blast wave duration. The dominant period in the blast wave may be estimated as twice the negative phase length or about  $2.4 \lambda$ . Taking the U.S.S.R. shot of August 5, 1962 [with yield of 30 MT according to Glasstone, 1962] as an example, the estimated blast wave period would be about 80 sec. By contrast, the records exhibited by Donn and Shaw [1967] have periods predominantly in the 3 to 15 minute range. In the context of the energy point source model, a 80 sec. source duration would appear virtually instantaneous in so far as predicting this low frequency portion of the signal. Thus one could, for all intents and purposes, set

$$f_E(t) = \delta(t) \int_0^{\infty} f_E(t) dt \quad (28)$$

which is equivalent to an impulsive energy source. An interesting consequence of this is that the resulting waveform would be directly proportional to yield and have a shape independent of yield. This behavior of the low frequency waveform has also been predicted by different methods [Hunt, Palmer, and Penney, 1960; Pierce and Moo, 1967].

#### Acknowledgments

The research reported in this paper was sponsored by the U.S. Air Force Cambridge Research Laboratories, Office of Aerospace Research. The author would like to thank Mrs. E.F. Iliff for many helpful discussions on the problem.

#### References

- Araskog, R.U. and H. Wagner, Long range transmission of atmospheric disturbances, *Nature*, 193, 907-971, 1962.
- Bhartendu and B.W. Currie, Atmospheric waves from U.S.S.R. nuclear test explosions in 1962, *Can. J. Phys.*, 42, 632-637, 1964.
- Brode, H., Numerical solutions of spherical blast waves, *J. Appl. Phys.*, 26, 766-775, 1955.
- Carpenter, E.W., G. Harwood, and T. Whiteside, Microbarograph records from the Russian large nuclear explosions, *Nature*, 189 (4805), 847, 1961.
- Dieminger, W. and H. Kohl, Effects of nuclear explosions on the ionosphere, *Nature*, 193, 963-4, 1962.
- Donn, W.L. and M. Ewing, Atmospheric waves from nuclear explosions, *J. Geophys. Res.*, 67, 1855-1866, 1962a.
- Donn, W. L. and M. Ewing, Atmospheric waves from nuclear explosions, 2, The Soviet test of October 31, 1961, *J. Atmospheric Sci.*, 19, 264-273, 1962b.
- Donn, W. L. and D. M. Shaw, Exploring the atmosphere with nuclear explosions, *Rev. of Geophys.*, 5, 53-82, 1967.
- Eckart, C., *Hydrodynamics of Oceans and Atmospheres*, Pergamon Press, 1960.
- Forsythe, G. E. and W. R. Wasow, *Finite-Difference Methods for Partial Differential Equations*, Wiley, 1960.
- Glasstone, S., *The Effects of Nuclear Weapons*, U.S. Government Printing Office, 1962.
- Harkrider, D. G., Theoretical and observed acoustic-gravity waves from explosive sources in the atmosphere, *J. Geophys. Res.*, 69, 5295-5321, 1964.
- Hayes, W. D., The propagation upward of the shock wave from a strong explosion in the atmosphere, *J. Fluid Mech.*, 317-331, 1968.
- Hines, C. O., Atmospheric gravity waves; a new toy for the wave theorist, *Radio Sci.*, 690, 375-380, 1965.
- Hines, C. O., On the nature of traveling ionospheric disturbances launched by nuclear explosions, *J. Geophys. Res.*, 72, 1877-1882, 1967.
- Hunt, J. N., R. Palmer, and W. Penney, Atmospheric waves caused by large explosions, *Phil. Trans. Roy. Soc. London, A.*, 252, 275-315, 1960.
- Jones, R.V., Sub-acoustic waves from large explosions, *Nature*, 193, 229-232, 1962a.

- Jones, R. V. and S. T. Forbes, Sub-acoustic waves from recent nuclear explosions, *Nature*, 196, 1170-1171, 1962b.
- Kohl, H., Acoustic-gravity waves caused by the nuclear explosion on October 30th, 1961, in Electron Density Distribution in Ionosphere and Exosphere, edited by E. Thrane, pp. 160-169, North-Holland, 1964.
- Kompaneets, A. S., A point explosion in an inhomogeneous atmosphere, *Soviet Physics - Doklady*, 5, 46-48, 1960.
- Lamb, H., The Dynamical Theory of Sound, Edward Arnold, 1925 [reprinted by Dover, 1960].
- Morse, P.M. and H. Feshbach, Methods of Theoretical Physics, Vol. 1, McGraw-Hill, 1954.
- Pfeffer, R. L. and J. Zarichny, Acoustic gravity wave propagation in an atmosphere with two sound channels, *Geofis. Pura Appl.*, 55, 175-199, 1963.
- Pierce, A.D., Propagation of acoustic-gravity waves from a small source above the ground in an isothermal atmosphere, *J. Acoust. Soc. Amer.*, 35, 1798-1807, 1963.
- Pierce, A. D., Propagation of acoustic-gravity waves in a temperature and wind-stratified atmosphere, *J. Acoust. Soc. Amer.*, 37, 218-227, 1965.
- Pierce, A. D., Justification of the use of multiple isothermal layers as an approximation to the real atmosphere for acoustic-gravity wave propagation, *Radio Science*, 1, 265-267, 1966.
- Pierce, A. D., The multilayer approximation for infrasonic wave propagation in a temperature- and wind-stratified atmosphere, *J. Comp. Phys.*, 1, 343-366, 1967a.
- Pierce, A. D., Guided infrasonic modes in a temperature- and wind-stratified atmosphere, *J. Acoust. Soc. Amer.*, 41, 597-611, 1967b.
- Pierce, A. D. and C. A. Moo, Theoretical study of the propagation of infrasonic waves in the atmosphere, Final report on contract AF 19(628)-3891, Report No. AFCRL-67-0172, (Avco Space Systems Division, Wilmington, Mass., Feb., 1967).
- Raizer, Yu P., Motion produced in an inhomogeneous atmosphere by a plane shock of short duration, *Soviet Physics - Doklady*, 8, 1056-1058, 1963.
- Rose, G., J. Oksman, and E. Kataja, Round-the-world sound waves produced by the nuclear explosion on Oct. 30, 1961 and their effect on the ionosphere at Sodankyla, *Nature*, 192, 1173-1174, 1961.
- Row, R. V., Acoustic-gravity waves in the upper atmosphere due to a nuclear detonation and an earthquake, *J. Geophys. Res.*, 72, 1599-1610, 1967.
- Taylor, G. I., The formation of a blast wave by a very intense explosion, *Proc. Roy. Soc., A*, 201, 159-174, 1950.
- Tolstoy, I., The theory of waves in stratified fluids including the effects of gravity and rotation, *Rev. Mod. Phys.*, 35, 207-230, 1963.
- Weston, V. H., The pressure pulse produced by a large explosion in the atmosphere, *Canad. J. Phys.*, 39, 993-1009; 1961; Part II, 40, 431-445, 1962.
- Weston, V. H. and D. B. Van Hulsteyn, The effects of winds on the gravity wave, *Canad. J. Phys.*, 40, 797-804, 1962.
- Wexler, H. and W. A. Hass, Global atmospheric pressure effects of the October 30, 1961 explosion, *J. Geophys. Res.*, 67, 3875-3887, 1962.
- Whitaker, W. A., E. A. Nawrocki, C. E. Needham, and W. W. Troutman, Theoretical calculations of the phenomenology of HE detonations, AFWL-TR-66-141, Vol. 1, Air Force Weapons Laboratory, November, 1966.
- Wickersham, A.F., Jr., Identification of acoustic-gravity wave modes from ionospheric range time observations, *J. Geophys. Res.*, 71, 4551-4555, 1966.
- Yamamoto, R., The microbarographic oscillations produced by the explosions of hydrogen bombs in the Marshall Islands, *Bull. Am. Meteor. Soc.*, 37, 406-409, 1956.
- Yamamoto, R., A dynamical theory of the microbarographic oscillations produced by the explosions of hydrogen bombs, *J. Meteor. Soc. Japan*, 35, 32-40, 1957.



# ACOUSTIC-GRAVITY WAVES PRODUCED BY ENERGY RELEASE\*

J. D. COLE

California Institute of Technology  
Pasadena, California

and

The RAND Corporation  
Santa Monica, California

and

C. GREIFINGER

The RAND Corporation  
Santa Monica, California

A complete asymptotic analysis is carried out for the flow field produced by the instantaneous release of energy, at a point on the ground, in an isothermal atmosphere. A double integral representation of the flow is constructed from Laplace-Hankel transforms of the linearized equations. An asymptotic approximation to the integral is obtained by two successive applications of the method of stationary phase. It is found that there are three principal groups of dispersive waves behind the spherical acoustic front. One of these groups is contained in a high frequency band, and the other two in a low frequency band. The spatial domain of the low frequency waves is cut off by a front (caustic), the location of which is calculated. Some characteristics of the flow are discussed.

## I. INTRODUCTION

The problem of waves in a stratified atmosphere has received much attention and many different cases have been considered. The case which is analyzed here is one for which a complete asymptotic analysis can be carried out and an overall view of the resulting wave motion obtained. The principal simplification is that the waves are small disturbances to an isothermal atmosphere. The problem worked out in detail is the flow field produced by the instantaneous release of energy at a point in the ground plane (the analysis is easily extended to cases of energy release at a point above the ground). This case does not seem to have been discussed previously, although similar problems for monochromatic waves have been discussed (Pierce, 1963).

The basic method used for obtaining the asymptotic approximation is the repeated application of the method of stationary phase. The kinematic aspects of the groups of waves produced could have been based on the dispersion relation and the considerations of Whitham (1961) and Lighthill (1965). But, it turned out to be more convenient for this paper to base all the calculations on the Fourier integrals derived by Laplace-Hankel transforms of the linearized equations. In any case there are three principal groups of waves, one in a high frequency band and two in a low frequency band. The spatial domain of the low frequency waves is cut off by a front (caustic). This phenomenon was first noted by Mowbray and Rarity (1967) in their study of dispersive waves in an incompressible stratified fluid. A similar phenomenon appears in the pattern of waves around a moving ship.

In Section II the basic equations are given and the linearization is carried out in suitable dimensionless units. The basic small parameter is shown to be the ratio of the energy released to the internal energy in a volume of scale height dimensions. In addition, due to the exponential decay of density, there is an exponential growth of disturbances unfavorable for the validity of the theory. However, there should still be a considerable range in which the approximation is quantitatively correct as well as qualitatively instructive.

In Section III the application of Laplace transform in time and Hankel transform with respect to cylindrical radius enables an integral representation of the exact solution to be obtained. In Section IV it is shown how the acoustic spherical wave front is contained in the representation. Non-linear effects are probably most important in describing the amplification of the front into a shock wave and its subsequent propagation. However, the main residual disturbance is a system of dispersive waves behind the front. By studying the double integral representation, it is seen that a cylindrical ground wave exists in addition to propagating waves in low and high frequency bands. Section V studies these propagating dispersive groups and presents the final description of the flow as well as some numerical results.

---

\*This work was sponsored by the United States Air Force and the Advanced Research Projects Agency.

## II. THE BASIC EQUATION

We consider motion in an isothermal atmosphere above a ground plane produced by instantaneous energy release at a point on the ground, the origin in Fig. 1. The equilibrium atmosphere is thus characterized by the usual exponential distributions with scale height  $h$ ,

$$\frac{P_0(z)}{P^*} = e^{-\frac{z}{h}} = \frac{\rho_0(z)}{\rho^*} \quad (1)$$

$P^*, \rho^*, T^*$  = sea level ( $z = 0$ ) pressure, density, temperature,  $h$  = scale height =  $\frac{RT^*}{g}$ . Note that  $c^* = \sqrt{\gamma} c_g$  where  $c^*$  = isentropic sound speed =  $\sqrt{\gamma RT^*}$ ,  $c_g$  = gravity wave speed =  $\sqrt{gh}$ . The dimensionless equations of motion, continuity, momentum, entropy for a perfect gas are

$$\frac{\partial \rho}{\partial t} + \text{div } \rho \vec{q} = 0 \quad (2)$$

$$\frac{\partial \vec{q}}{\partial t} + \vec{q} \cdot \nabla \vec{q} = -\frac{1}{\gamma \rho} \nabla P - \frac{1}{\gamma} \vec{k} \quad (3)$$

$$\left( \frac{\partial}{\partial t} + \vec{q} \cdot \nabla \right) \frac{P}{\rho \gamma} = \frac{1}{\rho \gamma} \epsilon \delta(x) \delta(y) \delta(z) \delta(t). \quad (4)$$

Here lengths have been referred to the scale height  $h$ , velocities to  $c^*$ , times to  $h/c^*$ , pressure to  $P^*$ , and density to  $\rho^*$ . The basic parameter of the problem is

$$\epsilon = \frac{(\gamma-1)Q_0}{h^3 P^*} \quad (5)$$

where  $Q_0$  = energy released at  $t = 0$ ;  $\epsilon$  roughly measures the energy release compared to the internal energy stored in a scale height volume. The initial conditions at  $t = 0$  are

$$P = \rho = e^{-z}, \quad \vec{q} = 0, \quad (6a)$$

the boundary conditions at  $z = 0$  is

$$q_z = 0. \quad (6b)$$

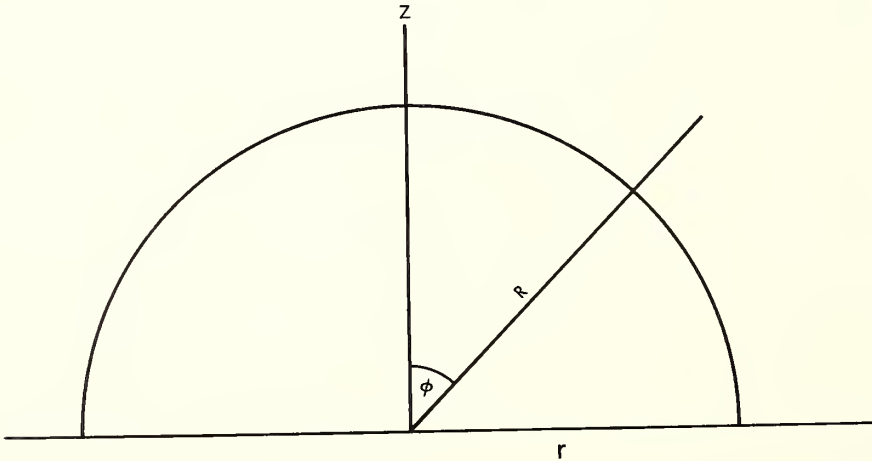


Fig. 1 - Co-ordinate system, with origin at the point of energy release.



## ACOUSTIC EXPANSION

The acoustic expansion is based on  $\epsilon \ll 1$  and represents the flow as small changes superimposed on the ambient state:

$$\vec{q} = \epsilon \vec{u} + \dots, \quad \vec{u} = (u, w) \quad (7)$$

where  $u$  = radial component  
 $w$  = vertical component

$$P = e^{-Z} \{1 + \epsilon p + \dots\} \quad (8)$$

$$\rho = e^{-Z} \{1 + \epsilon \sigma + \dots\} . \quad (9)$$

The equations of order  $\epsilon$  that result from (2), (3) and (4) are thus, for the case of axial symmetry,

$$\sigma_t + u_r + \frac{u}{r} + w_z - w = 0 \quad r = \sqrt{x^2 + y^2} \quad (10)$$

$$u_t = -\frac{1}{\gamma} p_r \quad (11)$$

$$w_t = -\frac{1}{\gamma} p_z + \frac{p-\sigma}{\gamma} \quad (12)$$

$$p_t - \gamma \sigma_t + (\gamma-1)w = \frac{1}{2\pi} \frac{\delta(r)}{r} \delta(z) \delta(t) . \quad (13)$$

The initial and boundary conditions for the perturbations are

$$p = \sigma = \vec{u} = 0 \quad \text{at } t = 0- \quad (14)$$

$$w = 0 \quad \text{at } z = 0, \quad t > 0 \quad (15)$$

and the main wave motion is assumed outgoing. The characteristic surfaces of the system ((10)-(13)) are given by

$$\phi_t^2 = 0, \quad \phi_t^2 - \phi_z^2 - \phi_r^2 = 0 \quad (16)$$

where  $\phi(r, z, t) = \text{const.}$  on a characteristic surface in  $(r, z, t)$  space. The first factor in (16) represents possible discontinuity surfaces along fixed cylinders  $r(z)$  in space while the second shows the possibility of a spherical acoustic front (the sound speed is constant everywhere in this model).

## III. FORMAL SOLUTIONS

A formal integral representation of the solution is constructed by a combination of Laplace and Hankel transformation. Let

$$\bar{g}(s) = \int_0^\infty e^{-st} g(t) dt \quad (\text{Laplace transform})^* \quad (17)$$

so that the system ((10)-(13)) has  $\frac{\partial}{\partial t} \rightarrow s$ , with the zero initial conditions.

$$s\bar{\sigma} + \bar{u}_r + \frac{\bar{u}}{r} + \bar{w}_z - \bar{w} = 0 \quad (18)$$

$$s\bar{u} + \frac{1}{\gamma} \bar{p}_r = 0 \quad (19)$$

---

\*We intend to use the usual inversion formula

$$g(t) = 1/2\pi i \int_{-i\infty}^{i\infty} e^{st} \bar{g}(s) ds.$$

$$\frac{1}{\gamma} \bar{\sigma} + s \bar{w} + \frac{1}{\gamma} (\bar{p}_z - \bar{p}) = 0 \quad (20)$$

$$-\gamma s \bar{\sigma} + (\gamma - 1) \bar{w} + s \bar{p} = \frac{1}{2\pi} \frac{\delta(r)}{r} \delta(z). \quad (21)$$

Using the Hankel transforms

$$f(r) = \int_0^\infty F(w) J_\nu(wr) w dw, \quad F(w) = \int_0^\infty f(r) J_\nu(wr) r dr \quad (\nu > -\frac{1}{2}) \quad (22)$$

note that

$$\frac{\delta(r)}{2\pi r} = \int_0^\infty \tilde{\delta}(w) J_0(wr) w dw, \quad \tilde{\delta}(w) = \int_0^\infty \frac{\delta(r)}{2\pi r} J_0(wr) r dr = \frac{1}{2\pi}. \quad (23)$$

Thus, let

$$(\bar{\sigma}, \bar{w}, \bar{p}) = \int_0^\infty (R, W, P) J_0(kr) k dk \quad (24)$$

$$\bar{u} = \int_0^\infty U(k) J_1(kr) k dk. \quad (25)$$

The choices in (24) and (25) are made consistent with the overall symmetry of the equations and insure that  $\lim_{r \rightarrow 0} ru_r \rightarrow 0$ , so that the behavior at the axis of symmetry is regular. Using the properties of  $J_0, J_1$ , etc. the basic system, ((18)-(21)), becomes

$$sR + kU + \frac{dW}{dz} - W = 0 \quad (26)$$

$$sU - \frac{k}{\gamma} P = 0 \quad (27)$$

$$\frac{1}{\gamma} R + sW + \frac{1}{\gamma} \left( \frac{dP}{dz} - P \right) = 0 \quad (28)$$

$$-\gamma sR + (\gamma - 1)W + sP = \frac{1}{2\pi} \delta(z). \quad (29)$$

This system is linear and second order with respect to  $z$ , so that there are two basic roots  $\lambda_1, \lambda_2$ , for solutions of the form  $(R, U, W, P) \sim e^{\lambda z}$ . The characteristic determinant from ((26)-(29)) is

$$\begin{vmatrix} s & k & \lambda - 1 & 0 \\ 0 & s & 0 & -k/\gamma \\ \frac{1}{\gamma} & 0 & s & \frac{1}{\gamma}(\lambda - 1) \\ -\gamma s & 0 & \gamma - 1 & s \end{vmatrix} = 0 \quad (30)$$

and the characteristic equation is

$$(\lambda - 1)^2 + (\lambda - 1) - \left\{ s^2 + k^2 \left( 1 + \frac{\gamma - 1}{2 + s} \right) \right\} = 0. \quad (31)$$

The basic roots are

$$\lambda_{1,2} = \frac{1}{2} \pm \sqrt{\frac{1}{4} + s^2 + k^2 \left( 1 + \frac{\gamma - 1}{2 + s} \right)}. \quad (32)$$

For definiteness the contour in the  $\mathbb{S}$  plane is at first chosen so that  $\operatorname{Re} \sqrt{\phantom{x}} \geq 0$  in (32).

In order to formulate "jump" conditions it is most convenient to eliminate  $(R, U)$  from the system ((26)-(29)) and obtain

$$\gamma \frac{dW}{dz} - W + \left(\frac{k^2}{s} + s\right)P = \frac{1}{2\pi} \delta(z) \quad (33)$$

$$\left\{ \gamma^2 s^2 + (\gamma-1) \right\} W + \gamma s \left( \frac{dP}{dz} - P \right) + sP = \frac{1}{2\pi} \delta(z). \quad (34)$$

Integration of (33) from  $(0- \text{ to } 0+)$  yields the jump condition

$$[W]_{z=0} = \frac{1}{2\pi\gamma}, \quad (35)$$

Since the solution should vanish ahead of the acoustic wave front ( $\sqrt{r^2 + z^2} > t$ ) only the root  $\lambda_2$  of (32) need be considered and we write

$$\lambda = \frac{1}{2} - \mu(s, k; \gamma) \text{ where } \mu = \sqrt{\frac{1}{4} + s^2 + k^2 \left(1 + \frac{\beta^2}{s^2}\right)}, \quad (36)$$

and

$$\beta^2 = \frac{\gamma-1}{\gamma}.$$

Note that  $0 < \beta^2 < \frac{1}{4}$ ; ( $\gamma = 1.4$ ,  $\beta^2 = .22$ ) for realistic values of  $\gamma$ . Since  $W = 0$ , for  $z = 0-$ , the jump condition (35) provides the boundary conditions for  $W$  as  $z \rightarrow 0+$  and the solution for  $W$  is

$$W(z; s, k) = \frac{1}{2\pi\gamma} e^{\frac{1}{2}z} e^{-\mu z}. \quad (37)$$

It follows from (33), for  $z > 0$ , that

$$P(z; s; k) = \frac{1}{2\pi} \frac{\frac{2-\gamma}{2\gamma} + \mu}{s^2 + k^2} s. \quad (38)$$

Applying the double inversion of Laplace and Hankel transforms, we obtain a formal representation of the perturbation pressure field

$$e^{-\frac{1}{2}z} p(r, z, t) = \frac{1}{2\pi} \int_0^\infty J_0(kr) F(k; z, t) k dk \quad (39)$$

where

$$F(k; z, t) = \frac{1}{2\pi i} \int_{-i\infty}^{i\infty} e^{st - \mu(s, k)z} \frac{\frac{2-\gamma}{2} + \mu}{s^2 + k^2} s ds. \quad (40)$$

The integration of (40) is regarded as carried out first, for a fixed real  $k$ . This integration over  $\mathbb{S}$  is carried out, at first, along a path parallel to the imaginary axis to the right of all singularities in the  $\mathbb{S}$  plane, so that the initial conditions are satisfied. The  $\mathbb{S}$  plane is cut suitably so that  $\operatorname{Re}(\mu) \geq 0$  on the contour.

The pressure field is the main quantity of interest but all the other quantities easily follow from the system ((26)-(29)).

#### IV. APPROXIMATE AND ASYMPTOTIC EVALUATIONS

In this note the main interest is centered on the dispersive waves behind the acoustic front. This is the main disturbance which contains eventually most of the energy put in at  $t = 0$ .

However, first, a crude approximation valid near the acoustic wave front comes from considering large  $(k, s)$  in (39), to obtain

$$p(r, z, t) \doteq e^{\frac{1}{2}zz} \frac{1}{4\pi i} \int_{-i\infty}^{i\infty} s e^{st} ds \int_0^\infty \frac{e^{-z\sqrt{s^2+k^2}}}{\sqrt{s^2+k^2}} J_0(kr) k dk. \quad (41)$$

The second integral is a special case of an integral evaluated in Watson's Bessel functions (Watson, 1922).

$$\int_0^\infty \frac{e^{-z\sqrt{s^2+k^2}}}{\sqrt{s^2+k^2}} J_0(kr) k dk = \frac{e^{-s\sqrt{r^2+z^2}}}{\sqrt{r^2+z^2}} \quad (42)$$

so that (41) is

$$p(r, z, t) \doteq e^{\frac{1}{2}zz} \frac{1}{2\pi R} \int_{-i\infty}^{i\infty} s e^{s(t-R)} ds \quad (43)$$

where  $R = \sqrt{r^2+z^2}$  = spherical radius. According to the usual interpretation the integral in (43) is the derivative of a delta function, or

$$p(r, z, t) \doteq e^{\frac{1}{2}zz} \frac{1}{2\pi R} \delta'(t-R) \quad (44)$$

$\delta'(t-R)$  is the acoustic version of the compression followed by an expansion that is felt near the wave front. The intensity is doubled, due to the ground plane, over that of a point source in free space. Further, the factor  $e^{\frac{1}{2}zz}$  represents the amplification of the waves proportional to  $\rho_0(z)^{-\frac{1}{2}}$ , according to the usual local energy considerations.

Asymptotic integration of (39), (40) which is valid in the main wave zone for large  $(r, t)$  can be carried out by repeated applications of the method of stationary phase coupled with the use of an asymptotic representation of  $J_0$ .

In order to give definite meaning to the integral the following plan is adopted. The  $s$  plane is suitably cut and the integral of (40) for  $F(k; z, t)$  is expressed as an integral along segments of the imaginary axis ( $s=i\omega$ ). That is, it is expressed as a Fourier integral over the frequencies  $\omega$  which, for a given  $k$ , can propagate. In doing this, the residues at certain poles (due to the presence of the ground), have to be evaluated. Next, in the real double integrals,  $(\omega, k)$ , the order of integration is changed, since the stationary phase approximation can more easily be carried out in the  $k$ -integral. However, this can only be done if the asymptotic approximation for  $J_0$  is used. After this is completed, the answer is expressed as a Fourier integral. This integral is again of such a form that the method of stationary phase can be used and its qualitative features are easily discussed. (See Section V.) In addition some quantitative results are also presented. Some details of the procedure just outlined are now given.

First note that the exponent in (40)

$$\mu(s, k) = \frac{1}{s} \left\{ s^4 + (\frac{1}{2} + k^2)s^2 + \beta^2 k^2 \right\}^{\frac{1}{2}} \quad (45)$$

can be written as

$$\mu = \frac{1}{s} \left\{ \xi^2 + \omega_1^2(k) \right\} (s^2 + \omega_2^2(k)) \Bigg\}^{\frac{1}{2}} \quad (46)$$

so that the integrand has branch points at  $s = \pm i\omega_1, \pm i\omega_2$  where

$$\omega_2(k) = \frac{1}{2} \left[ (\frac{1}{2} + k^2 + 2\beta k)^{\frac{1}{2}} + (\frac{1}{2} + k^2 - 2\beta k)^{\frac{1}{2}} \right] \quad (47)$$

$$\omega_1(k) = \frac{1}{2} \left[ (\frac{1}{2} + k^2 + 2\beta k)^{\frac{1}{2}} - (\frac{1}{2} + k^2 - 2\beta k)^{\frac{1}{2}} \right] \quad (48)$$

$\omega_2$  is a lower cut-off frequency,  $\omega_1$  an upper cut-off frequency. (See Fig. 2.) In addition, the integrand of (40) has poles at  $s = \pm ik$ , and an essential singularity (due to  $\mu$  in the exponent) at the origin. It can be verified that the integrand is one-valued in the entire plane with barriers as shown, if the principal branches of the angles associated with each branch point are chosen as shown in Fig. 3. The picture is drawn for a given  $k$  and is qualitatively the same for all  $k$ . Note the arguments of  $\mu$  at the various points on the imaginary axis.

$$\arg \mu_A = \arg \mu_D = \arg \mu_E = \arg \mu_H = \pi/2 \quad (49)$$

$$\arg \mu_B = \arg \mu_C = \arg \mu_F = \arg \mu_G = -\pi/2. \quad (50)$$

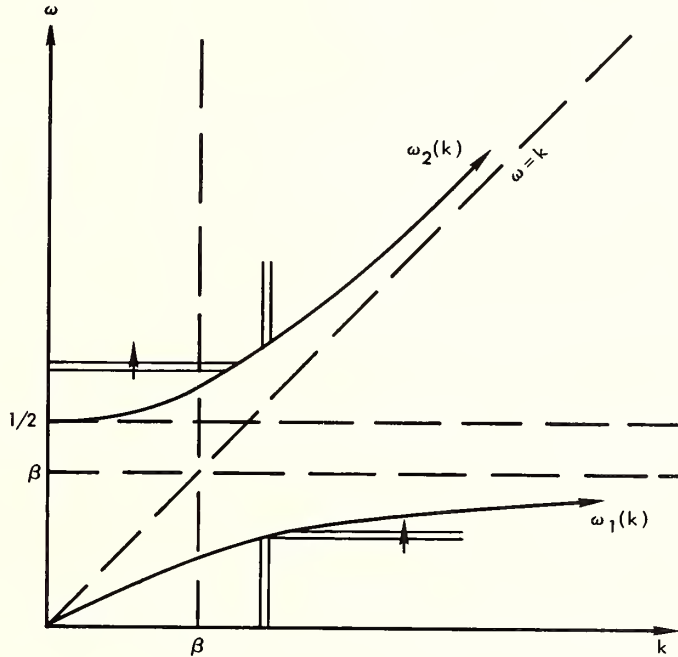


Fig. 2 - Location of the cutoff frequencies, given by Eqs. (47) and (48), which arise from the change in the order of integration of Eq. (41).

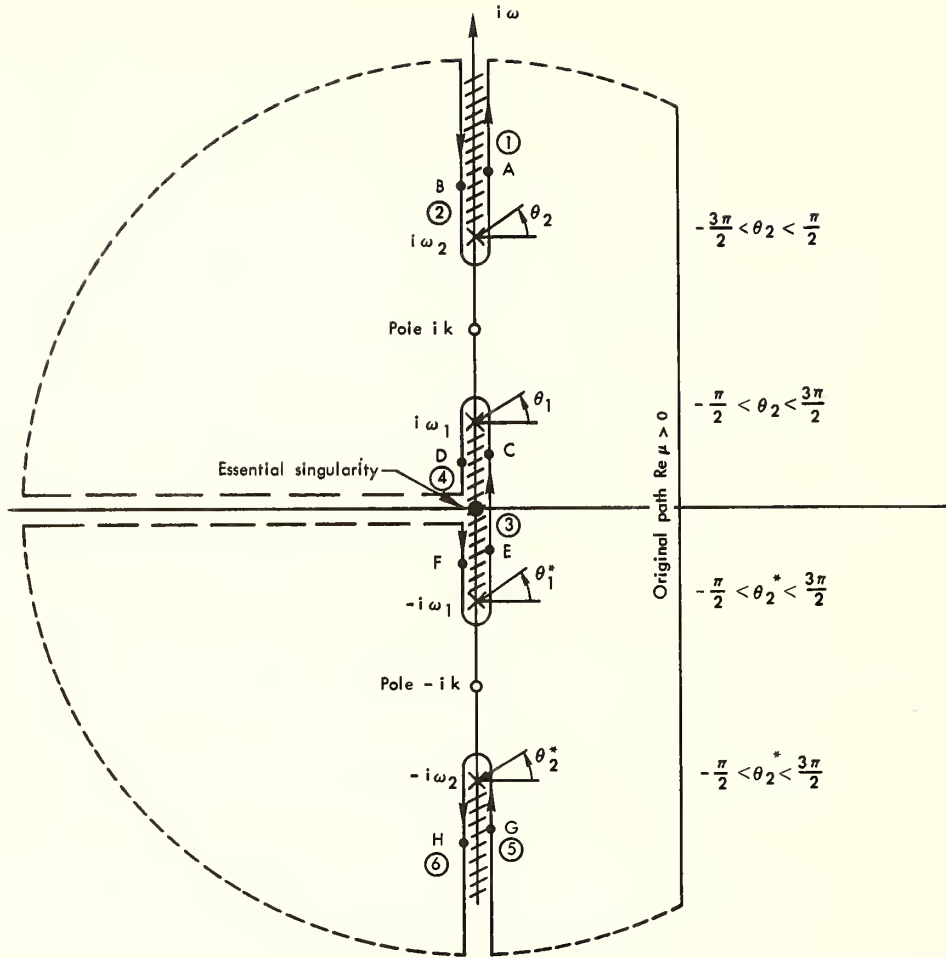


Fig. 3 - Contour for carrying out the integration in the  $s$ -plane, with the location of poles, branch points, and essential singularity as indicated.

The application of Cauchy's theorem enables the integral of  $F$  on the original path to be expressed as integrals on segments of the imaginary axis as shown, plus  $(2\pi i) \times (\text{sum of the residues})$  at the poles ( $s = \pm ik$ ). This is true since the integral on a large circle in the left half plane vanishes ( $\text{Re}(s) < 0$ ). Also, the essential singularity at the origin is outside the contour used for Cauchy's theorem, and thus does not contribute a residue. Thus

$$F(k; z, t) = \left( \sum_{s=\pm ik} \text{Res} \right) + F_1 + F_2 + F_3 + F_4 + F_5 + F_6 \quad (51)$$

where

$$F_1(k) = \frac{1}{2\pi i} \int_{\omega_2(k)}^{\infty} e^{i(\omega t - \mu_1 z)} \frac{\left( \frac{2-\gamma}{2\gamma} + i\mu_1 \right)}{\omega^2 - k^2} \omega d\omega \quad (52)$$

$$F_2(k) = \frac{1}{2\pi i} \int_{-\infty}^{-\omega_2} e^{i(\omega t + \mu_1 z)} \frac{\left( \frac{2-\gamma}{2\gamma} - i\mu_1 \right)}{\omega^2 - k^2} \omega d\omega \quad (53)$$



and  $\mu = i\mu_1$  on 1, etc.

$$\mu_1 = \frac{1}{\omega} \sqrt{(\omega^2 - \omega_1^2)(\omega^2 - \omega_2^2)} = \frac{1}{\omega} \sqrt{\omega^4 - (\frac{1}{2} + k^2)\omega^2 + \beta^2 k^2} \quad (54)$$

$$F_5(k) = \frac{1}{2\pi i} \int_{-\infty}^{-\omega_2} e^{i(\omega t + \mu_5 z)} \frac{\frac{2-\gamma}{2\gamma} - i\mu_5}{\omega^2 - k^2} \omega d\omega \quad (55)$$

$$F_6(k) = \frac{1}{2\pi i} \int_{-\omega_2}^{-\infty} e^{i(\omega t - \mu_5 z)} \frac{\frac{2-\gamma}{2\gamma} + i\mu_5}{\omega^2 - k^2} \omega d\omega \quad (56)$$

Noting that  $\mu_5 = -\mu_1$  these integrals can be combined to

$$F_1 + F_2 + F_5 + F_6 = \frac{1}{2\pi i} \int_{-\infty}^{\infty} \frac{\omega d\omega}{\omega^2 - k^2} \left\{ \left( \frac{2-\gamma}{2\gamma} + i\mu_1 \right) e^{i(\omega t - \mu_1 z)} - \left( \frac{2-\gamma}{2\gamma} - i\mu_1 \right) e^{i(\omega t + \mu_1 z)} \right\} \quad (57)$$

$|\omega| > \omega_2(k)$

The integration is carried out in (57) only over those frequencies  $|\omega| > \omega_2(k)$  which can propagate as waves. In a similar way,

$$F_3 + F_4 = \frac{1}{2\pi i} \int_{-\omega_1}^{\omega_1} \frac{\omega d\omega}{k^2 - \omega^2} \left\{ \left( \frac{2-\gamma}{2\gamma} + i\mu_1 \right) e^{i(\omega t - \mu_1 z)} - \left( \frac{2-\gamma}{2\gamma} - i\mu_1 \right) e^{i(\omega t + \mu_1 z)} \right\} \quad (58)$$

Thus, all these integrals can be combined to a Fourier integral on only those frequencies which can propagate

$$F_1 + F_2 + F_3 + F_4 + F_5 + F_6 = \frac{1}{2\pi i} \int_{-\infty}^{\infty} \frac{\omega d\omega}{|\omega^2 - k^2|} \left\{ \left( \frac{2-\gamma}{2\gamma} + i\mu_1 \right) e^{i(\omega t - \mu_1 z)} - \left( \frac{2-\gamma}{2\gamma} - i\mu_1 \right) e^{i(\omega t + \mu_1 z)} \right\} \quad (59)$$

$|\omega| < \omega_1, \quad |\omega| > \omega_2$

Further, the residue at  $s = \pm ik$  is easily calculated:

$$\begin{aligned} (\mu^2(ik) &= \frac{1}{2} - \beta^2 = \left( \frac{2-\gamma}{2\gamma} \right)^2 \\ \text{Res}(s = \pm ik) &= \frac{2-\gamma}{2\gamma} e^{-\frac{2-\gamma}{2\gamma} z} e^{\pm ikt} \end{aligned} \quad (60)$$

Thus

$$\sum_{s=\pm ik} \text{Res} = \frac{2-\gamma}{\gamma} e^{-\frac{2-\gamma}{2\gamma} z} \cos kt. \quad (61)$$

The pressure field is calculated by applying the Hankel transform to (59) and (61) as in (39). The part produced by the residue at the poles (61) is called the ground wave  $P_G$  and thus has the representation

$$e^{-\frac{1}{2}z} p_G = \frac{1}{2\pi} \frac{2-\gamma}{\gamma} e^{-\left(\frac{2-\gamma}{2\gamma}\right)z} \int_0^\infty J_0(kr) \cos kt k dk. \quad (62)$$

The integral in (62) is divergent, but can be interpreted as

$$\frac{\partial}{\partial t} \int_0^\infty \sin kt J_0(kr) dk = - \frac{t}{(t^2 - r^2)^{3/2}}. \quad (63)$$

Then,

$$e^{-\frac{1}{2}z} p_G = \frac{1}{2\pi} \left(\frac{2-\gamma}{\gamma}\right) e^{-\frac{2-\gamma}{2\gamma}z} \left( \frac{-t}{(t^2 - r^2)^{3/2}} \right) \quad (64)$$

Equation (64) represents a cylindrical wave, which exists only behind the spherical front. It is an exact solution to the original equations as given in Lamb (1945). The wave is excited from the axis ( $r=0$ ) by the vertical passage of the spherical acoustic wave. The remainder of the pressure field comes from the Hankel transform of (59). The order of integration is changed and the integral is broken up into low and high frequency bands (cf. Fig. 2).

$$p = p_G + p_I + p_{II} \quad (65)$$

$$e^{-\frac{1}{2}z} p_I = \frac{1}{2\pi i} \int_{-\beta}^{\beta} \omega d\omega \frac{1}{2\pi} \int_{k_1(\omega)}^{\infty} \frac{J_0(kr)k}{k^2 - \omega^2} \left\{ \left(\frac{2-\gamma}{2\gamma} + i\mu_1\right) e^{i(\omega t - \mu_1 z)} - \left(\frac{2-\gamma}{2\gamma} - i\mu_1\right) e^{i(\omega t + \mu_1 z)} \right\} dk \quad (66)$$

$$e^{-\frac{1}{2}z} p_{II} = \frac{1}{2\pi i} \int_{|\omega| > \frac{1}{2}}^{\infty} \omega d\omega \frac{1}{2\pi} \int_{k_1(\omega)}^{\infty} \frac{J_0(kr)k}{\omega^2 - k^2} \left\{ \left(\frac{2-\gamma}{2\gamma} + i\mu_1\right) e^{i(\omega t - \mu_1 z)} - \left(\frac{2-\gamma}{2\gamma} - i\mu_1\right) e^{i(\omega t + \mu_1 z)} \right\} dk. \quad (67)$$

Here

$$k_1(\omega) = |\omega| \sqrt{\frac{\omega^2 - \frac{1}{4}}{\omega^2 - \beta^2}}$$

from (54). These integrals can be expressed as integrals over positive frequencies in low and high frequency bands.

$$e^{-\frac{1}{2}z} p_I = \frac{1}{\pi} \operatorname{Im} \int_0^{\beta} \omega e^{i\omega t} G_I(\omega) d\omega \quad (68)$$

$$e^{-\frac{1}{2}z} p_{II} = \frac{1}{\pi} \operatorname{Im} \int_{\frac{1}{2}}^{\infty} \omega e^{i\omega t} G_{II}(\omega) d\omega \quad (69)$$

where

$$G_I(\omega) = \frac{1}{2\pi} \int_{k_1}^{\infty} \frac{J_0(kr)k}{k^2 - \omega^2} \left\{ \left(\frac{2-\gamma}{2\gamma} + i\mu_1\right) e^{-i\mu_1 z} - \left(\frac{2-\gamma}{2\gamma} - i\mu_1\right) e^{i\mu_1 z} \right\} dk \quad (70)$$

$$G_{II}(\omega) = \frac{1}{2\pi} \int_0^k \frac{J_0(kr)k}{\omega^2 - k^2} \left\{ \left( \frac{2-\gamma}{2\gamma} + i\mu_1 \right) e^{-i\mu_1 z} - \left( \frac{2-\gamma}{2\gamma} - i\mu_1 \right) e^{i\mu_1 z} \right\} dk. \quad (71)$$

The asymptotic formula

$$J_0(kr) \approx \sqrt{\frac{2}{\pi kr}} \cos \left( kr - \frac{\pi}{4} \right) = \frac{1}{\sqrt{2\pi kr}} \left\{ e^{i kr - i \frac{\pi}{4}} + e^{-i kr + i \frac{\pi}{4}} \right\} \quad (72)$$

is now used in (70), (71). This approximation is very good for  $r$  large except for those  $k$  near zero (in  $G_{II}$ ). But for  $k$  close to zero the integrand is small anyway so that the approximation of (72) is probably excellent. The apparent singularity at ( $r=0$ ) in (72) in fact disappears from the answer later. Thus,

$$G_I \approx \frac{1}{(2\pi)^{3/2} \sqrt{r}} \int_{k_1(\omega)}^{\infty} \frac{\sqrt{k} dk}{k^2 - \omega^2} \left\{ \left( \frac{2-\gamma}{2\gamma} + i\mu_1 \right) (e^{i\theta_1(k)} + e^{i\theta_1(-k)}) - \left( \frac{2-\gamma}{2\gamma} - i\mu_1 \right) (e^{i\theta_2(k)} + e^{i\theta_2(-k)}) \right\} \quad (73)$$

$$G_{II} \approx \frac{1}{(2\pi)^{3/2} \sqrt{r}} \int_0^{k_1(\omega)} \frac{\sqrt{k} dk}{\omega^2 - k^2} \left\{ \left( \frac{2-\gamma}{2\gamma} + i\mu_1 \right) (e^{i\theta_1(k)} + e^{i\theta_1(-k)}) - \left( \frac{2-\gamma}{2\gamma} - i\mu_1 \right) (e^{i\theta_2(k)} + e^{i\theta_2(-k)}) \right\}. \quad (74)$$

Here

$$\theta_1(k) = kr - \mu_1(k)z - \frac{\pi}{4} \operatorname{sign} k \quad \theta_1(-k) = -kr - \mu_1 z + \frac{\pi}{4} \quad (75)$$

$$\theta_2(k) = kr + \mu_1 z - \frac{\pi}{4} \operatorname{sign} k \quad \theta_2(-k) = -kr + \mu_1 z + \frac{\pi}{4}$$

$$\mu_1 = \frac{1}{\omega} \sqrt{(\beta^2 - \omega^2)k^2 - \omega^2 \left( \frac{1}{4} - \omega^2 \right)} = \frac{1}{\omega} \sqrt{\omega^2 \left( \omega^2 - \frac{1}{4} \right) - (\omega^2 - \beta^2)k^2}. \quad (76)$$

Note that

$$\frac{d\mu_1}{dk} = \frac{\beta^2 - \omega^2}{\omega} \frac{k}{[(\beta^2 - \omega^2)k^2 + \omega^2(\omega^2 - \frac{1}{4})]^{\frac{3}{2}}} = \frac{\beta^2 - \omega^2}{\omega^2} \frac{k}{\mu_1} \begin{matrix} > 0 \text{ in } G_I \\ < 0 \text{ in } G_{II} \end{matrix} \quad (77)$$

$$\frac{d^2\mu_1}{dk^2} = -\omega \frac{(\frac{1}{4} - \omega^2)(\beta^2 - \omega^2)}{[(\beta^2 - \omega^2)k^2 + \omega^2(\omega^2 - \frac{1}{4})]^{3/2}} < 0, \text{ always.} \quad (78)$$

Now, the method of stationary phase is applied to the integrals in (73) and (74) with the rapidly oscillating exponents  $\theta_{1,2}(\pm k)$ . The main contribution comes from wave numbers where  $\theta'(k_s) = 0$  (main group). Details of the calculation are shown only for  $G_I$ . The point of stationary phase in  $\theta_1$  is given by

$$\frac{d\mu_1}{dk} = \frac{r}{z}. \quad (79)$$

Since  $\frac{d\mu_1}{dk} > 0$  in  $G_I$ , only  $\theta_1(k)$ ,  $\theta_2(-k) = -\theta_1(k)$  have stationary points and contribute the dominant terms to the answer. Thus

$$\left(\frac{d\mu_1}{dk}\right)^2 = \frac{r^2}{z^2} = \frac{(\beta^2 - \omega^2)k_s^2}{\omega^2[(\beta^2 - \omega^2)k_s^2 + \omega^2(\omega^2 - \frac{1}{2})]}$$

or

$$k_s = \omega^2 \sqrt{\frac{\omega^2 - \frac{1}{2}}{\omega^2 - \beta^2}} \frac{\sin \varphi}{\sqrt{\omega^2 - \beta^2 \cos^2 \varphi}}. \quad (80)$$

Here  $\varphi$  is the pole angle in physical space,  $r = R \sin \varphi$ ,  $z = R \cos \varphi$ . According to (80), a stationary point occurs in  $G_I$  only for those frequencies  $\omega > \beta \cos \varphi$ . According to the method, the integrand is evaluated at the stationary point except for the exponent which is approximated as

$$\theta_1(k) = \theta_1(k_s) + \frac{(k - k_s)^2}{2} \theta_1''(k_s) \quad (81)$$

(subscript  $s$  denotes quantities evaluated at the stationary point). Due to the rapid oscillation away from  $k - k_s$ , the limits of integration can be extended to  $\infty$  without introducing a significant error. Note the formulas

$$\omega^2 - k_s^2 = \frac{\omega^2 D(\omega, \varphi)}{(\omega^2 - \beta^2)(\omega^2 - \beta^2 \cos^2 \varphi)} \quad (82)$$

where

$$D(\omega, \varphi) = (\omega^2 - \beta^2)^2 \cos^2 \varphi + (\frac{1}{2} - \beta^2) \omega^2 \sin^2 \varphi > 0 \quad (83)$$

$$\mu_s = \cos \varphi \sqrt{\frac{(\frac{1}{2} - \omega^2)(\beta^2 - \omega^2)}{\omega^2 - \beta^2 \cos^2 \varphi}} \quad (84)$$

$$\theta_{1s} = R \sqrt{\frac{\frac{1}{2} - \omega^2}{\beta^2 - \omega^2}} \sqrt{\omega^2 - \beta^2 \cos^2 \varphi} - \frac{\pi}{4} = \theta_{2s}. \quad (85)$$

For  $G_{II}$ , the only stationary points occur in  $\theta_2(k)$  and  $\theta_1(-k)$ . Thus, the stationary phase approximation yields,

$$G_I \approx \frac{1}{(2\pi)^{3/2} \sqrt{r}} \frac{\sqrt{k_s}}{k_s^2 - \omega^2} 2i \operatorname{Im} \left\{ \left( \frac{2 - \gamma}{2\gamma} + i\mu_s \right) e^{i\theta_{1s}} \int_{-\infty}^{\infty} e^{\frac{i}{2}(k - k_s)^2 \theta_{1s}''} dk \right\} \quad (86)$$

$$G_{II} \approx \frac{1}{(2\pi)^{3/2} \sqrt{r}} \frac{\sqrt{k_s}}{\omega^2 - k_s^2} 2i \operatorname{Im} \left\{ \left( \frac{2 - \gamma}{2\gamma} + i\mu_s \right) e^{-i\theta_{2s}} \int_{-\infty}^{\infty} e^{-\frac{i}{2}(k - k_s)^2 \theta_{1s}''} dk \right\}. \quad (87)$$

The integrals in (86), (87) are

$$\int_{-\infty}^{\infty} e^{\frac{i}{2}(k - k_s)^2 \theta_{1s}''} dk = \frac{\sqrt{2\pi}}{\sqrt{\theta_{1s}''}} e^{i \frac{\pi}{4}} \quad (\text{since } \theta_{1s}'' = -z\mu_{1s}'' > 0) \quad (88)$$

$$\int_{-\infty}^{\infty} e^{-\frac{i}{2}(k-k_s)^2 \theta''_{2s}} dk = \frac{\sqrt{2\pi}}{\sqrt{|\theta''_{2s}|}} e^{i \frac{\pi}{4}} \quad (\text{since } \theta''_{2s} = z\mu''_{1s} < 0). \quad (89)$$

Using the expressions at the stationary point tabulated above, we obtain for (86), (87)

$$G_I \approx \frac{\cos \varphi}{2\pi R} \frac{(\beta^2 - \omega^2)(\frac{1}{2} - \omega^2)^{\frac{1}{2}}}{D(\omega, \varphi)} 2i \operatorname{Im} \left\{ \left( \frac{2-\gamma}{2\gamma} + i\mu_s \right) e^{-iR \sqrt{\frac{(\frac{1}{2} - \omega^2)}{(\beta^2 - \omega^2)}} (\omega^2 - \beta^2 \cos^2 \varphi)} \right\} \quad (90)$$

$$G_{II} \approx \frac{\cos \varphi}{2\pi R} \frac{(\omega^2 - \beta^2)(\omega^2 - \frac{1}{2})^{\frac{1}{2}}}{D(\omega, \varphi)} 2i \operatorname{Re} \left\{ \left( \frac{2-\gamma}{2\gamma} + i\mu_s \right) e^{-iR \sqrt{\frac{(\omega^2 - \frac{1}{2})}{(\omega^2 - \beta^2)}} (\omega^2 - \beta^2 \cos^2 \varphi)} \right\}. \quad (91)$$

Thus, the pressure in the far field can be written as integrals over the important frequency bands (cf. (68), (69)):

$$e^{-\frac{1}{2}z} p_I \approx \frac{\cos \varphi}{2\pi^2 R} \operatorname{Im} \int_{\beta \cos \varphi}^{\beta} \frac{\omega(\beta^2 - \omega^2)(\frac{1}{2} - \omega^2)^{\frac{1}{2}}}{D(\omega, \varphi)} \left\{ \left( \frac{2-\gamma}{2\gamma} + i\mu_s \right) e^{i(\omega t + \Omega R)} - \left( \frac{2-\gamma}{2\gamma} - i\mu_s \right) e^{i(\omega t - \Omega R)} \right\} d\omega \quad (92)$$

$$e^{-\frac{1}{2}z} p_{II} \approx \frac{\cos \varphi}{2\pi^2 R} \operatorname{Re} \int_{\frac{1}{2}}^{\infty} \frac{\omega(\omega^2 - \beta^2)(\omega^2 - \frac{1}{2})^{\frac{1}{2}}}{D(\omega, \varphi)} \left\{ \left( \frac{2-\gamma}{2\gamma} + i\mu_s \right) e^{i(\omega t - \Omega R)} + \left( \frac{2-\gamma}{2\gamma} - i\mu_s \right) e^{i(\omega t + \Omega R)} \right\} d\omega \quad (93)$$

where

$$\Omega(\omega, \varphi) = \sqrt{\frac{(\frac{1}{2} - \omega^2)}{(\beta^2 - \omega^2)}} (\omega^2 - \beta^2 \cos^2 \varphi). \quad (94)$$

The representation ((92), (93)) shows spherical waves with a spherical phase and group velocity depending on angle  $\varphi$ . These integrals can again be approximated by the method of stationary phase. Details are given in the next section.

## V. ASYMPTOTIC PRESSURE FIELD, NUMERICAL RESULTS

In this section, we shall examine some of the properties of the pressure field given by (92) and (93). The field has been expressed in terms of integrals of the form

$$\int f(\omega, \cos \varphi) e^{i(\omega t \pm \Omega R)} d\omega \quad (95)$$

over two bands of propagating frequencies, with  $\Omega(\omega, \varphi)$  given by (94). For large  $R$  and  $t$ , the exponentials are rapidly oscillating and the method of stationary phase can be applied to these integrals. The points of stationary phase, if any, are given by

$$\frac{t}{R} \pm \frac{d\Omega}{d\omega} = 0. \quad (96)$$

The existence and number of stationary points in each frequency band is best illustrated graphically.



We first consider the high frequency band,  $\frac{1}{2} \leq \omega < \infty$ . In Fig. 4, we have plotted  $\Omega(\omega, \varphi)$  vs  $\omega$  for a typical value of  $\varphi$ . The function  $\Omega$  is a monotonically increasing function of  $\omega$ , starting out as  $\sqrt{\omega - \frac{1}{2}}$  for  $\omega$  near  $\frac{1}{2}$  and asymptotically approaching  $\omega$  as  $\omega \rightarrow \infty$ . The derivative  $\frac{d\Omega}{d\omega}$  decreases continuously from  $\infty$  to 1 as  $\omega$  increases from  $\frac{1}{2}$  to  $\infty$ . Since  $\frac{d\Omega}{d\omega} > 0$ , it is clear that only the exponential with the minus sign can have a stationary point. It is also clear from the above discussion that there will be a single stationary point in this frequency range for all  $t/R$  such that  $1 \leq t/R < \infty$ , i.e., for all points behind the spherical front.

For the low frequency band,  $\beta \cos \varphi \leq \omega \leq \beta$ , the situation is somewhat different, as can be seen from Fig. 5. The function  $\Omega$  increases monotonically with  $\omega$  in this band, starting out as  $\sqrt{\omega - \beta \cos \varphi}$  for  $\omega$  near  $\beta \cos \varphi$  and approaching  $\infty$  as  $\frac{1}{\sqrt{\omega - \beta}}$  when  $\omega$  approaches  $\beta$ . It is clear that the function has an inflection point  $\omega_c$  in this frequency range. The derivative  $\frac{d\Omega}{d\omega}$  decreases from  $\infty$  to some minimum value as  $\omega$  increases from  $\beta \cos \varphi$  to  $\omega_c$ , and then increases again to  $\infty$  as  $\omega$  increases from  $\omega_c$  to  $\beta$ . For any given  $\varphi$ , the minimum value of  $\frac{d\Omega}{d\omega}$  represents the minimum value of  $t/R$ , or the maximum value of  $R/t$ , for which a stationary point exists (again only for the exponential with the minus sign). For values of  $R/t$  greater than the maximum, there are no stationary points for the given  $\varphi$ , whereas for values smaller than the maximum there are clearly two stationary points. At the maximum value of  $R/t$ , the two stationary points coincide.

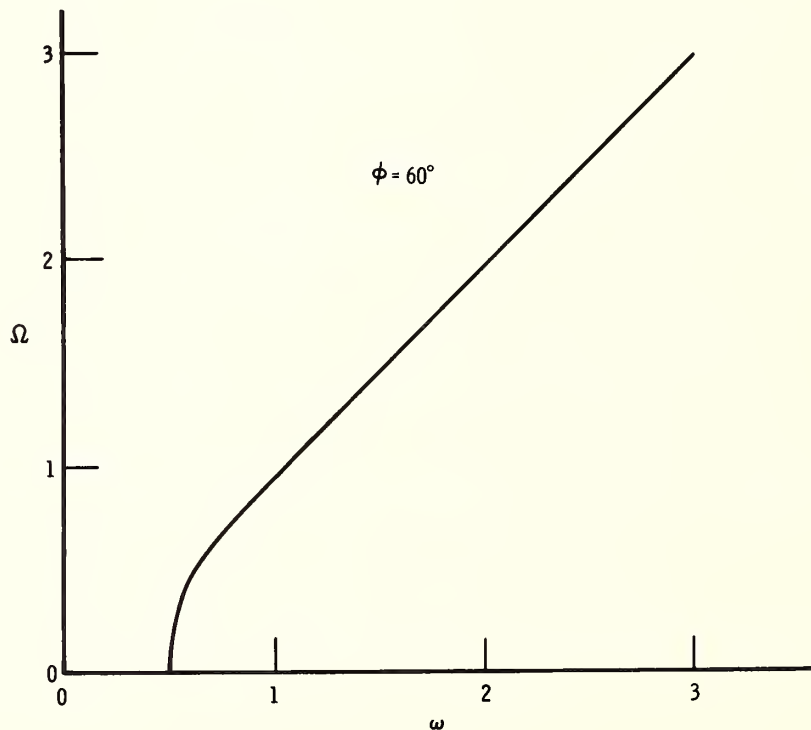


Fig. 4 - High frequency branch of the function  $\Omega(\omega, \varphi)$  (Eq. (94)) for  $\varphi = 60^\circ$ . For a given  $\omega$ , the slope of the curve is the value of  $t/R$  for which the phase is stationary at that frequency.

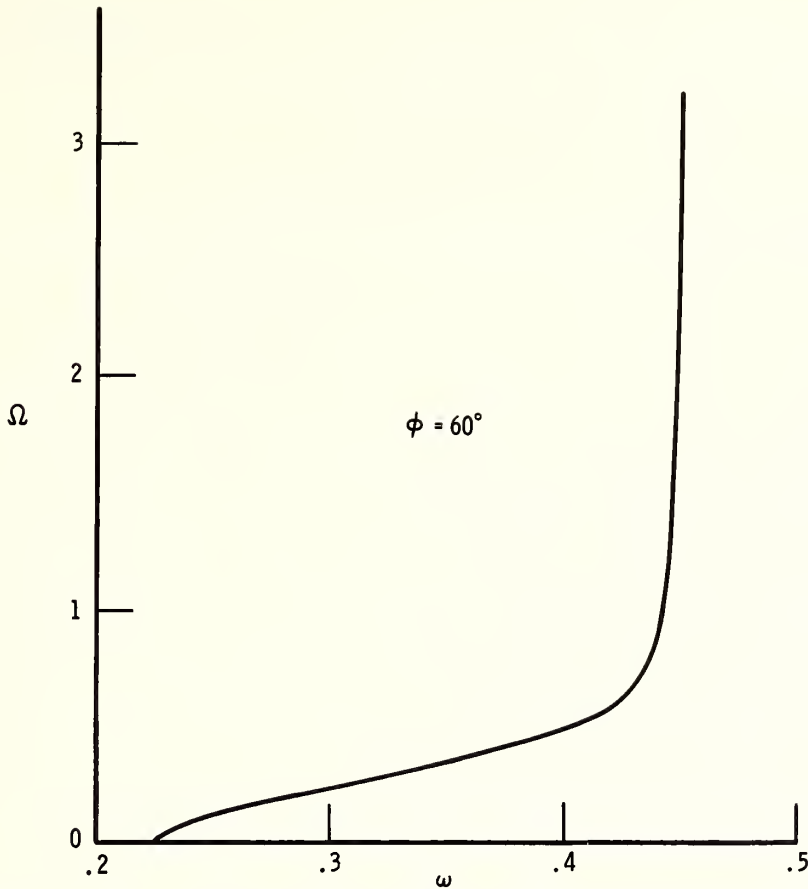


Fig. 5 - Low frequency branch of the function  $\Omega(\omega, \phi)$  (Eq. 94) for  $\phi = 60^\circ$ . For a given  $\omega$ , the slope of the curve is the value of  $t/R$  for which the phase is stationary at that frequency. Note existence of inflection point, at which the slope has its minimum value.

This situation is identical to that which arises in the case of incompressible flow in a density stratified liquid considered by Mowbray and Rarity (1967). The physical consequences are the same as for the incompressible case: the locus in physical space of the double points of stationary phase defines a front, or "caustic," representing the onset of the disturbance. Between the caustic and the spherical front, the low frequency part of the disturbance is exponentially small, and the main contribution comes from the high frequency band.

For the purposes of calculating the location of the front, it is convenient to use the variables

$$\begin{aligned}\zeta &= \frac{r}{t} \\ \eta &= \frac{z}{t}\end{aligned}\tag{97}$$

where  $r = R \sin \phi$  is the cylindrical radius and  $z = R \cos \phi$  is the altitude. In terms of these variables, a line of constant phase  $\Phi = \omega - \frac{R}{t} \Omega$  can be written

$$\frac{\omega^2}{(\beta^2 - \omega^2)} \zeta^2 - \eta^2 = \frac{(\omega - \Phi)^2}{(\frac{1}{2} - \omega^2)}\tag{98}$$

while the condition for stationary phase (96) becomes

$$\frac{\beta^2 \omega (\frac{1}{2} - \omega^2)}{(\omega - \Phi) (\beta^2 - \omega^2)^2} \zeta^2 - \frac{\omega (\omega - \Phi)}{(\frac{1}{2} - \omega^2)} = 1.\tag{99}$$

For a given value of the parameter  $\xi$ , which corresponds to a particular value of the phase at a given time, (98) and (99) are parametric equations for a line in the  $(\zeta, \eta)$ -plane along which the particular phase is stationary. Each point on such a line corresponds to a different value of  $\omega$ , the point of stationary phase. A line of constant and stationary phase intersects the locus of double stationary points in a cusp. The condition for a cusp is

$$\frac{d\zeta}{d\omega} = \frac{d\eta}{d\omega} = 0. \quad (100)$$

Applying this to (99), we can obtain  $\xi$  as a function of  $\omega$  along the front. Equations (98) and (99) then provide a one to one mapping from  $(\xi, \omega)$  to  $(\zeta, \eta)$ . The wave front obtained in this manner is shown in Fig. 6, where we have also plotted a few lines of constant  $\xi$  for the purposes of illustration.

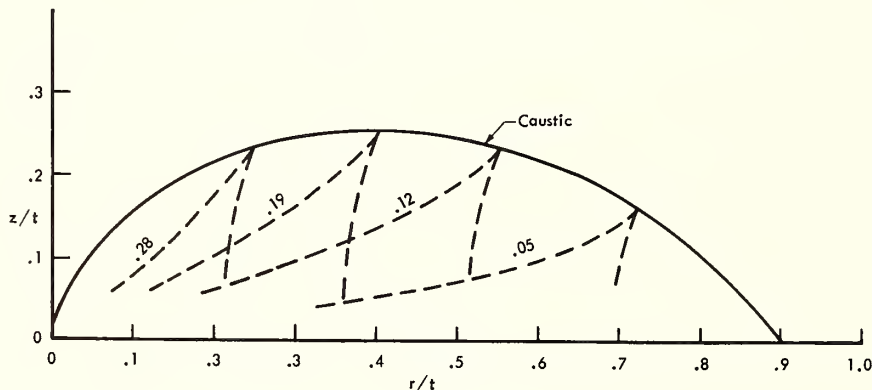


Fig. 6 - Location of the caustic in  $(r/t, z/t)$  space. The dashed lines are lines of stationary phase along which the phase is constant at any instant.

The co-ordinates  $(\zeta, \eta)$  of any point on the front are the horizontal and vertical components, respectively, of the velocity of the front at that point. The point moving along the ground has a velocity  $\zeta/t = 2\beta = .9c^*$ . The maximum vertical velocity is  $.26c^*$ , and occurs at an angle of about  $32^\circ$  with the horizontal. (Every point on the front moves radially outward from the origin.)

As just indicated, each point on the caustic is associated with a given angle  $\phi$  in physical space, given by  $\phi = \tan^{-1} \eta/\zeta$ . Associated with this point on the caustic is also the frequency  $\omega_c$  of the double point of stationary phase. This is the first frequency (in the low frequency band) to arrive at a given  $\phi$ , after which the signal splits into two frequency components, one of which increases with time towards  $\beta \cos \phi$ . In Fig. 7, we plot in polar co-ordinates the frequency  $\omega_c$  as a function of the pole angle  $\phi$ .

In light of the above discussion, it is now possible to describe briefly the frequency-time history of the signal at any location. The first disturbance to arrive at any location  $(R, \phi)$  is the acoustic spherical front, containing the very high frequencies. As time progresses, the principal frequency in this part of the disturbance decreases asymptotically towards  $\frac{1}{2}$ . Some time after the passage of the spherical front, the caustic arrives, carrying the frequency associated with the angle  $\phi$  (Fig. 7). As discussed above, this part of the signal then splits into two frequencies, one tending toward  $\beta$  and the other toward  $\beta \cos \phi$  as time progresses. Thus, at any location, the signal consists asymptotically of the three frequencies  $\frac{1}{2}$ ,  $\beta$ , and  $\beta \cos \phi$ . This information is summarized in Fig. 8, which is a polar graph of the various groups. Each dashed line represents the location in  $(R/t, \phi)$  space of a group of a given frequency. The solid line is the caustic, which appears as the envelope of the low frequency band. Outside of the caustic, only the high frequency band is present, whereas inside of the caustic both bands clearly contribute to the signal.

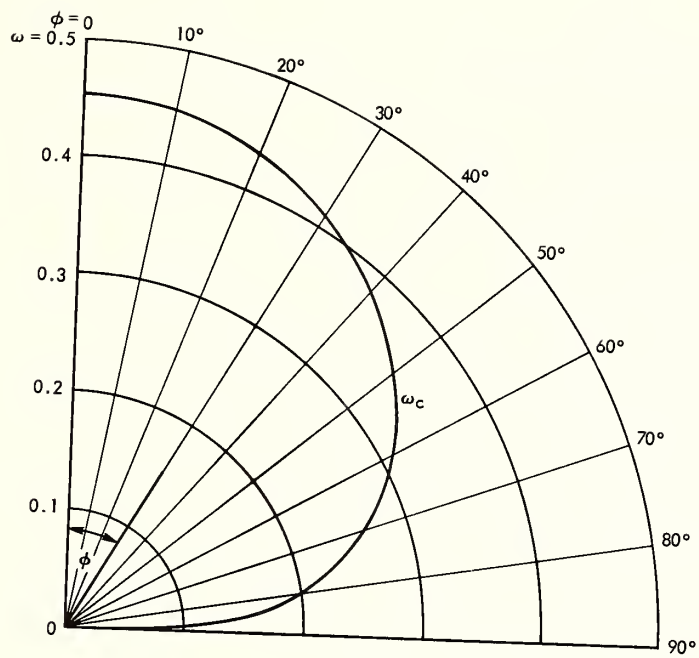


Fig. 7 - Angular frequency at the caustic, in units of  $c^*/h$ , as a function of the pole angle  $\phi$ .

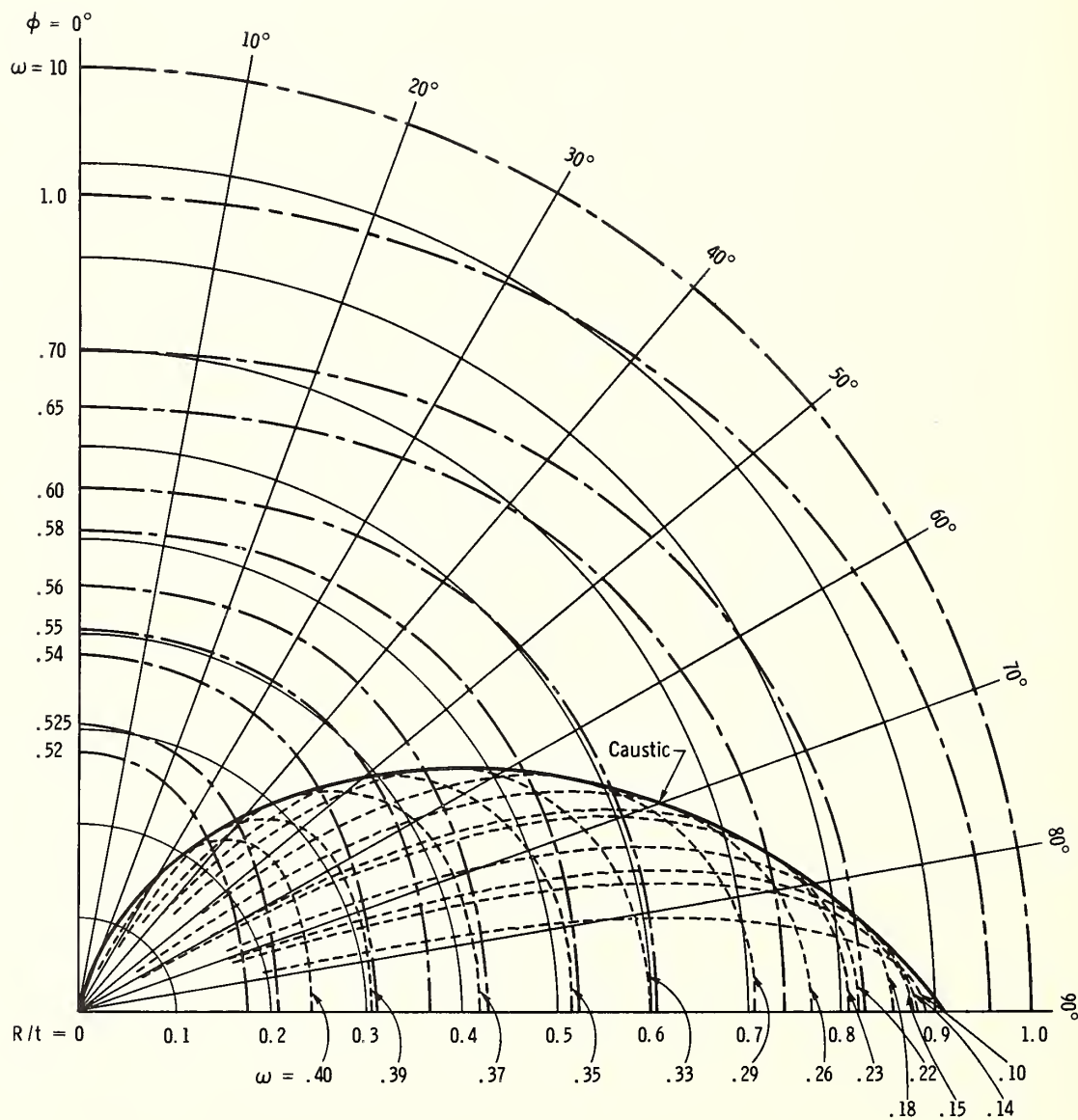


Fig. 8 - Location in  $(R/t, \phi)$  space of groups of a given frequency.  
The solid line is the caustic, which appears as the envelope  
of the low frequency band.



#### REFERENCES

- Lamb, H. Hydrodynamics, p. 548, Dover Publications, Inc., New York, 1945.
- Lighthill, M. J., Group Velocity, J. Inst. Maths. Applics., 1, 1-28, 1965.
- Mowbray, D.E. and B. S. H. Rarity, A Theoretical and Experimental Investigation of Internal Waves of Small Amplitude in a Density Stratified Liquid, J. Fluid Mech., 28, 1-16, 1967.
- Pierce, A. D., Propagation of Acoustic-Gravity Waves from a Small Source Above the Ground in an Isothermal Atmosphere, J. Acoust. Soc. Am., 35, 1798-1807, 1963.
- Watson, G. N., A Treatise on the Theory of Bessel Functions, Cambridge Univ. Press, 1922.
- Whitham, G. B., Group Velocity and Energy Propagation for Three-Dimensional Waves, Comm. Pure Appl. Math., 14, 675-691, 1961.



Theoretical Calculations of Traveling Ionospheric  
Disturbances Generated by Low-Altitude  
Nuclear Explosions

J. S. Greene, Jr., and W. A. Whitaker  
Air Force Weapons Laboratory  
Kirtland Air Force Base, New Mexico

The Air Force Weapons Laboratory SHELL and SAP hydrodynamic computer codes have been used to calculate the generation and to a limited extent the propagation of ionospheric disturbances originating from low-altitude nuclear explosions. These codes solve Newton's equations. The free field fluid quantities of density, pressure, energy, and velocity are calculated continuously as a function of space and time. Our original intention was to investigate overhead disturbance arrival times, but we have been able to continue the calculations to one hour and twenty minutes after the burst. By this time the ionosphere is disturbed 3600 km from the burst axis. The calculations show that the first perturbation in the F-layer critical frequency, even at these distances, is created by the primary acoustic shock wave traveling radially outward at about 750 m/sec. The subsequent  $f_oF_2$  perturbations are due to traveling disturbances with pressure-velocity relationships characteristic of long period internal atmospheric gravity waves. These gravity waves are generated in the region of rapid temperature increase near the 120 km altitude level. The generation processes are associated with an acceleration and fold-over of the shock waves passing through this region.

INTRODUCTION

From the early days of testing, it has been well known [Daniel and Harris, 1953] that large yield weapons lead to disturbances in the ionosphere. The Novaya Zemlya tests in October, 1961, gave rise to ionospheric disturbances which travelled great distances around the globe [Beynon and Jones, 1962; Obayashi, 1962, 1963; Stoeffregen, 1962]. Similar observations have been documented for the 1962, United States Housatonic test [Kanellakos, 1967].

Obayashi [1962, 1963] proposed that these observations be explained in terms of long period gravity waves. This widely accepted view was developed further by Kohl [1964] and has been advocated more recently by Hines [1967]. In a conflicting view, Wickersham [1966] has appealed to an interpretation of the successive surges of  $f_oF_2$  observed [Stoeffregen, 1962; Kanellakos, 1967] over distant stations in terms of the passage of separate wave groups. On the basis of a probability distribution of group speed for different modes [Wickersham, 1965], he associates each surge with the passage of one or more modes of propagation of fully ducted acoustic-gravity waves. Tolstoy [1967] has proposed that the disturbances be explained in terms of energy propagating as a long-period surface type gravity wave on the thermal incline at the 120 km altitude.

The basic equations of motion for a stratified compressible fluid in a gravitational field have been given in several equivalent forms [Lamb, 1945; Eckart, 1960; Tolstoy, 1963; and Hines, 1960, 1965]. These treatments assume a perturbation theory and find a wave solution to the linearized equations. Generally an isothermal atmosphere in the absence of background winds have been assumed, although considerable effort has been devoted in the last few years to more elaborate and realistic atmospheric models [Press and Harkrider, 1962; Pfeffer and Zarichny, 1963; Pierce, 1963; Harkrider, 1964; Friedman, 1966; Midgley and Liemohn, 1966; Hines and Reddy, 1967].

The calculations of the present paper represent a distinct departure from the philosophy of the wave theorists. In fact we pretend not to know anything about waves -- acoustic waves, gravity waves, or surface waves. We just solve Newton's equations in some considerable detail, conserving mass, momentum, and energy. Having achieved moderate success at predicting shock pressures, precursor effects, fireball rise and mach numbers, we decided to try to predict

the arrival times of disturbances at ionospheric heights. In particular we wanted to investigate the difference between the one dimensional SAP and two dimensional SHELL computer code calculations, although this was pushing the two dimensional code far beyond its original purposes.

These two computer codes have been developed by many people at the Air Force Weapons Laboratory during the past ten years. SAP is a one dimensional Lagrangian hydrodynamic code. SHELL is a two dimensional pure Eulerian hydrodynamic code. SAP has been specialized to the problem of atmospheric blast in order to increase its speed and accuracy. Written in the spherical coordinate system it can calculate hydrodynamic shocks at any angle to the horizontal. It is capable of handling over 1000 zones. For the problem of this paper an automatic rezone capability was included in the code. The SHELL code is a versatile two dimensional hydrodynamic code. It can be used to solve problems in any medium whose motions can be analyzed on the basis of inviscid hydrodynamic behavior of a cylindrically symmetric compressible fluid.

In the SHELL code, the atmospheric region of interest is divided into cells to each of which is assigned a mass, pressure, internal energy, and velocity. The partial differential equations for nonviscous, nonconducting compressible fluid flow are solved by a finite difference scheme which advances the cell field quantities explicitly to new values at time  $t + \Delta t$  in terms of the values at time  $t$ . To simulate a nuclear explosion an 11,000°K isothermal sphere surrounded by ambient atmosphere is assumed as initial condition. The radius of the sphere is chosen so that the region within will have the desired energy at ambient density. This sphere is then allowed to expand hydrodynamically into zones with properties of the ambient atmosphere.

The 1962 U.S. Standard mid-latitude atmosphere model was used in all of the calculations. The atmosphere model has been modified slightly to be hydrodynamically stable in an  $R^{-2}$  gravitational field [Brackbill, et al., 1967] even in the differenced scheme. A brief description of the SHELL code is included as an appendix to this paper. Those who are interested in a more detailed discussion of the finite differencing scheme are referred to the appropriate references particularly [Whitaker, et al., 1966].

#### OVERHEAD ARRIVAL TIMES

Figure 1 shows the location of successive maxima and minima in the relative pressure as a function of altitude over the burst point versus time. Each pressure maximum is indicated by a small circle and each minimum by a dash. Without looking at the actual numerical values associated with these dots and dashes, it is difficult to identify which is the important feature. For this reason two lines have been added connecting some of the dots. Initially the primary shock moves upward with a velocity of approximately 380 m/sec. As the shock passes through the 100 km region where the ambient temperature begins to increase very rapidly an acceleration is observed. By 200 km the shock speed has increased to about 1050 m/sec. Above this altitude it continues to increase slowly.

The origin of the secondary shock wave may be identified. By looking at the pressure values and velocity values (not shown here) it is possible to trace the second shock back to its origin. Behind the primary shock there is a negative phase region in which the velocities are downward. This negative phase region essentially extends from about 120 seconds out to 300 seconds between the primary and secondary curves shown on Figure 1. Just below the curve identifying the second shock at times like 140 to 150 seconds, there is a row of minus signs which can be traced back to the beginning of the plot. These minus signs indicate the location of the fireball center which has stabilized at approximately 20 km. The secondary shock has its origin in the interaction of the downward moving air of the negative phase with the stabilized fireball. In effect then, the disturbance which eventually dominates as the second shock at ionospheric heights developed as a reflection of the downward moving air of the negative phase off the stabilized fireball. It will be observed that the rise velocity of the second shock is somewhat lower than that of the primary shock. In particular the second shock does not show the marked acceleration as it passes through the 100 km region which the primary shock shows. From this plot it may be observed that the primary shock arrives at the 120 km level at about 300 seconds and the second shock arrives at this level at about 440 seconds. These times compare well with the times [see e.g., Daniels and Harris, 1953] at which the ionosphere over the burst point is typically observed to be disturbed.



If the burst occurs some distance above ground, a downward moving shock will be reflected off the ground back up into the atmosphere. Typically the reflected downward moving shock arrives at the ionosphere after the second shock shown in this calculation. We can say then that the first three disturbances to arrive over the burst may be attributed to the primary shock wave moving upward, a shock wave resulting from an interaction of the negative phase with the stabilized fireball, and a downward moving shock which has been reflected from the ground. The presence of this third shock is of course dependent on the altitude of the burst.

#### GRAVITY WAVE GENERATION

Figures 2 through 6 are plots of constant relative pressure as a function of altitude and radial distance at five successive times. In Figure 2 the primary shock wave has just passed the 130 km altitude. At this time the center of the shock has begun to accelerate and flatten on the sides. By 360 seconds (Figure 3) the shock has reached 200 km, the flattening on the right side is considerably more pronounced and a distinctly different feature has begun to develop at the 120 km level. At 400 seconds (Figure 4) the disturbance at 120 km has become an important feature on the relative pressure plots. By this time the second shock wave has reached an altitude of 110 km. At 500 seconds (Figure 5) a similar disturbance has begun to develop behind the secondary shock wave. The primary shock wave above these centers is in a region of higher sound speeds and has bowed out considerably so that the right hand boundary of the primary shock is already well ahead of the disturbances at 120 km. At 600 sec (Figure 6) the disturbance at 120 km has become the dominant feature of the relative pressure pattern. The contour scale shown in the upper right hand corner of the relative pressure plots indicated rather large overpressures. These high relative overpressures, which we now understand, have been the occasion of considerable concern. We will return later in this paper to a discussion of them. For now we want to direct our attention to the development at 120 km which was illustrated in the last five figures.

The most striking difference between this disturbance and the originating shock wave occurs in the characteristic particle motion. In the shock wave the particle motion is longitudinal in the direction of the shock propagation as would be expected. In these disturbances at 120 km the particle motion is rotational. In the shock waves the relative over pressure, relative over density, and horizontal and vertical velocities are all in phase with each other. In the disturbances at 120 km the relative over pressure and horizontal velocities are in phase while the vertical velocity is out of phase with these two parameters and out of phase in just such a way as to lead to a rotational motion of the fluid. The easiest way to see this rotational motion is through the use of vorticity plots or velocity vector plots. These features enable us to identify these disturbances as long period gravity waves.

The literature contains a considerable amount of speculation on the nature of the disturbances creating observed  $f_oF_2$  fluctuations. The most plausible theory has been that advanced by Hines [1967]. Hines has assumed from the propagation characteristics that the gravity waves are generated at low altitudes. He then interprets the major perturbations of the F-layer critical frequency in terms of long period gravity waves. The essential feature of this interpretation is that the longer period waves will travel more nearly horizontally, arriving at ionospheric heights at greater distances. We have gone to considerable effort to try to substantiate Hines' work. Although our calculations do not justify comment on the propagation characteristics at this time, they do show, for reasons which will be considered next, that the long period gravity waves are generated at the 120 km level.

The first strong evidence for expecting a transfer of energy from a one dimension to a two dimension motion came from a comparison of the SHELL and SAP code results. Figure 7 compares calculations made using the SHELL code with those made with the SAP code. The plot shows values of relative overpressure at the peak of the primary shock as a function of distance along a ray at  $45^\circ$  above the horizontal. The numbers along the data points of the curves indicate the time in seconds at which the shock peak reached the values indicated. The relative pressures in the SHELL calculations are somewhat larger than those of the SAP calculation. This difference follows naturally from the nature of the codes. In the SAP code, the  $r = 0$  point is tied to the center of the fireball throughout the entire calculation. The SHELL code, being a two dimensional code, can allow the fireball to rise through the mesh. The rising fireball prevents the shock from relieving backwards. This is particularly true

for megaton yield weapons which have a significant fireball rise velocity. For smaller yield weapons the effect would be less dramatic. The difference between the two calculations is greatest along the axis directly above the burst, while horizontally outward both codes give nearly the same values of pressure.

The most distinctive feature of this plot is the cross-over at 120 km. We interpret this cross-over as being due to a draining off of energy from the one dimensional acoustic shock energy into a two dimensional type of motion which the SAP calculation is not capable of describing.

In order to test Hines' theory even further we performed a special calculation in which an imaginary horizontal barrier was placed at 60 km altitude and extending from 80 km to the right boundary. It was not possible for any information to be transmitted through this barrier. Figure 8 shows a plot of relative pressure contours for the calculation with the barrier. This plot is made at the same problem time as Figure 5. The maximum relative pressures at these times are nearly identical and the character of the curves show very little difference. There was no way for the gravity wave disturbance to pass by line of sight from the burst point to its present position. The primary shock wave refracted around the barrier as would be expected. At later times, one would expect the intensity of the disturbance above the barrier would be diminished because approximately 2/5 of the problem energy is being removed. Indeed this is just what is observed at later times. The fact that the gravity wave disturbance developed at 100 km and propagated radially outward in spite of the barrier indicates that the energy did not propagate directly from the burst point.

One naturally wants to know what is so distinctive about this region of the atmosphere and how do the gravity waves form at this altitude. The 1962 U.S. Standard Atmosphere temperature has a very rapid increase at the 120 km level. In order to show that the generation mechanism is dependent on this steep temperature gradient, a calculation was run with an isothermal atmosphere above 90 km. The results of this calculation are shown in Figure 9. At 380 seconds the shock wave has reached an altitude of 200 km. The shock front shows no indication of flattening as the previous ones did. In fact there is no indication of any development at the 120 km level. This shock wave propagated on out with a hemispherical wave front and no indication of any disturbance developing behind it. As a further test of the influence of the temperature gradient on the region of formation of the long period gravity waves, we performed an additional calculation in which a model atmosphere was built with a large temperature increase at about 40 km and an isothermal region above the stratopause. In this calculation the gravity waves develop strongly at the region of maximum temperature increase. These two calculations indicate that the region of gravity wave formation is strongly dependent upon temperature and in fact the gravity waves do not develop in an isothermal atmosphere.

At about 120 km there is an interesting region of the atmosphere at which the Brunt-Vaisala frequency is greater than the acoustic cutoff frequency. This region of the atmosphere has recently received more attention [Tolstoy 1967; Johnston, 1967]. In order to get a better understanding of what is happening in this region of the atmosphere, we computed the local Brunt-Vaisala frequency in the disturbed region behind the shock wave. Two interesting effects were observed. Generally the altitude range over which the Brunt-Vaisala frequency exceeded the acoustic cutoff frequency was increased. In addition there was a region around 100 km where the Brunt-Vaisala frequency tended to be imaginary. Under the latter conditions the vertical wave number of simple wave theory would tend to become imaginary so that the gravity waves would be reflected from this region, or would lead to turbulence. While we do not want to place much emphasis on this point, the implication would be that gravity waves generated below this level would not reach the 120 km region.



## DISTURBANCES AT GREAT DISTANCES

The most serious limitations to the approach of this paper are those imposed by the storage capacity of the present day computers. Our computer allows us to use a mesh with 22,000 zones. The problem becomes one of arranging these cells in such a way as to cover the region of interest and still maintain a cell size which is sufficiently small to define the characteristic length scales of interest. Two approaches to this problem have been used in the calculations of this paper. In the first approach, an automatic rezone capability is utilized. In this case the mesh size automatically expands when the shock reaches the boundary of the mesh. Using this technique a majority of the available cells are always being used. This method works fine for following shock wave development. When gravity wave development at 120 km is being studied the method has its limitations. The rezone is still set by the advancing shock far up in the atmosphere. By the time the problem time has reached about 600 sec (Figure 6) only about one third of the mesh is being used to define the gravity wave region. As the vertical rezoning continues there is an artificial movement of mass upward in the grid so that densities as a whole are larger at a given altitude than would be found in the ambient atmosphere.

An additional effect is also operating to enhance the computed relative pressures in these regions. By these times the zone size at the bottom of the mesh has become large compared to the local pressure scale height. This means that a major part of the problem mass is contained in the bottom row of zones. Small instabilities in the bottom zone then tend to initiate additional shock waves which propagate upward, pumping additional energy into the disturbances at 120 km. While this is somewhat unfortunate as far as defining the amplitudes of the disturbances at 120 km, it does shed some light on the generation mechanisms, since this energy was continually pumped into the gravity-wave-like disturbance at 120 km. For these reasons, the calculations shown in Figures 2 through 6 lead to extremely large over pressures if carried to later times.

In order to overcome this entirely unrealistic growth problem, we have had to resort to a gimmick. First we introduced a transmissive upper boundary fixed at 290 km. For reasons which will be pointed out later this turned out to be an unfortunately low choice for following the propagation of the gravity waves at great distances. Next we used a variable vertical zone dimension with a zone size of about 0.1 km at the bottom increasing to about 6.0 km at the 290 km altitude. The problem was never rezoned vertically. After the problem was run about 1000 sec, we began to remove rows of cells from the bottom of the mesh, adding them to the right boundary. The upper zones were maintained with their original vertical dimensions and altitudes. After the mesh size reached 80 zones vertically by 252 zones horizontally, rezone to the right was used again.

Using this approach it has been possible to carry the calculation out to problem times of 1 hour and 20 minutes at which time the ionosphere was disturbed 3600 km from the burst point. At these times, values of maximum relative over pressure were less than 3.0. While these values are somewhat larger than most people would like to assume, they are a vast improvement over our first attempts.

In order to compare these calculations with observations, a model ionosphere has been assumed and local plasma frequencies computed as a function of space for a number of times. When these plots are combined with relative pressure, velocity, and vorticity plots, it is possible to identify the nature of the successive disturbances as well as to specify the arrival times of the various disturbance types at great distances from the burst axis. Table I is a brief summary of the arrival times at various distances of the disturbances. The first disturbance to arrive at a station is the primary shock front. For this reason the onset is very rapid as may be observed in  $f_oF_2$  observations [See, e.g., Kanellakos, 1967, "Group I" stations]. This first disturbance has traveled horizontally at a speed of about 750 m/sec.

In column three of Table I the arrival distances of the first gravity wave energy is identified for a few times. At 1200 seconds the center of the first gravity wave disturbance was calculated to about 250 km from the burst axis. By 1800 seconds the center of this disturbance has moved out to approximately 500 km suggesting a velocity of a little over 200 m/sec. Because of the circular motion of the gravity waves, mass is continually carried out of the top of the mesh and not replaced. For this reason the energy of a

gravity wave disturbance was slowly dissipated so that by 3000 seconds, we were no longer able to clearly identify them. For this reason the distances of first onset of the gravity wave disturbances in Table I are only shown out to 3000 seconds. In the automatically re-zoned problem, the gravity wave disturbance remained clearly distinct, but by these times the zone size had become so large that diffusion effects prevented a clear identification of the cell centers. Further, zone size problems tended to give an unreasonably large effective velocity to the gravity wave disturbances.

In spite of the limitations, these calculations have been able to effectively compute the onset times of the  $f_oF_2$  frequency fluctuations at distant stations. Even more important, it has been shown for the first time that the first and second  $f_oF_2$  fluctuations are fundamentally different. The first fluctuation is due to the acoustic shock wave. The second fluctuation is due to long period gravity waves. Finally, subject to the problems of following the gravity wave disturbance, the present calculations indicate that the gravity wave disturbance increases in altitude about 1 km for every 40 km that it travels horizontally.

### CONCLUSIONS

The most significant facts to be drawn from these calculations are that large computer calculations of the type presented in this paper can meaningfully predict the overhead shock arrival times and the onset of  $f_oF_2$  frequency fluctuations at great distances from the burst point. In addition the calculations have shown that the first  $f_oF_2$  surge is due to the primary acoustic shock wave, and the second surge is due to long period gravity waves. While the code to date has not been impressively successful at following the gravity wave disturbances, it has clearly shown that the generation occurs in the 120 km region of rapid temperature increase. Finally, the calculations have shown that this temperature incline is of fundamental importance to the generation process.

## APPENDIX

The equations solved in SHELL are the partial differential equations for nonviscous, non-conductive compressible fluid flow. These equations are the equations of conservation of mass, momentum and energy together with an appropriate equation of state. The SHELL calculation advances explicitly in steps or cycles. That is the cell quantities are calculated for time  $t + \Delta t$  in terms of those at time  $t$ . The time step is chosen to prohibit the transmission of a signal or mass across more than one zone in one time cycle. This requirement is imposed by consideration of stability of finite difference equations. After the time step has been determined SHELL performs the hydrodynamic calculations in two phases. This is done according to a finite difference approximation to the hydrodynamic equations. In the first phase the advective terms are omitted and the fluid is treated as if it were at rest with respect to the cell. The velocity and specific internal energy are advanced tentatively one time step according to the equations.

$$\frac{\partial \vec{u}}{\partial t} = - \frac{1}{\rho} \nabla p + \nabla \phi$$

and

$$\frac{\partial I}{\partial t} = - \frac{p}{\rho} \nabla \cdot \vec{u}$$

where  $\rho \equiv$  density in gms/cm<sup>3</sup>

$\vec{u} \equiv$  velocity in cm/sec

$p \equiv$  pressure in dynes/cm<sup>2</sup>

$I \equiv$  specific internal energy in ergs/gm

$t \equiv$  time in sec

$\phi \equiv$  potential of external force field in ergs/gm.

Two passes in succession are made through the first phase of the calculation of each cycle. In the first pass tentative new values of velocity are calculated for a full time step. The internal energy is updated by half a time step using the old velocities. In the second phase the new internal energy is updated another half a time step using tentative new velocities calculated in the first pass. The energy is treated in this fashion for considerations of stability as well as accuracy in the behavior of fluid entropy [Harlow, 1964]. If the internal energy in any cell becomes negative the code has the provision to integrate back to the previous time and decrease the time step. The total energy  $[E = I + 1/2 (u^2 + v^2)]$  of the system is conserved identically even in the finite difference scheme.

In the second phase, continuous mass transport is calculated according to the equation of mass conservation

$$\frac{\partial \rho}{\partial t} = - \nabla \cdot \rho \vec{u}$$

in a finite difference form. After the mass transferred over all faces of the cell has been determined the momentum and total specific energy associated with this mass are computed. Then by conserving both radial and axial momentum, the final new velocities are calculated. The total energy carried by the transported mass is subtracted from the donor cell and added to the re-

ceiver cell. Then by conserving total energy the new internal energy of each cell is the difference between the new total energy and the new kinetic energy. The new specific internal energy is the new internal energy divided by the new mass.

The equations used in the first phase of the calculations are unstable since they do not contain a dissipative mechanism necessary for a finite difference scheme to calculate shocks. Harlow [1964] has shown that the treatment of mass movement in the second phase of the calculation produces dissipative effects that gives stability to the calculation. It may be shown that by expanding the difference equations in a Taylor series about some central space in time, the resulting equations to first order in  $\Delta t$  are:

Conservation of mass

$$\frac{\partial \rho}{\partial t} + \frac{\partial (r\rho u)}{r\partial r} + \frac{\partial (\rho v)}{\partial z} = \frac{1}{r} \frac{\partial}{\partial r} \left( \frac{1}{2} \frac{r\lambda_u}{\rho} \frac{\partial \rho}{\partial r} \right) + \frac{\partial}{\partial z} \left( \frac{1}{2} \frac{\lambda_v}{\rho} \frac{\partial \rho}{\partial z} \right)$$

Conservation of momentum-r direction

$$\rho \frac{\partial u}{\partial t} + \rho u \frac{\partial u}{\partial r} + \rho v \frac{\partial u}{\partial z} + \frac{\partial p}{\partial r} = \frac{1}{r} \frac{\partial}{\partial r} \left[ r \lambda_u \frac{\partial u}{\partial r} \right] + \frac{\partial}{\partial z} \left[ \lambda_v \frac{\partial u}{\partial z} \right] + \frac{\lambda_u}{\rho} \frac{\partial \rho}{\partial r} \frac{\partial u}{\partial r} + \frac{\lambda_v}{\rho} \frac{\partial \rho}{\partial z} \frac{\partial u}{\partial z}$$

Conservation of momentum-z direction

$$\rho \frac{\partial v}{\partial t} + \rho u \frac{\partial v}{\partial r} + \rho v \frac{\partial v}{\partial z} + \frac{\partial p}{\partial z} + \rho g = \frac{1}{r} \frac{\partial}{\partial r} \left[ r \lambda_u \frac{\partial v}{\partial r} \right] + \frac{\partial}{\partial z} \left[ \lambda_v \frac{\partial v}{\partial z} \right] + \frac{\lambda_u}{\rho} \frac{\partial \rho}{\partial r} \frac{\partial v}{\partial r} + \frac{\lambda_v}{\rho} \frac{\partial \rho}{\partial z} \frac{\partial v}{\partial z}$$

Conservation of energy

$$\rho \frac{\partial I}{\partial t} + \rho u \frac{\partial I}{\partial r} + \rho v \frac{\partial I}{\partial z} + p \left[ \frac{1}{r} \frac{\partial (ur)}{\partial r} + \frac{\partial v}{\partial z} \right] = \frac{1}{r} \frac{\partial}{\partial r} \left( r \lambda_u \frac{\partial I}{\partial r} \right) + \frac{\partial}{\partial z} \left( \lambda_v \frac{\partial I}{\partial z} \right) + \lambda_u \left[ \left( \frac{\partial u}{\partial r} \right)^2 + \left( \frac{\partial v}{\partial r} \right)^2 \right] + \lambda_v \left[ \left( \frac{\partial u}{\partial z} \right)^2 + \left( \frac{\partial v}{\partial z} \right)^2 \right]$$

where  $\lambda_u = 1/2\rho|u|\Delta r$

$\lambda_v = 1/2\rho|v|\Delta z$

These equations are the same as the original hydrodynamic differential equations plus some additional terms that have the appearance of true viscosity and heat conduction terms. They are called effective viscosity and effective heat conduction. It has been shown [Bjork, et al., 1963; Papetti, 1964; and Kaplan et al., 1966] that any attempt to relate the terms appearing on the right hand side of the equations above to distinct physical effects leads to many contradictions. Moreover the values of these terms far exceed the magnitude of the analogous physical terms. Therefore these terms cannot be thought of as anything but errors but they do make SHELL a practical code.



## REFERENCES

- [1] Beynon, W.J.C., and E. Jones, Ionospheric effects of nuclear explosions, Nature, 196, 253-254, 1962.
- [2] Bjork, R., N. Brooks, and R. Papetti, A numerical technique for solution of multi-dimensional hydrodynamic problems, RM-2628-PR, Rand Corporation, Santa Monica, California, December 1963.
- [3] Brackbill, J. U., E.A. Nawrocki, and W.A. Whitaker, Atmospheric models for use in hydrodynamic computer codes, AFWL-TR-67-75, Air Force Weapons Laboratory, Kirtland AFB, New Mexico, August 1967.
- [4] Daniel, F.B., and A.K. Harris, Effects of atomic explosions on the ionosphere, Operation Snapper, WT-547, Signal Corps Engineering Laboratories, Fort Monmouth, N.J., January 1953.
- [5] Eckart, C., Hydrodynamics of oceans and atmospheres, Pergamon Press, New York, 1960.
- [6] Friedman, J.P., Propagation of internal gravity waves in a thermally stratified atmosphere, J. Geophys. Res., 71, 1033-1054, 1966.
- [7] Harkrider, D.G., Theoretical and observed acoustic-gravity waves from explosive sources in the atmosphere, J. Geophys. Res., 69, 5295-5321, 1964.
- [8] Harlow, F.H., The particle-in-cell computing method for fluid dynamics, in Fundamental Methods in Hydrodynamics (Methods in Computational Physics, Vol. 3, B. Alder, S. Fernbach, and M. Rotenberg, editors), 319, Academic Press, New York, 1964.
- [9] Hines, C.O., Internal atmospheric gravity waves at ionospheric heights, Can. J. Phys., 38, 1441-1481, 1960.
- [10] Hines, C.O., Atmospheric gravity waves: a new toy for the wave theorist, Radio Sci., 690, 375-380, 1965.
- [11] Hines, C.O., On the nature of traveling ionospheric disturbances launched by low altitude nuclear explosions, J. Geophys. Res., 72, 1877-1882, 1967.
- [12] Hines, C.O., and C.A. Reddy, On the propagation of atmospheric gravity waves through regions of wind shear, J. Geophys. Res., 72, 1015-1034, 1967.
- [13] Johnston, T.W., Atmospheric Gravity Wave Instability?, J. Geophys. Res., 72, 2972-2974, 1967.
- [14] Kanellakos, D.P., Response of the ionosphere to the passage of acoustic-gravity waves generated by low altitude nuclear explosions, J. Geophys. Res., 72, 4559-4576, 1967.
- [15] Kaplan, M.A., and R.A. Papetti, An analysis of the two-dimensional particle-in-cell method, RM-4876-PR, Rand Corporation, Santa Monica, California, September 1966.
- [16] Kohl, H., Acoustic gravity waves caused by the nuclear explosion on October 30th, 1961, in Electron Density Distribution in Ionosphere and Exosphere (E. Throne, Editor), North-Holland Publishing Co., Amsterdam, pp. 160-169, 1964.
- [17] Lamb, H., Hydrodynamics, Dover Publications, New York, 1945.
- [18] Midgley, J.E., and H.B. Liemohn, Gravity waves in a realistic atmosphere, J. Geophys. Res., 71, 3729-3748, 1966.

References (continued)

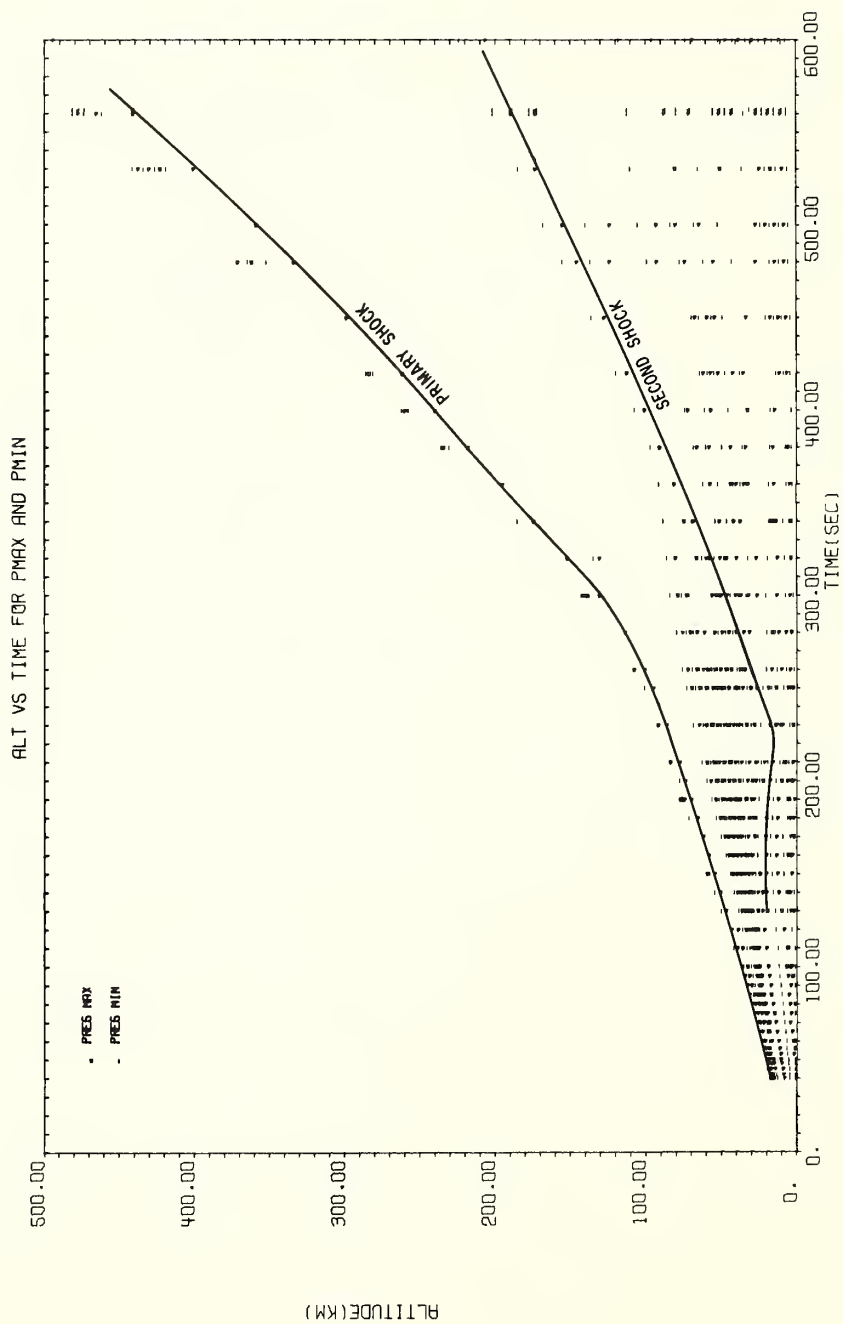
- [19] Obayashi, T., Wide-spread ionospheric disturbances due to nuclear explosions during October 1961, Rep. Iono. Space Res. Japan, 16, 334-340, 1962.
- [20] Obayashi, T., Upper atmospheric disturbances due to high-altitude nuclear explosions, Planet. Space Sci., 10, 47-63, 1963.
- [21] Papetti, R.A., An analysis of the particle-in-cell numerical process in one-dimensional problems, RM-3613-PR, Rand Corporation, Santa Monica, California, April 1964.
- [22] Pfeffer, R.L., and J. Zarichny, Acoustic-gravity wave propagation from nuclear explosions in earth's atmosphere, Geofis. Pura Appl., 55, 175-199, 1963.
- [23] Pierce, A.D., Propagation of acoustic-gravity waves from a small source above the ground in an isothermal atmosphere, J. Acoust. Soc. Am., 35, 1798-1807, 1963.
- [24] Press, F., and D.G. Harkrider, Propagation of acoustic-gravity waves in the atmosphere, J. Geophys. Res., 67, 3889-3909, 1962.
- [25] Stroffregen, W., Jonosfarstroningar Observerade I Samband Med Karnladdningsprov Vid Novaja Semlja Den 23 Och 30, FOA3-Rept. A517, Res. Inst. Natl. Defence, Electronics Dept., Stockholm 80, Sweden, May, 1962.
- [26] Tolstoy, I., The theory of waves in stratified fluids including the effects of gravity and rotation, Rev. Mod. Phys., 35, 207-230, 1963.
- [27] Tolstoy, I., Hydromagnetic gradient waves in the ionosphere, J. Geophys. Res., 72, 1435-1442, 1967.
- [28] Whitaker, W.A., E.A. Nawrocki, C.E. Needham, and W.W. Troutman, Theoretical calculations of the phenomenology of HE detonations, Vol. 1, AFWL-TR-66-141, Air Force Weapons Laboratory, Kirtland AFB, New Mexico, November 1966.
- [29] Wickersham, A.F., Jr., Comparison of velocity distributions for acoustic-gravity waves and traveling ionospheric disturbances, J. Geophys. Res., 70, 4875-4883, 1965.
- [30] Wickersham, A.J., Jr., Identification of acoustic-gravity wave modes from ionospheric range time observations, J. Geophys. Res., 71, 4551-4555, 1966.



TABLE I

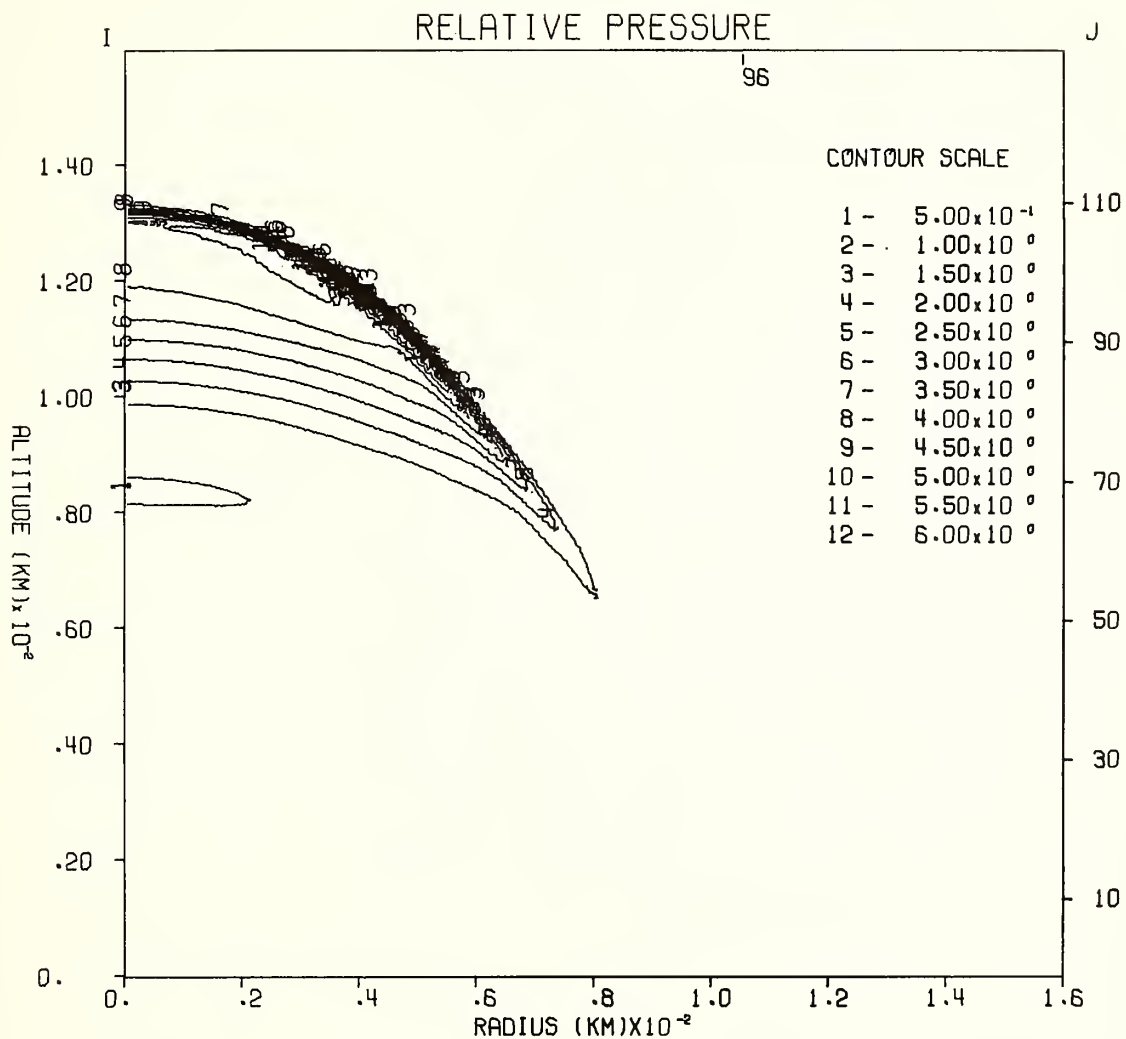
DISTANCES AT WHICH  $f_oF_2$  PERTURBATIONS DUE TO THE ACOUSTIC  
SHOCK WAVE AND GRAVITY WAVE DISTURBANCES ARE  
FIRST SEEN FOR A NUMBER OF TIMES.

<u>TIME</u>	<u>SHOCK WAVE</u>	<u>GRAVITY WAVE</u>
20 min	650 km	250 km
30 min	1100 km	375 km
40 min	1550 km	500 km
50 min	2000 km	---
60 min	2450 km	---
70 min	2900 km	---
80 min	3350 km	---



AFWAL SHELL CALC OF 4 MT AT SEA LEVEL (43.008)

Figure 1.



AFWL SHELL CALC OF 4MT SEA LEVEL ISOTHERMAL SPHERE.

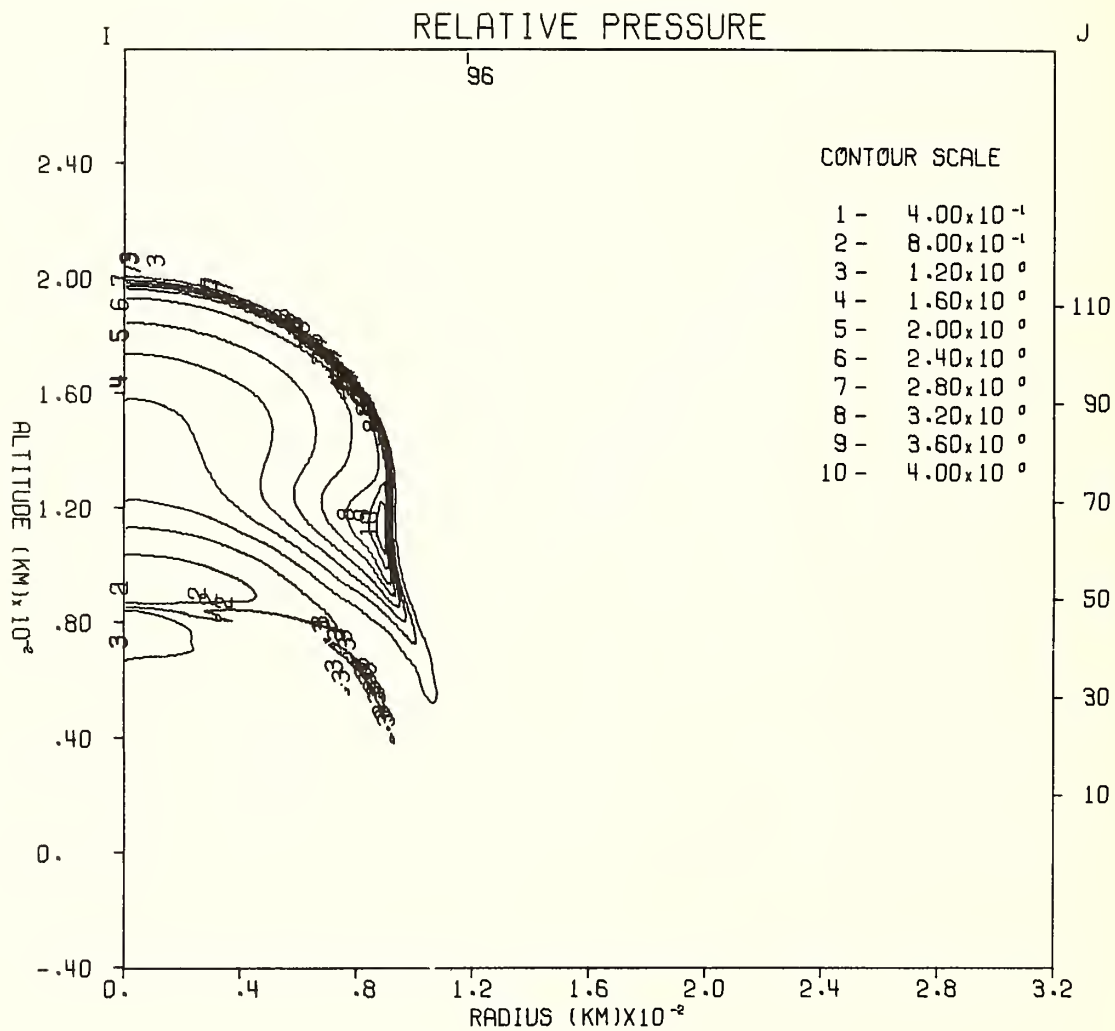
TIME 300.000 SEC

CYCLE 5938

PROBLEM

43.0080

Figure 2.



AFWL SHELL CALC OF 4MT SEA LEVEL ISOTHERMAL SPHERE.

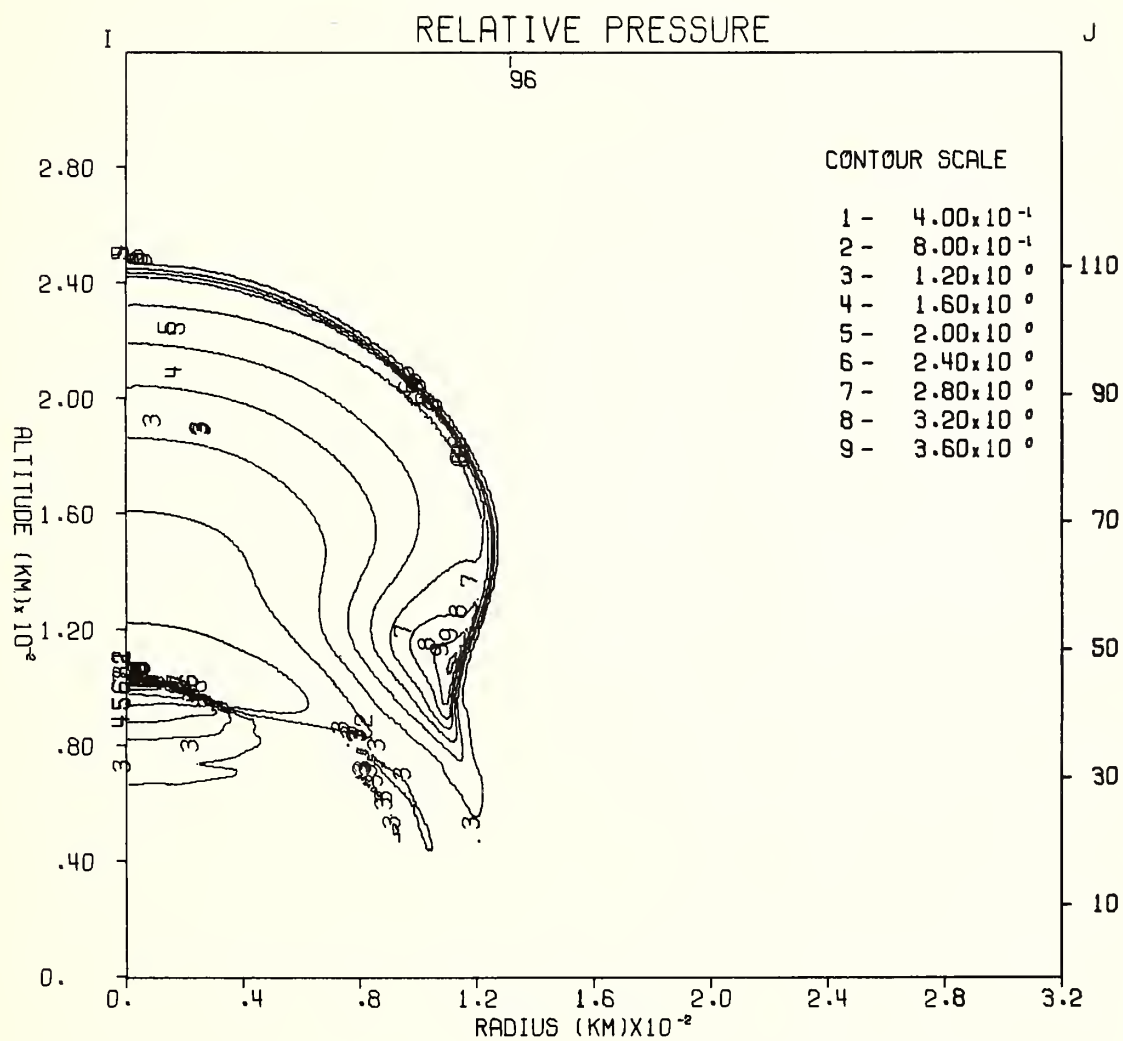
TIME 360.000 SEC

CYCLE 5999

PROBLEM

43.0080

Figure 3.



AFWL SHELL CALC OF 4MT SEA LEVEL ISOTHERMAL SPHERE.

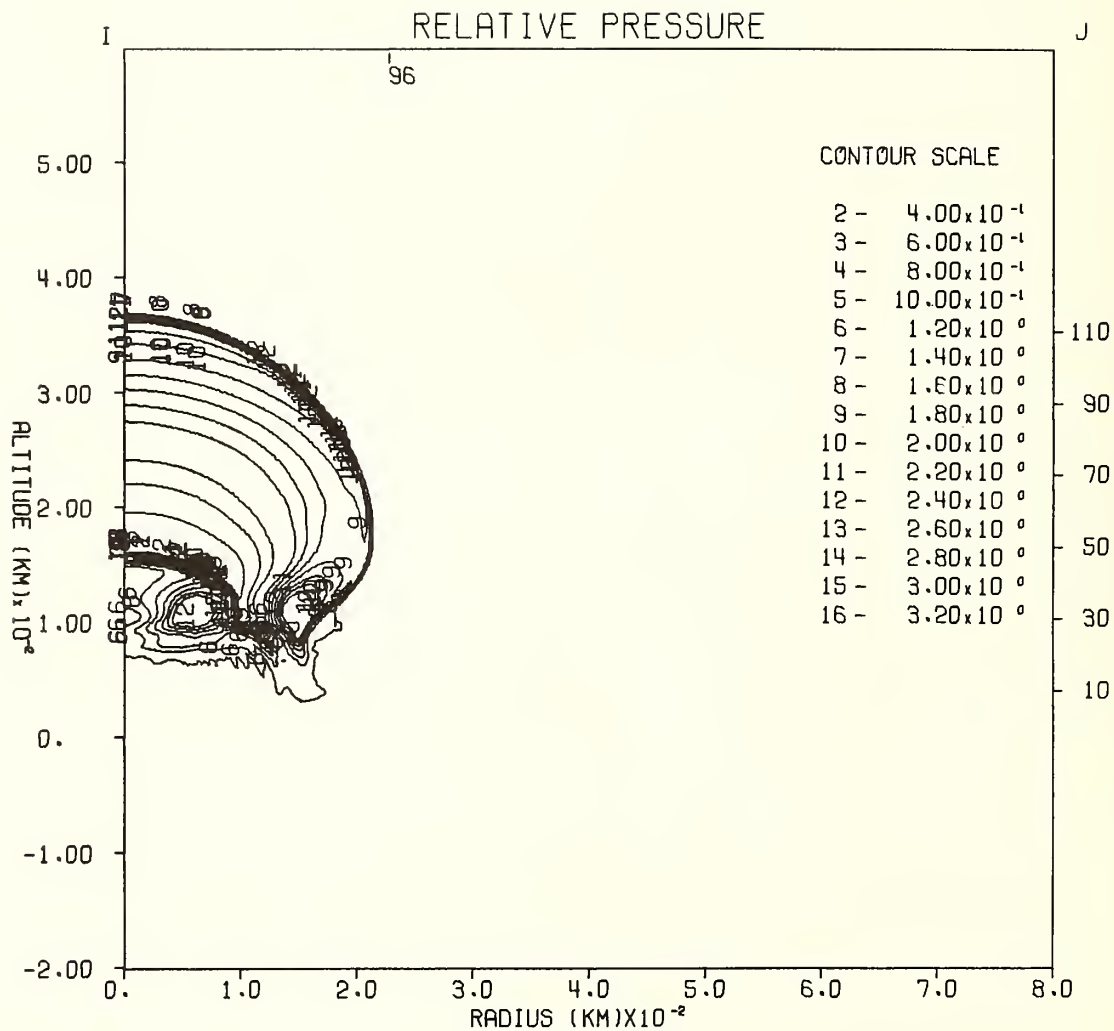
TIME 400.000 SEC

CYCLE 6039

PROBLEM

43.0080

Figure 4.



AFWL SHELL CALC OF 4MT SEA LEVEL ISOTHERMAL SPHERE.

TIME 500.000 SEC

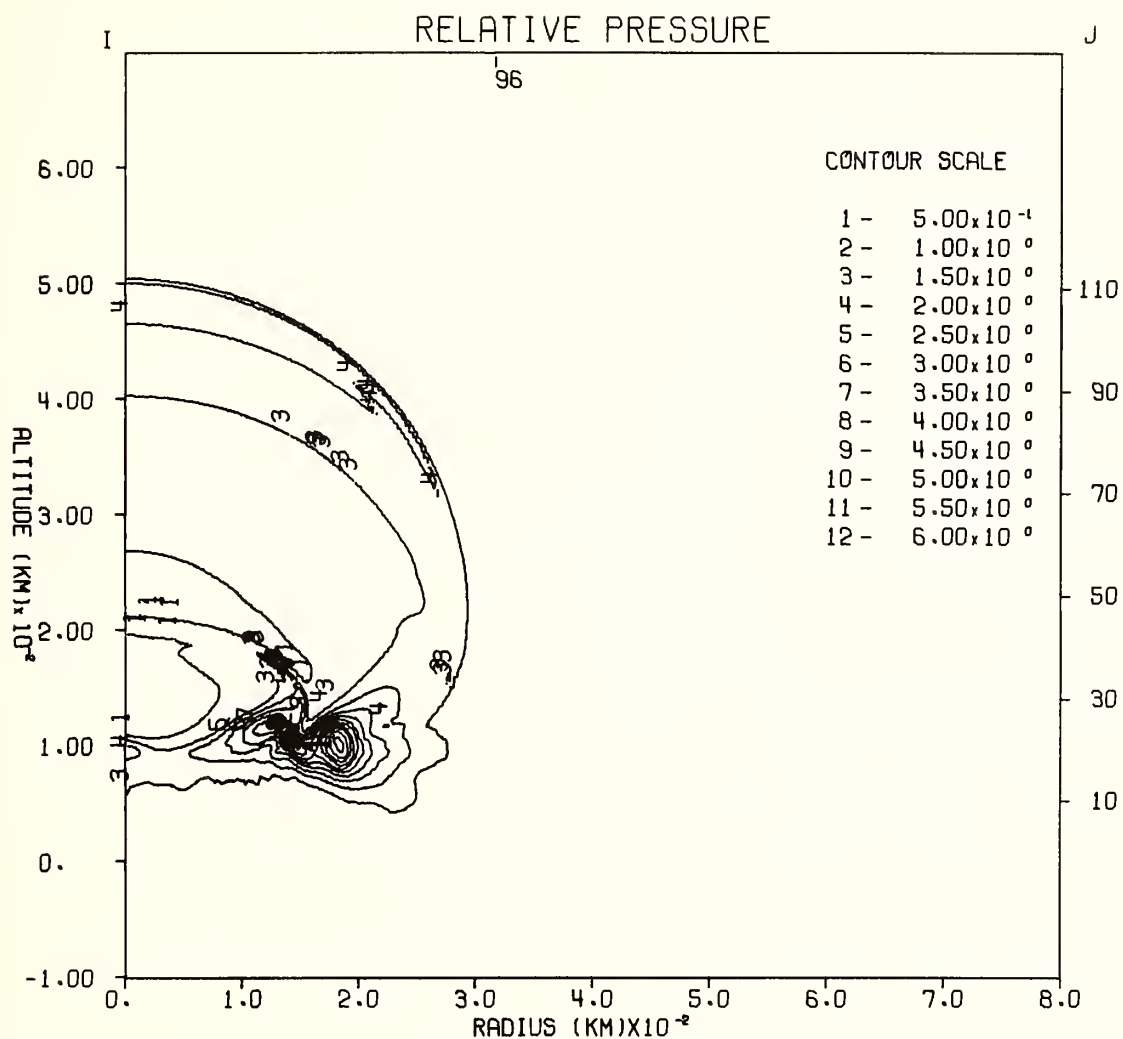
CYCLE 6117

PROBLEM

43.0080

Figure 5.





AFWL SHELL CALC OF 4MT SEA LEVEL ISOTHERMAL SPHERE.

TIME 600.000 SEC

CYCLE 6177

PROBLEM

43.0080

Figure 6.

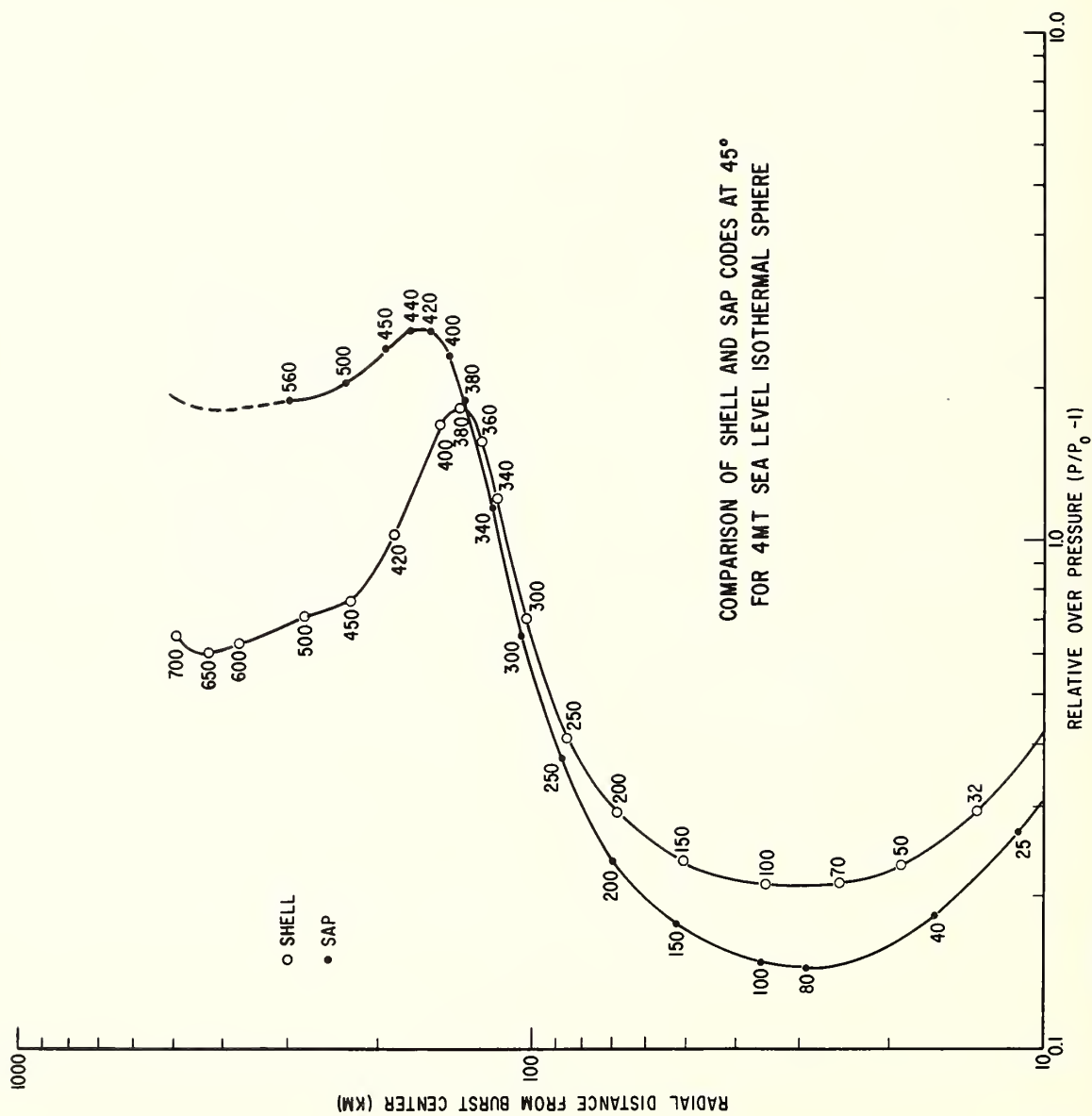
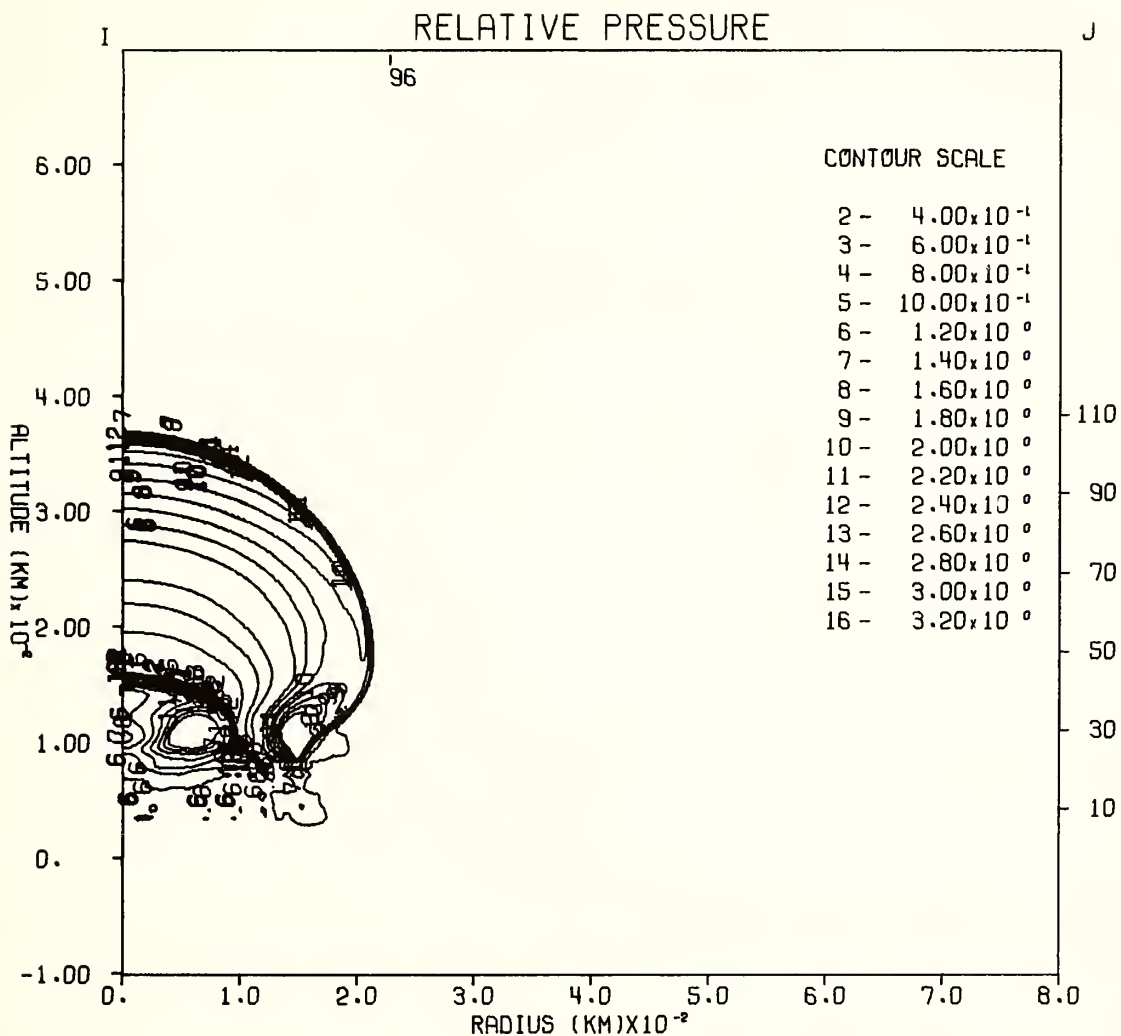
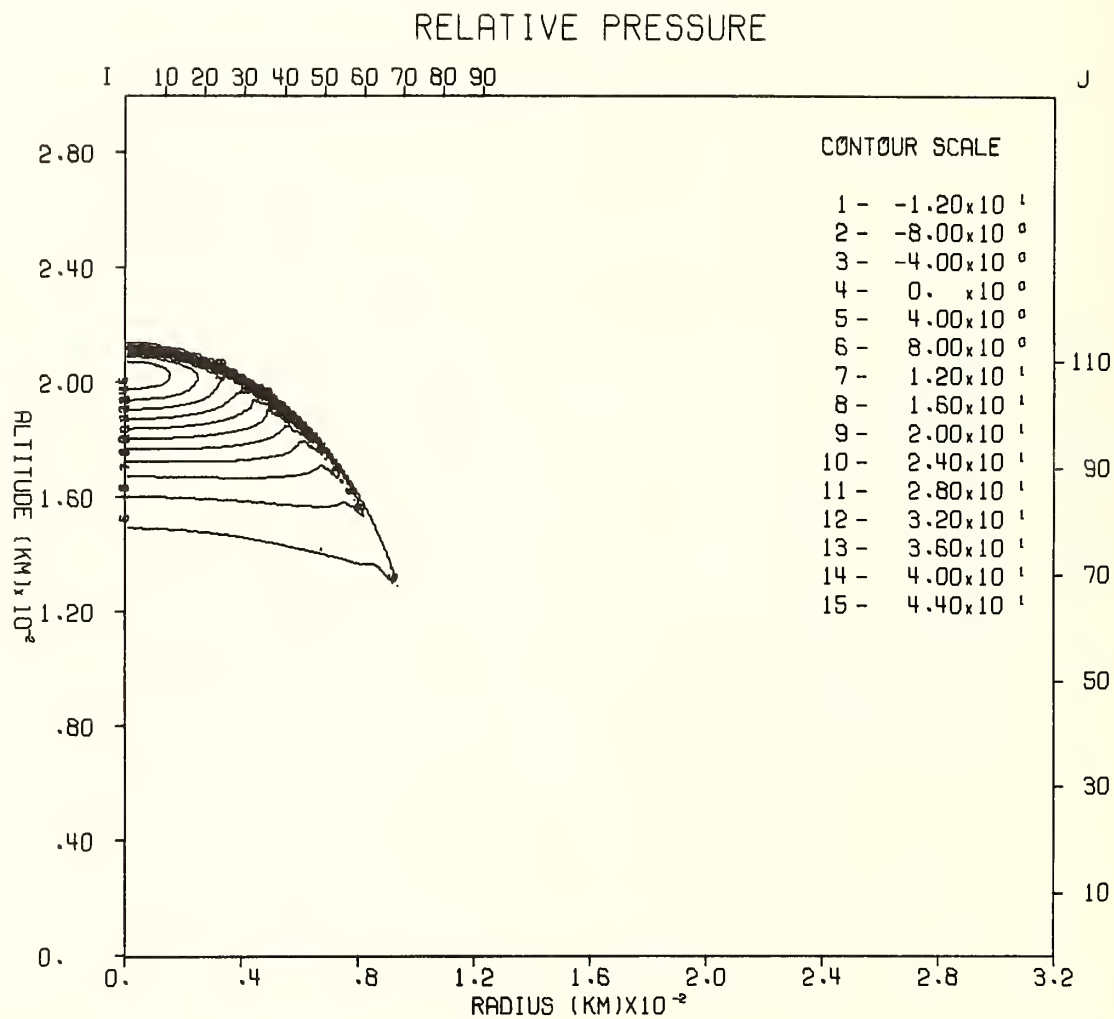


Figure 7.



AFWL SHELL CALC OF 4MT SEA LEVEL ISOTHERMAL SPHERE (BARRIER AT 60KM AND GT 80KI  
 TIME 500.000 SEC      CYCLE 6354      PROBLEM 43.0080

Figure 8.



AFWL SHELL CALC OF 4MT SEA LVL ISOTH SPHERE. ISOTH ATMOSPHERE ABOVE 90KM.  
 TIME 380.0 SEC CYCLE 5992 PROBLEM 43.0081

Figure 9.

## NOTE ON COMPRESSIBLE BORES\*

Wallace D. Hayes

Princeton University and Stanford Research Institute

In analogy with the classical bores or hydraulic jumps of classical hydrodynamics, bores can propagate in a stratified atmosphere. The calculations reported by Whitaker and Greene (1968) show a phenomenon reminiscent of a bore. The purpose of this note is to outline some of the properties such bores should have. Although compressible, they have certain properties in common with classical bores. In particular, they are nonlinear, and are dissipative and irreversible. When weak, they are related to the linear wave modes described by Harkrider (1968). One type of atmospheric bore has been mentioned by Lighthill (1967) as represented by the California Sierra Wave.

Compressible bores in a stratified atmosphere are nonlinear waves, which appear as discontinuities to a distant observer. As with classical bores, they have a structure which is dissipative. In the classical incompressible case, mechanical energy is conceptually separated from total energy, and the dissipation appears as a loss of this mechanical energy. In the atmospheric compressible case, this separation cannot conveniently be made, and total energy is conserved. The dissipation appears as an entropy increase.

Although viscosity and heat conduction provide the mechanisms for the eventual dissipation as measured by an increase in entropy, for either classical or compressible bores the direct action of viscosity or heat conduction is generally completely negligible. Two principal direct mechanisms are present in classical bores, with a third also present in compressible bores. These dissipative mechanisms are: (a) the creation of dispersive wavelets of high wave number behind the bore; (b) the production of turbulence; and (c) the entropy increase across shock waves. In weak classical bores, and presumably also in weak compressible bores, (a) is the principal mechanism. In considering strong compressible bores, we must keep in mind that turbulence in this case would be compressible turbulence, with part of the dissipative process the creation of shock waves. Thus, we should consider mechanism (c) associated with a quasipermanent shock wave system travelling with the bore. With a compressible bore, energy can also be transferred away from the bore in the form of internal acoustic-gravity waves.

We can expect a basic relation to hold between compressible bores and the linear modes treated by Harkrider (1968). The linear or weak wave limit of a compressible bore should correspond precisely, in wave propagation speed and mode shape, to the zero-wave-number limit of one of the "S" acoustic-gravity modes of Harkrider. This relation is suggested by the corresponding relation for classical bores.

Thus, a consideration of atmospheric compressible bores should start with gravity-acoustic waves, in particular in the limit of zero wave number. Gravity waves, either classical or in the atmosphere, are dispersive at finite wave number and nondispersive in the limit of zero wave number. At fixed wave number, there are a number of modes, each in general of different frequency and propagation speed. In the classical water-wave problem only one mode appears, but this is a consequence of the assumption of constant density with only a single discontinuity (or free) surface. A stratified incompressible liquid with several constant-density layers has several gravity-wave modes, while one with a continuous stable density distribution has an infinite number.

The manner of excitation of gravity waves which produces weak bores is one corresponding to a constant-velocity piston (either for planar waves or for axis-symmetric waves). The velocity of the piston may be a function of altitude, and is constant only in time. The amplitudes of the

---

\*Not presented at the Symposium, but included here because of its relevance to the previous paper.

modes excited depend on the particular function of altitude. The piston velocity must be small in comparison to the propagation speeds of the modes excited.

For the excited modes to separate from one another as distant weak bores travelling with different speeds, nonlinearity must play a part. Each bore has a structure, with a total width that varies roughly inversely as the square root of the amplitude. As the excitation becomes stronger with increasing piston velocity, the waves steepen into recognizable bores, with widths characteristic more of a vertical scale height than of the amplitude. In addition, bores which are distinct at low amplitudes may merge into a smaller number at larger amplitude. The structure of a bore, as well as its propagation speed, may depend upon the particular way in which it is excited.

The classical weak-bore or shallow-water wave speed is  $\sqrt{gh}$ , where  $h$  is the depth. In an atmosphere, an analogous wave generally has small amplitude below some characteristic altitude, and the propagation speed is approximately  $\sqrt{gh}$ , where  $h$  is the scale height at the characteristic altitude. But  $g$  times the scale height is also approximately the square of the speed of sound. Thus, the atmospheric weak-bore or small-wave-number propagation speed is approximately the speed of sound at the characteristic altitude. The maximum speed of sound in the atmosphere serves as an absolute upper bound for the propagation speed. The only lower bound is zero, and in a weakly stable atmosphere modes with propagation speeds far below the speed of sound can exist.

A bore must satisfy certain conservation relations. We assume that the atmosphere ahead of the bore is quiescent, without winds, and that the bore moves with velocity  $U$  from right to left. In the frame of reference of an observer also moving to the left with velocity  $U$ , the bore appears as a steady flow, as indicated in Figure 1.

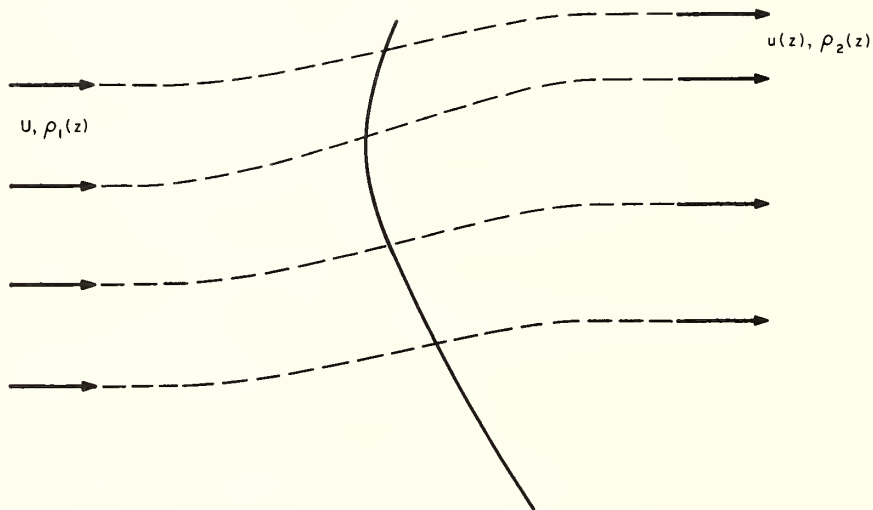


Fig. 1 ATMOSPHERIC COMPRESSIBLE BORE (SCHEMATIC)



Mass conservation is ensured by the condition

$$U \int_0^{\infty} \rho_1 dz = \int_0^{\infty} \rho_2 u dz \quad (1)$$

This condition is automatically ensured through the replacement of the altitude  $z$  as independent variable by the stream function  $\psi$  defined by

$$\psi = U \int_0^{\infty} \rho_1 dz = \int_0^{\infty} \rho_2 u dz \quad , \quad (2)$$

with the integrals--indefinite ones--equal to zero at the lower limit. The altitude  $z_1$  or  $z_2$  is then given by

$$z_1 = \frac{1}{U} \int_0^{\psi} \frac{d\psi}{\rho_1} \quad ; \quad z_2 = \int_0^{\psi} \frac{d\psi}{\rho_2 u} \quad . \quad (3)$$

The total mass flow, equal to the integrals of Eq. (1), is designated  $\psi_{\infty}$ .

Hydrostatic equilibrium is assumed to hold on both sides of the bore. Thus, we have

$$p_1 = g \int_0^{\infty} \rho_1 dz = \frac{g}{U} ( \psi_{\infty} - \psi ) \quad , \quad (4a)$$

$$p_2 = g \int_0^{\infty} \rho_2 dz = g \int_0^{\psi_{\infty}} \frac{d\psi}{u} \quad , \quad (4b)$$

with the integrals--negative indefinite ones--equal to zero at the upper limit. Conservation of horizontal momentum leads to the condition

$$\int_0^{\infty} p_1 dz + U^2 \int_0^{\infty} \rho_1 dz = \int_0^{\infty} p_2 dz + \int_0^{\infty} \rho_2 u^2 dz \quad , \quad (5)$$

or, after an integration by parts,

$$\frac{g}{U^2} \int_0^{\infty} d\psi \int \frac{d\psi}{\rho_1} + U \psi_{\infty} = g \int_0^{\infty} \frac{d\psi}{u} \int \frac{d\psi}{\rho_2 u} + \int_0^{\infty} u d\psi \quad . \quad (6)$$

Conservation of energy leads to the condition

$$\int_0^{\infty} (h_1 + \frac{g}{U} \int \frac{d\psi}{\rho_1} d\psi + \frac{1}{2} U^2 \psi_{\infty} = \int_0^{\infty} (h_2 + \frac{1}{2} u^2 + g \int \frac{d\psi}{\rho_1 u} d\psi \quad . \quad (7)$$

The second law of thermodynamics may be expressed

$$\int_0^{\infty} S_1 d\psi \leq \int_0^{\infty} S_2 d\psi , \quad (8)$$

with equality holding only in the limit of very weak bores. If there is no turbulent mixing in a range of  $\psi$ , the stream function  $\psi$  serves as a Lagrangian "label" for the material in the flow. Then, Eqs. (7) and (8) hold in a stronger form:

$$h_1(\psi) + \frac{1}{2} U^2 + gz_1(\psi) = h_2(\psi) + \frac{1}{2} u^2(\psi) + gz_2(\psi) , \quad (9)$$

and

$$S_1(\psi) \leq S_2(\psi) . \quad (10)$$

In a portion of the flow in which the dissipation is negligible, such as low in the atmosphere for a high-altitude bore, the equality in Eq. (10) may be used.

The conservation conditions given above are simply global conditions which must be met by a steady two-dimensional bore. The principal condition for the existence of a bore is the existence of a solution for the detailed structure of the flow. We can expect that, with the bore speed  $U$  given, there should be a continuous family of solutions with different structures, corresponding to some continuous family of excitation of downstream boundary conditions.

With particular reference to the ionosphere, considered as the high-temperature region above the low-temperature mesopausal acoustic duct, there is a low-wave-number gravity-wave mode whose main motion is in the ionosphere and whose propagation velocity is approximately the speed of sound there. Corresponding bores should exist, with propagation speeds higher than that of the linear gravity wave. Some experimental evidence of these bores exists, and the calculations reported by Whitaker and Greene (1968) indicate that they may be initiated by an explosion in the lower atmosphere. Bores of this type, propagating outward radially from a center, should be attenuated by the radial (cylindrical) divergence and by the effect of rarefaction gravity waves catching up with the bore. For there to be no attenuation with this geometry, the excitation would have to come from an equivalent of a radial piston with constant velocity or a source whose strength increases linearly with time.

Acknowledgment The research reported here was supported by the Advanced Research Projects Agency, Washington, D.C. through the Office of Naval Research, under contract No. Nonr 4913(00), ARPA Order 215.

#### REFERENCES

- Whitaker, W. A., and J. S. Greene, Jr., Theoretical calculations of shock arrival times at ionospheric heights for low altitude nuclear tests, Proc. ESSA/ARPA Symposium on Acoustic-Gravity Waves, ESSA Research Labs., Boulder, Colorado, 1968.
- Harkrider, D. G., The excitation and dispersion of the atmospheric surface wave, Proc. ESSA/ARPA Symposium on Acoustic-Gravity Waves, ESSA Research Labs., Boulder, Colorado, 1968.
- Lighthill, M. J., Waves in fluids, Comm. Pure Appl. Math., 20, 267-293, 1967.

# Propagation Velocity of Acoustic Gravity Wave due to Large Nuclear Explosion

RYOZABURO YAMAMOTO  
Kyoto University, Kyoto

Distribution of propagation velocities of the primary wave  $A_1$  and the returning one  $B_1$  due to the Soviet nuclear explosion, October 30, 1961 is examined over Northern Hemisphere, using the isochrone maps of wave arrival by Wexler and Hass[1962]. The wind effects may be excluded from the mean propagation speed of the both waves, confirming that the both waves have the opposite propagation direction and that there is no appreciable time change in structure of the atmosphere. Over large part of the area analyzed here, the mean speed is in the range from 275 m/sec to 350 m/sec. The values of mean speed higher than 350 m/sec over central Pacific and lower than 275 m/sec over Arctic region and off England are not easily explained with the observed temperature structure up to the lower stratosphere. Difference of the propagation speed between  $A_1$  and  $B_1$  wave gives the wind-induced increment of velocity, which exceeds 50 m/sec over Davis Strait and 20 m/sec north of West Indies. Such wind distribution that may give these velocity increments cannot be found in the layer below the height of 25 km.

## INTRODUCTION

A gigantic nuclear explosion by the Soviet Union on October 30, 1961 has generated a quite remarkable barometric wave, which could be traced over a large portion of the world, even the wave returning after passing through the antipode. Wexler and Hass[1962] have attempted a world-wide collection of barograms and illustrated a global feature of the wave propagation with the aid of maps of arrival time of the primary wave  $A_1$  and the returning one  $B_1$ . Another example of similarly remarkable barometric wave of more intensity had been caused by Krakatoa eruption in 1883. It had been detected that the wave went round the globe three times or more, and the global features of its propagation were illustrated on the isochrone maps of wave travel by Symons[1888], basing upon the barograms at about 50 stations. Noticing that the isochrones of the returning wave assumes a non-circular shape in the vicinity of Karakatoa, Taylor[1929] has attributed such shape to horizontal distribution of the prevailing winds rather than that of the air temperature. More accurate and more detailed information of propagation of the wave due to the Soviet explosion in 1961 can be anticipated than that of Krakatoa eruption, because of much increase of the observing stations since the last century. Actually, Wexler and Hass[1962] have collected the barograms of approximately 1000 stations or ships. This makes the present author to attempt a detailed analysis of the isochrone maps presented by Wexler and Hass.

## HEMISPHERICAL DISTRIBUTION OF PROPAGATION VELOCITY OF THE WAVE DUE TO THE SOVIET EXPLOSION ON OCTOBER 30, 1961

Isochrone maps of the wave travel presented by Wexler and Hass[1962] are analyzed from the viewpoint of delineating quantitatively the large-scale features of the propagation. For the area north of 20°N except the vicinity of the North Pole and the explosion site, the arrival times of  $A_1$  and  $B_1$  wave are read at the points of every 10 degree latitude and 10 degree longitude. Averaging the times zonally

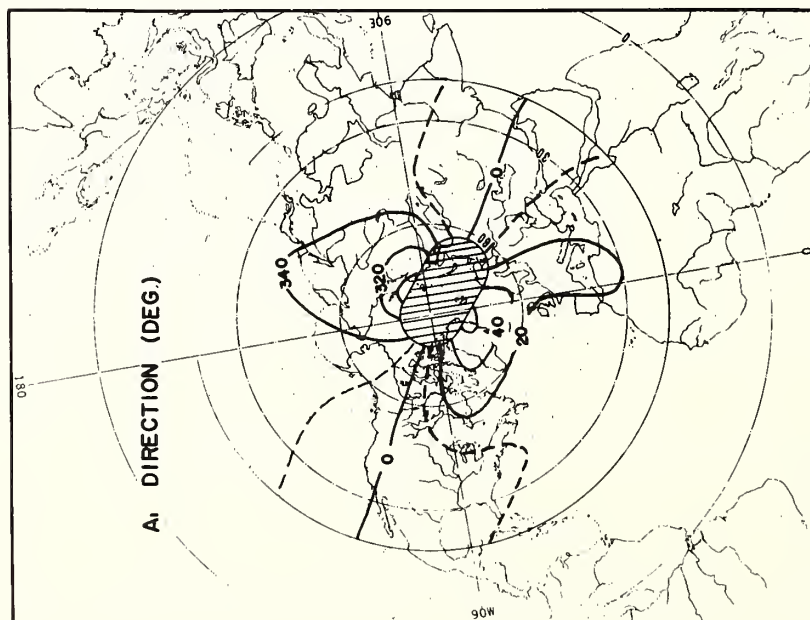


Fig.1. Distribution of propagation direction of the primary wave( $A_1$ ), in degree.

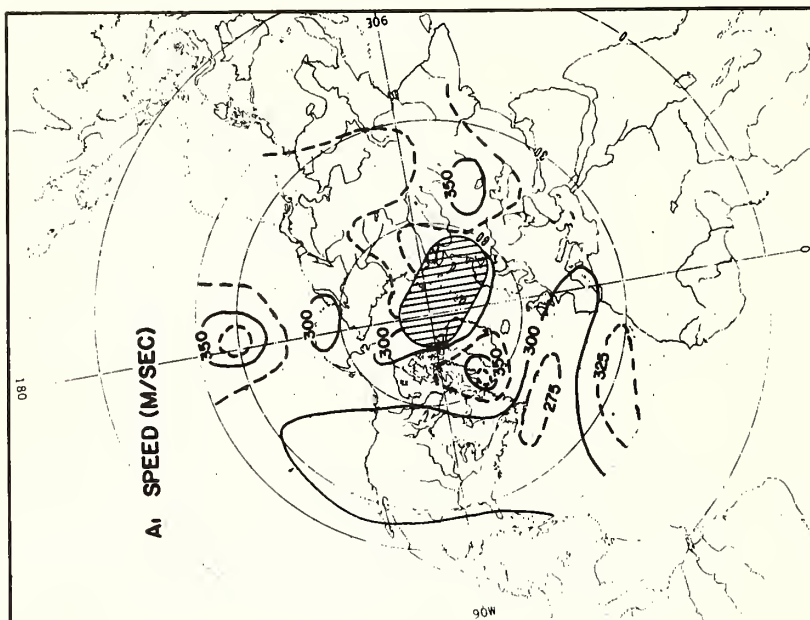


Fig.2. Distribution of propagation speed of the primary wave( $A_1$ ) in m/sec.

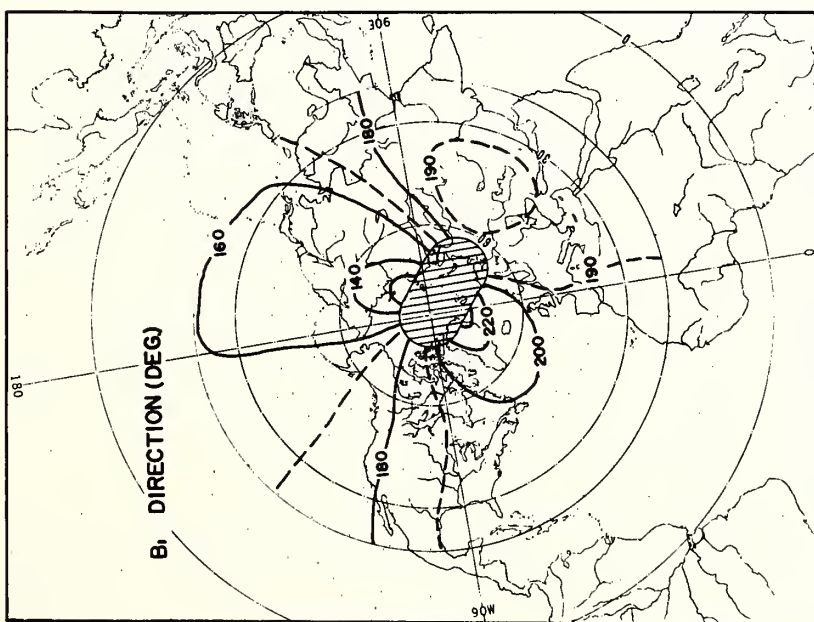


Fig.3. Distribution of propagation direction of the returning wave( $B_1$ ), in degree.

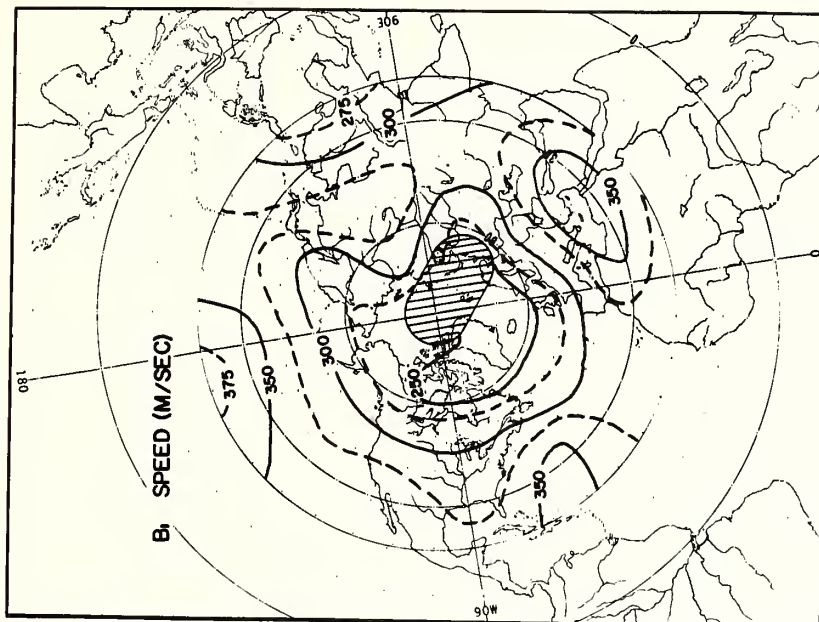


Fig.4. Distribution of propagation speed of the returning wave( $B_1$ ) in m/sec.



over 30 degree longitude, the speed and the direction of propagation are calculated. Their distributions are given in Figs. 1, 2, 3 and 4. Here, the propagation direction is expressed in the same way as the wind direction in meteorology.

TABLE 1. Longitudinally Averaged Speed of the Primary Wave( $A_1$ ) and the Returning Wave( $B_1$ ) in m/sec.

Lat( $^{\circ}$ N)	80	70	60	50	40	30	20	80-20	North Pole ↔ South Pole
$A_1$	295	318	321	308	309	317	316	314	320
$B_1$	249	265	271	295	328	333	324	308	308
Mean of $A_1$ and $B_1$	272	292	296	302	319	325	320	311	314

The general feature of propagation direction of the both waves is such that the waves progress along the great-circle path. Some appreciable deviations from the path, however, are seen for  $B_1$  wave over central part of Eurasia. Propagation speeds of the both waves are, in the most part of the area analyzed here, in the range from 250 m/sec to 350 m/sec. Speed higher than 375 m/sec can be found near Midway Island, central Pacific and over Davis Strait for  $A_1$  wave, and south of Midway Island for  $B_1$  wave. Over Arctic region from northern Canada to Scandinavia, the speed of  $B_1$  wave is lower than 250 m/sec. A general tendency of decreasing speed with increasing latitude is noticed for  $B_1$  wave, although it is not so clear for  $A_1$  wave. Such tendency is clearer for the longitudinally averaged speed given in Table 1, which includes the speed averaged over the area from 20°N to 80°N and the mean speed from North Pole to South Pole and vice versa. The mean speed of  $A_1$  and  $B_1$  waves over the area concerned here is about 311 m/sec, and almost equal to Wexler and Hass' value of 310 m/sec determined by use of the successive transit times at stations where the data are highly reliable. The mean speed of  $A_1$  and  $B_1$  waves from pole to pole is 314 m/sec, and agrees approximately with that of Krakatoa wave (310 m/sec). From analysis of microbarograms at 9 stations for  $A_1$ ,  $B_1$  and  $A_2$  waves, Donn and Ewing [1962] give the speed of 324 m/sec, which is larger than the values presented here by about 3 per cents.

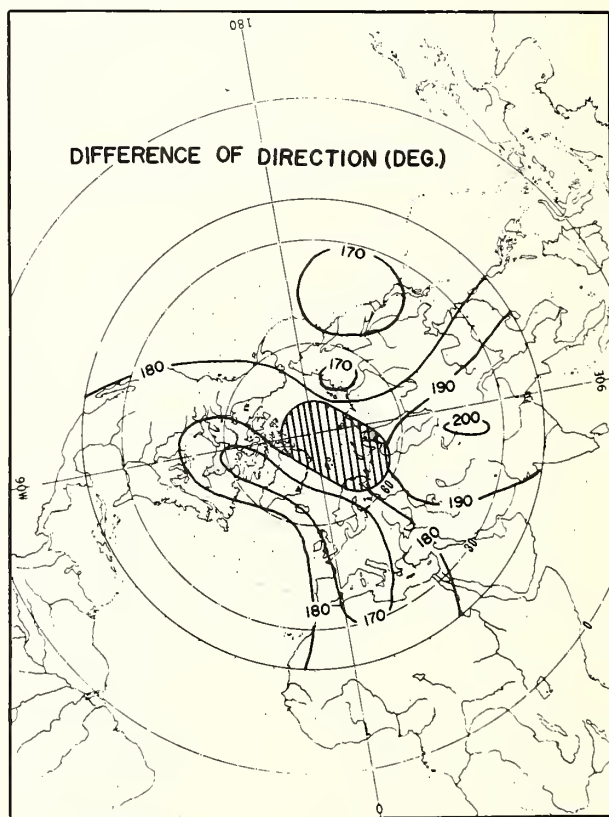


Fig. 5. Deviation of the propagation direction of the primary wave( $A_1$ ) from that of the returning wave( $B_1$ ) in degree.

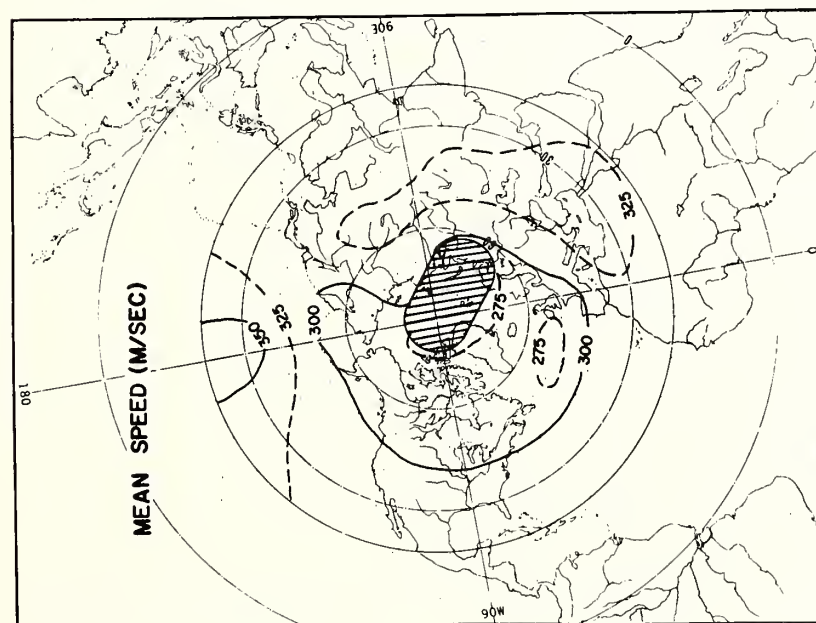


Fig.6. Distribution of the mean speed of the primary wave( $A_1$ ) and the returning wave( $B_1$ ) in m/sec.

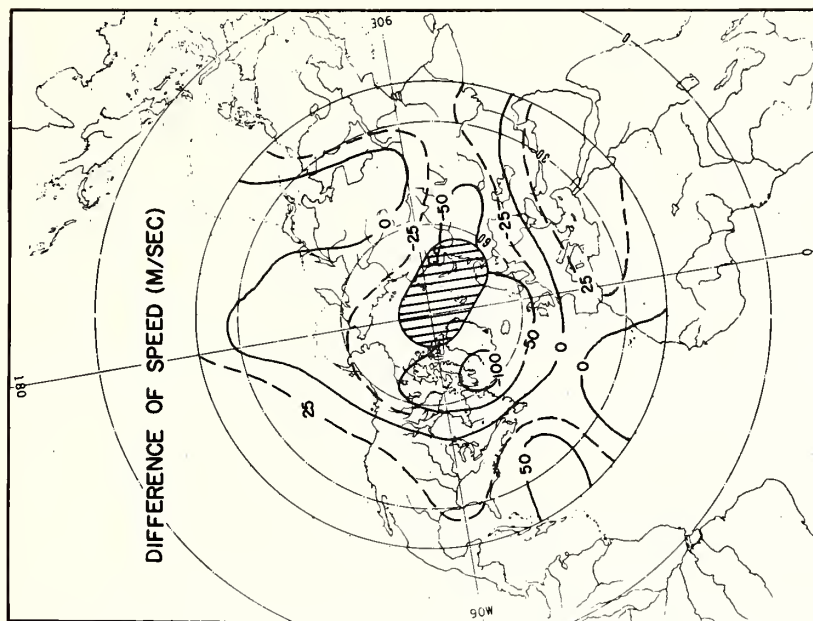


Fig.7. Difference of speed between the returning wave( $B_1$ ) and the primary wave( $A_1$ ) in m/sec.

Fig.5 shows the distribution of deviation of the propagation direction of  $A_1$  wave from that of  $B_1$  wave. Isogonal line of 180 degree means that the propagation directions of the both waves are exactly opposite, and lines of 190 degree and 170 degree that the both directions deviate each other by 10 degree. Although the angle of deviation is smaller than 10 degree over large portion of the area, larger deviations are found over a banded area extending from Baffin Island to Europe, central part of Eurasia and northeast of Japan. Deviation larger than 20 degree is noticed over Tibetan Plateau. This might be perhaps some influence of mountain range, which was suggested by Wexler and Hass[1962]. Since the deviation is not so large, arithmetic mean of the speeds of  $A_1$  and  $B_1$  wave has an implication of mean propagation speed, the distribution of which is given in Fig.6. In the greater part of the area, the mean speed is in range from 275 m/sec to 350 m/sec. The speed higher than 350 m/sec is found near Midway Island, and the speed lower than 275 m/sec off England and over Arctic region. In this distribution, the general tendency of increasing speed with decreasing latitude is clearly seen. Distribution of the difference of speed between  $B_1$  and  $A_1$  waves is given in Fig.7. Although the difference is, in general, smaller than 50 m/sec, larger differences are seen over northern Canada, northeast Europe and north of West Indies.

#### DISCUSSIONS

Theoretical treatments of the propagation of acoustic gravity waves have recently been made by many authors for various models of the atmosphere, taking particular interests on the dispersive characters[e.g., Press and Harkrider, 1962; Pfeffer and Zarichny, 1962, 1963; Harkrider, 1964; Pierce, 1966; MacKinnon, 1967, 1968]. The results of these treatments may be available for examining the features of the wave propagation described in the previous section. A theory[Pierce, 1966] predicts that the early-arriving detectable signals are associated with the  $GR$  mode with period of several minutes, the  $S_0$  mode with period of a few minutes and the

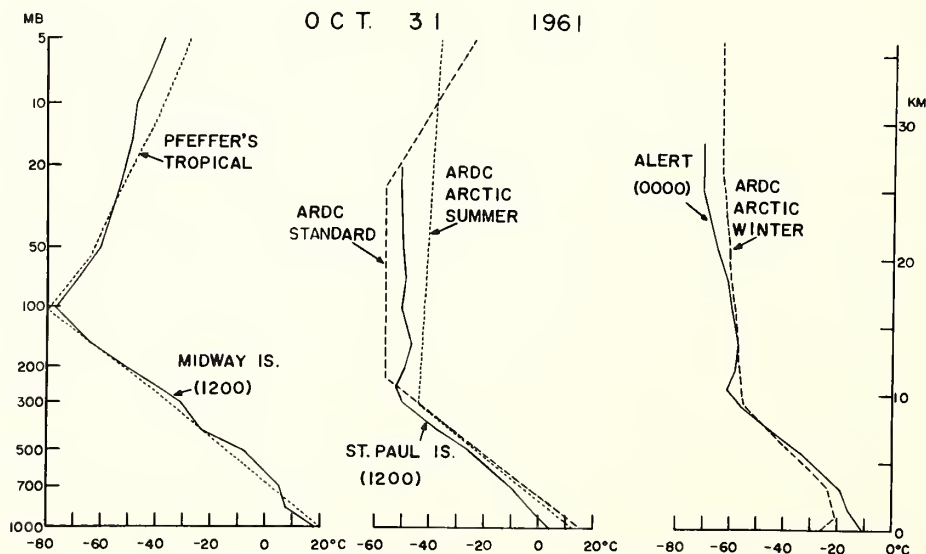


Fig.8. Temperature profiles at Midway Island, St. Paul Island and Alert on October 31, 1961. Numeral in bracket signifies the observational time in UT. Profiles of several model atmosphere are also given, for which Press and Harkrider[1962] and Pfeffer and Zarichny[1963] have given the numerical values of the group velocity.

$S_1$  mode with period less than a few minutes. The largest group velocity for the  $GR_0$  mode is larger than those of the latter two modes. It may be reasonable to presume that the phase taken by Wexler and Hass[1962] may be associated with the  $GR_0$  mode. For a particular model atmosphere, Pierce[1966] has obtained a conclusion that for the  $GR_0$  mode with period longer than 5 minutes and for the  $S$  mode with period from 2.5 minutes to 4 minutes, the wind effect to the wave propagation is normal and the wind-induced increment of group velocity holds the so-called cosine law.

Assuming that structure of the atmospheric layer effective to group velocity of the  $GR_0$  mode does not appreciably change for interval between the transit times of  $A_1$  and  $B_1$  waves, the wind effects should be eliminated in the field of the mean propagation speed of  $A_1$  and  $B_1$  waves illustrated in Fig.6. And the temperature structure in the atmospheric layer below the height of 50 km must govern the pattern of this mean speed [Press and Harkrider, 1962], to which the theoretical results for windless model may be applied. Fig.6 shows a remarkable variation of the mean speed along the 180 degree meridian, with the speeds higher than 350 m/sec near  $30^\circ N$  and lower than 275 m/sec near Arctic region. Although Wexler and Hass[1962] mentioned that the fast speed over central Pacific was somewhat less well supported, this high speed was too remarkable to be attributed only to the error, being noteworthy for some detailed discussions.

Fig.8 shows the temperature profiles observed by radiosonde at Midway Island, central Pacific ( $28^\circ 13' N$ ,  $177^\circ 22' W$ ), St. Paul Island near Aleutain Islands ( $57^\circ 09' N$ ,  $170^\circ 13' W$ ) and Alert, Arctic region ( $82^\circ 30' N$ ,  $62^\circ 20' W$ ), in the vicinity of which the mean propagation speed is higher than 350 m/sec, nearly equal to 295 m/sec and lower than 275 m/sec, respectively. The temperature profiles of several model atmosphere are also given in Fig.8, for comparison. The temperature structure below the height of 25 km at Midway Island does roughly agree with that of Pfeffer and Zarichny's model[1963], within several degree centigrade, for which they have given maximum group velocity of the  $GR_0$  mode of 315 m/sec. This is smaller than the observed one in the vicinity of Midway Island by more than 10 per cents.

Such disagreement is too large to be explained with the difference between the actually observed temperature and that of the model. The temperature profile at St. Paul Island is intermediate between those of ARDC

Standard Atmosphere and ARDC Arctic Summer Atmosphere, except systematic lower-temperature in the troposphere.

The maximum group velocity of the  $GR_0$  mode falls in the range from 311 m/sec to 313 m/sec [Press and Harkrider, 1962].

Difference of the velocity between the calculated and the observed is nearly equal to 5 per cents, and may probably be diminished by taking account of the observed lower-temperature in the troposphere.

Alert temperature profile is somewhat higher than that of ARDC Arctic Winter Atmosphere in the troposphere and somewhat lower in the stratosphere. The maximum group velocity of 302 m/sec is given to the  $GR_0$  mode for the model by Press and Harkrider[1962], and this value is larger than the observed one near Alert by about 10 per cents.

It cannot be anticipated for this difference to be diminished by taking account of the temperature difference

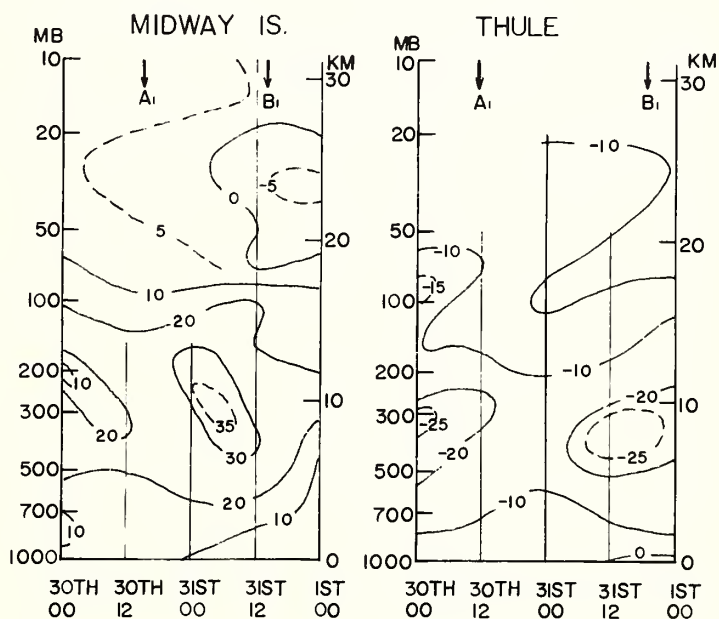


Fig.9. Time sections of the wind component in the propagation direction of  $A_1$  wave at Midway Island and Thule, in m/sec. The arrows show the transit times of  $A_1$  and  $B_1$  waves.



between the actual and the model atmosphere.

If the prevailing winds in the atmosphere vary appreciably from the transit time of  $A_1$  wave to that of  $B_1$  wave, the wind effects might be remained in the value of mean propagation speed. Fig.9 is the time sections of the wind components in the propagation direction of  $A_1$  wave at Midway Island and Thule, Greenland ( $76^{\circ}34'N$ ,  $68^{\circ}49'W$ ), in the vicinity of which the propagation direction of  $B_1$  wave is almost exactly opposite to that of  $A_1$  wave. At Midway Island, the time change of the wind component at each level from the transit time of  $A_1$  wave to that of  $B_1$  wave is 10 m/sec or less below the height of 30 km, which gives at most an increment of 5 m/sec to the mean propagation speed. This increment does not essentially affect the fast mean speed near Midway Island. The time change of wind component at Thule is less than that at Midway. Small value of the mean

propagation speed near Thule (275 m/sec) is not substantially modified by this wind change. The above discussions imply that comprehensive interpretation of the observed mean propagation speed needs to take the temperature structure in the upper stratosphere into consideration, referring to Harkrider's [1964] conclusion that the high temperature region at the height of about 50 km controls the early-arriving gravity modes. And the great spatial variation of the mean speed suggests remarkable variation of the temperature in the upper stratosphere.

From the reasoning mentioned in the first part of this section, it may be considered that the difference of speed between  $B_1$  and  $A_1$  waves represents twice of the effective wind component along the wave propagation direction. Remarkable variation of the speed difference can be noticed along  $70^{\circ}W$  meridian.  $B_1$  wave has, just north of West Indies, speed higher than that of  $A_1$  by 50 m/sec or more, and the lower speed by 100 m/sec or more over Davis Strait. Pierce [1966] and MacKinnon [1968] have concluded that the speed of initial long-period wave depends mainly on the wind structure below the height of 25 km or 20 km.

Fig.10 is  $70^{\circ}W$  meridional cross-section of the geostrophic wind component in the propagation direction of  $B_1$  wave. Such wind structure that can illustrate at least qualitatively the speed difference cannot be found below the height of 25 km. Above this height, the positive component of wind at lower latitude and negative one at higher latitude appear, the senses of which agree with those of the wave speed difference.

This shows, together with the discussions on the temperature structure, that comprehensive analysis of the global propagation of acoustic gravity wave should be made by taking account of the atmospheric structure, at least, up to the upper stratosphere. Since the world-wide network of meteorological rocket observation is not yet established, it is not easy to obtain the hemispherical structure of the upper stratosphere with the aid of conventional synoptic method of rocket data analysis. To understand sufficiently the wave propagation in question is one of

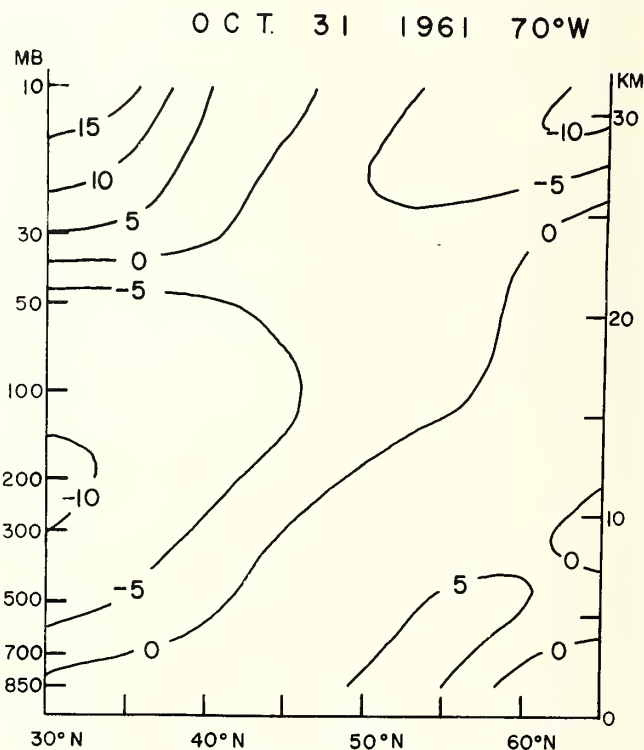


Fig.10. Meridional cross-section along  $70^{\circ}W$  of the geostrophic wind component in propagation direction of  $B_1$  wave in m/sec.



problems in the future, after the large-scale structure of the upper stratosphere will be speculated with some appropriate method[e.g., Yamamoto, Kawahira and Iwashima, 1968].

#### REFERENCES

- Donn, W.L., and M. Ewing, Atmospheric waves from nuclear explosions—Part II: Soviet test of 30 October 1961, J. Atmospheric Sci., 19, 264-273, 1962.
- Harkrider, D.G., Theoretical and observed acoustic-gravity waves from explosive sources in the atmosphere, J. Geophys. Res., 69, 5295-5320, 1964.
- MacKinnon, R.F., The effects of winds on acoustic-gravity waves from explosions in the atmosphere, Quart. J. Roy. Meteorol. Soc., 93, 436-454, 1967.
- MacKinnon, R.F., Effects of winds in atmospheric pressure waves produced by hydrogen bombs, J. Meteorol. Soc. Japan, 46, 45-59, 1968.
- Pfeffer, R.L., and J. Zarichny, Acoustic gravity wave propagation from nuclear explosions in the earth's atmosphere, J. Atmospheric Sci., 19, 256-263, 1963.
- Pfeffer, R.L., and J. Zarichny, Acoustic gravity wave propagation in an atmosphere with two sound channels, Geofis. Pura Appl., 55, 175-199, 1963.
- Pierce, A.D., Guided infrasonic modes in a temperature- and wind-stratified atmosphere, Sci. Rep. 6, AVCO Corp., Contract No. AF19(628)-3891, 1966.
- Press, F., and D.G. Harkrider, Propagation of acoustic-gravity waves in the atmosphere, J. Geophys. Res., 67, 3889-3908, 1962.
- Symons, G.J., The eruption of Krakatoa, Trübner and Co., London, 1888.
- Taylor, G.I., Wave and tide in the atmosphere, Proc. Roy. Soc. London, A, 126, 169-183, 1929.
- Wexler, H., and W.A. Hass, Global atmospheric pressure effects of the October 30, 1961 explosion, J. Geophys. Res., 67, 3875-3887, 1962.
- Yamamoto, R., K. Kawahira and T. Iwashima, Large-scale disturbances in the winter stratosphere and mesosphere, 11th Plenary Meeting of COSPAR, Tokyo, May 1968.



# ACOUSTIC WAVES IN THE IONOSPHERE FOLLOWING NUCLEAR EXPLOSIONS

by

Donald M. Baker  
Space Disturbances Laboratory  
Research Laboratories, ESSA  
Boulder, Colorado 80302

Following several atmospheric nuclear explosions in 1961 and 1962 wavelike disturbances were observed at 150 to 200 km above the United States. The disturbances, detected as oscillatory variations in the frequencies of radio signals reflected from the F region, had periods ranging from 5 min down to less than 1 min, with periods of about 1 min being predominant. The speed of propagation of the disturbances was about 300 m/sec. The periods, propagation speeds, and dispersion exhibited by the ionospheric disturbances are essentially the same as those observed in ground-level pressure variations (microbarograms) following the same explosions.

These ionospheric disturbances are interpreted as manifestations of imperfectly ducted acoustic waves. The bulk of the acoustic-wave energy was confined to lower heights (probably below 120 km); some of the energy, however, leaked upward into the F region of the ionosphere. For one specific event (30 October 1962) an upper limit to the energy flux at 190 km is found to be  $0.5 \text{ erg cm}^{-2}\text{sec}^{-1}$ .

## 1. INTRODUCTION

Following seventy-five nuclear explosions in the atmosphere during 1961 and 1962 wavelike disturbances were observed in the ionosphere above the United States. The existence of these ionospheric disturbances was pointed out by Baker and Davies (1968); the present paper is a summary of portions of a more complete report by Baker (1968).

The ionospheric disturbances we shall discuss were detected with the high-frequency Doppler technique which has been described by Davies and Baker (1966) and Baker (1968). Since these disturbances have predominant periods of about one minute and travel with acoustic speeds, we have chosen to refer to them as "acoustic-wave" disturbances in order to distinguish them from the longer period (tens of minutes) "gravity-wave" disturbances which have been discussed by Kanellakos (1967), Breitling et al. (1967), Hines (1967), and Row (1967).

## 2. CHARACTERISTICS OF THE DISTURBANCES

We shall confine our discussion to the event of 30 October 1962, shown in figure 1, which illustrates the essential features of the disturbances. This figure shows the variations of the frequencies of 4 and 5 MHz radio signals after reflection from the ionosphere at nearly vertical incidence at Boulder. The frequency deviation increases positively upward and the time (in UT) increases from left to right. The nuclear device which generated this disturbance had a yield in the megaton range (TNT equivalent) and was detonated at 1601:56 on 30 October 1962 near Johnston Island in the Pacific (Donn and Shaw, 1967).

The exact time of arrival of the bomb-related disturbance is uncertain because of the background frequency variations which are present even during "quiet" periods. We believe that the disturbance from the explosion arrived at 2210 UT. This belief is based on the fact that features similar to those between 2210 and 2230 of figure 1 can be found at similar time delays following several other explosions. Based on a great-circle path from the source to Boulder of 7084 km, this arrival time (2210) corresponds to a propagation speed of about 320 m/sec.

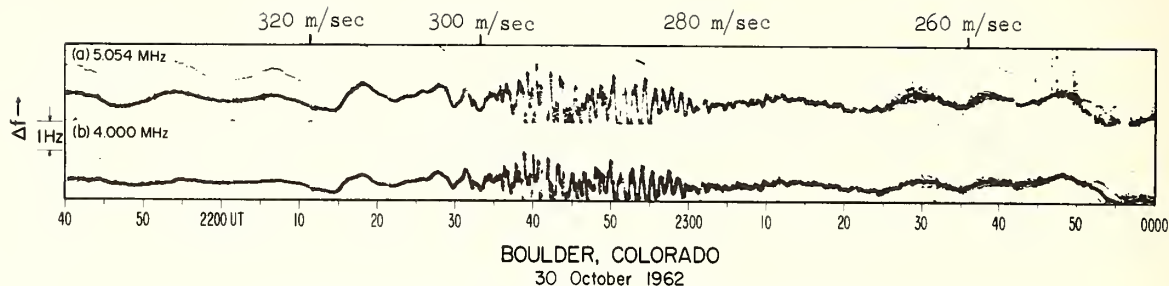


Figure 1. Doppler signature of an ionospheric disturbance above Boulder following nuclear explosion near Johnston Island on October 30, 1962 (1602 UT). Explosion yield was in megaton range. Times corresponding to various propagation speeds from the source to Boulder are indicated. Secondary trace on each record is a harmonic of main trace.

The characteristic short-period disturbance which makes these events stand out on the records begins at 2230. This disturbance consists of an extended train of oscillations with periods ranging from 30 to 90 sec. These oscillations are of relatively large amplitude from 2230 to 2300 and then appear to persist at reduced amplitude until 2330. The propagation speeds of these short-period features range from about 300 m/sec down to 260 m/sec. Finally, there is strong evidence that the short-period oscillations are superimposed on a longer-period (10 to 20 min) wave.

### 3. COMPARISON OF IONOSPHERIC AND GROUND-LEVEL EFFECTS

Pressure waves from large nuclear explosions have been observed at ground level by a global network of microbarographs (Donn and Shaw, 1967). It is of interest to compare the ionospheric disturbances with the ground-level pressure variations. Figure 2 shows the microbarographs obtained at Poughkeepsie, New York and Berkeley, California and the frequency variations of 5 MHz at Boulder following the explosion of 30 October 1962. In this figure the approximate distance of each observation from the explosion is given and the times corresponding to various propagation speeds are indicated. The records are aligned at times corresponding to a speed of 300 m/sec. A cursory examination is sufficient to reveal a striking similarity between the general features of the ground-level and ionospheric observations. The periods and speeds of the disturbances on the ground are essentially the same as those in the ionosphere.

One significant difference between the ionospheric and ground-level disturbances appears to be their observable lifetimes. Following the largest explosions the microbarographs detected the wave which traveled directly from the explosion to the detector (the  $A_1$  wave), the wave which reached the detector after having passed through the antipode of the source (the  $A_2$  wave), and the second passage of the direct wave after it had completely circled the globe (the  $A_3$  wave). We have, however, been able to detect only the direct wave ( $A_1$ ) on the ionospheric records. This difference in the apparent lifetimes of the ground-level and ionospheric disturbances may be a result of the propagation mechanisms involved and/or a difference in the sensitivities of the observing techniques.

The dispersion (group speed versus period) for seven ionospheric events, as determined by the peak-and-trough method of Ewing and Press (1954), is shown in figure 3. The dispersion curves for the ground-level pressure variations are also shown for three of the events. The figure illustrates once again that the periods and speeds observed on the ground and in the ionosphere are essentially the same. For the particular event we are discussing, 30 October 1962, the group speeds observed on the ground at Socorro, New Mexico for the 50 to 100 sec range of periods differ from those observed in the ionosphere over Boulder by only a few meters per second. For periods greater than 100 sec the velocities of the ionospheric disturbances are from 10 to 20 m/sec greater than those on the ground, but the ionospheric data follow the same trend as the microbarograph data. This lends support to our assertion that the longer-period features which begin at 2210 of figure 1 are the earliest arriving disturbances from the explosion.

In summary, we have seen that the ionospheric disturbances are similar to the pressure waves recorded on the ground. This leads us to conclude that the two phenomena are closely related.

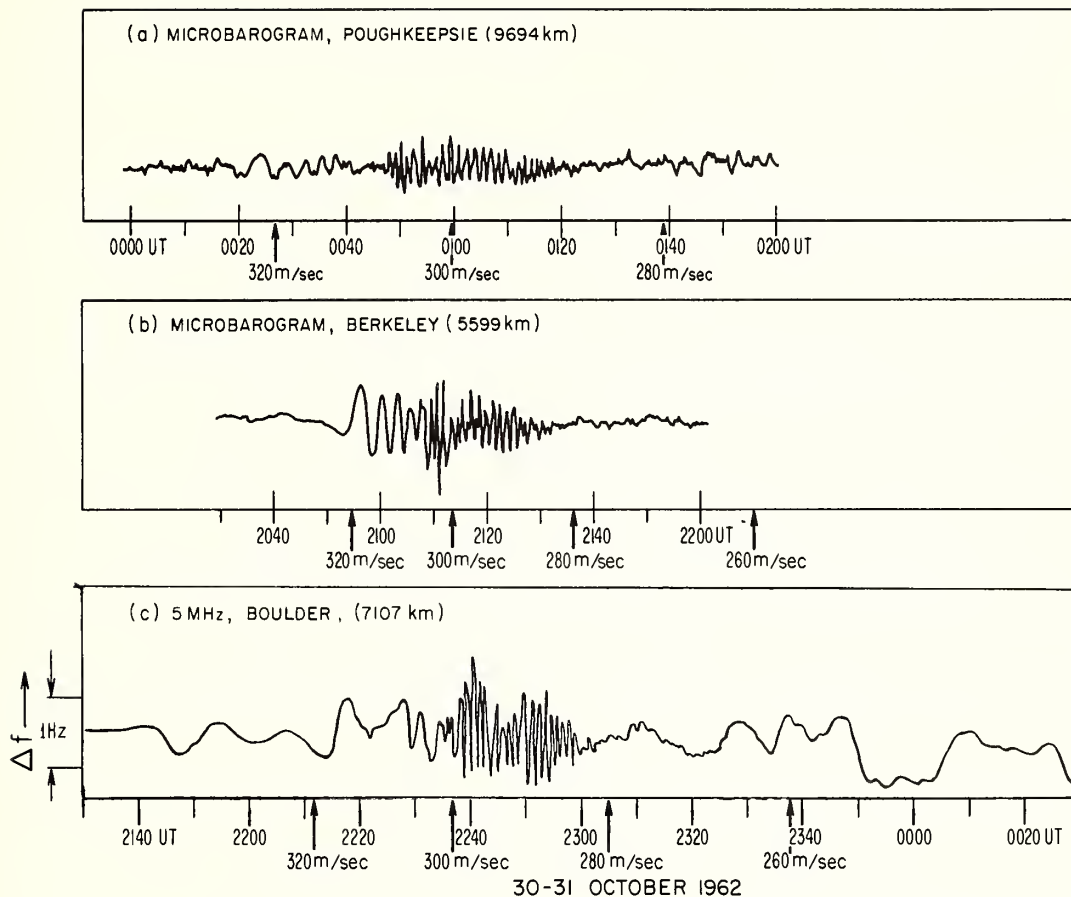


Figure 2. Comparison of microbarograms obtained at Poughkeepsie, New York (a) and Berkeley, California (b) with ionospheric disturbance above Boulder (c) following nuclear explosion on October 30, 1962. The records are aligned at times corresponding to a propagation speed of 300 m/sec. The microbarograms are reproduced through the courtesy of William L. Donn.



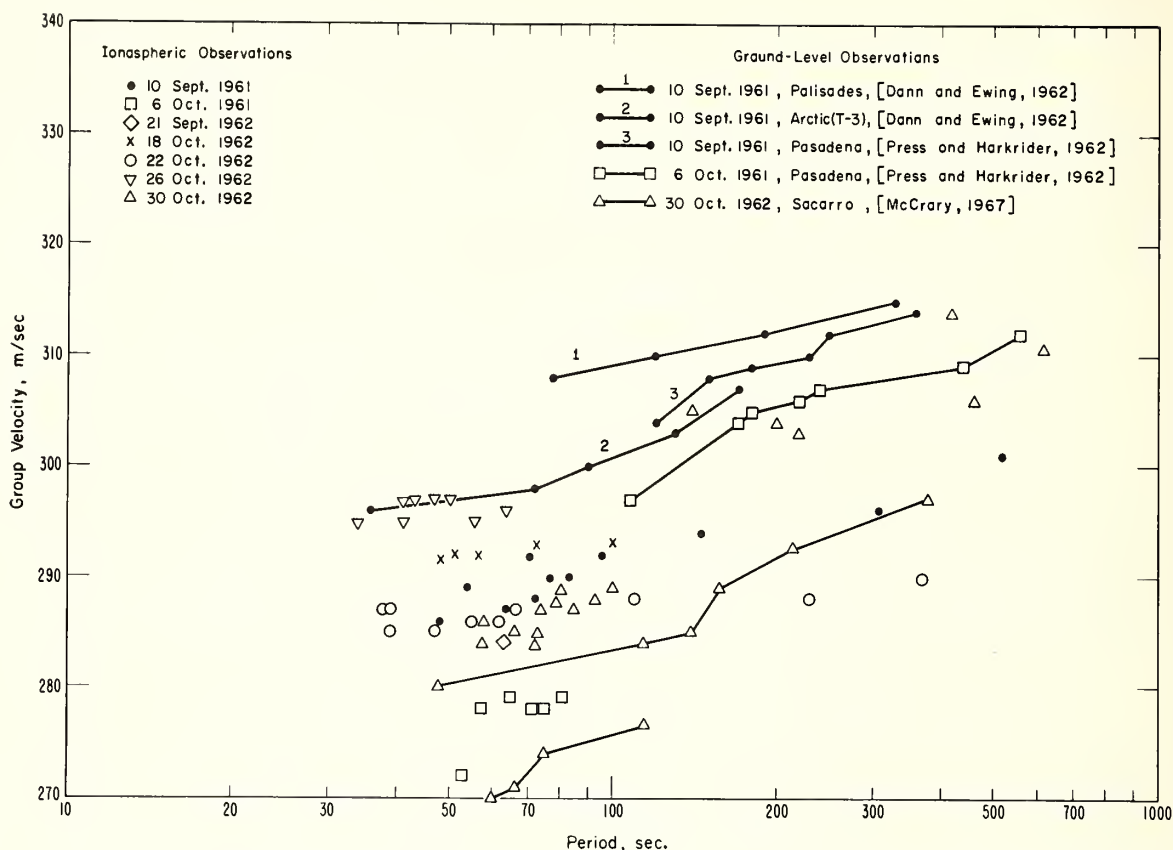


Figure 3. Group velocity dispersion exhibited by ionospheric disturbances and ground-level pressure waves following several nuclear explosions.

#### 4. INTERPRETATION OF THE IONOSPHERIC DISTURBANCES

The pressure waves observed on the ground have been interpreted as ducted acoustic-gravity waves by Press and Harkrider (1962), Pfeffer and Zarichny (1963), and Harkrider (1964). The similarities found in the last section prompt us to seek a similar interpretation for the ionospheric events. We can obtain some information on the height at which the ionospheric disturbances were observed from figure 1. We see that the frequency deviation of 5 MHz was larger than that of 4 MHz ( $\Delta f_5/\Delta f_4 \approx 1.3$ ). This implies, based on the simplest theoretical considerations (Davies and Baker, 1966, p 546), that the changes which produced the frequency variations must have extended up to the height of reflection for 5 MHz. Furthermore, from figure 4 we see that there is a phase difference between the effects observed on 4 and 5 MHz, with a given feature appearing on 4 about 17 sec before it appears on 5. True-height analysis of the Boulder ionogram for 2230 UT gives 180 and 190 km for the reflection heights of 4 and 5 MHz, respectively. If we assume that the major part of the Doppler shift was imposed at the height of reflection, the disturbance must have had a vertical trace velocity of about 600 m/sec, which is the right order of magnitude for the sound velocity at 180-190 km. In other words, the ionospheric disturbance above Boulder appeared to be traveling upward from a source in some region directly below.

These observations lead to the following interpretation: The explosion generated acoustic waves which became ducted in the sound channels of the atmosphere. Some of the energy which was trapped in the upper sound channel (between 50 and 120 km) leaked out of the duct and propagated upward, perturbing the electrons in the ionosphere as it progressed. These perturbations of the ionospheric electrons produced the observed Doppler shifts in the HF radio waves. This

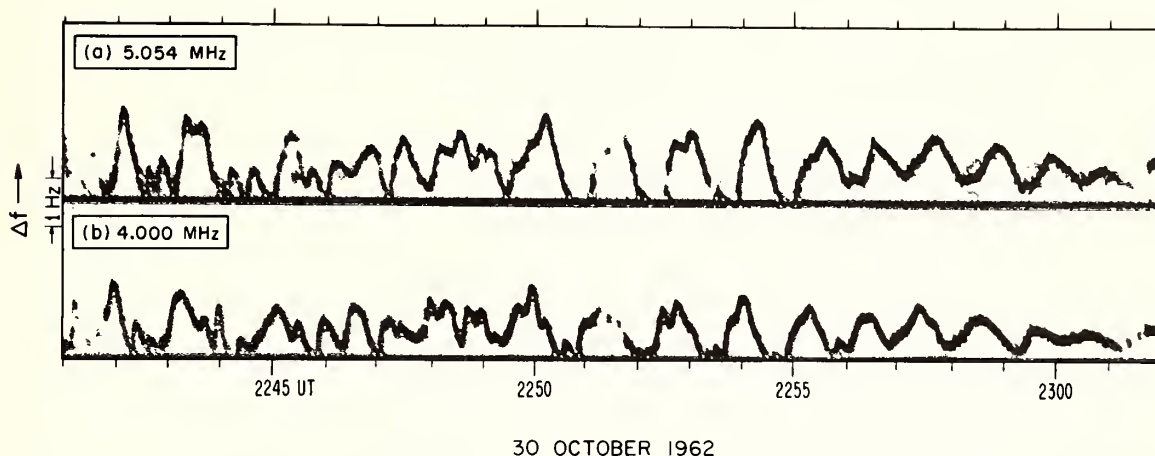


Figure 4. Detail of ionospheric disturbance above Boulder on 30 October 1962 illustrating phase difference between disturbances on 4 MHz (reflected from 180 km) and 5 MHz (reflected from 190 km).

interpretation is consistent with the relatively low propagation speed (about 300 m/sec) with which the disturbance traveled from the source to Boulder. This speed suggests that the waves traveled most of the way in the lower regions of the atmosphere where the sound speed itself is about 300 m/sec.

In order to obtain an estimate of the pressure perturbation at 190 km necessary to cause the observed frequency shifts, we have developed the model for the time rate of change of electron density as a function of height and time which is shown in figure 5a. This model shows a wavelike structure with amplitude increasing with height. This growth in amplitude is caused partly by the growth of the neutral particle displacement, which is itself caused by the decrease in the density of the air. The model was constructed for a vertically-traveling, plane acoustic wave of 90 sec period, and the electrons were assumed to follow the component of the neutral air motions along the magnetic field.

The frequency variations of 4 and 5 MHz resulting from this model are shown in figure 5b. We see that the model gives a Doppler shift on 5 MHz which is larger than that on 4 MHz and also predicts a phase difference, with the effect on 4 MHz leading that on 5 MHz. Both of these features are required by the observations, and comparison with the experimental records for 30 October 1962 reveals good quantitative agreement if the dispersion and small-scale details of the observations are neglected, as is shown in figure 6.

To make the model fit the observations requires a relative pressure perturbation at 190 km of 13 percent and an energy flux of  $0.5 \text{ erg cm}^{-2}\text{sec}^{-1}$ . Because of the nature of the calculations, these values must be regarded as upper limits. The maximum peak-to-peak amplitude of the pressure perturbation at Poughkeepsie (figure 2a) was about 175 microbars (William L. Donn, private communication) which corresponds to a relative pressure perturbation of only  $10^{-4}$  and an energy flux of  $160 \text{ ergs cm}^{-2}\text{sec}^{-1}$ . Thus we see that, relative to the ground-level values, the over-pressure at ionospheric heights is large but the energy flux involved is small.

##### 5. ACKNOWLEDGEMENTS

I wish to thank Dr. William L. Donn of the Lamont Geological Observatory for permission to reproduce the microbarograms shown in figure 2. The records of ionospheric disturbances used in this paper were collected under the sponsorship of the National Bureau of Standards, Central Radio Propagation Laboratory (now part of the Research Laboratories of the Environmental Science Services Administration) and the analysis of the data was supported by the Advanced Research Projects Agency, Nuclear Test Detection Office under ARPA Order No. 932, Amendment 2, Task VII.

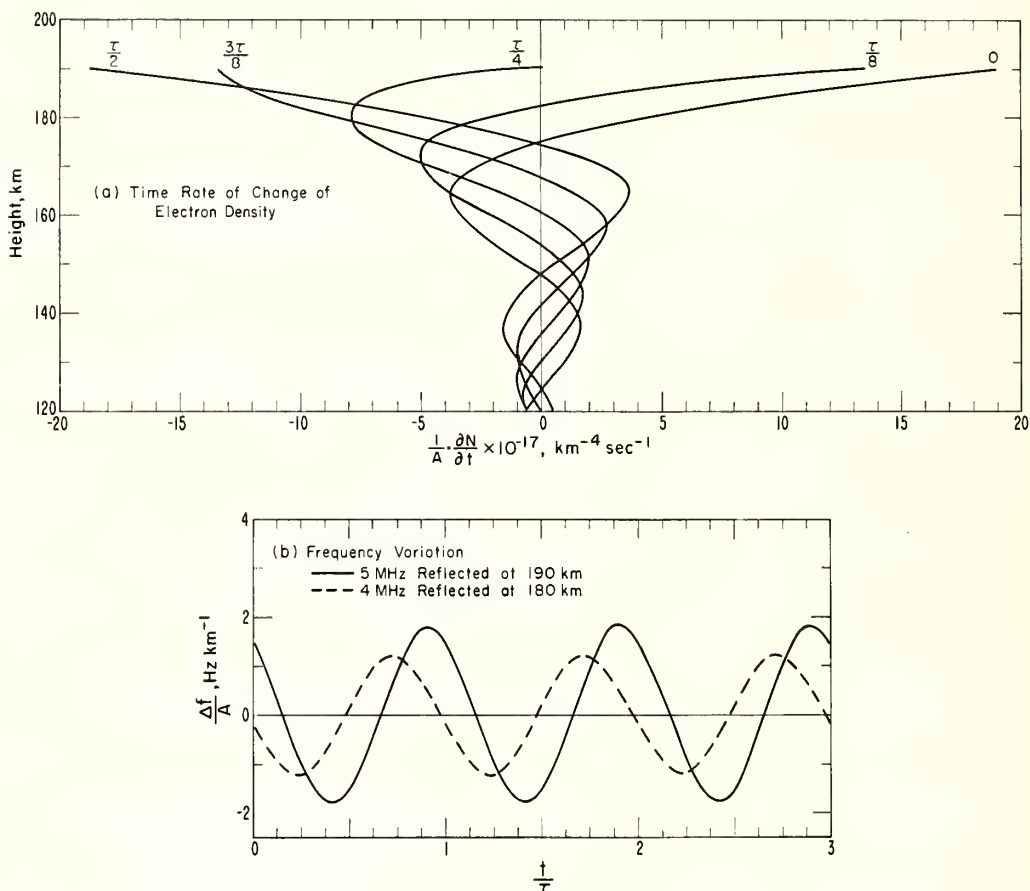
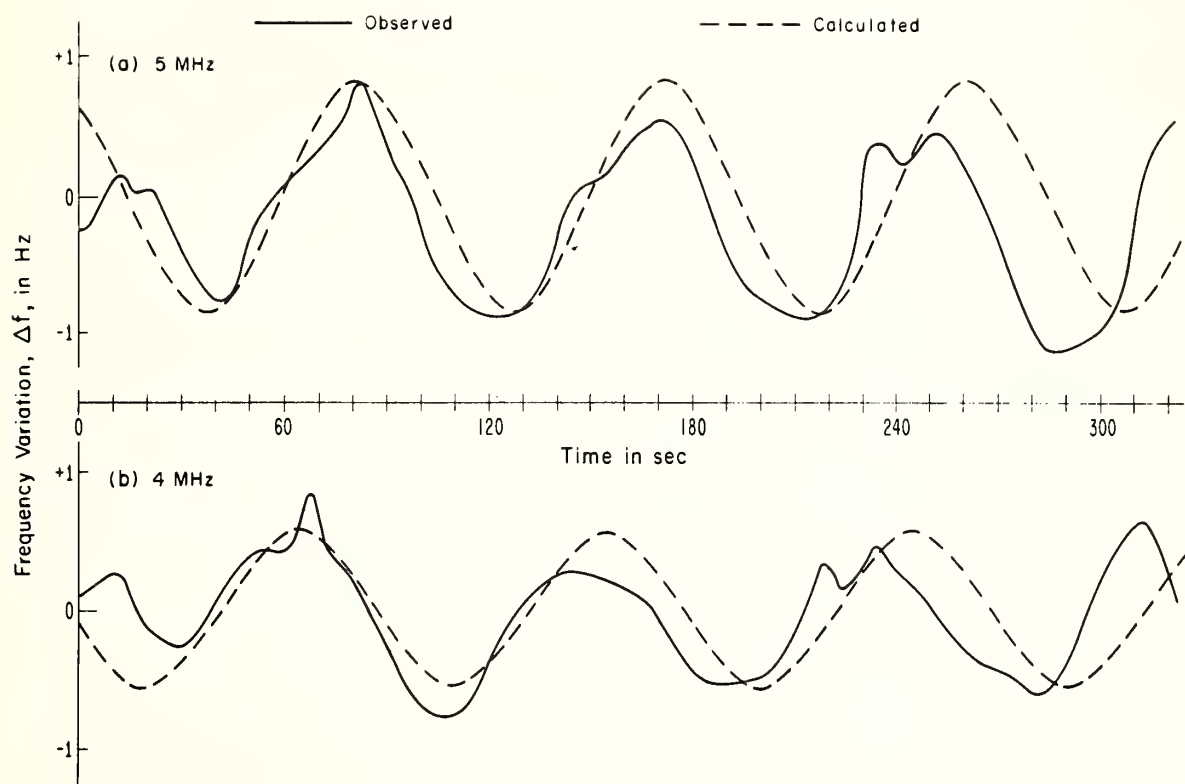


Figure 5. (a) Variation of the time rate of change of electron density with height and time as caused by a vertically propagating acoustic wave of 90 sec period. The rate of change of electron density is expressed in terms of the amplitude, A, of the neutral particle displacement at 190 km.

(b) Doppler shifts of 4 and 5 MHz caused by model shown in (a). Doppler shift is also expressed in terms of the amplitude factor, A.



30 OCTOBER 1962

Figure 6. Theoretical and observed Doppler shifts on 4 and 5 MHz, 30 October 1962. Observed variations are taken from figure 1. The origin of time corresponds to 2249 UT. The theoretical curves are taken from figure 5b with the amplitude factor chosen to make the peak-to-peak deviation on 5 MHz agree with the observations.

## 6. REFERENCES

- Baker, D.M., "Observations of acoustic waves in the ionosphere following nuclear explosions," to be published as an ERL Tech. Rep., 1968.
- Baker, D.M. and K. Davies, "Waves in the ionosphere produced by nuclear explosions," J. Geophys. Res., 73, No. 1, 448-451, 1968.
- Breitling, W.J., R.A. Kupferman and G.J. Gassmann, "Traveling ionospheric disturbances associated with nuclear detonations," J. Geophys. Res., 72, No. 1, 307-315, 1967.
- Davies, K. and D.M. Baker, "On frequency variations of ionospherically propagated HF radio signals," Radio Sci., 1 (New Series), No. 5, 545-556, 1966.
- Donn, W.L. and M. Ewing, "Atmospheric waves from nuclear explosions," J. Geophys. Res., 67, No. 5, 1855-1866, 1962.
- Donn, W.L. and D.M. Shaw, "Exploring the atmosphere with nuclear explosions," Rev. Geophys., 5, No. 1, 53-82, 1967.
- Ewing, M. and F. Press, "An investigation of mantle Rayleigh waves," Bull. Seis. Soc. Am., 44, 127, 1954.
- Harkrider, D.G., "Theoretical and observed acoustic-gravity waves from explosive sources in the atmosphere," J. Geophys. Res., 69, No. 24, 5295-5321, 1964.
- Hines, C.O., "On the nature of traveling ionospheric disturbances launched by low-altitude nuclear explosions," J. Geophys. Res., 72, No. 7, 1877-1882, 1967.
- Kanellakos, D.P., "Response of the ionosphere to the passage of acoustic-gravity waves generated by low-altitude nuclear explosions," J. Geophys. Res., 72, No. 17, 4559-4576, 1967.
- McCrory, R.A., "Atmospheric pressure waves from nuclear explosions," J. Atmospheric Sci., 24, No. 4, 443-447, 1967.
- Pfeffer, R.L. and J. Zarichny, "Acoustic-gravity wave propagation in an atmosphere with two sound channels," Geofis. Pura Appl., 55, No. 2, 175-199, 1963.
- Press, R. and D.G. Harkrider, "Propagation of acoustic-gravity waves in the atmosphere," J. Geophys. Res., 67, No. 10, 3889-3908, 1962.
- Row, R.V., "Acoustic-gravity waves in the upper atmosphere due to a nuclear detonation and an earthquake," J. Geophys. Res., 72, No. 5, 1599-1610, 1967.



PROPAGATING ENERGY IN THE UPPER ATMOSPHERE INCLUDING  
LOWER IONOSPHERE GENERATED BY ARTIFICIAL SOURCES \*

by

Uri Fehr

Lamont Geological Observatory (Columbia University)  
Palisades, New York.

Explosions at 50 km level, and large space vehicles (the Saturn V vehicle through its travel up to 190 km) are used as generators of propagating energy. The explosions are produced on the West coast. Both artificial sources are monitored by a variety of sensors; including infrasonic sensors, ELF and VLF E and B field sensors, and several ionosonde stations. The monitoring stations cover from short to long range observations (a few tens of kilometers to about 2000 km). Energy propagation characteristics in the different layers are discussed and related to the propagation of many types of waves involved.

INTRODUCTION

At 21h53m40sUT on June 14, 1967, a 172.4 lb chemical bomb was exploded at an altitude of 48.8 km above San Nicholas Island (about 70 miles off the coast of Southern California). Its effect was observed by geomagnetic, geo-acoustic and other types of stations placed around Southern California and San Nicholas Island (Fehr 1968). At 17h11m28sUT and at 17h53m21.4sUT on June 13, 1968, two similar bombs were exploded at altitudes 49.9 and 49.4 km respectively above San Nicholas Island. Their effects were observed by the same stations monitoring the 1967 explosion.

At 12h01mUT on November 11, 1967 and at 12h01mUT on April 4, 1968 two Saturn V vehicles were launched from Kennedy Space Center in Florida. Their effects were observed by geoacoustic stations at Cape Kennedy, Florida, Grand Bahama Island, Cape Hatteras, North Carolina, Fort Monmouth, New Jersey and Palisades, New York. Also, ionosonde and VLF monitors have shown disturbances related to these launches.

Various results related to the acoustic energy released by the Saturn V launches had been reported elsewhere (Donn 1968). The observation was carried out in the frequency range of 0.1 to 10 cps. The observation by the Lamont Geological Observatory station was centered between 0.1 to 1 cps, while the stations at Cape Hatteras, Virginia and Fort Monmouth were operated by the Army at the frequency range of 0.5 to 10 cps. A station was established in Grand Bahama Island on April 1968 which monitored the Saturn V launch of April 4. It covered the whole frequency range of 0.05 to 20 cps. The results are reported in this paper. The sensors at the different stations had different characteristics and the results had to be evaluated, bearing in mind the various characteristics as reported by Fehr (1967).

OBSERVED RESULTS FROM EXPLOSIONS

On November 2, 1967 at 23h35m15.36sUT an explosive of 172.4 lbs of TNT was discharged at an elevation of 240 meters. It served as a calibrator for the acoustic data. Figures 1 and 2 are some examples of the acoustic energy associated with the detonation. They represent the information from three sensors which are lined with the explosion center. They represent power spectrum of a stretch of 2.56 seconds, where the signal detected was 2 seconds in width. Figure 1 shows three power spectrum curves fit together by multiplying the dashed curve by 3 and the continuous curve by 6 in order to be able to notice the frequency change with distance. As may well be understood, the closest station is the one designated by dashes and dots; the second is the dashed curve; and the last one which is the farthest is the continuous

\* Lamont Geological Observatory (Columbia University) Contribution No. 1225



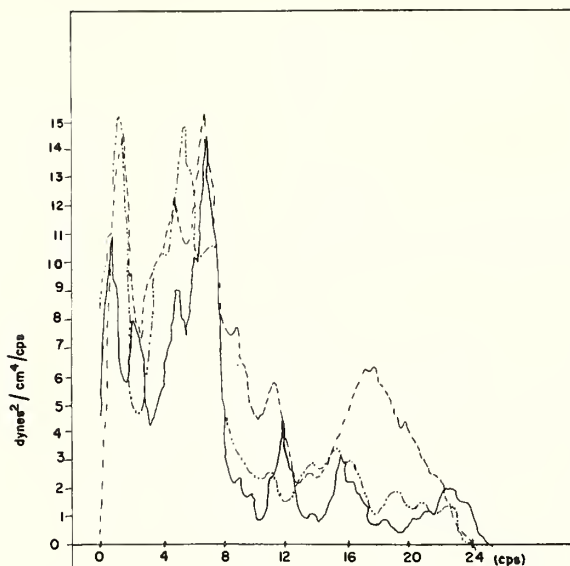


Fig. 1. Power spectrum distribution at three sensor sites on San Nicholas Island from the Nov. 2, 1967 explosion.

curve. Fig. 2 represents the total energy in each station by the dashed area. Fig. 2a is the closest station while 2c is the farthest. The explosions at 50 km altitude showed the same width of signal of 2 seconds. However, the difference between stations was negligible as the distance from the source was almost the same for all three of them.

The above figures give a clear view of the attenuation of the acoustic energy with distance and with frequency. The attenuation related to the signal from the high altitude explosion is being studied from the three tests in order to get a statistical evidence.

Fig. 3 represents electromagnetic fluctuations at VLF frequencies. Fig. 3a is the original signal arriving at the instant of the explosion (Nov. 2, 1967) while 3b represents 7 reflections arriving 64 seconds later. The frequencies involved are between 3 to 4 KHz. The reflections are slightly attenuated which agrees within a factor of 2 with Helliwell's (1968) model who calculated a minimum for absorption of VLF at 2 KHz.

He points out that reflection occurs in the vicinity of the lower hybrid resonance frequency where the wave normal of the whistler can become transverse. Fig. 3b shows a variety of dispersion forms which represent the original signal. According to Helliwell (1968) wave-particle interaction could be the cause of such dispersion. A statement in his paper could well answer both types of time scattering observed in these reflections. The rate of change of frequency with time at a given location of the interaction region with respect to the geomagnetic equator can be understood by the following: as electrons approach the equator, their gyrofrequency increases and hence, the frequency of emission decreases with time. Conversely, as the particles depart from the equator, the frequency of their gyration about the lines of force increases with time, and hence, the generated frequency rises with time.

An ELF electromagnetic signal of 16 seconds in duration was also observed from that low altitude explosion and it was deduced that this signal was generated and propagated on the ocean surface (Fehr 1968).

The high altitude explosions (near to 50 km level) from which three have been monitored in the last year between June 1967 and June 1968 have disturbed the earth's magnetic field and produced a detectable signal as observed by a magnetometer and reported by Fehr (1968). Another interesting observation was the disturbance which appeared on the ionosonde observation at about 0.4 MHz with apparent height of 140 km.

Observed Results from the Saturn V of April 4, 1968.

Fig. 4 is the acoustic signal generated by the Saturn V as heard by the three sensors station in the Grand Bahama Island. It can easily be seen that the signal consists of a continuous signal of about 160 seconds and three additional pulses arriving at later times with tens of seconds gaps among themselves and between the continuous signal and the first pulse. Direction angles, Fig. 5, show that all signals mentioned have come from the Saturn V. The group velocity for the first arrival, assuming it relates to the ignition of the first stage, is 307.4 m/s. The conclusion that the first part of the signal relates to the ignition is deduced from the observed low frequency waves which consist of the initials of the

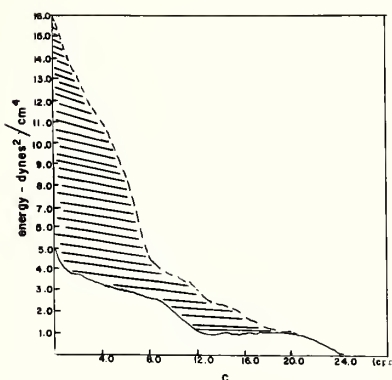
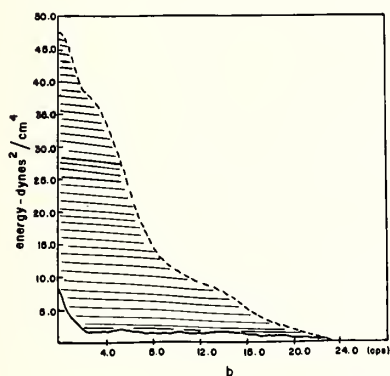
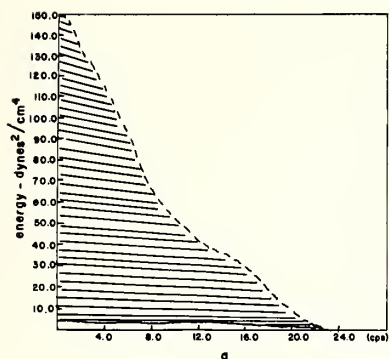


Fig. 2. Total energy distribution in the frequency range of 0 to 24 cps from the same test and sites as Fig. 1.

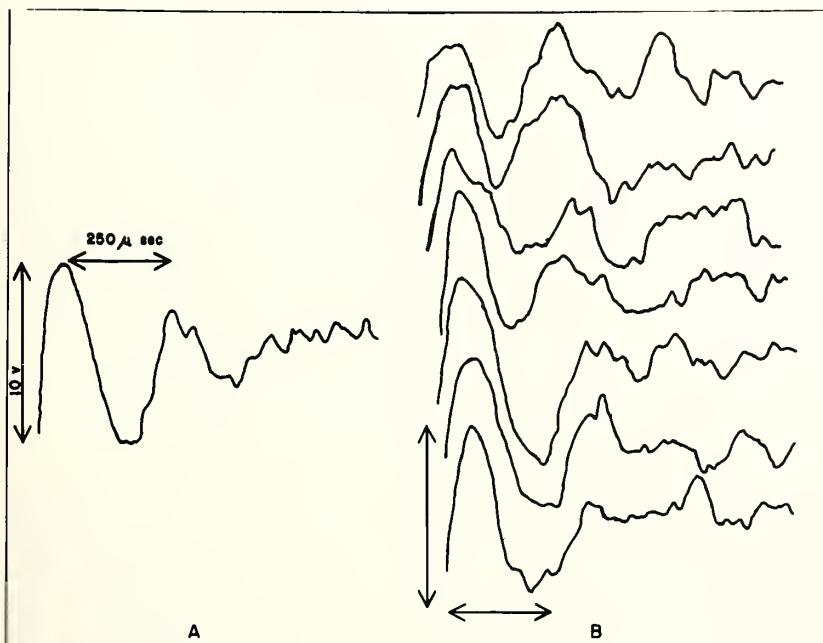


Fig. 3. a) an electromagnetic signal generated by the Nov. 2 explosion received at a station 180 km away; b) seven reflections of (a) arriving 64 seconds later.

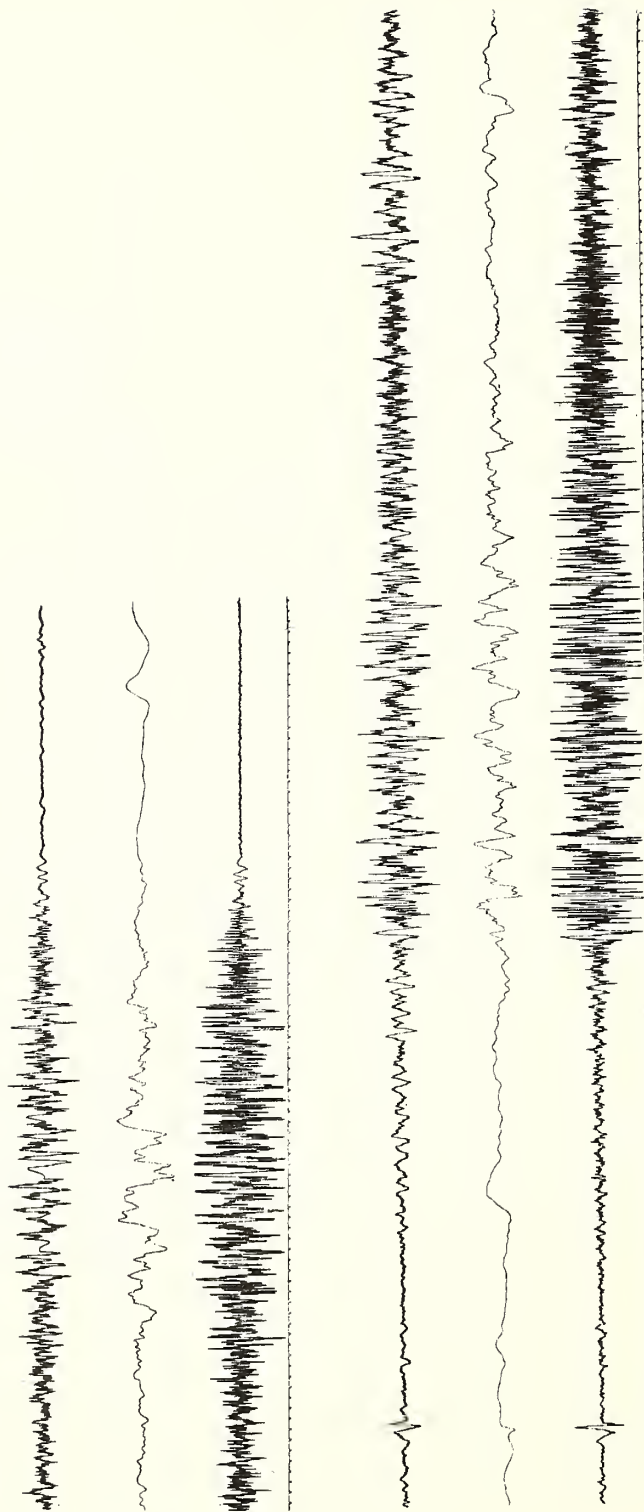


Fig. 4. The acoustic signal at Grand Bahama Island as received by three sensors station. The top shows the first arrival with first group; the bottom shows the second group and one of the pulses. Time goes from right to left.

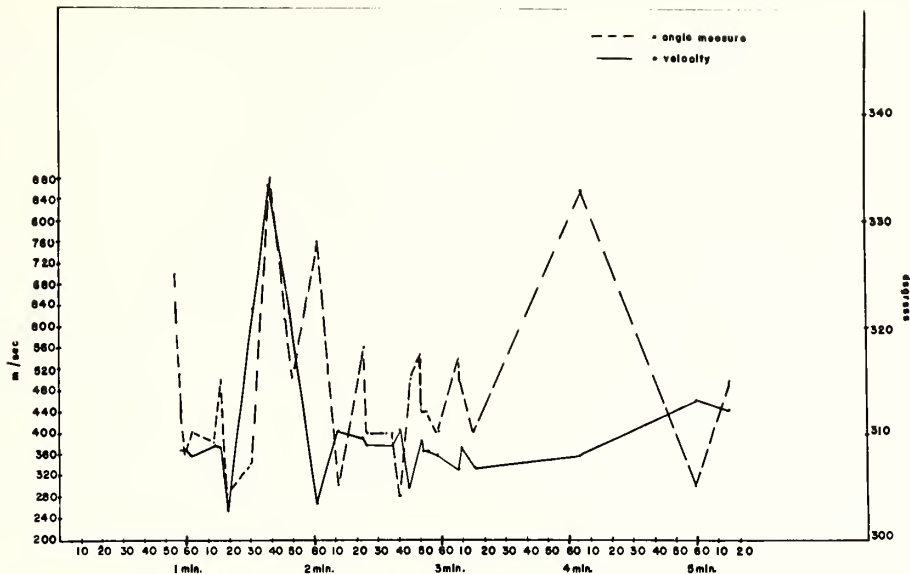


Fig. 5. Graph of change of phase velocity and angle of arrival with time, for the signal received at Grand Bahama. The last three points are the three pulses observed.

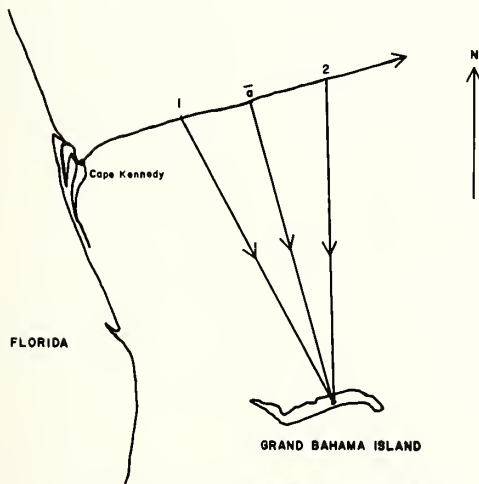


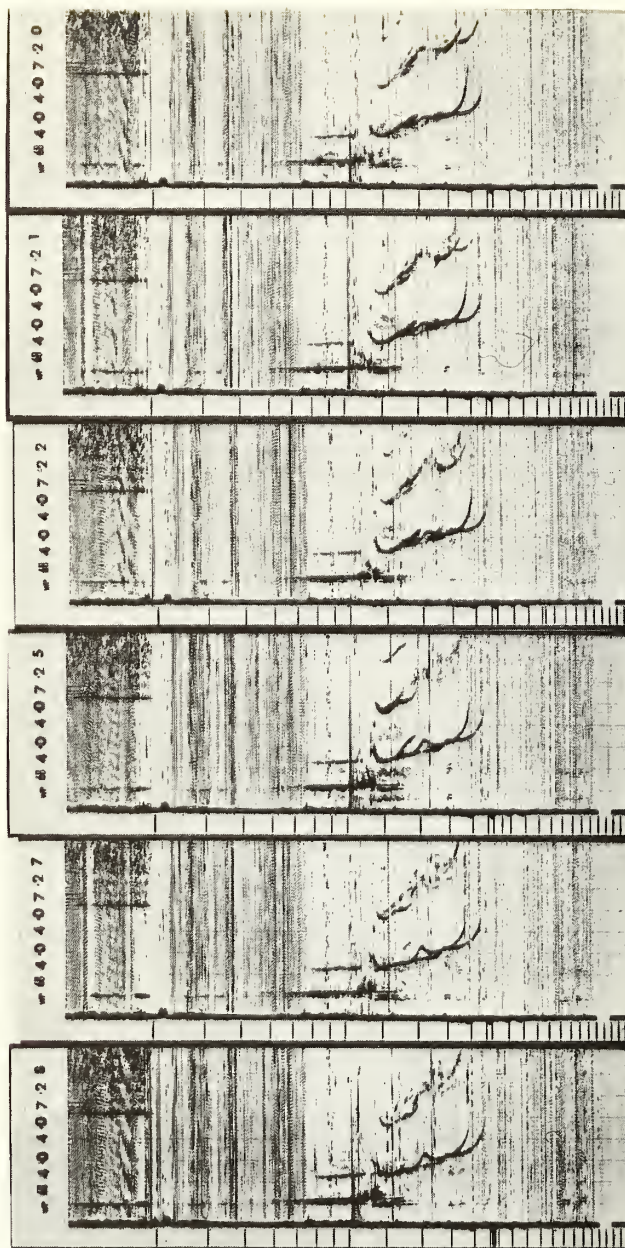
Fig. 6. The trajectory of April 4, 1968 Saturn V in respect with Grand Bahama Island. Lines 1 and 2 present direction angles of min and max of signal arrival and a is the average direction for that group.

continuous signal. However, the ignition as monitored in the vicinity of the launch area at about three miles distance, showed that this low frequency signal had a high amplitude in respect to the regular engine noise. This fact requires the identification of the continuous signal which consists of three groups: the first group, an intermediate group and the second group, which is of highest amplitude. The highest amplitude is in the order of  $20 \text{ dynes/cm}^2$ .

It is necessary to determine if the groups relate to the exhaust energy or to the ballistic wave produced by the rocket. The ignition might be highly attenuated by molecular absorption effect and would necessarily mean that the signal is not observed from the first few kilometers. Fig. 5 indicates that part of the first group could have been associated with the second stage, while parts of the intermediate and second group came from first stage. The determination of whether most of the signal is ballistic or exhaust energy might resolve this problem.

The Saturn V signal from April 4, 1968 was observed in addition to the Grand Bahama site only by the Lamont site. However, here the signal was very low in amplitude with respect to the November 9, 1967 signal (Donn 1968), and it lasted for half the duration. Although two groups were easily recognizable, their durations were less than seven minutes each. Also, their direction vectors were pointing more westward covering only the range observed by the Grand Bahama Island station. In this case, it was seen that no signal from above 110 km reached any of the stations, although the November 9, 1967 picture indicated signals arriving from as high as 170 km altitude. Fig. 6 is a map of the Saturn V trajectory in the April 4





a.

Fig. 7a. Ionograms at Wallops Island of an echo from Saturn V of April 4, 1968.

with altitude. In the last few years it has been found that acoustic phenomena is closely tied in with disturbances in the ionosphere. One of the best examples is the observations of nuclear explosions by microbarovariographs on the ground and by Dopplersondes in the ionosphere. A strong similarity between the dispersion characteristics of both types of observations has been shown by Balachandran (1968). The anomalies of acoustic propagation have been used already since World War I as an indication of change of wind with season. Tremendous artillery barrages at the time of battles in the northern part of France and Flanders were

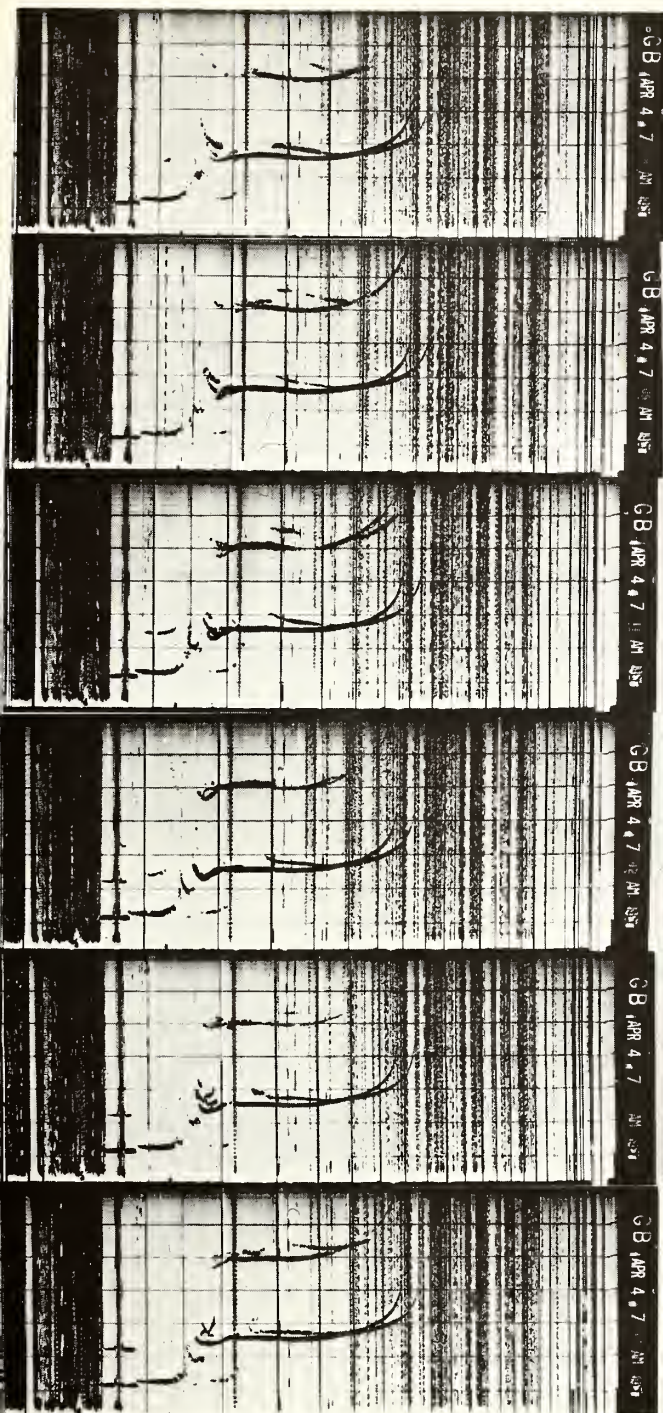
flight and the Grand Bahama station. Direction angles which represent a minimum, a maximum and an average direction of a group of acoustic waves arriving at the island have been traced. The maximum angle points to an altitude of 108 km and a distance of 283.3 km from the stations. The group velocity for that part of the signal is 322 m/s. The minimum angle in that group of waves gives us a group velocity of 309 m/s. The discrepancy in group velocities occurs generally because of the different curvature and the different waves propagated. This will be explained in the next section.

Ionospheric variations after the launch of the Saturn V were recorded on vertical incidence ionograms at two stations at Grand Bahama Island and at Wallops Island. Figs. 7a, b, c are samples from both stations at various periods after launch. Disturbances have been observed at the Grand Bahama Island for a period of almost two hours, from 12h08mUT to 14h00mUT. The frames in Grand Bahama were obtained every 30 seconds, while those of Wallops Island are 60 second frames. Disturbances such as these, have been observed from chemical releases, (Golomb 1963). However, the disturbances here are much sharper with faster changes and with gaps of quiet times in between disturbances. On the other hand, the November 9 Saturn V launch has not shown any disturbance noticeable by the ionosonde study at Grand Bahama Island.

#### USE OF ACOUSTIC PROPAGATION FOR RESEARCH INTO THE UPPER ATMOSPHERE

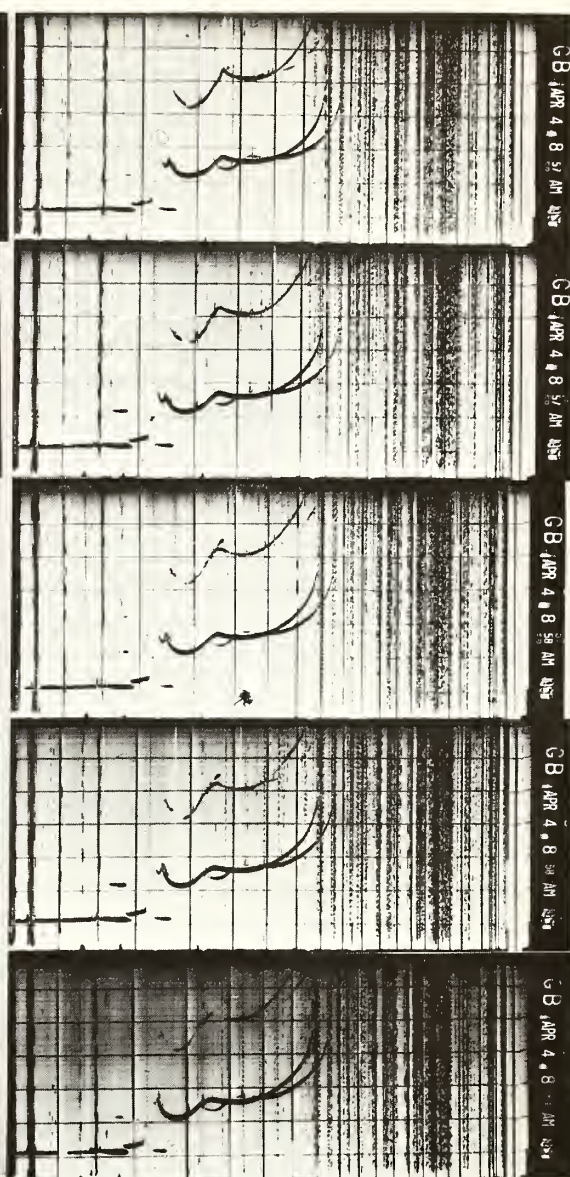
Both explosion and rocket noise can be utilized for the study of the upper atmospheric characteristics. The rocket grenade technique was utilized for temperature and wind measurements up to 90 km by the method of explosion noise. Others, such as Bushman (1966), utilized rocket noise to determine winds, or such as Fehr (1967) to get cut-off frequencies





b.

Fig. 7b. First disturbance observed at Grand Bahama Island as received by ionograms from same Saturn V launch.



c.

Fig. 7c. Last disturbance as observed by the Grand Bahama Island ionosonde station.

heard in winter in the western part of Germany, but they could not be heard in summer. However, the opposite was observed in London - the thundering of the barrages was heard in summer, but not in winter (Khvostikov, 1964). Observations at Lamont of launches from Cape Kennedy in Florida has shown exactly the same phenomenon: rocket signals were observed during the months of January to May and October to December. However, during June to September or October no signal reached our station. From the study of microbarom propagation (Posmentier 1968) it was found that tidal winds at 110 km altitude influenced strongly the microbaroms' propagation. Many experiments have shown that acoustic waves of audio frequencies cannot reach high altitudes without dissipating. This requires winds to reflect them at altitudes of 20 to 30 km so that the audio frequencies would reach long range as observed from World War I. On the other hand, winds at 60 km will effect sound between 4 to 12 Hz which cannot reach above 90 km as determined by the cut-off frequencies with altitude (Fehr 1967) and the lower frequencies by the winds of 110 km or above. These deductions are still a speculated possibility. In order to determine if it is valid it is necessary to utilize other types of observations in addition to much larger arrays of acoustic sensors. The problem of acoustic attenuation with distance and frequency while traveling at different levels of the atmosphere has yet to be determined and experiments such as these can give some numerical results which would aid in predicting focussing or superbloom phenomenon.

The attenuation problem is being studied by the array of sensors in San Nicholas Island as shown in Fig. 8 and by the array in Fig. 9, which shows all other stations on the southern coast of California (the E, F, G, H and L stations are all acoustic at infrasonic frequencies). The explosion sketched on Fig. 9 was carried out on February 20, 1968 at 23h03mUT and the data is now being analyzed. Ray tracings have shown average group velocity along a ray curve in between 305 to 320 meters/sec which agrees with our observations of the Saturn V in the Grand Bahama Islands.

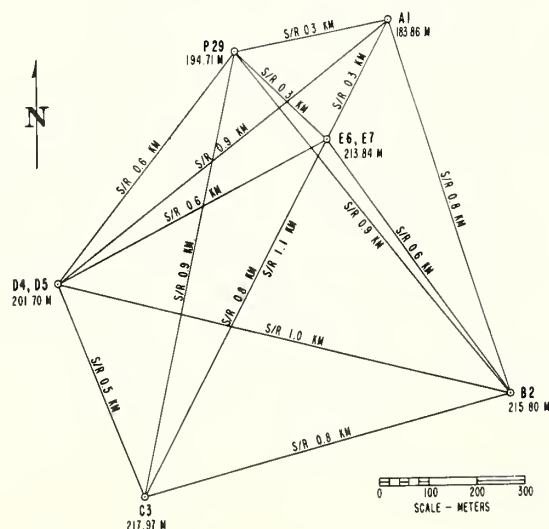


Fig. 8. The infrasonic sensor array configuration at San Nicholas Island used for the tests in 1968.

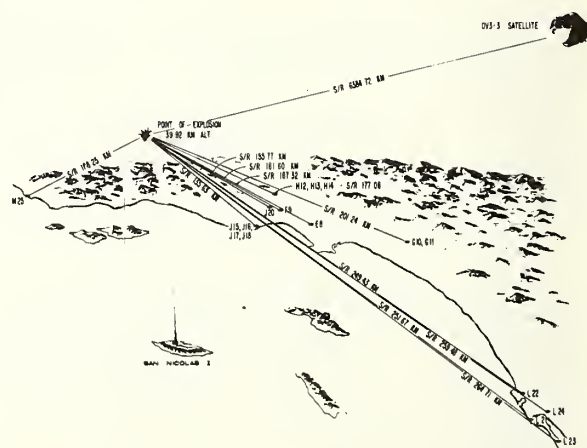


Fig. 9. A sketch of Southern California high explosive test designating position of observation station in respect to explosion of Feb. 20, 1968.



## PROBING OF THE IONOSPHERE

The medium we deal with is a gas of neutral molecules in which is embedded a statistically homogeneous mixture of free electrons and neutralizing heavy positive ions, in the presence of an imposed uniform magnetic field. For all purposes we consider the ionosphere as homogeneous on the horizontal scale and stratified vertically. There is a region in the lower ionosphere where continuum motion existing in the lower atmosphere is supposed to be damped out (Hines 1960). The meaning of acoustic wave propagation is an ordered motion in a random velocity field. In that field many factors attenuate the wave: the viscosity, thermal conductivity diffusion, radiation of heat and humidity (molecular absorption factor). In the lower ionosphere where, if once ordered motion has been established, it might grow within some ducts and propagate with hardly any attenuation at all.

When a rocket passes through the lower ionosphere it generally produces a hole in it. However, when a rocket does fire during its flight through the ionosphere, as the Saturn V vehicle, then there is a large enhancement of ionized gas. In an undisturbed ionosphere, the total mass of ionized gas is only a few milligrams per cubic kilometer, and therefore the hot exhaust gas ejected by the rocket flight introduces a large addition of ionized particles and electrons. Furthermore, the particles have a high thermal velocity with respect to the surroundings. The question would arise as to why we do not observe any radio interference at lower altitudes, and why do the radio reflections concentrate between 2 to 4 MHz and between 150 to 400 km (Fig. 7). Table I gives a few numbers related to some characteristics in the lower ionosphere which were used in calculating some factors related to observed signals which were produced in the ionosphere from the artificial sources of disturbances. From Table I we do see two very important factors: one the Alfvén velocity has a channel with a minimum between 300 to 400 km, and the second is that the acoustic velocity grows fast from 120 km and upwards, bending almost any acoustic wave propagating toward space. In addition, the magnetic field is still very large, up to 400 km. These numbers will limit any echo disturbance to the range above, if this echo is a result of either acoustic or hydromagnetic propagation. The hydromagnetic disturbance may be determined by magnetometers which will be included in future tests. The acoustic are discussed in the following.

The only other ionogram records available to the author, related to a rocket flight from Kennedy Space Center, were the ones taken when the Vanguard II was launched on 17 February 1959. The ionograms show a signature in existence for about 30 minutes in much higher frequencies which substantiate the hole concept. The frequencies are about 6 to 16 MHz at the heights of 300 to 700 km. However, the Saturn V has shown smaller signature shapes and, also, the longest disturbance duration from it was 10.5 minutes, which was the first observed echo (Fig. 7b). The times of the other disturbances were becoming smaller and smaller in duration and amplitude. The last, almost two hours after launch, lasted for 2.5 minutes, (Fig. 7c). If there were any other disturbances, after 2 hours, it would be hard to distinguish because 2 hours after launch the rate of frame taking was changed from 30 second sweeps to 15 minute sweeps. The only good identified signal at Wallops Island is in Fig. 7a. Both Wallops Island and Grand Bahama Island are off the trajectory of the rocket. However, Wallops Island is about 1000 km from the trajectory while the Grand Bahama station can be as close as 250 km. That means, on our ionograms, we observe a propagation of disturbance in the ionosphere which occurred at some horizontal distance from the stations. Now, if electrons have been removed within a bounded region, it would cause a sharp discontinuity of refractive index across the boundary. However, a compression of the ambient ionization by the expansion of the material from the propagating disturbance would increase the electron density, which would result by a strong echo. Most of the energy of the rocket exhaust is ultimately dissipated in the form of heat: the heated region expands and the ion density within it becomes smaller, which will produce a region of change in electron density from which an echo is returned. The first observation of disturbance occurred at 12h08m30sUT on April 4, 1968. At that time, the second stage was close to burnout and at 180 km altitude and at least 600 km away from Grand Bahama Island. As a result it would be easier to

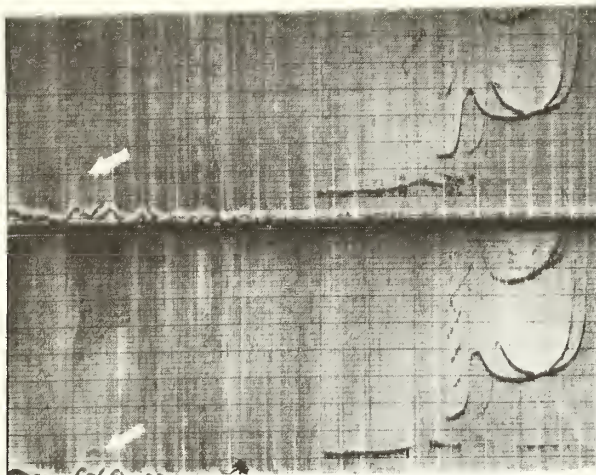


Fig. 10. Ionograms as received by the Vandenberg station from explosion on June 14, 1967. The disturbance appeared first on the bottom frame and then on the top. It is designated by the arrow.

assume that we observe disturbances that occurred when the rocket passed into the F region, which would be almost at 12h04m30s or four minutes away from Grand Bahama Island. This would require an approximate velocity of 1 km/sec for the disturbance to reach Grand Bahama Island by the previously mentioned time. A velocity of this type was observed by Wright (1964) from Project Firefly. This velocity is slightly higher than the acoustic speed at the altitudes of the echo observation. This estimation of velocity might be in error by a factor of 1.5 at most, due to the wide angle of observation of the vertical antennae (from the delta type). A second evidence of this velocity existence is given by the disturbance observed in Fig. 7a at Wallops Island, which would require a velocity of about 0.7 km/sec in order to reach that station in the observed time. Fig. 10 shows ionograms taken on June 14, 1967 after an explosion release at 48.8 km. The echo designated by the thick arrow at the bottom frame is seen at 140 km apparent height. At the top frame, the echo has reached 200 km apparent height which requires at least a propa-

gation velocity of 0.5 km/sec as the time difference between both frames is two minutes. From the above it is seen that most ionospheric disturbances monitored have been some form of acoustic mode of propagation which would limit the echo's to the interval observed.

#### SUMMARY

It is noted that in the ionosphere, while disturbed by small disturbances such as explosions and rockets, acoustic modes are generated and propagate to long distances. Similarly, the acoustic long range propagation as observed by ground sensors has shown coupling with several upper atmosphere characteristics. The wind and temperature effects are partially known. However, the dissipation effects of other factors and the low collision frequencies at the upper atmosphere, as well as the possibility of energy coupling are still unresolved and require a stronger effort in both experimentation and analytical methods in order to determine all the factors involved. A cooperation of several ionospheric scientists and experts on wave phenomenon should operate in close coordination in observing future phenomenon. This must be done in order to be able to control the many factors involved in trying to solve the intermixed complex medium of the upper atmosphere including the lower ionosphere.

#### ACKNOWLEDGMENTS

I would like to thank Mr. L.C. McGahan who made these experiments with the explosives at the West coast possible; to Capt. Raymont; to A. Fiske and the people of GBI for their help in establishing the GBI station; to Mr. George Kaschak for his coordination on long range acoustic propagation; to the Navy in Point Mugu for the data handling and last but not least to J. Roberts for her patience in a hard task of reducing and reworking of the data not once but three times. This research was supported by U.S. Army Research Office Durham Contract DAHC 0037.

TABLE I

ALT. (km)	ELECTRON DENSITY $10^{-2}$ (cm <sup>-3</sup> ) Ne	ION DENSITY $10^3$ (cm <sup>-3</sup> ) N+	ION COLL- ISION FREQ (sec <sup>-1</sup> ) v+	ELECTRON COLLISION FREQUENCY $10^2$ (sec <sup>-1</sup> ) ve	ACOUSTIC SPEED $10^4$ cm/sec C	ALFVEN SPEED $10^8$ cm/sec Va	TOT. FLD. gauss Bo	NEUTRAL M.F.P. (cm) $\Lambda$	ELECTRON ELASTIC COLLISION FREQUENCY $10^3$ (sec <sup>-1</sup> ) ve eff	AVERAGE IONIC MOLECULAR WEIGHT W
60	0.1	8			3.1	10.52	0.4278	$4.9 \times 10^{-2}$	47000	
65	0.3	3				17.14	0.4268			
70	1.0	5			2.82	13.26	0.4258	$1.4 \times 10^{-1}$	14000	
75	1.5	8				10.44	0.4245			
80	6.0	5	$2.05 \times 10^5$	32900	2.53	13.18	0.4235	$8.8 \times 10^{-1}$	1700	29.0
85	6.0	6				12.00	0.4225			
90	100.0	14	$3.24 \times 10^4$	5420	2.62	7.839	0.4215	2.1	760	29.0
95	500.0	50			2.76	4.137	0.4205			
100	1000.0	100	$5.37 \times 10^3$	1000	2.85	2.919	0.4195	$1.0 \times 10$	170	28.4
110	1500.0	150			3.18	2.374	0.4180	$3.5 \times 10$	51	
120	1200.0	120	$3.12 \times 10^2$	7.93	3.74	2.642	0.4160	$1.1 \times 10^2$	18	26.7
130	1300.0	130			4.66	2.526	0.4140	$5.1 \times 10^2$	4.8	
140			$7.44 \times 10$	76.6	5.42		0.4120			25.7
150	1500.0	150			6.10	2.329	0.4100	$8.2 \times 10^2$	3.4	
160			$2.83 \times 10$	13.7	6.57		0.4080			24.7
180			$1.33 \times 10$	8.86	7.03		0.4045			23.7
200	5000.0	500	6.94	6.46	7.36	1.245	0.4000	$8.2 \times 10^3$	1.6	23.0
250			2.01	3.97	7.94		0.3915			21.0
300	18000.0	1800	$8.25 \times 10^{-1}$	3.83	8.41	0.6281	0.3830	$1.0 \times 10^5$	2.7	19.5
350			$3.91 \times 10^{-1}$	4.20	8.78		0.3745			18.4
400	15000.0	1500	$1.94 \times 10^{-1}$	4.43	9.12	0.6573	0.3660	$6.9 \times 10^5$	1.4	17.4



#### REFERENCES

Balachandran, N.K., W.L. Donn, Dispersion of atmospheric waves from nuclear explosions, Proceedings of the ESSA/ARPA Acoustic-Gravity Wave Symposium, 1968.

Bushman, W.W., O.E. Smith, An acoustic wind measuring technique, Presented at AIAA, 4th Aerospace Sciences Meeting, Los Angeles, Calif., June 27-29, 1966.

Donn, W.L., E. Posmentier, U. Fehr, N.K. Balachandran, Infrasound at long range from Saturn V, (in press, Science), 1968.

Donn, W.L., E. Posmentier, Infrasonic waves from natural and artificial sources, Proceedings of the ESSA/ARPA Acoustic-Gravity Wave Symposium, 1968.

Fehr, U., Instrumentational role in the observation of geoacoustical phenomena from artificial sources, J. Acoust. Soc. Am., 42, 5, 991-1000, 1967.

Fehr, U., L.C. McGahan, Energy coupling in the lower ionosphere by artificial disturbances in the 50 km atmospheric level - part I, Navy Report, (in press), 1968.

Golomb, D., N.W. Rosenberg, J.W. Wright, R.N. Barnes, Formation of an electron depleted region in the ionosphere by chemical releases, Space Research IV, North-Holland Pub. Co., 1964.

Helliwell, R.A., A study of the mechanism of Whistler propagation and VLF emission generation, Rept. AFOSR 68-0219, Jan. 1968.

Hines, C.O., Internal atmospheric gravity waves at ionospheric heights, Can. J. of Phys. 38, 1441, 1960.

Khvostikov, I.A., The upper layers of the atmosphere, NASA Rept. TTF-315, May 1965.

Wright, J.N., Ionosonde studies of some chemical releases in the ionosphere, Radio Science J. of Res., NBS, Vol. 68D, No. 2, Feb. 1964.

## II Natural sources of atmospheric waves- theory



# THE LAUNCHING OF LOW FREQUENCY TRAVELLING DISTURBANCES BY AURORAL CURRENTS

G. Chimonas

Department of Physics, University of Toronto, Toronto 5

It is shown that an auroral current discharge, coupling to the neutral atmosphere through the Lorentz force  $\bar{J} \times \bar{B}_0$ , can act as a powerful source of low frequency travelling waves. We propose that through this mechanism auroral storms give rise to TID's which can be observed at great distances from the auroral regions.

## INTRODUCTION

The accumulation of experimental evidence suggesting that auroral storms are responsible for travelling ionospheric disturbances (TID's) observed at lower latitudes (Chan and Villard, 1962; Hunsucker and Tveten, 1967; King, 1967) makes an investigation of the link between the two phenomena desirable.

The low-frequency propagation characteristics of the atmosphere have been studied extensively, and can be well understood on the basis of gravity wave theory (Hines, 1960) and the many 'explosion propagation' calculations (Press and Harkrider, 1962; Weston, 1962; Pierce, 1963; Row, 1967; Harkrider, 1964).

In fact if a coupling mechanism between an auroral discharge and the surrounding atmosphere is to be examined, by far the least well-known aspects of the problem concern the morphology of the discharge. Data on the coarse structure of auroral currents (total flow, approximate height etc.) are available, but the fine structure such as the space-time distribution has not yet been obtained.

It becomes necessary in our calculations to assume a form for these distributions. We have kept this form as simple as possible, hoping to reproduce the important quantitative features of a discharge without introducing too much model dependence into the calculation.

## THE MODEL FOR AURORAL CURRENTS AND THE COUPLING MECHANISM

The currents flowing through the ionosphere during a period of high auroral activity often extend thousands of kilometers along the direction of flow, yet remain highly localized in the plane perpendicular to the flow (eg., Boström, 1964). It is thus quite reasonable to use a two-dimensional current model of the discharge. Little is known about the shape of these currents perpendicular to the flow direction, so we will use the mathematically convenient form of a two-dimensional Gaussian distribution. Time development probably follows that of a magnetic substorm, with a relatively rapid buildup, a more-or-less steady phase, and a subsequent decay. Fluctuations within the substorm will of course occur, and will alter the response in detail. Our calculation of gross characteristics is quite insensitive to such structure however, and it is sufficient for present purposes to use a form such as that shown in Fig. 1.

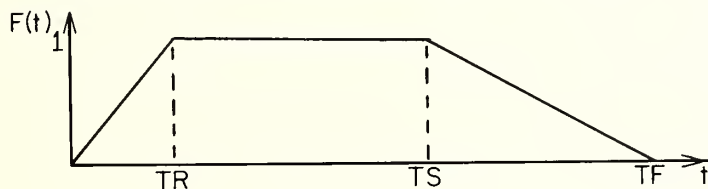


Figure 1. Model form for the time evolution  $F(t)$  of the discharge currents.

We will therefore have a current density  $\bar{j}(x, z, t)$  given by

$$\bar{j}(x, z, t) = \hat{y} A F(t) \exp \left[ -\alpha_1^2 (x - x_0')^2 - \alpha_2^2 (z - z_0')^2 \right],$$

where  $z_0'$  is the 'height' of the current above the earth's surface, and  $\hat{y}$  is the unit vector in the direction of flow (nearly East-West).

Because of the geomagnetic field  $\bar{B}_0$ , the neutral atmosphere will be coupled to the current by the Lorentz force  $\bar{j} \times \bar{B}_0$ . This provides a source of neutral disturbance, which then propagates out of the auroral regions. The work we wish to report here examines the efficiency of the body force (force per unit mass)

$$\bar{F}(x, z, t) = \bar{j} \times \bar{B}_0 / \rho_0 \quad (\rho_0 = \text{neutral mass density})$$

as a source of low frequency atmospheric disturbances, and finds that the larger currents detected in auroral displays are very likely to be responsible for TID's observed thousands of kilometers equator-wards.

#### RESPONSE OF THE ATMOSPHERE TO A PERTURBING FORCE

The equations of hydrodynamics governing the behaviour of the atmosphere when a body force  $\bar{F}(x, z, t)$  is present are

(i) Continuity

$$\frac{D\rho}{Dt} + \rho \nabla \cdot \bar{v} = 0$$

(ii) Adiabatic equation of state

$$\frac{D}{Dt} (p \rho^{-\gamma}) = 0 \quad 1.$$

(iii) Force equation

$$\rho \frac{D\bar{v}}{Dt} = \rho \bar{F} + \rho \bar{g} - \nabla p$$

Taking the atmosphere to be isothermal with scale height  $h$ , we proceed in the usual way to linearise the set 1 in perturbing amplitudes, and Fourier transform the resulting equations with respect to time. Some algebraic manipulation then yields an inhomogeneous second order partial differential equation for the  $\omega$  component of the fractional pressure perturbation.

$$\frac{p - p_0}{p_0} = \frac{1}{2\pi} \int_{-\infty}^{+\infty} d\omega e^{i\omega t} p^{(\omega)}; \quad p^{(\omega)} = e^{z/2h} \Phi^{(\omega)}$$

$$\left( \frac{\partial^2}{\partial x^2} + A_1 \frac{\partial^2}{\partial z^2} + A_2 \right) \Phi^{(\omega)} = S^{(\omega)}(x, z) \quad 2.$$

where

$$A_1 = \frac{\omega^2}{(\omega^2 - \omega_B^2)}; \quad A_2 = \frac{(\omega^4 - \omega^2 \omega_A^2)}{c^2 (\omega^2 - \omega_B^2)}; \quad \omega_B = \frac{(\gamma - 1)^{\frac{1}{2}} g}{c}; \quad \omega_A = \frac{\gamma g}{2c}; \quad c^2 = \gamma gh$$

and



$$S^{(u)}(x, z) = \frac{e^{-z/2h}}{gh} \left( \nabla \cdot \bar{F}^{(u)} + \frac{\omega_B^2}{(\omega^2 - \omega_B^2)} \frac{\partial F_z^{(u)}}{\partial z} - \frac{\omega^2 \omega_B^2}{(\gamma - 1) g(\omega^2 - \omega_B^2)} F_z^{(u)} \right).$$

A Green's function may be constructed for 2, and through its use the appropriate solution found to be

$$\Phi^{(u)}(x, z) = \iint dx' dz' \frac{i}{4\omega} (\omega^2 - \omega_B^2)^{\frac{1}{2}} S^{(u)}(x', z') H_0^2 \left\{ \left[ \frac{(\omega^2 - \omega_A^2)(\omega^2 - \omega_c^2)}{(\omega^2 - \omega_B^2)} \frac{R^2}{c^2} \right]^{\frac{1}{2}} \right\} \quad 3.$$

with

$$\omega_c = \frac{(z - z')}{R} \omega_B; \quad R^2 = (x - x')^2 + (z - z')^2.$$

$H_0^2$  is Hankel's Bessel function of the third kind of order zero (Watson, 1944). Fourier inverting 3 we formally obtain the fractional pressure perturbation as a triple integral. However, by making approximations appropriate for studying the low frequency portion of the pressure response at distances well removed from the source region, we can perform two of these integrations directly, leaving

$$\begin{aligned} p(x, z, t) \simeq & - \frac{\omega_B}{2\pi gh \rho_0(\bar{z}_0)} e^{-(\frac{1}{4} h \alpha_2)^2 + (z - \bar{z}_0)/2h} \frac{B_z \pi A}{\alpha_1 \alpha_2} \frac{(x - \bar{x}_0)}{R^2} \\ & \times \int_0^\infty ds e^{-(\omega_B s / 2R \alpha_2)^2} \left\{ \frac{F(t - \sqrt{s^2 + t_0^2})}{(1 + s^2/t_0^2)} \frac{\cos \omega_B s(z - \bar{z}_0)}{R} \right. \\ & + \frac{1}{t_0} I(t - \sqrt{s^2 + t_0^2}) \left[ \frac{1}{(1 + s^2/t_0^2)^{\frac{3}{2}}} \frac{\cos \omega_B s(z - \bar{z}_0)}{R} \right. \\ & - \frac{\omega_B s}{R(1 + s^2/t_0^2)} \frac{\sin \omega_B s(z - \bar{z}_0)}{R} \\ & \left. \left. - \frac{\omega_B s^2}{R \alpha_2} \frac{1}{2(1 + s^2/t_0^2)^{\frac{1}{2}}} \frac{\cos \omega_B s(z - \bar{z}_0)}{R} \right] \right\} \quad 4. \end{aligned}$$

with

$$t_0 = \frac{R \omega_B}{c \omega_A}; \quad \bar{x}_0 = x_0'; \quad \bar{z}_0 = z_0' + \frac{1}{4h \alpha_2^2}; \quad I(t) = \int_0^t dt' F(t').$$

A numerical computation now produces the pressure field. As a typical result we show in Fig. 2 the shape of the pressure pulse received at the point  $(x - \bar{x}_0) = 1500$  km,  $(z - \bar{z}_0) = 100$  km when the parameter values used are

$$h = \frac{1}{\alpha_2} = 10 \text{ km}, \text{ TR} = 10 \text{ mins}, \text{ TS} = 40 \text{ mins}, \text{ TF} = 70 \text{ mins}.$$

The zero of time is measured from current commencement.

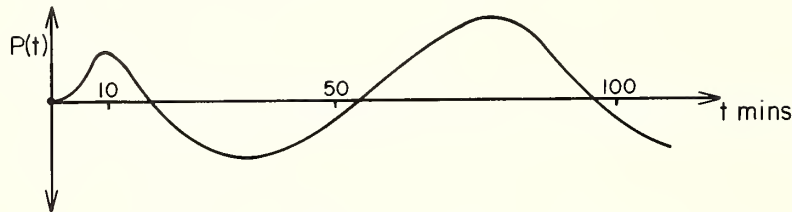


Figure 2. The pressure pulse received at lateral distance 1500 km from, and vertical distance 100 km above, the source currents.

Evaluating the absolute amplitude of the pulse, we find that if  $\bar{z}_0$  is 110 km above the earth's surface, while the total steady period current  $\pi A/\alpha_1 \alpha_2$  is  $10^6$  amps, the fractional pressure 'perturbation' recorded at this field point reaches order unity at its peaks. Such a response raises questions about the use of linear propagation theory, but leaves no doubt as to the ability of the (model) discharge to launch detectable TID's.

#### VISCOUS DAMPING

An estimate of viscous damping is needed both to find the atmospheric heating caused by passage of a TID, and to examine the associated decay of the TID itself. If we take the pressure pulse to locally simulate a plane gravity wave, we can use Hines' (1960) formula to find the rate of viscous dissipation of energy.

A rather striking result of this calculation is that the head of the pulse is less strongly damped than the tail. This provides a very convenient way of limiting the observable length of a TID, where otherwise the linear theory would predict a very long observable tail.

#### ACKNOWLEDGMENTS

The suggestion that the Lorentz force in an auroral discharge could be the source of travelling disturbances, was made to me by Dr. C. O. Hines, whose constant interest and help in the development of this work are gratefully acknowledged.

#### REFERENCES

- Bostrom, R., A model of the auroral electrojets, J. Geophys. Res. 69, 4983, 1964.
- Chan, R. L. and O. G. Villard, Jr., Observation of large-scale travelling ionospheric disturbances by spaced-path high-frequency instantaneous-frequency measurements, J. Geophys. Res. 67, 973, 1962.
- Harkrider, R., Theoretical and observed acoustic-gravity waves from explosive sources in the atmosphere, J. Geophys. Res. 69, 5295, 1964.
- Hines, C. O., Internal atmospheric gravity waves at ionospheric heights, Can. J. Phys. 38, 1441, 1960.

- Hunsucker, R. D. and Tveten, L. H., Large travelling-ionospheric-disturbances observed at mid-latitudes utilizing high resolution h.f. backscatter technique, *J. Atmos. Terr. Phys.* 29, 909, 1967.
- King, G. A. M., The ionospheric disturbance and atmospheric waves, *J. Atmos. Terr. Phys.* 29, 161, 1967.
- Pierce, A. D., Propagation of acoustic-gravity waves from a small source above the ground in an isothermal atmosphere, *J. Acoust. Soc. Am.* 35, 1798, 1963.
- Press, F. and Harkrider, D., Propagation of acoustic-gravity waves in the atmosphere, *J. Geophys. Res.* 67, 3889, 1962.
- Row, D. V., Acoustic-gravity waves in the upper atmosphere due to a nuclear detonation and an earthquake, *J. Geophys. Res.* 72, 1599, 1967.
- Watson, G. N., A treatise on the theory of Bessel's functions, Cambridge Univ. Press, 1944.
- Weston, V. H., The pressure pulse produced by a large explosion in the atmosphere, Part II, *Can. J. Phys.* 40, 431, 1962.



## MESOSCALE PRESSURE FLUCTUATIONS IN THE ATMOSPHERE

Ivan Tolstoy\*

Hudson Laboratories of Columbia University  
Dobbs Ferry, New York 10522

Plausible mechanisms of input and transmission of long period ( $1 \text{ min} < T < 2 \text{ hr}$ ) pressure perturbations are examined, together with some of the experimental evidence. It is pointed out that both internal gravity waves and shear-flow stability waves can be expected to play a role. There appears to be good evidence that this is so in the case of pressure fluctuations due to the jet stream and recorded on the Hudson Laboratories microbarograph system.

### Introduction

This paper discusses some theoretical problems raised by naturally occurring, traveling pressure fluctuations in the 2-90 min period passband. Our attention will be focussed specifically on a class of fluctuations excited by the tropospheric jet stream.

In order to put this discussion into some kind of perspective relationship to the observations, a few words must be said about the nature of the experimental evidence.

One meaningful type of description of background pressure fluctuation levels is provided by power spectrum studies. Figure 1 reproduces a power spectrum analysis given over ten years ago in a classic paper by Gossard [1960]. The region of particular interest to us here lies in the  $10^{-2}$  Hz to  $10^{-4}$  Hz range. Figure 2 shows some more detailed studies of this band, i. e., smoothed power spectra computed from a great many observations [Tolstoy and Herron, to be published]. A typical characteristic of the power spectra in this range is their knee-like shape, with a somewhat steeper fall-off for periods shorter than 10 min or so.

Another interesting property of this type of background is provided by its anisotropy, and, in particular, by frequently observed and well-defined directions and speeds of propagation, which correlate quite well, over long periods of time, with those of the jet stream aloft near the 200 mbar level [Flaurand et al., 1954; Young, 1968; Madden and Claerbout, 1968; Cook, 1968]. Systematic measurements of this correlation have been supplied recently by Tolstoy and Herron [to be published].

Another significant characteristic of these fluctuations is their rapid decorrelation. Cross-spectrum and coherence studies performed in the Dobbs Ferry area indicate that, for the typical jet stream type of activity described above in the 10-90 min passband, all spectral components decorrelate in the direction of propagation, over distances less than a wavelength. (On the other hand, traveling pressure perturbation systems generated by frontal activity, thunderstorms, etc., appear to remain coherent over larger distances.)

Such are the chief observations relevant to this discussion. In what follows we shall examine a plausible hypothesis relating some measured characteristics of the jet stream to the ground level pressure observations. In all of this we shall view the jet stream as a steady wind system superimposed upon which one has a spectrum of perturbations. General characteristics of this system will be found in Reiter's book [1963]. Kao and Woods [1964] have published some power spectra of these jet-level wind perturbations obtained from aircraft measurements. We will discuss here how a power spectrum such as the one shown in Fig. 3, representing the longitudinal wind perturbations at about 10 km, can be converted to a ground-level spectrum of pressure fluctuations.

### Formulation

The simplest pertinent physical problem can be stated as follows: Given a stratified fluid in a vertical gravity field and in a state of steady horizontal shear flow  $U_0(z)$ , and given a velocity perturbation field at some level  $z$ , calculate the concomitant pressure and velocity fields at ground level. The relevant equations are, ideally, the linearized Navier-Stokes equations. However, even in their linearized form, these equations lead to great mathematical difficulties. We therefore choose, at this juncture, to neglect viscosity. This leads to the linearized Euler or Boussinesq equations:

---

\* Now at Florida State University, Geophysical Fluid Dynamics Institute, Tallahassee, Florida.



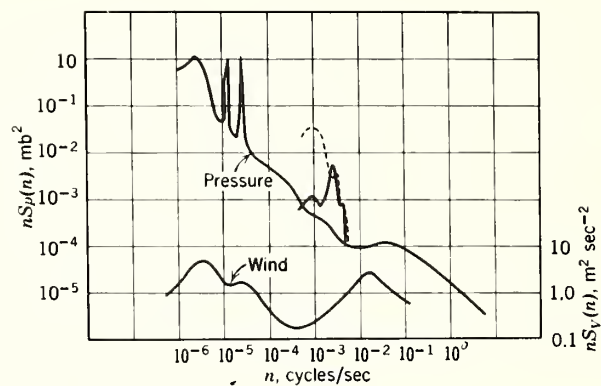


Fig. 1. Pressure power spectrum of the atmosphere after E. E. Gossard [1960].

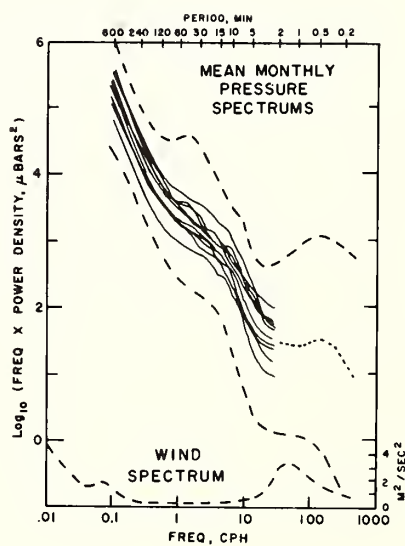


Fig. 2. Pressure power spectrum of the range from about  $10^{-2}$  to  $10^{-4}$  Hz, after Tolstoy and Herron [to be published].

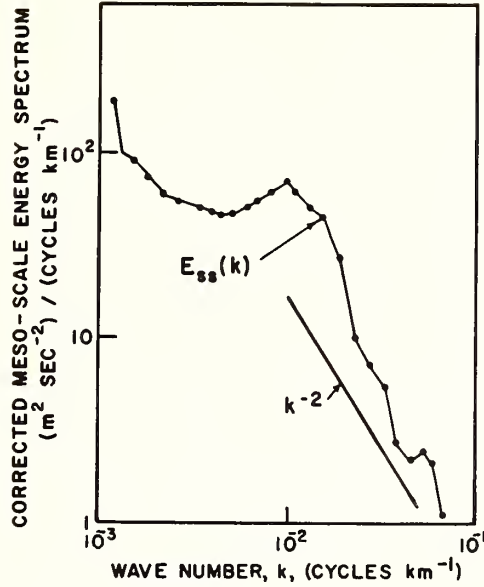


Fig. 3. Wind fluctuation power spectrum at a height of the order of 10 km, from Kao and Woods [1964].

$$\rho_0 \frac{d\vec{v}}{dt} = -\nabla p_1 + \vec{g} \rho_1 + \rho_0 \vec{v} \wedge \vec{\Omega} \quad (1)$$

where  $\vec{v}$  is the perturbation velocity,  $p_1$  and  $\rho_1$  the perturbation pressure and density respectively,  $\rho_0$  the steady mean density,  $\vec{g}$  the acceleration of gravity and  $\vec{\Omega}$  the Coriolis vector, and

$$\frac{d\vec{V}}{dt} = \frac{\partial \vec{V}}{\partial t} + U_0 \frac{\partial \vec{V}}{\partial x} + \vec{i}_z w U_0' \quad (2)$$

We take  $\rho_0$ ,  $U_0$  as functions of  $z$  only. If we neglect the Coriolis force we may use the two-dimensional system of Cartesian coordinates and conventions shown in Fig. 4. Furthermore, we may consider a harmonic perturbation field, i. e.:

$$\vec{v} = (u, w) \propto e^{i(ax - \omega t)} \quad (3)$$

where  $a$  is the horizontal component of the wavenumber and

$$c = \frac{\omega}{a} \quad (4)$$

is the horizontal phase velocity.

We may also assume that this perturbation field is essentially that of an incompressible fluid, as long as we limit ourselves to flows and perturbation velocities appreciably smaller than the speed of sound [Prandtl, 1952], i. e.:

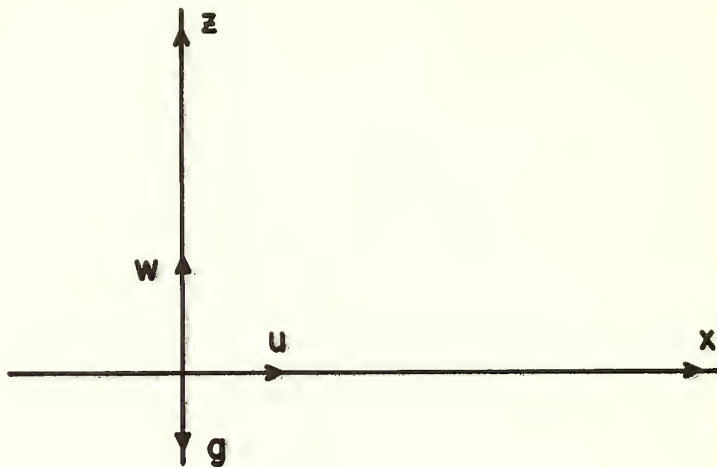


Fig. 4. Coordinate system used.

$$iau = -w_z \quad . \quad (5)$$

If then we write

$$w = \rho_o^{-1/2} h \quad , \quad (6)$$

it is easily demonstrated that the problem is reduced to the solution of a Helmholtz equation for  $h$  :

$$h_{zz} + \gamma^2 h = 0 \quad (7)$$

where

$$\gamma^2 = \frac{a^2}{\omega^2} \cdot \frac{N^2}{\left(1 - \frac{U_o}{c}\right)^2} \left[ a^2 + \frac{1}{4} \left( \frac{d}{dz} \ln \rho_o \right)^2 + \frac{1}{2} \frac{d^2}{dz^2} \ln \rho_o \right] + \frac{U_o'' + U_o' \frac{d}{dz} \ln \rho_o}{c - U_o} \quad . \quad (8)$$

Here the primes also indicate differentiation with respect to  $z$  .

$\gamma$  may be interpreted as the vertical component of the wavenumber and  $N$  is Väisälä or Brunt-Väisälä frequency:

$$N^2 = -g \frac{d}{dz} \ln \rho_o \quad . \quad (9)$$

It represents the angular frequency of oscillation of a small parcel of fluid displaced from its position of equilibrium and allowed to oscillate freely under the restoring force of buoyancy in a static medium. For static stability it is clearly required that  $N^2 > 0$ , i.e.,  $(d/dz) \ln \rho_0 < 0$ , consistently with Fig. 4.

The other terms containing derivatives of  $\rho_0$  in (8) represent the effect of variation of momentum density with  $z$  and can frequently be neglected [Phillips, 1966]. However in this latter procedure, care must be exercised: for example, in the case of a linear  $U_0(z)$  law (plane Couette flow) in a stratified medium, it is clearly not permissible to neglect the term  $U_0' (d/dz) \ln \rho_0$ , especially when  $c \approx U_0$ . Also, even in the absence of steady shear flow, these terms cannot be neglected for very long wavelengths ( $\alpha \rightarrow 0$ ).

The two special cases corresponding to the neglect of stratification or of the flow have been extensively studied in the literature. Thus:

1) If, in Eq. (8), we make  $U_0$  vanish everywhere, we have

$$\gamma^2 = \frac{\alpha^2}{\omega^2} N^2 - \left[ \alpha^2 + \frac{1}{4} \left( \frac{d}{dz} \ln \rho_0 \right)^2 + \frac{1}{2} \frac{d^2}{dz^2} \ln \rho_0 \right] \quad (10)$$

and we recover the usual equation for internal gravity waves in an incompressible fluid at rest. In general terms the theory of these waves is well understood [Yih, 1965; Tolstoy, 1963; Eckart, 1960]. Their possible relevance to atmospheric motions has been stressed by a number of authors in various contexts [Eckart, 1960; Hines, 1965; Tolstoy, 1967]. Both in oceanic and atmospheric dynamics we may drop the last two terms in (10) for a wide range of frequencies and wavenumbers, and write:

$$\gamma^2 = \frac{N^2}{c^2} - \alpha^2 \quad (11)$$

where  $c$  is the horizontal phase velocity defined in Eq. (4).

2) If we make  $\rho_0 = \text{const}$ , then

$$\gamma^2 = \frac{U_0''}{c - U_0} - \alpha^2 \quad (12)$$

and we obtain the standard form of the equation of small perturbations of a steady shear flow for the inviscid case [Drazin and Howard, 1966; Lin, 1955]. These have been variously named: we shall call them here stability waves in shear flow. There are obvious and well-known mathematical difficulties inherent in their treatment when one neglects viscosity as we are doing here. Clearly there is an essential singularity of the differential equation near  $U_0 = c$ . There is also a solution branch point connected with this value of  $z$  [Lin, 1955]. However, once viscosity is introduced these difficulties disappear: the full solution of the fourth order differential equation (the Orr-Sommerfeld equation) which then replaces (12) is perfectly regular and well behaved near  $c = U_0$ . Furthermore, one may always appeal to a well-known connection formula which enables one to relate the integration constants of the solution of (12) to both sides of  $c = U_0$  and to define the proper branch of the solutions to be used [Lin, 1955]. Thus, as long as one does not attempt to draw conclusions concerning the amplitude of the perturbation field itself near  $c = U_0$ , we may treat the solutions of Eq. (12) like those of any other Helmholtz equation. In particular, we may define most of the standard propagation properties for wave systems, such as wavenumber components, phase velocities, and perhaps group velocities, etc. Since the early studies of Rayleigh [Lin, 1955], hydrodynamicists have devoted a great deal of effort to the study of both the viscous and the inviscid problem of the propagation of small perturbations in shear flow.

Indeed, this is the core and substance of hydrodynamic stability theory [Lin, 1955]. However, the hydrodynamicist's principal interest in this problem has been in determining, for a number of typical shear flows, whether or not a given steady flow field  $U_0(z)$  is stable, and in determining the value of the critical Reynolds number  $Re_{cr}$ , if any. The procedure, both in the viscous and inviscid approximations, is to assume wave-like solutions such as (3), to take  $\alpha$  real and, having satisfied suitable boundary conditions, to calculate the complex eigenvalues for  $\omega = \omega_r + i\omega_i$ . If  $\omega_i < 0$  the solution (3) is stable, and it is unstable if  $\omega_i > 0$ . The boundary between the domains of stability and instability corresponds to  $\omega_i = 0$ . Even in quite simple flow models, this is quite a formidable computational problem. Once it has been solved, the hydrodynamical theorist usually loses further interest in the subject.

However, for the geophysicist interested in wave motions in atmospheric wind shear systems (or in ocean current systems!), the wave properties of the disturbance are often of greater interest than the stability criteria, particularly for cases that are either slightly stable (small damping) or weakly unstable (slow growth rate). From this point of view, a good procedure is to assume  $\omega$  real and to calculate the real and imaginary components of  $\alpha$ . If the imaginary component of  $\alpha$  is shown to be small, it is then possible to neglect it in many applications. In fact, if we fix our attention on problems which are known to be stable in the absence of boundaries - such as plane Poiseuille flow - we may omit this step entirely and, by virtue of our knowledge of the regular behavior of the complete viscous perturbation solutions near  $U_0 = c$ , proceed immediately to discuss some of the wave properties in the inviscid context of Eq. (7).\*

A point of some general interest regarding Eq. (7) is that, if we define

$$k^2 = \alpha^2 + \gamma^2 \quad (13)$$

one may rewrite (12) as

$$\omega = \alpha U_0 + \frac{\alpha}{k^2} U_0'' \quad (14)$$

which is isomorphic to the so-called "  $\beta$  plane" Rossby wave approximation:

$$\omega = \alpha V_0 + \frac{\alpha}{k^2} \beta \quad (15)$$

where  $V_0$  is the constant velocity of the stream and

$$\beta = -\frac{\partial \Omega}{\partial y} = \text{const} \quad (16)$$

is the meridional rate of change of the normal component of the Coriolis vector  $\vec{\Omega}$ .

Equation (14) differs somewhat from the usual Rossby wave approximation in that both  $U_0$  and  $U_0''$  may be functions of the transverse coordinate ( $z$  in our case,  $y$  for Eq. (15)). However, for plane Poiseuille flow with a maximum velocity at  $z = h$ :

$$U_0 = U_m - \frac{U_m}{h^2} (z - h)^2 \quad (17)$$

The analogy between (14) and (15) is closest for disturbances propagating near the axis  $z = h$ , since here  $U_0 \approx U_m$  is approximately constant.

Actually, the isomorphism between the dispersion equations (15) and (14) could have been foreseen formally from the equations of motion (1) which become, for constant  $\rho_0$ :

$$\frac{d\vec{v}}{dt} = -\frac{1}{\rho_0} \nabla p + \vec{v} \wedge \vec{\Omega} \quad (18)$$

if

$$\vec{\omega} = \text{curl } \vec{v} \quad (19)$$

We have, taking the curl of both sides of (18):

$$\frac{\partial \vec{\omega}}{\partial t} + \text{curl} [(\vec{\omega} + \vec{\Omega}) \wedge \vec{v}] = 0 \quad (20)$$

---

\* It has been pointed out by Case [1962] and Warren [1968] that the initial value problem bypasses many of these difficulties entirely.



If now we write,

$$\vec{v} = \vec{U}_0 + \vec{u} \quad (21)$$

and

$$\vec{\omega} = \vec{\omega}_0 + \vec{\omega}_1 \quad (22)$$

where

$$\vec{\omega}_0 = \text{curl } \vec{U}_0 \quad (23)$$

$$\vec{\omega}_1 = \text{curl } \vec{u} \quad (24)$$

then the linearized (perturbation) equation for  $\vec{\omega}_1$  is:

$$\frac{\partial \vec{\omega}_1}{\partial t} + \text{curl} \left[ \left( \vec{\omega}_1 + \vec{\omega}_0 + \vec{\Omega} \right) \wedge \vec{u} \right] = 0 \quad (25)$$

Thus, it is clear that  $\vec{\omega}_0$  and  $\vec{\Omega}$  play similar roles. In the case of a plane shear flow of the type discussed above,

$$\vec{\omega}_0 = \vec{1}_z U'_0 \quad (26)$$

Both Rossby and stability waves in shear flow exist by virtue of gyroscopic-type restoring forces which ensure the constancy of vorticity, i. e., of the angular momentum of each infinitesimal cylinder of fluid. Actually this process may be viewed as resulting from a balance of forces involving a field of vortex filaments parallel to the transverse axis (  $y$  , in our coordinate system), as pointed out by C. C. Lin [1955].

#### Excitation of Wave by Moving Disturbances

In treating an inviscid model of the Earth's atmosphere one should, in principle, use Eqs. (7) and (8), keeping in mind at all times the difficulties inherent to this model because of the singularity and branch points at  $U_0 = c$  . It is feasible to some extent to steer clear of these mathematical subtleties thanks to the existence of careful analyses and of connection formulae for the  $\rho_0 = \text{const}$  case, but one is still faced with the fact that, in practice,  $U_0$ ,  $N^2$ ,  $\rho_0$  are functions of  $z$  and that  $\gamma^2$  has a fairly complex dependence upon  $z$  . Thus the problem of extracting the correct behavior of the various possible modes of wave propagation from Eqs. (7) and (8) has never been successfully and fully resolved. Thus the relatively simpler question of stability for the stratified flows remains unclear. The actual value of the critical Richardson number, and even its significance for real problems, is still a matter of debate [Case, 1962].

In the following we shall not attempt to attack even the limited problem corresponding to Eqs. (7) and (8) and we will modestly confine ourselves to estimating orders of magnitude for the two limiting cases of vanishing  $\rho'_0$  and of  $U_0 = 0$  . This will enable us at least to shed a little light on the relationship of these problems to the theory of a class of atmospheric pressure perturbations in the 2-90 min period bandpass.

We will assume that a sinusoidal disturbance such as (3) is moving at some height close to the jet stream axis with a velocity  $c$  matching that of the wind, and we shall estimate the magnitude of the pressure perturbations recorded at ground level in the case of two highly over-simplified models. This moving sine wave is taken to represent both a spectral component of the Kao and Woods jet-stream perturbation field and the value of the generated wave field at this height. This is equivalent to assuming that the Kao and Woods wind spectrum is coupled into the wave field with 100% efficiency - an assumption which is obviously open to question unless one assumes that the measurements of Kao and Woods correspond to a fully established perturbation wave field.

The first model we shall consider only briefly: it is that of a homogeneous, incompressible fluid with a parabolic wind distribution - i. e., the case of plane Poiseuille flow corresponding to Eq. (7) and sketched in Fig. 5. In this case, the relevant equations are (7) and (12), and the relationship between pressure  $p$  and longitudinal particle velocity  $u$  (i. e., wind perturbation) is, in the linear approximation,

$$p = \rho c u \quad (27)$$

where  $c$  is the phase velocity (4).

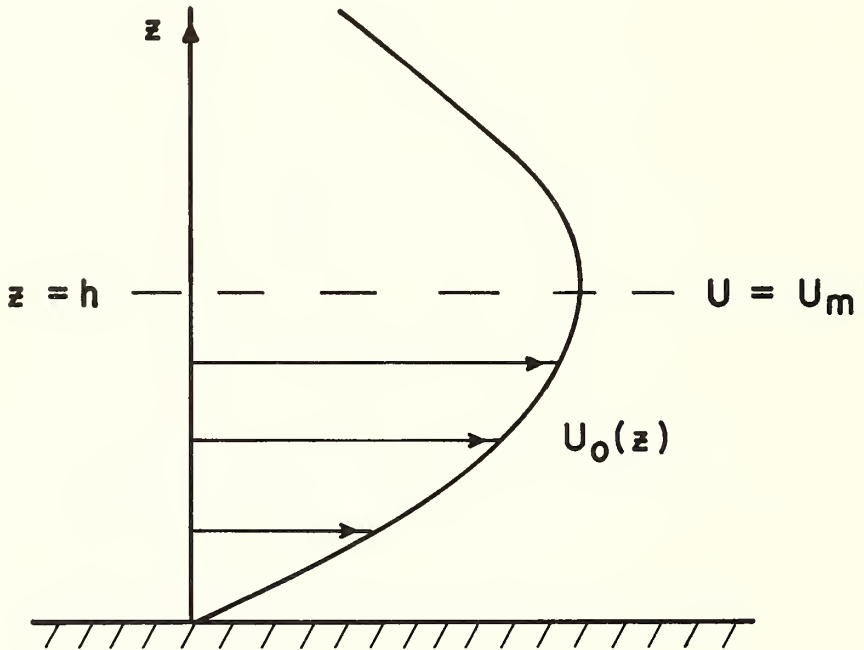


Fig. 5. Plane Poiseuille flow.

The difficulty one faces here concerns what to do with the singular plane at  $c = U_0$ . This is, in turn, related to the problem of how close can one get to this singularity and still get proper approximations for the wave field amplitudes by means of Eqs. (7) and (12). We can side-step this problem to a considerable extent by assuming that the reference level  $z = z_0$  at which we take our traveling wave is far enough from the plane  $c = U_0$ , and computing field amplitudes only in the direction of increasing  $|c - U_0|$  from this reference level.

For example, let us assume the reference level

$$z = z_0 = 0.9 \times 10^4 \text{ m} \quad (28)$$

at which level the wave system is traveling with a phase velocity  $c$  matching the value of the flow on axis:

$$c = U_0(h) = U_m. \quad (29)$$

Then, using (17) and (12) gives

$$\gamma^2 = -\frac{2}{(z-h)^2} - a^2 \quad (30)$$

$\gamma^2$  is thus negative for  $0 \leq z < h$ . In the W.K.B. approximation, solutions of (7) will have the form:

$$h \propto |\gamma|^{-1/2} e^{\pm s} \quad (31)$$

where

$$s(z) = \int^z |\gamma| dz \quad (32)$$

Thus, by virtue of (5) and (6), and assuming that only exponentially decreasing solutions of the type (31) are relevant here, we have:

$$u = U_o \left| \frac{\gamma_o}{\gamma} \right|^{1/2} e^{s_o - s} \quad (33)$$

where the subscript  $o$  refers to quantities calculated at the reference level (28) and

$$s(z) = a \left\{ \left[ \frac{2}{a^2} + (z-h)^2 \right]^{1/2} - \frac{\sqrt{2}}{a} \ln \left| \frac{\frac{\sqrt{2}}{a} + \left[ \frac{2}{a^2} + (z-h)^2 \right]^{1/2}}{z-h} \right| \right\} \quad (34)$$

If now we assume a period of  $T = 20$  min and a phase velocity  $c = U_m = 20 \text{ m sec}^{-1}$ , giving a wavelength of the order of 24 km, and  $a = 2.6 \times 10^{-4} \text{ m}^{-1}$ , for  $h = 10 \text{ km}$ , these results give us  $u/u_o < 10^{-2}$ . Calculations performed for other values of  $c$ ,  $T$  in this general range yield comparable answers.

This mechanism of transmitting perturbations of the jet stream to ground level does not therefore appear to be a very efficient one, in marked contrast to the internal gravity wave mechanism which we can estimate approximately as follows.

First of all, we note that in (8) reasonable orders of magnitude for  $(d/dz) \ln \rho_o$ ,  $N$ , averaged for the atmosphere below the jet stream are given by assuming

$$N \approx 1 \times 10^{-2} \text{ rad} \cdot \text{sec}^{-1} \quad (35)$$

and if

$$\rho = \rho_o e^{-2\nu z} \quad (36)$$

with

$$\begin{aligned} \nu &\approx 5 \times 10^{-5} \\ \nu^2 &\approx 2.5 \times 10^{-9} \end{aligned} \quad (37)$$

and

$$\gamma^2 \approx \frac{N^2}{(c - U_o)^2} - (a^2 + \nu^2) + \frac{U_o'' - 2\nu U_o'}{c - U_o} \quad (38)$$

The last (shear flow) term is essentially zero at ground level  $z = 0$ , whereas at  $z \approx h$ ,  $|U_o''| \gg |2\nu U_o'|$ . Elsewhere therefore, the ratio of the gravitational to the shear flow term is of the order of  $r = |N^2/c U_o''|$ . For the type of model chosen  $|U_o''| = 2(U_m/h^2)$  and, assuming again  $c \approx U_m$ , gives

$$r = \frac{N^2 h^2}{2c^2} \approx 0.5 \times 10^4 \times \frac{1}{c^2} . \quad (39)$$

Thus,  $r \gg 1$  if  $c^2 \ll 0.5 \times 10^4$ , i. e., for  $c \ll 0.7 \times 10^2$ . Assuming this to hold true, we see that for all practical purposes:

$$\gamma^2 \approx \frac{N^2}{(c - U_0)^2} - a^2 . \quad (40)$$

This implies that buoyancy forces as modified by a wind distribution  $U_0(z)$  play the dominant role. For a given  $c \neq U_0$ , the effect of the shear flow is equivalent to modifying the  $N(z)$  stratification of the static case.

As a first approximation we may treat the case of

$$U_0 = 0$$

$$N = 1 \times 10^{-2} \text{ rad} \cdot \text{sec}^{-1} = \text{const} . \quad (41)$$

The jet stream is then represented by the traveling corrugation (3) with  $c = U_m$ , and:

$$\gamma^2 \approx \frac{N^2}{c^2} - a^2 . \quad (42)$$

Here, as long as  $\omega = ac < N$ , we have  $\gamma^2 > 0$ , the solutions of (7) are sinusoidal:

$$u(z) = u_0 \sqrt{\frac{\rho_0}{\rho}} \cos \gamma (z - z_0) \quad (43)$$

where, as before, the  $_0$  subscript refers to the reference level  $z_0$ . It follows from (27) that the ground-level pressure is, in terms of  $u_0$ :

$$p(z) = c \sqrt{\rho \rho_0} u_0 \cos \gamma (z - z_0) \quad (44)$$

For  $\omega > N$ , i. e., for periods shorter than the Väisälä period,  $\gamma^2$  in (42) is negative and we replace  $\gamma$  by  $\gamma' = (a^2 - N^2/c^2)^{1/2}$ . We should then replace the trigonometric functions in (43) and (44) by exponentials and  $z$ , for  $z < z_0$ :

$$p(z) = c \sqrt{\rho \rho_0} u_0 e^{\gamma' (z - z_0)} . \quad (45)$$

Thus the contribution of jet-stream perturbations to ground-level pressure perturbations, for given  $c$ , falls off quite rapidly for  $\omega > N$ .

These results enable us to convert quite simply the Kao and Woods wind velocity fluctuation spectrum to ground-level pressure perturbations. Thus taking the time average of the  $p^2$  and smoothing in frequency by replacing  $\cos^2 \gamma (z - z_0)$  by  $1/2$  (this assumes insufficient resolution to separate the resulting fine structure in the spectrum), gives:

$$\langle p^2 \rangle \approx c^2 \rho \rho_0 \frac{1}{2} \langle u_0^2 \rangle . \quad (46)$$

in MKS units  $\rho \approx 1$ ,  $\rho_0 \approx 0.4$ , and the conversion in these units is:

$$\Pi \approx 0.2 c^2 P_o \quad (47)$$

where  $\Pi$  is the ground-level power spectrum of pressure and  $P_o$  is the jet-stream longitudinal wind velocity fluctuation power spectrum.

To use the Kao and Woods  $E_{ss}(\kappa)$  from Fig. 3 we take

$$P_o = k E_{ss} \quad (48)$$

where  $k$  is in cycles  $\text{km}^{-1}$ . Converting this to  $(\mu\text{bar})^2$  times cph and taking the log we obtain results comparable to those of Tolstoy and Herron of Fig. 2. In Fig. 6, we show the comparison for the model of Eq. (41) with a dotted line. It is seen that appropriate orders of magnitude are obtained this way. The rapid falloff of the calculated spectrum for periods shorter than ten minutes or so is due to one's having to use (45): for periods shorter than the Väisälä period this mechanism for transmission of pressure fluctuations to ground level is very inefficient.

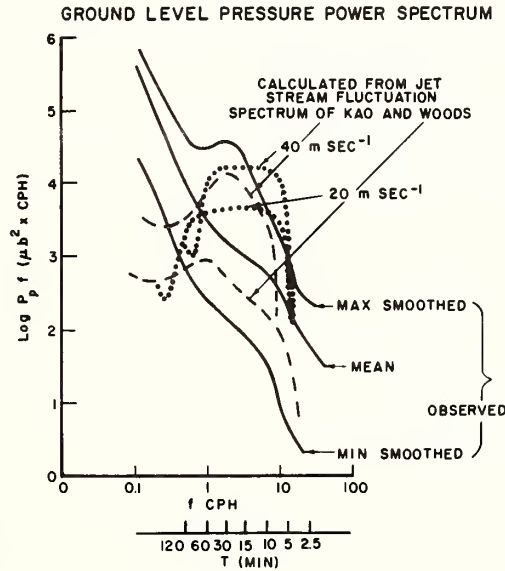


Fig. 6. Comparison of smoothed average and extremal pressure spectra observed at Dobbs Ferry (solid line) with spectra calculated from the jet-stream wind spectrum of Kao and Woods shown in Fig. 3. Two different velocities were tested, 20 and 40 m  $\text{sec}^{-1}$ , and two hypotheses, corresponding to constant  $N = 1 \times 10^{-2} \text{ rad} \cdot \text{sec}^{-2}$  (dotted line) and no wind shear, and to  $N$  varying according to Eq. (56) (dashed line). The latter hypothesis is approximately equivalent to using a constant  $N$  and a variable wind velocity, increasing with height, and is seen to give the best results.



In view of Eq. (40) and our previous discussion, it is worth making some simple calculations in models neglecting wind, but with  $N(z)$  increasing with height. In view of what was said above, this will, for given  $c$ , provide at least a qualitative estimate of the effect of  $U_0(z)$ , if we use an increasing  $N(z)$ . For example, assuming:

$$\begin{aligned} N(z) &= 1 \times 10^{-2}, & z &= 0 \\ N(z) &= 2 \times 10^{-2}, & z &= h \end{aligned} \quad (49)$$

implies that, if  $c = U_m$  = jet-stream velocity, then the reference level is chosen so that  $U_0 = 0.75 c = 0.75 U_m$ . A realistic wind profile model would place this level at some height between 9 and 10 km [Reiter, 1963]. The model of Eq. (49) with no wind should then yield somewhat improved conversion factors for transforming the Kao and Woods spectrum to a ground-level pressure fluctuation spectrum, since it is effectively equivalent to using (35) with a variable  $U_0$ .

The W.K.B. approximation applied to Eq. (7) gives, in this case:

$$u(z) = u_0 \sqrt{\frac{\rho_0 \gamma_0}{\rho \gamma}} \cos s \quad (50)$$

where

$$s = \int_0^{z_0} \gamma dz \quad (51)$$

for the domain of real  $\gamma$ , i.e., as long as  $\omega < N(z)$ .

For regions of  $\omega > N(z)$ , the internal gravity wave modes have only an exponential type of penetration and we replace  $\cos s$  in (50) by  $e^{-\sigma}$  where:

$$\sigma = \int_0^{z_0} |\gamma| dz \quad (52)$$

$$|\gamma| = \sqrt{a^2 - \frac{N^2}{c^2}} \quad (53)$$

The conversion formula, after squaring and smoothing is, for the trigonometric spectrum, the same as (47) except for a factor  $\gamma/\gamma_0$ :

$$\Pi \approx 0.2 c^2 \frac{\gamma}{\gamma_0} P_0 \quad (54)$$

and, of course, the exponentially decreasing modes fall off as  $e^{-2\sigma}$ :

$$\Pi \approx 0.2 c^2 \frac{|\gamma|}{\gamma_0} P_0 e^{-2\sigma} \quad (55)$$

Equations (54) and (55) are, of course, valid only as long as  $\gamma_0 \neq 0$ , i.e., we must exercise care to stay away from the turning points of Eq. (7) at which the W.K.B. approximations are invalid. It is well known that this only involves a narrow range of parameters which is easily avoided in practice [Brekhovskikh, 1960].

Assuming a law such as (49), with

$$\begin{aligned} N^2 &= 1 \times 10^{-4} + az, \\ a &= 3 \times 10^{-8} \text{ m}^{-1} \text{ sec}^{-2} \end{aligned} \quad (56)$$

enables us to calculate the dashed line spectra shown in Fig. 6: this appears to show a behavior of the power-spectrum which is somewhat more in consonance with observation.

#### Discussion

We have demonstrated by means of some very simple model calculations that it is possible to correlate quantitatively the wind-fluctuation power spectra measured by aircraft at jet-stream heights with ground-level pressure fluctuation power spectra. These calculations support the point of view that the primary effect is one of radiation of internal gravity waves by the perturbed jet stream. These internal gravity waves have phase velocities matching the mean flow velocity somewhere near the jet-stream core. The effect of wind shear can be qualitatively taken into account, and appears to significantly affect the shape of the pressure spectrum at ground level. However this can be approximately taken into account by using, for a given phase velocity, a model without winds but with an effective Väisälä frequency which increases upward.

A difficulty of this model lies in the somewhat unrealistic assumption that each component of the wind perturbation spectrum can be treated as a perfectly coupled corrugation of the medium traveling with the mean jet-stream velocity  $U_m = c$ . The fact remains, however, that this assumption gives the right orders of magnitude. A way of side-stepping the issue therefore suggests itself: the jet-stream wind perturbation spectra published by Kao and Woods might well correspond to fully developed internal gravity wave fields, in which case our model would be valid. This may enable us to avoid the issue, but the problem of how these fields are in fact generated by the jet stream remains. This is undoubtedly a question of considerable complexity, deserving further study - it is almost certainly related to the difficult problems of internal gravity wave generation by turbulence and perhaps, conversely, to the theory of clear air turbulence.

#### Acknowledgments

This work was supported by the Office of Naval Research and the Advanced Research Projects Agency under Contract Nonr-266(84). Reproduction in whole or in part is permitted for any purpose of the United States Government. It is Hudson Laboratories of Columbia University Contribution No. 330.

#### References

- Brekhovskikh, L. M., *Waves in Layered Media*, Academic Press, New York and London (1960).
- Case, K. M., Hydrodynamic stability and the initial value problem, *Proc. of Symposia on Appl. Math.*, 13, 25-33, Am. Math. Soc. (1962).
- Cook, R. C., Subsonic atmospheric oscillations, *Boulder Symposium on Acoustic-Gravity Waves in the Atmosphere*, (A), 50 (1968).
- Drazin, P. G., and L. N. Howard, *Hydrodynamic Stability of Parallel Flow of Inviscid Fluid*, *Advances in Appl. Mech.*, 9, Academic Press, New York (1966).
- Eckart, C., *Hydrodynamics of Oceans and Atmospheres*, Pergamon Press, Oxford, England (1960).
- Flaurand, E. A., A. H. Mears, F. A. Growley, Jr., and A. P. Crary, Investigation of Microbarometric Oscillations in Eastern Massachusetts, AFCRL Tech. Rept. 54-11, *Geophys. Res. Papers* No. 27 (1954).
- Gossard, E. E., Spectra of atmosphere scalars, *J. Geophys. Res.*, 65, 3339-3351 (1960).
- Hines, C. O., in *Physics of the Earth's Upper Atmosphere*, by C. O. Hines, I. Paghis, T. R. Hartz, and J. A. Fefer, Prentice-Hall, New Jersey (1965).
- Kao, S. K., and H. D. Woods, Energy spectra of meso-scale turbulence along and across the jet stream, *J. Atmos. Sci.*, 21, 513 (1964).
- Lin, C. C., *The Theory of Hydrodynamic Stability*, Cambridge University Press, Cambridge (1955).
- Madden, T. R., and Jon Claerbout, Observations of jet-stream gravity waves and their implications concerning jet-stream stability, *Boulder Symposium on Acoustic-Gravity Waves in the Atmosphere*, (A), 51 (1968).

- Phillips, O. M., The Dynamics of the Upper Ocean, Cambridge Monographs on Mechanics and Applied Mathematics, Cambridge University Press, Cambridge (1966).
- Prandtl, L., Essentials of Fluid Dynamics, with Applications to Hydraulics, Aeronautics, Meteorology and Other Subjects, Hafner Publishing Co., New York (1952).
- Reiter, Elmar E., Jet-Stream Meteorology, The University of Chicago Press, Chicago (1963).
- Tolstoy, I., The theory of waves in stratified fluids including the effects of gravity and rotation, Rev. Mod. Phys., 35, 207-230 (1963).
- Tolstoy, I., Long period gravity waves in the atmosphere, J. Geophys. Res., 72, 4605-4622 (1967).
- Tolstoy, I., and T. Herron, A model for atmospheric pressure fluctuations in the mesoscale range (to be published).
- Warren, F. W. G., Transient energy flux and the initial value problem, Boulder Symposium on Acoustic-Gravity Waves in the Atmosphere, (A), 9 (1968).
- Yih, C. S., Dynamics of Nonhomogeneous Fluids, The Macmillan Co., New York (1965).
- Young, J. M., Experimental observations of tropospheric jet-stream waves, Boulder Symposium on Acoustic-Gravity Waves in the Atmosphere, (A), 51 (1968).

## JET STREAM ASSOCIATED GRAVITY WAVES

and

## IMPLICATIONS CONCERNING JET STREAM STABILITY

T.R. Madden and J.F. Claerbout<sup>1</sup>

Geology and Geophysics Department, Massachusetts Institute of Technology

Data collected from a 20 km array of microbarographs situated in the vicinity of Boston, Massachusetts frequently show well correlated pressure fluctuations in the 5 to 50 minute period range that move across the array with velocities and directions typical of the overhead tropospheric jet stream. Comparisons of the gravity wave phase velocities and the upstream jet profile imply that the gravity waves emanate from the region of the jet that is least dynamically stable. These correlations are strongest when the jet stream is nearly unstable, although gravity waves are still observed when the upper air summaries indicate that the jet stream is quite stable on a gross scale. Upwards continuation of the observed pressure fields show, however, that the shears associated with the gravity wave induced winds can exceed the Richardson stability criteria at distances of as much as one third to one half a kilometer below the critical layer.

### Introduction

An increasing importance is being assigned to atmospheric gravity waves in explanations of dynamical effects in the upper atmosphere and ionosphere. The tropospheric jet streams appear as likely contributors of such waves as the jet stream represents a very large reservoir of dynamical energy, and the jet stream velocities are comparable to some of the horizontal phase velocities associated with the upper atmospheric effects. It is known that if the jet stream velocity shear exceeds twice the local Brunt frequency the flow is dynamically unstable, and since gravity waves can match the velocity of any flow that is subsonic, one would expect these instabilities to radiate out gravity waves. The height at which the flow velocity matches the horizontal phase velocity is known as the critical layer, and it has been shown that linear theory predicts the gravity wave will give up its momentum to the mean flow at this layer if the flow profile is stable (Booker, 1967; Bretherton, 1966). Thus there may well be an interplay between gravity waves and jet streams that could result not only in energy being radiated out to the upper atmosphere, but also could result in modifications of the jet stream profile. The true picture of these interactions is difficult to track down because of the non-linear character of the phenomenon near the critical layer. In this paper we will be mainly concerned with our observations made on the ground of jet stream associated waves and their correlation with the degree of dynamical instability of the jet as determined from the upper air summaries of wind and temperature.

### Observational Evidence of Jet Stream Waves

In Eastern Massachusetts we are monitoring pressure fluctuations in the period band of 1 to 50 minutes with a triangular array of 20 kilometers to a side. Records of the pressure fluctuations show two common types of coherent features that cross the array. One type is associated with moving weather sources such as fronts.

<sup>1</sup> Now at Geophysics Department, Stanford University, Stanford, California.

Figure 1 shows such an example

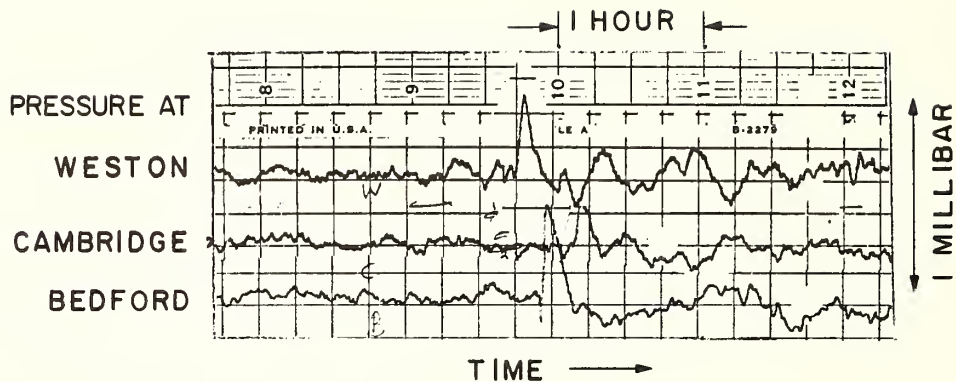


Figure 1 Pressure fluctuations associated with moving weather

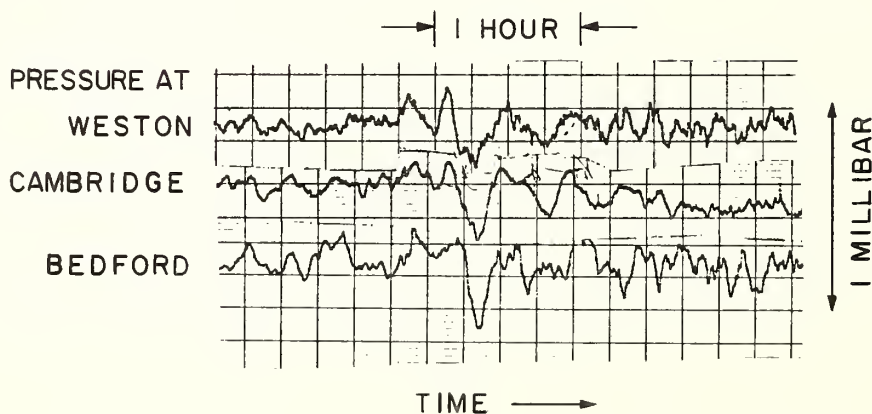


Figure 2 Pressure fluctuations associated with tropospheric jet stream

These weather features move across the array with velocities of 5 to 15 meters/sec. and can include, as the example in Fig. 1, quite a wide spectrum of frequencies. The other common type consists of waves of higher velocities with a marked absence of high frequency components. Such an example is shown in Figure 2. The velocity



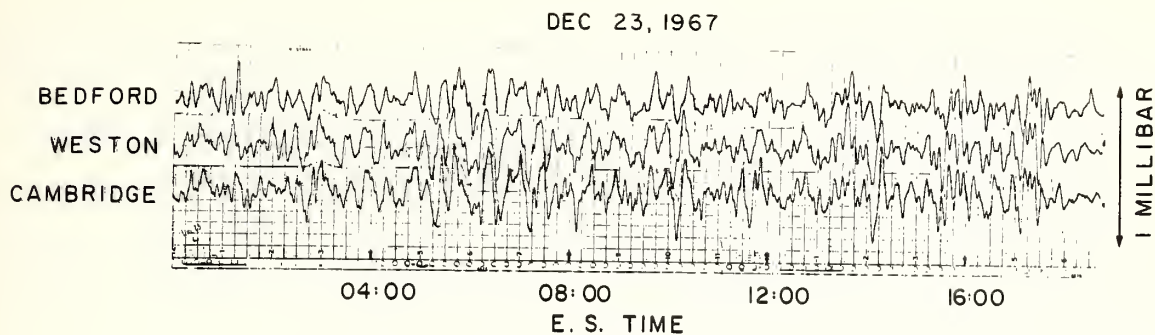


Figure 3 An example of very strong jet stream associated gravity waves

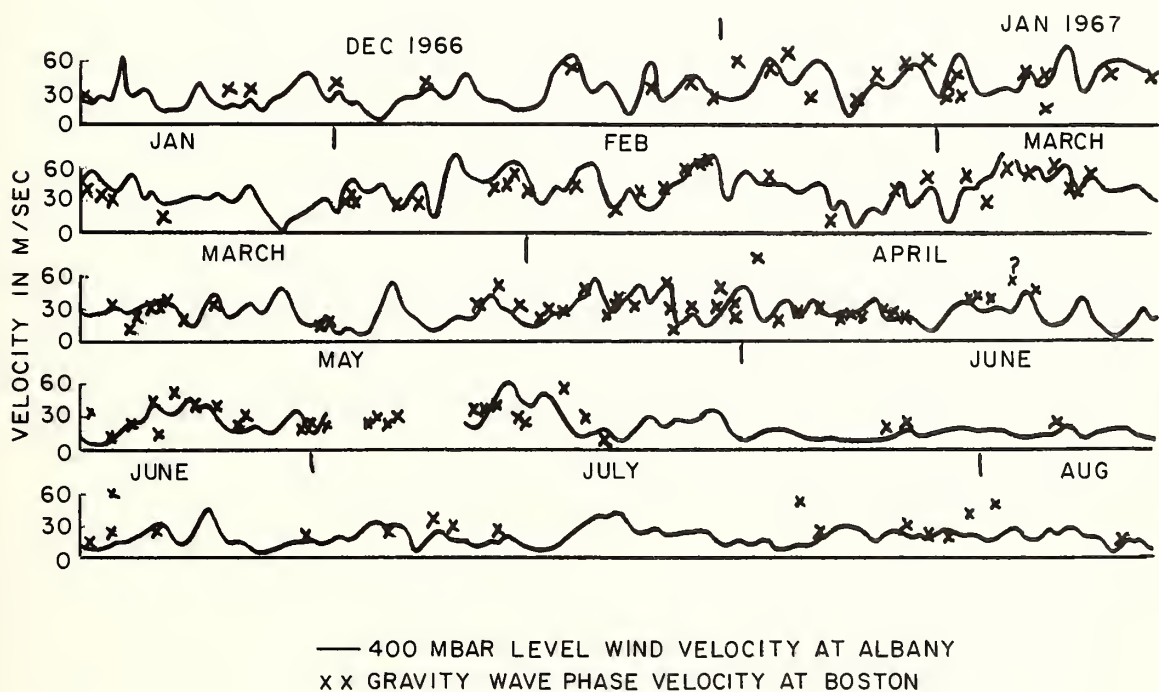


Figure 4 Jet stream and gravity wave activity near Boston, Dec. 1966 - Aug. 1967

of these waves ranges from 20 to 90 meters/sec and are predominantly in the eastward direction. Waves of this type were first reported by Flauraud (Flauraud, 1954) from measurements also made in the vicinity of Boston and were correlated with the overhead tropospheric jet stream. On some occasions these waves can completely monopolize the pressure fluctuations and produce very coherent records across the 20 km array. Figure 3 shows such an example. The coherency is most remarkable in this example near the end of the record and just before a dramatic quieting of the pressure fluctuations took place.

When the coherency is quite good across the array one can make an estimate of the wave phase velocity from a visual examination of the analog records and in Figure 4 we show a plot of the velocities determined in this fashion during a nine month period. The overhead jet stream velocity at the 400 mbar level is also shown. These velocity determinations are very crude, but Figure 4 does show that coherent wave activity is not uncommon and is generally correlated with strong overhead jet stream activity. A similar result is obtained in plotting wind and wave directions.

While the example of Figure 3 showing strong correlations across all the sensors of the array is somewhat unusual, it is not uncommon for very strong correlations to exist between two stations that are on the same streamline. Cambridge lies almost due east of Weston and eastward is the dominant jet stream flow direction, and we find that the Weston-Cambridge coherency is often very pronounced. Figure 5 shows two examples of Weston-Cambridge records. During the winter and early spring months when the jet stream is at its strongest over Boston, these two stations are well correlated most of the time. The weaker correlations across the flow lines must imply that the waves have some spectrum of across flow wavelengths of less than 80 kilometers.

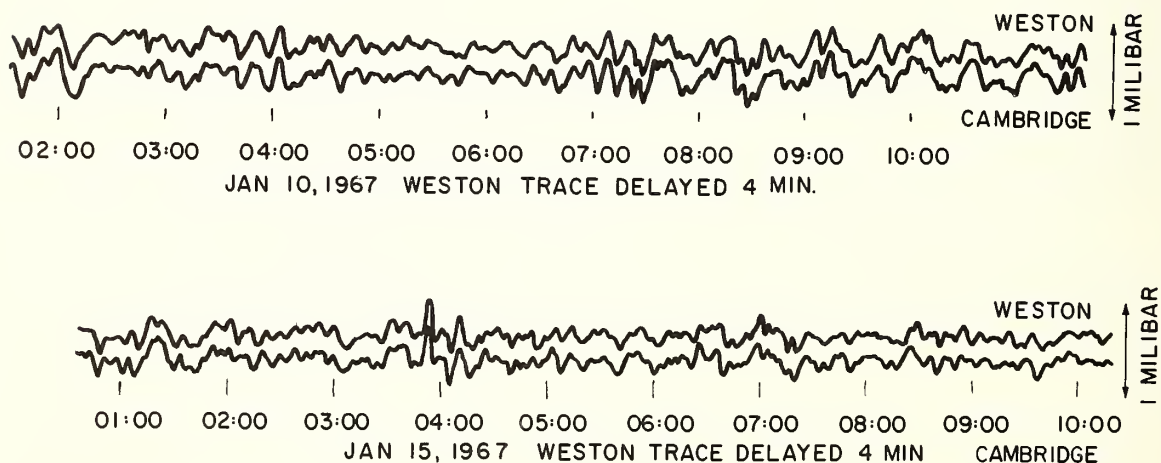


Figure 5 Pressure fluctuations at Weston and Cambridge showing high down stream correlation between stations 20 km apart.

Another feature of these waves that is deducible from the strong visual coherency of the waves is their non-dispersive character; that is, all the frequency components have the same horizontal phase velocity.

#### Propagation Characteristics of Gravity Waves

In order to make a more quantitative study of these waves, one must carry out spectral and coherency analyses of the data and study the propagation characteristics of acoustic-gravity waves in the presence of wind shears. From the linearized equations (Claerbout, 1967) we have

$$\tilde{u} = \frac{k_x \tilde{P}}{\bar{\rho} \Omega} - i \frac{\bar{u}_z}{\Omega} \tilde{w} \quad (1)$$

$$\frac{d}{dz} \begin{bmatrix} \tilde{P} \\ \bar{\rho} \tilde{w} \end{bmatrix} = \begin{bmatrix} -g/c^2 & i(\Omega - \frac{q}{\bar{\rho}} (\frac{1}{c^2} \bar{P}_z - \bar{\rho}_z)) \\ i(\Omega/c^2 - k_x^2/\Omega) & -\frac{k_x}{\Omega} \bar{u}_z - \frac{1}{\bar{\rho}} (\frac{1}{c^2} \bar{P}_z - \bar{\rho}_z) \end{bmatrix} \begin{bmatrix} \tilde{P} \\ \bar{\rho} \tilde{w} \end{bmatrix} \quad (2)$$

$\tilde{u}$ =horizontal wave wind	$\tilde{P}$ =wave pressure
$\tilde{w}$ =vertical wave wind	$k_x$ =horizontal wave number
$\bar{u}_z$ =wind shear	$\Omega = \omega - k_x u$ =doppler shifted frequency seen by moving media
$\bar{\rho}$ =mean density	$c$ =sound speed
$\bar{P}$ =mean pressure	$\gamma$ =ratio of specific heats
$u$ =mean wind	$q$ =gravitational force

These equations can be rewritten in many forms. Pierce (1966) and Claerbout (1967) derived new variables so that the variables remained continuous in the presence of density and wind shear discontinuities, and gave sinusoidal solutions in regions of constant temperature and constant wind. A somewhat simpler appearing form can be obtained by seeking transmission like equations or what is sometimes called a canonical form (Eckart, 1960)

$$\frac{d}{dz} \begin{bmatrix} e^{\int dz/\delta H} \tilde{P} \\ \frac{\omega}{\bar{\rho}} e^{\int dz/\delta H} \tilde{w} \end{bmatrix} = - \begin{bmatrix} 0 & \frac{\bar{\rho}}{-i\omega} e^{2\int dz/\delta H} (\omega_b^2 - \Omega^2) \\ \frac{i\omega}{\bar{\rho}} e^{\int dz/\delta H} (\frac{k_x^2}{\Omega^2} - \frac{1}{c^2}) & 0 \end{bmatrix} \begin{bmatrix} e^{\int dz/\delta H} \tilde{P} \\ \frac{\omega}{\bar{\rho}} e^{\int dz/\delta H} \tilde{w} \end{bmatrix} \quad (3)$$

$$\omega_b^2 = (\text{Brunt frequency})^2 = \frac{q}{\bar{\rho}} \left( \frac{1}{c^2} \frac{d\bar{P}}{dz} - \frac{d\bar{\rho}}{dz} \right)$$

$$H = \text{scale height} = c^2/\gamma q$$

The simplicity of this form allows us to study the qualitative behavior of these

waves, but this form has the disadvantage of allowing discontinuities in the variables if discontinuities in density exist. From the analogy to transmission lines we have (Schelkunoff, 1943) for the vertical propagation

$$k_z^2 = (\omega_b^2 - \Omega^2)(k_x^2/\Omega^2 - 1/c^2) \quad (4)$$

and for the characteristic impedance

$$\frac{\tilde{P}}{\tilde{\omega}} e^{2z/\delta H} \frac{\Omega}{\omega} = \frac{\bar{P}}{\omega} e^{2z/\delta H} \left( \frac{\omega_b^2 - \Omega^2}{k_x^2/\Omega^2 - 1/c^2} \right)^{1/2} \quad (5)$$

These results are locally correct, but the  $k_z$  value is not an accurate description of the  $z$  dependence of the variables unless the impedance is a slowly varying function of heights, so that the  $k_z$  behavior is a sort of WKB approximation. It tells us that for doppler shifted frequencies less than the Brunt frequency vertical propagation takes place only if the horizontal phase velocity is less than the speed of sound, and for frequencies greater than the Brunt frequency propagation only occurs if the horizontal phase velocity is greater than the speed of sound. A special solution for all frequencies called the Lamb wave also exists for a constant temperature, constant wind atmosphere. This is really an acoustic wave with no vertical motions. A more complete analysis for a windless atmosphere will also show that the changing impedance with height prevents vertical propagation for waves with frequencies between the Brunt frequency and 1.1 times the Brunt frequency (Eckart, 1960).

When the wind speed is close to the wave speed the doppler shifted frequency seen by the moving fluid,  $\Omega$ , is very small and equation (4) shows that the vertical wave number becomes very large. In this case the WKB approximation is more valid. From equations (1), (4), and (5) we have for low frequency low velocity gravity waves

$$\text{when } \Omega \ll \omega_b, \quad \frac{\Omega}{k_x} \ll c$$

$$\lambda_z = (V-U) \text{ (Brunt period)} \quad (6)$$

$$\tilde{u} = \frac{\tilde{P}}{\bar{P}} \frac{(1 \pm i\tilde{u}_z/\omega_b)}{V-U} \quad (7)$$

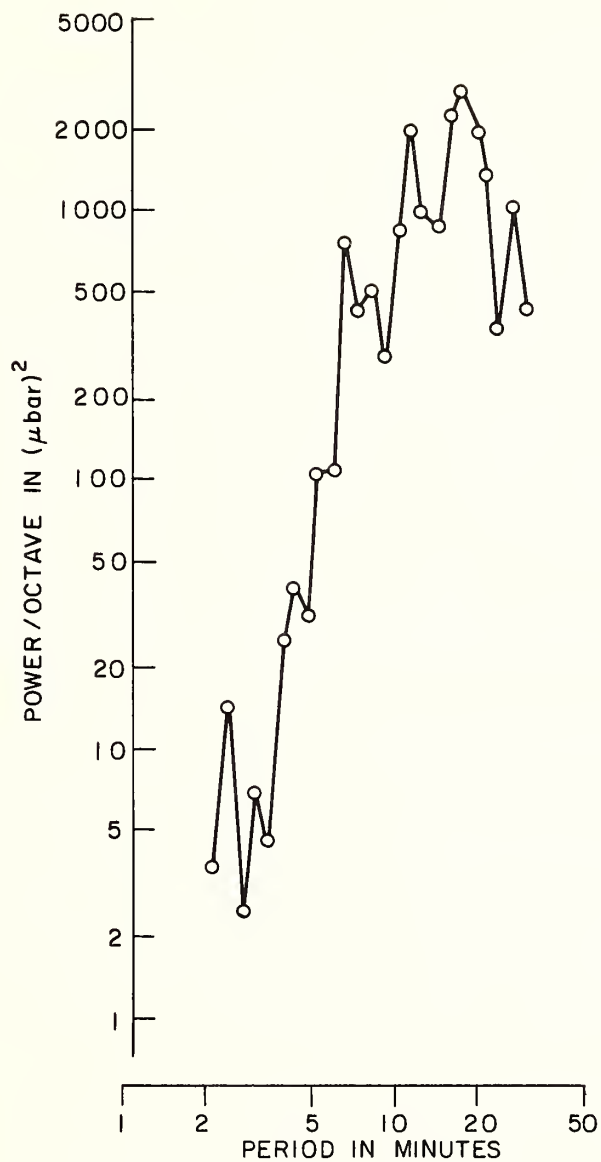
$$\tilde{\omega} = \pm \frac{\tilde{P}}{\bar{P}} \frac{\text{(Brunt period)}}{\text{(horizontal wavelength)}} \quad (8)$$

$V$  = horizontal phase velocity

$U$  = wind velocity

Since  $\tilde{P}/\bar{P} = 200 \text{ (m/sec)}^2$  for a 1 mbar wave at the 500 mbar level one sees that catastrophic wave wind effects will result even considerably away from the critical layer for finite amplitude waves.

When typical jet profiles and gravity wave velocities are considered we find that the impedance change in a distance equal to  $\lambda_z$  is not small even as  $\Omega$  goes to zero, so that the WKB approximation is not truly valid and the above results are only good for order of magnitude calculations.



CROSS POWER OF WESTON AND CAMBRIDGE PRESSURE  
00:00-04:00 APRIL 4 1966

Figure 6 Cross-power spectrum showing the typical low pass behavior of jet stream gravity waves



If we consider a disturbance of the jet stream to be our source, it can resonantly couple with gravity waves having the same horizontal velocity for any wavelength since the doppler shifted frequency will be zero. As the waves propagate down away from the source area, the doppler shifted frequency will increase, and the short wavelength disturbances will have acoustic frequencies and their vertical propagation will become evanescent. Thus the distance between the source area and the ground acts like a low pass filter that has a cutoff at the Brunt frequency. In the troposphere the Brunt period is about 10 minutes, so that waves emanating from the jet stream should show a distinct cutoff for periods shorter than 10 minutes. In figure 6 is shown the cross-power spectrum between Weston and Cambridge during a period when well correlated waves were crossing the array. The very remarkable cutoff at 5 to 10 minute periods is a good indication that the source is well up into the troposphere. On the other hand the sudden pressure jump seen in Figure 1 is an indication that the source was essentially at ground level.

As a general rule the background pressure fluctuations always show this cutoff at the Brunt frequency which implies that most of the sources are above the ground. When the waves are very slowly moving, however, a much shorter vertical distance is required to accomplish the same amount of filtering. From equation (4) we have for high frequencies and low velocities

$$\Omega \gg \omega_b, \quad \frac{\Omega}{k_x} \ll c \quad k_z = i k_x \quad (9)$$

This means that the high frequency components will have their amplitudes reduced by a factor of

$$e^{-\left(\frac{2\pi (\text{source height})}{v(\text{wave period})}\right)}$$

The data in Figure 6 involved waves of about 65 m/sec, and the amplitudes at periods of 3 minutes was about 1/20 the 10-20 minute period amplitudes. This leads to an estimate of 7 km for the source height, which is about the height of the 65 m/sec winds at that time. These calculations, of course, are subject to the assumption that the source spectrum has a rather flat power/octave frequency dependence, which is not unreasonable for geophysical data. More exact calculations of the source height effect will be shown later.

#### Detailed Comparisons of Gravity Wave and Jet Stream Behavior and Stability Criteria

In order to examine more closely the relationship between the gravity waves and the overhead jet stream, numerical calculations of the array correlations were performed. The lag value that gave the maximum correlation was taken as the delay time, and the ratio of the peak cross-correlation to the root mean zero lag auto-correlations was taken as the coherency. The use of a straight correlation analysis was justified by the non-dispersive nature of the waves. The bandwidth of the data was limited artificially by a leak filter in the pressure transducer and a further stage of high pass filtering in the electronic amplifier, both filters having cutoffs of about 50 minute periods. The delay times obtained by this analysis were used to determine the gravity wave phase velocities, assuming plane wave fronts, and the coherencies were used to give confidence limits on these velocities. The self consistency of the three delay times was also used as a check on these confidence limits. The presence of several wave velocities, and of curved wave fronts, as well as the presence of incoherent pressure fluctuations all tend to lower the apparent coherency of the records. In determining apparent phase velocities only consistent data with coherencies of over 30 percent for a four hour averaging time was used.

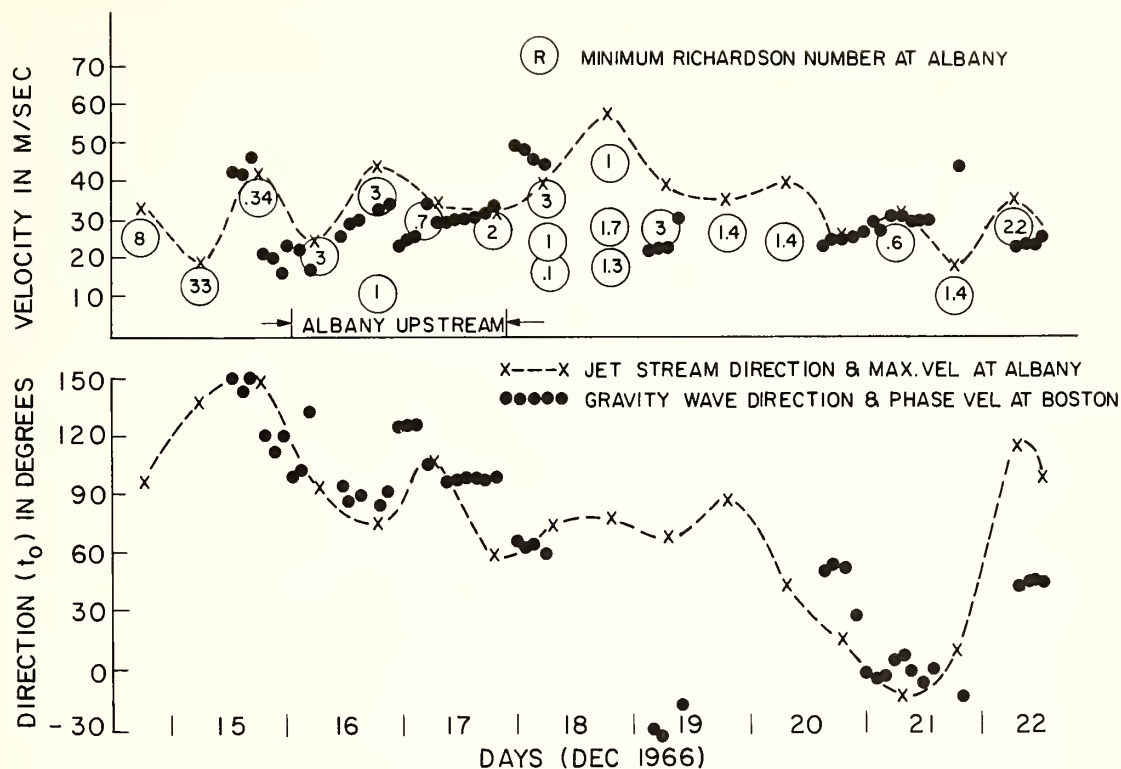


Figure 7 Comparison of gravity wave and jet stream behavior Dec. 15-22, 1966

Figures 7, 8, and 9 show the results of such analyses and also comparisons with the jet stream parameters measured at Albany, New York, about 270 km to the west of Boston.

The jet streams have a whole range of velocities from the relatively low velocities near the surface to the peak velocity which is usually found at the height of the tropopause. The streaming direction, however, remains fairly constant throughout the jet profile. Thus the gravity wave phase velocity direction is a good parameter to examine in checking for a jet stream association.

In figure 7 is shown data taken while a kink in the jet stream was passing over the area. Because of this kink an unusual variation of jet stream directions took place, and, if we ignore a few anomalous points, the coherent gravity wave fluctuations followed all these changes of direction. In figure 8 the variation of direction is greatly reduced, but the agreement in direction of the waves and the stream is equally good. This correlation of the direction of the jet stream and the gravity waves is taken as further evidence that the source of the gravity waves is in the jet stream.

If the gravity wave emanates from the jet stream we expect its velocity to not only match the direction of the stream, but also the magnitude of the stream velocity at the source level. Thus the gravity wave phase velocity should have a value which is not greater than the peak jet stream velocity. The comparisons of gravity waves in Boston with the jet stream over Albany cannot be expected to be very true when Boston is not downstream from Albany, but this limitation on the wave velocities is generally well upheld.

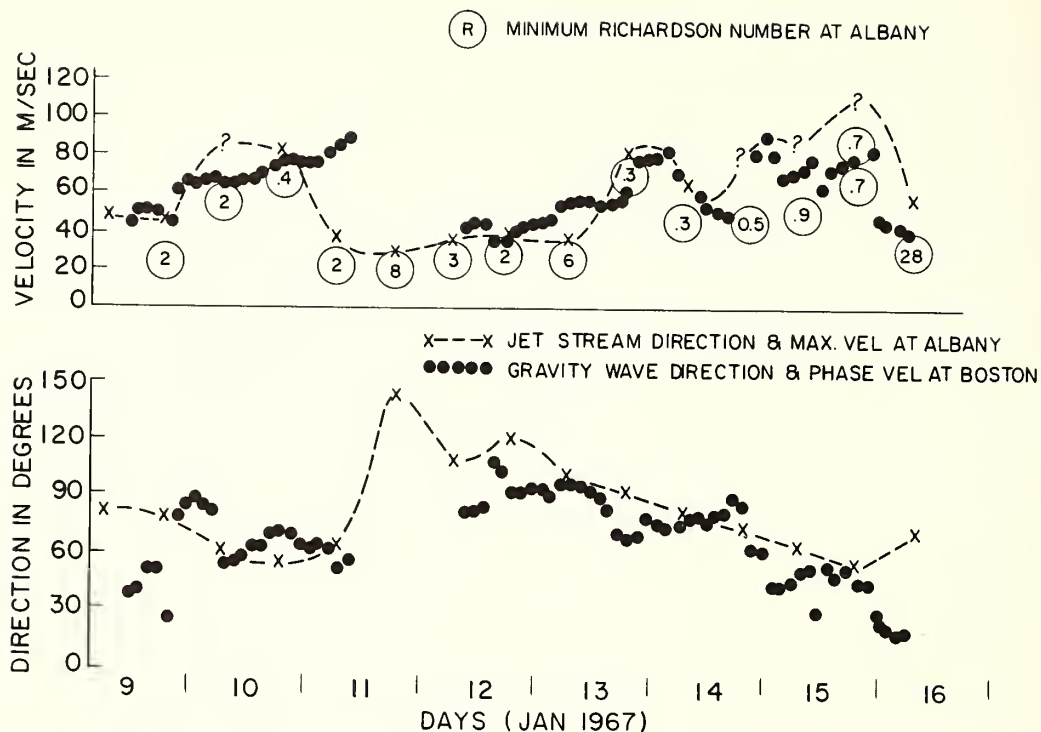


Figure 8 Comparison of gravity wave and jet stream behavior Jan. 9-16, 1967.

The nature of the source of these waves is one of the major points that needs clarification in studies of this phenomenon. The pressure gradients that drive the jet stream are the result of horizontal temperature gradients, and these cannot be expected to have rapid variations. Thus, it is natural to look for spontaneous generation of the waves by the jet stream. The temperature decrease with height in the troposphere is a destabilizing factor, but the gradient at the jet stream level is usually only about one half the adiabatic gradient. The instability must therefore involve the dynamical effect of the wind shear. This problem has a long history and has some peculiar aspects. It has been shown that if the wind shear is continuous and has a continuous derivative the stream is stable to small perturbations of all wavelengths as long as the Richardson number is greater than  $1/4$  at all points of the profile (Taylor, G.I., 1931; Synge, J.L., 1933; Miles, J.W., 1961; Howard, L.N., 1961).

$$Ri = \text{Richardson number} = \frac{\omega_b^2}{U_z^2} > 1/4 \text{ for stability} \quad (10)$$

The importance of the continuity of the shear derivative is demonstrated in one of the examples worked out by G.I. Taylor, but one would expect the natural jets to be smooth enough for the criteria of equation (10) to hold.

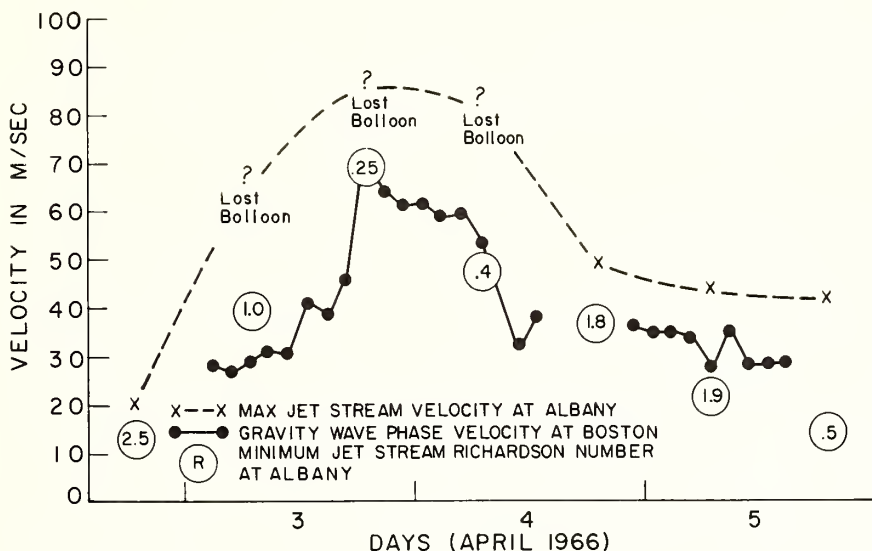


Figure 9 Comparison of gravity wave and jet stream behavior April 3-5, 1966.

When the stability criterion is exceeded we should expect the wind to spontaneously amplify incipient gravity waves and these waves would have a horizontal phase velocity that reflects the wind velocity at the level of the instability. In order to examine this behavior the minimum Richardson number and the velocity of the wind at the level of this minimum are also indicated in figures 7, 8, and 9. The Richardson number as determined by the smoothed upper air summaries never seem to exceed the stability criteria, but whenever the value approaches the value .25, the gravity waves appear to have the velocity of the nearly unstable level. This is especially evident in the data shown in figure 9, but is also seen in figures 7 and 8. Gravity waves are also observed when the smoothed profiles appear quite stable, but since Albany is some distance away from Boston, and since we lack details concerning the small scale wind structure and horizontal wind shears, these negative results may not be very meaningful.

Unstable wind shears are also commonly found near the surface but our analysis has ignored very slow velocity waves and we have not included the low level Richardson numbers.

#### Upwards Continuation of the Wave Fields and Linearity Considerations.

It is quite apparent from the ground observations that much of the gravity wave activity seen at the ground emanated from the jet stream overhead. It is not clear, however, that the activity seen at the ground is a measure of the gravity wave activity escaping out from the top of the jet stream. We believe the source level is usually on the underside of the jet, for the minimum Richardson numbers were always on the underside. This is not because the wind shears are greater on the underside but rather because the temperature gradients on the underside lowered the Brunt frequency. If the waves are generated on the lower side of the jet, they must penetrate another critical layer on the upper side of the



jet before escaping into the upper atmosphere, and linear theory predicts very little energy would escape. Further complications arise due to the ground reflecting back the gravity waves into the source area.

The critical layer effect guarantees infinite amplitudes, but if viscosity and heat conduction are introduced, the singularities disappear and the predictions of the linear theory are upheld. The observed fields, however, have quite finite amplitudes, and it becomes apparent that viscosity and heat conduction will not be able to keep the phenomenon in the linear region.

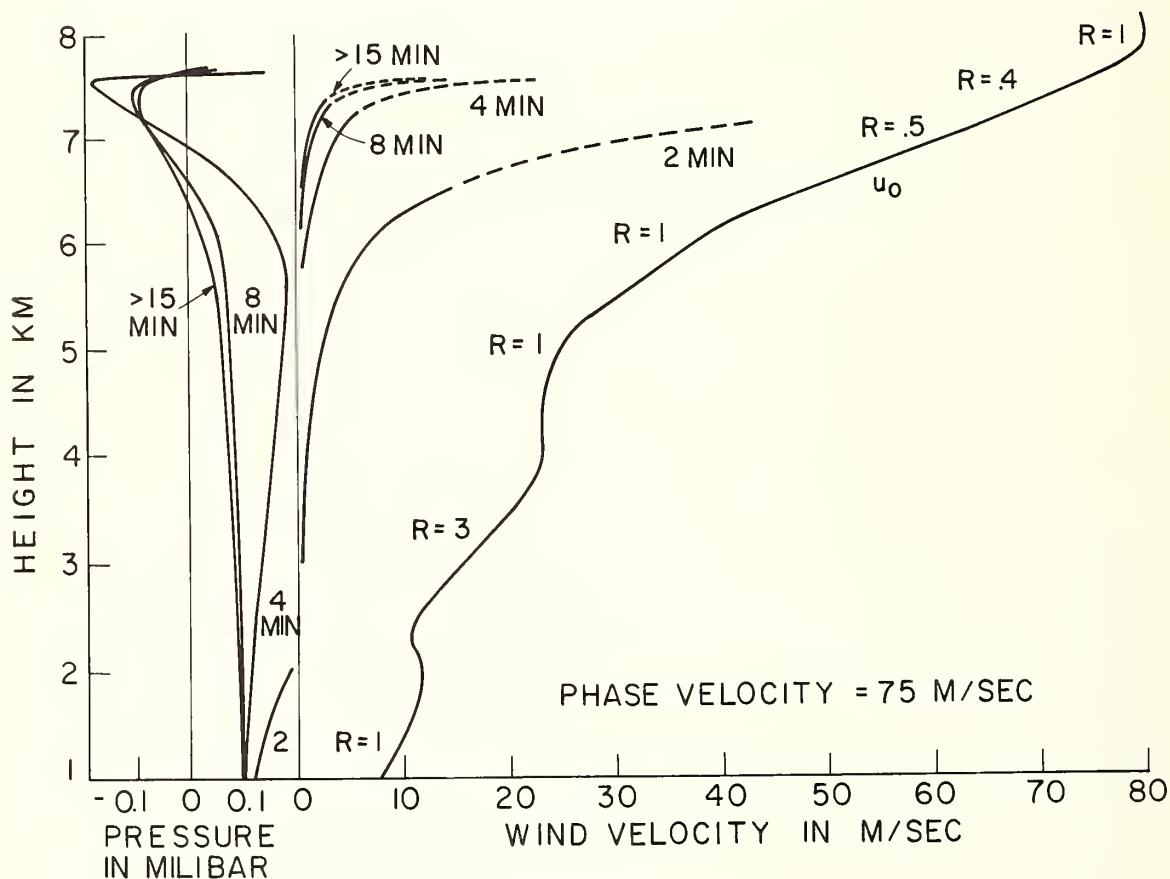


Figure 10 Upwards projection of gravity wave fields in the presence of the jet stream, Jan. 10-11, 1967.

Figure 10 shows calculations of a multilayered media approximation to an actual jet wind and temperature profile that gave the upwards projections of the surface wave fields. The qualitative results of our earlier analysis are upheld. The low frequencies all behave alike with their vertical wavelengths shortening and their horizontal wave winds increasing as they approach the critical layer. This double effect of increasing amplitude and decreasing vertical wavelength



results in large wind shears and in figure 10 we have dotted the wave wind velocities when these shears would cause a breakdown of the stability criteria. Since these calculations assumed a 0.1 mbar surface pressure and since the actual fluctuations often exceed this, one finds the waves becoming non-linear in their shears long before the linear dissipative forces are important. The upwards projections usually become non-linear about 1/3 to 1/2 a km below the critical layer and in some extreme cases almost a km away. Exactly how the waves really behave is not known at present, but it seems unavoidable that some turbulence must set in.

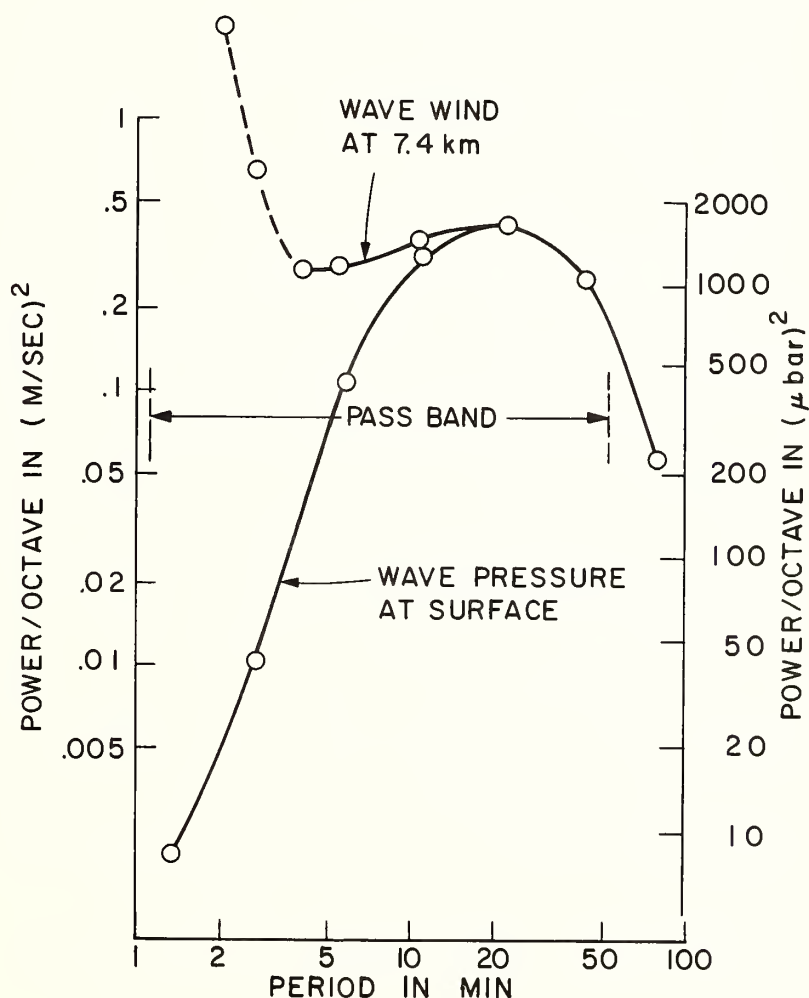


Figure 11 Power spectrum of surface pressure fluctuations and upwards projected wave wind, Jan. 9-11, 1967.

These same calculations could also be used to check the predictions of the high frequency filtering. In figure 11 we show the power spectrum of the ground pressure fluctuations and the upwards projected wave wind. The upwards projected winds do appear to have a rather flat power/octave spectrum. The fall off at the long period end is due to the filtering of the observing equipment. The rise at the low period end may be due partially to having carried the upwards projection too far. The surface fluctuation at these frequencies was so low, however, it must have included some contribution from very local sources.

## Conclusions

The evidence from ground observations of pressure fluctuations clearly shows that the tropospheric jet stream produces a good deal of gravity wave energy. The data suggest that this energy is derived from instabilities of the jet wind shears. The finite amplitude of these waves leaves some doubt about the predictions of the linear theory concerning the escape of this energy through the critical layers, so that at present it is not known how the ground observations will relate to the upper atmosphere gravity waves. The same is true concerning the parallel problem of the modification of the jet profile by the interaction of the wind shears and the gravity waves.

## Acknowledgements

This work was supported by U.S. Army Research Office Project 2M014501B52B. Some initial support was also obtained from NASA through the M.I.T. Center of Space Research. One of the authors held a NASA traineeship during the course of these investigations.

We would also like to thank Prof. F.P. Bretherton, Dr. E. Gossard, Prof. W. Munk, and Prof. N. Phillips for helpful discussions concerning these phenomena. Mr. Roger Breeding did the data analysis recorded in figure 4.

## References

- Booker, J.R. and F.P. Bretherton, Critical layer for internal gravity waves in a shear flow, J. Fluid Mech., 27, 513-539, 1967.
- Bretherton, F.P., The propagation of groups of internal gravity waves in shear flow, Quart. J. Roy. Met. Soc., 92, 466-480, 1966.
- Claerbout, J.F., Electromagnetic effects of atmospheric gravity waves, Ph.D. thesis at Massachusetts Institute of Technology, 1967.
- Eckart, D., Hydrodynamics of Oceans and Atmospheres, Pergamon Press, London, 1960.
- Flauraud, Mears, Crowley, and Creary, Investigations of microbarometric oscillations in eastern Massachusetts, Geophysical Research Paper 27, Air Force Research Center, 1954.
- Howard, L.N., Note on a paper of John W. Miles, J. Fluid Mech., 10, 509-512, 1961.
- Miles, J.W., On the stability of heterogeneous shear flows, J. Fluid Mech., 10, 496-508, 1961.
- Schelkunoff, S.A., Electromagnetic Waves, D. Van Nostrand Co., New York, 1943.
- Synge, J.L., The stability of heterogeneous liquid, Trans. Roy. Soc. Cam. (3), 27, 1, 1933.
- Taylor, G.I., Effect of variations of density on the stability of superposed streams of fluid, Proc. Roy. Soc. A., 132, 499-523, 1931.

## ELECTROMAGNETIC EFFECTS OF ATMOSPHERIC GRAVITY WAVES

J. F. Claerbout<sup>1</sup> and T. R. Madden

Geophysics Department, Massachusetts Institute of Technology

Continuous observations of pressure fluctuations at gravity wave periods (5-30 minutes) in eastern Massachusetts show that the only important pressure fluctuations not associated with moving weather sources are pressure fluctuations associated with the jet stream. These fluctuations appear to be non-dispersive and move a little slower than the maximum overhead jet stream velocity. The coupling between gravity wave modes and fluctuations in the jet stream is examined to investigate the pumping of energy from the jet stream into the upper atmosphere. There are two major problems in understanding the nature of the disturbance at the critical altitude where the velocity of the disturbance matches the velocity of the mean wind. The first problem involves the origin of the disturbance in the vicinity of such a critical altitude. Theoretically, the energy flux emitted is amplified by the wind shear as the wave moves away from the critical altitude. The second problem involves a wave originating elsewhere moving into a critical zone. A wave packet moving into a critical zone becomes so compressed before it reaches the critical altitude that the wind shear within the wave itself causes the atmosphere to become locally unstable. The exact mechanism for the transport of energy across a critical altitude is not known. If by symmetry it is presumed that the amplitude of the wave will be comparable on either side of the critical altitude, the wave amplitudes in the upper atmosphere can be predicted.

Energy propagation to the ionospheric D-region (80 km) takes 10 hours under average conditions where typical amplitudes will be 10 meters/second. Shorter propagation times occur when mesospheric temperature gradients are low and winds above the jet stream are directed opposite to the jet. The waves are strongly reflected by temperature gradients in the lower thermosphere, consequently, it takes a long time to accumulate any energy at height. Energy typically propagates upward to about 115 km where it is dissipated by electromagnetic forces in 20 to 1000 hours. The induced magnetic field when integrated back to the ground is an order or two magnitude less than the quiet-time ambient field. Therefore we have not observed a correlation between atmospheric pressure and the magnetic field on the ground but expect that pressure may be correlated to some measure of activity in the ionospheric D-region.

### Introduction

This paper is an abstraction of the first author's thesis supervised by the second author. The thesis is concerned with the propagation, generation, and dissipation of gravity waves in the atmosphere. In eastern Massachusetts the observed gravity waves are generated principally in the jet stream and are thought to propagate up to the ionosphere where they are dissipated by electromagnetic processes.

Our pressure observations over the course of 14 months have shown no waves emitted by storms which travel any faster than the storms themselves. On the other hand, of frequent occurrence were disturbances of jet stream speed. Theoretically these faster disturbances can be expected to propagate to the ionosphere much more readily than disturbances of weather front speed.

The strength of these "jet waves" may be explained by the strong wind shear at jet stream altitudes. When the wind shear (which has physical dimensions of frequency) becomes comparable to the atmospheric vertical resonance frequency the atmosphere becomes dynamically unstable. At any height where this frequency ratio predicts instability one may expect a disturbance to form and be swept over ground observers at the speed of the wind at that height. A height where a gravity wave velocity matches a wind velocity is called a critical height; here coupling may occur and the wave can be amplified. Theory predicts the vertical

---

<sup>1</sup>Now at Geophysics Department, Stanford University, Stanford, California 94306

energy flux of a gravity wave to be amplified by the wind shear as the wave emerges from the critical height. As the waves propagate vertically they may encounter more critical heights. These may act as barriers or they may transmit the energy; this is an important topic for future research. In any case the waves emerging from the last critical height propagate upward having their energy amplified by the wind shear and their amplitude further magnified by the decreasing atmospheric density.

Propagation upward to the ionospheric D-region (80 km) will take about 10 hours. This travel time is quite variable depending on the wind and thermal state of the intervening air. The particle velocities at this altitude, if they can pass through the critical heights without energy loss, will be about 10 meters per second in both horizontal and vertical directions. This should be measurable by some independent means.

Further propagation into the ionosphere is greatly retarded by strong thermal gradients. Typically, disturbance energy is going so nearly horizontal that it reaches 115 kilometers only after 20 to 1000 hours. In this amount of time the disturbance will be well spread out in space and will be dissipated by electromagnetic processes. Greatly diminished amounts of energy may get further up and still be important because the amplitudes continue to increase for awhile due to the decreasing  $\rho$ .

When the gravity wave neutral air molecules drag ions and electrons across the earth's magnetic field electric currents are set up which in turn induce magnetic fields. The currents (.3 microamps/meter<sup>2</sup>) that we extrapolate from the pressure data are quite comparable to other currents thought to be present in the ionosphere. Due to the fairly short (20 km) vertical wavelengths of the wave, the effects of the currents tend to cancel in the production of magnetic fields. When the magnetic fields are integrated back to earth they are smaller than the observed quiet-time variations by one or two orders of magnitude.

# I. Acoustic Gravity Wave Formula Derivations

## A. Stratified Wind and Temperature

### 1. From Basic Equations to Stratified Media

We use the conventional definitions: pressure  $p$ , density  $\rho$ , sound speed  $c$ , particle velocity  $\vec{v}=(u,v,w)$ , angular frequency  $\omega$ , wave numbers  $k$  and  $\ell$ , gravity  $g$ , and ratio of specific heats  $\gamma$ . As subscripts,  $x$ ,  $z$ , and  $t$  are partial derivatives. A bar over a quantity indicates its time average. A tilde over a quantity represents the perturbation part due to the presence of a wave. By a stratified media we mean one in which the media properties are functions of only the vertical  $z$  coordinate. We take plus  $z$  upward. The trial solutions are:

$$(1) \quad \begin{bmatrix} p \\ \rho \\ u \\ v \\ w \end{bmatrix} = \begin{bmatrix} \bar{p}(z) \\ \bar{\rho}(z) \\ \bar{u}(z) \end{bmatrix} + \begin{bmatrix} \tilde{p}(z) \\ \tilde{\rho}(z) \\ \tilde{u}(z) \\ \tilde{v}(z) \\ \tilde{w}(z) \end{bmatrix} e^{-i\omega t + ikx + i\ell z}$$

Linearization means that products of elements in the righthand vector will be ignored as being small. The equations of adiabatic state (energy), momentum conservation, and mass conservation are:

$$(2) \quad \frac{Dp}{Dt} = c^2 \frac{D\rho}{Dt} ; \quad \rho \frac{D\vec{v}}{Dt} = \rho \vec{g} - \nabla p ; \quad \frac{\partial \rho}{\partial t} + \nabla \cdot (\rho \vec{v}) = 0$$

Define  $\Omega = \omega - \vec{k} \cdot \vec{v}$ , eliminate  $\tilde{\rho}$  and  $\tilde{u}$ , and collect  $z$ -derivatives on the left to get:



$$(3) \quad \frac{d}{dz} \begin{bmatrix} \tilde{p} \\ \bar{\rho} \tilde{w} \end{bmatrix} = \begin{bmatrix} -g/c^2 & i(\Omega - \frac{g}{\Omega \bar{\rho}} (\frac{1}{c^2} \bar{p}_z - \bar{\rho}_z)) \\ i(\frac{\Omega}{c^2} - \frac{k^2 + l^2}{\Omega}) & -\frac{k}{\Omega} \tilde{u}_z - \frac{1}{\bar{\rho}} (\frac{1}{c^2} \bar{p}_z - \bar{\rho}_z) \end{bmatrix} \begin{bmatrix} \tilde{p} \\ \bar{\rho} \tilde{w} \end{bmatrix}$$

It is useful to put equation 3 into a form where the matrix of coefficients has the following properties: 1) it contains no  $z$  derivatives; 2) it is constant in a constant temperature constant wind velocity region; 3) it contains no complex numbers, and its trace is zero. Then the solutions will have the following properties: 1) continuous functions of  $z$ ; even if wind and temperature are discontinuous at layer boundaries; 2) sinusoidal or exponential in a constant temperature constant wind region.

A somewhat detailed algebraic development (thesis) gives

$$(4) \quad \frac{d}{dz} \begin{bmatrix} \tilde{p} \\ \bar{\rho} \tilde{w} \end{bmatrix} = \begin{bmatrix} g(\frac{\gamma}{2c^2} - \frac{k^2}{\Omega^2}) & -\frac{\Omega^2}{c^2} + \frac{g^2 k^2}{2\Omega^2} \\ (1 - c^2 \frac{k^2}{\Omega^2}) & -g(\frac{\gamma}{2c^2} - \frac{k^2}{\Omega^2}) \end{bmatrix} \begin{bmatrix} \bar{p}^{-1/2} (\tilde{p} + g\bar{\rho} \frac{\tilde{w}}{i\Omega}) \\ \bar{p}^{1/2} \frac{\tilde{w}}{i\Omega} \end{bmatrix}$$

which is the polished form of the equations. These equations were derived in a different way by Pierce (1966).

The procedure of deriving (4) from (3) was originally a difficult one, and the presentation of a sequence of unmotivated algebraic steps seemed impossible to avoid. It would be valuable to know just how broad a class of problems can be reduced to a polished form by the weighting and addition transformations and to know if the reduction can proceed in a systematic way. This might be in the literature on Lyapunov transformations but a cursory investigation has failed to find it. For example, it would be nice to know if a polished form is possible for a layer of constant Brunt frequency. If so, extremely realistic atmospheric models would be constructed with very few layers.

In summary, in this section we have deduced equation (4) from fundamentals. This equation can be integrated to produce the state of the media at one position given the state at another. It shows that the variables  $\tilde{p} + g\bar{\rho} \tilde{w}/(i\Omega)$  and  $\tilde{w}/\Omega$  are continuous functions of height even though the temperature and wind may be discontinuous. (Notice that every element of the matrix in (4) is always finite but that the matrix of (3) contains infinities at layer boundaries.)

Since one expects the vertical velocity to be continuous at layer boundaries, why is it that  $\tilde{w}/\Omega$  is continuous rather than  $\tilde{w}$ ? Consider a point where the boundary is deformed to a sine wave with wind on one side and not the other. At the zero crossing of the sine wave the particles on the windless side may have no vertical velocity, but by virtue of the wind, particles on the other side are sliding up or down the sine wave on its steepest slope. An observer moving along with the particles interprets  $\tilde{w}/(-i\Omega)$  as the amplitude of the deformed boundary and that is why it must be the same to observers on either side of the boundary.

One also expects the total pressure to be continuous at the deformed boundary. The wave pressure is augmented by a hydrostatic pressure due to the deformation  $\tilde{w}/(-i\Omega)$  of the boundary. Thus the total pressure

$$\tilde{p} + \frac{d\bar{p}}{dz} \delta z = \tilde{p} + (-\rho g) \frac{\tilde{w}}{-i\Omega} = \tilde{p} + \rho g \frac{\tilde{w}}{i\Omega}$$

is continuous as equation (4) shows.

In the next sections we use equation (4) to study the transport of energy and momentum by acoustic gravity waves.



## I-A-2 Energy and Momentum Principles

In this section we will derive formulas for energy density, momentum density, and transport of these densities in a stratified medium. In the simplest type of wave propagation the phase velocity and the group or energy velocity have the same direction and speed. Bringing in gravity causes these velocities to differ in both direction and speed. Bringing in a stratified wind causes further complication because the energy in a wave packet is not conserved as the packet propagates from one altitude to another. In a media at rest  $1/2 \operatorname{Re} \tilde{P} \tilde{W}^*$  is identified as the vertical energy flux. If  $1/2 \operatorname{Re} \tilde{P} \tilde{W}^*$  does not vanish at a boundary of the system, it represents the power flowing into the system at the boundary. We will subsequently show that  $\operatorname{Re}(\tilde{P} \tilde{W}^*/\Omega)$  is altitude invariant in a region of no sources. Hence, the quantity  $\operatorname{Re} \tilde{P} \tilde{W}^*$  is not constant in a windy medium where  $\Omega$  is z-dependent. Since  $1/2 \operatorname{Re} \tilde{P} \tilde{W}^*$  represents the amount of power which may be absorbed by a viscous absorber, it is clear that an observer at some altitude seeing a wave can have no idea how much power it took to generate the wave unless he knows the ratio of his translation speed to the source's translation speed.

The situation is not so strange as it may seem. Consider an observer riding on a flat car in a railroad switching yard full of flatcars. If he sees a snowball flying over his flatcar he cannot tell how much energy went into launching the snowball unless he knows the relative velocity of the flatcar from which it was launched. If a steady state were set up by continuous snowball-throwing, there is one thing all flatcar observers would agree on and that is the momentum flux or mass current perpendicular to the tracks.

In our acoustic-gravity wave problem the constancy in  $z$  of  $\operatorname{Re}(\tilde{P} \tilde{W}^*/\Omega)$  can also be interpreted as a current, not a current of energy or mass but as related to a vertical current of horizontal momentum. This will be interpreted more fully after we verify that  $\operatorname{Re}(\tilde{P} \tilde{W}^*/\Omega)$  is indeed altitude invariant.

Introducing the definition of Brunt frequency  $\omega_b$

$$(5) \quad \omega_b^2 = \frac{g}{\rho} \left( \frac{1}{c^2} \bar{P}_z - \bar{\rho}_z \right)$$

and recalling the equilibrium equation  $\bar{P}_z = -\bar{\rho}g$  we get from (I-A-3)

$$(6) \quad \frac{d}{dz} \begin{bmatrix} \tilde{P} \\ \frac{\tilde{W}}{-i\Omega} \end{bmatrix} = \begin{bmatrix} -g/c^2 & \bar{\rho}(\Omega^2 - \omega_b^2) \\ \frac{1}{\bar{\rho}} \left( -\frac{1}{c^2} + \frac{k^2}{\Omega^2} \right) & +g/c^2 \end{bmatrix} \begin{bmatrix} \tilde{P} \\ \frac{\tilde{W}}{-i\Omega} \end{bmatrix}$$

We abbreviate this

$$(7) \quad \frac{d}{dz} \begin{bmatrix} X_1 \\ X_2 \end{bmatrix} = \begin{bmatrix} A_{11} & A_{12} \\ A_{21} & -A_{11} \end{bmatrix} \begin{bmatrix} X_1 \\ X_2 \end{bmatrix}$$

Now we can get an equation for  $X_1 X_2^*$  as follows

$$(8) \quad \frac{d}{dz} (X_1 X_2^*) = \frac{dX_1}{dz} X_2^* + X_1 \frac{dX_2^*}{dz} = A_{21}^* X_1 X_1^* + A_{12} X_2 X_2^*$$

$$(9) \quad \frac{d}{dz} \frac{\tilde{P} \tilde{W}^*}{i\Omega^*} = \frac{1}{\bar{\rho}} \left( -\frac{i}{c^2} + \left( \frac{k^2}{\Omega^2} \right)^* \right) \tilde{P} \tilde{P}^* + \bar{\rho} (\Omega^2 - \omega_b^2) \frac{\tilde{W} \tilde{W}^*}{\Omega \Omega^*}$$

This we may split into real and imaginary parts

$$(10) \quad \frac{d}{dz} \operatorname{Im} \frac{\tilde{P} \tilde{W}^*}{\Omega} = \frac{1}{\bar{\rho}} \left( -\frac{1}{c^2} + \operatorname{Re} \frac{k^2}{\Omega^2} \right) \tilde{P} \tilde{P}^* + \bar{\rho} (\operatorname{Re} \Omega^2 - \omega_b^2) \frac{\tilde{W} \tilde{W}^*}{\Omega \Omega^*}$$

$$(11) \quad \frac{d}{dz} \left( -\operatorname{Re} \frac{\tilde{P} \tilde{W}^*}{\Omega^*} \right) = -\frac{1}{\bar{\rho}} \left( \operatorname{Im} \left( \frac{k^2}{\Omega^2} \right)^* \right) \tilde{P} \tilde{P}^* + \bar{\rho} (\operatorname{Im} \Omega^2) \frac{\tilde{W} \tilde{W}^*}{\Omega \Omega^*}$$

Equation (11) shows that in a source free region in the steady state ( $\omega, k$  real) that  $\text{Re}(\tilde{P}\tilde{W}^*/\Omega)$  is constant, independent of  $z$ . We can define a current  $F$  by the formula  $F = (k/\pi)\text{Re}(\tilde{P}\tilde{W}^*/\Omega)$ , where  $F$  has the dimensions of momentum density per unit volume times velocity. Having also physical dimensions of force per unit area it is a stress. Without the  $\pi$  it is called the Reynolds stress.

We will now show that  $F$  is the time rate of momentum lost by a uniform wind blowing over a unit area of a perfectly rigid sinusoidally undulating ground. The situation is depicted in Figure (1).

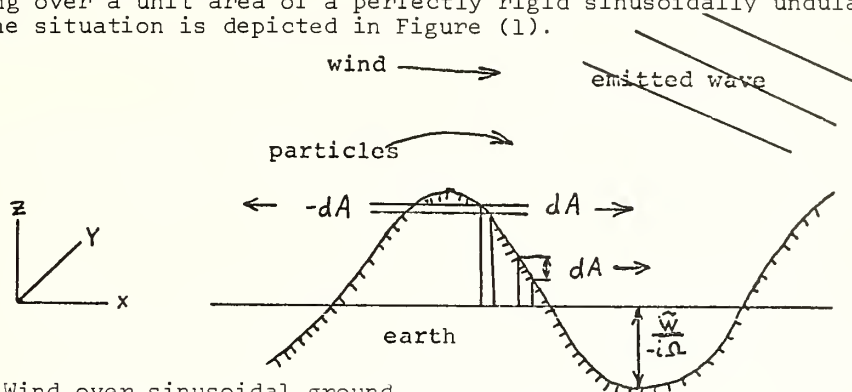


Figure 1. Wind over sinusoidal ground.

The lost momentum is accounted for by the radiation to infinity of an acoustic-gravity wave. If the atmosphere is topped by a rigid boundary or if frequencies and velocities are such that the disturbance is evanescent then investigation shows that  $F$  vanishes by virtue of  $\tilde{P}$  and  $\tilde{W}$  being out of phase. The force acting on the ground in the horizontal direction is proportional to the pressure times the effective area. The amount of area for the force to act on in the horizontal direction is proportional to the amplitude of the ground displacement. Both pressure and area are sinusoidal functions of  $x$ . A negative pressure acting on a negative area gives a force in the same horizontal direction as a positive force on a positive area. In  $1/4$  wavelength along  $x$  the area is  $\tilde{W}/\Omega$  dy. Thus the area per unit length on the  $x$ -axis is  $\text{Re}(dA)$  where

$$dA = \frac{4}{\lambda_x} \frac{\tilde{W}}{\Omega} e^{ikx} dy$$

The integral of the pressure times the effective area over one wavelength along the  $x$ -axis is the force.

$$\text{Force} = \int_0^{\lambda_x} (\text{Re } \tilde{P})(\text{Re } dA) dx = \frac{4}{2} \text{Re} \frac{\tilde{P}\tilde{W}^*}{\Omega} dy$$

Hence the shearing force per unit area acting on the ground is

$$F = \text{Force/area} = \frac{2}{\lambda_x} \text{Re} \frac{\tilde{P}\tilde{W}^*}{\Omega} = \frac{k}{\pi} \text{Re} \frac{\tilde{P}\tilde{W}^*}{\Omega}$$

The momentum density  $M$  of the waves may be defined by its continuity equation.

$$(12) \quad 0 = \frac{\partial M}{\partial t} + \text{div } F = 0$$

Taking  $k$  real, this becomes

$$(13) \quad 0 = \frac{\partial M}{\partial t} + \frac{d}{dz} \left( \frac{k}{\pi} \text{Re} \frac{\tilde{P}\tilde{W}^*}{\Omega} \right)$$

In the case where  $\omega$  is real we have already shown the righthand term to be zero. Generalizing to complex  $\omega$ ,  $\omega = \omega_r + i\omega_i$ , we will be able to define  $\partial M / \partial t$ . Since  $M$  is a quadratic function of field variables and either of the field variables is

$$(14) \quad \varphi = \varphi(z) e^{ikx - i\omega_r t} e^{\omega_i t}$$

then

$$\frac{\partial}{\partial t} \varphi \varphi^* = \frac{\partial}{\partial t} \varphi(z) \varphi^*(z) e^{2\omega_i t} = 2\omega_i \varphi \varphi^*$$

So we may substitute  $\partial/\partial t M = 2\omega_i M$  into (13) and also bring (11) into (13) getting

$$(15) \quad 2\omega_i M = \frac{k}{\pi} \left\{ \frac{1}{\bar{\rho}} \left( \partial_m \frac{k^2}{\Omega^2} \right) \tilde{P} \tilde{P}^* + \bar{\rho} (\partial_m \Omega^2) \frac{\tilde{W} \tilde{W}^*}{\Omega \Omega^*} \right\}$$

Take  $\Omega = \Omega_r + i\omega_i$  to be complex, but keep  $k$  real. Thus we are considering a time transient problem with sources and sinks to be of infinite extent in  $x$  and  $y$ . For algebraic simplicity take  $|\omega_i| \ll |\Omega_r|$ . Then (15) gives the momentum density as

$$(16) \quad M = \frac{k}{\pi \Omega_r} \left\{ \frac{1}{\bar{\rho}} \frac{k^2}{\Omega_r^2} \tilde{P} \tilde{P}^* + \bar{\rho} \tilde{W} \tilde{W}^* \right\}$$

Now using the momentum continuity equation (12) and the knowledge that the energy current is  $1/2 \operatorname{Re} \tilde{P} \tilde{W}$  we will derive a continuity equation for energy density and it shows how gradients of the mean flow can amplify waves going through them. Expand out equation (13)

$$0 = \frac{\partial M}{\partial t} + \frac{d}{dz} \operatorname{Re} \frac{k}{\pi} \frac{\tilde{P} \tilde{W}^*}{\Omega^*} = 0 = \frac{\partial}{\partial t} \left( \frac{\pi}{k} M \right) + \frac{d}{dz} \left[ \frac{(\operatorname{Re} \tilde{P} \tilde{W}^*)(\operatorname{Re} \Omega)}{\Omega \Omega^*} - \omega_i \partial_m \frac{\tilde{P} \tilde{W}^*}{\Omega \Omega^*} \right]$$

Again use  $\omega_i \ll \Omega_r$  so  $\Omega \Omega^* = \Omega_r^2$ .

$$(17) \quad 0 = \frac{\partial}{\partial t} \left( \frac{\pi}{k} M \right) - \frac{d \Omega_r}{dz} \operatorname{Re} \tilde{P} \tilde{W}^* + \frac{1}{\Omega_r} \frac{d}{dz} \operatorname{Re} \tilde{P} \tilde{W}^* - \omega_i \frac{d}{dz} \left[ \partial_m \frac{\tilde{P} \tilde{W}^*}{\Omega_r^2} \right]$$

Multiply by  $\Omega_r/\alpha$  and identify  $2\omega_i$  with  $\partial/\partial t$

$$(18) \quad 0 = \frac{\partial}{\partial t} \frac{1}{2} \left[ \frac{\pi \Omega_r M}{k} - \frac{\Omega_r}{2} \frac{d}{dz} \left( \partial_m \frac{\tilde{P} \tilde{W}^*}{\Omega_r^2} \right) \right] + \frac{k}{2} \frac{d \bar{u}}{dz} \operatorname{Re} \frac{\tilde{P} \tilde{W}^*}{\Omega_r} + \frac{d}{dz} \frac{1}{2} \operatorname{Re} \tilde{P} \tilde{W}^* \\ = \frac{\partial}{\partial t} (\text{Energy density}) + (\text{shear amplification}) + (\text{divergence of flux})$$

We identify the rightmost term with the divergence of energy flux. The center term is wave amplification due to the flux of wave momentum across the mean wind shear. The leftmost term is the time derivative of the energy density  $E$  and we next examine it further.

$$(19) \quad 2E = \frac{\pi \Omega_r}{k} M - \frac{\Omega_r}{2} \frac{d}{dz} \partial_m \frac{\tilde{P} \tilde{W}^*}{\Omega_r^2} = \frac{\pi \Omega_r}{k} M - \frac{1}{2} \frac{d}{dz} \partial_m \frac{\tilde{P} \tilde{W}^*}{\Omega_r} + \frac{d \Omega_r}{2 dz} \partial_m \frac{\tilde{P} \tilde{W}^*}{\Omega_r}$$

Now let  $\omega$  be real and substitute (16) into the first term and (10) into the second

$$(20) \quad 2E = \left[ \frac{1}{\bar{\rho}} \left( \frac{k}{\Omega} \right)^2 \tilde{P} \tilde{P}^* + \bar{\rho} \tilde{W} \tilde{W}^* \right] - \frac{1}{2} \left[ \frac{1}{\bar{\rho}} \left( -\frac{1}{c^2} + \frac{k^2}{\Omega^2} \right) \tilde{P} \tilde{P}^* + \bar{\rho} (\Omega^2 \omega_i^2) \frac{\tilde{W} \tilde{W}^*}{\Omega^2} \right] + \frac{\Omega_r}{2 \Omega} \partial_m \frac{\tilde{P} \tilde{W}^*}{\Omega}$$

$$E = \frac{1}{4} \left\{ \frac{1}{\bar{\rho}} \left( \frac{1}{c^2} + \frac{k^2}{\Omega^2} \right) \tilde{P} \tilde{P}^* + \bar{\rho} \left( 1 + \frac{\omega_i^2}{\Omega^2} \right) \tilde{W} \tilde{W}^* - \frac{d \bar{u}}{dz} \frac{k}{\Omega} \partial_m \frac{\tilde{P} \tilde{W}^*}{\Omega} \right\}$$

A  $1/4$  scale appears instead of a  $1/2$  because  $\tilde{P}$  and  $\tilde{W}$  are the peak, not the R.M.S. amplitudes of the sinusoidal time dependence. Now we have derived expressions for momentum density (equation 16) and energy density (equation 20) in terms of the two complex variables  $\tilde{P}$  and  $\tilde{W}$ . The media could also be described at a point by giving two independent complex variables representing

upgoing and downgoing wave solutions. It could be described by giving four real quantities, say pressure, density and two components of velocity. By means of the equations of motion any of these descriptions can be derived from the others so they are mathematically equivalent. Some choices give a more intuitive feel for the situation than others. For example take the horizontal component of Newton's equation

$$(21) \quad \bar{\rho} \tilde{u}_p = \bar{\rho} \left( \tilde{u} + \frac{d\bar{u}}{dz} \delta z \right) = \frac{k}{\Omega} \tilde{p}$$

Introducing the horizontal component of Newton's equation (21) into the momentum flux definition we get

$$(22) \quad F = \frac{k}{\pi} \operatorname{Re} \frac{\tilde{p} \tilde{W}^*}{\Omega} = \frac{\bar{\rho}}{\pi} \operatorname{Re} \tilde{u}_p \tilde{W}^*$$

Introducing the horizontal component of Newton's equation (21) into the energy density (20) and  $\delta z = W / -i\Omega$  for the vertical displacement we get

$$(23) \quad 4E = \bar{\rho} (\tilde{u}_p \tilde{u}_p^* + \tilde{W} \tilde{W}^*) + \frac{\tilde{p} \tilde{p}^*}{\bar{\rho} c^2} + \bar{\rho} \omega_b^2 (\delta z) (\delta z)^* - \bar{\rho} \operatorname{Re} \tilde{u}_p \left( \frac{\partial \bar{u}}{\partial z} \delta z \right)^*$$

The first term is clearly the kinetic energy of a parcel. The second term is the potential energy of adiabatic compression. In the third term the factor  $\rho \omega_b^2$  is like a spring constant. Gravity appears explicitly when the definition of  $\omega_b^2$  is substituted giving

$$g \left( \frac{1}{c^2} \frac{d\bar{p}}{dz} - \frac{d\bar{\rho}}{dz} \right) (\delta z)^2 = \text{gravitational adiabatic compression energy} + \text{density stratification perturbation energy}$$

The fourth term in (23) is a correlation between the parcel momentum and the velocity of the equilibrium mean wind at the parcel position. If they correlate the wave perturbation represents a lesser energy perturbation than if they don't, hence the minus sign for the term. If a sizable wave perturbation  $\tilde{p}$  or  $\tilde{W}$  corresponds to nearly zero energy due to the negativity of the wind shear term then we are near the disastrous situation that a very small energy may produce a large  $\tilde{p}$  or  $\tilde{W}$ . Consider a wind layer; when its boundaries are distorted into sinusoids the centrifugal force inside the layer does work against the boundaries to tend to make the sinusoidal amplitude increase. Thus, energy from the mean flow can be absorbed by a growing wave. We will next see that the fourth term acts toward giving the wave a negative energy density. The contradiction implied by negative energy means that the actual solutions are exponentials, not sinusoids as we have assumed.

The possibility of a negative wave energy density arises not just from the wind shear term. It could also come from the gravitational term if the density were stratified with the (potentially) heaviest air on top. A precise condition for the positiveness of the energy quadratic comes by writing (20) in matrix form

$$(24) \quad E = \frac{1}{4} \begin{bmatrix} \tilde{p} & \tilde{W} \end{bmatrix}^* \begin{bmatrix} \frac{1}{\bar{\rho}} \left( \frac{1}{c^2} + \frac{k^2}{\Omega^2} \right) & -\frac{i}{2} \frac{d\bar{u}}{dz} \frac{k}{\Omega} \\ +\frac{i}{2} \frac{d\bar{u}}{dz} \frac{k}{\Omega} & \bar{\rho} \left( 1 + \frac{\omega_b^2}{\Omega^2} \right) \end{bmatrix} \begin{bmatrix} \tilde{p} \\ \tilde{W} \end{bmatrix}$$

The Hermitian matrix is positive definite if we have

$$0 < \left( 1 + \frac{\omega_b^2}{\Omega^2} \right) \quad \text{and} \quad 0 < \frac{\Omega^4}{k^2} \left\{ \left( \frac{\Omega^2}{c^2 k^2} + 1 \right) (\Omega^2 + \omega_b^2) - \frac{1}{4} \left( \frac{d\bar{u}}{dz} \right)^2 \right\}$$

The first inequality is satisfied if the atmosphere has a stable temperature stratification (so  $\omega_b$  is real). The second inequality may be violated in strong wind shears. This gives rise to dynamic instability described in the next section.



Somewhat different developments by Bretherton (1966) and Elaissen and Palm (1960) have not included in the energy the term which is negative in the presence of wind shear.

### I-A-3 The Instability of Waves Interacting with High Altitude Winds

Coupling is frequently observed between two phenomena which move at the same speed. Here we will study what happens to acoustic gravity waves propagating at a velocity which equals that of the wind. Since the wind velocity is generally a continuously changing function of height one is concerned with a discrete set of points called critical heights where the wind speed equals the horizontal component of the wave speed. Of particular interest in the real atmosphere are the jet stream winds. Their speed frequently exceeds 20% of the speed of sound. The first thing to notice about a critical height  $z_c$  is that an observer moving with the wind at the critical height sees the frequency of the disturbance doppler shifted to zero. In the precise treatment the doppler frequency  $\Omega = \omega - ku$  occurs as a divisor which leads to some mathematical complexity. An idea of what happens to the wave may be gotten by seeing what happens in a wind-free, isothermal medium when the frequency is lowered keeping the horizontal wavelength fixed. The phase velocity becomes vertical, the group velocity and particle motions become horizontal, and the vertical wavelength becomes very small. The progress of a wave packet emitted from the ground heading toward the critical height is depicted below in Figure (2).

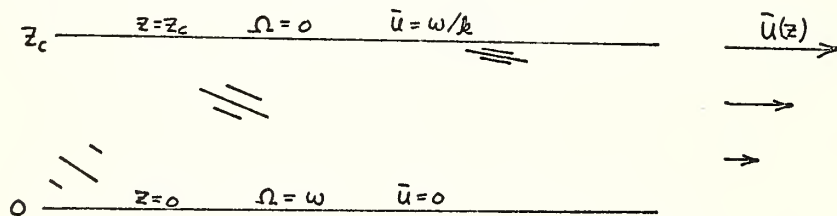


Figure 2. Wave packet emitted from the ground heading toward critical height.

If there is a continuing source on the ground the momentum density of the wave builds up to infinity at the critical height. Also very large shears develop in the wave itself.

In the solutions we will develop for the vicinity of the critical height we can see the effect of increasing the wind shear. Above a certain critical shear the solutions blow up catastrophically. Looking back to the solution in a stable wind shear we recall that the shear in the wave itself blows up at  $z_c$ . Thus, any real wave of finite amplitude at the ground creates the conditions<sup>c</sup> for instability at some point below  $z_c$ .

An attempt to give an intuitive idea of this so-called Richardson instability goes as follows:

Gravity will tend to stabilize the atmosphere with the densest layer on the bottom. However, if the bottom layer has a lot of kinetic energy in the form of wind, there is no energetic reason why it could not move up to replace a less dense layer losing some of its wind energy to do it. Perturbation on the stratified wind flow may tend to grow with time just like kinks in a water hose tend to grow because of the centrifugal force on the water. Stability will be assured only if the gravitational energy of some perturbed state is greater than the wind kinetic energy available for the perturbation. Specifically let two altitudes in a wind stratified incompressible fluid be separated by a distance  $dz$  have a horizontal velocity difference  $du$  and a density difference  $d\rho$ . Then the stability condition is

$$\text{Kinetic energy} < \text{potential energy}$$

$$\frac{1}{2} \rho (du)^2 < g (d\rho) (dz)$$



$$\frac{1}{2} \rho \left( \frac{du}{dz} dz \right)^2 < g \left( \frac{d\rho}{dz} dz \right) dz$$

$$\frac{1}{2} \left( \frac{du}{dz} \right)^2 < \frac{g}{\rho} \frac{d\rho}{dz}$$

The righthand side is the square of the Brunt frequency of an incompressible fluid (equation 5) and the inequality is within a factor of 2 of the Richardson stability criterion.

We begin the analytical deduction with equation (3)

$$\frac{d}{dz} \begin{bmatrix} \tilde{p} \\ \bar{\rho} \tilde{w} \end{bmatrix} = \begin{bmatrix} -g/c^2 & i(\Omega - \frac{g}{\bar{\rho}} (\frac{\bar{p}_z}{c^2} - \bar{\rho}_z)) \\ i(\frac{\Omega}{c^2} - \frac{k^2}{\bar{\rho}}) & -\frac{k}{\Omega} \bar{u}_z - \frac{1}{\bar{\rho}} (\frac{\bar{p}_z}{c^2} - \bar{\rho}_z) \end{bmatrix} \begin{bmatrix} \tilde{p} \\ \bar{\rho} \tilde{w} \end{bmatrix}$$

In the vicinity of  $\Omega=0$  we may drop all terms without  $\Omega$  in the denominator.

$$(25) \quad \frac{d}{dz} \begin{bmatrix} \tilde{p} \\ \bar{\rho} \tilde{w} \end{bmatrix} = \frac{1}{\Omega} \begin{bmatrix} 0 & \frac{g}{\bar{\rho}} (\frac{\bar{p}_z}{c^2} - \bar{\rho}_z) \\ -k^2 & -k \bar{u}_z \end{bmatrix} \begin{bmatrix} \tilde{p} \\ \bar{\rho} \tilde{w} \end{bmatrix}$$

Now it is convenient to introduce the definition of the Brunt frequency  $\omega_b$ .

$$(26) \quad \omega_b^2 = \frac{g}{\bar{\rho}} \left( \frac{\bar{p}_z}{c^2} - \bar{\rho}_z \right) \cong \frac{g}{T} \left( \frac{\partial T}{\partial z} + 9.5 \text{ } ^\circ\text{C}/\text{km} \right)$$

If we take the wind profile to be a linear function  $u(z) = u_0 + u_1 z$  of altitude near the singularity, then we have

$$(27) \quad \frac{1}{\Omega} = \frac{1}{\omega - k(u_0 + u_1 z)} = \frac{(-k u_1)^{-1}}{z - u_1^{-1}(\frac{\omega}{k} - u_0)} = \frac{(-k u_1)^{-1}}{z - z_c}$$

Substituting (26) and (27) into (25) gives

$$(28) \quad \frac{d}{dz} \begin{bmatrix} \tilde{p} \\ \bar{\rho} \tilde{w} \end{bmatrix} = \frac{1}{z - z_c} \begin{bmatrix} 0 & -\omega_b^2 / k u_1 \\ k / u_1 & 1 \end{bmatrix} \begin{bmatrix} \tilde{p} \\ \bar{\rho} \tilde{w} \end{bmatrix}$$

Taking  $\omega_b$  constant near the singularity we can integrate (28) in the vicinity of  $z_c$ . Let the matrix of coefficients be temporarily denoted by  $A$  and the solution vector by  $x$ . Then (28) is written

$$(29) \quad (z - z_c) \frac{d}{dz} x = A x$$

Define a new independent variable  $y$  by  $e^y = (1 - z/z_c)$

$$(30) \quad \frac{d}{dy} x = A x$$

This equation may be integrated to give the solution  $x_+$  at a point  $y_+$  from the solution  $x_-$  at  $y_-$ . Integration of (30) gives

$$(31) \quad x_+ = e^{A(y_+ - y_-)} x_- = \left[ e^{A \ln \frac{z_c - z_+}{z_c - z_-}} \right] x_- = P x_-$$

Let the matrix  $P$  be expanded by Sylvester's theorem.

$$(32) \quad P = \left[ \text{adj}(A - \lambda_1 I) \right] e^{\lambda_1 \ln \frac{z_c - z_+}{z_c - z_-}} + \left[ \text{adj}(A - \lambda_2 I) \right] e^{\lambda_2 \ln \frac{z_c - z_+}{z_c - z_-}}$$

Here "adj" represents matrix adjoint and  $\lambda_1$  and  $\lambda_2$  are the eigenvalues of A. The eigenvalues are the solution of

$$(33) \quad 0 = \det(A - \lambda I) = \lambda^2 - \lambda - \omega_b^2/u_i^2$$

$$(34) \quad \lambda = 1/2 \pm \sqrt{1/4 - \omega_b^2/u_i^2} = 1/2 \pm i\sqrt{R - 1/4} = 1/2 \pm i\mu$$

The quantity R as we have seen earlier is called the Richardson number by meteorologists and is a measure of the dynamic stability of the atmosphere. It is usually greater than 1/4 so we will take  $\mu$  as real until later when we consider instability.

The momentum flux associated with each of these solutions was shown in the last section to be a constant. The analysis actually breaks down at any point where  $\Omega=0$  as may be seen by re-examining equation 11. By means of (31) and (32) we will attempt to carry the integration across the critical height. Take the upward going wave and look at the z- dependent part of the momentum flux.

$$\operatorname{Re} \frac{1}{\Omega} \tilde{P} \tilde{W}^* \sim \frac{z_c - z_-}{z_c - z_+} \left| e^{(1/2 - i\mu) \ln \frac{z_c - z_+}{z_c - z_-}} \right|^2$$

As long as  $z_+$  and  $z_-$  are on the same side of  $z_c$  the logarithm is real and the above quantity is a constant equal to unity. If  $z_-$  stays fixed but  $z_+$  migrates to the other side of  $z_c$  the flux undergoes a jump at  $z_c$ . Evaluating it where  $|z_+ - z_c| = |z_- - z_c|$  we get the amount of the jump.

$$\operatorname{Re} \frac{\tilde{P} \tilde{W}^*}{\Omega} \sim (-1) \left| e^{(1/2 - i\mu) \ln(-1)} \right|^2 = - |(-1)^{1/2 - i\mu}|^2 = - |e^{\pm i\pi(1/2 - i\mu)}|^2 = - e^{\pm 2\pi\mu}$$

The sign ambiguity has been resolved by Booker and Bretherton by consideration of an initial value problem. In it one takes  $\omega$  hence  $z_c$  to be complex. Complex integration shows that the wave is attenuated by an amount  $e^{-2\pi\mu}$  on traversal of the critical height.

Hines and Reddy did the problem from a slightly different point of view and got a different answer. Instead of integrating first ( $dz \rightarrow 0$ ) and then letting the imaginary part of  $\omega$  go to zero, they did it in reverse order. They took  $\omega$  real and integrated in steps of width  $\Delta z$ . If the singular point is kept at a layer boundary it has no effect even as ( $\Delta z \rightarrow 0$ ) and  $\operatorname{Re}(\tilde{P} \tilde{W}^*/\Omega)$  stays constant.

In any case, one may calculate that the time it takes to propagate a disturbance through  $z_c$  is infinity.

$$\begin{aligned} \text{time} &= \int_{z_-}^{z_+} \text{momentum density } dz / \text{momentum flux} \\ &\sim \int_{z_-}^{z_+} \frac{dz}{(z_c - z)^2} / \text{const.} \sim \frac{1}{(z_+ - z_c)} \xrightarrow{z_+ \rightarrow z_c} \infty \end{aligned}$$

If one observes a continuing random disturbance on one side of a critical height and is to decide the amplitude of the disturbance on the other side of the critical height none of the above analyses are appropriate because of further complications. These complications have to do with non-linearity and instability which for real finite amplitudes arise before the disturbance gets to  $z_c$ .

Equations (28) to (32) show that at  $z = z_+$

$$(35) \quad \tilde{P} \sim \tilde{W} \sim (z_c - z)^{1/2}$$

Reference to the equations of motion shows that

$$(36) \quad \tilde{P} \sim \tilde{U} \sim (z_c - z)^{-1/2}$$

Differentiating gives  $u_z = du/dz \sim (z_c - z)^{-3/2}$

The further complication is that (36) et seq. diverge at the critical height. For any realistic non-zero amplitude (36) implies we get into problems of non-linearity even before the critical height is reached. The wind shear of the wave itself will become very large and violate the Richardson stability criterion before the critical height is reached. A numerical calculation shows that for realistic parameters under the jet stream the stability criterion is violated before the non-linearity criterion.

# I- B-1 Electrical Phenomena with Prescribed Neutral Velocity

Now we derive equations which enable us to calculate the electrical effects of acoustic gravity waves. In this section we take the behavior of the neutral atmosphere to be completely determined by the acoustic equations and we use the neutral particle velocities as sources to drive Maxwell's equations. Since we are concerned with millicycle per second frequencies we can drop time derivatives in Maxwell's equations and take the electric field  $E$  to be derivable from a potential  $\varphi$  and the divergence of the current  $J$  to vanish

$$(37,38) \quad \nabla \varphi = -\vec{E} \quad \nabla \cdot \vec{J} = 0$$

One may develop (thesis) the electrical conductivity expression

$$(39) \quad \vec{J} = \underline{\sigma} \vec{E} + \underline{\tau} \vec{V}$$

where  $\vec{V}$  is the velocity of the neutral wind. Inserting (39) into (37) we get

$$(40) \quad \nabla \varphi = -\underline{\sigma}^{-1} \vec{J} + \underline{\sigma}^{-1} \underline{\tau} \vec{V} = -\underline{r} \vec{J} + \vec{s}$$

where  $\underline{r}$  is the resistivity matrix and  $\vec{s}$  will be called the source vector. We take solutions to be of the form

$$(41) \quad \begin{bmatrix} J_x \\ J_y \\ J_z \\ \varphi \end{bmatrix} = \begin{bmatrix} J_x(z) \\ J_y(z) \\ J_z(z) \\ \varphi(z) \end{bmatrix} e^{ikx + i\ell y}$$

Inserting (41) into (40) and into (38) we get

$$(42) \quad \begin{bmatrix} & ik & & \\ & i\ell & & \\ & & \frac{\partial}{\partial z} & \\ ik & i\ell & \frac{\partial}{\partial z} & 0 \end{bmatrix} \begin{bmatrix} J_x \\ J_y \\ J_z \\ \varphi \end{bmatrix} = \begin{bmatrix} S_x \\ S_y \\ S_z \\ 0 \end{bmatrix}$$

Bringing terms without  $z$  derivatives to the right and interchanging the last two equations we get

$$(43) \quad \frac{d}{dz} \begin{bmatrix} 0 \\ 0 \\ J_z \\ \varphi \end{bmatrix} = - \begin{bmatrix} r_{xy} & r_{xy} & r_{xz} & ik \\ r_{yx} & r_{yy} & r_{yz} & i\ell \\ ik & i\ell & 0 & 0 \\ r_{zx} & r_{zy} & r_{zz} & 0 \end{bmatrix} \begin{bmatrix} J_x \\ J_y \\ J_z \\ \varphi \end{bmatrix} + \begin{bmatrix} S_x \\ S_y \\ 0 \\ S_z \end{bmatrix}$$

Next we partition this  $4 \times 4$  into a  $2 \times 2$  of  $2 \times 2$ 's

$$(44) \quad \frac{d}{dz} \begin{bmatrix} 0 \\ x_2 \end{bmatrix} = - \begin{bmatrix} A_{11} & A_{12} \\ A_{21} & A_{22} \end{bmatrix} \begin{bmatrix} x_1 \\ x_2 \end{bmatrix} \begin{bmatrix} S_1 \\ S_2 \end{bmatrix}$$

solving the top equation for  $x_1$ ,  $x_1 = A_{11}^{-1}(-A_{12}x_2 + S_1)$ , and inserting back into the bottom of (44)

$$(45) \quad \frac{d}{dz} x_2 = (A_{21}A_{11}^{-1}A_{12} - A_{22})x_2 + (-A_{21}A_{11}^{-1}S_1 + S_2)$$

This is the desired 2 x 2 set of equations which we may write symbolically as

$$(46) \quad \frac{d}{dz} \begin{bmatrix} J_z \\ \varphi \end{bmatrix} = \begin{bmatrix} A(z) \end{bmatrix} \begin{bmatrix} J_z \\ \varphi \end{bmatrix} + \begin{bmatrix} c(z) \end{bmatrix}$$

These equations are solved in principle by matrizants (Gantmacher Vol. 2 p. 131) and in practice by various numerical integration schemes. (Further details are in the thesis.)

Finally we come to calculate the perturbation in the magnetic field  $H$ . For this we use  $\text{curl } H = J$  and  $\text{div } H = 0$ . Arranging as a matrix

$$(47) \quad \begin{bmatrix} 0 & -\partial_z & ik \\ \partial_z & 0 & -ik \\ -ik & ik & 0 \\ ik & ik & \partial_z \end{bmatrix} \begin{bmatrix} H_x \\ H_y \\ H_z \end{bmatrix} = \begin{bmatrix} J_x \\ J_y \\ J_z \\ 0 \end{bmatrix}$$

Similar manipulations (thesis) give rise to

$$(48) \quad \frac{d}{dz} \begin{bmatrix} H_x \\ ikH_z \end{bmatrix} = \begin{bmatrix} 0 & 1 \\ (k^2, l^2) & 0 \end{bmatrix} \begin{bmatrix} H_x \\ ikH_z \end{bmatrix} + \begin{bmatrix} J_y \\ -ikJ_z \end{bmatrix}$$

## II. Results of Calculations

### A. Pure Acoustic Gravity

#### 1.1 Free Space Dispersion Curves

Figure (3) is the free space dispersion curve given by Hines (1960). It may be derived by specializing our layer integration formula (equation 4) by replacing  $d/dz$  by  $ik_z$ . Hines' dispersion relation may be thought of as the eigenvalue  $k_z$  as a function of  $k_x$  and  $\omega$ . The direction of the propagation vector  $\vec{k}$  is given by a vector from the origin to the curve. This is the direction of the phase velocity. The group velocity is given by  $\nabla_{\vec{k}} \omega$ . It is perpendicular to the curve at the tip of the  $\vec{k}$  vector in the direction of increasing frequency (decreasing period). Notice that at the long (gravity wave) periods a  $\vec{k}$  vector with an upward vertical component implies a downward component of the group velocity. Also notice that in the long period limit all group velocities become horizontal and phase velocities become vertical. That limit must be approached in the jet stream when one observes a steady disturbance at the ground traveling at jet stream speed because an observer moving with the jet sees the disturbance frequency doppler shifted to zero.

Figure (4) gives a picture of group velocity magnitudes as a function of frequency and direction. It is notable that a low frequency cannot propagate vertically.

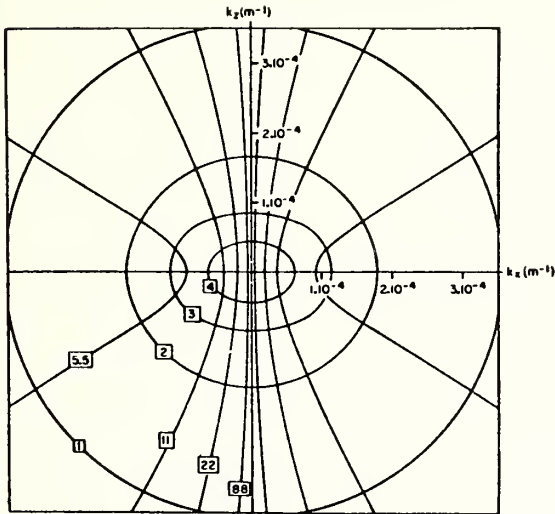


Figure 3. After Hines (1960). Free space dispersion curves of acoustic gravity waves. The numbers in the boxes are periods in minutes.

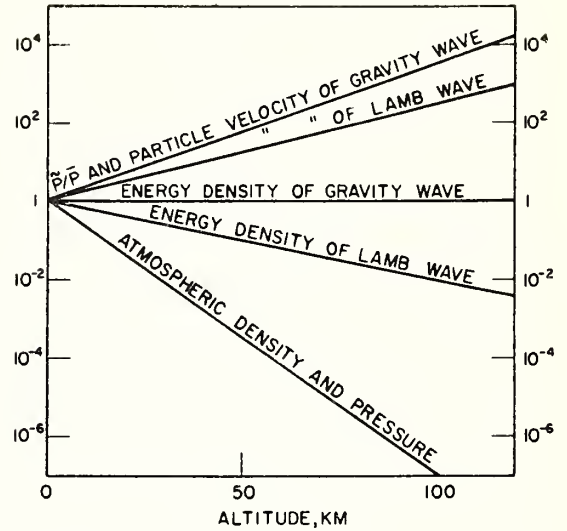


Figure 5. Altitude scaling of various properties of acoustic gravity waves in a free space of constant temperature.

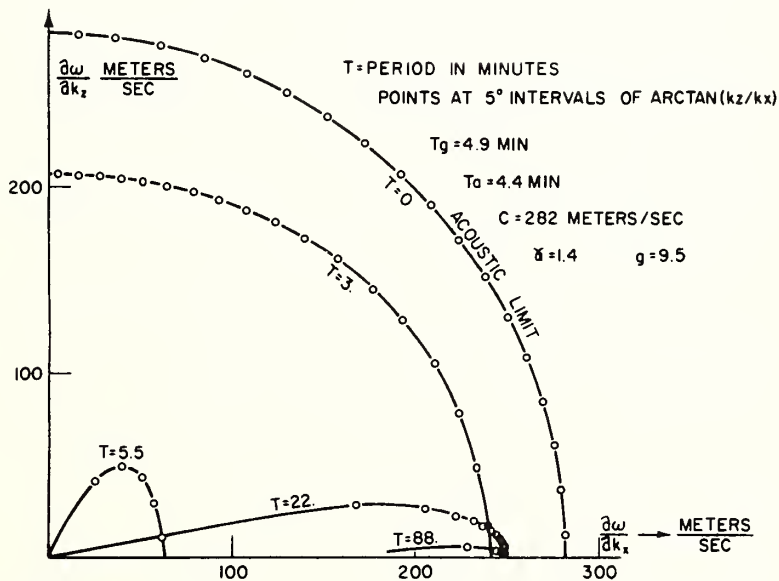


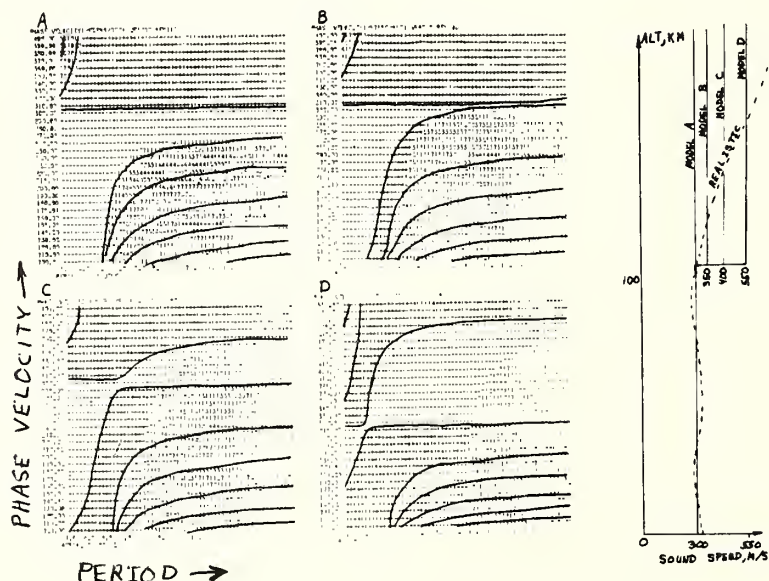
Figure 4. Group velocity of acoustic gravity waves as a function of period.

Figure (5) shows the altitude dependence of various parameters. One sees immediately that the non-linearities will arise when weak but observable disturbances on the ground propagate to ionospheric altitudes.



## II-A-1.2 Thermal Effects

With the mathematical formulation used in this thesis and the computer programs developed, there is no need to consider layer models for the atmosphere's temperature and wind structure. We still like layer models because of the insight they afford compared to realistic models for which cause and effect are harder to unscramble. Therefore we introduce the thermo-jet or T-J layer model. It shows all the principle modal behavior of a realistic model. The T-J model has a constant sound speed of 300 meters/sec between 0 and 100 km altitude, and 550 meters/sec above 100 km (thermosphere), and a 75 meter/sec jet stream between 8 and 10 km in an otherwise quiescent atmosphere. Figure (6) shows how dispersion curves undergo the transition from an isothermal atmosphere to the T-J model. Pluses and minuses refer to the sign of the dispersion relation. Where the sign changes a mode is possible. At some periods and phase velocities the half-space solution is not evanescent but is an outgoing wave solution. In the nomenclature of I-A-2 "outgoing" means that the sign of the vertical wave number in the half-space is chosen to make the energy flux  $\text{RePW}^*$  positive. The numbers in the upper lefthand corner of the dispersion diagram are vertically leaking acoustic waves. The numbers in the lower right are vertically leaking gravity waves. Modal solutions for these leaky waves require complex frequencies or complex horizontal wave numbers. We have instead kept the frequency real and put in a pressure source at jet stream level. In these regions of the T-V plane numbers are printed which represent the octant of the phase angle of the  $p$  source. The real part changes sign at practically the same frequency as the real part of the dispersion relation for a leaky mode so the leaky and non-leaky regions merge smoothly.



altitude. This is of mathematical significance but not practical significance because the node is at high altitude on the tail of the energy distribution. At these longer periods another wave has become the fundamental mode. Its speed at the long period limit is about 500 meters/second. Its energy density is maximum at the 100 km thermosphere boundary and it damps off in both directions. In the limit of a very hot (light) thermosphere and very cold (heavy) air layer and long period (incompressible medium), this wave resembles a surface wave on water.

One expects high altitude (100 km) nuclear explosions to excite the 500 meter/second mode and near surface explosions to excite the 300 meter/second mode.

### II-A-1.3 Jet Stream Effects

In Figure (7) one sees the effect of the 75 meter/sec jet stream from 8 to 10 kilometers altitude is to cause a cluster point of modes around 75 meters per second. From Figure (3) one sees that long period waves have a short vertical wavelength. This explains the cluster point. If an observer outside the jet sees a 76 meter/second wave, an observer inside sees a 1 meter/second wave with a very short vertical wavelength whose period is doppler shifted to be very long. Since the vertical wavelength gets arbitrarily short, the mode number gets arbitrarily large, hence the cluster point in the mode diagram.

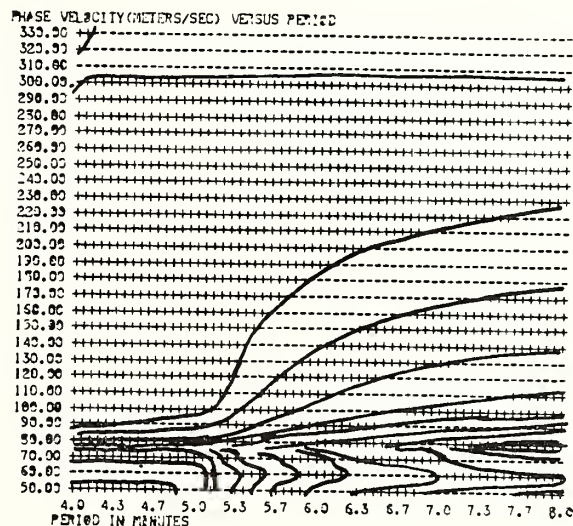


Figure 7. Dispersion curves for a model with a jet-stream layer with a speed of 75 meters/second.

A modal diagram of this type showing velocities less than the jet stream speed is somewhat questionable due to the integration through two singular points. This was discussed extensively in section I-A-3. A computer program working with layers experiences no difficulty because the singular point is missed being at the point of discontinuity between layers. Below 75 meters/second one simply has a backward going wave in the jet coupled to a forward going wave outside the jet. An important reason for showing the modes below 75 meters/second is that if the T-J model were the real atmosphere, observational experience shows that the jet sources are probably located below the peak of the wind velocity profile.

The non-dispersed modes at short periods are gravity waves inside the jet and acoustic waves outside. Since acoustic waves do not propagate outside the jet the modal profile is strongly damped outside the jet. This is quite in agreement with our observations in the real atmosphere which show very little energy above the Brunt frequency. The Brunt frequency in the troposphere is actually lower (about 10 minutes) than the Brunt frequency in the T-J model

due to the temperature lapse in the troposphere. Thus in a more realistic model, the curves of Figure (7) would be shifted more to the right.

#### II-A-1.4 Vertical Group Velocity

Strictly speaking there is no way to define vertical group velocity in the medium we are considering because it can produce such strong reflections. Nevertheless energy does migrate upward from low altitude sources to high altitudes where it is dissipated. Without solving the time transient problem we can calculate reasonable measures of vertical energy transport. Consider a source at a perfectly reflecting ground overlain by a simple layer and half-space with a 99% reflection coefficient at the half-space. If the group travel time from the ground to the half-space is  $t_0$ , an observer just above the layer in the half-space might regard  $50t_0$  or  $100t_0$  as a better estimate of the time for vertical energy transport than just  $t_0$ . The time  $t_0$  might perhaps be more accurately called a signal velocity and might very well be the appropriate velocity to consider for some experiments, but it would not be the vertical energy transport time.

We have here defined the vertical energy travel time from the jet to an altitude  $h$  by putting a source just above the jet and a perfect, non-reflecting absorber at  $h$ . The travel time is then said to be the integral of the energy density between the two points divided by the vertical energy flux.

$$\text{energy travel time} = \frac{\int_{\text{source}}^{\text{absorber}} \text{energy density } dh}{\text{energy flux}}$$

When this formula was calculated for the real atmosphere it was found as expected that vertical acoustic waves have just the delays ordinary ray theory would predict because the reflections are small; however for jet stream waves reflections can be very strong. This is graphed later (figure 13) for a range of horizontal phase speeds. The most notable thing about the graph is the very large vertical travel time taken by slow disturbances and the extreme sensitivity of vertical travel time to the horizontal velocity. In going from 60 meter/sec waves to 30 meter/sec waves the transport time to 100 kilometers altitude goes from 20 hours to 2000 hours. It is also clear that temperature gradients around eighty kilometers play a strong role in retarding the energy. Since these temperature gradients are not really well known and are thought to disappear in winter it is clear that situations could arise in which energy could propagate to the ionosphere much more rapidly than computed in Figure (13). Another situation which could result in very rapid vertical transport is if the wind overlying the jet stream were in the opposite direction. This would effectively increase the horizontal phase velocity of the waves and reduce the reflecting effect of temperature gradients.

#### II-A-2 Particle Motions

Figure (8) shows the particle motions of the Lamb wave. The wave is propagating to the right along the x-axis in a T-J model atmosphere. Below 100 km one sees the horizontal particle velocities one expects, purely longitudinal. Because the thermosphere is hotter, hence lighter than the air beneath, the particles tend to burst out into the thermosphere from the point of maximum compression below. On the figure this is at 50 kilometers on the x-axis and 100 kilometers on the z-axis.

Figure (9) shows the particle motions in the T-J model for a disturbance of a fast jet stream velocity (85 m/s) and 20 minute period. The most obvious difference with the Lamb waves is the standing wave pattern due to reflections at the thermosphere boundary. The wave is propagating to the right, and as it does the phase fronts in the ionosphere appear to move downward. The air currents are circulating and there are no obvious regions of compression and rarefaction as with the Lamb waves. For the realistic atmosphere particle motions are a great deal more complicated due to their vertical wavelength being comparable in scale to vertical changes in temperature.



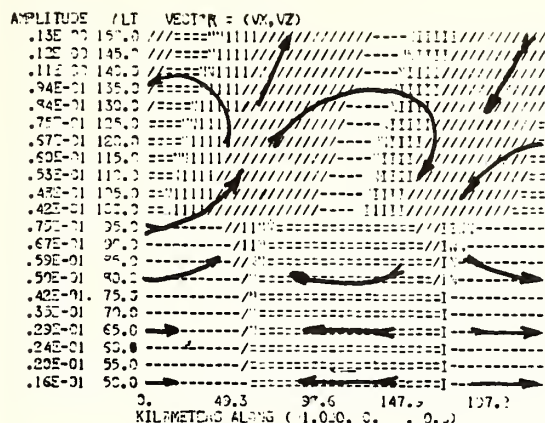


Figure 8. Particle motions of Lamb waves in the T-J model.

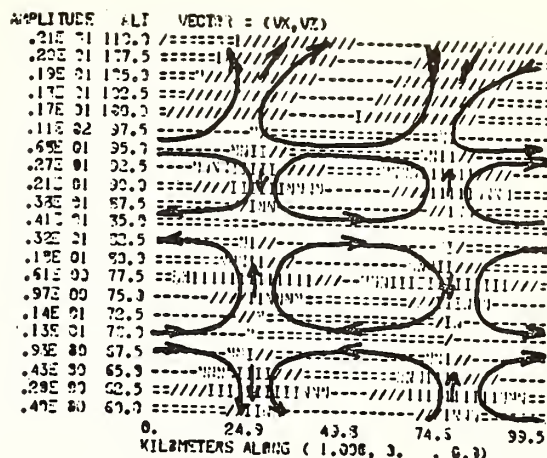


Figure 9. Particle motions in the T-J model for a disturbance of a fast jet stream velocity (85 meters/second) and a 20 minute period.

Figure (10) shows particle velocities of a wave going just slightly faster than the jet at its peak. The wave propagates to the right and must be sustained by a source at the ground. Phase fronts move downward as the energy is radiated outward. The wind increases linearly (actually in 20 constant layers) to 50 meters/second at 10 kilometers altitude and then decreases linearly at the same rate. It is notable that the wind gradient does not seem to set up partial reflections as temperature gradients do. As the wave propagates up to the point of maximum wind velocity its frequency is doppler lowered and the phase fronts become parallel horizontal.

In Figure (11) the source has been moved up to 5.5 kilometers altitude. This has the effect of producing a standing wave pattern below it due to reflections off the ground.

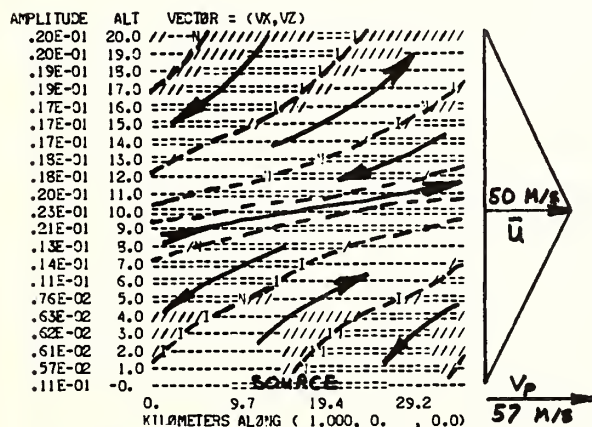


Figure 10. Particle velocities of a wave going slightly faster than the peak speed in the jet. The wave propagates to the right and must be sustained by a source at the ground.

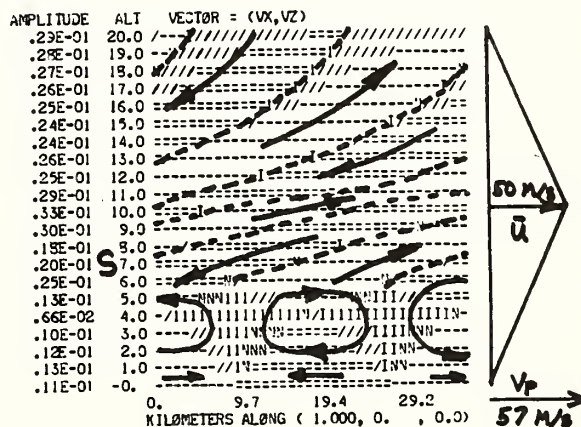


Figure 11. Particle velocities of a wave sustained by a source at jet stream altitude.

In Figure (12) the phase velocity has been reduced below the maximum jet speed. Thus there are two critical heights near 5 and 10 kilometers where the

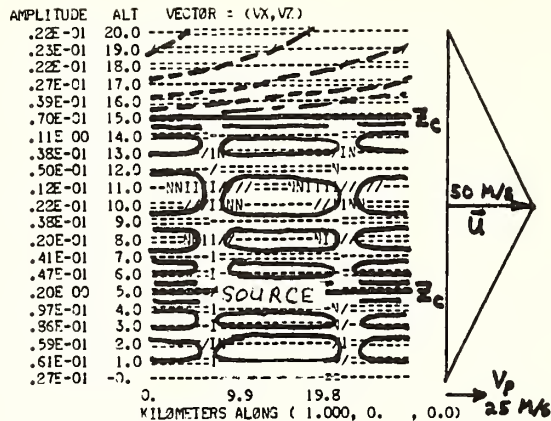


Figure 12. Particle velocities of a wave traveling slower than the jet stream.

integration must pass through a singularity. (See section I-A-3.) The program sidesteps this problem by putting the singularity at a layer interface. This problem was discussed theoretically in chapter I-A-3. Briefly the conclusion was that the group velocity becomes horizontal at the critical height. The source then feeds finite power into the region of the critical height and the energy density becomes so large linearity breaks down. Even before linearity breaks down, the wave has very large horizontal shears and itself violates the Richardson stability criterion at the critical height. For lack of a better approach at the present time we might then regard the critical height as a secondary source, due to the onset of some turbulent motions driven by the waves. The actual effect of this situation on the waves and the waves' ability to cross these critical zones remains an important unsolved problem. We will refer to this problem again when we examine the observational data.

## II-B-1 Gravity Wave Dissipation and Heating

Profiles of electromagnetic dissipation rate  $(V_p \cdot V_n) / (V_n \cdot V_n)$  have been computed for a variety of acoustic gravity wave modes. Generally the profile is within a factor of 2 or so of the profile of dissipation rate of ionospheric winds. However, for the modes the dissipation is not so smooth a function of altitude due to the vertical wavelengths of the modes. In fact, at some altitudes electromagnetic effects may be acting to strengthen the gravity wave rather than diminish it.

As a mechanism for dissipation of acoustic gravity waves electromagnetic effects are fairly independent of frequency and wave-number quite unlike dissipation due to heat conduction and molecular viscosity.

A comparison of the results of this work with Midgley and Liemohn's calculation of viscous damping shows that electromagnetic dissipation is more important for all velocities comparable to the jet stream. At some lower velocity (shorter vertical wavelength) these must become equal but exact comparison is difficult due to differences in techniques and thermal models.

Finally we come to the heating of the ionosphere by energy lost from ionospheric winds and gravity waves. Along with wind profiles and the specific heat  $C_p$  everything needed is a profile of dissipation rate because the heating rate is

$$\text{heating rate} = - \frac{\nabla p \cdot V_n}{\rho C_p} \quad \text{degrees C/sec}$$

$$\text{heating time} = - \frac{\rho C_p}{\nabla p \cdot V_n} = \frac{C_p T}{V_n \cdot V_n} = \frac{10^3 T}{V_n \cdot V_n} \quad \text{sec/degree C}$$

Since  $T$  is actually graphed in units of hours we may also read the same graph as hours to raise the temperature one degree if the time axis is scaled by



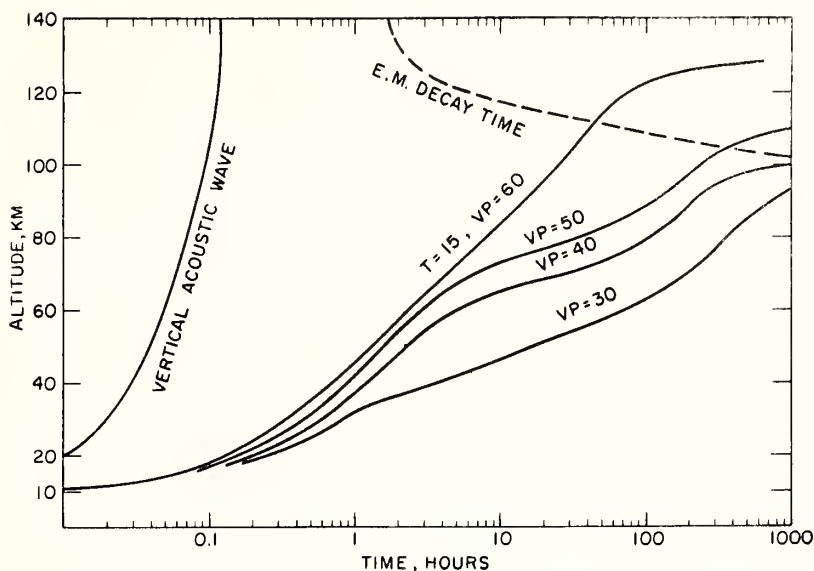


Figure 13. Vertical energy transport time for acoustic gravity waves originating in the jet stream.

$10^3/V^2$ . Since ionospheric winds of 100 meters/sec at 125 km altitude are fairly typical where decay times are typically 20 hours we get

$$\text{heating time} = 10^3 \cdot 20 / 100^2 = 2 \text{ hours/degree centigrade}$$

Gravity waves associated with the jet stream are dissipated at about  $110 \pm 10$  km altitude where the vertical group velocity is 50 hours per kilometer and the decay time is 300 hours. Both observations and modal calculations agree that 100 meters/sec is a reasonable particle velocity at that altitude and this implies a heating rate of 30 hours per degree. Due to uncertainties in the altitude and velocity magnitude involved the reliability of this number is taken to be an order of magnitude.

## II-B-2 Electromagnetic Effects of the Lamb Wave

Figure (14) shows the particle motions of the Lamb wave in a realistic temperature model.

The amplitude of the vectors is scaled to correspond to what we consider the quietest atmospheric conditions, an r.m.s. pressure at the ground of 10 microbars. Everything scales linearly. Multiply by a factor of 10 to get typical noise amplitudes observed on the ground (100 microbars) or by a factor of 50 to get unusually large amplitudes (.5 millibar). All vector amplitudes are in rationalized MKS units.

Subsequent figures are calculated from the theory developed in section I-B-1. Superposed on the T-J model we have a uniform magnetic field at  $45^\circ$  in the x-z plane. The wave we are considering is traveling southward at mid-latitude in the northern hemisphere. The neutral particles collide with charged particles and tend to drag them along. This is depicted in Figure (15). At high altitudes, however, the charged particles tend to follow magnetic field lines. In Figure (16) we see the electric fields induced by the Lamb wave. At high altitudes the electric fields tend to be perpendicular to the magnetic field due to the high conductivity along field lines. At low altitudes charge

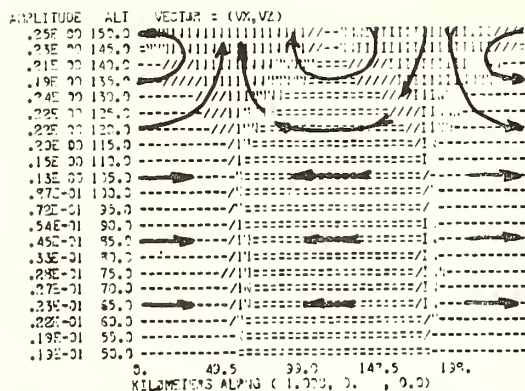


Figure 14. Particle velocities (MKS Units) for a Lamb wave propagating along the x-axis in a realistic atmosphere.

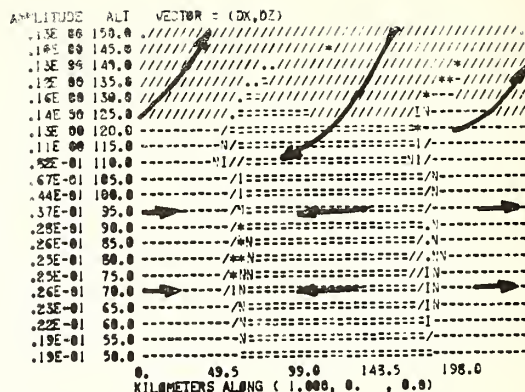


Figure 15. Drift =  $(V_{ion} + V_{electron}) / 2$  in meters/sec induced by the Lamb wave in Figure (14). Drift follows neutrals at low altitude and follows magnetic field lines at high altitudes.

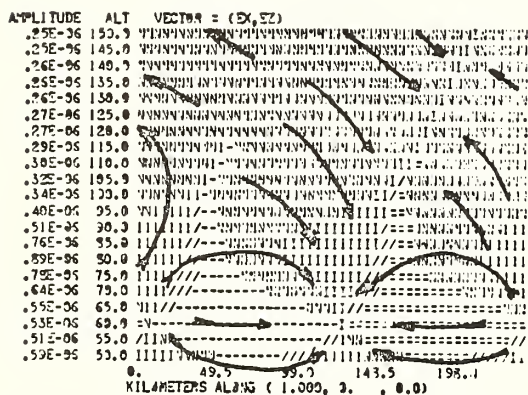


Figure 16. Electric fields induced by the Lamb wave. The induced electric fields are perpendicular to the magnetic field at high altitude. At low altitude charge concentration gives a divergence of  $E$ .

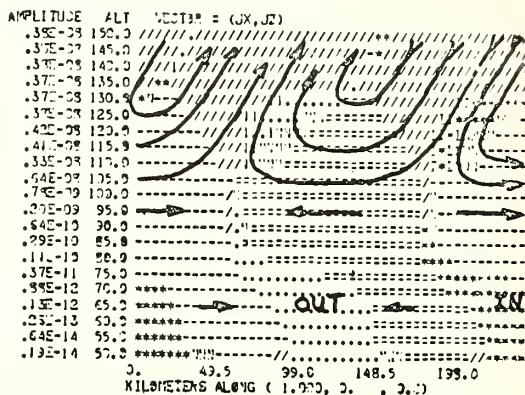


Figure 17. Electric currents induced by the Lamb wave. The electrical currents behave like the drifts except at low altitude where electric fields influence the currents.

concentration produces a divergence of  $E$  which is clearly apparent on the figure at 10 and 135 kilometers on the x-axis.

Figure (17) shows the induced electrical currents. They behave somewhat like the charged particle drift but differ at low altitudes because they are influenced in addition by the electric fields. Figure (18) shows the induced magnetic fields. One may crudely verify  $\text{curl } H = J$  by comparison of Figures (17) and (18). Near the bottom one sees the magnetic field satisfying  $\text{curl } H = 0$ .

## II-B-3 The Westerly Jet Wave

Calculations similar to the last section have been done for the westerly

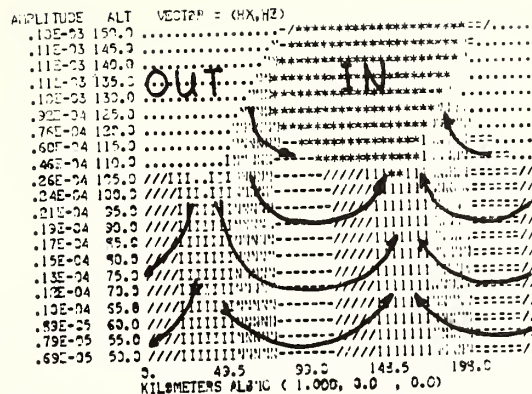


Figure 18. The magnetic field induced by the Lamb wave. The magnetic fields are obtained by solving  $\text{curl } \mathbf{H} = \mathbf{J}$ . This may be qualitatively verified by comparison with Figure (17).

jet wave. The effect of cellular motions has also been considered (thesis). The parcel motion is too complicated and dependent on details of the model to merit graphical presentation. To calculate the magnetic fields as seen on the earth a number of approximations have been made. First of all the acoustic gravity wave is computed as a steady state wave with no dissipation. Then since electromagnetic dissipation is dominant above 110 km the currents induced above 110 km are neglected insofar as production of magnetic fields is concerned. When the magnetic fields were integrated back down to the ground it was found that even under optimistic conditions (85 m/s gravity wave, 15 min period, 1/2 millibar pressure at the ground) the magnetic field seen at the ground ( $H = 5 \times 10^{-8}$ ) was two orders of magnitude below magnetic noise during quiet conditions.

#### References

- Booker, J.R., Bretherton, F.P., Critical layer for internal gravity waves in a shear flow, *J. of Fluid Mech.*, 27 513-539, 1967.
- Bretherton, F.P., The propagation of groups of internal gravity waves in a shear flow, *Transaction of Royal Society*, 551.511.3:532.59, 466-480, Mar. 25, 1966.
- Claerbout, J.F., Electromagnetic effects of atmospheric gravity waves, Ph.D. thesis at Massachusetts Institute of Technology, 1967, available from Clearinghouse, Department of Commerce, Springfield, Virginia 22151, accession number AD-661650, \$3.
- Donn, W.L., Ewing, M., Atmospheric waves from nuclear explosions, Part II - The Soviet test of Oct. 30, 1961, *J. Atmos. Sci.*, 19, 246, 1962.
- Gossard, E., Munk, W., Gravity waves in the atmosphere, *Quart. J. of Royal Meteorological Soc.*, 81, No. 349, July 1955.
- Hines, C.O., Internal atmospheric gravity waves at ionospheric heights, *Can. J. Physics*, 38, 1440-1481, 1960.
- Hines, C.O., Reddy, C.A., On the propagation of atmospheric gravity waves through regions of wind shear, *J.G.R.*, 72, No. 3, 1015-1034, 1967.
- Martyn, D.F., Cellular atmospheric waves in the ionosphere and troposphere, *Proc. Royal Soc., London, Ser. A*, 201, 216-234, 1950.
- Midgley, J.E., Liemohn, H.B., Gravity waves in a realistic atmosphere, *J.G.R.*, 71, No. 15, p. 3729-3748, Aug. 1966.
- Pierce, A.D., Propagation of acoustic-gravity waves from a small source above the ground in an isothermal atmosphere, *J. of Acous. Soc. of Amer.*, 35, No. 11, 1798-1807, Nov. 1963.
- Press, F., Harkrider, D., Propagation of acoustic-gravity waves in the atmosphere, *J. Geophys. Res.*, 67, 3889-3908, 1962.



### **III Natural sources of atmospheric waves- observations**





The Auroral Zone as a Source  
of  
Traveling Ionospheric Disturbances  
by

W. L. Flock, University of Colorado  
and  
R. D. Hunsucker, ESSA Research Laboratories

Certain characteristics of the aurora and experimental data concerning traveling ionospheric disturbances (TIDs) suggest that the aurora is a likely source of some TIDs. Observations by a number of investigators have shown the existence of TIDs that move from higher to lower latitudes, in some cases penetrating into the opposite hemisphere as well. Hunsucker and Tveten showed that, in the case of a certain group of TIDs, about half were preceded by auroral activity that might have initiated them. Large amounts of energy are dissipated in the auroral oval in conjunction with particle precipitation and the flow of intense electric currents, and it has been shown that auroral activity can generate infrasonic waves. It is now widely believed that TIDs are a gravity wave phenomenon and other investigators are analyzing theoretically the possibility that gravity waves can be initiated by auroral activity that has sufficient intensity and appropriate characteristic dimensions and period. Particle precipitation at locations other than the auroral oval may also be a source of some TIDs.

Key Words: Auroral zone, Energy source, Traveling ionospheric disturbance,  
Gravity wave, Experimental evidence, Electrojet.

Introduction

Traveling ionospheric disturbances (TIDs) are observed commonly to travel towards the south in the northern hemisphere and towards the north in the southern hemisphere. Munro's extensive observations in Australia (Munro, 1958) however, showed TIDs traveling generally towards the north in the southern hemisphere winter and towards the south in the northern hemisphere winter. The directions of travel and other evidence have prompted suggestions (DuCastel and Faynot, 1964; Liszka and Taylor, 1965; Thome, 1966; King, 1966; Hunsucker and Tveten, 1967) that at least a significant fraction of TIDs originate in the auroral zone. It is now widely believed that TIDs are a gravity wave phenomenon (Hines, 1960; Friedman, 1966; Hines, 1964) and theoretical analyses of the possibility that auroral activity launches gravity waves are being undertaken by Blumen and Hendl (1968) and Chimonas (1968). This paper reviews the experimental evidence concerning this point.

In considering TID observations it is useful to distinguish the different types of disturbances as has been done by Georges (1968). The medium scale disturbances he describes are not associated with magnetic activity (at the point of observation) and travel with velocities in agreement with imperfectly ducted gravity wave theory (Friedman, 1966). They may have their source in the auroral zone, being initiated by auroral activity taking place there when little magnetic activity is evident at middle latitudes. The very large disturbances accompany magnetic storms and travel with higher velocities. They also may be generated in the auroral zone or, more precisely, in the auroral oval. The latter moves to lower latitudes during magnetic storms.

Related topics include the generation of infrasonic waves by auroral activity and effects of particle precipitation at locations other than the auroral zone. Wilson and Nichparenko (1967) and Wilson (1967) have shown clearly by measurements in the general area of the auroral zone that auroral activity does initiate infrasonic waves. Infrasonic signals observed at temperate latitudes also have been attributed to an auroral source. It has not been possible,

however, to follow individual infrasonic events from the auroral zone to temperate latitudes. In the case of TIDs, a study comparable to that of Wilson has not been carried out, but ionospheric disturbances have been followed over distances of up to 3000 km (Heisler, 1958; Wright, 1961; Chan and Villard, 1962). Paulikas et.al. (1966) and Gledhill et.al. (1967) have discussed electron precipitation at middle latitudes and resulting ionospheric disturbances.

#### Observations of TIDs Propagated from High Latitudes

Certain TID observations of interest to this discussion are listed in Table 1, and some of the table entries are discussed further in this section.

Bowman has studied TIDs extensively and has pointed out an association between spread F, sporadic E, and TIDs. His 1965 paper reports source locations for three TIDs which he considered to be initiated by sudden commencements (SCs) of geomagnetic storms. The sources in each case are specified to be a pair of conjugate high latitude sources. Ionosonde data and assumed travel velocities were used to determine these source locations. Chan and Villard (1962) also reported an association between TIDs and SCs. They used HF Cw doppler measurements from several long paths which crossed the United States. The disturbances were observed to come from the north. Auroral index data which has become available since the papers were written, however, indicates that auroral activity rather than effects associated with SCs could well have the source of the TIDs reported on by both Bowman and Chan and Villard.

Heisler (1958) and Wright (1961) followed TIDs by using ionosonde data. Heisler followed medium scale disturbances north from Hobart to Townsville, a distance of 3000 km, and Wright followed very large disturbances from Campbell Island to Christchurch, a distance of 1100 km. The latter disturbances occurred during times of magnetic storms, and velocities between 406 and 691 m/sec were observed. Chan and Villard (1962) followed disturbances associated with magnetic activity over distances as great as 1200 km and observed velocities between 400 to 765 m/sec.

Hunsucker and Tveten (1967) observed TIDs with high-resolution HF backscatter equipment during November and December, 1963, and, assuming a constant velocity of travel and an auroral zone source, calculated the predicted times of auroral activity at College, Alaska. For about 50% of the 37 events, auroral activity was observed at the predicted time.

The work of Munro (1958), carried out over a period of nine years, is one of the most statistically significant studies. The TIDs he observed traveled on the average towards the northeast (30° east of north) in the southern hemisphere winter and towards the southeast (120° east of north) in the northern hemisphere winter. Thus the winter polar region may be the source of the TIDs that Munro reported. Munro's data refers primarily to the day-time and to medium scale TIDs.

In general, all of the observations listed in Table 1 report propagation from higher to lower latitudes and in that respect are consistent with auroral zone sources.

Table 1  
TID Observations

<u>Investigator</u>	<u>Technique</u>	<u>Speed</u>	<u>Comments</u>
1. Bowman (1965)	Ionosonde	361 m/sec, 722 m/sec (assumed)	Reports sources as conjugate high-latitude locations. TIDs occurred following SCs.
2. Chan & Villard (1964)	Cw Doppler	400-765 m/sec	TIDs occurred following SCs.
3. DuCastel & Faynot (1964)	Satellite signals	180 m/sec	Simultaneous upper and lower ionospheric data. Suggest high-latitude origin.
4. Georges (1968)	Cw Doppler	Two groups: < 300 m/sec, > 300 m/sec	Medium scale and very large TIDs. From north.
5. Goodwin (1968)	Ionosonde	30 m/sec	Large-scale frontal irregularities in E region. Suggests origin near geomagnetic pole.
6. Heisler (1958)	Ionosonde	97-207 m/sec	Followed TIDs 3000 km from Hobart to Townsville.
7. Hunsucker & Tveten (1967)	High-resolution HF backscatter	82-325 m/sec	52% preceded by auroral activity at suitable time for auroral origin.
8. King (1966)	Ionosonde	200 m/sec	Accepts infrasonic evidence as to auroral source.
9. Liszka & Taylor (1965)	Faraday rotation of satellite signals	200-300 m/sec	Suggest auroral zone source.
10. Munro (1958)	Three 5, 8 MHz pulsed transmitters	120-150 m/sec	Waves come from winter polar region. Nine years of data.
11. Thome (1966)	Thomson backscatter sounder at Arecibo, f-430 MHz.	50-100 m/sec	Suggests auroral electrojet as source.
12. Titheridge (1968)	Faraday rotation or polarization of satellite signals	50 m/sec	Waves in New Zealand traveled towards the north.
13. Wright (1961)	Ionosonde	406-691 m/sec	Followed TIDs 1100 km from Campbell Island to Christchurch.

#### An Unusual Event of Possible Middle Latitude Origin

Possible effects of middle latitude particle precipitation were reported by Hunsucker, Tveten, and Flock (1967) for January 20, 1967 when ionospheric virtual height variations of over 250 km at 3.2 MHz were observed at Texarkana, Ark. Simultaneously a large TID and a large azimuthal direction-of-arrival variation of the signal from an HF transponder, along

with spread-F on another vertical ionosonde were observed in the same geographical region. Some of these data are shown in Fig. 1. During this period there was no significant magnetic activity at Boulder or Dallas, and auroral activity at College and Churchill seemed to occur too late to be a likely source of the disturbance. Ionosonde records from other midlatitude stations showed no anomalies.

Thus the disturbance appeared to be quite localized and is cited as an example of a rather intense disturbance that is difficult to associate with auroral activity.

#### Pertinent Characteristics of the Aurora

Concepts of the auroral oval and of auroral substorms are basic to this discussion and are described briefly in this section. Certain special features of the aurora are then mentioned. For further information concerning the aurora the reader is referred to references such as Akasofu (1965, 1966, a,b), Davis (1965), McCormac (1967), Piddington (1964), and Hultquist (1968).

Studies of the aurora have shown that auroral arcs tend to lie in an oval belt that encircles, but is eccentric with respect to the geomagnetic pole. The belt is displaced towards the dark hemisphere. What has been called the auroral zone is the locus of the midnight part of the oval where the most intense auroral activity tends to take place. Auroral activity occurs nearly every night in the auroral zone, but the intensity of the activity is quite variable. Intense auroral activity takes place during times of worldwide magnetic storms, but is not necessarily restricted to such times. The auroral oval shifts toward the equator during magnetic storms, so that a location that is on the oval normally, may be inside the oval during a magnetic storm.

In a normal night of auroral activity a typical sequence of cycle of events is observed. Such a sequence may be repeated more than once in one night. The term, auroral substorm, is used to describe the expansive and recovery phases of one cycle or sequence of activity. The onset of the auroral substorm is sudden, and Akasofu has used the term "explosive phase" and spoken of an explosive release of energy at the time.

Stable visible arcs with an east-west dimension of thousands of kilometers and a north-south width of only several hundred meters are usually the first sign of auroral activity. It is more common for several arcs to be in the field of view than for only one arc to be present. The arcs are commonly separated by distance of 30-40 km. After the arcs have remained rather quiet for perhaps several hours, they first brighten and then advance poleward, this movement initiating the expansive phase of the substorm. In addition to the poleward expansion, a surge travels westward along the pre-existing arcs, and to the east the arcs disintegrate into patches which drift eastward. Thus, the whole auroral system is activated from the midnight sector. The recovery phase of the auroral substorm involves a contraction of the thickness of the auroral oval and a return to quiet conditions.

The geomagnetic field at a fixed observing point near the auroral oval varies in a characteristic way during a cycle of auroral activity. During the period of quiet auroral arcs the horizontal component of the field is greater than previously, this increase being referred to as a positive bay. During the explosive phase of a substorm, corresponding to what is commonly called the auroral breakup, the horizontal component of the geomagnetic field decreases abruptly and a negative bay is initiated. The negative bays are associated with a strongly concentrated intense westward current, that is, with a westward auroral electrojet. There has been a difference of opinion as to whether an eastward auroral electrojet or merely a return flow of a westward electrojet occurring elsewhere is responsible for the positive bay.

Examples of magnetic records from the auroral zone are shown in Fig. 2. The upper record is a storm magnetograph (taken with reduced sensitivity) showing an intense magnetic storm that started with an SC shortly before 2400 UT, Feb. 15, 1967. The main phase on Feb. 16



shows a negative excursion of about 2000  $\gamma$ . The magnetic record from Boulder, Colorado was also highly disturbed, but reference to the calibration indicates a deviation of only about 125  $\gamma$ . The lower record for March 17-18, 1967, taken at normal sensitivity for College, shows a negative deviation of 620  $\gamma$ . At this time the Boulder record shows no significant activity. Points to notice are the small effect of the SC as compared to the main phase and the fact that the March 17-18 record shows that quite intense magnetic activity can take place in the auroral zone when magnetically quiet conditions prevail elsewhere. Assuming a simple line current source at a height of 110 km for the Feb. 16 magnetic storm and using the relation

$$\Delta B = \frac{\mu_0 \Delta I}{2\pi r}, \text{ where } r \text{ is distance, shows that a current of about } 10^6 \text{ amps could be responsible}$$

for the observed  $\Delta B$  deviation of  $2 \times 10^{-6}$  weber/m<sup>2</sup> or 2000  $\gamma$ . Such a calculation is crude and should indicate only the order of magnitude of the electrojet current. On March 18 the corresponding current value is about  $3.5 \times 10^5$  amps.

A valuable measure of auroral electrojet activity is provided by the auroral electrojet indices (Davis and Sugiura, 1966). The Geophysical Institute of the University of Alaska has published a series of Scientific Reports which give the auroral electrojet indices for the years 1958 through 1964. Example of the plots of AE indices are shown in Figures 3 and 4. Points to notice are that values of 500  $\gamma$  are commonly reached (the 2000  $\gamma$  figure for Feb. 16, 1967 is unusually high) and that auroral activity can be moderately high for a rather large percentage of the time. The electrojet indices represent weighted average values of variations in the horizontal component of the earth's magnetic field and are determined by using data from seven auroral-zone observatories. The magnetic records from the seven sites are plotted against UT and overlain, and the AE index represents the difference between the upper and lower envelopes.

Having described some well known characteristics of the aurora, attention is now directed to certain special auroral or high-latitude features. Visual auroral forms sometimes move with supersonic velocities, and Wilson and Nichparenko (1967) and Wilson (1967) found that these forms are specifically responsible for the generation of infrasonic waves. Infrasonic waves nevertheless do occur most frequently during intense auroral substorms. A related study by Cresswell (1968) has been concerned also with fast auroral waves in his case with forms which propagate southward from the vicinity of College, Alaska on rare occasions after midnight. Large field aligned "sheets" or irregularities in the auroral zone extending from the lower F region up to 1000 km in height and of hundreds of kilometers in longitudinal extent have been reported by Lund, Hunsucker, Bates, and Murcray (1967). In one instance, a large sheet was observed to be moving southward at approximately 18 km/sec. Hill (1963) has reported large sporadic increases in F region concentration at high latitudes. Recently Maehlum (1968) reported maxima of electron flux in the northern polar regions at the time of maxima of Hill's "sporadic-F". The features mentioned here may have some relation to the generation of infrasonic or gravity waves, especially the former in the case of the rapidly moving forms.

The factors that would determine whether gravity waves can be launched by auroral activity include the intensities and efficiencies and the time and spatial variations of the source mechanisms. Heating due to particle precipitation, Joule heating due to current flow, and motions imparted to the neutral air by charged particle motions or currents have been proposed as suitable mechanisms. The first of these mechanisms was analyzed by Maeda and Watanabe (1964) and Taffe (1966) for the case of infrasonic waves and the second was treated by Blumen and Hendl (1968), for the case of gravity waves. Piddington (1964) has suggested the last mechanism. He discussed the two possibilities of Pedersen and Hall drift but put emphasis on Pedersen drift, that is, on motion imparted to the neutral air in the direction of the electric field. The  $J \times B$  force on a unit volume of fluid is being considered by Chimonas (1968) in an analysis of the initiation of gravity waves by auroral activity. The interaction between particle precipitation and Joule heating has recently been discussed by Maehlum and O'Brien (1968). These two effects are not independent of each other. In general it appears that all the proposed mechanisms for the generation of gravity waves by the aurora can operate at the same time.

As already stated, infrasonic waves have been found to be generated by supersonic auroral forms. Gravity waves, having longer periods and wavelengths, however, may be generated by more slowly varying effects or effects of greater spatial extent and they may relate more directly to the intensity of auroral activity. In so far as the intensity of auroral activity is important to the launching of gravity waves, the auroral electrojet indices are pertinent.

### Atmospheric Characteristics

If gravity waves responsible for traveling ionospheric disturbances are presumed to be generated in the auroral zone, the question of whether they can propagate frequently over long distances to temperate latitudes needs to be asked. A body of experimental and theoretical evidence suggests that they can. It is not clear, however, whether conditions that are favorable for the propagation of infrasonic waves and conditions that are favorable for the propagation of gravity waves tend to occur simultaneously or not. The same remark can be made about gravity wave propagation and ducted HF electromagnetic wave propagation. The interesting long-range propagation of HF signals, presumably on the basis of ionospheric ducting, from Alaska to Massachusetts has been observed by Mullen, Allen and Aarons (1965). The conditions required for gravity wave and e-m wave ducting are, of course, not the same, but both conditions could possibly tend to occur simultaneously. The times of day and the season at which Mullen et. al. observed ducted HF signals correspond to the times and season at which Hunsucker & Tveten (1967) observed TIDs.

Winds in the middle atmosphere, and especially the combination of wind and temperature effects, can cause some degree of directional filtering of gravity waves favoring propagation in a north-south direction (Hines and Reddy, 1967). The effects of the earth's magnetic field and of tendencies for observational selectivity on the part of the techniques used may also favor the observation of north-south traveling disturbances (Hooke, 1968). Thus a preponderance of observations indicating north-south directions of travel for TIDs is not conclusive evidence that the disturbances originate in high latitudes.

### Conclusion

A rather impressive amount of evidence shows that many TIDs propagate from higher to lower latitudes, perhaps crossing the equator and continuing into the other hemisphere as well. In some cases TIDs have been followed over distances up to 3000 km. On the basis of measured TID velocities and records of auroral activity, Hunsucker and Tveten showed that about half of the TIDs they observed in a certain period could have originated in the auroral zone. Auroral substorms occurring in the auroral oval thus seem to be a likely source of at least a significant fraction of TIDs. Particle precipitation at other times and locations may also initiate some TIDs. Tropospheric sources may also initiate TIDs. These have not been considered in this paper, but it is recognized that some TIDs that come from the direction of the auroral zone may actually be generated by jet streams in the troposphere.

In further experimental work a distinction should be made between the medium scale slowly traveling disturbances which are not associated with widespread magnetic activity and very large rapidly traveling disturbances which are associated with magnetic storms. In North America further observations in the region between that where TIDs have been frequently identified and the auroral zone would be valuable. Cw Doppler, Ionosonde, HF high-resolution backscatter, and Faraday rotation techniques could be used for the purpose.

### Acknowledgements

This research was partly supported by the ESSA Research Laboratories through Contract E22-108-67(N), arranged by the HANDS program with University of Colorado.

## References

- Akasofu, S. -I., Dynamic morphology of auroras, *Space Sci. Rev.*, 4, 488-540, 1965.
- Akasofu, S. -I., The auroral oval, the auroral substorm, and their relations with the internal structure of the magnetosphere, *Planetary Space Sci.*, 14, 587-595, 1966a.
- Akasofu, S. -I., S. Chapman, and A. B. Meinel, The aurora, in *Handbuch der Physik*, vol. 49, part 1, Springer-Verlag, Berlin, 1966b.
- Blumen, W. and R. G. Hendl, NCAR symposium on gravity waves, June, 1968.
- Bowman, G. G., Traveling disturbances associated with ionospheric storms, *J. Atmospheric Terrest. Phys.*, 27, 1247-1261, 1965.
- Bowman, G. G., Movements of ionospheric irregularities and gravity waves, *J. Atmospheric Terrest. Phys.*, 30, 721-734, 1968.
- Chan, K. L. and O. G. Villard, Jr., Observation of large-scale traveling ionospheric disturbances by spaced-path high-frequency instantaneous-frequency measurements, *J. Geophys. Res.* 67, 973-988, 1962.
- Chimonas, G. (these proceedings), 1968.
- Cresswell, G. R., Fast temporal and spatial changes in auroras, Geophysical Institute, University of Alaska, College, Alaska, Scientific Report, February, 1968.
- Davis, T. N., The aurora, in *Introduction to Space Science*, edited by W. N. Hess, pp. 205-250, Gordon and Breach Science Publisher, New York, 1965.
- Davis, T. Neil and Masahisa Sugiura, Auroral electrojet activity index AE and its universal time variations, *J. Geophys. Res.*, 71, 785-801, 1966.
- DuCastel, F., J. M. Faynot, Some irregularities observed simultaneously in the upper and lower ionosphere at middle latitudes, *Nature*, 204, 984-985, 1964.
- Friedman, Jack P., Propagation of internal gravity waves in a thermally stratified atmosphere, *J. Geophys. Res.*, 71, 1033-1054, 1966.
- Georges, T. M., H-f doppler studies of traveling ionospheric disturbances, *J. Atmospheric Terrest. Phys.*, 30, 735-746, 1968.
- Gledhill, J. A., D. G. Torr, and Marsha R. Torr, Ionospheric disturbance and electron precipitation from the outer radiation belt, *J. Geophys. Res.*, 72, 209-214, 1967.
- Goodwin, G. L. Some horizontally-moving ionospheric irregularities at high latitudes, *Planetary Space Sci.*, 16, 273-283, 1968.
- Heisler, L. H., Anomalies in ionosonde records due to traveling ionospheric disturbances, *Aust. J. Phys.* 11, 79-90, 1958.
- Hill, Geoffrey E., Sudden enhancements of F-layer ionization in polar regions, *J. Atmospheric Terrest. Phys.*, 20, 492-497, 1963.
- Hines, C. O., Internal atmospheric gravity waves at ionospheric heights, *Can. J. Phys.*, 38, 1441-1481, 1960.
- Hines, C. O., Comments on paper by A. F. Wickersham, Jr., 'Identification of ionospheric motions detected by the high-frequency backscattering technique', *J. Geophys. Res.*, 69, 2395, 1964.
- Hines, C. O. and C. A. Reddy, On the propagation of atmospheric gravity waves through regions of wind shear, *J. Geophys. Res.*, 72, 1015-1034, 1967.
- Hooke, W. H., (these proceedings), 1968.
- Hultqvist, Bengt, Aurora, in *Physics of Geomagnetic Phenomena*, Volume I, edited by S. Matsushita and Wallace H. Campbell, pp. 664-791, Academic Press, New York, 1967.
- Hunsucker, R. D., L. H. Tveten, and W. L. Flock, Investigation of the structure and motion of large ionospheric irregularities at middle latitudes, XIV General Assembly, I. A. G. A., St. Gall, Switzerland, 1967.
- Hunsucker, R. D., and L. H. Tveten, Large traveling-ionospheric-disturbances observed at mid latitudes utilizing the high resolution h.f. backscatter technique, *J. Atmospheric Terrest. Phys.*, 29, 909-916, 1967.
- King, G. A. M., The ionospheric disturbance and atmospheric waves, I - general discussion, *J. Atmospheric Terrest. Phys.*, 28, 957-963, 1966.
- Liszka, L., and G. N. Taylor, A synoptic study of large scale ionospheric irregularities using observations of the Faraday rotation of satellite signals, *J. Atmospheric Terrest. Phys.*, 27, 843-854, 1965.



- Lund, D. A., R. D. Hunsucker, H. F. Bates, and W. B. Murcray, Electron number densities in auroral irregularities: comparison of backscatter and satellite data, *J. Geophys. Res.*, 72, 1053-1059, 1967.
- Maeda, K. and T. Watanabe, Pulsating aurorae and infrasonic waves in the polar atmosphere, *J. Atmospheric Sci.*, 21, 15-29, 1964.
- Maehlum, Bernt N., Universal-time control of the low-energy electron fluxes in the polar regions, *J. Geophys. Res.*, 73, 3459-3468, 1968.
- Maehlum, Bernt N., and Brian J. O'Brien, The mutual effect of precipitated auroral electrons and the auroral electrojet, *J. Geophys. Res.*, 73, 1679-1684, 1968.
- McCormac, Billy M. (editor), *Aurora and Airglow*, Reinhold Publishing Corporation, New York, 1967.
- Mullen, J. P., R. S. Allen, and J. Aarons, Long Range propagation observed on the ORBIS experiment, *Planetary Space Science*, 14, 155-162, 1966.
- Munro, G. H., Travelling ionospheric disturbances in the F region, *Aust. J. Phys.*, 11, 91-112, 1958.
- Paulikas, G. A., J. B. Blake, and S. C. Freden, Precipitation of energetic electrons at middle latitudes, *J. Geophys. Res.*, 71, 3165-3172, 1966.
- Piddington, J. H., Geomagnetic storms, auroras, and associated effects, *Space Sci. Rev.*, 3, 724-780, 1964.
- Taffe, W. J., Comparison of micropulsation and infrasonic wave records and discussion of a Joule heat source for infrasonic waves, ESSA Technical Report IER 20-ITSA 20, December, 1966.
- Thome, G. D., A study of large-scale traveling disturbances in the ionosphere using the arecibo UHF radar (Ph.D. thesis), Cornell University, CRSR 236, 1966.
- Titheridge, J. E., Periodic disturbances in the ionosphere, *J. Geophys. Res.*, 73, 243-252, 1968.
- Wilson, C. R. and Sue Nichparenko, Infrasonic waves and auroral activity, *Nature*, 214, 1299-1302, 1967.
- Wilson, C. R., Infrasonic pressure waves from the aurora: a shock wave model, *Nature*, 216, 131-133, 1967.
- Wright, M. D., Possible identification of atmospheric waves associated with ionospheric storms, *Nature*, 190, 898-899, 1961.

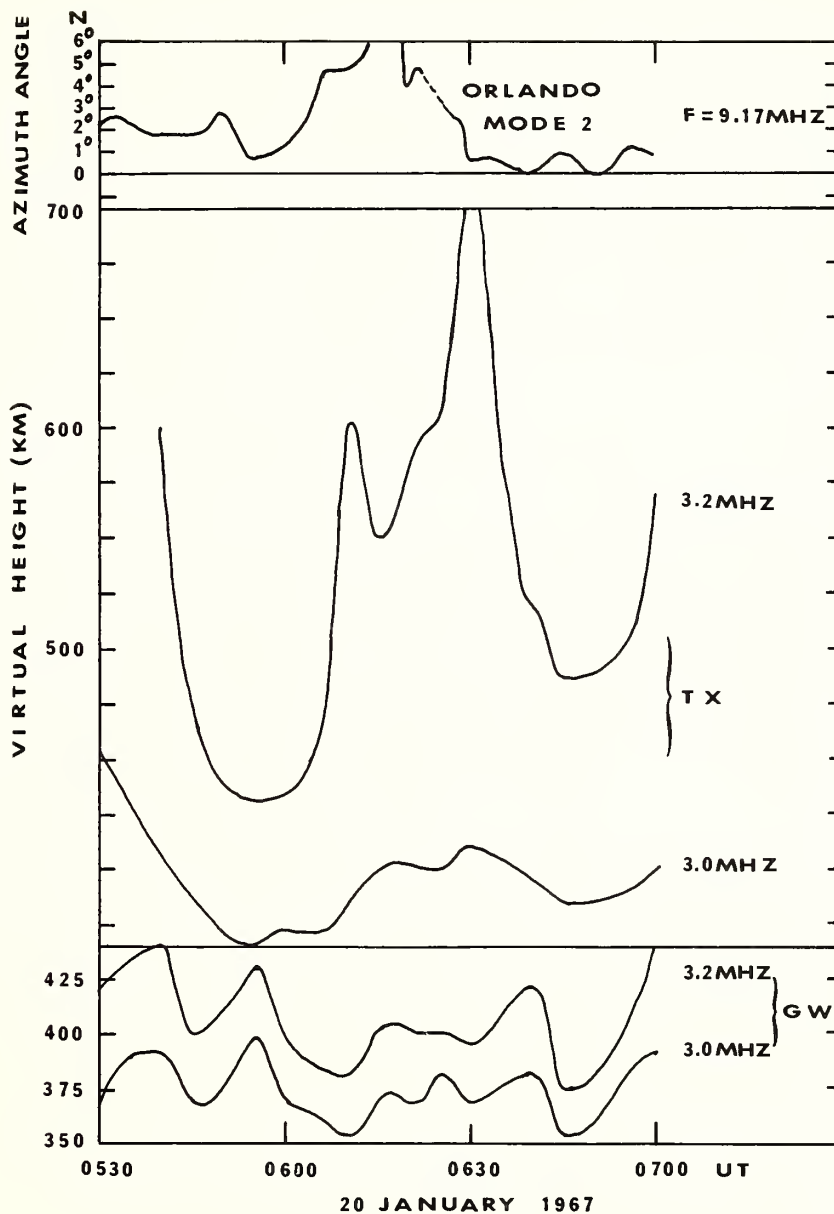


Fig. 1. Simultaneous azimuth direction-of-arrival variations of HF signal from Orlando, Fla., measured at Boulder, Colo., and virtual height variations observed at Texarkana, Ark., and Greenwood, Miss.



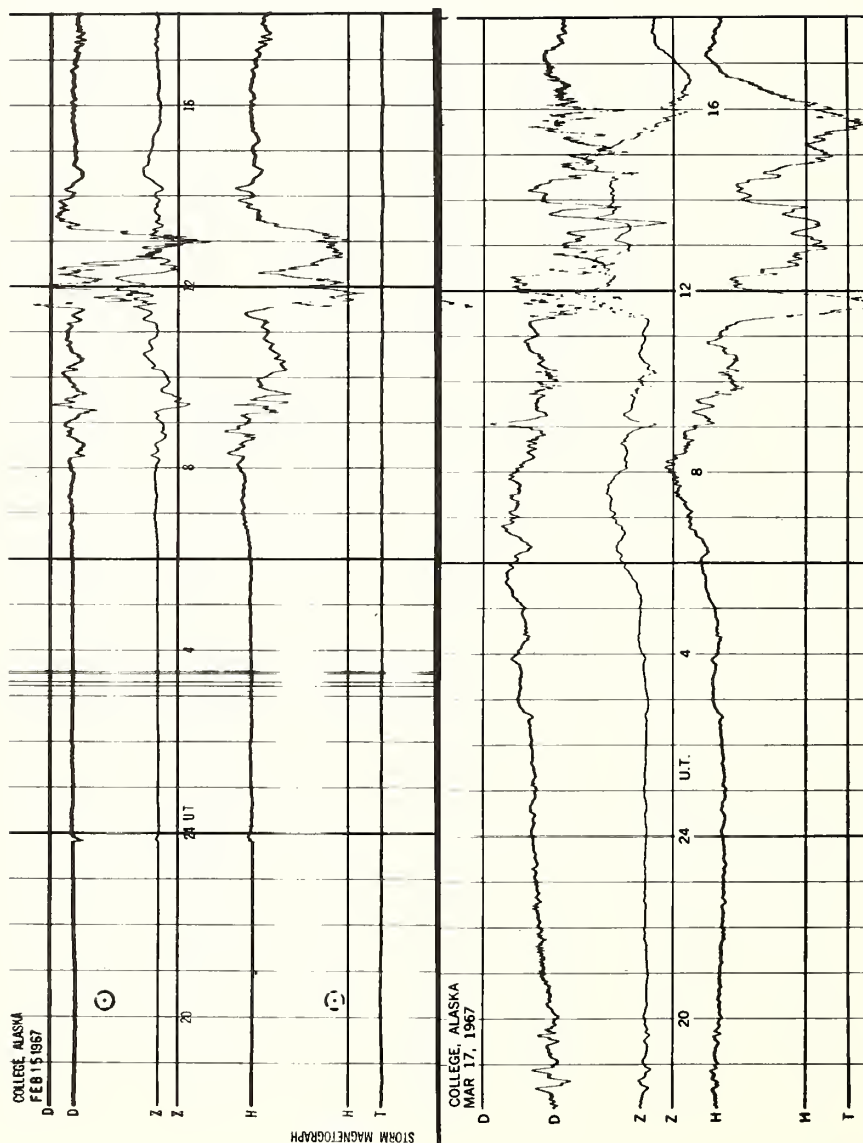


Fig. 2. Magnetographs from the College, Alaska Observatory.

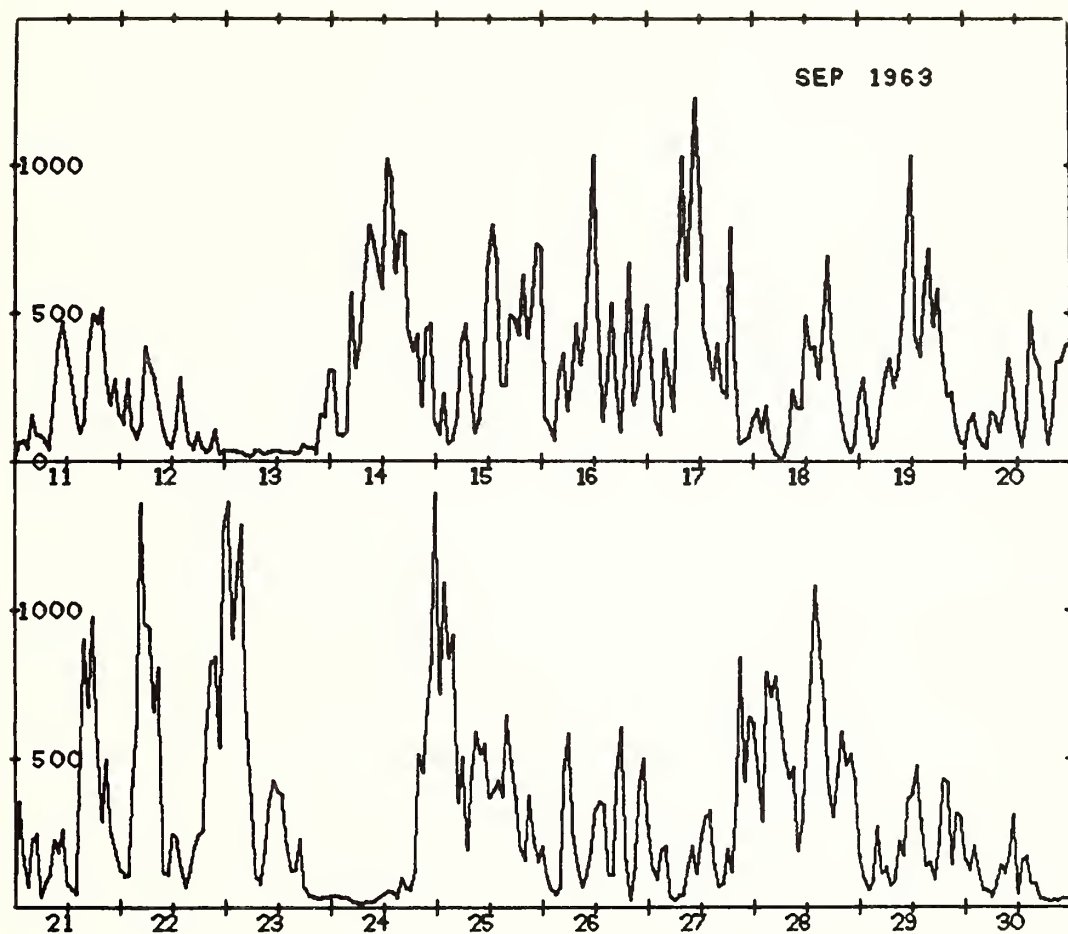


Fig. 3. Auroral electrojet (AE) Index plot for September 11-30, 1963. This illustrates the daily activity during an equinoctial month.

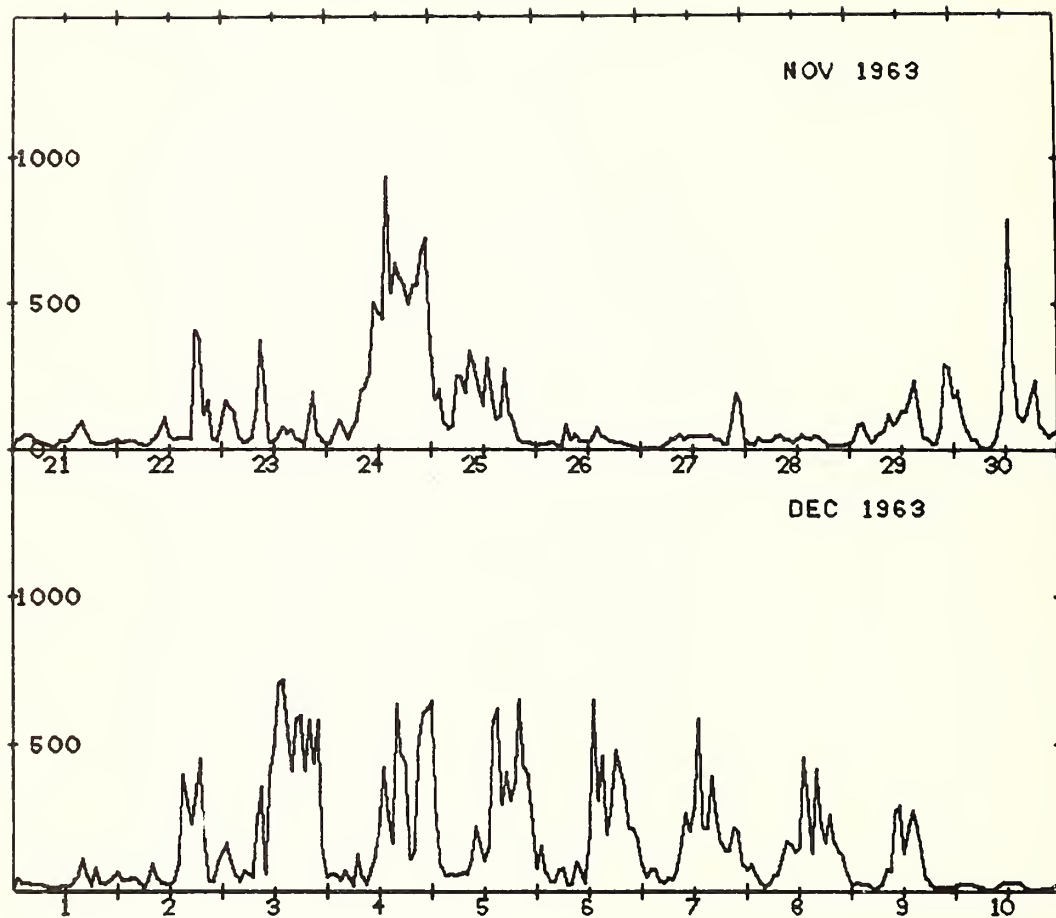


Fig. 4. AE Index plot for November 21-December 10, 1963 during the period when many TIDs were observed from Boulder by Hunsucker and Tveten [1967].

## SHORT-PERIOD IONOSPHERIC OSCILLATIONS ASSOCIATED WITH SEVERE WEATHER

T. M. Georges  
ESSA Research Laboratories  
Boulder, Colorado 80302

This paper reports progress in connecting localized wavelike ionospheric disturbances with certain features of tropospheric weather activity. The ionospheric disturbances are observed as nearly sinusoidal fluctuations of about 3-min period in the frequencies of HF radio waves reflected from the F region. Weather activity below the ionospheric reflection points is recorded hourly by weather radars. Analysis of one year of continuous radio and weather-radar data shows a convincing connection between the ionospheric oscillations and strong thunderstorm cells with tops over 40,000 ft. A previous interpretation of the disturbances as acoustic waves being filtered by atmospheric absorption and acoustic-cutoff effects still seems reasonable. Turbulence connected with cumulus formation is suggested as a source.

### INTRODUCTION

It has lately been fashionable to suggest that sources of atmospheric waves in the troposphere are responsible for some of the wavelike and irregular motions detected in the ionosphere by radio means. If the troposphere is indeed the source of energy for some kinds of natural ionospheric motions, it should be possible to detect the simultaneous appearance of distinctive ionospheric motions and unusual wave-generating processes in the troposphere. A few tenuous associations have been found between tropospheric weather events and various phenomena in the E and F regions (cf. Bauer, 1958; Rastogi, 1962 and references therein), but the subject has been one of long-standing skepticism and controversy. As far as we are aware, no natural event in the lower atmosphere has yet been conclusively associated with a particular ionospheric disturbance. This paper reports some success in connecting certain features of severe weather activity in the troposphere with short-period wavelike motions observed at heights of about 250 km in the F region of the ionosphere.

### THE OBSERVATIONS

The technique for monitoring the ionospheric motions is the spaced-path CW Doppler-sounding network that has been described in previous publications (Georges, 1967b, 1968). The motions in question are quasi-periodic electron density fluctuations whose periods are always close to 3 min and are detected as fluctuations in the frequencies of HF radio waves reflected in the F region at night. The oscillations typically last a few hours, and the peak-to-peak frequency deviations are of the order of 0.25 Hz on a 4.0 MHz radio wave, with deviations occasionally approaching 1 Hz. Similar fluctuations have been observed sporadically for several years on Doppler soundings made at Boulder, Colorado, and more recently over a 1300-km oblique path from Havana, Illinois, to Boulder (D. M. Baker, personal communication). Such oscillations were first associated with tropospheric weather on the basis of a few events that appeared on data from the spaced-transmitter network near Little Rock, Arkansas, at times when weather maps showed strong local thunderstorm activity (Georges, 1967b). These oscillations were attributed to the influence on the ionosphere of acoustic waves generated by some process -- perhaps turbulence -- connected with heavy thunderstorms. The monochromatic appearance of the ionospheric disturbances was attributed to a narrow-band atmospheric filtering process involving acoustic-cutoff and absorption effects.

To explore further the connection between the ionospheric oscillations and tropospheric weather, we have examined all the radio data obtained at Little Rock during the year 1967 and compared the occurrence and characteristics of short-period oscillations with the distribution and intensities of tropospheric storms as displayed on ESSA radar summary charts. The charts are hourly maps showing the locations and characteristics of weather-radar echoes from clouds and storm systems over virtually all of the eastern United States. A portion of







such a chart is shown in figure 1. Because redundancies in the observing systems offset equipment outages, both the weather-radar and ionospheric data were available continuously during the whole year.

#### ANALYSIS

The portion of the radar charts studied was limited to a circle 600 km in diameter centered on Little Rock, Arkansas. The transmitting stations of the spaced-path radio-sounding network roughly form a triangle inscribed in this circle. This area was chosen for analysis after a preliminary study revealed that the ionospheric oscillations generally correlated best with storm activity within about 250 km of the radio reflection points. The 600 km circle was not interpreted as a rigid boundary; for example, some very strong cells located just outside the boundary were counted in the statistics.

Only times between 00 and 12 hours UT (approximately local nighttime) were studied because the radio frequencies of the Doppler-sounding network reflect in the F region only at night, and the disturbances are seen only in the F layer.

Six indicators of weather activity within the area were chosen, which can be rather easily identified on radar summary charts:

1. Cloud echoes.
2. Thunderstorm activity.
3. A line of cloud echoes.
4. A civilian or aviation severe-weather warning that intersects the area surveyed.
5. Strong, isolated storm cells.
6. Echoes with tops exceeding 40,000 ft.

Severe-weather warnings are less significant than the other indicators of the actual existence of severe weather, since they are man-made predictions and are not always fulfilled.

The results of the one-year analysis are given in table 1, which shows the days on which short-period (1-5 min) ionospheric oscillations were seen and the days on which each of the six weather indicators appeared on the radar charts.

To distinguish between oscillations of different intensities, two kinds of marks appear on the portion of the chart pertaining to the ionospheric effects. Oscillations that are weak or intermittent and last for less than 4 hours, or are continuous and last for an hour or less, are denoted by slant lines. Those which are intermittent or weak but last for more than four hours, or are continuous and last longer than an hour, are called "sustained" oscillations and are denoted by X. Ionospheric oscillations are also broken down into two classes with regard to period: those with periods between 1 and 2 min, and those with periods between 3 and 5 min.

The arrangement of the weather indicators in table 1 is intended to be roughly in order of increasing severity, so that the spaces tend to be filled in downwards with increasing severity of a weather event.

The statistics contained in the table can be summarized as follows:

1. On 31 (8.5%) of the 365 days studied, at least five of the weather indicators were noted, but 15 (48%) of these days showed sustained 3-to-5-min ionospheric oscillations.
2. On 26 (7.1%) of the days studied, sustained 3-to-5-min oscillations were observed, but 15 (58%) of these days showed at least five of the weather indicators.

3. The order of occurrence frequencies of the weather features on the days when 3-to-5-min ionospheric oscillations were observed is as follows: area echoes (77% of the days), thunderstorms (77%), line of echoes (73%), tops of echoes greater than 40,000 ft (62%), strong cells (58%), and severe-weather warnings (42%).
4. Nine (35%) of the instances of sustained 3-to-5-min oscillations were accompanied by fewer than four of the weather indicators, and five were accompanied by none at all.
5. On 16 of the 31 days on which five or more of the weather indicators were seen, no short-period ionospheric effects were observed.
6. Little, if any, connection appears between the weather features and the 1-to-2-min oscillations, or with the instances of intermittent or weak 3-to-5-min events.
7. Seventeen (65%) of the 3-to-5-min sustained oscillations and 22 (71%) of the days when at least five of the weather indicators were noted occurred in March through June, while in September through December only one of the 3-to-5-min oscillations was seen, and only 3 days contained five or more of the weather indicators.

Although the connection between the tropospheric and ionospheric events is convincing from a statistical point of view, some of the possible reasons why the correlation is not much better should be mentioned.

In comparing weather-radar and ionospheric records, we noted that in a few instances where ionospheric effects would have been expected on the basis of the weather situation, only a general blurring or spreading of the Doppler traces was seen. The cause of such spreading has not yet been discovered, but it resembles spreading that has come to be associated with magnetically disturbed periods. Small-amplitude oscillations would be masked during such times.

No attempt has been made to distinguish short-period-oscillations that may be geomagnetically related, though they have been found to be somewhat more intermittent than those we associate with severe weather. They can also be distinguished by their simultaneous appearance at widely spaced locations (Georges, 1967b, p. 261). The source of these oscillations is as yet unknown.

Perhaps more convincing of the relationships between the ionospheric and tropospheric events than the statistical data are a few examples where particularly strong cells were identified in places and at times that match well with the relative amplitudes and durations of the 3-min oscillations on the spaced-path radio transmissions. Figures 1 and 2 show two instances where 3-min oscillations were observed on the frequencies of radio signals traversing paths passing near strong cells and were not observed, or were observed with decreased intensity, on signals traversing paths farther away from centers of storm activity.

The top half of figure 1 is a reproduction of a portion of a radar chart showing the locations of strong cells (black dots) and their heights (in hundreds of feet) at 0245 UT on 24 April. Strong cells, one extending to 50,000 ft, were observed in the vicinity between about 00 and 04 UT. The bottom portion of the figure shows that 3-min oscillations were quite strong on the Greenwood (G) signal during the same period, while the fluctuations were much weaker on the other two signals. (The longer-period fluctuations are not relevant to the present discussion.)

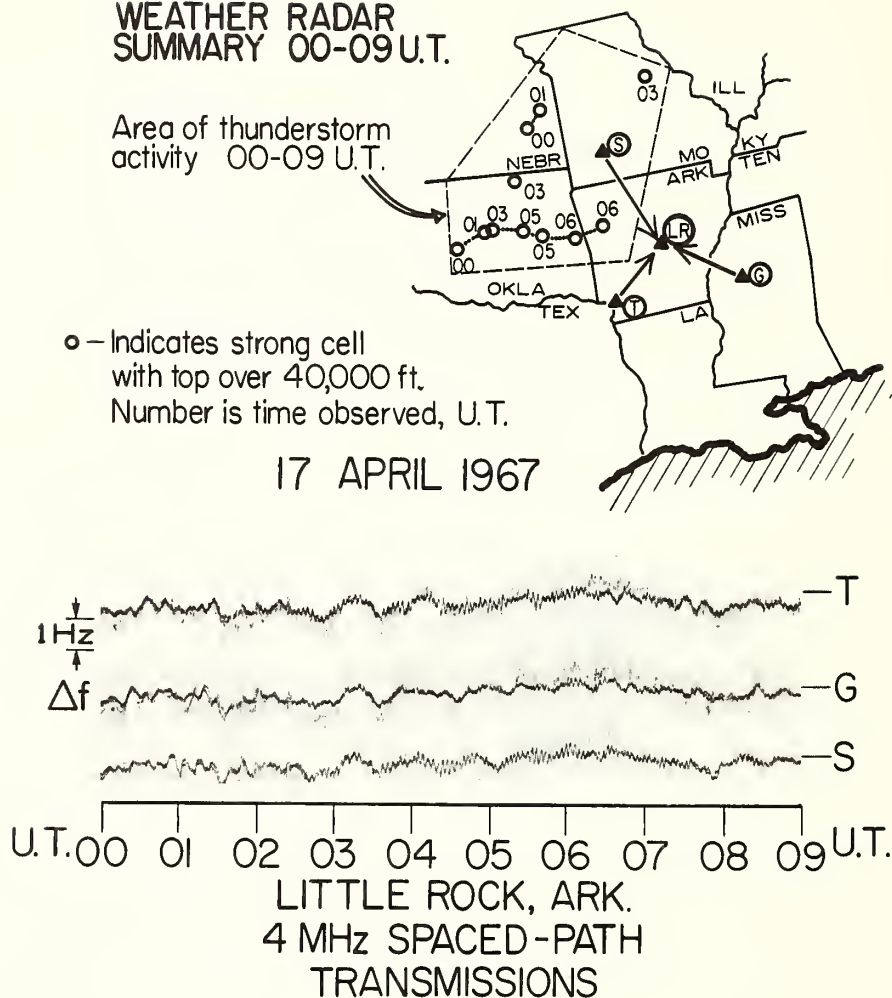
Figure 2 shows the locations of strong cells with tops over 40,000 ft during the period 00-09 UT on 17 April. Activity began in central Oklahoma and reached western Arkansas by 0600, then died out slowly. Doppler soundings show 3-min oscillations on all three radio signals, being strongest on the Springfield (S) path between about 0400 and 0630 UT, slightly weaker on the Texarkana (T) path, and barely detectable on the Greenwood (G) path. (The three radio paths are indicated by arrows on figure 2.)



Area of thunderstorm activity 00-09 U.T.

- — Indicates strong cell with top over 40,000 ft. Number is time observed, U.T.

17 APRIL 1967



-176-



In these two cases, as well as two or three others, the relationships between the positions and lifetimes of the strong-cell echoes and the radio-path midpoints and their variations with time closely match the relative intensities of the oscillations on the three radio paths and their time variations. The connection between the strong-cell echoes and the ionospheric oscillations thus appears unmistakable.

## DISCUSSION

A previous interpretation (Georges, 1967a; 1968) of the 3-min oscillations as upward-traveling acoustic waves interacting with the ionosphere seems to be reinforced by these observations.

The apparent upward phase progression of the disturbances mentioned in previous papers has been further confirmed by additional multifrequency observations; the appearance of the oscillations on higher frequencies always lags their appearance on lower frequencies, typically by a few tens of seconds. Because precise estimates of the radio reflection heights are not usually possible, exact determinations of the vertical phase speeds are not available, but the delays are of the right order to match the sound speed at F-region heights. (One determination at Boulder yielded 500-600 m/s.) It has not been possible to determine directly the horizontal trace velocities of the waves because the stations of the radio-sounding network are too far apart. However, the geographically localized nature of the ionospheric effects and their effects on the obliquely propagated signals suggest that the wavefronts are nearly horizontal. (The effects of wavelike electron density fluctuations of such short period on an obliquely propagating radio wave would be largely "averaged out" if the wavefronts were greatly inclined.)

That the ionospheric disturbances are not normally observed more than about 250 km horizontally from the assumed sources is thought to be caused by acoustic-wave reflection and defocusing in the thermosphere. Some acoustic ray-tracing plots (Barry, 1963) show qualitatively that in realistic model atmospheres, defocusing and reflection in the thermosphere permit waves from ground-level sources to reach F-region heights only within a couple of hundred kilometers horizontally from the source. Energy density appears to fall off rapidly at greater distances. There is, however, some question whether ray-tracing results are applicable at this wave period, because the wavelength of 3-min waves varies from about 50 km in the troposphere to over 100 km in the thermosphere, a size comparable to the thermal structure of the atmosphere.

The explanation of the monochromatic nature of the ionospheric oscillations in terms of atmospheric filtering (Georges, 1968, fig. 9) still seems plausible. The relatively high percentage of days with five or more of the weather indicators on which 3-to-5-min oscillations were not seen suggests that the presence of an appropriate source may not be a sufficient condition for the appearance of ionospheric effects. The proposed filtering mechanism would be rather sensitive to the temperature and neutral density in the thermosphere, so that only slightly enhanced defocusing or absorption could close the 3-min "window" entirely.

While earlier Boulder observations indicated that the ionospheric oscillations seldom appeared, perhaps only a few times a year, the search through the 1967 spaced-path soundings at Little Rock has shown that the oscillations are much more common than previously suspected. The reason seems to be partly that a facility for recognizing oscillations of smaller intensity has been developed, and partly the increased frequency of the events at the new Arkansas location, an area rather well-known for frequency of thunderstorms. The Boulder area, on the other hand, experiences severe storms relatively infrequently. Hence, ionospheric effects connected with severe weather activity would be more numerous at the Little Rock location.

The specific source mechanism responsible for the ionospheric effects cannot yet be identified, but the results given here may encourage further observations of the effect and stimulate examination of the mechanics of severe convective storms from the point of view of



wave-generation processes. Pierce and Coroniti (1966) have suggested that buoyancy oscillations near the tops of strong convective cells (thunderstorms) would be expected to generate atmospheric wave energy near the local Brunt frequency, and that sufficient wave energy may reach ionospheric heights to cause ionization motions. However, a 3-min period is rather short for buoyancy oscillations.

In searching for a source mechanism, it does not seem necessary to find one that favors a 3-min period, only one whose energy spectrum includes 3 min. The atmospheric-filtering process, if it operates as described, would account for the nearly monochromatic appearance of the waves at ionospheric heights. A suitable source may be found in the turbulence associated with the strong convection currents known to give rise to cumulus formation. Lighthill (1952; 1954) has indicated that the acoustic intensity generated by a turbulent flow increases approximately as the eighth power of the mean velocity of flow. The connection between the ionospheric effects and strong cells with tops over 40,000 ft reinforces this idea, since the height of a cumulus top is an indication of the strength of the updraft current.

#### ACKNOWLEDGMENT

The radar summary charts were supplied on microfilm by the National Weather Records Center, ESSA, Asheville, N. C. 28801

#### REFERENCES

- Barry, G. H., Ray tracings of acoustic waves in the upper atmosphere, *J. Atmos. Terrest. Phys.* 25, 621-629, 1963.
- Bauer, S. J., An apparent ionospheric response to the passage of hurricanes, *J. Geophys. Res.* 63, 265-269, 1958.
- Georges, T. M., Evidence for the influence of atmospheric waves on ionospheric motions, *J. Geophys. Res.* 72, 422-425, 1967a.
- Georges, T. M., Ionospheric effects of atmospheric waves, ESSA Technical Report IER 57-ITSA 54, 341pp, 1967b.
- Georges, T. M., HF Doppler studies of traveling ionospheric disturbances, *J. Atmos. Terrest. Phys.* 30, 735-746, 1968.
- Lighthill, M. J., On sound generated aerodynamically, 1, general theory, *Proc. Roy. Soc. Lond. A211*, 564-587, 1952.
- Lighthill, M. J., On sound generated aerodynamically, 2, turbulence as a source of sound, *Proc. Roy. Soc. Lond. A222*, 1-32, 1954.
- Pierce, A. D., and S. C. Coroniti, A mechanism for the generation of acoustic-gravity waves during thunderstorm formation, *Nature* 210, 1209-1210, 1966.
- Rastogi, R. G., Thunderstorms and sporadic-E layer ionization over Ottawa, Canada, *J. Atmos. Terrest. Phys.* 24, 533-540, 1962.

# DISPERSION OF ACOUSTIC-GRAVITY WAVES IN THE ATMOSPHERE \*

by

N.K. Balachandran and William L. Donn

Lamont Geological Observatory (Columbia University)  
Palisades, New York.

A normal mode theory for the propagation of acoustic-gravity waves in a multi-layer model of the atmosphere with constant temperature and uniform wind in each layer, is developed. Solutions are obtained by an iterative procedure giving rise to theoretical group velocity dispersion curves. Empirical dispersion curves are determined from time-stepped Fourier analysis of pressure records from nuclear explosions in the atmosphere. The theoretical dispersion curves for appropriate atmospheric models show good agreement with empirical dispersion curves. The theory is able to account for both the normal and inverse dispersion of acoustic-gravity waves. Strong winds at altitudes near 100 km, in the direction of propagation of the waves and opposing low altitude winds are favorable for inverse dispersion at long periods. Acoustic-gravity waves give rise to ionospheric disturbances with similar dispersion characteristics as those of pressure fluctuations detected at the ground.

## INTRODUCTION

Air waves from nuclear explosions in the atmosphere, meteoritic falls, volcanic eruptions, and earthquakes give rise to pressure oscillations in the period range of 0.5 to 20 min. which are recorded on microbarographs even at large distances from the source. A striking feature of these waves is their dispersion, a systematic variation of the period of the waves with time. Characteristically, these waves are normally dispersed, the period of the waves gradually decreasing with time. Close examination of each train of waves shows that the dispersion is more complicated. Donn and Ewing (1962) and Donn, Pfeffer and Ewing (1963) observed that along with a normally dispersed branch (group velocity increasing with period), some pressure records from nuclear explosions show an inversely dispersed branch (group velocity decreasing with increasing periods). Visual analysis (Fig. 1) indicated that the normally dispersed group of waves are superimposed on inversely dispersed longer period waves when present. The group velocity dispersion curves obtained by Donn, Pfeffer and Ewing (1963) by using the trough and crest analysis of Ewing and Press (1954) are given in Fig. 2. Some of these curves show both the normally and inversely dispersed branches merging in Airy phases in maxima of group velocity. We will give, later in this paper, the dispersion curves obtained by subjecting a number of pressure records to Fourier analysis. These curves indicate several modes with normal and inverse dispersion.

Pfeffer (1962), Press and Harkrider (1962) and Pfeffer and Zarichny (1963) have developed a normal mode theory of acoustic-gravity waves in a multi-layer temperature-stratified model of the atmosphere. Wind effects were neglected. These authors have been successful in explaining many of the observed features of wave speed and dispersion but they could not account for the observed inverse dispersion and some of the observed wave speeds. Realizing that wind stratification in the atmosphere may significantly affect the propagation of acoustic-gravity waves we have modified the multi-layer model theory of Pfeffer (1962) to include wind structure. Pierce (1967) and MacKinnon (1967) have also developed a theory of propagation of acoustic-gravity waves in a temperature and wind stratified atmosphere, using an integration technique different from ours. But their results also fail to explain many of the observed dispersion features because they were not fitted to observational data. With atmospheric models having suitable wind structure we have been able to explain most of the observed features of acoustic-gravity waves.

---

\* Lamont Geological Observatory (Columbia University) Contribution No. 1222.

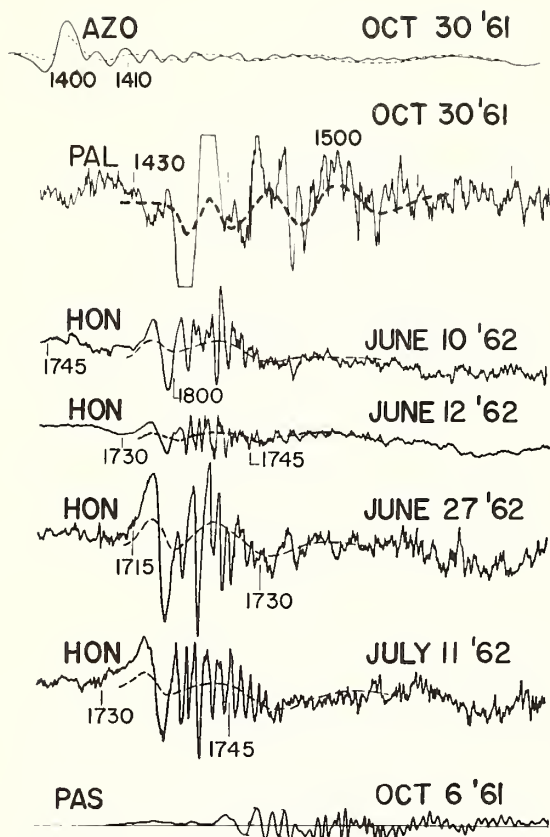


Fig. 1. Air wave recordings from selected explosions showing the visual interpretation (broken over printed line) of waves that are inversely dispersed. AZO: Azores, PAL: Palisades, HON: Honolulu, PAS: Pasadena.

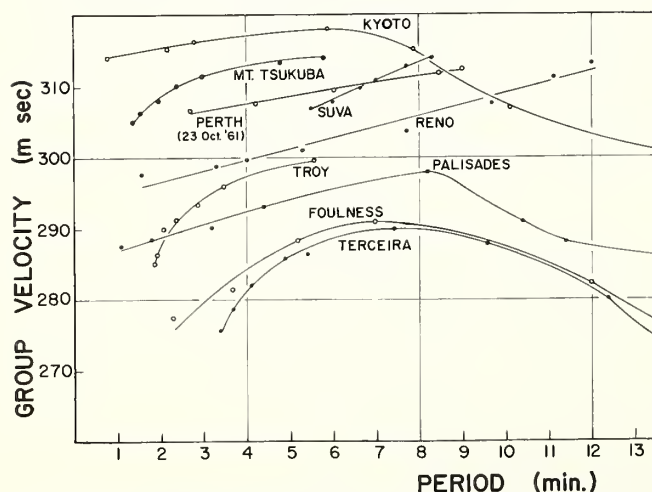


Fig. 2. Empirical dispersion curves for air waves from the Soviet nuclear test of 23 October 1961, recorded at various stations around the globe.

## THEORY AND COMPUTATIONAL PROCEDURE

Using a multilayer model of the atmosphere with constant wind and temperature in each layer, we obtain normal mode solutions by an iterative procedure following the method of Pfeffer (1962) and Press and Harkrider (1962). A summary of the detailed theory and procedure of Balachandran (1968) is given here.

We employ a linear perturbation method, assuming that at large distances from the source, the waves produced by a disturbance travel as small amplitude perturbations superimposed on the equilibrium state of the atmosphere. In the equilibrium state the atmosphere is assumed to be in hydrostatic balance with only steady horizontal motions and with pressure and density varying only in the vertical direction.

For the observed wavelengths and periods, the earth may be treated as flat and the coriolis force ignored. The x-axis is taken along the line joining the source and the receiver and the z-axis along the vertical. The notations used are:

$\bar{\rho}, \rho$  equilibrium and perturbed values of density

$\bar{p}, p$  equilibrium and perturbed values of pressure

$U, u$  mean and perturbed velocities in the x-direction

$w$  perturbed velocity in the vertical (z) direction (unperturbed vertical velocity is zero)

$t$  time

$g$  acceleration due to gravity

$C$  sound speed

$\gamma$  ratio of specific heats

$d \frac{\partial u}{\partial x} + \frac{\partial w}{\partial z}$ , the divergence.

We then assume that  $p$ ,  $w$  and  $d$  vary as

$$\{p, w, d\} = \{P(Z), W(Z), D(Z)\} e^{i(\sigma t - kx)}$$

$\sigma$  being the angular frequency and  $k$  the wave number. The differential equation

$$\frac{d^2 D}{dz^2} - \frac{g\gamma}{C} \frac{dD}{dz} + \left\{ -k^2 + \frac{\omega^2}{C^2} + \frac{g^2 k^2}{\omega^2 C^2} (\gamma-1) \right\} D = 0 \quad (1)$$

where  $\omega = \sigma - ku$  applies to each layer of the atmosphere with constant temperature and wind.

Equation (1) is an ordinary differential equation with constant coefficients and is easily solved giving the dispersion relation

$$\omega^4 - \omega^2 C^2 (k^2 - \eta^2) + (\gamma-1) g^2 k^2 - \frac{\gamma^2 g^2 \omega^2}{4C^2} = 0 \quad (2)$$

where  $\eta$  is the vertical wave number.

Equations (1) and (2) apply to each layer of the medium. For a multilayered model, we impose the following boundary conditions:

- 1) At the ground the vertical velocity is zero;
- 2) The total kinetic energy of the atmosphere is finite;
- 3) Across each interface between any two layers, the vertical displacement and total pressure are continuous; and
- 4) For the propagation of waves over large distances, the energy does not leak out of the medium (atmosphere).

The last condition implies that  $\eta$  for the uppermost layer is real. This leads to cut-off conditions (either at high or low periods) for each model.

If  $H_n$  is the thickness of any  $n$ th layer, then using boundary conditions (3),  $W$  and  $P$  at the bottom of the  $(n+1)$ th layer can be related to  $W$  and  $P$  at the top of the  $n$ th layer by the matrix equation,

$$\begin{bmatrix} W_B \\ P_B \end{bmatrix}_{n+1} = \frac{\omega_{n+1}}{\omega_n} \begin{bmatrix} 1 & 0 \\ \frac{ig(\Delta\bar{P})_n}{\omega_{n+1}} & \frac{\omega_n}{\omega_{n+1}} \end{bmatrix} \begin{bmatrix} W_H \\ P_H \end{bmatrix}_n \quad (3)$$

where  $\Delta\bar{P}_n = \bar{P}_H(n) - \bar{P}_B(n+1)$  and  $H$  and  $B$  indicate values at the top and bottom of the respective layers. Also, we can relate  $W$  and  $P$  at the bottom of any layer to  $W$  and  $P$  at the bottom of the layer above by the relation

$$\begin{bmatrix} W_B \\ P_B \end{bmatrix}_{n+1} = [M]_n \begin{bmatrix} W_B \\ P_B \end{bmatrix}_n \quad (4)$$

the matrix  $[M]_n$  being defined as

$$[M]_n = \begin{bmatrix} \frac{\omega_{n+1}}{\omega_n} & 0 \\ \frac{ig(\Delta\bar{P})_n}{\omega_n} & 1 \end{bmatrix} \begin{bmatrix} L_1 & L_2 \\ L_3 & L_4 \end{bmatrix}_n$$

where

$$L_1 = \left( \frac{g(2-\gamma)}{2C^2\eta} \sinh \eta H + \cosh \eta H \right) \exp(\Gamma H)$$

$$L_2 = \left( \frac{(C^2 k^2 - \omega^2) i}{C^2 \eta \omega \bar{\rho}_B} \sinh \eta H \right) \exp(\Gamma H)$$

$$L_3 = \left( \frac{g^2 (\gamma-1) - \omega^2 C^2}{\omega C^2 \eta} \sinh \eta H \right) i \bar{\rho}_H \exp(\Gamma H)$$



$$L_4 = \left[ \cosh \eta H - \frac{g(2-\gamma)}{2C^2\eta} \sinh \eta H \right] \frac{\bar{\rho}_H}{\bar{\rho}_B} \exp(\Gamma H)$$

where  $\Gamma = \frac{g\gamma}{2C^2}$

By successfully applying (4) to each pair of layers, the values of W and P at the bottom of the ground-based layer (layer 1) is related to values of W and P at the bottom of the top-most layer (Nth layer). This involves the product of (N-1) matrices. If we write this product as

$$[M_{N-1}][M]_{N-2} \dots [M]_2[M]_1 = \begin{bmatrix} \theta^{(1)} & \theta^{(2)} \\ \theta^{(3)} & \theta^{(4)} \end{bmatrix}$$

then using the boundary condition (1), the final frequency equation for the problem is written as

$$\theta^{(2)}(\bar{\rho}\epsilon)_{B(N)} - \theta^{(4)}\beta_{HN} = 0 \quad (5)$$

where

$$\epsilon = \frac{i\omega}{g^2k^2 - \omega^4} \left[ \frac{g^2\gamma}{2} - \omega^2C^2 - gC^2\eta \right]$$

$$\beta_B = \frac{1}{g^2k^2 - \omega^4} \left[ g^2C^2k^2 - \frac{g\gamma\omega^2}{2} - \omega^2C^2\eta \right]$$

Equation (5) is solved by an iterative procedure. The top-most (Nth) layer is assumed to extend to infinity. The assumption that  $\eta$  for this layer has to be real leads to cut-off conditions depending on the temperature and wind speed used for this layer. In a  $(\sigma, k)$  plane there are lines separating regions of real and imaginary values of  $\eta_N$ . Also, in the region of real values of there is a set of curves which satisfy equation (5). These curves are defined as the various modes of solution for the problem. The point where the left-hand - side of (5) changes sign along the boundary separating the real and imaginary values of  $\eta_N$  is taken as the starting point for tracing a particular mode.

Using the classification of Pfeffer (1963) we identify each mode as the fundamental, acoustic or gravity mode. The acoustic modes disappear when the medium is assumed to be incompressible. The gravity modes disappear when the acceleration due to gravity is assumed to be zero. The fundamental mode behaves like a gravity mode for long periods and like an acoustic mode for short periods. Each mode is given a number equal to the number of times the vertical profile of pressure crosses zero for this mode.

In the computational scheme given a particular atmospheric model, we trace the various modes of solution for this model. For each mode we plot both the phase and group-velocity dispersion curves. The computational scheme also provides plots of vertical profiles of normalized amplitudes of perturbation pressure, vertical velocity and kinetic energy per unit mass. The normalization is such that the perturbed pressure at the ground is unity and the values are computed at the base of each layer of the model for a particular  $(\sigma, k)$  solution of equation (5).

The layer at the top of the model extending to infinity and having constant temperature and uniform wind may not be very realistic. The wind speed and temperature used in this layer determine the longest period of the waves which are trapped in the wave guide. Tolstoy (1967) has used a free surface at the top of his atmospheric model and Press and Harkrider (1962) have used a rigid surface at the top of some of their models. The solutions are extended to longer periods by using such boundary conditions. In our case we have resorted to the use of negative winds (winds in a direction opposite to that of propagation of the waves) as a means of extending the solutions to longer periods. The use of such a boundary condition does not significantly affect the short-period solutions.



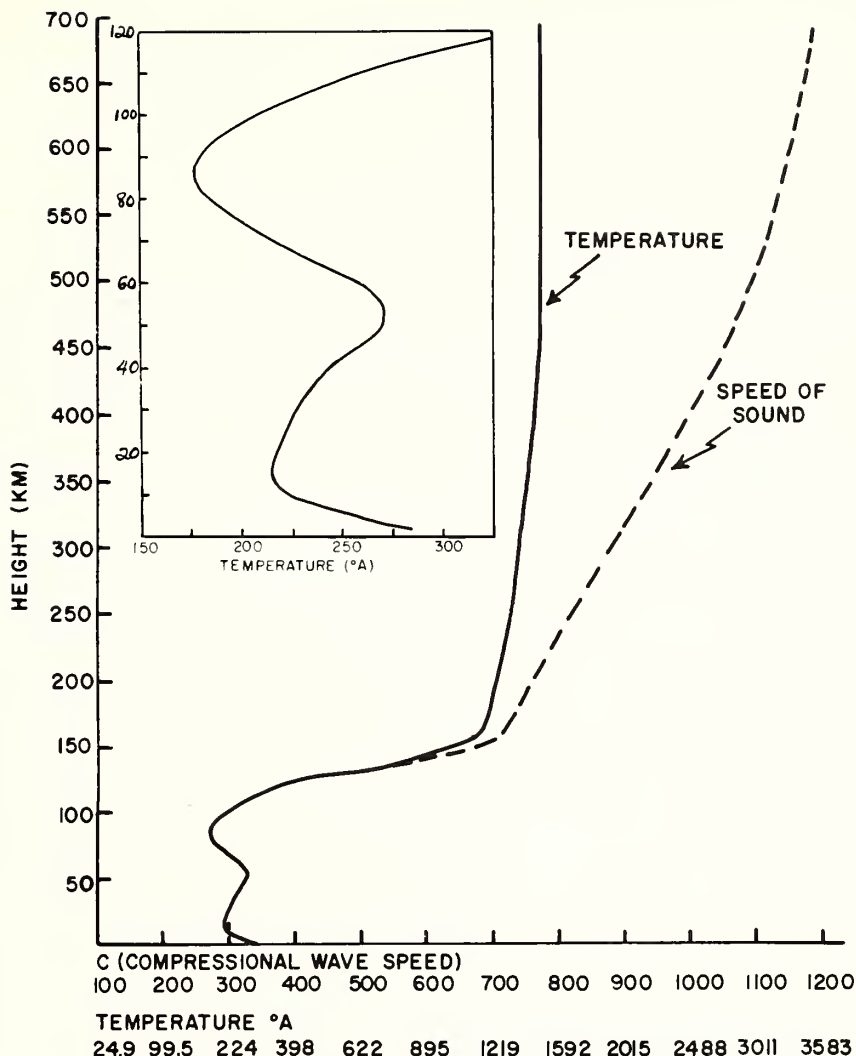


Fig. 3. Temperature and sound velocity structure for the COSPAR international reference atmosphere

For our atmospheric models we use the temperature and density structures as in the COSPAR model atmosphere shown in Fig. 3. Suitable winds are included in the COSPAR model to generate theoretical group velocity dispersion curves. These theoretical dispersion curves are then compared with those determined empirically.

#### EFFECTS OF WIND ON THE PROPAGATION OF ACOUSTIC-GRAVITY WAVES

Detailed study of the effects of wind at various levels of the model on the dispersion curves will be given in a separate paper. A summary is given here.

Strong positive winds (winds in the direction of propagation of waves) at all levels in general, give rise to increased group velocities for all periods, the winds near the ground being more effective than winds at high elevations, due to the higher density of air at lower altitudes. In an atmospheric model with two temperature-produced sound channels, the wind conditions which decrease the effective strength of the upper sound channel and increase the effective strength

of the lower channel give rise to inverse dispersion at long periods; the opposite wind conditions give rise to normal dispersion at all periods. In other words, strong positive winds in the top layers of the model and strong negative winds near the ground (in the altitude of about 0-20 km) give rise to inverse dispersion at long periods.

## COMPARISON OF THEORY AND OBSERVATIONS

### Data Analysis

Our observational data have been taken from the recordings of the Lamont global microbarovariograph system. The instrument is adjusted by means of suitable leaks, to respond to pressure variations in the period range of approximately 0 - 25 minutes. The microbarovariograph and the recording system have been fully described by Donn, Shaw and Hubbard (1963) and Donn, Pfeffer and Ewing (1963).

The pressure records from nuclear explosions were digitized at intervals of 6 seconds for Fourier analysis. The basic Fourier analysis program used in this work comes from Cooley and Tukey (1965). This basic program was modified for computing a "running amplitude spectrum". In the procedure followed, the record was divided into different segments of specified length and suitable overlap. The pressure values in each segment were weighted by means of a "cosine window" in order to avoid spurious peaks in the spectrum. The importance of using such "windows" has been discussed by Balckman and Tukey (1958). Each pressure value  $P(t)$  in a segment with a total of  $N$  values is modified to get the weighted value  $W(t)$  using the relation

$$W(t) = P(t) \frac{1}{2} \left( 1 - \cos \frac{2\pi I}{N-1} \right)$$

where  $t$  goes from 1 to  $N$  and  $I = t-1$ . Outside the segment,  $W(t)$  is assumed to be zero. The weighted data is subjected to Fourier analysis giving a distribution of amplitudes versus frequencies (or periods) for the particular segment. The window is moved along the record in a specified amount (time steps) and another spectrum computed. The process is repeated for the entire record. The amount of overlap between successive spectra is specified for each analysis.

Depending on the range of periods under investigation, we used different lengths of record for each individual segment and step. The time resolution is an inverse function of the length of the window. Increasing the window length increases frequency resolution but decreases time resolution, and the reverse. Normally, the time corresponding to the middle point of a particular window is taken as the time of arrival of all periods present in that window. But here we tried to improve time resolution by subjective interpretation of the record and the matching spectrum. The data of the origin times and distances from various microbarovariograph locations for the Soviet and United States nuclear tests have been provided by Donn and Shaw (1967). From these data and the times of arrival of various periods in the running-spectrum analysis, we computed the group-velocity dispersion curves. These empirical dispersion curves are then matched with the theoretical ones for an atmospheric model. In the atmospheric model, we assume temperatures and pressures as in the COSPAR atmosphere and use suitable winds to get reasonable agreement between the theoretical and empirical dispersion curves. For the wind-structure, we used actual data as far as available and assumed reasonable values for the rest. Normally, daily upper wind data is available to an altitude of about 30 km. We then adjusted winds at higher altitudes to get good agreement between theory and observation.

### Nuclear Test of 5 August 1962

Fig. 4 shows the pressure waves recorded at Palisades, N. Y. from the Soviet nuclear explosion in Novaya Zemlya of 5 August 1962. It also shows the running spectra for this record. In order to resolve the long periods present in the record, the length of each window used was 2362 seconds. Inverse dispersion from

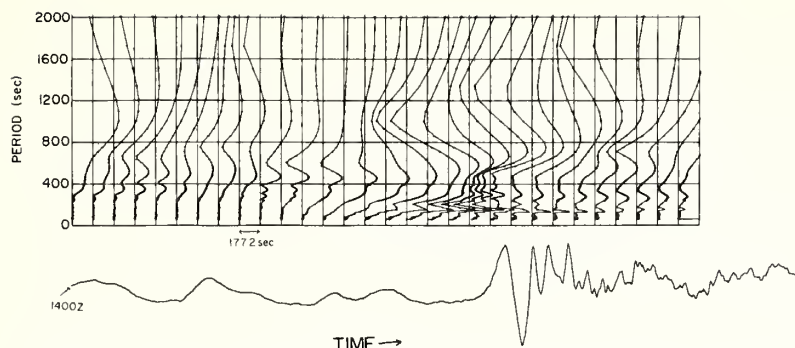


Fig. 4. Pressure record at Palisades and the running spectrum of the record (with window length of 2362 sec) for the Soviet nuclear test of August 5, 1962.

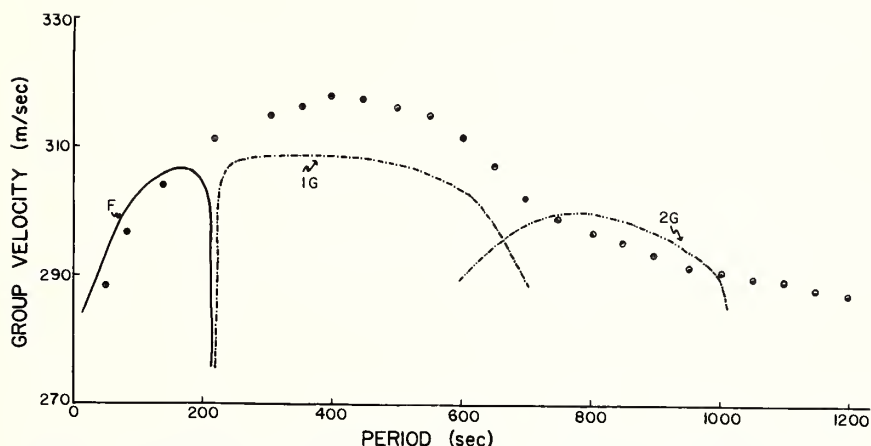


Fig. 5. Theoretical dispersion curve for Model 1 with empirical data from the analysis of Fig. 4 (points within small circles).

periods of about 400 to 1200 seconds and normal dispersion from periods of about 400 to 100 seconds is evident in the analysis. From the analysis in Fig. 4 we computed the long-period branch (periods above 600 sec) of the dispersion curve. A shorter window (1181 sec) was used for computing the short-period branch.

The azimuth of approach of the pressure waves at Palisades was  $15^\circ$ . The wind data for New York show light winds near the ground and a maximum wind speed of 27 meters/sec from  $330^\circ$  at an altitude of 12 km. Thus, the component of wind in the direction of propagation of waves is very small. In the first wind model used, we took the wind component to be zero from ground up to an altitude of 44 km. The wind structure used above 44 km (Model 1) is given in Table 1 and the resulting theoretical dispersion curves are given in Fig. 5. The circled points in Fig. 5 are from the empirical analysis. There is reasonable agreement between theoretical and empirical group velocities for periods of about 750-1000 sec, but for periods less than 700 sec, theoretical velocities are less than empirical velocities by about 10 m/sec.

In order to extend the solutions to long periods and to get higher group velocities for periods less than 700 sec, we used the atmospheric structure as in Model 2 (Table 1). The resulting theoretical dispersion curves are given in Fig. 6 together with empirical data for 5 August. There is now good agreement between the theoretical and empirical curves, if we ignore the quasi-vertical portions for reasons given in the following paragraph.

A negative wind speed of 190 mps was used in Model 2 to extend the period

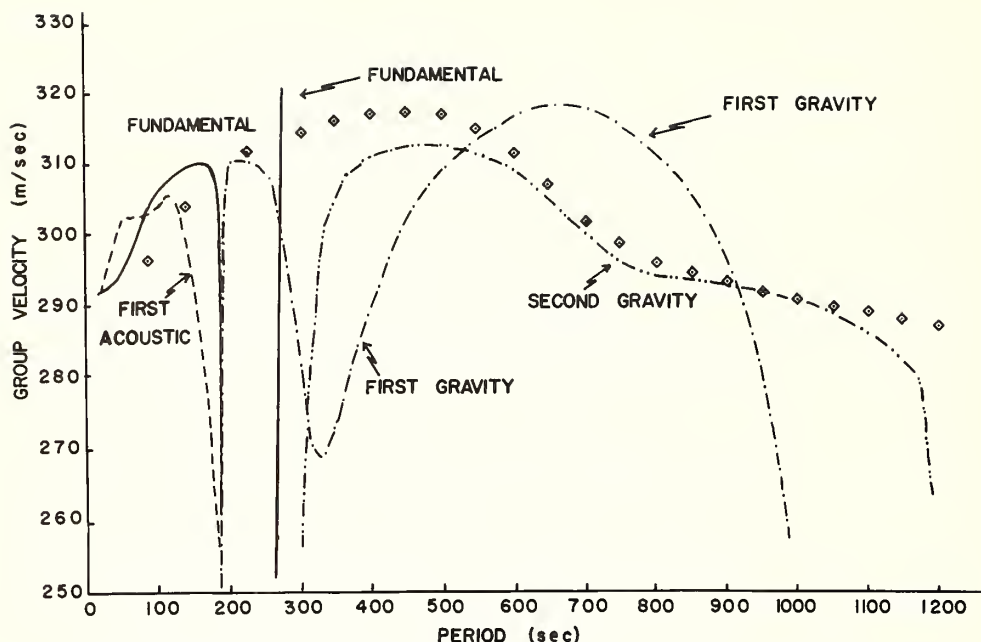


Fig. 6. Theoretical dispersion curves for Model 2 with empirical data plotted within small squares.

of the solution to about 1200 sec. Also, positive winds had to be used between the altitudes of 24-230 km, with speeds of 100 mps or more in the altitude range of 76-120 km.

Pfeffer and Zarichny (1963) observed that for their atmospheric models without wind, only the quasi-horizontal portions of the dispersion curves are relevant for waves observed at the ground. The quasi-vertical portions correspond to waves propagating mainly at high elevations (near 100 km), as indicated by the vertical profiles of kinetic energy. These conclusions are found to be relevant for the atmospheric models with wind also. The kinetic energy profiles for Model 2 are given in Fig. 7. It may be observed that the quasi-horizontal portions of the various modes correspond to wave propagation with energy concentration near the ground. Thus, energy considerations are important in interpreting theoretical dispersion curves. The empirical dispersion curve (Fig. 6) is interpreted as representing various segments of different theoretical modes.

The wind speeds used in Models 1 and 2 are not entirely arbitrary. There is observational evidence for the existence of such winds, for example, Kantor and Cole (1964), among others. These observations show high variability of winds around 100 km altitude which may explain why inverse dispersion is observed at certain times and not at others.

#### Nuclear Test of 30 October 1962

The pressure records from the United States nuclear test on Johnston Island on 30 October 1962 as recorded at Poughkeepsie, N. Y. and running spectra computed with two different windows are shown in Fig. 8. For the same test, the pressure record for Berkeley, California and its spectrum are shown in Fig. 9. The pressure records show mostly waves with periods below about 500 sec. The spectra show how our analysis separates the different modes present in the records.

The spectrum in Fig. 8a, whose window length was 1181 sec clearly shows one normally dispersed mode with period in the range of about 100-200 seconds, and other modes with shorter periods. To get better time resolution for short periods,



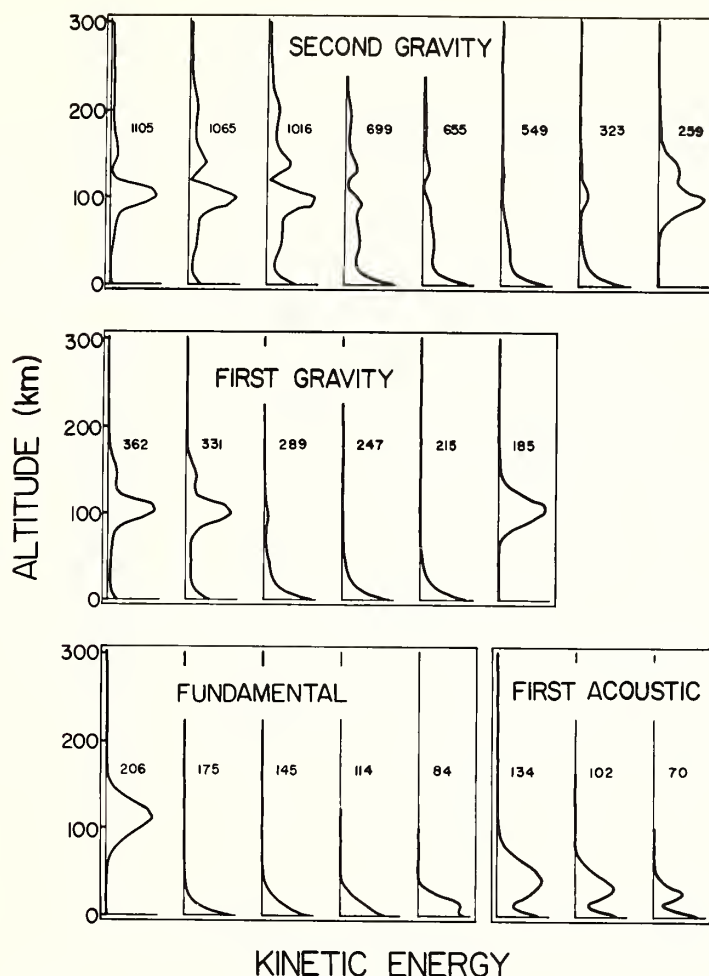


Fig. 7. Kinetic energy profiles for Model 2. The number adjacent to each profile is period in seconds.

a window of 590 seconds was used for the analyses presented in Figs. 8b and 9. These clearly indicate normally and inversely dispersed short-period branches.

Since only short-period pressure waves were detected, we used a 130 km model (described below) for generating the theoretical dispersion curves. Only the fundamental and the acoustic modes are appropriate for comparison. Fig. 10 shows the theoretical dispersion curves together with the points obtained from the empirical analysis of the Poughkeepsie and Berkeley pressure records. According to this analysis the normally dispersed empirically determined branch with periods in the range of 100-200 seconds does follow the fundamental mode closely and the other branches follow the acoustic modes. Though the Berkeley data show the same dispersive trend as the Poughkeepsie data, the Berkeley velocities are somewhat lower. This can be explained by the effect of the relatively strong tropospheric westerlies between Berkeley and Poughkeepsie.



POUGHKEEPSIE, N.Y. OCT. 30-31, 1962

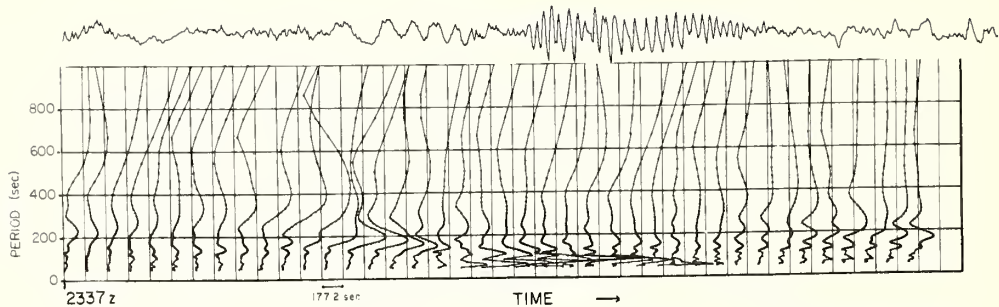


Fig. 8a. Pressure record and running spectrum analysis with window length of 2362 sec for the United States nuclear test of 30 October 1962.

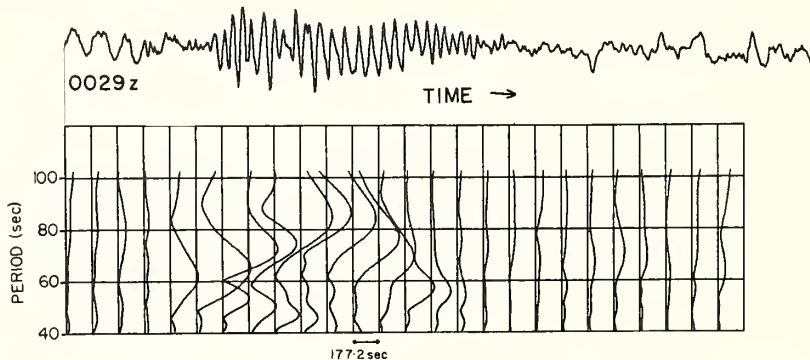


Fig. 8b. Same as above with window length of 590 sec.

The atmospheric model used in the computation was primarily developed to fit the Poughkeepsie empirical data.

The wind data used in the computation of the theoretical dispersion curves of Fig. 10 are given in Table 2. The maximum observed group velocity of the pressure waves was about 320 m/sec and wind speeds up to 30 meters/sec at low altitudes were required to generate the matching dispersion curves. Wind data at Albany, New York at 0000 GMT on 31 October 1962 indicate strong tropospheric winds; a maximum of 41 meters/sec is observed at an altitude of 10 km from a direction of 240°. These observations substantiate the use of the model used to compute the dispersion curves in Fig. 10.

Baker (1968) observed ionospheric disturbances produced by the nuclear test of 30 October 1962. He noted the similarity in periods and velocities between the pressure oscillation at Poughkeepsie and Berkeley and the ionospheric disturbance at Boulder, Colorado. We subjected the Boulder ionogram to running spectrum analysis with results shown in Fig. 11. A striking similarity between the dispersion patterns of the pressure record for Poughkeepsie and the ionogram for Boulder is evident. Both running spectra show normal and inverse dispersion in roughly the same period range. This confirms with great certainty Baker's observations of the effect of acoustic-gravity waves on the ionosphere.

At ionospheric heights, although the pressure perturbations due to the passage of acoustic-gravity waves are small, the velocity perturbations are significant due to the low air density at these heights. A continuous study of this effect is being made.

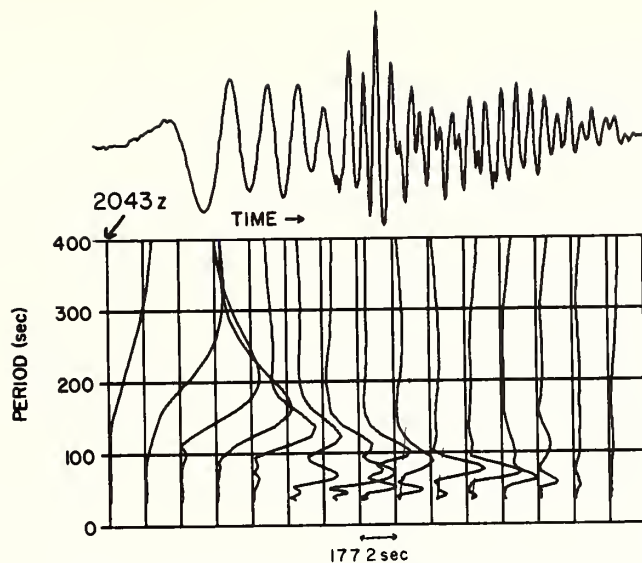


Fig. 9. The Berkeley pressure record and its running spectrum analysis (window length of 590 sec) for the United States nuclear test of 30 October 1962.

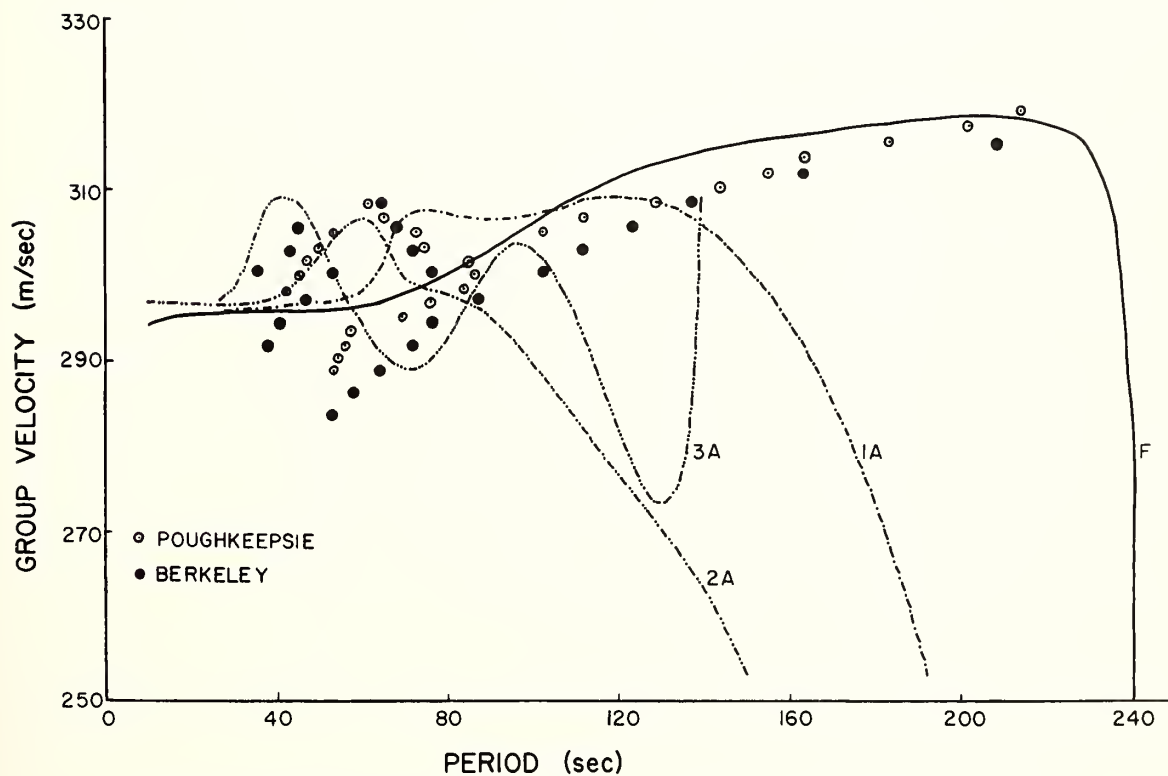


Fig. 10. Theoretical dispersion curves for the 130 km model of Table 2 along with empirical points.

# ACKNOWLEDGMENTS

This research was supported by National Science Foundation Grants GP 5136 and GA 1333 and U.S. Army Research Office Durham Contract DAHC 0037. R. Pfeffer and J. Zarichny provided their original computer program for solutions without wind and Mr. Zarichny gave helpful suggestions in further programming.

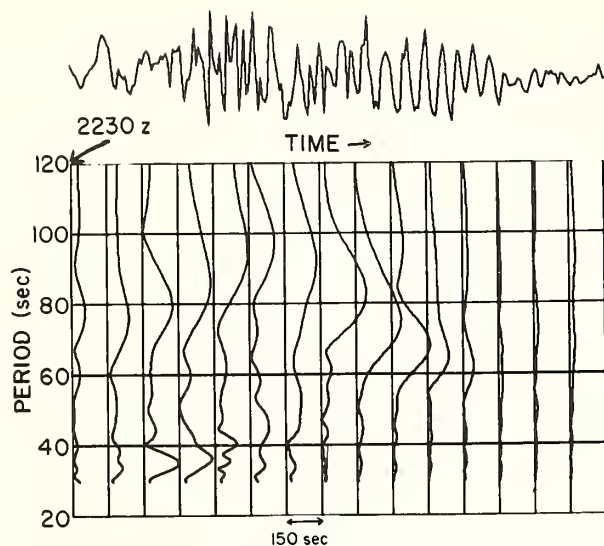


Fig. 11. Ionogram (recorded at Boulder, Colorado) and its running spectrum analysis for the nuclear test of 30 October 1962.

TABLE 1

Altitude km	Temperature °K	Model 1 Wind Speed m/sec	Model 2 Wind Speed m/sec
0 - 2	268.8	0.0	0.0
2 - 4	275.3	0.0	0.0
4 - 6	256.7	Wind	0.0
6 - 8	239.8		0.0
8 - 10	227.4	is	0.0
10 - 12	219.5		0.0
12 - 14	215.4	zero (0.0)	0.0
14 - 16	214.1		0.0
16 - 18	214.6	up	0.0
18 - 20	216.1		0.0
20 - 22	218.1	to	0.0
22 - 24	220.3		0.0
24 - 26	222.5	46 km.	5.0
26 - 28	224.7		10.0
28 - 30	227.1		15.0
30 - 32	229.7		20.0
32 - 34	232.8		25.0
34 - 36	236.4		30.0
36 - 38	240.6		31.0
38 - 40	245.4		32.0
40 - 42	250.5		33.0
42 - 44	255.6		30.0
44 - 46	260.6		25.0
46 - 48	264.9	12.0	20.0
48 - 50	268.2	26.0	15.0
50 - 52	270.1	40.0	20.0

CONT. OF TABLE 1

Altitude km	Temperature °K	Model 1 Wind Speed m/sec	Model 2 Wind Speed m/sec
52 - 54	270.4	40.0	25.0
54 - 56	268.9	50.0	30.0
56 - 58	265.6	60.0	35.0
58 - 60	260.7	70.0	40.0
60 - 62	254.3	80.0	45.0
62 - 64	246.8	80.0	52.0
64 - 66	238.6	80.0	60.0
66 - 68	230.0	80.0	70.0
68 - 70	221.3	80.0	80.0
70 - 72	213.0	80.0	85.0
72 - 74	205.5	80.0	90.0
74 - 76	198.4	70.0	95.0
76 - 78	192.2	60.0	100.0
78 - 80	187.1	50.0	110.0
80 - 82	183.2	60.0	110.0
82 - 84	180.5	70.0	110.0
84 - 86	179.1	80.0	110.0
86 - 88	179.0	85.0	110.0
88 - 90	180.4	90.0	110.0
90 - 100	197.7	85.0	110.0
100 - 110	239.5	73.0	100.0
110 - 120	305.7	58.0	100.0
120 - 130	459.5	40.0	30.0
130 - 140	689.0	10.0	80.0
140 - 150	912.5	- 5.0	84.0
150 - 160	1092.0	-10.0	84.0
160 - 170	1173.3	-15.0	84.0
170 - 180	1193.1	-20.0	84.0
180 - 190	1210.0	-20.0	88.0
190 - 200	1227.6	-25.0	90.0
200 - 210	1245.0	-25.0	90.0
210 - 220	1261.7	-30.0	50.0
220 - 230	1277.8	-30.0	10.0
230 - 240	1292.6	-35.0	-30.0
240 - 250	1307.0	-35.0	-70.0
250 - 260	1319.0	-40.0	-110.0
260 - 270	1332.0	-40.0	-150.0
270 - 280	1344.1	-45.0	-160.0
280 - 290	1356.4	-45.0	-170.0
290 - 300	1366.3	-50.0	-180.0
300 - ∞	1358.5	-100.0	-190.0

TABLE 2

Wind structure for the model used to obtain the theoretical dispersion curve of Fig. 10. The temperature structure for this model is the same as in Table 1.

Altitude km	Wind Speed m/sec	Altitude km	Wind Speed m/sec
0 - 2	0.0	66 - 68	30.0
2 - 4	5.0	68 - 70	10.0
4 - 6	15.0	70 - 72	0.0
6 - 8	20.0	72 - 74	10.0
8 - 10	30.0	74 - 76	20.0
10 - 12	25.0	76 - 78	30.0
12 - 14	20.0	78 - 80	40.0
14 - 16	10.0	80 - 82	50.0
16 - 18	5.0	82 - 84	60.0
18 - 44	0.0	84 - 86	70.0
44 - 46	10.0	86 - 88	80.0
46 - 48	20.0	88 - 90	100.0
48 - 50	30.0	90 - 100	100.0
50 - 52	40.0	100 - 110	70.0
52 - 54	50.0	110 - 120	30.0
54 - 56	60.0	120 - 130	10.0
56 - 58	70.0	130 - $\infty$	0.0
58 - 60	80.0		
60 - 62	70.0		
62 - 64	60.0		
64 - 66	50.0		

## REFERENCES

Baker, D.M., Observations of acoustic waves in the ionosphere following nuclear explosions, Proceedings of the ESSA/ARPA Acoustic-Gravity wave Symposium, 1968.

Balachandran, N.K., Acoustic-gravity wave propagation in a temperature- and wind-stratified atmosphere, J. Atmos. Sci., 25(5), 1968.

Blackman, R.B. and J.W. Tukey, The measurement of power spectra from the point of view of communications engineering, Part I, The Bell System Tech. Jour., XXXVII(1), 185, 1958.

Cooley, J.W. and J.W. Tukey, An algorithm for the machine calculations of complex Fourier series, Math. of Comp., 19, 297-301, 1965.

Donn, W.L. and M. Ewing, Atmospheric waves from nuclear explosions - Part I, J. Geophys. Res., 67 (5), 1855-1866, 1962.

Donn, W.L. and M. Ewing, Atmospheric Waves from nuclear explosions - Part II, The Soviet test of 30 Oct. 1961, J. Atmos. Sci., 19, 264-273, 1962.



Donn, W.L. and R. Pfeffer and M. Ewing, Propagation of air waves from nuclear explosions, Science, 139, 307-317, 1963.

Donn, W.L. and D.M. Shaw and A.C. Hubbard, The microbarographic detection of nuclear explosions, IEEE Trans. Nuc. Sci., NS-10, 285-296, 1963.

Donn, W.L. and D. Shaw, Exploring the atmosphere with nuclear explosions, Reviews of Geophysics, 5, 53-82, 1967.

Ewing, M. and F. Press, An investigation of mantle Rayleigh waves, Bull. Seis. Soc. Amer., 44, 127, 1954.

Kantor, A.J. and A.E. Cole, Zonal and meridional winds to 120 kilometers, J. Geophys. Res., 69, 5130-5140, 1964.

MacKinnon, R.F., The effects of winds on acoustic-gravity waves from explosions in the atmosphere, Quart. J. Roy. Meteor. Soc., 93, 436-454, 1967.

Pfeffer, R.L., A multi-layer model for the study of acoustic-gravity wave propagation in the earth's atmosphere, J. Atmos. Sci., 19, 251-255, 1962.

Pfeffer, R.L., and J. Zarichny, Acoustic-gravity wave propagation in an atmosphere with two sound channels, Geofis. Pura, Appl., 55, 175-199, 1963.

Pierce, A.D., Guided infrasonic modes in a temperature- and wind-stratified atmosphere, J. Acoust. Soc. Am., 41, 597-611, 1967.

Press, F. and D. Harkrider, Propagation of acoustic-gravity waves in the atmosphere, J. Geophys. Res., 67, 3889-3908, 1962.

Tolstoy, I., Long-period gravity waves in the atmosphere, J. Geophys. Res., 72, 4605-4622, 1967.



# INFRASONIC WAVES FROM NATURAL AND ARTIFICIAL SOURCES \*

by

William L. Donn and Eric Posmentier

Lamont Geological Observatory (Columbia University)  
Palisades, New York.

A tripartite array of capacitor microphones has been used at the Lamont Geological Observatory to record infrasonic waves in a 1 to 10 sec bandpass. Peak energy of natural sounds in this band, which occurs at about 5 sec, has been shown to originate in marine storms mostly off the eastern coast of the United States but occasionally off the western coast of Canada. These waves, known as microbaroms, show a characteristic semidiurnal variation caused by the changing directions of the semidiurnal atmospheric tidal winds above 100 km. Maximum microbarom amplitudes occur when the azimuth of the source and of the tidal winds coincide; amplitude minima occur when the two azimuths are  $180^\circ$  apart. The time of maximum microbaroms corresponds approximately to the hour angle of the source as measured from north.

Microbaroms have spectra which are very similar or nearly identical with microseisms, and have been explained as originating in interfering ocean waves by a mechanism similar to that used by Longuet-Higgins to explain microseisms. But in eastern United States microbaroms can be detected from storms beyond the continental shelf whereas microseisms generated in the same storms cannot penetrate the continental margin.

Infrasound has been detected at Palisades, N. Y. (Lamont) from Atlas and Saturn rockets launched at Cape Kennedy. The signals contain strong energy between 1 and 8 sec periods and appear to emanate from points along the trajectory at least as high as 180 km, indicating that both generation and propagation of infrasound is possible in the ionosphere.

## INSTRUMENTATION AND DATA ANALYSIS

A tripartite array of capacitor microphones has been in nearly continuous operation at the Lamont Geological Observatory (Palisades, N. Y.) since the Spring of 1966. Signals are telemetered via leased telephone lines to the laboratory where they are recorded on both analog magnetic tape and a visual triple-drum recorder for signal monitoring.

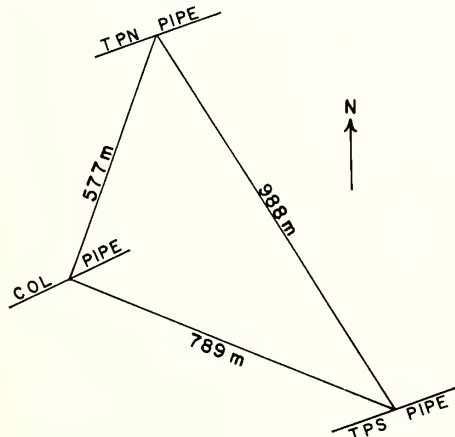


Fig. 1. Scale drawing of the Lamont tripartite array of capacitor microphones centered in Daniels noise-reducing pipes.

The tripartite array, (Fig. 1), is nearly a right triangle the length of whose sides is close to the wavelength of the 5 sec acoustic waves we record most commonly. It has been shown by Barber (1963), who considered the resolving power with a triangular array, that the optimum detector separation is about one-half the wavelength.

During the first two years of operation we mostly used the Globe microphone which had been adjusted to give an essentially flat response from 0.05 to 10 sec period. The response was further adjusted in the laboratory by the use of three Krohn-Hite filters set for a bandpass of 1 to 10 sec with signals outside this range being attenuated by 18 db per octave. This removes

\* Lamont Geological Observatory (Columbia University) Contribution No. 1221.

much of the strong wind-pressure noise between 10 and 30 seconds.

Further improvement in the signal to noise ratio is obtained by installing the microphones in the center of symmetrically tapered 1000-foot pipes as described by Daniels (1959). The three pipes in our array are oriented in the same direction to avoid phase differences that would otherwise result. For waves of a period of about 5 sec and longer the pipes are essentially omnidirectional. Although the transducer and filter responses are essentially flat between 1 and 10 sec, the pipes introduce increasing signal suppression as the wave period decreases from 5 sec. At 1 sec the system response is reduced about 50 percent. An example of the effectiveness of the pipe system is shown in Fig. 2 for both quiet and "noisy" days. The comparison of the records for the quiet interval shows the lack of any signal distortion by the pipe. Noise reduction during

the windy day is of the order of a factor of 10. Data analysis has been by both visual and machine processing. Signal amplitudes and periods, timing of events and rapid correlations among the tripartite elements can be made easily on the drum type records in view of their 24-hour presentation and large time scale. Quadrants of wave approach can be estimated quickly by phase matching on the overlaid semi-transparent records.

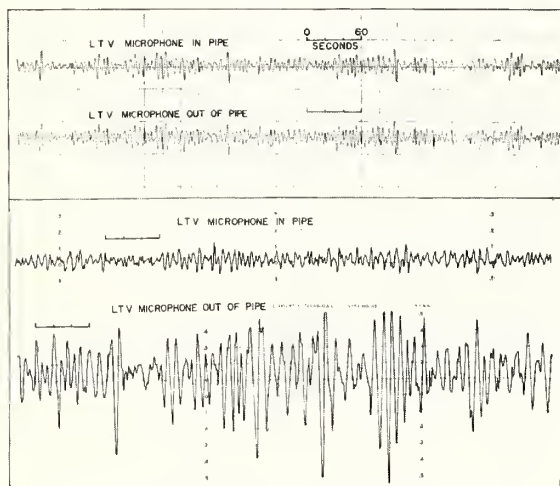


Fig. 2. Comparison of records to show the effect of the Daniels pipes.

A more precise determination of the above parameters is made on our analog computer, the Noratom ISAC (Instrument for Statistical Analog Computation). Output from this instrument, whose operation has been described elsewhere (Donn and Posmentier, 1967) and Posmentier and Donn (in press) include power spectrum analysis, amplitude distribution and auto- and cross-correlation. Time lags determined from the cross-correlation procedure permit the computation of infrasound wave vectors.

#### MICROBAROMS

The characteristic natural signal between 1 and 10 cps is the form of infrasound first reported by Benioff and Gutenberg (1939) who called the phenomenon microbaroms. These are detected as small pressure fluctuations of the order of a few microbars (dynes/cm<sup>2</sup>) which persist for hours or days. Microbaroms characteristically travel with about the speed of sound in air and originate in storms at sea. Ocean wave and weather data, as provided by the U. S. Weather Bureau and the Navy Fleet Weather Central, are used in our analyses.

#### Microbaroms and Marine Storms

Infrasound detected in Palisades, N. Y. (Lamont Geological Observatory) has been correlated with strong low pressure areas in the Atlantic and Pacific Oceans. Cases for the former are more common and of greater intensity in view of the proximity of the Atlantic region to the station.

Figure 3 illustrates a case described more completely by Donn and Posmentier (1967). Illustrated here is the magnetic tape playback of three channels of infrasound signal from our tripartite array and one channel of microseisms, the latter to be discussed in a subsequent section.

An example of the correlation procedure is given in Fig. 4 which shows the cross-correlation function obtained by comparison of 30 minutes of record from two of the three microphone stations. The best correlation occurs at the time lag where the function has maximum amplitude as indicated by the arrow. This procedure is unambiguous if a single source exists and the signal can be assumed to



be monochromatic or at least quasimonochromatic. If signals from two simultaneous sources exist, the wave vectors for each can be computed after internal filtering in the computer permits resolution of the separate arrivals. At times of low wind noise on the tape, the accuracy with which time lags can be measured yields errors of  $\pm 3^\circ$  in direction and 5m/sec in speed.

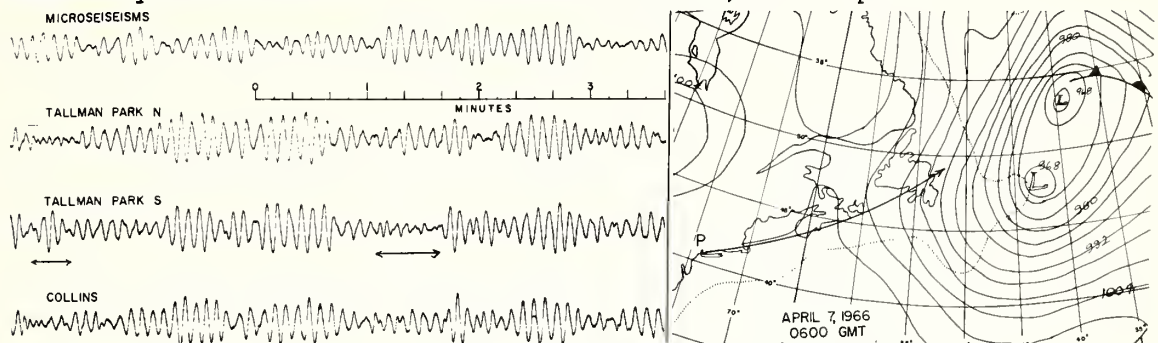


Fig. 3. Microbaroms and microseisms from the storm indicated by the computed direction (arrow).

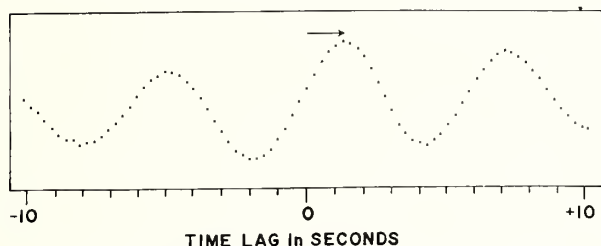


Fig. 4. Example of the cross-correlation function between two signals.

examination reveals examples of incoherence. The coherence calculated between TPN and TPS by means of the analog computer is 0.8.

Posmentier (1968) shows how coherence varies as a function of source size for different values of the angle between the ray from the storm center and the line between receivers, and for different ratios of receiver spacing to wavelength. Fig. 5 (from Posmentier) represents the theoretical relationships for a source distance of 600 km when the ray is normal to the line separating the receivers - as is nearly true in the case under discussion for Tallman Park N. and Tallman Park S. (TPN and TPS). The diagram shows coherence as a function of source radius (DECX) where the radius is taken as the distance from the center to the point where the ocean wave height has fallen to half the maximum value (see Theory of Microbaroms, below), or 15 ft.

To apply these results to the present case, note that the ratio of receiver separation to wave length is about 0.5 and the coherence is 0.8 for quasi-monochromatic waves from a single large source. Since Fig. 5 is developed for a particular source distance of 600 km, the theoretical source radius for a storm distance of 1700 km (the present case) can be found by linear extrapolation to be 510 km, in good agreement with the average radius of the 15 ft ocean wave contour (the half-width value of the disturbed sea source). The coherence between the records of receivers TPN and TPS are thus explained by this effect. A further consequence of waves arriving from a broad source is a consistent overestimate of wave speed by the array method (Posmentier, 1968).

Another typical case is that of 11-14 April 1968. A cyclonic depression which has developed in the western North Atlantic Ocean off Cape Hatteras late on 11 April, moved so slowly northeastward during the next three days as to be



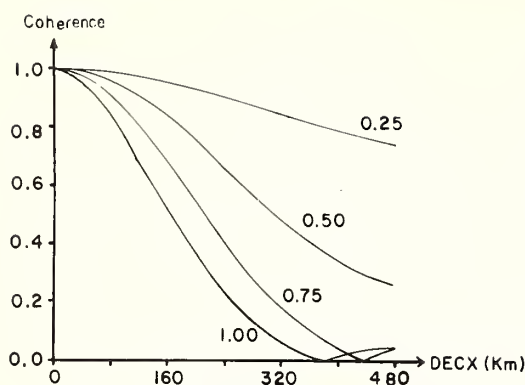
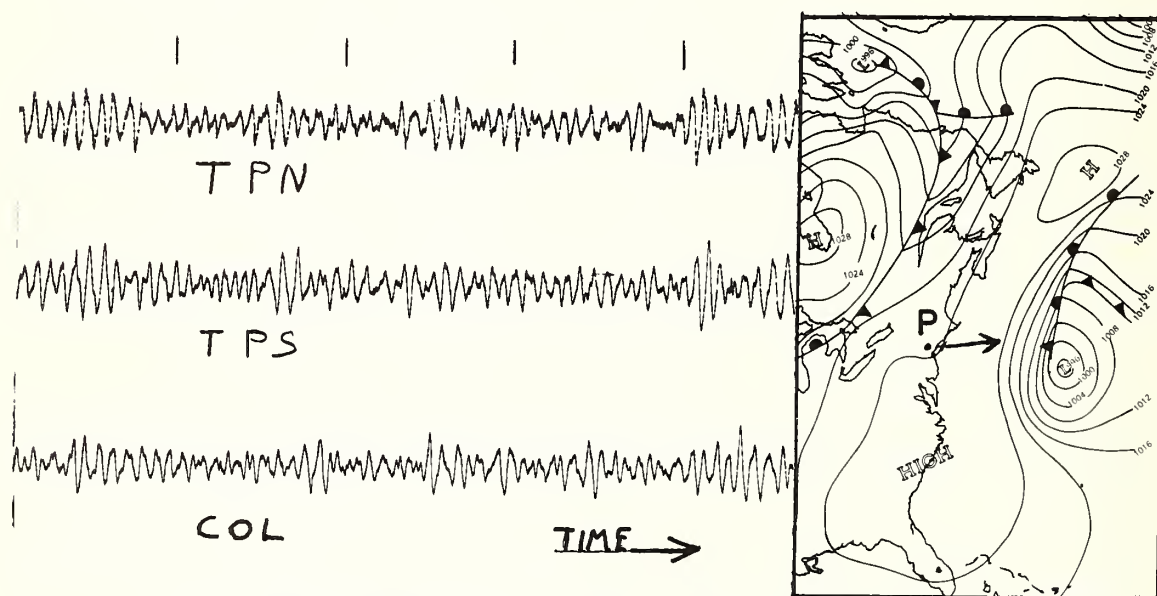


Fig. 5. Coherence vs source width (DECX) for different ratios of receiver separation/wavelength with a source at 600 km (Posmentier, 1968).

nearly stationary in the position shown in the chart in Fig. 6 for 13 April at 1300 EST. A consistent pattern of microbaroms was recorded at Palisades during the life of this storm. Examples for the tripartite station are shown also in Fig. 6 for 0400 April 14. (Although the times do not coincide, no significant difference occurred in either the weather or the microbarom pattern between these times).

Signals at both TPN and COL lag those at TPS by about the same time interval (2 sec). On the basis of the geometry in Fig. 1, this lag corresponds to a wave vector having an average azimuth of  $110^\circ$  as shown by the arrow on the chart of Fig. 6 which clearly indicates the storm.



## Microbaroms and Microseisms

Microseisms are small amplitude, continuous earth tremors long known to be related to storminess at sea. Although storm microseisms occur in two distinct period ranges, the dominant type are most commonly from 4 to 6 sec in period with a range from about 3 to 6 sec. Donn (1957) established that microseisms recorded in eastern United States require the generating area to be on the continental shelf.

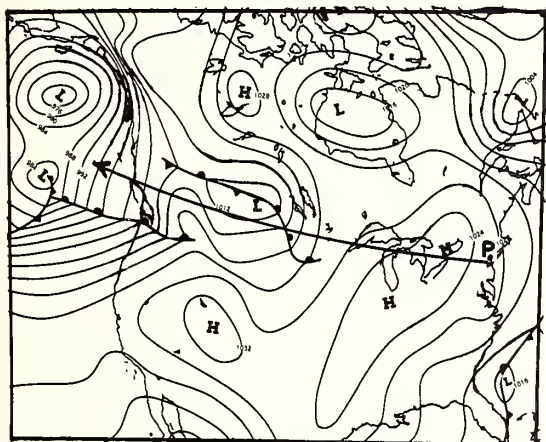


Fig. 7. Weather Map -  
13 Dec. 1966, 1300 EST.

Donn and Posmentier (1967) showed a clear relationship between a large cyclonic storm off the coast of Newfoundland and microbaroms and microseisms recorded at Palisades. Both types (Figs. 3 and 8) of signals had nearly identical appearance and power spectra and arrived from the direction of the storm. As indicated by the spectra, microbarom amplitudes varied with time while the source was unchanged, but microseism amplitudes showed no significant time variation. This relationship appears to be characteristic of microbaroms and microseisms recorded at Palisades. Microbaroms from a unique source usually show a semidiurnal variation whereas related microseisms maintain a continuously high level.

Not only do microbaroms and microseisms show common spectral features, they also vary with time in the same way when received from the same source. In the case of the strong microbaroms and microseisms on 3 January 1967, the computed arrival direction of microbaroms shown by the arrow in Fig. 9 indicates the intense cyclone to the east of the station. The power spectra of microbaroms and microseisms determined at six-hour intervals on this day (Fig. 10) show very good agreement in general characteristics and in many details. Both show a gradual increase in period with time. All of our results confirm in detail the earlier observations of Baird and Banwell (1940) who noted an agreement between the periods of concurrent microbaroms and microseisms recorded in New Zealand.

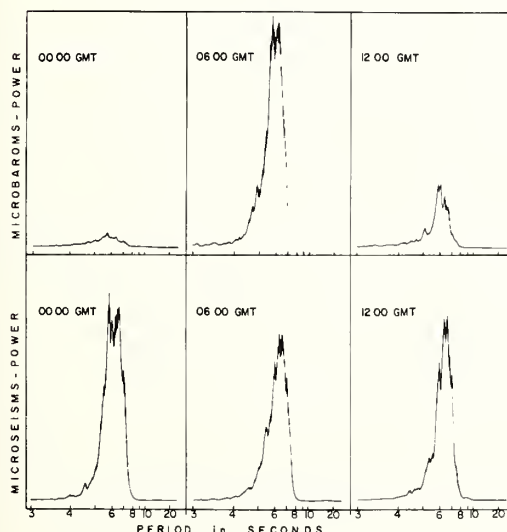


Fig. 8. Power spectra of the  
simultaneous microbaroms and  
microseisms shown in Fig. 3.

The cases documented here are but examples of the large number accumulated during the operation of our infrasonics array. Although microbarom vectors can be computed with accuracy, microseism vectors have been determined more crudely by a comparison of records from a three component seismograph system. On the assumption that microseisms are composed dominantly of Rayleigh waves, (whose ground-particle motion is in the form of a vertically polarized retrograde ellipse) the quadrant of wave approach can be determined. Such quadrants have always been in agreement with the storms indicated by microbarom vectors when unique sources were present.

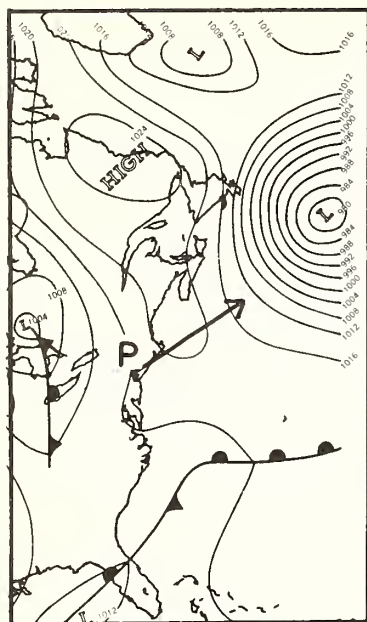


Fig. 9. Weather Map -  
3 Jan. 1967, 1300 EST.

When the generating area is beyond the continental shelf microbaroms are often detected but not microseisms as a consequence of the inability of microseisms from deep water storms to penetrate the eastern continental margin.

#### The Origin of Microbaroms

The simultaneous occurrence, directions of signal arrival and similarity of spectra indicate strongly that the origin of microbaroms is closely related to the origin of microseisms. Generation of microbaroms by local coupling is ruled out by their pressure amplitudes in comparison with microseisms as well as by the time variation of the former. The perturbation pressure that is radiated upwards by local microseism ground motion is given by

$$p = \rho c v \quad (1)$$

where  $\rho$  is the air density,  $c$  the acoustic speed in air and  $v$  the vertical velocity of the ground. Resulting pressures are inadequate to explain microbaroms. The possibility that microbaroms are generated by resonant coupling to microseisms along the path of propagation is negated both by the known prominent time variations of microbaroms (to be elaborated in the following section) while microseism intensity shows no change and by the fact that microseisms have a phase velocity some ten times greater than that of microbaroms.

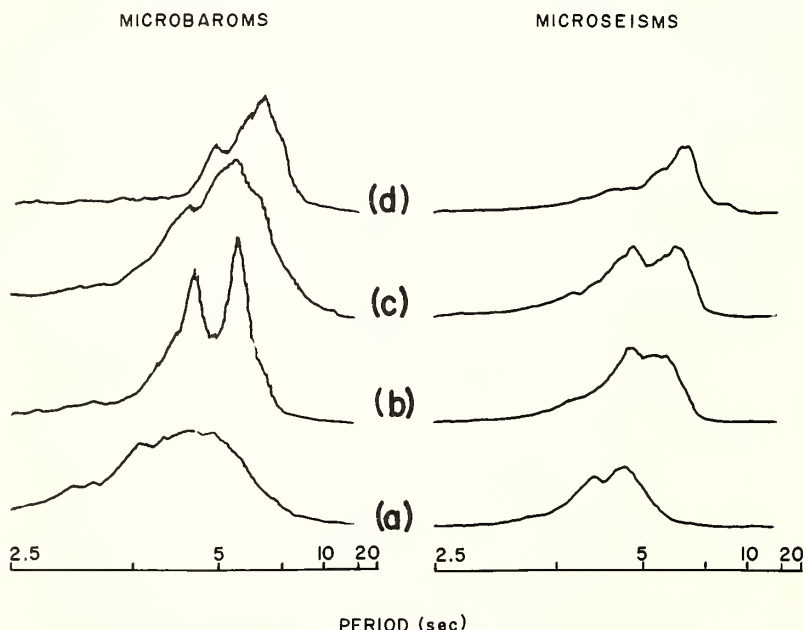


Fig. 10. Power spectra of microbaroms and microseisms for 3 January 1967.

These arguments lead to the conclusion that microbaroms and microseisms have the same source. Since neither are generated by storms when over land but develop quickly when storms reach the sea, ocean waves appear to be the only possible common marine source.

Posmentier (1968) proposed a theory, analogous to the Longuet-Higgins (1950) theory of microseisms, to explain the generation of microbaroms by standing water waves associated with marine storms. Fig. 11 shows four stages of one period of standing wave motion, along with four stages of one period of an analogous pendulum motion. Although both the standing waves and the pendulum complete one cycle of motion in the time illustrated, the height



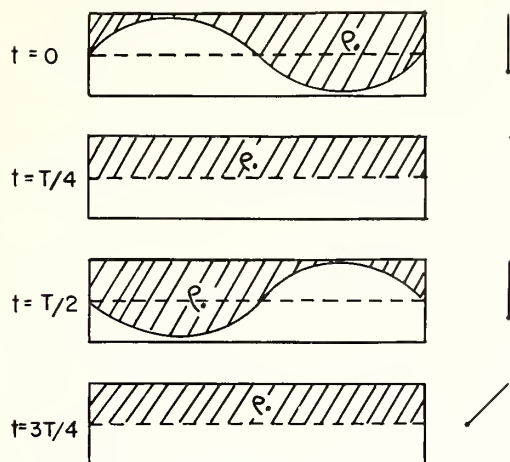


Fig. 11. Motion of air and water in a standing wave. (Modified from Longuet-Higgins, 1953).

of the center-of-gravity of both the air above the standing waves (shaded area with density  $\rho_a$ ) and the pendulum bob complete two cycles. Therefore, the vertical forces on each must oscillate at twice the frequency of their motions. In the case of the air above the standing waves, this means that the mean surface pressure on the plane of the standing waves varies at twice the frequency of the waves. If the vertical displacement of the surface is

$$2a \cos k_0 x \cos \omega t$$

the perturbation pressure,  $p$ , will be

$$p = -2\rho_a a^2 \omega^2 \cos 2\omega t \quad (2)$$

It is this pressure variation which produces microbaroms. Eq. (2) remains valid if the compressibility of air is taken into account.

Posmentier (1968) has shown further that for ocean wave models more realistic than an infinite plane of standing waves, the predicted magnitude of microbaroms agree well with observations. For example, if a storm having a half-width of only 80 km in radius has standing waves of 12.6 sec periods produced by the interaction of 23.6 foot waves with 2.36 foot waves, and if the standing wave motion is coherent over distances not more than 10 ocean wavelengths, microbaroms 600 km distant will have half-amplitudes of 1.6 microbars and periods of 6.3 sec. A rather conservative example of a marine storm is thus capable of generating strong microbaroms with periods the same as microseisms predicted by the Longuet-Higgins theory (half the ocean wave period).

Semi-empirical forecasts of ocean wave heights and periods as well as charts of computer-drawn wave height contours have been provided by the U. S. Fleet Numerical Weather Facility at Monterey, California and transmitted to use by the Fleet Weather Central in Norfolk Virginia. Our microbarom vectors usually indicate the region of strong wave activity within a storm or the region where ocean wave interference producing standing waves, is most likely to occur. This has been documented in more detail by Posmentier and Donn (in press).

#### The Semidiurnal Oscillation of Microbaroms

Donn (1967) called attention to a characteristic semidiurnal variation of microbaroms as illustrated for example in Fig. 12 for three different situations. In the case of 3 January, already referred to in the previous section, each of these separate cases are portions of 24-hour drum records and each line shows about 4 minutes of the one-hour line on the original record.

In the case of 2-3 January 1968, (also referred to in the previous section) maximum amplitudes occur between 0100 and 0200 local time and again at local noon. The source was mostly east-northeast of the station during this time (Fig. 9). Note also in Fig. 9 the incipient low pressure system just developing off southeastern United States.

The record for 4-5 January shows microbarom maximum at 0400 and 1600 EST. Azimuths at these times are from  $105^\circ$  and  $152^\circ$  respectively, the direction of the newly developed cyclone system, now closer and to the east-southeast of the station (Fig. 13). According to the standing wave theory of microbaroms, the computed wave vectors actually indicate the average position of maximum wave interference which is rarely the central portion of the storm.

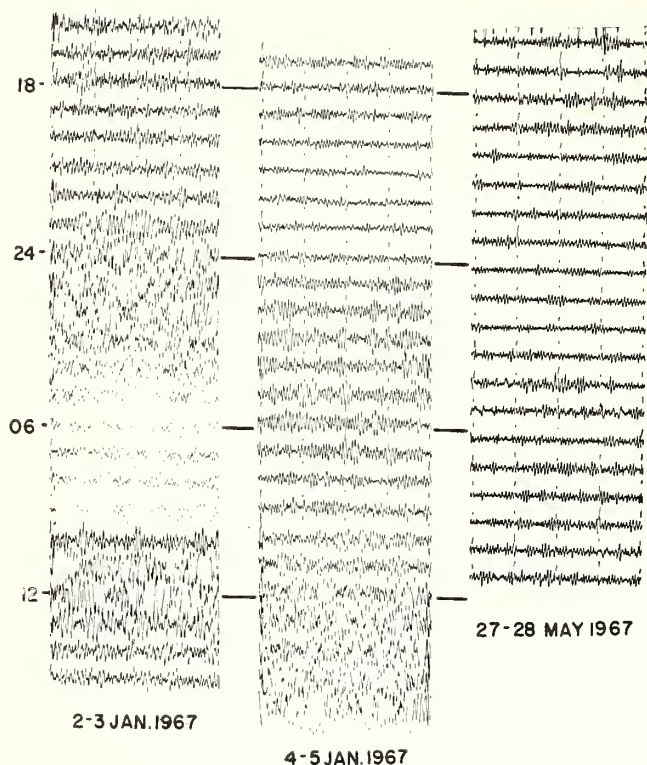


Fig. 12. Cases illustrating semidiurnal variation of microbaroms for storms of different azimuths from Palisades.



Fig. 13. Weather Map - 4 Jan. 1967, 1300 EST.

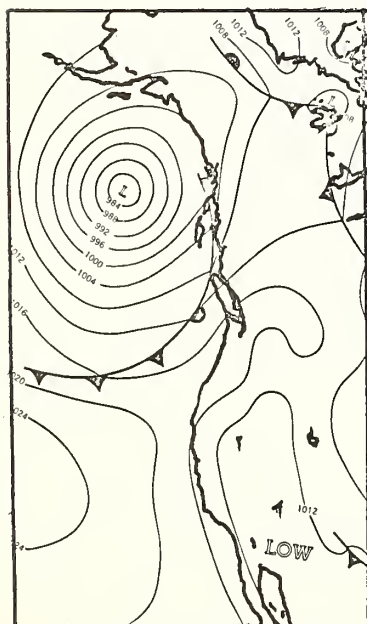


Fig. 14. Weather Map - 27 May, 1967, 1300 EST.

The record of Fig. 12 for 27-28 May 1967 shows microbarom maxima which precede local noon and midnight by several hours. In fact, midnight (2400) is the time of a distinct minimum. The computed azimuths of  $245^{\circ}$  for this case indicates a westerly source but not the strong low off northwestern Canada (Fig. 14) which developed wave heights forecast to be 33 ft. The inaccuracy of the vector in this case is probably due to the inability of the array to resolve two sets of simultaneous arrivals, one from the northwest and the other, a storm receding to the northeast.

Observations in the cases just given, and of numerous others we have studied, permit the generalization that the time of microbarom maxima approximately match the azimuth of the source as measured in hours from north. This lends support to the suggestion of Donn (1967) that the cause of the semidiurnal variation of microbaroms might be the upper atmospheric tidal winds whose directions shift in a clockwise manner every 12 hours.

To test this hypothesis a temperature-wind model from the surface to 120 km was developed for  $45^{\circ}\text{N}$  during the winter. A detailed statement of the model and sources of data is being prepared separately (Donn and Posmentier in preparation). The rather conservative wind profile used in ray solutions of sound propagation is shown in Fig. 15, which includes the total wind from  $45^{\circ}$  (NE) at 0430 and 1030 local time (at  $45^{\circ}\text{N}$ ).



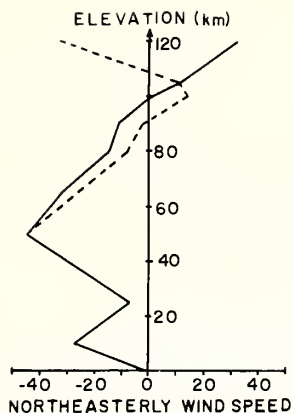


Fig. 15. Atmospheric wind model used to compute ray solutions of Fig. 16. The broken line shows winds at 0430; the full line at 0430 and 1230.

The tidal winds have shifted direction by  $180^\circ$  during this time, the effect being most important above 100 km.

Ray solutions for this model and winter temperature from the U. S. Standard Atmosphere were carried out by Andrew Thompson of the U. S. Army Ballistics Research Laboratory. The Thompson program computes ray paths in a multi-layered wind and temperature stratified atmosphere with the assumption that sound and wind speed vary linearly in each layer. We believe that the first order theory used provides sufficient accuracy for the purpose of this study.

Ray solutions were developed for eight times at equal intervals with a point source of sound at  $45^\circ$  azimuth, or northeast of Palisades, the direction of the most common marine storms. All rays with initial elevation angles of  $0^\circ$  to  $40^\circ$ , in steps of  $5^\circ$ , were considered. Results are shown in Fig. 16a and b for the hours of least favorable and most favorable propagation from  $45^\circ$ , or 0430 and 1030 local time respectively. Complete results show a symmetrical ground insonification about the time of minimum (0430) and of maximum (1030). The numerical output indicates that signal strength is about the same at both times when different attenuation is balanced by compensating focussing effects.

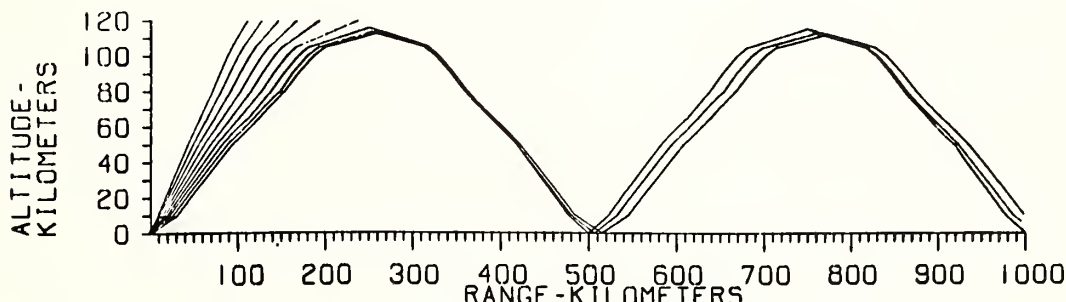


Fig. 16a. Ray solutions for winds at 0430 - opposite wave propagation.

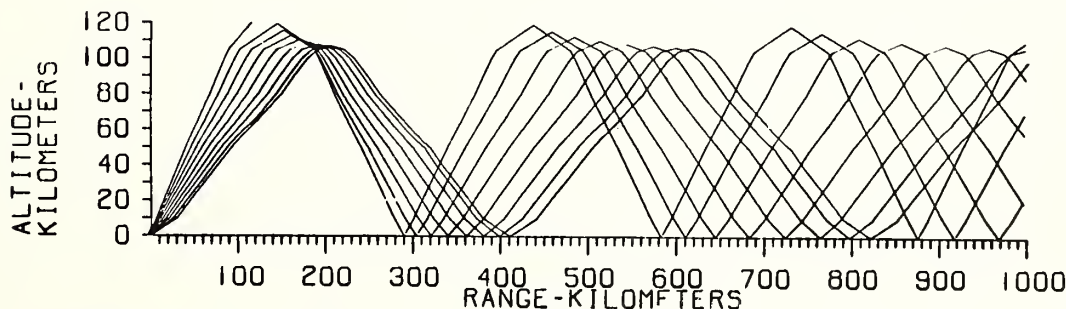


Fig. 16b. Ray solutions for winds at 1230 - in direction of propagation.

Note that the real source is probably an extended region of ocean waves so that the resulting signal strength at the ground must be in a sense averaged over an area equal to the source area. With a broad source, considerable reinforcement of sound will occur in the insonified regions. The ratio of sound intensity between times of maximum and minimum ground insonification will be in the proportion of the insonified segments of the range. In the case of the first returns in Fig. 16, the intensity at 1030 would be six times that at 0430. Also, the separation between the zones of audibility and zones of silence will not be sharp as for a point source. This again matches observations which nearly always show the weaker signals at times of minimum activity coming from the same source as at times of maximum, providing the source is unique.

Although these results demonstrate that the relatively high velocity tidal winds can enhance or diminish infrasound from surface sources, there is not perfect agreement between the times of theoretical and observed microbarom maxima. For the case developed, predicted maxima at 1030 (and 2230) precede times of observed maxima from northeast storms by about two hours. This time discrepancy may be within the experimental error resulting from the atmospheric model used. At the same time, the results tend to confirm the presence of strong rotating tidal winds in the upper atmosphere. It should be noted that the effects of less periodic but equally strong winds at lower levels, as revealed by grenade explosion, would be superimposed on the effects of tidal winds. This could account for intervals of a third maximum occasionally observed. Also, a very extended storm gives a less restricted interval of maximum infrasound.

#### ATMOSPHERIC WAVES FROM EARTHQUAKES

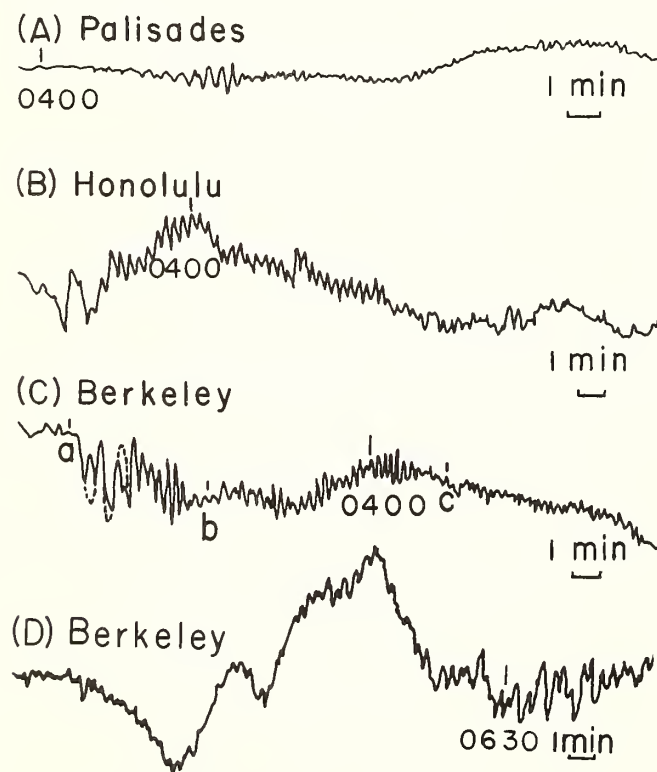


Fig. 17. Pressure waves associated with the Alaskan earthquake - 27 March 1964.

A number of stations have detected infrasonic waves associated with strong earthquakes. These sounds include acoustic waves traveling directly from the source and those generated locally by coupling to Rayleigh waves. Donn and Posmentier (1964) described and interpreted both types of waves recorded from the Alaskan earthquake of 27 March 1964 by our long-period sensors at Honolulu, Berkeley and Palisades. Records from these stations are illustrated in Fig. 17. The short period waves on records A, B, and C represent atmospheric infrasound generated by 15-30 sec Rayleigh waves passing the respective stations, while the high amplitude, long period arrival beginning about 0615 on the Berkeley record represents the direct acoustic wave traveling through the atmosphere from the epicenter. Donn and Posmentier showed that the velocity dispersion of the short-period waves recorded at the three sites agree very closely with typical seismic dispersion curves for first mode continental Rayleigh waves in the case of Palisades, first mode oceanic Rayleigh waves in the case of Honolulu, and both continental and oceanic Rayleigh waves in the case of Berkeley.

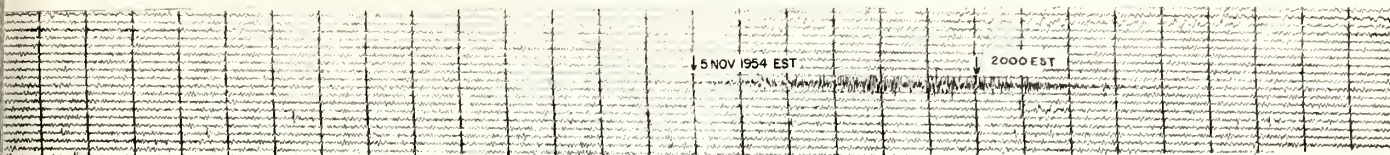


Fig. 18a. Infrasonic signal from the Atlas launching at Kennedy Space Center of 5 November 1967, 1837 EST. One-minute time marks are on record.

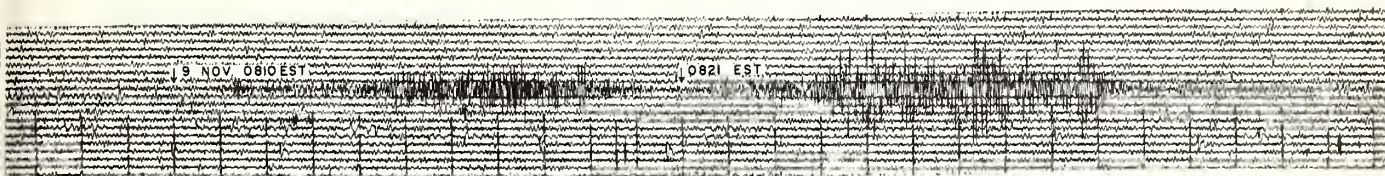


Fig. 18b. Infrasonic signal from Saturn V launching at Kennedy Space Center of 9 November 1967, 0700 EST.

#### INFRASOUND FROM ROCKET LAUNCHINGS

The Lamont array has detected a large number of dynamic rocket firings from a number of launch sites including various NASA launchings from Kennedy Space Center, Florida (1485 km away). Two examples of such recordings are shown in Fig. 18. The upper trace represents a 10-minute signal beginning at 1954 EST from the launching of an Atlas-Agena rocket on 5 November 1967. The Atlas thrust is 360,000 pounds. The effect of the Agena is insignificant. The range of periods estimated from this record is about 1 to 6 sec. Since the rocket was launched at 1837 on 5 November, the travel time of the first arrival was 77 min and the group velocity was 321 m/sec on the basis of a range distance of 1485 km.

Fig. 18b is the trace of the first Saturn V launch on 9 November 1967, also from Kennedy Space Center. Obvious difference between this records and that from the Atlas are the presence of two wave groups and the higher amplitudes in the Saturn signal. The high amplitudes of the latter are readily explained by the hitherto unprecedented thrust of its first and second stages which were 7.5 and 1 million pounds, respectively.

Since the Saturn launch time was 0700, the travel time and group velocity of the beginning of the second wave group is 81 minutes and 306 m/sec, respectively, compared to the anomalously high velocity of 351 m/sec for the first group if we use the Kennedy Space Center distance for both sets of computations. In a detailed analysis of this case, Donn *et al*, (in press), computed average wave vector azimuths of  $194^\circ$  from Palisades for the Atlas signals and  $196^\circ$  for the second of the Saturn signals. Average azimuths computed for the first wave group of the Saturn signals was  $178^\circ$  from Palisades. Donn *et al* further showed that the anomalously high group velocity of the first signal and the low azimuth of  $178^\circ$  can be explained if the first wave group represents either the second stage of Saturn V or the first stage reentry, and the second wave group represents the first stage. This results from high velocity component of the vehicle toward the receiver.

A consequence of a second stage source is that infrasound observed from the second stage was generated at elevations from 120 to 180 km and then propagated by multipath reflections from these elevations. The quieter interval between the two groups is suggested to occur from the passage of the vehicle through the strong upper sound channel centered at an elevation of about 87 km. Ray solutions (by A. Thompson) for the source at different elevations (Fig. 19) support the argument of weak surface returns when the rocket crossed the upper sound channel.



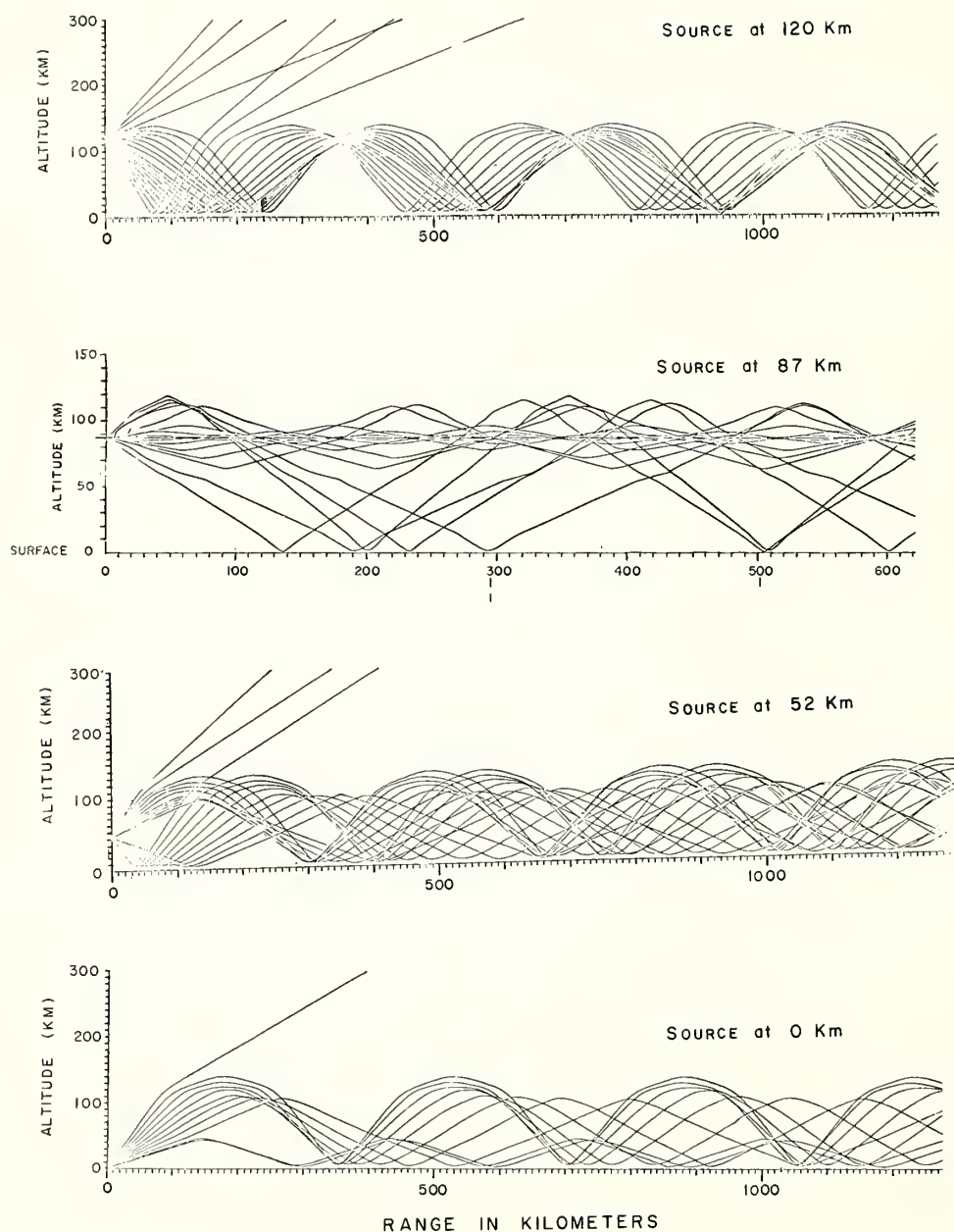


Fig. 19. Ray solutions computed for a source at different elevations on the basis of a winter atmosphere between Florida and Palisades.

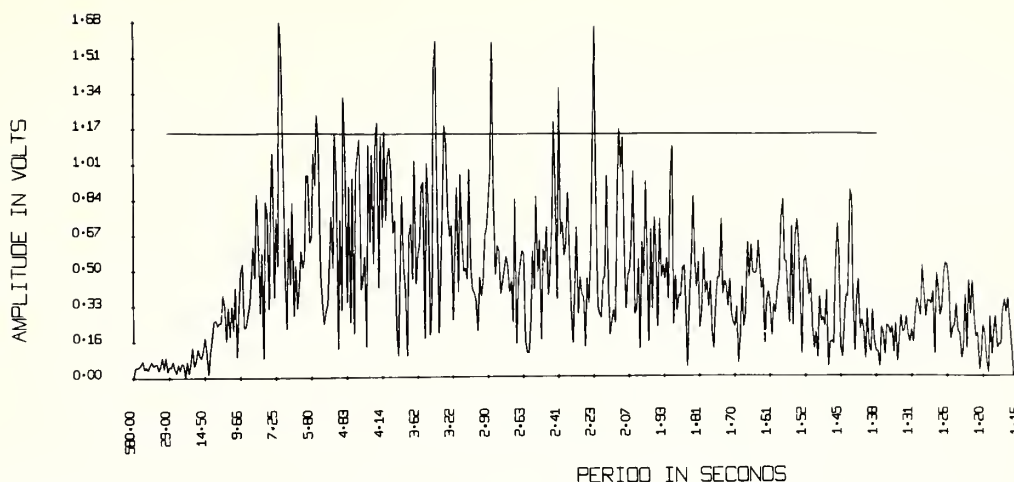


Fig. 20a. Fourier analysis of the first Saturn V wave group. The horizontal line represents the 95 percent confidence limit.

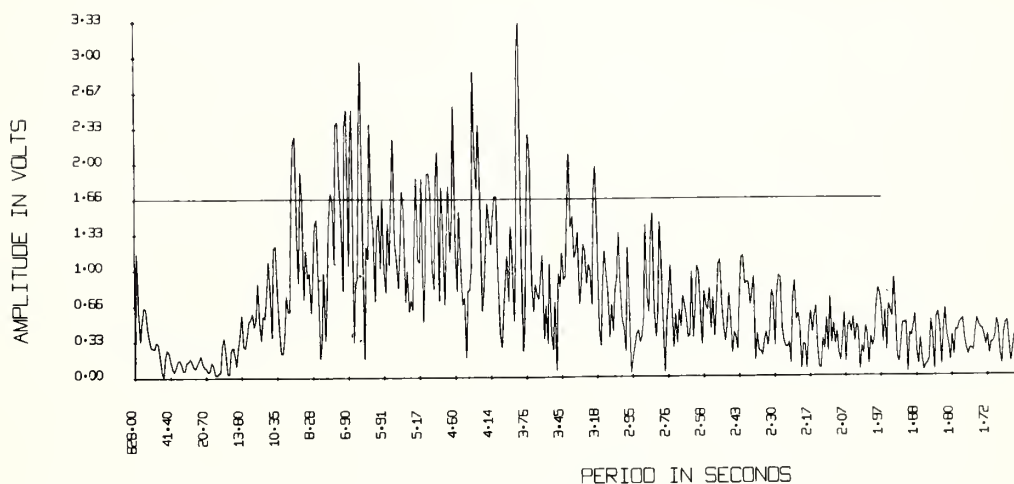


Fig. 20b. Fourier analysis of the second Saturn V wave group.

A Fourier analysis (from Donn et al, in press) of the two wave groups in the Saturn V signal is reproduced in Fig. 20. As noted earlier, our system is operated within a 1-10 sec electronic bandpass with additional signal suppression imposed below 5 sec period by the noise-reducing pipes. Of significance is the relatively low frequency extent of the spectrum. These results indicate the value of increasing the bandpass of receivers usually used to monitor long range rocket sounds in view of the more efficient propagation of long wavelengths.



#### ACKNOWLEDGMENTS

The research described was supported by National Science Foundation Grants GP 5136 and GA 1333 and U. S. Army Research Office Durham Contract DAHC 0037. We wish to thank Mr. Andrew Thompson for his ray tracing solutions and are grateful to the U. S. Weather Bureau, U. S. Navy Fleet Weather Central and the National Aeronautics and Space Administration for data and information vital to this research.

#### REFERENCES

Baird, H.F. and C. Banwell, Recording of air pressure oscillations associated with microseisms at Christchurch, N.Z., J. Sci. Tech. 21B, 314, 1940.

Barber, N.F., The directional resolving power of an array of wave detectors in Ocean Wave Spectra, Prentice-Hall, Englewood, N.J., 1963.

Benioff, H. and B. Gutenberg, Waves and currents recorded by electromagnetic barographs, Bull. Am. Meteorol. Soc. 20, 41, 1939.

Daniels, F.B., Noise reducing line microphones for frequencies below 1 cps, J. Acoust. Soc. Am. 31, 529, 1959.

Donn, W., A case study bearing on the origin and propagation of 2 to 6 second microseisms, Trans. Am. Geophys. Un. 38, 354, 1957.

Donn, W., Natural infrasound of five seconds period, Nature, 215, 1469, 1967.

Donn, W. and E. Posmentier, Ground-coupled air waves from the great Alaskan earthquake, J. Geophys. Res. 69, 5357, 1964.

Donn, W. and E. Posmentier, Infrasonic waves from the marine storm of April 7, 1966, J. Geophys. Res. 72, 2053, 1967.

Donn, W., E. Posmentier, U. Fehr, N. Balachandran, Infrasound at long range from Saturn V, 1967, (subm. to Science).

Longuet-Higgins, M.S., A theory of the origin of microseisms, Phil. Trans. Roy. Soc. 24, No. 3, 1, 1950.

Longuet-Higgins, M.S., Can sea waves cause microseisms, Symposium on Microseisms, 1952, Natl. Acad. Sci.-Natl. Res. Council. Pub. 306, 74, 1953.

Posmentier, E., A theory of microbaroms, Geophys. J. 13, 487, 1967.

Posmentier, E., Source size as a theoretical limit on the determination of wave vectors by detector arrays, J. Acoust. Soc. Am. 43, 5, 1968

Posmentier, E. and W. Donn, Natural atmospheric infrasound of 0.1-0.4 Hz, (subm. to J. Geophys. Res.)

## SUBSONIC ATMOSPHERIC OSCILLATIONS

Richard K. Cook

Environmental Science Services Administration  
Geoacoustics Group  
Rockville, Maryland 20852

Some long-period oscillations, 300 seconds and greater, of sound pressure in the atmosphere travel at subsonic phase velocities, 30 m/s and greater, over the earth's surface. The subsonic waves are evidently generated by the jet stream. The distributions of sound pressures and atmospheric motions are obtained at various altitudes.

### Introduction

The passage of a jet stream in the atmosphere over the eastern (Atlantic) seaboard of the United States is occasionally accompanied by large oscillations in barometric pressure at infrasonic frequencies. The periods of oscillation are usually greater than five minutes, and the pressure fluctuations at the earth's surface are of the order of 100 dynes/cm<sup>2</sup>.

The jet stream is a thin layer of fairly high-speed wind. The location of the layer in the atmosphere is in the neighborhood of the tropopause, at an altitude of about 10 km. The thickness of the stream is about three kilometers. The wind speed along the axis is at least 30 meters/sec, and sometimes as great as 80 meters/sec. The wind blows towards a direction between northeast and southeast, and the width of the stream (in a direction transverse to the direction of flow) is generally at least 100 km.

The oscillations in barometric pressure, hereinafter referred to as "sound pressure," are measured by means of line-microphones located on the ground. The Washington station of our laboratory has an array of four such microphones located at ground level and spaced about 5 - 10 km apart. Each line microphone produces frequency-modulated voltages proportional to the sound pressure in the atmosphere. The voltages are transmitted by telephone wires to a recording location. Here they are demodulated, amplified and filtered, and recorded in analog form both as ink-on-translucent-paper traces, and on magnetic tape. An important feature of the recordings is the provision of accurate timing schemes. More complete technical details of the electroacoustical equipment are given in Reference (1).

The microphone array at the station is currently designed for the measurement of four principal characteristics of infrasonic waves. These are (1) the amplitude and waveform of the incident sound pressure, (2) the direction of propagation of the wave, (3) the horizontal phase velocity, and (4) the dominant period (or periods) of oscillation.

The results of observations made at our station in Washington, D. C. show that almost all sound waves coming from subsonic oscillations of the jet stream have wavefront surfaces of constant phase which are almost plane. The sound pressure has the following features when the jet stream is blowing. (1) The direction of propagation of lines of constant-phase sound pressure across the Washington area is very close to the direction of the jet stream over Washington. (2) The horizontal phase velocity  $c_0 = 30$  to 100 m/sec is about the same as the speed of the jet. (3) The sound pressures are mainly in the range 50 - 400 dynes/cm<sup>2</sup>. (4) Periods of oscillation  $T = 300$  to 1000 seconds.

A brief summary of a few observations made in Washington is given in Figure 1. The data show the correlation between the features of the sound pressure, and the characteristics of the jet stream causing the sound pressure. A detailed study of the waves observed at the Washington station has been made by Mary W. Hodge and her associates, see Reference (2). Further data on the Washington waves have been summarized by A. J. Bedard in Reference (3). Sound pressures caused by the jet stream have been observed elsewhere; a comprehensive report on waves in the Boston, Massachusetts area has been prepared by Elizabeth A. Flauraud and her associates, Reference (4).

The sound pressure probably has its origin in flow instability of the jet stream. The mechanism of the instability is not known. We can conjecture that it arises from a combination of viscous shear between the jet stream and the surrounding atmosphere, and unstable temperature gradients. We assume that the jet stream oscillations force the atmosphere into oscillation. The purpose of the investigation is determination of the

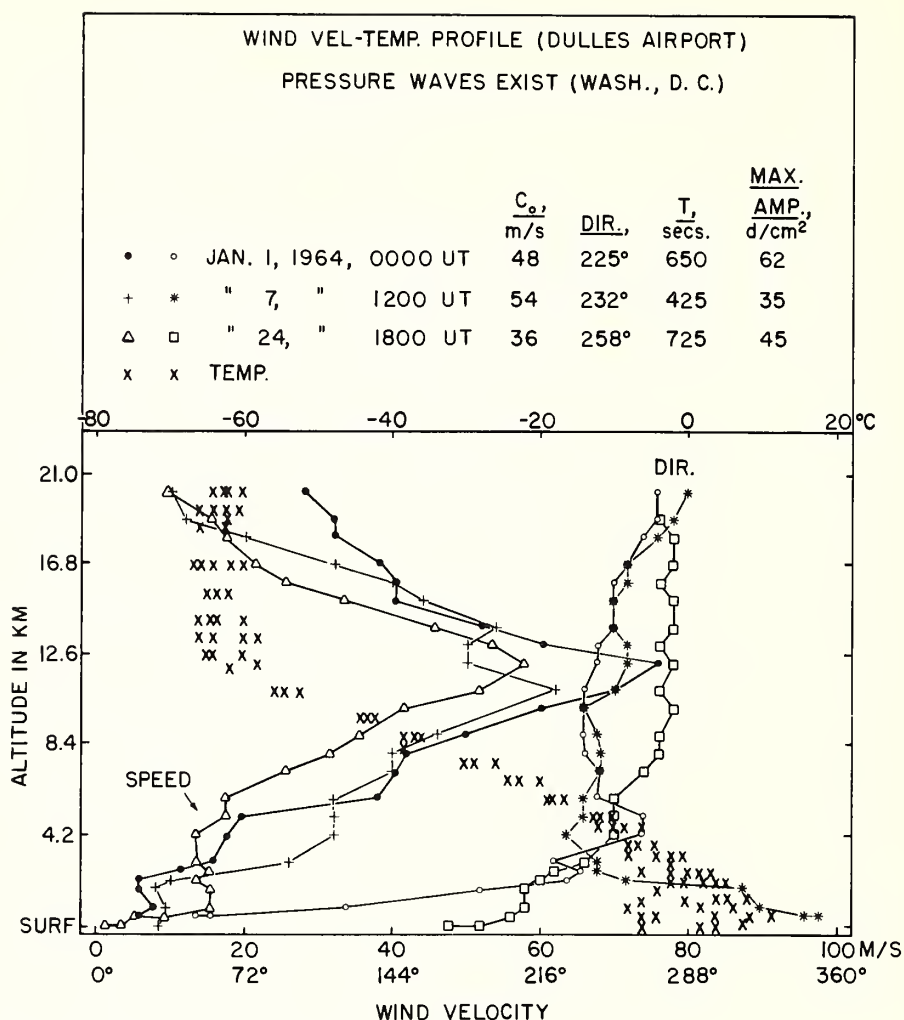


Figure 1. Observations on jet stream oscillations

relationship between the measured sound pressure and the oscillatory displacement of the jet.

#### Equations of Atmospheric Motion

The well-known equations of motion for sound waves in a wind-free atmosphere, see for example Reference (5), are presented here subject to the following conditions: (1) The atmosphere is isothermal and wind-free. (2) The waves are sinusoidal in time, and all quantities vary like  $\exp(i\omega t)$ . (3) All motions are in the  $x$ - $z$  plane, and so the particle velocity, with components  $u$ ,  $v$ ,  $w$ , has its  $y$ -component  $v \equiv 0$ , see Figure 2. (4) The traces of the straight lines of constant-phase sound pressure on the  $x$ - $y$  plane have a phase velocity  $c_o = \omega/k_o$ , and so all quantities vary like  $\exp(-ik_o x)$ ; the waves are advancing in the  $(+x)$  direction. The equations of motion reduce to

$$\frac{\partial}{\partial x} \left( \frac{\partial u}{\partial x} + \frac{\partial w}{\partial z} \right) + k^2 u - (g/c^2) \frac{\partial w}{\partial x} = 0 \quad (1)$$

$$\frac{\partial}{\partial z} \left( \frac{\partial u}{\partial x} + \frac{\partial w}{\partial z} \right) + k^2 w - (g/c^2) \frac{\partial w}{\partial z} - (\gamma - 1)(g/c^2) \left( \frac{\partial u}{\partial x} + \frac{\partial w}{\partial z} \right) = 0$$

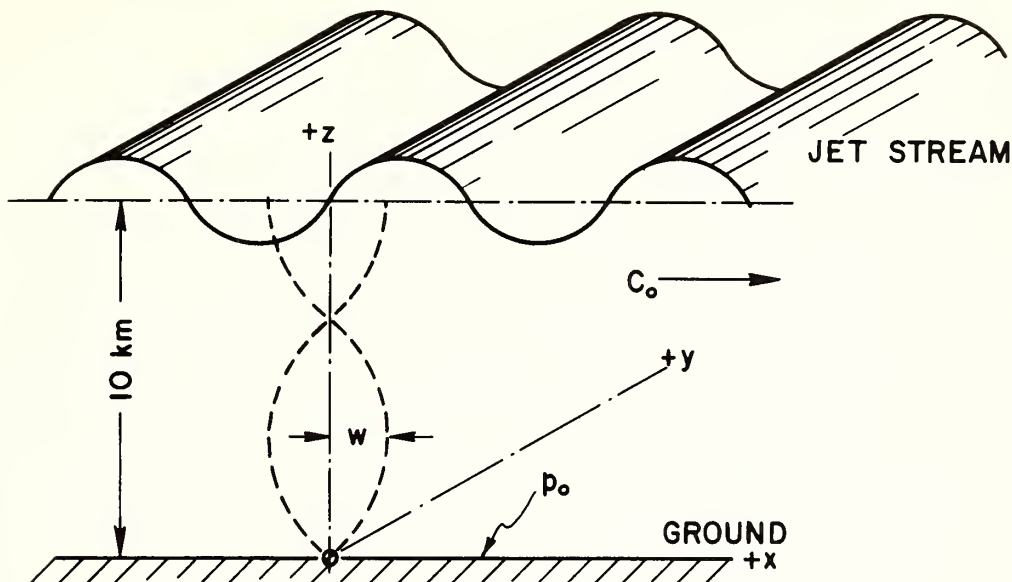


Figure 2. Radiation of sound pressure by jet stream oscillations

with the boundary condition  $w = 0$  at the  $xy$ -plane.  $\gamma = 1.40$  for the atmosphere,  $c$  = velocity of sound  $= \omega/k$ , and  $g$  = the acceleration of gravity. The components of particle velocity,  $\underline{u}$  and  $\underline{w}$ , vary with  $\underline{x}$  like  $\exp(-ik_0 x)$ , and with  $\underline{z}$  like  $\exp(Kz)$ .

$$\begin{aligned} u &= u_0 \exp(-ik_0 x + Kz) \\ w &= w_0 \exp(-ik_0 x + Kz) \end{aligned} \quad (2)$$

Introduction of these expressions into the equations of motion leads to a quadratic equation in  $K$ , from which the allowed values of  $K$  are given by

$$\begin{aligned} HK &= \frac{1}{2} \pm i \sqrt{\frac{\gamma-1}{\gamma} \cdot \frac{k_0^2}{k^2} - H^2(k_0^2 - k^2) - \frac{1}{4}} \\ &= \frac{1}{2} \pm i\beta \end{aligned} \quad (3)$$

where  $H$  = scale height of the atmosphere  $= c^2/\gamma g = 8.1$  km for an isothermal atmosphere with  $c = 333$  m/sec.

$\beta$  is a real number for a typical subsonic oscillation. By "subsonic" we mean that the phase velocity is less than the high-frequency limit for the speed of sound in an isothermal atmosphere. Between the jet stream and the ground, the atmosphere is traversed by both upward-going and downward-going plane waves, combined so as to have  $w = 0$  at the ground. The phase velocities are indicated in Figure 3 for two angles of incidence (and reflection),  $\alpha = 45^\circ$  and  $90^\circ$ . The curves are computed from Eq.(3).

The final expression for  $\underline{w}$  is

$$w = w_0 \sin(\beta z/H) \exp(z/2H - ik_0 x) \quad (4)$$

From this we see that the oscillatory amplitude of  $\underline{w}$  increases exponentially with altitude. The increase is inversely as the square root of the ambient atmosphere pressure.

The coefficient  $w_0$  can be computed from the measured sound pressure at the ground level,  $z = 0$ . The sound pressure is

$$p_0 = \frac{-\gamma \beta}{i\omega} \left( \frac{\partial u}{\partial x} + \frac{\partial w}{\partial z} \right), \text{ at } z = 0. \quad (5)$$

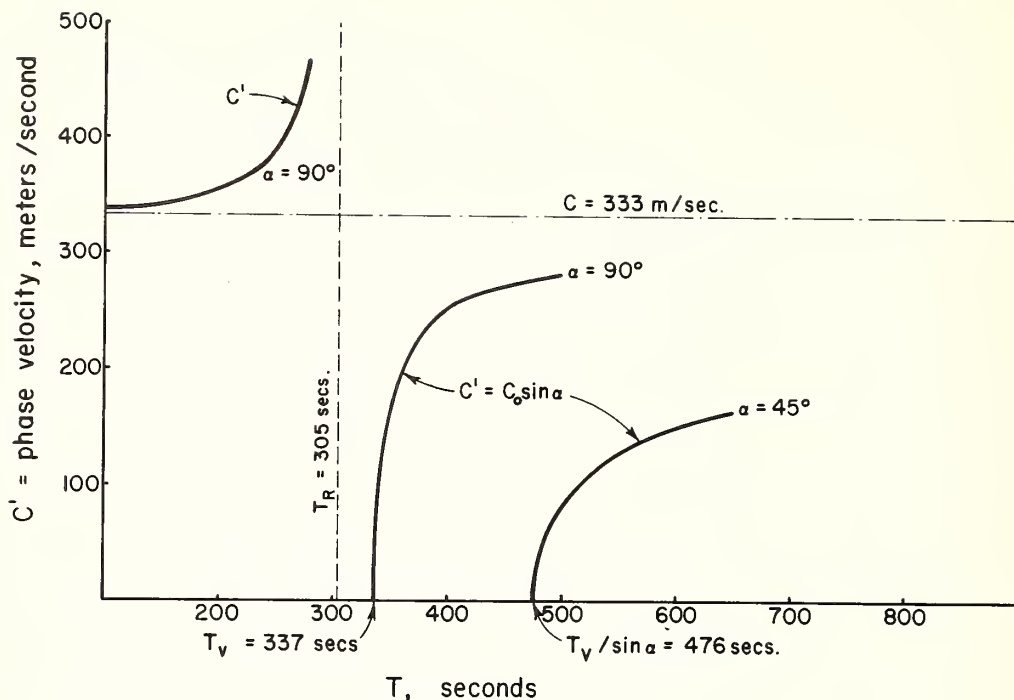


Figure 3. Phase velocities for sound waves in the atmosphere at very low frequencies

Combination of the expressions for  $\underline{w}$  and  $p_0$  with the equation of motion gives the following expression for the amplitude of the vertical component of particle displacement at the altitude  $z = 10$  km of the jet stream

$$\Delta z = 2H(k_0^2 - k^2) |p_0| / \beta \gamma B k^2 \quad (6)$$

As an example, consider a wave with  $T = 500$  secs,  $c_0 = 33$  m/sec ( $\approx c/10$ ), and  $|p_0| = 200$  dynes/cm<sup>2</sup>. We find  $\Delta z = 60$  meters, which must be the jet stream's vertical oscillatory displacement at an altitude of 10 km necessary to produce the measured sound pressure at the ground.

#### Standing-wave Hypothesis

The mechanism of the oscillation is not known, and there is no obvious limitation on the vertical component  $\beta/H$  of the wave-number vectors. We examine the conjecture that the vertical component  $\underline{w}$  of the particle velocity has a maximum at the jet stream's nominal altitude of 10 km, see Figure 1. From Eq.(4), this occurs approximately when

$$\beta z/H = \frac{\pi}{2}, \frac{3\pi}{2}, \frac{5\pi}{2}, \dots \quad (7)$$

Introduction of these values into Eq.(3) for  $\beta$  leads to a series of curves showing how the horizontal trace velocity  $c_0$  varies with the period of oscillation  $T$ . Two of the curves are shown in Figure 4. The curves all start with  $c_0 = 0$  at  $T_V = 337$  secs., this being the Väisälä period for the isothermal atmosphere ( $c = 333$  m/sec.) under consideration. Also plotted are some observed values of jet-stream horizontal phase velocities corresponding to well-defined periods of oscillation for the jet stream over Washington during January 1964. The data do not seem to confirm the hypothesis of Eq.(7). But evidently gravitational forces play a substantial role in the generation mechanism, since most of the observed oscillations occur at periods greater than the Väisälä  $T_V$ .



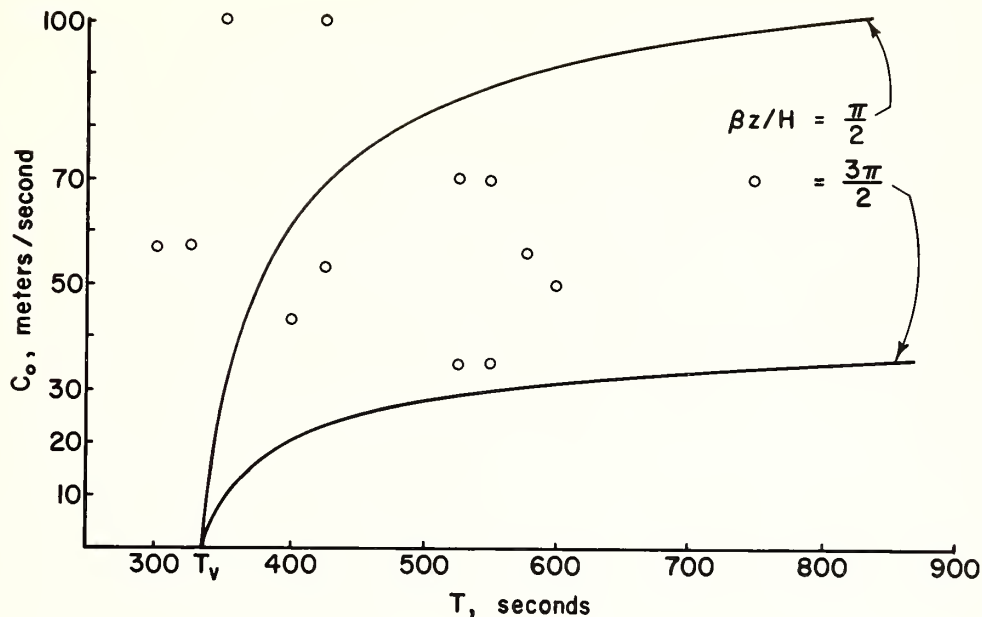


Figure 4. Horizontal phase velocities at various oscillation periods  
 o = observed velocities

#### Propagation to the Ionosphere

The displacement and velocity amplitudes in the jet stream, see Eqs.(6) and (4), can be expected to serve as sources for radiation of subsonic waves upward into the ionosphere. Eq.(4) shows that the amplitude of the vertical component  $\underline{w}$  of the particle velocity increases exponentially with altitude.

$$|\underline{w}| = w_j \exp[(z-10)/2H] \quad (8)$$

where  $\underline{w}_j = (2\pi/T)\Delta z$  = the amplitude at  $z = 10$  km. For the example given above,  $T = 300$  secs. etc., we find that at an altitude of  $z = 100$  km,  $|\underline{w}| \approx 100$  m/sec., and  $\Delta z \approx 9$  km. This estimate for  $|\underline{w}|$  is much greater than the phase velocity of the wave ( $\approx 30$  m/sec.). It appears that subsonic waves traveling upward will probably undergo substantial waveform changes, e.g., taking on a shock-wave configuration, well before reaching the ionosphere.

#### References

- (1) Richard K. Cook, "Strange sounds in the atmosphere" (Part I), Sound, Vol. 1, No. 2, pp. 12-16 (March 1962)
- (2) Mary W. Hodge & David T. Volz, "Possible relations of mesoscale surface pressure waves to the jet stream region and to clear air turbulence", Third National Conference on Aerospace Meteorology, pp 557-563 (New Orleans, Louisiana, May 6-9, 1968)
- (3) A. J. Bedard, Jr., "Some observations of traveling atmospheric pressure disturbances", National Bureau of Standards Report No. 9364 (July 1966)
- (4) E. A. Flauraud, A. H. Mears, F. A. Crowley, Jr., and A. P. Crary, "Investigation of microbarometric oscillations in Eastern Massachusetts", Geophysical Research Papers No. 27 of the Air Force Cambridge Research Center (May 1954)
- (5) H. Lamb, "Hydrodynamics", Dover Publications, New York (1945)



## "SUBSONIC" WAVES AND SEVERE WEATHER PHENOMENA

Howard S. Bowman

Environmental Science Services Administration

Geoacoustics Group

Rockville, Maryland 20852

A class of slow-traveling, low-frequency barometric-pressure associated waves was observed in the Washington, D. C. area. These waves are apparently associated with severe states of the local atmosphere. They were measured at the earth's surface and have characteristics similar to those of gravity waves. Experimental data are presented to verify a correlation.

At the infrasonic station in Washington, D. C., a class of slow-traveling, low-frequency waves was observed at the earth's surface. These waves have periods and velocities similar to certain internal gravity waves. In this report the waves are referred to as "subsonic" in the strict sense because their speed and frequency are below that of audible sound. Some of them have been associated with the jet stream near the tropopause, and some have been recently related to specific types of barometric pressure fluctuations. The literature (1,2,3,4,5) gives account of measurements of the movement of pressure systems across the earth's surface, and it is already known that some moving pressure systems are related to weather extremes. The object of this report is to present experimental data which tend to show a possible relation between a particular class of "subsonic" waves and severe or unusual weather phenomena. The particular weather conditions considered are those given in U. S. Department of Commerce's "Storm Data" reports containing data for the Washington, D. C. area between 1963 and 1968. In this paper, emphasis is placed on such weather types as severe snowstorms and hail-producing thunderstorms. Accounts of the particular weather phenomena are shown in the appendix.

Local weather information and barometric pressure data were obtained from the National Weather Records Center in Asheville, North Carolina; radar data were obtained from the Washington, D. C. National Airport weather station. Barometric pressure data were also obtained from records made in our laboratory on a specially designed, highly sensitive millibarograph that responds to short-period oscillations of atmospheric pressure in the order of minutes. Full-scale deflection on this instrument's recorder corresponds to ten millibars and the frequency response is within  $\pm 1$  dB between 0.1 and 0.001 Hz.

The "subsonic" waves were observed as ink tracings on transparent paper tapes. The tracings are the end product output of four infrasonic line microphones located about 5 to 10 km apart in the vicinity of Washington, D. C. The infrasonic measuring instrumentation has been described in the literature (6,7,8). Figure 1 is an example of four microphones' outputs. (In this figure and in Figure 3 a code is used to specify individual records, such as N9-8, D9-8, etc., where the letter refers to the microphone location, the first number refers to the pass band of interest, and the second number refers to the amplifier sensitivity setting.) The overlaid tracings in the lower portion of Figure 1 show the degree of coherence between the tracings when displaced along the time axis. The coherence of the overlay gives evidence of plane wave fronts passing the microphone array. Information on the time displacement of the overlaid traces and the known microphone locations was necessary to compute the horizontal trace velocity of the waves studied. The observed waves had periods between 4 and 15 min. and horizontal speeds between 10 and 100 m/s. The directions of the surface waves were associated with upper tropospheric jet winds and/or barometric pressure systems that were usually accompanied by severe local weather conditions.

The coherent waves noted on the overlaid tapes occurred during the same hour in which thunder was reported. These waves penetrated the high-frequency background pressure modulation of 7.6 m/s (17.0 mi/hr) local wind noise that existed throughout the entire interval. The "subsonic" waves and the thunder report were noted also during the time interval when the solid precipitation underwent a change of state (i.e., from light snow to light snow grains).

# SNOW AND THUNDER-RELATED SUBSONIC WAVES

WASH., D.C. AREA

( 1/13/64 )

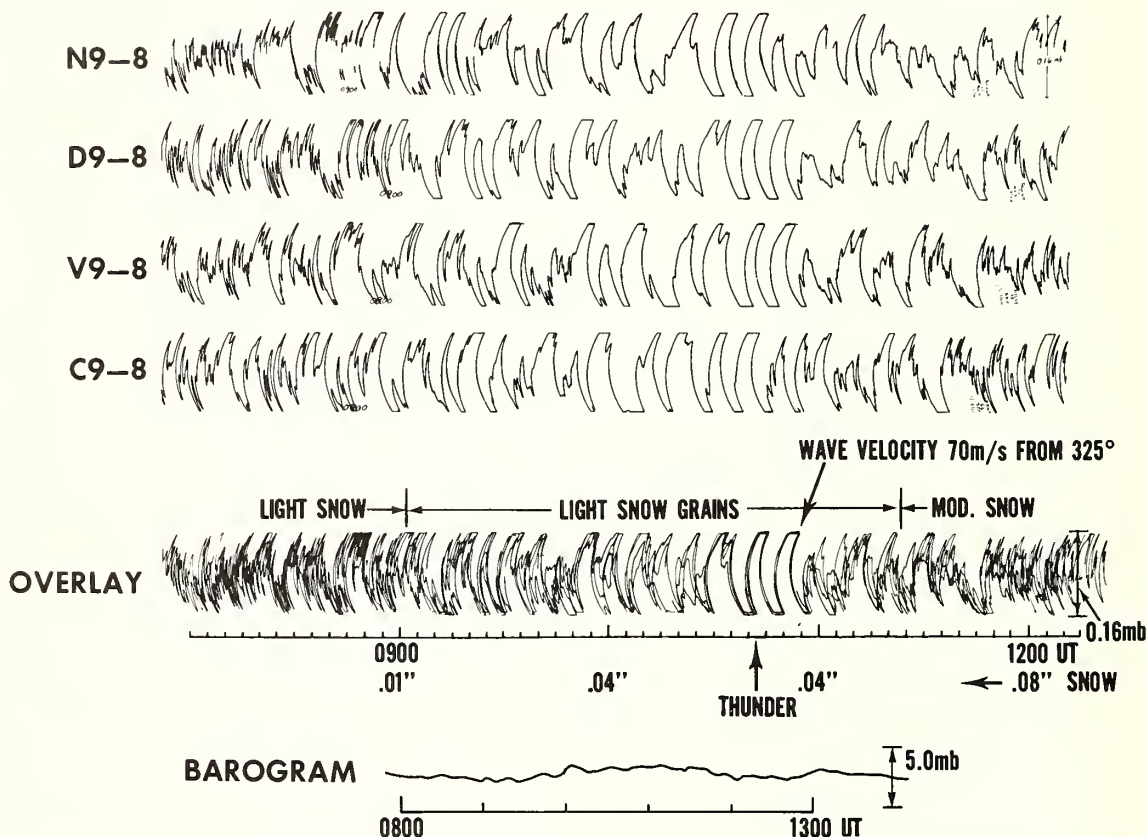


Figure 1. Tracings of four infrasonic microphones' outputs and corresponding barogram. The overlaid records and weather data show evidence of wave motion apparently associated with thunder and a change of state of solid precipitation in the area during a snowstorm.

The barogram given at the bottom of Figure 1 covers the same time interval as that of the curves above. The pressures considered in this report are peak-to-peak and not absolute values. The barometer used was a conventional aneroid type microbarograph which evidently does not respond to the short-period waves. In fact, the waves of approximately 7-min periods occurring at about 1045 UT are not shown on the barogram.

Concurrent records from the specially designed millibarograph and the infrasonic station showed a one-to-one correspondence between measurements of pressure changes. Figure 2 gives typical examples. The infrasonic wave phenomena displayed at the top left are characteristic of snow which started between 0840 and 0940 UT according to the radar report.

The snow-related waves were continuous during precipitation. The example for March 13, 1968, illustrates characteristic "subsonic" data related to a thunderstorm as compared with the atmospheric pressure data at the right. The first radar report of a thunderstorm coincides in time with the pulse on the infrasonic records and the pressure jump on the millibarograph record. Mr. A. J. Bedard, Jr., of our laboratory, associated "subsonic" waves with local thunderstorm

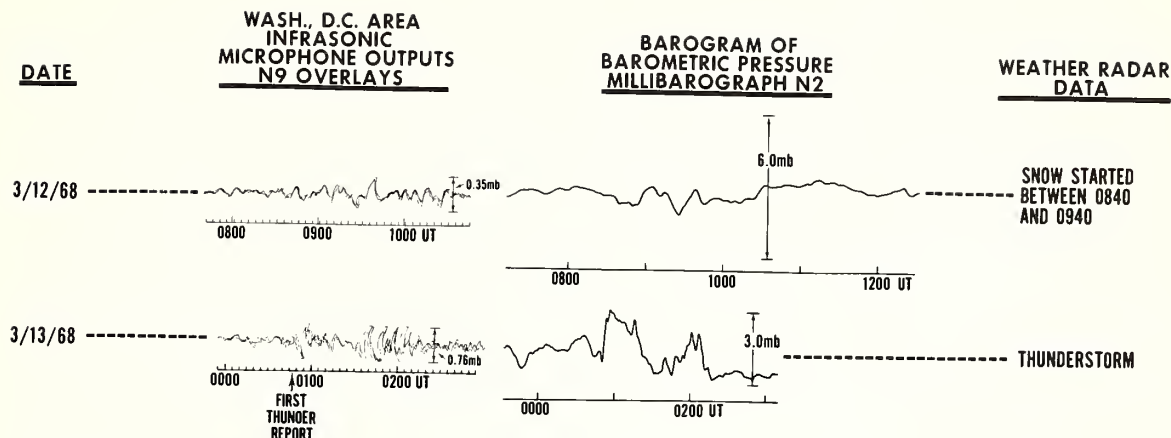


Figure 2. Records of infrasonic microphones' outputs with barometric pressure data from a highly sensitive millibarograph; also corresponding weather information.

activity, and the data presented here are in good agreement with his findings. The two events are not classed as severe. The data are shown in order to point out the fact that the infrasonic equipment responds to mild forms of certain weather phenomena.

An example of recorded "subsonic" pressure waves associated with a typical snowstorm yielding 3.4 in. of snow in 6-hr is given in Figure 3 for January 26, 1966. The computed horizontal trace velocity of the ground wave of 61 m/s from a direction of  $230^\circ$  is in good agreement with the winds near the tropopause. The vertical profiles of wind and temperature are shown at the right. The overlaid traces show good coherence throughout the interval.

Further examples of severe snowstorm-related "subsonic" waves are illustrated in Figure 4. The overlaid curves are presented, with corresponding weather data given below. The first set of curves for February 11, 1964, shows wave motion measured when 0.32 in. of snow and sleet fell during the 4-hr interval. Local wind speeds averaged 8.1 m/s (18.2 mi/hr) for the time shown. During this entire event local gusty winds reached gale proportions. The longest wave was noted when the radar echoes covered more than nine-tenths of the reported area. In that interval no jet stream existed aloft. However the speed of the "subsonic" waves at the earth's surface was approximately that of the wind speed near the tropopause. The set of curves for January 26, 1966, was discussed previously. Here the maximum pressure amplitudes measured approximately 240 dyn/cm<sup>2</sup>. In all cases the speed and direction of the ground waves were found to agree fairly well with the wind velocities in the neighborhood of the tropopause. This suggests a generating mechanism in that region. Waves of similar character have been observed in noctilucent clouds at altitudes near the mesopause, and their origin has been related to the region of the tropopause (9, 10). Whether the ground waves and noctilucent cloud waves stem from the same or similar source mechanism is a good question. The direction of the wave motion is in general the same as that of the moving weather systems as shown in Table I. Again, the wave motion is essentially continuous during the solid precipitation. The curves at the bottom of Figure 4 for January 29 and 30, 1966, are continuous data for the early stages of a snowstorm that reached blizzard proportions. Continuous coherent waves existed with constant velocity throughout the 12-hr interval shown.

The nature of the "subsonic" waves associated with thunderstorms was sporadic, and the longest period waves were in most cases related to hail-producing storms. Figure 5 gives examples of infrasonic data taken during times of typical hail-producing thunderstorms. The first two sets of curves show preliminary records for storms that produced hail about 5-hr later. The records show sporadic wave phenomena that coincide in time with the thunder reports. The two sets of curves at the bottom show infrasonic records for time intervals in which the hail was reported. The hail reports shown occurred for times corresponding to the long-period wave motion. Unfortunately the maximum amplitudes of these waves could not be determined because



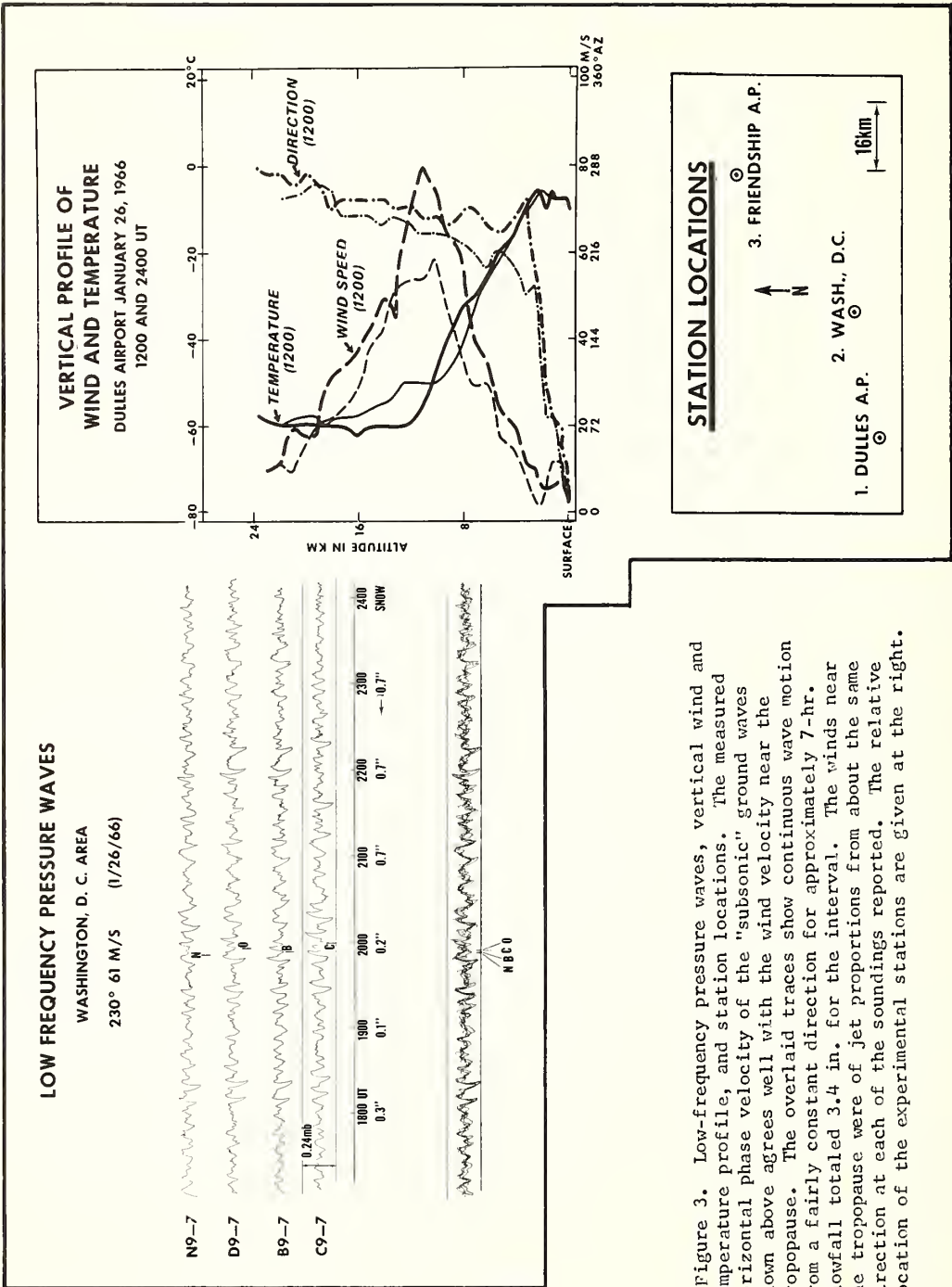
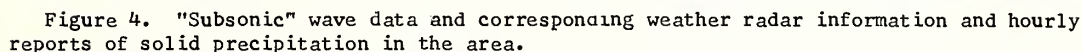


Figure 3. Low-frequency pressure waves, vertical wind and temperature profile, and station locations. The measured horizontal phase velocity of the "subsonic" ground waves shown above agrees well with the wind velocity near the tropopause. The overlaid traces show continuous wave motion from a fairly constant direction for approximately 7-hr. Snowfall totaled 3.4 in. for the interval. The winds near the tropopause were of jet proportions from about the same direction at each of the soundings reported. The relative location of the experimental stations are given at the right.

**WASH., D.C. AREA**



Date	Wave Data			Weather Data			
	Universal time	Azimuth degrees	Speed m/s	Universal time	Azimuth degrees	Speed m/s	Type
5/20/63	1752	307	13	1744	315	15	Thunder
1/27/67	1643	259	60	1641	260	12 1/2	Thunder
4/23/63	0745	262	28 1/2	1641	250	15	Thunder
				0744	286	24	Thunder & Hail
12/25/65	2000	271	17	1945	270	12	Thunder & Hail
1/13/64	1045	325	70	1044	340	20	Snow & Thunder
2/11/64	1245	220	29	1241	225	8	Snow
1/29/66	1900	209	78	1840	240	22 1/2	Snow

# HAILSTORM-RELATED SUBSONIC WAVES WASH., D.C. AREA

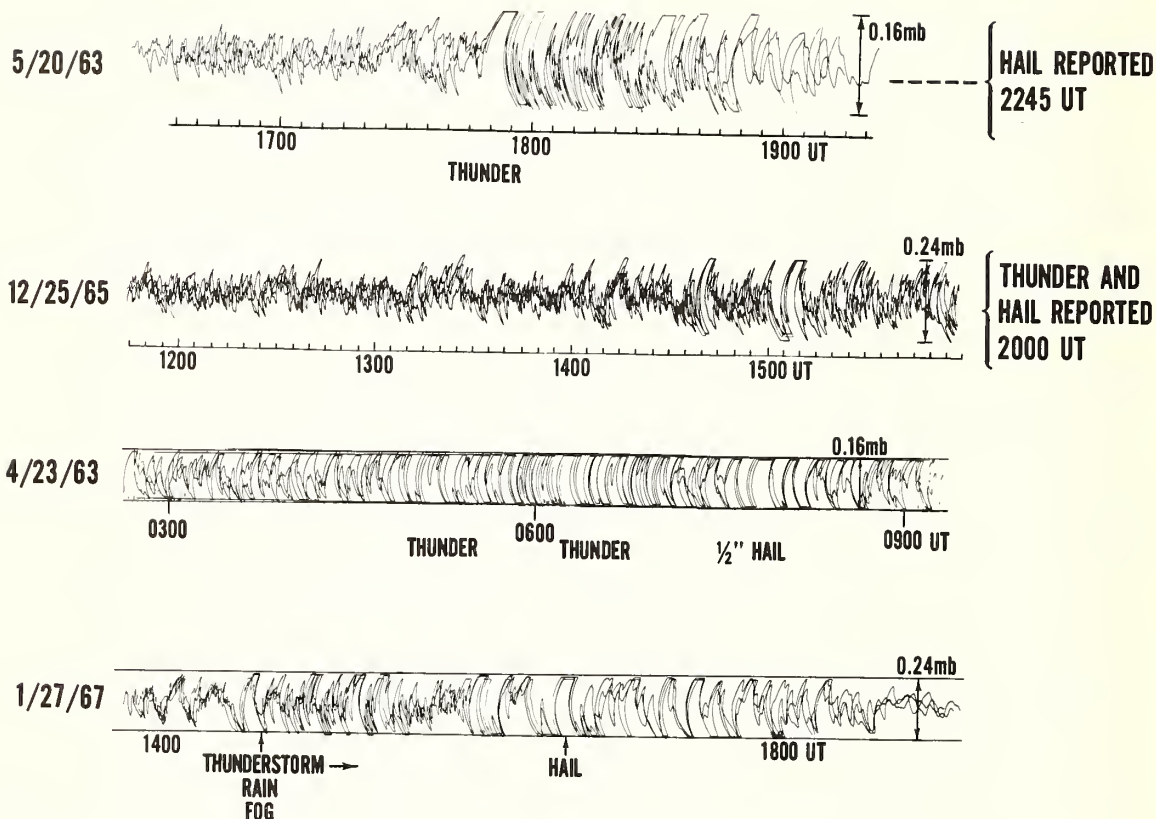


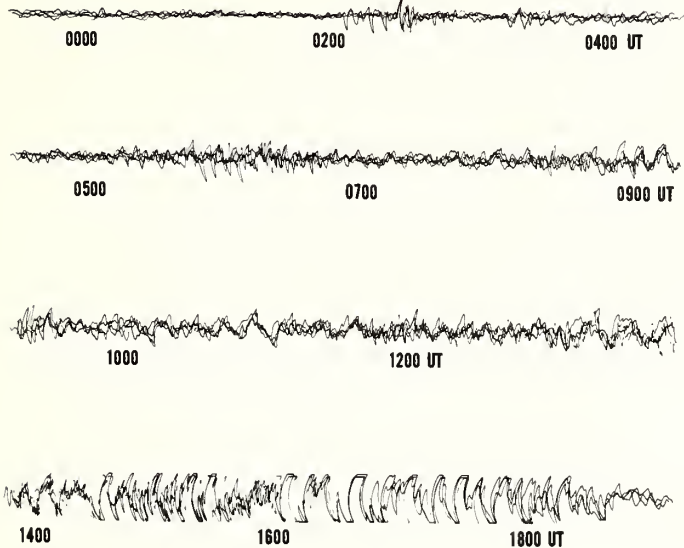
Figure 5. Hailstorm-related "subsonic" waves, with weather data noted as reported.

the recorders went over full scale at the time of the disturbances. These disturbances were not anticipated.

Observations were made during 18-hr before the occurrence of a tornado that was reported within a 60-mi radius of Washington, D. C., (See Appendix). Figure 6 shows the low-frequency information from the infrasonic station and the corresponding barometric pressure data from two ordinary aneroid barometers. All stations were inside the 60-mi radius. Being the only data available, these are shown merely to indicate their possible use in studying tornadic storms. A significant characteristic of the data is a series of sporadic events that occurred in about a 10-hr interval before 1805 UT when the tornado was observed about 60-mi away from the infrasonic microphones. The barogram trace for Dulles International Airport indicates a pressure jump of more than 5 mb at 1530 UT. The trace for Friendship International Airport about 65-mi away shows an even greater barometric pressure jump at 1630 UT. This information related favorably to an apparent moving pressure system and to the hail report in the Washington, D. C., area at about 1620 UT.

In conclusion, experimental evidence demonstrates that barometric-pressure-related "subsonic" waves are apparently associated with extreme weather phenomena. These particular waves were observed at the earth's surface on very sensitive infrasonic measuring equipment and were related to snowstorms and thunderstorms. The hail-producing thunderstorms were associated with waves of the longest periods. The directions of the moving waves were in general related to that of the weather systems and/or upper winds. The horizontal speed of the waves also appeared to be under the influence of winds aloft.

**LOW FREQUENCY PRESSURE WAVES**  
**WASH., D.C. AREA**  
**( 1/27/67 )**



**BAROMETRIC PRESSURE**  
**DATA**  
**(1/27/67)**

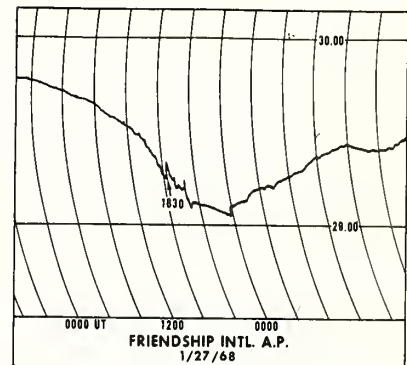
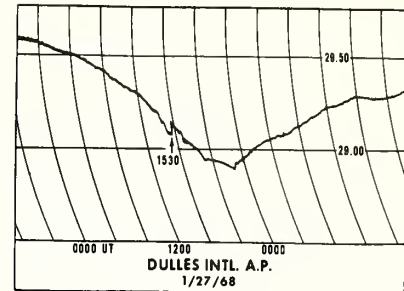


Figure 6. Low frequency pressure wave data and barometric pressure data for a time period associated with a tornado occurring at 1805 UT within a 60 mile radius of the Washington, D. C. infrasonic station.

Acknowledgements. I would like to thank Dr. Jessie M. Young for his invaluable suggestions, encouragement, and discussions of the material presented here. I am most grateful to the Geoacoustics staff whose splendid cooperation and teamwork were necessary for the completion of this work. Also my thanks and appreciation to Mr. Richard K. Estes, of ESSA's Graphic Arts Group, for his art work on this paper.

**References**

1. A.H.R. Goldie, "Waves at an Approximately Horizontal Surface of Discontinuity in the Atmosphere," Quart. J. Roy. Meteorol. Soc., Vol. 51, (1925)
2. R.D.M. Clark, "Atmosphere Micro-Oscillations," J. Meteorol. Vol. 7, (1949)
3. E.E. Gossard, "Gravity Waves in the Lower Troposphere over Southern California," U. S. Navy Electronics Lab. Report 709, San Diego, California, (1956)
4. C. East, "A Technique for Analysing Meso-Scale Pressure Patterns," McGill Univ. Scientific Report MW-35, (1961)
5. W.L. Donn & W.T. McGuinness, "Air Coupled Long Waves in the Ocean," J. Meteorol., Oct. (1960)
6. P. Chrzanowski, G. Greene, K. T. Lemmon, & J. M. Young, "Traveling Pressure Waves Associated with Geomagnetic Activity," J. Geophys. Res., Vol. 66, No. 11, Nov. 1961, pp. 3727-3733
7. R.K. Cook, "Subsonic Atmospheric Oscillations," presentation at the Symposium on Acoustic Gravity Waves, ESSA/ARPA, Boulder, Colorado, July 15-17, 1968
8. J. M. Young, "Experimental Observations of Tropospheric Jet Stream Waves," presentation at the Symposium on Acoustic Gravity Waves, ESSA/ARPA, Boulder, Colorado, July 15-17, 1968
9. B. Haurwitz, "Wave Motion in Noctilucent Clouds," presentation 49th Annual Meeting, American Geophysical Union, Washington, D. C. (1968)
10. A.D. Christie, "Synoptic Distributions of Noctilucent Clouds," presentation 49th Annual Meeting, American Geophysical Union, Washington, D. C. (1968)



# APPENDIX

## U. S. DEPARTMENT OF COMMERCE

C.R. SMITH Secretary

### ENVIRONMENTAL SCIENCE SERVICES ADMINISTRATION

#### ENVIRONMENTAL DATA SERVICE

### STORM DATA AND UNUSUAL WEATHER PHENOMENA

PLACE	DATE	TIME	LENGTH OF PATH (MILES)	WIDTH OF PATH (YARDS)	NO OF PERSONS				ESTIMATED DAMAGE	CHARACTER OF STORM
					KILLED	INJURED	PROPERTY	CROPS		

(JAN. 1964)

MARYLAND Statewide and District of Columbia	12-13				10	28	4	0		Snow, strong winds, high tides.
--	-------	--	--	--	----	----	---	---	--	---------------------------------

Snow, ranging from 4-6 inches in southern areas, to 16-18 inches in mountains, was heaviest in 3-6 years for some areas; over the coastal areas of southern Eastern Shore it was mostly rain. Drifting snow kept road crews busy. At least two traffic fatalities occurred during storm. Two deaths in Baltimore and at least one in the "wrens" (Goldboro) were caused by snow shoveling. Five deaths in Washington, D. C. were attributed to storm. At least 28 persons were treated in Baltimore hospitals for injuries from falls. High tides, 2 to 4 feet above normal, flooded many streets in Ocean City but little damage was reported. During snowstorm a thunderstorm was reported in both Talbot and Kent counties between 5 and 6 AM of 13th.

(FEB. 1964)

Statewide, including District of Columbia	10-11				0	0	4	0		Snow
---	-------	--	--	--	---	---	---	---	--	------

Storm yielded from 4 to over 11 inches of snow with heaviest amounts in the central and north-central sections. Heavy snow removal equipment brought out in force. Many minor traffic accidents reported. At least one death, that of a man in Washington, D. C. from overexertion in shoveling snow, was indirectly caused by storm.

(JAN. 1966)

Statewide and District of Columbia	26-27									Snow
------------------------------------	-------	--	--	--	--	--	--	--	--	------

A second major storm followed closely the weekend storm of January 22nd-23rd. Heaviest snowfall was in the southern and central portion where totals ranged from 10 to 17 inches; elsewhere it ranged from 6 to 10 inches except in western portion where totals were generally the least, from 2 to 5 inches. Snowfall, 11 to 14-inch in southern Eastern Shore and 12 to 17-inch in the St. Marys County area, was the heaviest since January 1940. Drifts up to 6 feet were reported in almost all areas; these greatly hampered transportation and travel. Traffic accidents, however, were generally the "fender-bender" variety. Newspapers listed at least four storm deaths, three in Maryland and one in District of Columbia. All were heart attack victims apparently from overexertion from shoveling snow or being stalled automobiles. Schools were closed one to two days.

(JAN. 1966)

Statewide and District of Columbia	29-30				12					Blizzard
------------------------------------	-------	--	--	--	----	--	--	--	--	----------

This third and the most severe storm since January 22nd, met the weather Bureau definition of a blizzard. Snowfall was heavy, 16 inches or more in Northern Central, Lower Southern and Central Eastern Shore Divisions and also in some areas of the Appalachian Mountain Division. The least amount was found in Garrett County area where 6 to 10 inches were reported. Winds, reaching gale force, caused heavy drifting generally 3 to 6 feet but as much as 12 to 15 feet. Near zero or sub-zero temperatures were recorded in the 27th and temperatures on both days did not generally reach 40°F above. This snowfall plus the previous snowfall gave some record of near record depths. Up to 20 inches or greater were found in all areas of the state; the greatest was 34 inches reported at Catoctin Mountain Park near Thurmont. Practically every highway was closed at one time or other. Helicopters were used to airlift patients and drop supplies. State newspapers reported at least 35 storm-related deaths in Maryland and 5 in District of Columbia; of these, as many as 20 were victims of heart attacks apparently from shoveling snow or trying to dig through snow. Many schools were closed as many as 5 days. The Coast Guard reported extremely hazardous conditions on the Chesapeake Bay with gale force winds and up to 7 inches of solid ice in the upper portion of the bay. The problem of getting and keeping roads and streets open was a most costly one for state, county and municipal governments. Fortunately, telephone and power service was little affected by this storm as well as the 2 earlier ones.

(APR. 1963)

MARYLAND Entire State	23	3:00 PM - 8:00 PM			1	10+	5	3		Wind
--------------------------	----	-------------------	--	--	---	-----	---	---	--	------

Agate winds reached 60-70 mph in gusts, breaking windows, blowing down signs and trees. One man was killed near Pocomoke when a tree fell on him. At least 6 others were injured by falling limbs and trees. Ten men were injured when winds caused the collapse of 2 apartment buildings at Silverdale. A brick bare wall was blown out in Carroll County. Half the stock of marble fell north of Hagerstown. Blossoms and spruce were blown from fruit trees. A Greenhouse at Bozman was damaged. Utility lines were broken and roads blocked by fallen trees.

(MAY 1963)

Beltair ★	20	Afternoon			0	1	4	0		Wind
-----------	----	-----------	--	--	---	---	---	---	--	------

Windstorm of "Tornado" force blew down trees and utility wires.

(DEC. 1965)

Central and Eastern Counties and District of Columbia	25	Afternoon and Evening			0	0	0	0		Thunderstorms
---	----	-----------------------	--	--	---	---	---	---	--	---------------

Numerous thunderstorms and unseasonably warm temperatures were reported on Christmas Day. Hail, 3-inch in size, was also observed in north central area. Rain totals were generally 3-inch or less. This was the first time thunderstorms were reported for this date by Baltimore Weather Bureau; records include period from 1893.

(JAN. 1967)

Statewide	27	Late morning & afternoon			0	0	5	0		Lightning, wind & hail
-----------	----	--------------------------	--	--	---	---	---	---	--	------------------------

Widespread thunderstorm activity was reported. Several homes were struck by lightning and a Baltimore club was damaged to the extent of several hundred thousand dollars by a fire apparently started by a lightning strike. Strong gusty winds caused some local damage, including the snapping of several telephone poles in Cambridge area. Hail was also reported but no size was given.

sollywood, St. Mary's County ★	27	1:05 p. m.	2N	30-50	0	0	3	0		Tornado
--------------------------------	----	------------	----	-------	---	---	---	---	--	---------

A black funnel cloud was observed, moving in a narrow line from SW to NE and touching ground in several places. Damage was limited to uprooting sixteen large trees in a line, ripping off a section of a school roof and demolishing several sheds.

† Storm damage are placed in categories varying from 1 to 9 as follows:

- 1 Less than \$50
- 2 \$50 to \$500
- 3 \$500 to \$5,000
- 4 \$5,000 to \$50,000
- 5 \$50,000 to \$500,000
- 6 \$500,000 to \$5,000,000
- 7 \$5,000,000 to \$50,000,000
- 8 \$50,000,000 to \$500,000,000
- 9 \$500,000,000 to \$5,000,000,000.

★ WITHIN 60 MI. RADIUS OF WASH., D.C.



## **IV** Atmospheric wave propagation in the terrestrial environment



Ducting of Internal Gravity Waves  
in a Temperature- and Wind-Stratified Atmosphere

C. A. Reddy

High Altitude Observatory  
National Center for Atmospheric Research  
Boulder, Colorado, 80302 U. S. A.

SUMMARY

One major feature of the Travelling Ionospheric Disturbances (TID's) is that they travel over large horizontal distances with comparatively small attenuation. This was explained by Hines [1960] as due to the continuous upward leakage of internal gravity waves which are imperfectly ducted between ground and different atmospheric levels with steep temperature gradients. Friedman [1966] made a thoroughgoing study of this ducting process caused by the temperature structure. The large scale wind systems in the middle atmosphere and in the lower ionosphere can cause substantial reflection of internal gravity wave energy [Hines and Reddy, 1967], and thus modify the mode structure involved in the process of energy leakage upward into the F-region. This effect of the atmospheric winds has been investigated, and some early results are reported here.

The temperature structure in the 0-240 km height range above ground has been adopted from the U. S. Standard Atmosphere 1965. It is shown in Figure 1. Then two wind models  $W_1$  and  $W_2$  are used in turn. Wind model  $W_1$  consists of a typical winter-time, mid-latitude zonal wind system in the 0-90 km region above ground, with a broad maximum of 82 meters  $\text{sec}^{-1}$  at about 65 km height, and a smaller but sharper second maximum of 35 meters  $\text{sec}^{-1}$  at 12 km level. Winds are assumed to be horizontal and in the same direction at all levels, and they are assumed to vanish above 90 km, in this model. In model  $W_2$ , a typical tidal wind system in the 90-150 km region is added to the wind system of model  $W_1$ . Again, the winds are assumed as horizontal and acting in the same vertical plane at all levels but the wind directions are assumed to differ by  $180^\circ$  at different height intervals. The two wind models are shown in Figure 2. Using the multilayer approximation (120 layers of 2 km thickness have been used), and using the appropriate upper, lower and interfacial boundary conditions, the possible 'modes' (i.e. the real and imaginary parts of the complex horizontal wave number) are identified for given wave periods in the range of 15-200 minutes. The 'modes' are identified for  $\phi = 0^\circ$  to  $180^\circ$ , where  $\phi$  is the angle between the direction of the horizontal wave velocity and the direction of the background wind.

A systematic (computer) search has been made in the domain of  $V_x = 50$  to 800 meters  $\text{sec}^{-1}$  and  $-k_i/k_x = 10^{-8}$  to 1 to identify all possible modes. All the modes with  $V_x \geq 110$  m/s at  $\phi = 90^\circ$  are listed in Table 1 for three values of  $\phi$ . Here  $V_x (= \omega/k_x)$  is the horizontal phase velocity, and  $k_x, k_i$  are the real and imaginary parts of the complex horizontal wave number. Many modes with  $V_x < 110$  m/s have been found but these are not shown here for the following reason: most of these lower  $V_x$  modes do not persist throughout the  $\phi$  range of  $0^\circ - 180^\circ$ , even though the critical level (i.e. where  $V_x = U$ , the background wind velocity)

has been avoided in all cases; and this behavior and its causes are still being investigated. The large effect of wind model  $W_2$  on two modes is shown in Fig. 3.

$\phi = 0$  case corresponds to waves with their horizontal phase propagation along the direction of the winds, while  $\phi = 180^\circ$  corresponds to horizontal phase propagation opposite to the wind direction. The effect of the winds is expected to be a maximum in each of these two cases, while it vanishes for  $\phi = 90^\circ$ , i.e. when the phase propagation is across the background wind. This case ( $\phi = 90^\circ$ ) gives the temperature modes that would obtain in the absence of winds at all levels. From Table 1 it is clear that  $V_x$  is greatly altered by the wind systems in almost all cases, while in many cases  $-k_i/k_x$  is also affected substantially.  $V_x$  values are found to decrease continuously in most cases as  $\phi$  is increased from  $0^\circ$  to  $180^\circ$ , though the rate of decrease is highly variable from mode to mode. On the other hand, the variation of  $-k_i/k_x$  with  $\phi$  is more complicated; for many modes,  $-k_i/k_x$  exhibits one or even two maxima in the range of  $\phi = 0^\circ$  to  $180^\circ$ .

The height variations of the kinetic energy density, the vertical wave number, and also the energy flow lines have been computed for most of the modes. These results are not reproduced here, but they show that the background wind systems modify - substantially for some modes and insignificantly for others - the ducting effects of the temperature structure at various levels.

In conclusion, the results indicate that in any detailed application of the 'mode analysis' to ionospheric observations, the effects of the atmospheric wind systems should be taken into account.

#### REFERENCES

- Friedman, J. P., Propagation of Internal Gravity Waves in a Thermally Stratified Atmosphere, J. Geophys. Res., 71, 1033-1054, 1966.
- Hines, C. O., Internal Atmospheric Gravity Waves at Ionospheric Heights, Canad. J. Phys., 38, 1441-1481, 1960.
- Hines, C. O., and C. A. Reddy, On the Propagation of Atmospheric Gravity Waves through Regions of Wind Shear, J. Geophys. Res., 72, 1015-1034, 1967.

Table 1 - Ducted Modes at a Frequency of  $\omega = 0.5 \times 10^{-3} \text{ sec}^{-1}$ ;  
(Modes with  $V_x < 110 \text{ m/s}$  at  $\phi = 90^\circ$  are not shown here;  
 $V_x$  is in meters  $\text{sec}^{-1}$ .)

	Wind Model $W_1$						Wind Model $W_2$					
	$\phi = 0$		$\phi = 90^\circ$		$\phi = 180^\circ$		$\phi = 0$		$\phi = 90^\circ$		$\phi = 180^\circ$	
	$V_x$	$-k_i/k_x$	$V_x$	$-k_i/k_x$	$V_x$	$-k_i/k_x$	$V_x$	$-k_i/k_x$	$V_x$	$-k_i/k_x$	$V_x$	$-k_i/k_x$
1	413	.214	413	.213	412	.213	416	.206	413	.213	410	.220
2	338	$7.7 \times 10^{-5}$	311	$3 \times 10^{-5}$	293	$2.6 \times 10^{-5}$	338	$1.2 \times 10^{-4}$	311	$3 \times 10^{-5}$	295	$4 \times 10^{-5}$
3	271	.083	271	.083	271	.084	275	.061	271	.083	277	.066
4	307	$2.7 \times 10^{-4}$	254	.004	(220) <sup>a</sup>	(.025) <sup>a</sup>	308	$5.6 \times 10^{-4}$	254	.004	207	.005
5	226	.013	216	.055	(217) <sup>b</sup>	(.054) <sup>b</sup>	252	.069	216	.005	212	.090
6	213	.047	181	.032	177	.066	222	$1.8 \times 10^{-3}$	181	.032	176	.027
7	186	.018	173	.043	154	.045	180	.092	173	.043	160	.060
8	174	.051	153	.039	139	.016	185	.002	153	.039	138	.004
9	160	.021	137	.024	126	.044	163	.004	137	.024	130	.061
10	148	.025	125	.035	112	.039	(148) <sup>c</sup>	(.010) <sup>c</sup>	120	.035	(106) <sup>c</sup>	(.035) <sup>c</sup>
11	140	.015	114	.031	100	.040	142	.038	114	.031	(108) <sup>a</sup>	(.031) <sup>a</sup>

a. values at  $\cos \phi = -.7$

b. Mode jumping might be present

c. This mode exists throughout  $\phi = 0$  to  $180^\circ$  only for some wave frequencies.



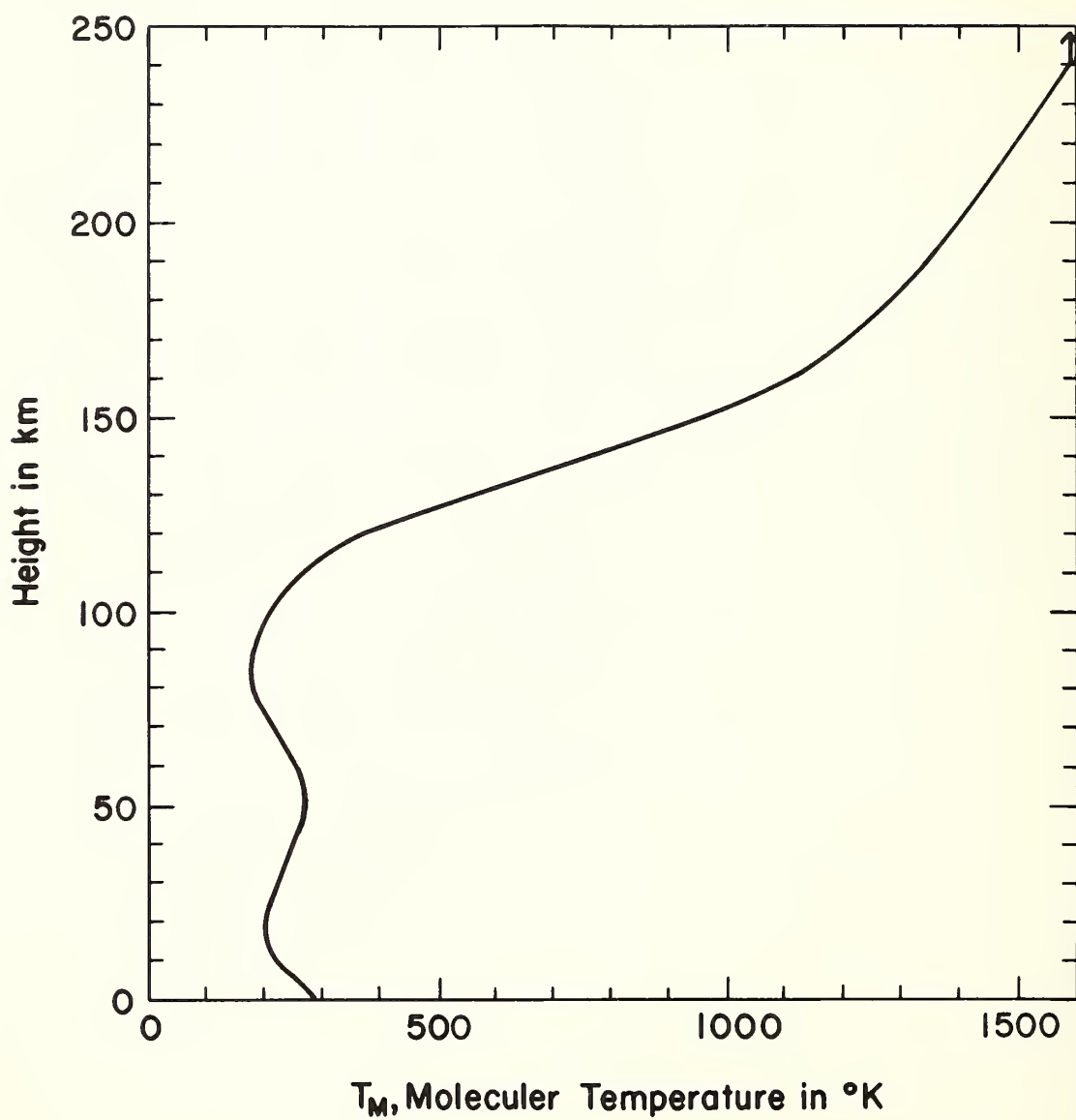


Fig.1

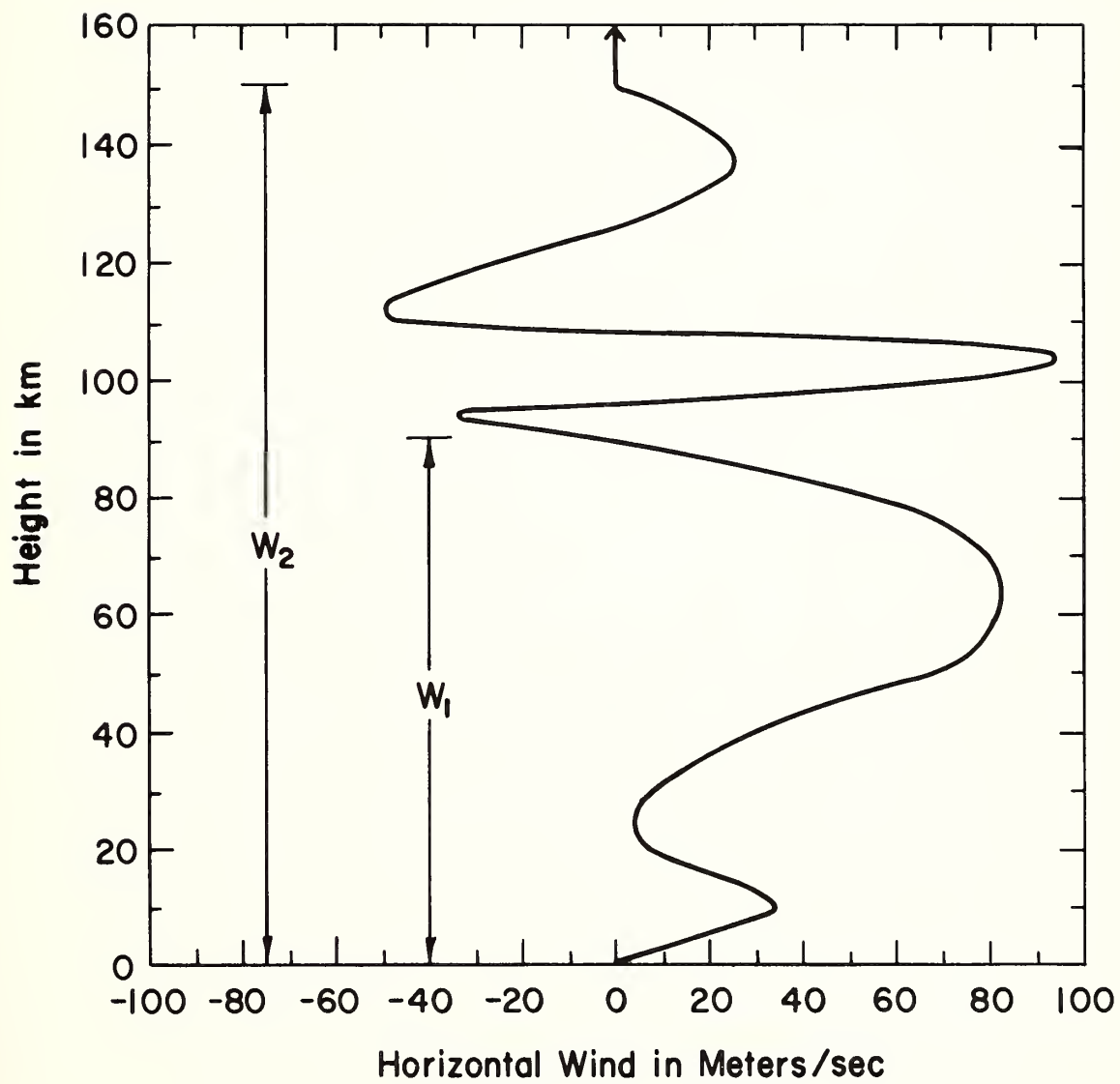


Fig.2

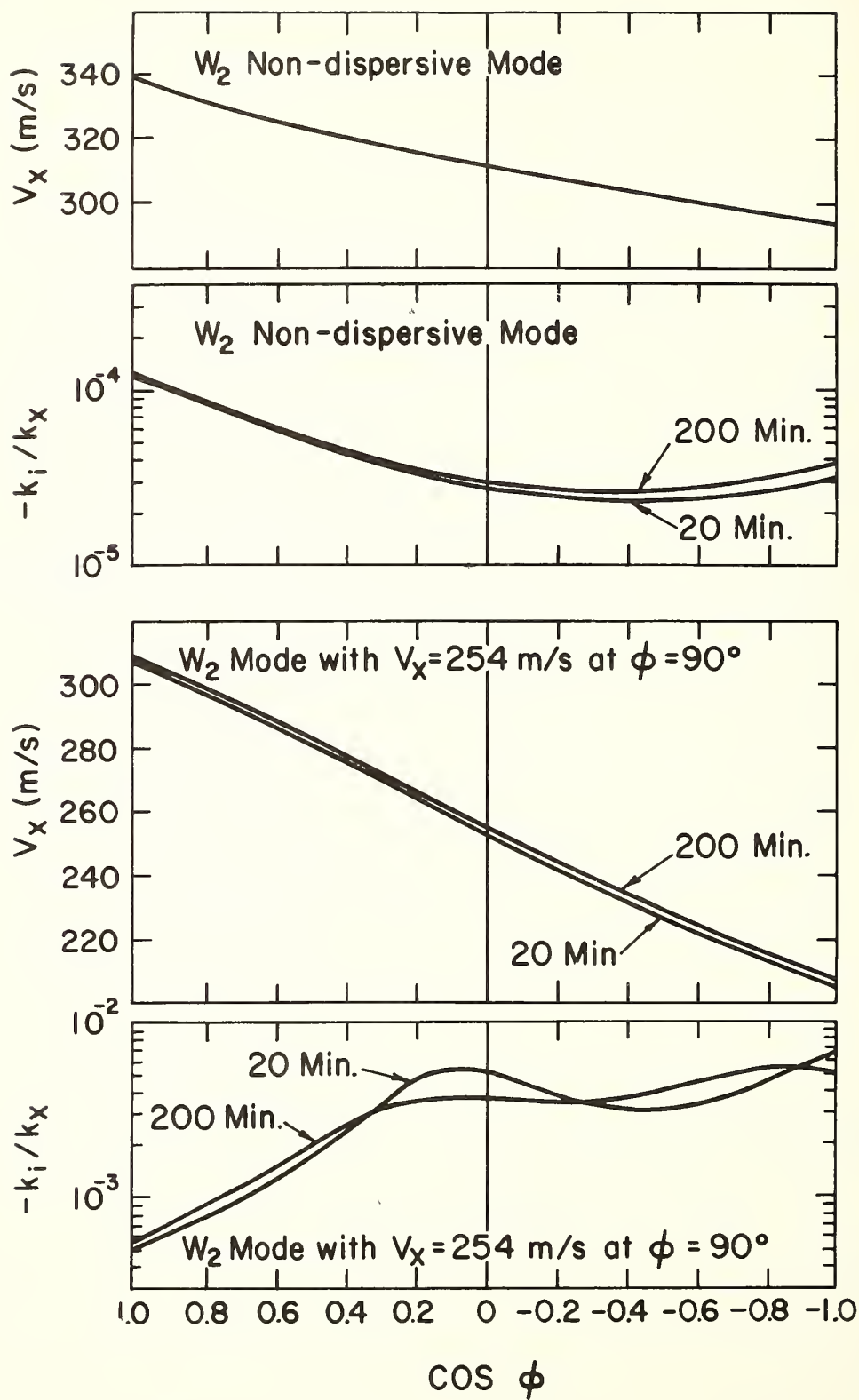


Fig.3

# SOME SPECULATIONS ON THE ROLES OF CRITICAL LEVEL INTERACTIONS BETWEEN INTERNAL GRAVITY WAVES AND MEAN FLOWS

Richard S. Lindzen  
University of Chicago

## 1. INTRODUCTION

There has been much recent interest in the effect of a mean horizontal flow on the propagation of internal gravity waves (Eliassen and Palm, 1960; Booker and Bretherton, 1967; Hines and Reddy, 1967; Jones, 1967). Especially significant is the absorption of internal gravity waves at levels where the mean zonal flow,  $U(z)$ , and the gravity wave's horizontal phase speed,  $c$ , are equal. Since upward propagating gravity waves are known to carry not only energy but horizontal momentum, the absorption of a wave by the mean flow must result in the absorption of that momentum by the mean flow and the consequent modification of that flow. Although we are, at present, unable to study the mutual interaction between waves and flow with mathematical rigor, it is possible, using models of varying degrees of idealization, to suggest some things gravity waves could do to a mean flow. The examples described are taken from a paper by Lindzen and Holton (1968) as is the basic analysis.

## 2. EQUATIONS FOR CHANGE OF MEAN FLOW

Let us consider an internal gravity wave of wave number  $k$ , and a phase speed,  $c$ , in some horizontal direction,  $x$ . Let the basic flow,  $U$ , be in the  $x$ -direction, and let  $U$  be a function only of altitude,  $z$ . Primed quantities will refer to wave fields, and overbars will refer to averages with respect to  $x$  and  $t$ . It was shown by Eliassen and Palm (1966) that  $\overline{p'w'}$  (where  $p'$  and  $w'$  are the pressure and vertical velocity fields associated with the wave) is the upward energy flux due to the wave, and that  $\rho_0 \overline{u'w'}$  (where  $\rho_0$  is the basic density distribution, and  $u'$  is the velocity field in the  $x$ -direction due to the wave) is the upward flux of momentum in the  $x$ -direction due to the wave. The following important relations were derived by Eliassen and Palm (1960):

$$\overline{p'w'} = -\rho_0(U - c) \overline{u'w'}, \quad (1)$$

and if  $U \neq c$

$$\frac{d}{dz} (\rho_0 \overline{u'w'}) = 0. \quad (2)$$

Let  $x$  represent the west to east direction, and let our wave source be below our region of interest. Then  $\overline{p'w'}$  will be positive and eqn. (1) states that waves whose phase speeds are westerly relative to  $U$  will carry westerly momentum upwards, while waves whose phase speeds are easterly relative to  $U$  will carry easterly momentum upwards. Equation (2) states that in the absence of a critical level where  $U = c$ , none of this momentum will be deposited in the mean flow. Eliassen and Palm (1960) do not deal with the problem of what occurs at a critical level. However, from (1) and (2) it is clear that something striking must happen. For example, assuming  $\overline{p'w'}$  remains positive as a wave goes through a critical level, then (2) certainly cannot remain true. Equation (1) suggests that  $\rho_0 \overline{u'w'}$  must, in fact, change sign--implying a large exchange of momentum between the wave and the mean flow. Booker and Bretherton (1967) have solved the problem of the behavior of internal gravity waves at critical levels, and their results confirm the above picture. Let the wave source be below the critical level and let

$$\rho_0 \overline{u'w'} = A \quad (3)$$

below the critical level. Booker and Bretherton show

$$\rho_0 \overline{u'w'} = -A e^{-2\pi \sqrt{\text{Ri} - \frac{1}{4}}} \quad (4)$$

above the critical level, where

$$Ri = \frac{\frac{g}{T_0} \left( \frac{\partial T_0}{\partial z} + \frac{g}{c_p} \right)}{\left( \frac{\partial U}{\partial z} \right)^2} \quad (5)$$

$Ri$ , known as the Richardson number, is generally greater than 1, and in such cases we see from (4) and (2) that the wave is almost completely absorbed by the mean field at the critical level. From (3) and (4) we see that an amount of momentum given by

$$A \left( 1 + e^{-2\pi \sqrt{Ri - \frac{1}{4}}} \right)$$

is absorbed at the critical level, and as Booker and Bretherton note, the absorption of a finite amount of momentum by a single level must lead to difficulty. The difficulty arises, as Booker and Bretherton note, from the assumption that a wave with finite energy and a single phase speed,  $c$ , will propagate for an infinite length of time through a medium with an unchanging basic velocity distribution having a critical level. We shall, in this paper, circumvent this difficulty by assuming that the disturbances consist of a spectrum of waves with a continuous distribution of phase speeds; i. e.,

$$\rho_0 \overline{u'w'} = \int_{-\infty}^{\infty} \hat{f}(c) dc, \quad (6)$$

where  $\hat{f}(c) dc$  = the momentum flux due to waves of all wave numbers,  $k$ , having phase speeds between  $c$  and  $c + dc$ . According to (2),  $\hat{f}(c)$  will be independent of  $z$  in any region where  $U \neq c$ . If  $\hat{f}(c) = A$  below a critical level, it will go to

$$- A e^{-2\pi \sqrt{Ri - \frac{1}{4}}}$$

above, as shown by (3) and (4). However, as long as  $\hat{f}(c)$  is finite, an infinitesimal layer will never absorb more than an infinitesimal amount of momentum. Unless otherwise indicated,  $\hat{f}(c)$  will refer to the distribution of  $\rho_0 \overline{u'w'}$  (i. e., Reynolds stress) at the base of the region of interest.

We now proceed to the derivation of a simple formula for the deposition of momentum in the mean flow by gravity waves. Consider first the case shown in figure 1a where  $dU/dz$  is positive. At a height  $z_0$ ,  $U = U_0$ . The amount of momentum absorbed (per unit time) in the altitude range  $dz$  will be

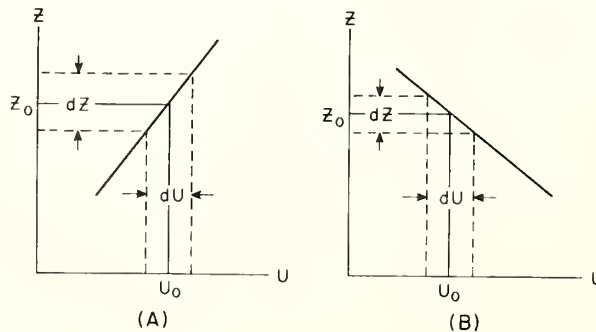


Figure 1. Geometry of the critical layer absorption process for westerly shear (a), and easterly shear (b).



$$\hat{f}(U_0)(1 + e^{-2\pi\sqrt{\text{Ri}(z_0) - \frac{1}{4}}}) |dU| ,$$

and the momentum flux divergence at  $z_0$  is given by

$$\frac{dF_{Mw}}{dz} = \hat{f}(U_0)(1 + e^{-2\pi\sqrt{\text{Ri}(z_0) - \frac{1}{4}}}) \left| \frac{dU}{dz} \right| , \quad (8)$$

where  $F_{Mw}$  = momentum flux due to waves. This result is independent of the sign of  $dU/dz$ . Moreover, waves whose critical level is at  $z_0$  will be westerly relative to  $U$  below  $z_0$ . Hence  $\hat{f}(U_0)$  is positive. Since  $dU/dz$  is also positive, (8) may be rewritten

$$\frac{dF_{Mw}}{dz} = |\hat{f}(U_0)| (1 + e^{-2\pi\sqrt{\text{Ri}(z_0) - \frac{1}{4}}}) \frac{dU}{dz} \quad (9)$$

For the case shown in figure 1b,  $dU/dz$  is negative. However, waves whose critical level is at  $z_0$  will now be easterly relative to  $U$  below  $z_0$ . Hence,  $\hat{f}(U_0)$  is also negative, and therefore (9) is correct for this case as well. For conciseness we may rewrite (9) as

$$\frac{dF_{Mw}}{dz} = f(U) \frac{dU}{dz} , \quad (10)$$

where  $f(U) = |\hat{f}(U)| (1 + e^{-2\pi\sqrt{\text{Ri}(z_0) - \frac{1}{4}}})$ ;  $f(U)$  is always positive. Equation (10) is appropriate regardless of the sign of the shear.

Equation (10) is based on the treatment by Booker and Bretherton (1967) wherein it was assumed that  $U(z)$  is independent of time. No such flows exist in nature. Moreover, the existence of momentum flux divergence implies that  $U$  will change in time. We shall assume, however, that the changes in  $U$  will occur sufficiently slowly for (10) to remain valid at any given moment. If this is the case, the equation for mean momentum in the  $x$ -direction becomes

$$\rho_0 \left( \frac{\partial U}{\partial t} + W \frac{\partial U}{\partial z} \right) = -f(U) \frac{\partial U}{\partial z} + \text{other terms} \quad (11)$$

When the nonlinear terms on the l. h. s. of (11) and the "other terms" are neglected, (11) describes the downward propagation of a distortion in  $U$ . The speed of propagation is given by  $-f(U)/\rho_0$ . It should be noted that if  $U$  is such that  $U(z_1) = U(z_0)$  and  $z_1 > z_0$ , then

$$f(U, z_1) = f(U, z_0) e^{-2\pi\sqrt{\text{Ri}(z_0) - \frac{1}{4}}} \quad (12)$$

One obstacle to the use of (11) is a lack of knowledge of the functional form of  $f(U)$ . At this point, there appear to be no cases where either observations or theory are adequate for the detailed specification of this form. However, it is often found that gravity waves have phase speeds confined primarily to a finite range. The simplest choice of  $f(U)$ , consistent with this, is

$$\begin{aligned} f(U) &= \text{constant}, \quad -c_r < U < c_r \\ f(U) &= 0, \quad c_r < |U| \end{aligned} \quad (13)$$

where  $c_r$ , a positive constant, is a high speed cut-off for the phase speeds. The distribution given by (13) will be used in the simple examples to which we now turn.

### 3. THE CREATION OF SHEAR LAYERS

In this example we consider a situation where local time changes in  $U$  are due solely to wave absorption. Equation (11) becomes

$$\rho_0 \frac{\partial U}{\partial t} = -f(U) \frac{\partial U}{\partial z}. \quad (14)$$

At  $t = 0$ , we let  $U = A + Bz$ , where  $A = -20 \text{ m sec}^{-1}$ , and  $B = 2/3 \text{ m sec}^{-1} \text{ km}^{-1}$ . The vertical distribution for  $\rho_0$  is taken from the equatorial standard atmosphere. For  $c_r$  (viz. (13)), we have taken  $5 \text{ m sec}^{-1}$ . For the constant in (13), we have chosen

$$1 \text{ km mo}^{-1} \times \rho_0(27 \text{ km}).$$

We have ignored the term  $e^{-2\pi\sqrt{\text{Ri} - \frac{1}{4}}}$  in (10), which is equivalent to assuming very high Richardson number. This is certainly the case initially. The above choice of parameters was in some instances governed by the author's interest in the meteorology of the equatorial stratosphere. However, for present purposes they may be considered perfectly arbitrary.

The solution for this case, obtained numerically, is shown in figure 2;  $t = 0$  is arbitrarily identified with 1 April 1960. We note the following important features:

- a) Only the region between 22.5 km and 37.5 km, where the mean wind is between  $-5 \text{ m sec}^{-1}$  and  $+5 \text{ m sec}^{-1}$ , is affected by wave absorption.
- b) Since  $\partial U / \partial z$  is positive, wave absorption causes the addition of westerly momentum. However, the maximum velocity which can be produced is  $5 \text{ m sec}^{-1}$ , since the mechanism ceases to operate for greater velocities.
- c) Wave absorption causes the level at which  $U = 5 \text{ m sec}^{-1}$  to descend at a rate given approximately by  $1 \text{ km mo}^{-1} \times (\rho_0(27 \text{ km})) / \rho_0(z)$ . Thus, the level descends about 8.5 km from 1 April to 6 July; it descends another 3.5 km by 14 October;

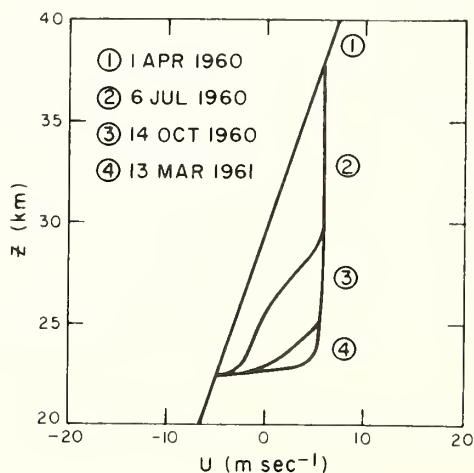


Figure 2. Numerical results for the time variation of zonal velocity profiles in the case where local time changes in  $U$  depend only on the wave absorption mechanism.

by 13 March it has descended only an additional 1.5 km. As long as the Richardson number is larger than one, the lowest level at which  $U = 5 \text{ m sec}^{-1}$  effectively shields the region above from the waves. This is independent of the distribution of  $U$  in the region above.

The above three features are common to all our examples. Somewhat peculiar to the present example is the development of a shear layer. The level at which  $U = 5 \text{ m sec}^{-1}$  cannot descend below 22.5 km. Thus, an increasingly sharp shear layer develops near 22.5 km. Presumably, when  $\partial U / \partial z$  gets sufficiently large, turbulence will set on, acting to diffuse the shear layer. The resulting shear layer may result from a balance between turbulent diffusion and wave absorption. This mechanism may be of importance for clear air turbulence--among other things.

#### 4. A POSSIBLE RELAXATION OSCILLATOR

In the following example, the shielding effect, mentioned above, plays a more prominent role. In addition to the processes involved in our first example, we introduce a restoring force in the form of a Rayleigh friction which attempts to maintain the initial distribution of  $U$ . Equation (11) becomes

$$\rho_0 \frac{\partial U}{\partial t} = -f(U) \frac{\partial U}{\partial z} + K[U(t=0) - U] , \quad (15)$$

where  $K = \rho_0 (27 \text{ km}) \cdot 1/365 \text{ days}$  -- this choice, again, being arbitrary. All other parameters are the same as in the first example. The numerically obtained solution is shown in figure 3. Again, the level at which  $U = 5 \text{ m sec}^{-1}$  descends. However, now the region above, shielded from the action of waves, relaxes to its initial form. For our particular choice of  $K$ , the relaxation is rather slow, but eventually we will be left with the initial profile except for a "spike" just above 22.5 km. What will happen now cannot be stated with certainty; however, the ingredients of a possible oscillation mechanism are evident. Let us assume that when the spike becomes sharp enough, it breaks down; presumably something close to the initial profile will be restored. There will then be no "shield" due to the spike, and the

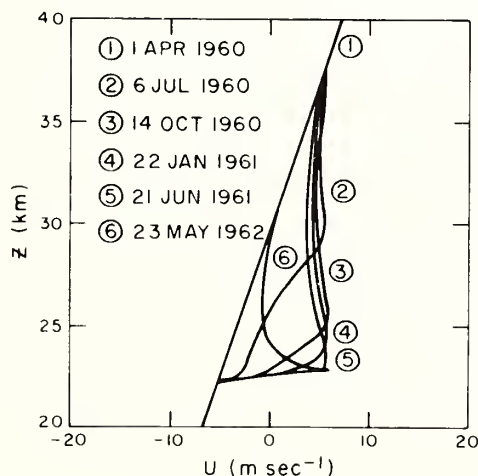


Figure 3. Same as figure 2 except that a Rayleigh friction which tends to restore the initial profile in  $U$  is included.

whole process will begin again, forming a relaxation oscillation whose period depends on  $K$ ,  $f(U)$ , and  $\partial U/\partial z$  ( $t=0$ ) (i. e., the distance between the levels where  $U = 5 \text{ m sec}^{-1}$  and  $U = -5 \text{ m sec}^{-1}$ ) and whose amplitude depends on the range of phase speeds over which  $f$  is nonzero. Though the idea is, at present, far fetched, it is by no means inconceivable that some such process is responsible for the solar cycle.

## 5. THE QUASI-BIENNIAL OSCILLATION IN THE EQUATORIAL STRATOSPHERE

The above examples were investigated largely in the course of a search for an explanation for one of the atmosphere's most interesting phenomena--the quasi-biennial oscillation of the equatorial stratosphere. Briefly, the wind in the equatorial stratosphere blows from east to west for about a year; it then blows from west to east for about a year; etc. The average period is 26 months--though individual cycles tend to vary in length by multiples of six months. The oscillation is, moreover, associated with a downward phase speed of about  $1 \text{ km mo}^{-1}$  at an altitude of 25 km. The amplitude of the oscillation is about  $20 \text{ m sec}^{-1}$  which is much larger than the amplitudes of the annual and semiannual cycles in this region (Reed, 1964; Wallace and Newel, 1966). There are a number of features of the equatorial atmosphere which suggest that this is a critical level phenomenon.

a) Much of the atmosphere's kinetic energy is in planetary scale waves with periods of about 5 days. Over much of the earth such waves are unable to propagate vertically because their frequency is less than twice the vertical component of the earth's rotation rate. However, at the equator where the latter quantity goes to zero, such waves can propagate vertically as internal gravity waves (Lindzen and Matsuno, 1968). Examples of such waves have already been observed with phase speeds between about  $-20 \text{ m sec}^{-1}$  and  $+20 \text{ m sec}^{-1}$  which suggests the use of  $c_r = 20 \text{ m sec}^{-1}$  in (13) (Maruyama, 1967; Wallace and Kousky, 1968).

b) In the equatorial upper stratosphere (ca. 45 km) there exists a strong semiannual oscillation in the zonal wind (Reed, 1965). The relevance of this phenomenon to the quasi-biennial oscillation will be seen later. The effect of the semiannual oscillation can be included in a study of the stratosphere by forcing a top level in the model (at about 40 km) to oscillate with a six-month period.

c) The waves mentioned in item a) above appear to have a peak energy density near the tropopause (Yanai, et al, 1968). It is assumed that this implies that the gravity waves we are concerned with are generated in the neighborhood of the tropopause. Lindzen and Holton (1968) incorporate this feature into a model of the quasi-biennial oscillation in the following way: As shown in section 3, the interaction of waves with the mean flow causes a shear layer to descend. They simply shut off the shielding effect of this shear layer when the middle of the layer descends below 19 km. While the layer is above 19 km, it effectively shields the region above it from the action of waves.

How the above three features could combine to produce a quasi-biennial oscillation is shown in figures 4a-4k. We take the constant in (13) to be such that a shear layer descends from 40 km to below 19 km in 15 mos. This choice leads to what we call a synchronized oscillation. The reason for this terminology will be explained later. Let us assume that at time  $t = 0$ , the semiannual oscillation is in its westerly phase, and that the region below is in an easterly phase. This is the situation in figure 4a. Since  $\partial U/\partial z$  is positive, wave absorption will cause the descent of a westerly ledge, and this ledge shields the region above from the further action of waves. Thus, the region above will continue to execute a semiannual oscillation. This situation is depicted schematically in figures 4b-4e. When  $t = 15 \text{ mos}$ , the middle of the westerly ledge is below 19 km and we assume that the waves can again propagate upwards. This is shown in figure 4f. The semiannual oscillation is in its easterly phase. Hence  $\partial U/\partial z$  is negative and wave absorption causes an easterly ledge to descend while the upper region continues to execute a semiannual oscillation. This is shown in figures 4g-4j. Finally when  $t = 30 \text{ mos}$  (fig. 4k) the middle of the easterly ledge has descended below 19 km and the semiannual oscillation is in its westerly phase; the whole process can now begin anew. The reason for calling the above



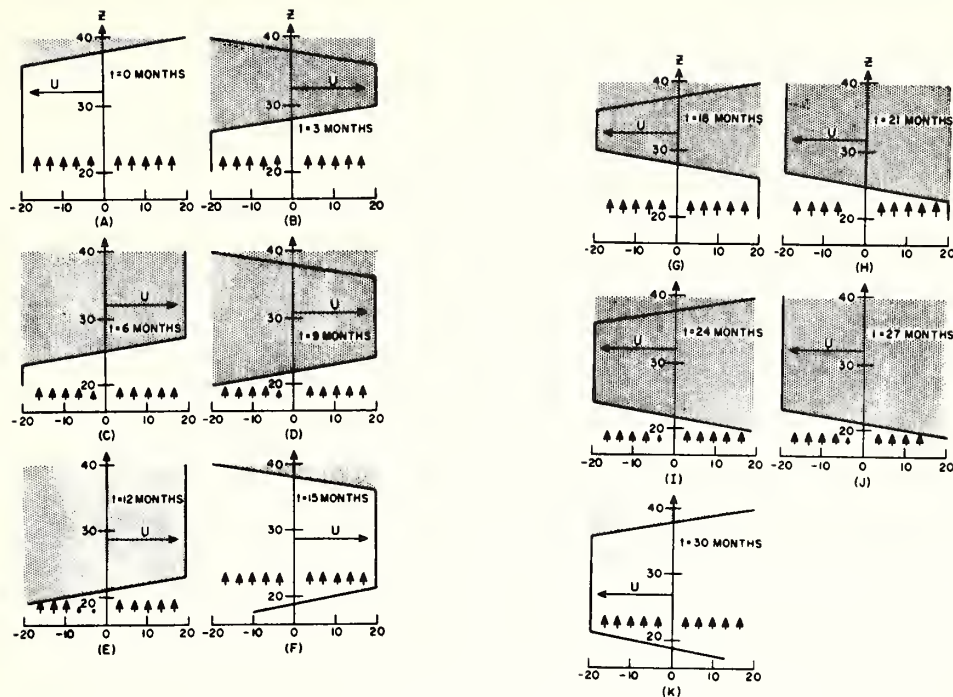


Figure 4 (a) - (k). A schematic time sequence illustrating the proposed theory of the quasi-biennial oscillation for the synchronous case. Vertical arrows indicate gravity wave propagation. Shaded regions are shielded from the waves. See text for details.

synchronized should be clear; when the middle of a westerly ledge descends below 19 km, the semiannual oscillation is in its easterly phase, and when the middle of an easterly ledge descends below 19 km, the semiannual oscillation is in its westerly phase. Synchronization requires a "ledge" to descend from 40 km to below 19 km in  $(2m + 1) \times 3 \text{ mos}$  ( $m = 0, 1, 2, 3, \dots$ ). Assuming easterly and westerly ledges can descend at different rates, we find that synchronous oscillations can take place with periods of

$$T_{\text{syn.}} = (p + 1) \times 6 \text{ mos}, \quad (16)$$

$$p = 0, 1, 2, 3, \dots$$

Equation (16) is excellently confirmed by observations. The period is merely the sum of the times it takes for the wave interaction to bring a westerly and an easterly ledge from 40 km to below 19 km. The observed wave amplitudes in the data of Wallace and Kousky (1968) are consistent with a momentum flux which suggests that  $p$  is around 3 or 4. An average period of 26 mos would result from two 24-month cycles and one 30-month cycle.

Of potentially greater interest to ionospheric physicists is what happens when we do not have synchronization. This is shown in figure 5. The oscillation is merely delayed for a length of time up to 3 mos until synchronization is re-established. In the mean time gravity waves simply continue to propagate upward beyond 40 km. Assuming no subsequent critical level above 40 km, these waves will give rise to appreciably enhanced wind variance at D levels and above. It should be added that these intervals of delay could be discerned in routine stratospheric wind data. These intervals would recur, moreover, with no regular periodicity.



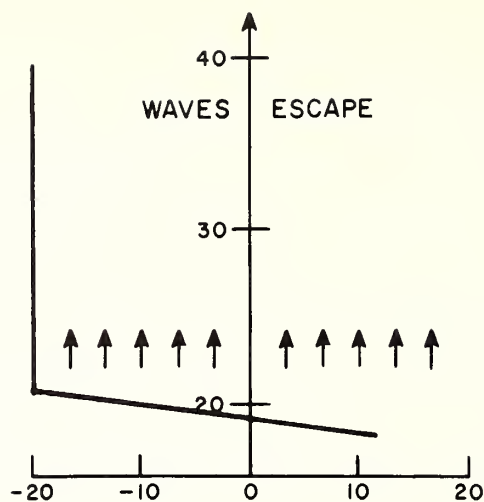


Figure 5. Schematic illustration of gravity wave escape for non-synchronous oscillation. See text for details.

A much more detailed study of the quasi-biennial cycle using numerical models may be found in Lindzen and Holton (1968). The results of that study differ in some details from the above schematic description; they, however, confirm the following features:

- a) The period of the oscillation is determined by 1) the upward flux of momentum due to gravity waves. This can-but need not-be a statistically steady quantity; and 2) the distance between the region dominated by the semiannual oscillation and the region of wave generation.
- b) The amplitude of the oscillation is determined by the range of phase speeds over which we have a significant energy density of gravity waves.

#### ACKNOWLEDGMENT

The preparation of this manuscript has been partially supported by NSF Grant GA-1622.

#### REFERENCES

- Booker, J. R. and F. P. Bretherton, The critical layer for internal gravity waves in a shear flow, J. Fluid Mech., 27, 513-519, 1967.
- Eliassen, A. and E. Palm, On the transfer of energy in stationary mountain waves, Geofys. Publ., 22, 1-23, 1960.
- Hines, C. O. and C. A. Reddy, On the propagation of atmospheric gravity waves through regions of wind shear, J. Geophys. Res., 72, 1015-1034, 1967.
- Jones, W. L., Propagation of internal gravity waves in fluids with shear flow and rotation, J. Fluid Mech., 30, 439-448, 1967.

- Lindzen, R. S. and J. R. Holton, A theory of the quasi-biennial oscillation, submitted to J. Atmos. Sci., 1968.
- Lindzen, R. S. and T. Matsuno, On the nature of large scale wave disturbances in the equatorial lower stratosphere, J. Meteor. Soc. Japan, 46, in press.
- Maruyama, F., Large scale disturbances in the equatorial lower stratosphere, J. Meteor. Soc. Japan, 45, 391-408, 1967.
- Reed, R. J., A tentative model of the 26-month oscillation in tropical latitudes, Quart. J. R. Meteor. Soc., 80, 441-466, 1964.
- Reed, R. J., Zonal wind behavior in the equatorial stratosphere and lower mesosphere, J. Geophys. Res., 71, 4223-4233, 1965.
- Wallace, J. M. and V. E. Kousky, Observational evidence of Kelvin waves in the tropical stratosphere, J. Atmos. Sci., 25, in press.
- Wallace, J. M. and R. E. Newell, Eddy fluxes and the biennial stratospheric oscillation, Quart. J. R. Meteor. Soc., 92, 481-489, 1966.
- Yanai, M., T. Maruyama, T. Nitta, and Y. Hayashi, Power spectra of large scale disturbances over the tropical Pacific, J. Meteor. Soc. Japan, 46, in press.



## Gravity Wave Propagation with a Time-Dependent Critical Level

David D. Houghton and Walter L. Jones  
National Center for Atmospheric Research  
Boulder, Colorado

A critical level has been defined as the level at which the horizontal trace velocity of a wave equals the mean fluid velocity; i.e., the intrinsic frequency of the wave approaches zero. The characteristics of critical level phenomena for gravity waves are studied numerically for cases where the mean horizontal wind flow is a function of time. An inviscid and compressible model, having an isothermal mean state and no rotation, is examined. Solutions are found for the initial and boundary value problem where wave energy is introduced at the lower boundary. The critical level is varied by making the mean horizontal velocity a function of time. Solutions are presented for the following three cases: (1) a critical level is present and stationary; (2) critical levels are established after the initial time; (3) a critical level initially present is gradually removed. The solutions demonstrate that gradual accelerations of the mean flow alter the wave frequency relative to a stationary frame of reference but not the intrinsic frequency of the wave. This means that critical levels can no longer be determined solely by the distribution of the mean flow in the stationary frame of reference.

### INTRODUCTION

The significance of a critical level in gravity wave propagation has been the subject of several recent papers (Bretherton [1966]; Booker and Bretherton [1967]; Hazel [1967]; and Jones [1967]). In these studies the critical level, defined as the level where the horizontal trace velocity of the wave equals the mean fluid velocity, was fixed in space by a time-invariant mean wind distribution. In this situation the critical level blocks the propagation of energy due to gravity waves and causes a transfer of energy from wave to mean motions if the Richardson number is equal to or larger than one quarter.

As pointed out by Booker and Bretherton [1967], the transfer of energy to the mean motions becomes increasingly large (without limit) in the critical zone, so that accelerations of mean motions in the critical zone will eventually become significant, regardless of the magnitude of the wave energy below the critical zone. Therefore, in order to determine when the linear model is valid, one must compare the time scale associated with this acceleration to the time scale for development of the stationary critical level.

In this study we anticipate the eventual analysis of nonlinear models and investigate the implications of time-varying mean motions on the waves. By varying mean motions, the critical level is changed, leading to discussions of how previous studies of stationary critical level models apply to this case. The mean accelerations considered have large time and height scales compared with the wave oscillations, making this study only the first step in a systematic transition from the linear to the nonlinear model.

### PHYSICAL MODEL

Because our model takes compressibility into account, it is more general than the model of Booker and Bretherton [1967]. However, for the class of motions studied, the two models may be considered virtually identical. A nonrotating Cartesian coordinate system is used with motions restricted to a vertical plane. Motions are adiabatic, and mean temperature is constant with height. The fluid is inviscid except above 100 km where a Rayleigh viscosity is introduced to minimize the reflection of wave energy. Wave motions are a function of space coordinates,  $x$  and  $z$ , and time,  $t$ ; whereas the mean velocity is a function only of  $z$  and  $t$ . The  $x$  variation of the wave variables is represented by only one Fourier component, with wavenumber  $k$  in the form  $e^{ikx}$ .

The linearized equations for this model include variables that are defined as follows:

c	speed of sound
g	acceleration of gravity
K	coefficient of viscosity
k	horizontal wavenumber
p	equal to $\rho_0^{-\frac{1}{2}} p^* e^{-ikx}$
$p^*$	perturbation pressure
t	time
$u_0$	mean velocity component in x direction
$u^*$	perturbation velocity component in x direction
u	equal to $\rho_0^{\frac{1}{2}} u^* e^{-ikx}$
$w^*$	perturbation velocity component in z direction
w	equal to $\rho_0^{\frac{1}{2}} w^* e^{-ikx}$
x	horizontal coordinate
z	vertical coordinate
$\rho_0$	mean density
$\rho^*$	perturbation density
$\rho$	equal to $\rho_0^{\frac{1}{2}} \rho^* e^{-ikx}$
$\beta$	stability factor equal to $\frac{1}{\rho_0} \frac{\partial \rho_0}{\partial z}$

The variables u, w, p, and  $\rho$  are the Fourier coefficients of the so-called field variables for velocity, pressure, and density.

The complex linearized equations for this model may be written

$$\frac{\partial u}{\partial t} = -iku_0 u - \frac{\partial u_0}{\partial t} \rho - \frac{\partial u_0}{\partial z} w - ikp - Ku \quad (1a)$$

$$\frac{\partial w}{\partial t} = -iku_0 w - \frac{\partial p}{\partial z} + \frac{\beta}{2} p - g\rho - Kw \quad (1b)$$

$$\frac{\partial \rho}{\partial t} = -iku_0 \rho + \frac{\beta}{2} w - iku - \frac{\partial w}{\partial z} \quad (1c)$$

$$\frac{\partial p}{\partial t} = -iku_0 p + \left( g - \frac{c^2 \beta}{2} \right) w - c^2 iku - c^2 \frac{\partial w}{\partial z} \quad (1d)$$

Equations (1a) and (1b) arise from the equation of motion, (1c) from the equation of continuity, and (1d) from the first law of thermodynamics.



## DISCUSSION

The intrinsic frequency of a wave,  $\omega'$ , is the frequency of this wave as observed from a frame of reference moving with the local mean velocity of the fluid. If  $\omega$  is the frequency in a fixed frame of reference,  $\omega' = \omega + k u_0$  for this model. Within the limitations of the geometrical optics approximation,

$$\frac{\partial \omega}{\partial t} = -k \frac{\partial u_0}{\partial t} \quad (2)$$

which implies that acceleration in the mean flow does not in itself alter the intrinsic frequency, cf. Bretherton and Garrett [1968], and Jones [1968]. That is, a critical layer action cannot be induced by mean accelerations alone, but still depends upon the movement of the waves through a region with velocity shear.

It can be concluded that the mean motion accelerations considered here affect critical layer phenomena only by altering the shear zone through which the waves subsequently propagate. Once mean accelerations have occurred, critical zones cannot be determined by the relationship of the mean winds to the fixed coordinate system, but must be determined by an examination of the intrinsic frequencies present in the fluid. The intrinsic frequencies will no longer be given by the original forcing frequency and the original or final mean wind distribution.

Using a time-varying mean state results in the creation of a multitude of critical levels or, rather, a wide critical zone for any given horizontal wavelength, tending to reduce the gradients of Reynolds stress or at least to limit their growth. Thus, in the nonlinear model we would expect slow mean accelerations to result in a feedback that tends to limit these accelerations.

## NUMERICAL EXPERIMENTS

The ideas set forth in the discussion have been demonstrated by numerical integration of the time-dependent equations (1). The numerical model treats these equations as an initial and boundary problem and uses a finite difference scheme of second order accuracy in time and space. A detailed discussion of the method, and comparison of the solutions with known analytical solutions, is given by Houghton and Jones [1968] for a time-independent mean state. The numerical method is shown to give satisfactory results until vertical wavelengths approach the resolution limit of the grid system.

Three experiments were run. In all cases constants were given the following values

$$\begin{aligned} c &= 300 \text{ m sec}^{-1} & g &= 9.8 \text{ m sec}^{-2} \\ \beta &= 1.524 \times 10^{-4} \text{ m}^{-1} & k &= 2\pi \times 10^{-5} \text{ m}^{-1}. \end{aligned}$$

The inviscid region where  $K = 0$  extended up to 100 km, and the Rayleigh damping region another 50 km above that. In the damping region, the coefficient of damping was given by

$$K = K_0 \left[ e^{(z-z_0)/L} - 1 \right] \quad (3)$$

where  $z_0 = 10^5 \text{ m}$ ,  $K_0 = \Delta t / [20(e^{5 \times 10^4/L} - 1)]$ ,  $L = 1.5 \times 10^4 \text{ m}$ , and  $\Delta t$  = time step. The grid spacing was 250 m and the time step was 0.75 sec. The lower boundary condition was

$$w = \left[ 1 - e^{(w/2)t} \right] e^{i\omega t} \quad (4)$$

in the first cases and

$$w = \left[ 1 - e^{(w/2)t} - e^{(w/2)(t_0-t)} \right] e^{i\omega t} \quad 0 < t < t_0 \quad (5)$$

and

$$w = 0 \quad t > t_0$$

in the last case, where  $\omega = 3.49 \times 10^{-3} \text{ sec}^{-1}$  and  $t_0 = 1.08 \times 10^4 \text{ sec}$ .

#### CASE 1

The first case was the control calculation where the mean winds were independent of time. The flow contained a stationary critical level corresponding to the analysis of Booker and Bretherton [1967]. Calculations were made for 12 hours of real time with a mean wind profile of

$$\begin{aligned} u_0 &= -10^{-3} z \text{ m sec}^{-1} & \text{for } z \leq 10^5 \text{ m} \\ u_0 &= -10^2 \text{ m sec}^{-1} & \text{for } z > 10^5 \text{ m} \end{aligned}$$

In this case there is a single critical level at 56.6 km. The solutions show close agreement with the theory of Booker and Bretherton [1967]. Figures 1 and 2 show the solutions for real  $u$  and real  $(uw')$ , respectively, at 12 hours, where  $w'$  is the complex conjugate of  $w$ . The quantity real  $(uw')$ , which is proportional to the momentum flux of the wave, shows a near discontinuity across the critical zone as anticipated by theory.

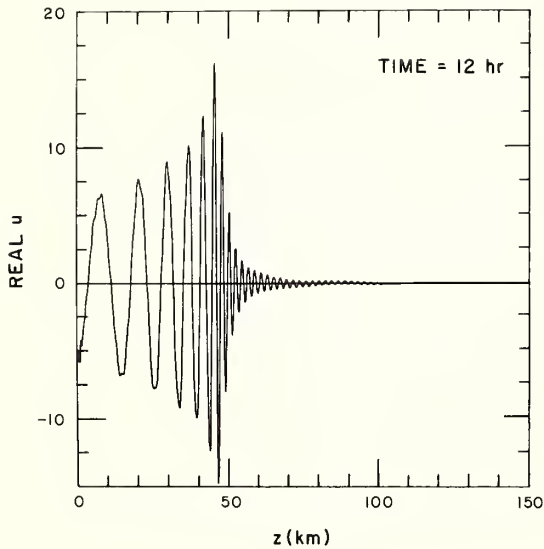


Fig. 1 Numerical solution for real  $u$  after 12 hours, Case 1.

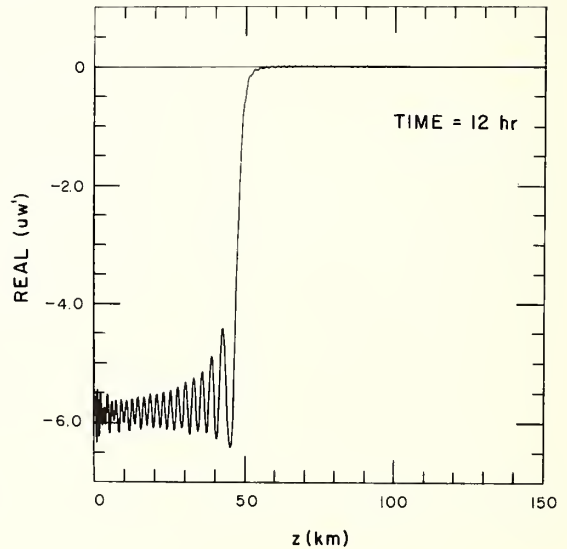


Fig. 2 Numerical solution for real  $(uw')$  after 12 hours, Case 1.

#### CASE 2

The mean winds are zero for the first 6 hours allowing a relatively uniform momentum flux to become established in the lower 100 km of the model. Between 6 and 11 hours the mean flow is accelerated at a constant rate so that the linear wind profile is maintained in the lower 100 km. At 11 hours, the wind profile becomes the same as in Case 1. Thereafter, it remains constant.

For waves at the lower boundary, the critical level appears at 100 km, at about 7.8 hours, and gradually lowers to 56.6 km by 11 hours. However, waves in the interior are accelerated in the horizontal by the acceleration of the mean motion. In the final stage the interior waves have critical levels that are a function of their position when the acceleration is applied. As a result of this acceleration, waves present at 6 hours have higher critical levels than those generated after 6 hours or no critical level at all. The waves appear to become blocked over a broad critical zone, and their distribution gradually reverts to the distribution observed in Case 1, since wave energy is continually absorbed within the broad critical band and supplied only from below. The energy supplied from the lower boundary after 11 hours is blocked by the final critical level at 56.6 km.

Figure 3 shows the real  $u$  solution after 6 hours. Figure 4 shows the real  $(uw')$  distribution after 6 hours, indicating the relative constancy of momentum flux established at 6 hours. Figure 5 shows the real  $u$  distribution after 15 hours. The gradual absorption of wave energy and the decreased vertical wavelength, characteristic of a critical level, are noted in a broad band above the final critical level. In addition, the accumulation of energy shown by increased amplitudes is present below the final critical level. Figure 6 shows the broad region of gradient that develops in the momentum flux or real  $(uw')$  field at 10 hours. Figure 7 shows the approach of the real  $(uw')$  distribution to that in Case 1 at 15 hours.

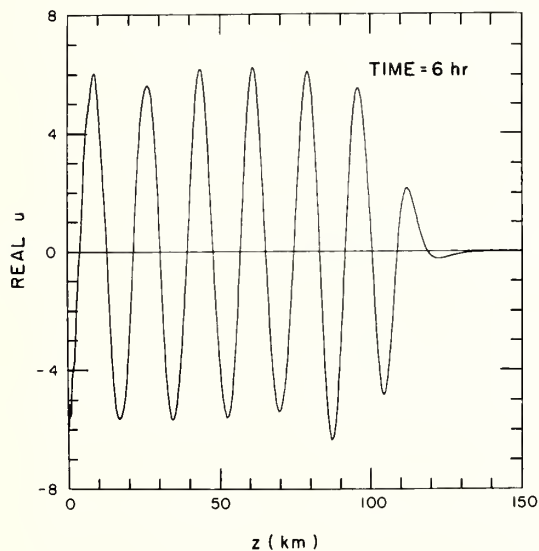


Fig. 3 Numerical solution for real  $u$  after 6 hours, Case 2.

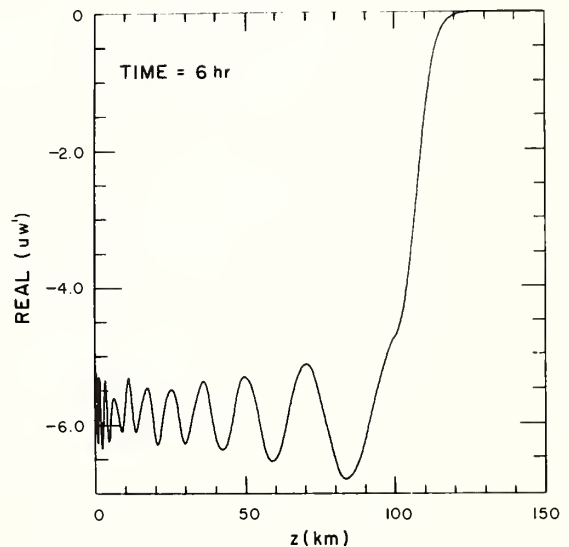


Fig. 4 Numerical solution for real  $(uw')$  after 6 hours, Case 2.

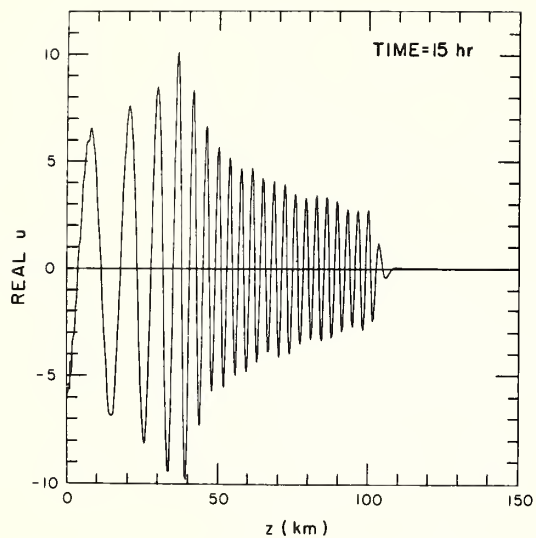


Fig. 5 Numerical solution for real  $u$  after 15 hours, Case 2.

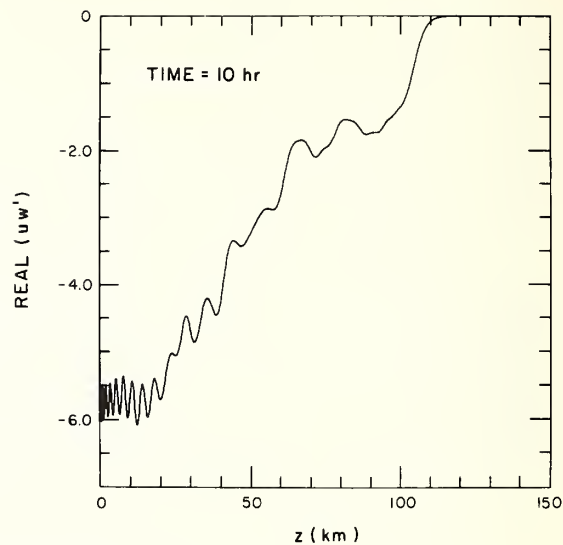


Fig. 6 Numerical solution for real  $(uw')$  after 10 hours, Case 2.

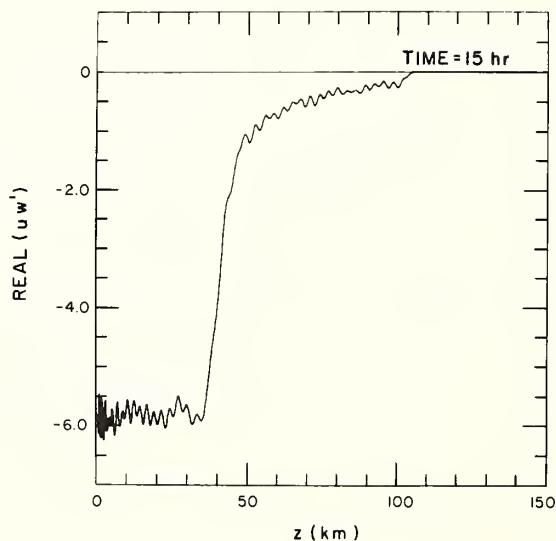


Fig. 7 Numerical solution for real  $(uw')$  after 15 hours, Case 2.

### CASE 3

The mean winds in Case 3 are the same as in Case 1 for the first 6 hours; however, wave energy is introduced at the lower boundary for only the first 3 hours. The wave packet sent up from the lower boundary becomes blocked on the lower side of the initial critical level at 56.6 km. By 6 hours the packet is well into a critical condition with a very low intrinsic frequency and a small upward group velocity. Between 6 and 16 hours a constant acceleration is applied to the mean winds so that the wind profile in the lower 100 km is always linear. The wind shear reverses at 11 hours and by 16 hours it is equal but opposite to the initial conditions. Thereafter, it remains constant.

The mean accelerations transfer the wave packet to the upward side of the critical zone. However, the low intrinsic frequency and the slow group velocity of the packet are not altered by the mean accelerations. Therefore, it takes considerable time for the packet to move away from a critical condition and to develop the rapid upward group velocity usually associated with the final mean velocity distribution.

Figures 8 and 9 show the wave packet at 6 hours in terms of the real  $u$  and real  $(uw')$  distributions. Figures 10 and 11 show the real  $(uw')$  distribution after 15 and 20 hours, respectively. The changes in magnitude indicate a loss of energy from the wave packet until the mean wind shear changes sign, after which they indicate a gain of energy. The energy (momentum flux) appears to be proportional to the intrinsic frequency as predicted by the theory of Bretherton and Garrett [1968]. The packet moves upward only 15 km between 6 and 15 hours (cf. Figures 9 and 10); it moves 30 km in the next 5 hours (cf. Figures 10 and 11). This indicates the slow response of the wave packet characteristics to the mean flow changes.

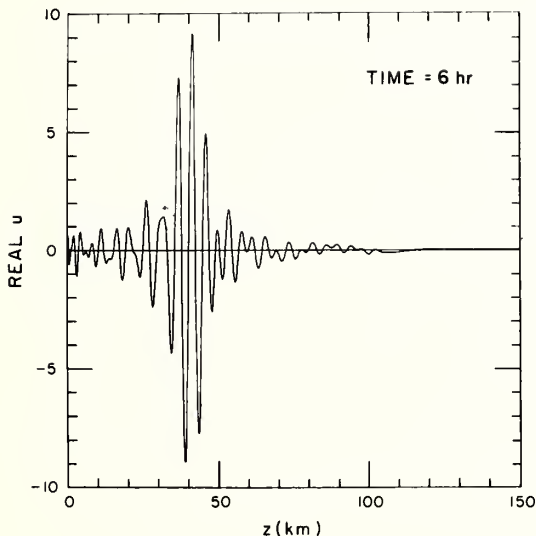


Fig. 8 Numerical solution for real  $u$  after 6 hours, Case 3.

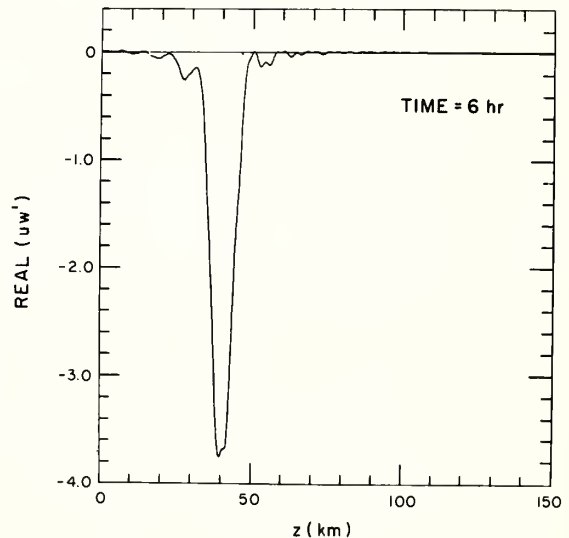


Fig. 9 Numerical solution for real  $(uw')$  after 6 hours, Case 3.



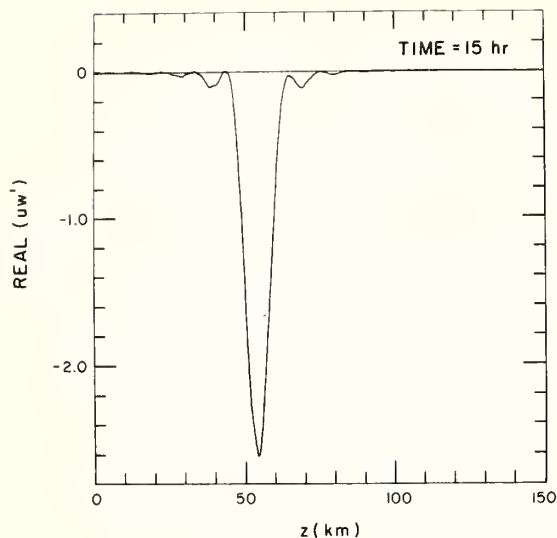


Fig. 10 Numerical solution for real ( $uw'$ ) after 15 hours, Case 3. Note the change in the ordinate scale from Figure 9.

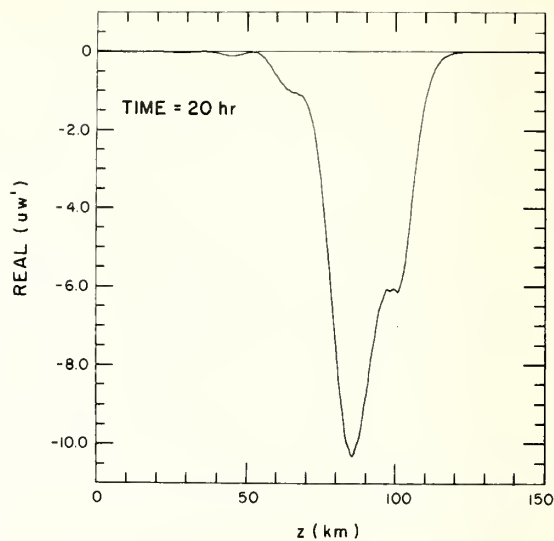


Fig. 11 Numerical solution for real ( $uw'$ ) after 20 hours, Case 3. Note the change in the ordinate scale from Figures 9 and 10.

#### SUMMARY

The numerical results show quite clearly the effects of slow acceleration of mean motions on wave propagation. They emphasize the importance of the intrinsic frequency that can be changed by propagation of the wave through a shear zone, but cannot be changed by slow mean motion accelerations. The results also show that the critical level must be considered relative to the wave and not to the coordinate system when mean accelerations are present. Such a consideration makes the critical concepts less useful, but not less valid, in attempting to understand gravity wave propagation in a shear flow.

#### REFERENCES

- Booker, J. R. and F. P. Bretherton, The critical layer for internal gravity waves in a shear flow, *J. Fluid Mech.*, **27**, 513-539, 1967.
- Bretherton, F. P., The propagation of groups of internal gravity waves in a shear flow, *Quart. J. Roy. Meteorol. Soc.*, **92**, 466-480, 1966.
- Bretherton, F. P. and C. J. R. Garrett, Wavetrains in inhomogeneous moving media, *Proc. Roy. Soc. London, A*, **302**, 529-554, 1968.
- Hazel, Philip, The effect of viscosity and heat conduction on internal gravity waves at a critical level, *J. Fluid Mech.*, **30**, 775-783, 1967.
- Houghton, D. D. and W. L. Jones, A numerical model for linearized gravity and acoustic waves, NCAR Manuscript No. 68-104, 1968.
- Jones, W. L., Propagation of internal gravity waves in fluids with shear flow and rotation, *J. Fluid Mech.*, **30**, 439-448, 1967.
- Jones, W. L., Ray tracing of internal gravity waves in fluids with spatial and temporal variations in mean flow, paper presented at Symposium on Acoustic Gravity Waves, ESSA, Boulder, July 15, 1968.

# Ray Tracing for Internal Gravity Waves

Walter L. Jones

National Center for Atmospheric Research, Boulder, Colorado

(Submitted to Journal of Geophysical Research)

Ray tracing techniques are applied to internal gravity waves in a fluid with spatially varying mean flows. It is shown that the effect of deformational mean flow is to shorten the wavelength, the effect being most pronounced for waves of modest spatial scale.

The model atmosphere used is incompressible, inviscid, Cartesian, non-rotating, and has a mean density  $\rho_0$  that varies as  $e^{-\beta z}$ . The mean wind has components  $u_0, v_0, w_0$ , all of which may vary in any direction and with time. The usual WKBJ approximation is made that a wave number varies slowly over a wavelength or cycle. In addition, it is assumed that

1. Vertical wind derivatives and horizontal derivatives of  $w_0$  are much less than  $(N^2 - \Omega^2)^{\frac{1}{2}}$ .
2. Horizontal derivatives of horizontal winds are much less than  $\Omega$ .
3. Time derivatives of horizontal winds are much less than  $\Omega\beta^{-1}(N^2 - \Omega^2)^{\frac{1}{2}}$ .
4. Time derivatives of vertical winds are much less than  $g$ .

Here  $N^2 = g\beta$  is the Brunt frequency,  $g$  the gravitational acceleration,  $\omega$  the wave frequency, and

$$\Omega = \omega - ku_0 - \ell v_0 - mw_0$$

the intrinsic frequency. The wave vector  $\underline{k}$  has components  $k, \ell, m$ .

Under these conditions, explicit derivatives of the mean wind may be dropped from the local dispersion equation, which becomes

$$(N^2 - \Omega^2)(k^2 + \ell^2) - \Omega^2(m^2 + \beta^2/4) = 0 \quad (1)$$

The eikonal or ray tracing techniques are those of Landau and Lifschitz (1959), Whitham (1960, 1961, 1965), Weinberg (1962), and Bretherton and Garrett (1968). When applied to the dispersion equation they yield

$$\frac{dx}{dt} = \frac{(N^2 - \Omega^2)k}{\Omega K^2} + u_0 \quad (2)$$

$$\frac{dy}{dt} = \frac{(N^2 - \Omega^2)\ell}{\Omega K^2} + v_0 \quad (3)$$

$$\frac{dz}{dt} = -\frac{m\Omega}{K^2} + w_0 \quad (4)$$

$$\frac{dk}{dt} = -k \frac{\partial u_o}{\partial x} - \ell \frac{\partial v_o}{\partial x} - m \frac{\partial w_o}{\partial x} \quad (5)$$

$$\frac{d\ell}{dt} = -k \frac{\partial u_o}{\partial y} - \ell \frac{\partial v_o}{\partial y} - m \frac{\partial w_o}{\partial y} \quad (6)$$

$$\frac{dm}{dt} = -k \frac{\partial u_o}{\partial z} - \ell \frac{\partial v_o}{\partial z} - m \frac{\partial w_o}{\partial z} \quad (7)$$

$$\frac{d\omega}{dt} = k \frac{\partial u_o}{\partial t} + \ell \frac{\partial v_o}{\partial t} + m \frac{\partial w_o}{\partial t} \quad (8)$$

where

$$K^2 = k^2 + \ell^2 + m^2 + \beta^2/4 \quad (9)$$

These equations describe the position, wave number components, and frequency of a wave packet as a function of time. They may be solved simultaneously, given an initial position, wave number, and frequency consistent with equation (1).

If it is assumed that the derivatives of the mean wind components are temporally and spatially constant, equations (5) - (7) constitute a closed set for  $k$ ,  $\ell$ ,  $m$  as functions of time. Solutions are of the form

$$\underline{k} = \underline{k}_1 e^{n_1 t} + \underline{k}_2 e^{n_2 t} + \underline{k}_3 e^{n_3 t} \quad (10)$$

where  $\underline{k}_1$ ,  $\underline{k}_2$ , and  $\underline{k}_3$  are integration constants, and  $n_1$ ,  $n_2$ , and  $n_3$  are solutions of the equation

$$n^3 + an + b = 0 \quad (11)$$

where

$$a = -\frac{1}{2}(\underline{D}:\underline{D} + \underline{Z}:\underline{Z}) \quad (12)$$

$$b = \det |\underline{D}_{ij} + \underline{Z}_{ij}| \quad (13)$$

$\underline{D}$  and  $\underline{Z}$  are the deformation and rotation tensors (Serrin, 1959) with components

$$\underline{D}_{ij} = \frac{1}{2} \left( \frac{\partial v_{oi}}{\partial x_j} + \frac{\partial v_{oj}}{\partial x_i} \right) \quad (14)$$

$$\underline{Z}_{ij} = \frac{1}{2} \left( \frac{\partial v_{oj}}{\partial x_i} - \frac{\partial v_{oi}}{\partial x_j} \right) \quad (15)$$

It can be shown that unless  $b = 0$  and  $a \geq 0$ , at least one  $n$  will have a positive real part, and thus the wave number will ultimately grow exponentially. Special conditions in which these conditions are met include

1. Purely rotational flow with no deformation
2. Two dimensional flow (no derivatives along an axis of any orientation) if the flow is predominantly rotational
3. Uni-directional flow, say only  $u_0(y, z)$ . There is a wave number growth, but it is linear.

The wave number growth may be interpreted physically by noting that the wave behaves much as if it were imbedded in the flow. A "stretching out" of the mean velocity component parallel to the wave vector "stretches" the wave, while a lateral shear of this velocity component rotates the wave vector. In deformational flow, the wave number increases along the axis of most negative dilatation.

If typical synoptic scale parameters are inserted, the wave number growth time constant is hours in deformational flow to a day or two in predominantly rotational flow. If an internal gravity wave passes through a "region" (e.g., the troposphere) in times short compared to these, it will not be much influenced. Slow moving waves will be greatly modified in a generalization of critical layer behavior. Waves apt to be so altered have small vertical and horizontal wavelengths, say less than 5 and 50 km, respectively.

#### REFERENCES

- Bretherton, F. P., and C. J. R. Garrett, Wavetrains in homogeneous moving media, Proc. Roy. Soc. A, 302, 509, 1968.
- Landau, L. D., and E. M. Lifschitz, Fluid Mechanics, Pergamon Press, London, 1959.
- Serrin, J., Mathematical principles of classical fluid dynamics, Handbuch der Physik, VIII/1, edited by J. Flugge, Springer-Verlag, Berlin, 1959.
- Whitham, G. B., A note on group velocity, J. Fluid Mech., 9, 347, 1960.
- Whitham, G. B., Group velocity and energy propagation for three-dimensional waves, Comm. Pure Appl. Math., 14, 675, 1961.
- Whitham, G. B., A general approach to linear and non-linear waves using a Lagrangian, J. Fluid Mech., 22, 273, 1965.
- Weinberg, J., Eikonal method in magnetohydrodynamics, Phys. Rev., 126, 1899, 1962.





Vertical Energy Flux in a Wind and  
Temperature Stratified Atmosphere.

Robert F. MacKinnon,  
Department of Mathematics,  
Imperial College, London, England.

**Abstract.** Calculations of nett mean energy flux due to a ground disturbance are presented for various altitudes in a wind-and temperature-stratified model atmosphere. Contributions to vertical energy flux are considered in turn for the continuous spectrum of acoustic waves, the discrete spectrum of trapped waves and the continuous spectrum of gravity waves. Each spectrum of waves presents its own difficulties which are discussed briefly as is the interdependence between the contributions from the various spectra. The effects of jet-stream winds are considered with particular attention given to vertical energy flux associated with gravity waves for which critical levels exist.

Introduction

Since the publication of a know well known paper by C.O. Hines (1960) many authors have given their attention to traveling ionospheric disturbances presumably caused by waves of periods greater than 10 min generated at low altitudes. Thermonuclear bombs have proved to be a source of widely observed ionospheric disturbances, most notably the low-altitude explosion of 30, October 1961 at Novaya Zemlya. Wickersham (1966) has interpreted ionospheric disturbances caused by this explosion as being evidence of the acoustic-gravity normal modes of propagation of the atmosphere such as are discussed by Pfeffer and Zarichny and others. Hines (1967) has disagreed with this interpretation and has reaffirmed his belief that such disturbances are due mostly to vertically propagating gravity waves of periods greater than 20 min. Recent theoretical studies concerning such long-period gravity waves have been made by Friedman (1966), Row (1967) and Tolstoy (1967).

Warren and Arora (1967) have derived expressions for nett mean vertical energy flux due to a transient source in an inviscid temperature-stratified atmosphere. An important feature of their results is that they represent a complete and rigorous solution to a mathematically well-posed problem. Their methods can be applied to a model atmosphere with winds. The addition of winds to the model atmosphere is a non-trivial alteration of theoretical and practical significance. It has been discussed independently by Booker and Bretherton (1967) and by Hines and Reddy (1967) how winds can hinder the upward progression of energy associated with waves for which critical levels exist. A critical level is an altitude at which the wind speed equals the phase speed of a wave of given frequency and wave-length. Jones (1967) and Hazel (1967) have shown this effect of the wind exists if viscosity or rotation are included in the formation of the problem. Pierce (1965, 1967) and MacKinnon (1967, 1968) have indicated some effects of winds upon the waves associated with normal modes of propagation.

In common with many previous authors we base our results upon the linearized equations of motion for a model consisting of an atmosphere of inviscid, perfect gas over a flat, non-rotating rigid earth. The atmospheric temperature - and wind-profiles are assumed continuous and piecewise linear. The model is bounded above by a calm, isothermal semi-infinite layer. Some limitations of such models have been discussed by Tolstoy (1967).

Nett Mean Vertical Energy Flux

It can be shown (Warren 1968b) that at a height  $z$  the rate of work,  $W(z,t)$ , being done by small oscillations of amplitude  $O(\delta)$  upon a stream surface not moving with the mean flow is given by

$$W(z,t) = \iint dx dy \left[ P(x,y,z;t) \frac{\partial Q(x,y,z;t)}{\partial t} + \text{the rate of work done by the hydrostatic pressure} \right] + O(\delta^2) \quad (1)$$

where  $t$  represents time,

$x, y, z$ , cartesian coordinates,  $z$  positive upwards,  
and  $P, Q$  are the perturbed pressure and displacement.

For simplicity unidirectional winds,  $U(z)$ , are assumed and a ground disturbance of the form

1. Now at Defence Research Establishment Pacific, F.M.O., Victoria, B.C., Canada.

evaluation of  $F(z)$ . Less important is the choice of  $b$ .

For purposes of convenience in the discussion below we define as 'flux functions'  $H$  and  $M$  such that  $H(z;w,k)$  is the imaginary part of the continuous spectrum integrand in Eq(3) and  $M(z;w,k)$  is the real part of the discrete spectrum integrand in Eq(3). Hence, apart from dimensional normalizing constants

$$F(z) = \pi^{-1} \int dk \int dw H(z;w,k) + \int dk M(z;w(k),k)$$

The 'downwind direction' is associated with integrals over positive  $k$  when winds are present.

#### Continuous Acoustic Spectrum

The contribution of the continuous acoustic spectrum to  $F(z)$  is independent of  $z$  since, as can be shown from the residual equations,  $\text{Im } p q$  is independent of  $z$  for given  $w$  and  $k$ . For large  $w$  it has been found numerically that

$$\text{Im } \bar{p} q |q(0)|^{-2} \propto w^{-1} (w^2 - N^2(0)) c(0) \quad (5)$$

where  $c(0)$  is the speed of sound at the ground, and  $N(0)$  is the Brunt frequency at the ground. This numerical result correlates with the WKBJ solution for  $p(z;w,k)$  which satisfies the upper boundary condition, viz

$$p(z;w,k) \propto (v^2(z) - N^2(z))^{\frac{1}{2}} S^{-\frac{1}{4}}(z) \exp i \int_0^z h(z) S^{\frac{1}{2}}(z) dz$$

where  $v = w - k$

$h = w/c(\infty)$

and for large  $w$ ,

$$S(z) \sim c^2(\infty)/c^2(z).$$

This correlation indicates that partial reflections at interfaces of discontinuous temperature gradient do not significantly affect energy flux for large  $w$ . From Eqs(3) and (5) it follows that for finite energy flux,

$$\int_0^\infty w^2 |S(w)|^2 dw < \infty$$

The integration of  $H$  over  $w$  can be performed in three parts. For small values of  $w$  near the boundary between the continuous and discrete spectra,  $p$  and  $q$  must be obtained through numerical integration (Runge-Kutta) of the residual equations. For moderate values of  $w$ ,  $p$  and  $q$  can be represented as a combination of WKBJ solutions. For small and moderate values of  $w$  integration was performed using the trapezoidal rule. For large values of  $w$  Eq(5) holds, so that the integral of  $H$  over  $w$  from a large value of  $w$  to infinity can be performed analytically for the ground perturbation chosen. The flux function  $\exp a k^2 H(z;w,k)$  is shown in Figure 2 for small values of  $w$  at two values of  $k$ . The peak appearing near  $w = 0.024 \text{ sec}^{-1}$  for  $k = 0.02 \text{ km}^{-1}$  is associated with the normal mode  $S$  which is shown in Figure 1 to originate at the spectrum boundary at a value of  $k = 0.073 \text{ km}^{-1}$ . This explains the absence of such a peak in Figure 2 at the larger value of  $k$ . It was found that the presence or absence of winds little affected the acoustic energy flux at the small values of  $k$  required (say  $k < 0.2 \text{ km}^{-1}$ ), even though winds can alter the low-frequency cut-offs of acoustic modes. For  $|f(k)|^2$  a rapidly decreasing function of  $k$  it was found that the acoustic energy flux is well approximated by

$$7.9 \pi^{-1} \int_0^\infty |f(k)|^2 dk$$

which for our case in particular is 0.16. As shown below this is by far the greater part of the total nett mean energy flux.

#### Discrete Spectrum

Using a result of Pierce (1965, Eq 5.Q) one can show that

$$M(z;w(k),k) = |g(w)|^2 |f(k)|^2 |p(0;w,k)|^2 I^{-2}(0;w,k) \{ v I(z;w,k) + p(z;w,k) q(z;w,k) \} \quad (6)$$

where

$$I(z;w,k) = \int_0^\infty (v |q|^2 + k^2 v^{-3} |p|^2) dz$$

and where  $p$  and  $q$  taken on real values.

Eq(6) was the form used in the calculations, Runge-Kutta integration being used to obtain  $p$  and  $q$  while the trapezoidal rule was used to calculate  $I(z;w,k)$ . The method of finding the solution to Eq(4) for a given modal curve is given by MacKinnon (1968b)

$M(z;w(k),k)$  was found to be a non-increasing function of altitude, otherwise varying with  $k$  and with wind conditions as well as the model order. Near the low-frequency cut-off of an acoustic mode  $M$  is nearly constant with height. For somewhat greater frequencies,  $M(z)$  for the same mode may decrease rapidly with altitude either in the upper or lower sound channel, so that little energy reaches the uppermost layer. Such a behaviour is indicated in Fig. 3 for the  $S$  mode in the downwind direction. Shifts in the concentration of associated energy from one sound channel to another manifest themselves in variations in modal dispersion curves

$m(t)n(x)$  is taken so that the  $y$ -integration in Eq(1) may be dropped with  $W(z,t)$  being defined per unit length in the  $y$ -direction. Table 1 gives the temperature and wind-profiles. An upper boundary condition taken at 120 km excluding waves in the uppermost layer which transport energy downwards leads directly to a division of waves into a continuous spectrum of acoustic waves, a discrete spectrum of trapped waves, and a continuous spectrum of gravity waves. The presence of winds leads to a continuous spectrum of waves for which critical levels exist. (Fig 1). The assumed model can be shown to be stable (Warren 1968a).

Adopting the methods of Warren and Arora (1967) we define the nett mean vertical energy flux,  $F(z)$ , as

$$F(z) = \lim_{\epsilon \rightarrow 0} \int_0^{\infty} dt W(z,t) \exp -\epsilon t \quad \text{as } \epsilon \rightarrow 0 \quad (2)$$

and find that

$$F(z) \propto \pi^{-1} \text{Im} \int_{-\infty}^{\infty} dk \int_{-\infty}^{\infty} dw w |g(w)|^2 |f(k)|^2 \bar{p}(z;w,k) q(z;w,k) |q(o;w,k)|^{-2} \\ + \sum \text{Re} \int_{-\infty}^{\infty} dk \frac{\partial}{\partial w_i} \{ w |g(w)|^2 \bar{p} q \} \frac{\partial q(o;w,k)}{\partial w_i} \bigg|_{w=w(k)} \quad (3)$$

where  $p, q$  represents appropriate solutions to the residual equation (the Zu and Yu of Pierce 1965),

$\bar{p}$  denotes the complex conjugate of  $p$ ,

$k$ , the horizontal wave-number,

$w$ , frequency,

$w_i = (w - \bar{w})/2$

$g(w) = \int_{-\infty}^{\infty} dt m(t) \exp iwt$  and  $f(k) = \int_{-\infty}^{\infty} dx n(x) \exp -ikx$

$C$  indicates the integration is to be taken over the continuous spectra of waves. The sum over  $n$  indicates a sum over normal modes of propagation. Integrals are taken over real values of  $w$  and  $k$ , however the differentiation  $\partial/\partial w_i$  is taken in the limit of  $w_i$  tending to zero through positive values, the last written integrand being evaluated at a point on a model curve.  $w(k)$  represents curves in the  $w$ - $k$  plane (termed 'model curves') prescribed by the condition

$$q(o;w,k) = 0 \quad (4)$$

Eq.(4) is satisfied for real  $w$  and  $k$  only for normal modes (Warren 1968b).

For the numerical results presented herein a ground perturbation is taken such that

$$m(t)n(x) \propto t \exp -bt \exp -0.5x^2/a^2,$$

so that

$$|g(w)|^2 |f(k)|^2 = (b^2 + w^2)^{-2} \exp -a^2 k^2$$

with

$$b = 1/15 \text{ sec}^{-1}, a = (200)^{1/2} \text{ km}$$

Only the longer horizontal wave-lengths are excited to an appreciable degree by such a disturbance. The large value of 'a' chosen assures that the expression in Eq(3) is a convenient one for numerical

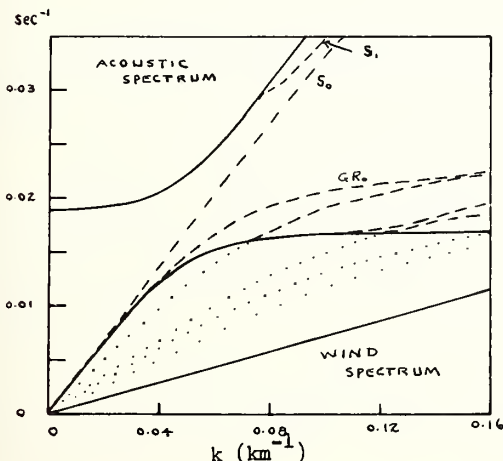


Fig. 1. The  $w$ - $k$  diagram for the downwind direction showing the regions of the various spectra of waves.

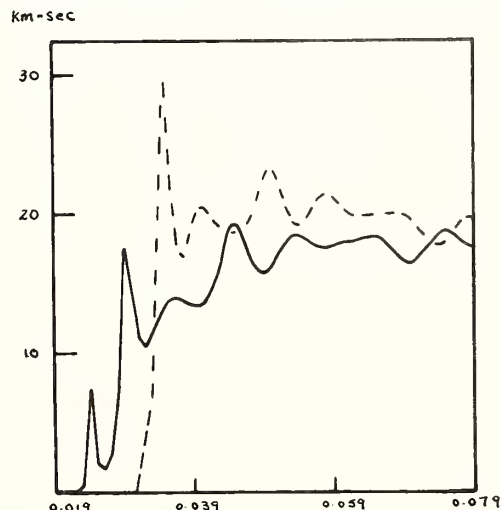


Fig. 2. The flux function in the continuous acoustic spectrum, downwind direction,  $k=0.01 \text{ km}^{-1}$ .



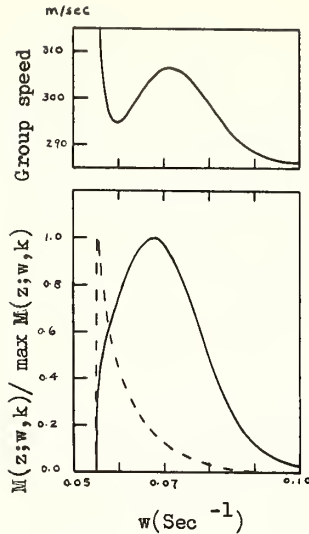


Fig. 3. The relationship between the dispersion curve of the  $S_3$  mode, downwind direction (A) and the behaviour of  $M(z;w,k)$  at an altitude of 119 km --- and at the ground — (B).

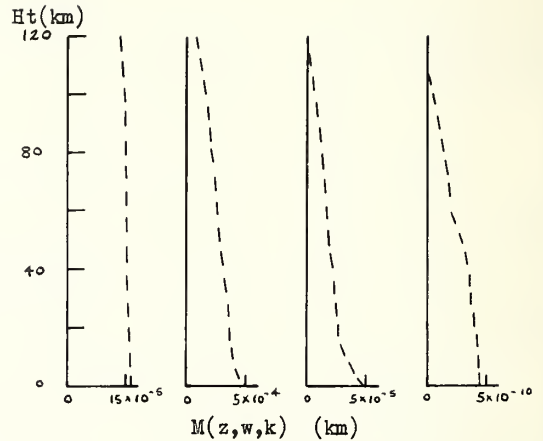


Fig. 4. The flux function,  $M(z;w,k)$ , for the S mode, downwind direction. For the panels from left to right the associated values of horizontal wave-length, period and group speed are as follows: 42 km, 114 sec, 359 m/sec; 39 km, 107 sec, 295 m/sec; 32 km, 90 sec, 306 m/sec; 22 km, 66 sec, 287 m/sec.

(Pfeffer and Zarichny 1963) Figs. 3 and 4 show how variations in horizontal group speed are related to the behaviour of  $M(z)$ .

MacKinnon (1968a) has presented modal dispersion curves for the modal atmosphere herein under study. (Note an error in Fig. 1 of that paper. The lowermost dotted curve represents the case here i.e. the "low-wind case", whereas the lowermost dashed curve represents the "high-wind case".) Differences in dispersion curves for differing wind conditions indicate that winds play an important role in determining the vertical distribution of energy flux. This is confirmed by results given in Tables 2-4. The sum of modal contributions to energy flux near the ground in upwind and downwind directions very nearly equals the modal energy flux in the no-wind case, however, at 119 km the modes of the calm atmosphere contribute more than the sum of the modes of the windy atmosphere. Taken as a whole the downwind modes are more efficiently trapped in the lower sound channel than are the upwind modes. Because of the rapid decrease of  $f(k)$  with  $k$  the differences between the modal contributions in the two wind directions are due mainly to the behaviour of the fundamental modes at longer periods.

The fundamental mode on the 120 km model without winds exhibits the three major phases shown in Figs. 5 and 6: at longer periods it represents energy trapped in the upper reaches of the upper sound channel; at intermediate periods it represents energy trapped near the ground; and at shorter periods it represents energy trapped near the center of the upper sound channel. The downward shift with period of energy concentration results in inverse dispersion at longer periods whereas the subsequent upward shift results in normal dispersion. The fundamental mode for the downwind direction resembles that of the calm atmosphere at shorter periods, but for all periods greater than 4 min it represents energy trapped near the ground.

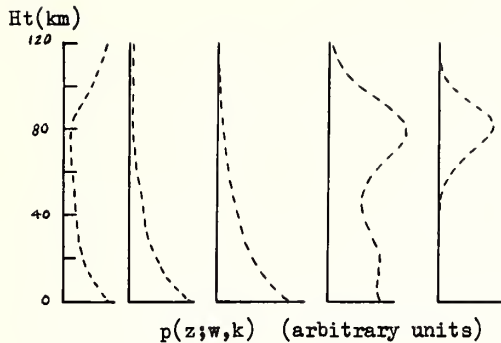


Fig. 5. The pressure eigenfunction,  $p(z;w,k)$ , for the So mode in a calm atmosphere. For the panels left to right the associated periods are 537, 428, 247, 100 and 66 sec, respectively.

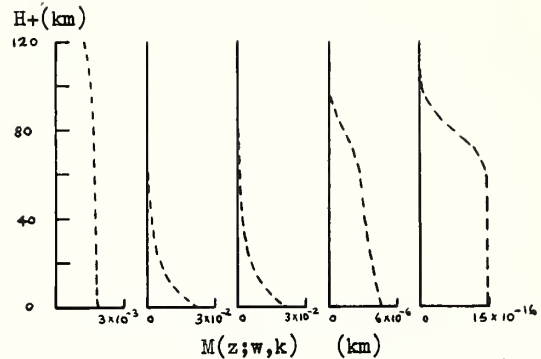


Fig. 6. The flux function,  $M(z;w,k)$ , for the So mode in a calm atmosphere. For the panels from left to right the associated values of horizontal wave-length, period and group speed are as follows: 179 km, 580 sec, 279 m/sec; 131 km, 425 sec, 307 m/sec; 79 km, 252 sec, 306 m/sec; 30 km, 100 sec, 286 m/sec; 19 km, 66 sec, 278 m/sec.

In the upwind direction the fundamental mode at periods between 1-6 min represents energy trapped near the ground, but at longer periods it resembles the fundamental mode for the calm atmosphere until it attains its cut-off frequency of 890 sec. At the longer periods it is the GRo mode rather than the fundamental which represents energy trapped near the ground in the upwind direction. It is a characteristic of the 120 km models that higher-order gravity modes contribute little to the total energy flux.

#### Continuous Gravity Spectrum

Winds play an important part in determining the contribution to energy flux by long-period waves included within the continuous gravity spectrum (Table 5). The flux function  $H(z;w,k)$  is shown in Fig. 7 for the downwind direction. For  $w/k$  less than 72 m/sec critical levels exist in the downwind direction which govern the behaviour of  $H$ . This point is taken up in the next section. Other than for such values of  $w$  and  $k$  in the downwind direction,  $H(z;w,k)$  is independent of altitude. As a function of  $w$  for fixed  $k$ ,  $H$  exhibits a series of peaks (Fig. 7). The peaks are due largely to variations in  $q(o;w,k)$  (Fig. 8). It is likely that the peaks are associated with zeroes of  $q(o;w,k)$  in the complex  $k$ -plane, i.e. with the 'leaky modes' found by Friedman (1966).

For small  $k$ , less than  $0.08 \text{ km}^{-1}$ , say, a large fraction of the integral of  $H$  with respect to  $w$  comes from these peaks. A particular peak may be thought of as progressing with increasing  $k$  through values of  $(w,k)$  in the continuous spectrum (the dotted paths of Fig. 1). The peak grows as it approaches the boundary with the discrete spectrum. It reaches the boundary at a cut-off frequency of an associated gravity mode. For somewhat larger values of  $k$  the peak has disappeared from the continuous spectrum. For the 120 km model the peaks associated with the GRo and R modes contribute greatly to the energy. Once these peaks have disappeared from the continuous spectrum the integral over  $w$  of  $H$  is largely reduced.

It is a major task for a computer to evaluate integrals of  $H$  over real  $w$  and  $k$ . For results given in Table 5 a 'brute force' technique was employed. For a fixed  $k$  the interval of integration over  $w$  was divided into quarters over which the trapezoidal rule was employed with decreasing step-length until agreeing estimates were obtained. The upper quarter contributes the most to the integral as it contains the largest peaks, hence it requires the largest numbers of evaluations of  $H$ . Runge-Kutta integration was employed to obtain estimates of  $H$ . Luckily the number of Runge-Kutta steps needed to obtain a sufficiently accurate estimate of  $H$  decreases with increasing  $w$  as so was least in the upper quarter. The integration over  $k$  was estimated by six- and seven-point Gauss-Laguerre formulae. That reasonable estimates could be obtained with so few values of



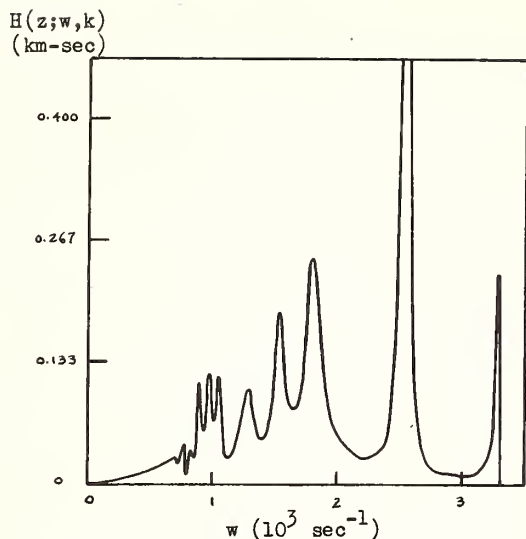


Fig. 7. The flux function,  $H(z; w, k)$ , for the gravity and wind spectra in the downwind direction. The horizontal wave-number is  $0.01 \text{ km}^{-1}$ .

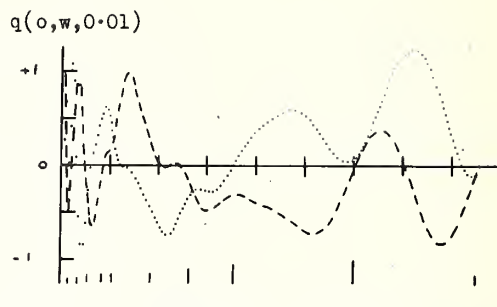


Fig. 8. The perturbed displacement function,  $q(o, w, k)$ , in the downwind direction at  $k=0.01 \text{ km}^{-1}$  over an interval of  $w$  corresponding to the continuous gravity spectrum: — — — real part of  $q$ ; ..... imaginary part of  $q$ . The sub-intervals of  $w$  indicated represent  $3 \cdot 10^{-4} \text{ sec}^{-1}$ . The vertical lines at the bottom of the diagram indicate local maxima of the flux function shown in Fig. 8.

$k$  was due to the nature of  $f(k)$ .

#### Continuous Wind Spectrum

For the downwind direction at small phase speeds the occurrence of critical levels alters the nature of  $p$  and  $q$  since at such altitudes  $w - kU(z)$  is zero so that the residual equations possess a singularity. The occurrence of critical levels defines an area of the  $w$ - $k$  plane which corresponds to a continuous wind spectrum. It overlaps parts of the continuous gravity spectrum and the discrete spectrum (Fig. 1.). Effects of critical levels in shear layers have been discussed by Miles (1961) and Booker and Bretherton (1967), the latter authors showing that the effect of critical levels on upward moving waves is to confine their energy to lower levels. In shear layers solutions to the residual equation about a critical level may be obtained from Frobenius series or through integration in the complex  $z$ -plane (See, for example, Zaat 1958). For the calculations given herein Frobenius series of nine terms were employed. The numerical procedure was to integrate the residual equations downwards from the uppermost layer using Runge-Kutta integration until the altitude of 24 km was reached, then to employ Frobenius series about the two critical levels which exist for the assumed wind profile, matching solutions at 24 km and 12 km. The function  $pq$  has a discontinuity at a critical level but is constant over any interval of  $z$  not containing a critical level. The flux function  $H$  is given in Table 6 for a fixed  $k$  and for three values of  $w$  which yield critical levels at various altitudes. In agreement with Booker and Bretherton (1967) a great reduction in  $H$  is to be noted for altitudes above the lower critical level. In Fig. 7 the flux function shown for values of  $w$  less than  $0.00072 \text{ sec}^{-1}$  is that at the ground. The great reductions are attributable mathematically to a phase shift in the function  $(w - kU(z))^{1/2}$  about the critical levels. Thus the wind spectrum energy flux is concentrated below altitudes of 12 km. (Table 7) A further wind effect is that the continuous gravity spectrum contribution to vertical energy flux is much reduced in the downwind direction (Table 5).

Another effect of the wind at short wave-lengths in the downwind direction is to prohibit modal curves for higher order gravity modes from originating at the boundary between the gravity spectrum and the discrete spectrum. Numerical results indicate that the boundary between the wind spectrum and the discrete spectrum ( $w/k=0.072 \text{ km/sec}$ ) becomes a limit line of an infinity of modal curves. To be noted in the regard are the rapid oscillations in the real part of  $q(o; w, k)$  shown in Fig. 8 near the boundary with the wind spectrum. Such modes cannot be expected to

contribute significantly to energy flux in the case under study because of the nature of  $f(k)$ , however they do contribute some small amount to the vertical energy. These modes represent gravity waves moving with the wind whose vertical energy flux decreases rapidly about the altitude of maximum wind.

**Acknowledgments.** This work was performed in cooperation with Dr F.W.G. Warren of Imperial College of Science and Technology, London, England, to whom the author is indebted for many hours of fruitful discussion. It was done during a period when the author was recipient of a scholarship from the Defence Research Board of Canada. Calculations were performed on the Atlas computer of the University of London.

#### References

- Booker, J.R. and F.P. Bretherton, The critical layer for internal gravity waves in a shear flow, *J. Fluid Mech.*, 27, 513-539, 1967.
- Friedman, J.P., Propagation of internal gravity waves in a thermally stratified atmosphere, *J. Geophys. Res.*, 71, 1033-1054, 1966.
- Hazel, P., The effect of viscosity and heat conduction on internal gravity waves at a critical level, *J. Fluid Mech.*, 30, 775-783, 1967.
- Hines, C.O., Internal atmospheric gravity waves at ionospheric heights, *Can. J. Phys.*, 38, 1441-1481, 1960.
- Hines, C.O., On the nature of traveling ionospheric disturbances launched by low-altitude nuclear explosions, *J. Geophys. Res.*, 72, 1877-1882, 1967.
- Hines, C.O. and C.A. Reddy, On the propagation of atmospheric gravity waves through regions of wind shear, *J. Geophys. Res.*, 72, 1015-1034, 1967.
- Jones, W.L., Propagation of internal gravity waves in fluids with shear flow and rotation, *J. Fluid Mech.*, 30, 439-448, 1967.
- MacKinnon, R.F., The effects of winds on acoustic-gravity waves from explosions in the atmosphere, *Quart. J. Roy. Meteorol. Soc.*, 93, 436-454, 1967.
- MacKinnon, R.F., Effects of winds on atmospheric pressure waves produced by hydrogen bombs, *J. Meteorol. Soc. Japan*, 1968a.
- MacKinnon, R.F., A comparative study of ground pressure waves in various atmospheric models, *Can. J. Phys.*, (to be published) 1968b.
- Miles, J.W., On the stability of heterogeneous shear flow, *J. Fluid Mech.*, 10, 496-508, 1961.
- Pfeffer, R.L., and J. Zarichny, Acoustic gravity wave propagation in an atmosphere with two sound channels, *Geophys. Pura Appl.*, 55, 173-199, 1963.
- Pierce, A.D., Propagation of acoustic gravity waves in a temperature- and wind-stratified atmosphere, *J. Acoust. Soc. Amer.*, 37, 218-227, 1965.
- Pierce, A.D., Guided infrasonic modes in a temperature- and wind-stratified atmosphere, *J. Acoust. Soc. Amer.*, 41, 597-611, 1967.
- Row, R.V., Acoustic gravity waves in the upper atmosphere due to a nuclear detonation and an earthquake, *J. Geophys. Res.*, 72, 1599-1610, 1967.
- Tolstoy, I., Long-period gravity waves in the atmosphere, *J. Geophys. Res.*, 72, 4605-4622, 1967.
- Warren, F.W.G., A note on Howard's proof of Miles' theorem, (to be published in August issue, *Quart. J. Mech. Appl. Maths.*) 1968a.
- Warren, F.W.G., Some calculations of vertical mechanical wave flux in the atmosphere, (to be published at this symposium) 1968b.
- Warren, F.W.G., and M.K. Arora, A problem of vertical distribution of mechanical wave energy in the atmosphere, *Quart. J. Mech. Appl. Maths.*, 20, 316-332, 1967.
- Wickersham, A.F., Jr., Identification of acoustic-gravity modes from ionospheric range-time observations, *J. Geophys. Res.*, 71, 4551-4555, 1967.
- Zaat, J.A., Numerical contributions to stability theory of boundary layers, in *Grenzschichtforschung* (H. Görtler, ed.), (Springer-Verlag 1958)

Table 1. Characteristics of the model atmosphere (Variations are linear between the indicated values)

Altitude (km)	Temperature (°K)	Wind Speed (m/sec)
120	334	0
120	334	0
84	189	0
48	258	0
28	212	0
24	212	0
12	212	72
0	289	0

Table 2. Contributions to F(z), the nett mean vertical perturbation energy flux, by normal modes of propagation in a calm atmosphere.

Height	$\frac{1}{2}$ Vertical Perturbation Energy Flux (Arbitrary Units)								
(Km)	S <sub>0</sub>	S <sub>1</sub>	S <sub>2</sub>	S <sub>3</sub>	S <sub>4</sub>	S <sub>5</sub>	GR <sub>0</sub>	GR <sub>1</sub>	GR <sub>2</sub>
119 2.00	(-5)*6.49	(-6) 0.84	(-5) 2.4	(-6) 1.7	(-7) 7.3	(-9) 2.11	(-5) 2.5	(-7) 0.8	(-8)
108 2.49	(-5) 1.06	(-5) 1.27	(-5) 3.7	(-6) 2.6	(-7) 1.1	(-8) 2.49	(-5) 3.6	(-7) 1.1	(-8)
96 3.06	(-5) 1.94	(-5) 2.01	(-5) 5.5	(-6) 3.6	(-7) 1.4	(-8) 2.82	(-5) 4.6	(-7) 1.3	(-8)
84 3.71	(-5) 3.67	(-5) 2.85	(-5) 6.6	(-6) 3.9	(-7) 1.6	(-8) 3.00	(-5) 5.6	(-7) 1.6	(-8)
72 4.81	(-5) 6.26	(-5) 3.26	(-5) 7.5	(-6) 4.6	(-7) 1.8	(-8) 3.05	(-5) 7.6	(-7) 1.8	(-8)
60 7.04	(-5) 8.50	(-5) 3.69	(-5) 9.1	(-6) 4.9	(-7) 2.0	(-8) 3.08	(-5) 1.3	(-6) 1.8	(-8)
48 1.145	(-4) 9.72	(-5) 4.80	(-5) 9.7	(-6) 5.8	(-7) 2.2	(-8) 3.13	(-5) 2.6	(-6) 1.8	(-8)
38 1.821	(-4) 1.022	(-4) 5.91	(-5) 1.03	(-5) 6.2	(-7) 2.5	(-8) 3.21	(-5) 4.8	(-6) 1.9	(-8)
24 3.762	(-4) 1.058	(-4) 6.98	(-5) 1.22	(-5) 6.7	(-7) 2.7	(-8) 3.47	(-5) 7.7	(-6) 1.9	(-8)
12 7.623	(-4) 1.084	(-4) 7.32	(-5) 1.29	(-5) 7.1	(-7) 2.9	(-8) 4.04	(-5) 8.7	(-6) 1.9	(-8)
6 1.1038	(-3) 1.108	(-4) 7.64	(-5) 1.34	(-5) 7.2	(-7) 3.0	(-8) 4.60	(-5) 8.9	(-6) 1.9	(-8)
0 1.6005	(-3) 1.145	(-4) 8.24	(-5) 1.44	(-5) 7.6	(-7) 3.2	(-8) 5.47	(-5) 9.1	(-6) 1.9	(-8)

\* The number in brackets denotes the position of the decimal point.  
Thus 2.00 (-5) = 2  $\cdot 10^{-5}$

Table 3. Contributions to F(z), the nett mean vertical perturbation energy flux, by normal modes of propagation associated with the downwind direction.

Height	Vertical Perturbation Energy Flux (Arbitrary Units)								
(Km)	S <sub>0</sub>	S <sub>1</sub>	S <sub>2</sub>	S <sub>3</sub>	S <sub>4</sub>	S <sub>5</sub>	GR <sub>0</sub>	GR <sub>1</sub>	GR <sub>2</sub>
119 2.4	(-6) 1.38	(-5) 1.09	(-5) 2.4	(-6) 1.5	(-7) 2.2	(-8) 0.8	(-6) 1.9	(-7) 3.2	(-8)
108 4.9	(-6) 2.35	(-5) 1.64	(-5) 3.6	(-6) 2.2	(-7) 0.3	(-8) 1.1	(-6) 2.8	(-7) 5.3	(-8)
96 1.05	(-5) 4.33	(-5) 2.50	(-5) 5.0	(-6) 2.8	(-7) 0.4	(-8) 1.4	(-6) 3.8	(-7) 6.7	(-8)
84 2.21	(-5) 7.83	(-5) 3.31	(-5) 5.6	(-6) 3.1	(-7) 0.5	(-8) 1.7	(-6) 4.7	(-7) 8.1	(-8)
72 4.47	(-5) 1.238	(-4) 3.64	(-5) 6.5	(-6) 3.5	(-7) 0.5	(-8) 1.8	(-6) 6.2	(-7) 9.4	(-8)
60 7.91	(-5) 1.558	(-4) 4.33	(-5) 7.3	(-6) 3.9	(-7) 0.6	(-8) 1.8	(-6) 1.0	(-6) 1.1	(-7)
48 1.269	(-4) 1.714	(-4) 5.43	(-5) 7.7	(-6) 4.4	(-7) 0.6	(-8) 1.8	(-6) 2.0	(-6) 1.3	(-7)
38 1.861	(-4) 1.827	(-4) 6.07	(-5) 8.9	(-6) 4.5	(-7) 0.7	(-8) 1.8	(-6) 3.6	(-6) 1.6	(-7)
24 3.845	(-4) 2.074	(-4) 6.46	(-5) 1.01	(-5) 5.0	(-7) 0.8	(-8) 1.8	(-6) 6.1	(-6) 1.8	(-7)
12 7.783	(-4) 2.484	(-4) 7.04	(-5) 1.10	(-5) 5.3	(-7) 0.8	(-8) 1.9	(-6) 7.3	(-6) 2.4	(-7)
6 1.212	(-3) 2.822	(-4) 7.71	(-5) 1.35	(-5) 5.7	(-7) 0.9	(-8) 1.9	(-6) 7.5	(-6) 2.5	(-7)
0 1.726	(-3) 3.218	(-4) 8.62	(-5) 1.44	(-5) 6.5	(-7) 1.0	(-8) 1.9	(-6) 7.6	(-6) 2.5	(-7)

Table 4. Contributions to F(z), the nett mean vertical perturbation energy flux, by normal modes of propagation associated with the upwind direction.

Height	Vertical Perturbation Energy Flux (Arbitrary Units)															
(Km)	S <sub>0</sub>		S <sub>1</sub>		S <sub>2</sub>		S <sub>3</sub>		S <sub>4</sub>		GR <sub>0</sub>		GR <sub>1</sub>		GR <sub>2</sub>	
119	1.96	(-5)	5.8	(-6)	1.0	(-5)	3.4	(-6)	3.3	(-7)	2.39	(-5)	3.3	(-7)	0.7	(-8)
108	2.85	(-5)	9.1	(-6)	1.6	(-5)	5.1	(-6)	5.2	(-7)	3.30	(-5)	4.6	(-7)	1.0	(-8)
96	3.84	(-5)	1.6	(-5)	2.5	(-5)	7.8	(-6)	7.5	(-7)	4.19	(-5)	5.7	(-7)	1.3	(-8)
84	4.61	(-5)	2.8	(-5)	3.7	(-5)	9.7	(-6)	8.2	(-7)	4.76	(-5)	6.7	(-7)	1.5	(-8)
72	5.25	(-5)	4.7	(-5)	4.4	(-5)	1.08	(-5)	9.7	(-7)	5.00	(-5)	9.0	(-7)	1.7	(-8)
60	6.57	(-5)	6.4	(-5)	4.8	(-5)	1.33	(-5)	1.04	(-6)	5.22	(-5)	1.5	(-6)	1.7	(-8)
48	9.70	(-5)	7.5	(-5)	6.0	(-5)	1.51	(-5)	1.32	(-6)	5.67	(-5)	2.9	(-6)	1.8	(-8)
38	1.509	(-4)	8.1	(-5)	7.7	(-5)	1.55	(-5)	1.37	(-6)	6.34	(-5)	5.2	(-6)	1.8	(-8)
24	3.124	(-4)	8.5	(-5)	1.02	(-5)	1.74	(-5)	1.46	(-6)	7.95	(-5)	8.0	(-6)	1.8	(-8)
12	5.905	(-4)	8.7	(-5)	1.11	(-4)	1.87	(-5)	1.59	(-6)	1.03	(-4)	8.8	(-6)	1.8	(-8)
6	8.173	(-4)	8.8	(-5)	1.16	(-4)	1.92	(-5)	1.62	(-6)	1.22	(-4)	9.0	(-6)	1.8	(-8)
0	1.196	(-3)	9.0	(-5)	1.26	(-4)	2.03	(-5)	1.71	(-6)	1.58	(-4)	9.2	(-6)	1.8	(-8)

Table 5. Contributions to  $F(z)$  from the regions of the continuous spectra for which no critical levels exist.

Continuous Spectrum	$\pi^{-1}$ Vertical Perturbation Energy Flux		
	Calm	Upwind	Downwind
Acoustic	4.90(-1)	2.45 (-1)	2.45 (-1)
Gravity	2.0 (-3)	1.31 (-3)	1.82 (-4)

Table 6. The flux function  $H(z;w,k)$  for  $k=0.05 \text{ km}^{-1}$  and for three values of  $w$  within the region of critical levels.

Height (km)	$H(z;w,0.05) \text{ (km - sec)}$		
	Location of Lower Critical Level		
	2 km	6 km	11 km
0	2.3 (-3)	2.2 (-2)	7.4 (-2)
4	-2.8 (-8)	2.2 (-2)	7.4 (-2)
10	-2.8 (-8)	-1.5 (-7)	7.4 (-2)
17	5.5 (-18)	-1.5 (-7)	-2.1 (-7)
24	5.5 (-18)	3.1 (-17)	4.2 (-17)

Table 7. Contributions to  $F(z)$  in the downwind direction from the region of critical levels

Height (km)	$\pi^{-1}$ Vertical Perturbation Energy Flux	
0	1.04	(-5)
2	1.03	(-5)
4	1.00	(-5)
6	0.90	(-5)
10	0.43	(-5)
12	1	(-10)





# THEORETICAL CALCULATIONS OF VERTICAL MECHANICAL WAVE ENERGY FLUX IN THE ATMOSPHERE

F. W. G. Warren  
Department of Mathematics  
Imperial College  
London S. W. 7, England

A disturbance in the lower part of a windy stratified atmosphere  
excites a dispersion system of waves. Expressions are derived for the  
vertical energy flux as a function of the height.

## INTRODUCTION

This paper is a sequel to an earlier paper (Warren and Arora, 1967) devoted to the same problem. The theory is here developed further and calculations are made for a windy non-isothermal model atmosphere. Disturbances within the atmosphere often excite gravity waves or compression (elastic, acoustic) waves or both, and that the basic task is to find how a local source of wave energy will distribute itself throughout the depth of the atmosphere. Some of the waves are reflected by the inhomogeneous atmosphere while the remainder radiate freely to large heights where the energy is absorbed by viscosity and other mechanisms. The reflected waves are also ultimately absorbed by viscous and similar processes, but this decay is relatively slow. In order to take account of the dissipation at very high altitudes a fictitious upper layer called the isosphere is introduced. This is an isothermal layer which extends indefinitely upwards from the level of the base of isosphere or 'top' of the atmosphere. Within this layer the wind speed and direction is by definition constant and so without loss of generality it may be supposed that there is no wind there. The physical justification for a model with an isosphere requires in reality the existence of an isothermal layer with no wind shear, in and below which the inviscid linearised equations make good approximation to the air flow. Further, within this layer there is negligible propagation of energy downwards. Yanowitch (1967) has shown that if viscosity is introduced into the model some reflection can occur at those upper levels where the atmosphere is tenuous and the dynamic viscosity very large. However this reflection occurs over a small frequency range and other factors, such as thermal conduction, are not considered. Thus while the introduction of a reflection coefficient (as a function of frequency and wavenumber) for the isosphere would be more realistic, the hypothesis is that there exists an optimum level for the isospheric base for which this coefficient is small. The estimation of this level, which will depend on the nature of the source spectrum is not attempted here. For present purposes it may be placed at say 120 km.

The governing equations are derived for instance by Eckart (1960) and the introduction of a horizontal wind is a straightforward modification. They read

$$\mathcal{L} \mathcal{R} = 0 \quad , \quad (1.1)$$

where  $\mathcal{L}$  is the operator

$$\left[ \begin{array}{cc} \alpha - \partial/\partial z & n^2 + d^2/dt^2 \\ \partial^2/\partial x^2 + \partial^2/\partial y^2 - c^{-2} d^2/dt^2 & d^2/dt^2 (\alpha + \partial/\partial z) \end{array} \right]$$

and  $\mathcal{R}$  is the vector

$$\mathcal{R}(x, y, z, t) = \begin{bmatrix} p(x, y, z, t) \\ \mathbf{2}(x, y, z, t) \end{bmatrix} .$$

Here

$$\alpha = g/c^2 + \frac{1}{2}\rho'/\rho ,$$

and

$$n^2 = -g^2/c^2 - g\rho'/\rho , \quad (n \text{ is the Väisälä-Brunt frequency})$$

where  $c$  is the basic local velocity of sound and  $\rho$  is the basic local density. Here and henceforth a prime denotes the differentiation with respect to  $z$ . The wind velocity is  $(u, v, 0) = \underline{u}$ , and

$$d/dt = \partial/\partial t + u \partial/\partial x + v \partial/\partial y .$$

The model is horizontally homogeneous and isotropic so that  $\alpha$ ,  $n$ ,  $c$ , and  $u$  are functions of height only.  $p$  and  $z$  are modified pressure-perturbation and displacement functions, such that the actual linearized pressure perturbation is  $\rho \frac{1}{2} p$  and vertical displacement of a fluid particle is  $\rho \frac{1}{2} z$ . The vertical velocity of a particle is  $\rho^{-\frac{1}{2}} dz/dt$ . The Cartesian axes  $(x, y, z)$  have the vertical  $z$  axis positive downwards, so that the base of the isosphere is at  $z = 0$  and sealevel is at

$$z = d > 0 .$$

No account is taken of the earth's curvature and rotation and the effects of ground topography are ignored, as also are effects of lateral variations in temperature and wind velocity. Further, the maximum wind velocity  $|\underline{u}|_{\max}$  is assumed to be less than the minimum velocity of sound in the model.

#### THE GREEN'S MATRIX FOR THE INITIAL VALUE PROBLEM

Generally, given the pressure and displacement fields (and their first time derivatives) at time  $t = 0$ , it is required to estimate the resultant nett flux through any horizontal level. The perturbation may also be defined as a local transient excitation of the pressure and/or particle displacement say at the lowest level. The numerical calculations were made for this latter case, but the theory is developed for the former which includes the latter.

The Fourier-Laplace transform

$$\int_{-\infty}^{\infty} dx \int_{-\infty}^{\infty} dy \int_0^{\infty} dt e^{-i(kx + ly - \omega t)}$$

reduces (1.1) to the form

$$\underline{\underline{L}} \underline{\underline{R}} = \underline{\underline{S}} \quad (2.1)$$

where  $\underline{\underline{L}}$  is the operator

$$\begin{bmatrix} \alpha - \partial/\partial z & n^2 - v^2 \\ k^2/v^2 - 1/c^2 & \alpha + \partial/\partial z \end{bmatrix} ,$$

$\underline{\underline{R}}$  is the vector

$$\begin{aligned} \underline{\underline{R}}(k, l, z, \omega) &= \begin{bmatrix} p(k, l, z, \omega) \\ q(k, l, z, \omega) \end{bmatrix} \\ &= \int_{-\infty}^{\infty} dx \int_{-\infty}^{\infty} dy \int_0^{\infty} dt R(x, y, z, t) e^{-(kx + ly - \omega t)} , \end{aligned}$$

and

$$\begin{aligned} v(k, l, z, \omega) &= \omega - ku(z) - lv(z) \\ &= \omega - \kappa U(z) \end{aligned}$$

where  $U(z) = \underline{u} \cdot \underline{u} / \kappa$  is the resolved velocity profile, with  $\underline{u} = (k, l, 0)$  and  $\kappa^2 = k^2$ ,  $\kappa \geq 0$ . The wave numbers  $k$  and  $l$  are real, while  $\text{im } \omega > 0$ .

$$\underline{S}(k, l, z, \omega) = \begin{bmatrix} S_1 \\ S_2 \end{bmatrix}$$

is given by

$$S_1 = -2i\nu \underline{Q}_0(k, l, z) + \underline{Q}_0(k, l, z) + i\omega \underline{Q}_0(k, l, z) ,$$

and

$$\begin{aligned} S_2 &= (2i/c^2 \nu) p_0(k, l, z) - (\partial/\partial z + \alpha)(2i/\nu) \underline{Q}_0(k, l, z) \\ &\quad - (\dot{p}_0(k, l, z) + i\omega p_0(k, l, z))/\nu^2 \\ &\quad + (\partial/\partial z + \alpha) (\dot{\underline{Q}}_0(k, l, z) + i\omega \underline{Q}_0(k, l, z))/\nu^2 . \end{aligned}$$

Here and hereafter a dot denotes differentiation with respect to the time, for example  $\dot{p}_0(k, l, z)$  denotes the first time derivative of the Fourier transform of  $p(x, y, z, t)$  at  $t = 0$ .  $\underline{S}$  has poles at points  $\omega_c$  on the real  $\omega$  axis where  $v(k, l, z, \omega_c)$  vanishes. Thus for fixed  $\omega$  there may exist a critical level  $z_c$  where the phase and wind speed are equal. A viscous thermally conducting model is more satisfactory for critical level flow. However for finite time intervals the limit of the corresponding solution of the transient initial value problem, as the viscosity and conductivity tend to zero, may be expected to coincide with the inviscid solution. This latter solution is reasonably well behaved for transient initial value problems provided the model is stable. The use of an inviscid model for this purpose has been the subject of some recent work by Booker and Bretherton (1967) and Hazel (1967).

A Green's function for the operator  $L$  is now constructed. Two fundamental solutions  $\underline{R}_{1,2}^{(0)}(k, l, z, \omega)$  of the homogeneous equation  $\underline{L}\underline{R} = 0$  form a basis where

$$\underline{R}_1^{(0)}(0) = \begin{pmatrix} 1 \\ 0 \end{pmatrix} \text{ and } \underline{R}_2^{(0)}(0) = \begin{pmatrix} 0 \\ 1 \end{pmatrix} .$$

Then in  $d > z > -\infty$  both  $\underline{R}_1^{(0)}$  and  $\underline{R}_2^{(0)}$  are analytic functions of  $k$ ,  $l$ , and  $\omega$  - except in the neighbourhood of the critical frequency  $\omega_c$  - provided  $n(z)$ ,  $\alpha(z)$ ,  $c(z)$ , and  $\underline{u}(z)$  are sufficiently well behaved. Sufficient conditions for this are a smooth vertical gradient of the basic temperature profile, and continuous velocity profile components which will also be assumed to be analytic functions of  $z$  in the neighbourhood of the real  $z$  axis, except possibly at a finite number of points of it. Then when  $z < 0$

$$\underline{R}_1^{(0)}(z) = \begin{bmatrix} \cosh \mu_0 z + (\alpha_0/\mu_0) \sinh \mu_0 z \\ (1/c_0^2 - k^2/\nu_0^2)/\mu_0 \sinh \mu_0 z \end{bmatrix} ,$$

and

$$R_2^{(0)}(z) = \begin{bmatrix} (n_0^2 - v_0^2)/\mu_0 \sinh \mu_0 z \\ \cosh \mu_0 z - (\alpha_0/\mu_0) \sinh \mu_0 z \end{bmatrix}.$$

Here

$$\mu_0 = \{\alpha_0^2 - (n_0^2 - v_0^2)(k^2/v_0^2 - 1/c_0^2)\}^{\frac{1}{2}},$$

and the suffic 0 here and henceforth denotes that  $z$  is to be set equal to zero so that  $v_0 = \omega$ . The branch of  $\mu_0$  is immaterial at this stage, but to avoid ambiguity that which has positive real part when  $\text{im } \omega \neq 0$  is selected.

In the case that the reflection coefficient is zero in the isosphere which therefore conducts no energy downwards the appropriate fundamental solutions are given by

$$\begin{aligned} \tilde{R}_+(z) &= (\alpha_0 + \mu_0) \tilde{R}_1^{(0)}(z) + (1/c_0^2 - k^2/v_0^2) R_2^{(0)}(z) \\ &= \begin{bmatrix} \alpha_0 + \mu_0 \\ 1/c_0^2 - k^2/v_0^2 \end{bmatrix} \exp(\mu_0 z) \text{ if } z \leq 0, \end{aligned}$$

and

$$\begin{aligned} \tilde{R}_-(z) &= (v_0^2 - n_0^2) \tilde{R}_1^{(0)}(z) + (\alpha_0 + \mu_0) R_2^{(0)}(z) \\ &= \begin{bmatrix} v_0^2 - n_0^2 \\ \alpha_0 + \mu_0 \end{bmatrix} \exp(-\mu_0 z) \text{ if } z \leq 0, \end{aligned}$$

and the Wronskian of these solutions is  $W = 2\mu_0(\alpha_0 + \mu_0)$ . Then by the radiation condition in the isosphere the solution of equation (2.1) contains only  $\tilde{R}_+(z)$ , if  $z < 0$ . As in Warren and Arora, 1967, solutions

$$\tilde{R}_{1,2}(z) = \begin{bmatrix} P_{1,2}(z) \\ q_{1,2}(z) \end{bmatrix}$$

are now constructed:

$$\begin{aligned} p_1(z) &= p_1(k, \ell, z, \omega; \zeta) = \{p_+(z)q_-(d) - p_-(z)q_+(d)\} p_+(\zeta); \\ &\quad d > z > \zeta \\ &= \{p_+(\zeta)q_-(d) - p_-(\zeta)q_+(d)\} p_+(z); \\ &\quad d > \zeta > z \end{aligned}$$

Similarly

$$\begin{aligned} q_1(z) &= \{q_+(d)q_-(z) - q_+(z)q_-(d)\} p_+(\zeta); \quad d > z > \zeta, \\ &= \{q_+(d)p_-(\zeta) - q_-(d)p_+(\zeta)\} q_+(z); \quad d > \zeta > z, \end{aligned}$$

$$p_2(z) = \{p_+(z)q_-(d) - p_-(z)q_+(d)\} q_+(\zeta); \quad d > z > \zeta, \\ = \{q_+(\zeta)q_-(d) - q_-(\zeta)q_+(d)\} p_+(z); \quad d > \zeta > z,$$

and

$$q_2(z) = \{q_+(d)q_-(z) - q_-(z)q_+(d)\} q_+(\zeta); \quad d > z > \zeta, \\ = \{q_+(d)q_-(\zeta) - q_-(\zeta)q_+(d)\} q_+(z); \quad d > \zeta > z.$$

Here the lower boundary condition, that the vertical displacement vanishes at the ground, has been anticipated:

$$(x, y, d, t) = q(k, l, d, t) = 0$$

for all  $t \geq 0$ . The appropriate solution of  $\tilde{L}\tilde{R} = \tilde{S}$  may now be written

$$\tilde{R}(k, l, \omega, z) = \int_{-\infty}^d d\zeta \{R_1(k, l, z, \omega; \zeta) S_2(\zeta) \\ + R_2(k, l, z, \omega; \zeta) S_1(\zeta)\} \\ / W(k, l, \omega) q_+(k, l, d, \omega). \quad (2.2)$$

Setting

$$\tilde{G}(k, l, z, \omega; \zeta) = \begin{bmatrix} p_2 & p_1 \\ q_2 & q_1 \end{bmatrix}$$

and using the inversion theorems, it follows that

$$\tilde{R}(x, y, z, k) = (1/8\pi^3) \int_{-\infty}^{\infty} dk \int_{-\infty}^{\infty} dl \int_{i\Omega-\infty}^{i\Omega+\infty} d\omega \int_{-\infty}^d d\zeta \\ \tilde{G}(k, l, z, \omega; \zeta) \cdot \tilde{S}(k, l, \zeta, \omega) e^{i(kx + ly - \omega t)} \\ / W(k, l, \omega) q_+(k, l, d, \omega), \quad (2.3)$$

where  $\Omega$  is real and positive so that the path of integration is a straight line  $L$  above the real  $\omega$  axis. Since  $\bar{p}_+(-k, -l, z, -\omega) = p_+(k, l, z, \omega)$  (where the bar denotes complex conjugate) as may be shown by arguments similar to those employed in (1), this result may be written

$$\tilde{R} = (1/4\pi^3) Rl \int_{-\infty}^{\infty} dk \int_{-\infty}^{\infty} dl \int_{L_{\frac{1}{2}}}^{\infty} d\omega \int_{-\infty}^d d\zeta \tilde{G} \cdot \tilde{S} e^{i(kx + ly - \omega t)} / W q_+(d),$$

where  $L_{\frac{1}{2}}$  is the path above the real axis from the origin to  $i\Omega + \infty$ . The integration over both  $\zeta$  and  $\omega$  ensure that  $\tilde{R}$  is a reasonably well behaved function of  $x, y, z$ , and  $t$ . (This is discussed further in the next section.) The above form enables the appropriate Green's functions to be found. For example for an initial pressure distribution  $p(x, y, z, 0)$ , with  $\dot{p}, \dot{z}$ , and  $\dot{z}$  initially



zero everywhere, the solution is

$$p(x, y, z, k) = \int_{-\infty}^{\infty} d\xi \int_{-\infty}^{\infty} d\eta \int_{-\infty}^d d\zeta G(x, y, z, k, \xi, \eta, \zeta) p(\xi, \eta, \zeta, 0), \quad (2.4)$$

where

$$G(x, y, z, k; \xi, \eta, \zeta) = (i/8\pi^3 c^2) \int_{-\infty}^{\infty} dk \int_{-\infty}^{\infty} d\ell \int_L d\omega \\ P_1(k, \ell, z, \omega; \zeta) e^{ik(x-\xi) + i\ell(y-\eta) - i\omega t} \\ / W(k, \ell, \omega) v^2(k, \ell, \zeta, \omega) q_+(k, \ell, d, \omega). \quad (2.5)$$

If necessary  $G$  is to be classed a generalised function. The integrands in the above expression are holomorphic functions of  $\omega$  in the upper half plane. That  $q_+(k, \ell, d, \omega)$  has no zeros in the upper half plane follows from an extension of the Miles-Howard theorem to the compressible case (Warren, 1968).

#### SOME PROPERTIES OF THE INTEGRAL SOLUTION AND ITS INTEGRAND

For a point source at the lowest level, the WKB approximation shows that for large  $\Omega$  the integrand of the integral in equation (2.3) is dominated by the factor

$$\exp[i k(x - \int_z^d (u/c) d\zeta) + i(y - \int_z^d (v/c) d\zeta) + i\omega \int_z^d (d\zeta/c) - \omega t],$$

where  $k$  and  $\ell$  are complex if the  $k$  and  $\ell$  paths are deformed into their respective complex planes. This factor, and hence the integral, tends to zero as  $\Omega \rightarrow \infty$  if  $(d-z) > c_{\max} t$  where  $c_{\max}$  is the maximum velocity of sound within the model. If also  $\text{im}(k, \ell) \rightarrow \infty$ , a similar argument shows that the integral vanishes if

$$(x^2 + y^2)^{\frac{1}{2}} > (|u|_{\max} + c_{\max}) t.$$

This confirms the expected bounds on the velocity of propagation of a disturbance.

The integrand has singularities in the complex  $\omega$  plane on the real  $\omega$  axis. Firstly there are branch points at the zeros of  $\mu_0(k, \ell, \omega)$ . In the absence of winds these points separate the discrete and continuous spectra. Generally the corresponding singularities in the  $\omega$  plane represent the behaviour of the reflection coefficient (in the isosphere) as a function of the frequency and wave number. Secondly, there are the simple isolated poles of  $q_+(k, \ell, d, \omega)$  on the real  $\omega$  axis which correspond to the fully trapped modes of oscillation of the model. There are also singularities on the real  $\omega$  axis which correspond to critical frequencies. In the first instance consider a strictly monotonic profile  $U(z)$  which is an analytic function of  $z$  in the neighbourhood of the segment  $(0, d)$  of the real  $z$  axis. There are singularities on the real  $\omega$  axis at points where  $v(k, \ell, z, \omega)$  vanishes. Since  $U'(z)$  does not vanish at the corresponding critical level on the  $z$  axis, these singularities correspond to regular singularities of the differential equation for  $R(z)$  through the relation  $v(\omega, z) = 0$ . The singularities in the  $z$  and  $\omega$  planes are therefore of the same type, and the Frobenius exponent is

$$\pm (\frac{1}{2} \pm ir_c), \quad (3.1)$$

where  $r_c$  is a modified Richardson number at the critical level,  $r_c^2 = n_c^2/U_c'^2 - 1/4 > 0$  for a stable model. In the complex  $\omega$  plane since the path is above the singularity, the corresponding path in the  $z$  plane is determined through  $\text{im}(\omega, z) > 0$  and so depends upon the sign of  $U'(z)$ .

Thus

$$\tilde{R}(z) - \tilde{R}(V) = \sum_{m=0}^{\infty} \begin{bmatrix} p_m V^{\frac{1}{2}} \\ q_m V^{-\frac{1}{2}} \end{bmatrix} V^m \pm i r_0 \quad (3.2)$$

if the transformation  $V = \omega/k - U(z)$  is made, where  $\text{im } V \geq 0$  on the path. These results are in accordance with Miles (1961), Booker and Bretherton (1967) and others. It follows from (3.1) that the residue about the singularity in the  $\omega$  plane vanishes. Thus for the transient problem there is no truly critical level for the displacement  $2(x, y, z, t)$ , but there exists a latent critical layer. A similar singularity exists at the point  $\omega_d$  where  $q_1(k, \ell, d, \omega_d) = 0$ . For the more general profile there are points ( $z_0$ ) or segments of the real  $z$  axis for which  $U'(z)$  vanishes, corresponding to irregular singularities of the differential equation for  $\tilde{R}(z)$ . Consider the case where  $U''(z_0) \neq 0$  and  $\text{im } v \neq 0$ . Set

$$w = v \{ \rho / (1 - v^2/k^2 c^2) \}^{\frac{1}{2}}$$

and eliminate  $p$ . The resulting equation for  $w(z)$  is

$$d^2 w / dz^2 + \{ (1 - v^2/k^2 c^2)^{-1} n^2 k^2 / v^2 - k^2 (1 - v^2/k^2 c^2)^{-1} - d^2 / dz^2 \{ \rho (1 - v^2/k^2 c^2)^{-\frac{1}{2}} / \{ \rho (1 - v^2/k^2 c^2) \} \} \} w = 0.$$

In the neighbourhood of  $z_0$ ,  $V$  is of the form

$$\sigma = - \left\{ \sigma + \frac{1}{2} U_0'' (z - z_0)^2 + O(z - z_0)^3 \right\},$$

where  $\sigma = U_0 - \omega/k$ . The WKB approximation for large  $|\sigma|^{-1}$  yields solutions of the type

$$\left\{ \sigma + \frac{1}{2} U_0'' (z - z_0)^2 \right\}^{\frac{1}{2}} \exp[ \pm i n_0 (2k/U_0'' \sigma)^{\frac{1}{2}} \tan^{-1} \{ (k U_0'' / 2\sigma)^{\frac{1}{2}} (z - z_0) \} ] .$$

These solutions tend to  $(\frac{1}{2} U_0'')^{\frac{1}{2}} (z - z_0) \exp \left\{ \frac{\pm i n_0}{(\frac{1}{2} U_0'')^{\frac{1}{2}} (z - z_0)} \right\}$  as  $\sigma \rightarrow 0$ , and are locally valid

in the neighbourhood of  $z_0$  if  $n_0 \neq 0$ . Hence the encounter in the  $z$  plane with the irregular singularity is such that very large increases in the modulus of the solution occur if  $\text{im } \omega \neq 0$ . That the exponentially large term is always present follows from arguments similar to those used by Warren (1968). (See appendix A.)

Similar arguments hold for segments of the real  $z$  axis where  $U(z)$  is constant. Thus in these cases the denominator of the integrand ensures that the latter is bounded in the vicinity of these singularities if  $\text{im } \omega > 0$ . Similar arguments hold for  $\text{im } \omega < 0$ . Hence the contribution from small semicircular paths about these singularities are negligibly small. This ensures the convergence of the infinite sum of residues from the infinite number of poles which may occur on the real  $\omega$  axis in the neighbourhood of such a singularity. A similar situation occurs in the case of a calm isothermal atmosphere of finite height  $H$  with a rigid lid upper boundary condition. There is in this case an infinite number of modes in the vicinity of the origin, at points given by  $\omega = n(1 + m^2 \pi^2 / k^2 H^2)^{-\frac{1}{2}}$  where  $m$  is an integer. For this present work, the excitation function is such that the contribution of this set of modes is negligible. Further, it is known that no singular modes exist. This is in accordance with Miles' Theorem IX (Miles, 1961) for a monotonic profile, which carries through for an upper boundary radiation condition, and for the non-monotonic profile, see appendix B. Some authors use layered models for which the layer velocity is constant. These models are unstable because of the discontinuities in the profile, and attenuation by the inviscid Reynolds stresses is absent. For sufficiently large values of  $k$ , the  $\omega_0$  type singularities enter the otherwise discrete spectrum. Since  $\omega_0$  is a branch point, this

implies that the wind has the property of lengthening the continuous spectrum at smaller wavelengths. Similar remarks apply to singularities of the  $\omega_d$  type, that is to monotonic profiles. The frontier of the continuous wind spectrum is possibly a limit point of modal wind-induced poles of the discrete spectrum.

Some group velocity properties of the trapped modes readily follows from the formula

$$\int_{-\infty}^z \{ (1/c^2 - k^2/v^2) |p|^2 + (n^2 - \bar{v}^2) |q|^2 \} dz = [\bar{p}q]_{-\infty}^z. \quad (3.3)$$

Set  $\omega = \omega(k)$  and differentiate with respect to  $k$  in the direction of the imaginary  $k$  axis. If  $z = d$ , selection of the real part of the resulting equation yields a familiar formula for the group velocity

$$d\omega/dk = \int_{-\infty}^d \{ (\omega/k) (k^2/v^3) p^2 + U v q^2 \} / \int_{-\infty}^d \{ (k^2/v^3) p^2 + v q^2 \}, \quad (3.4)$$

as found by Pierce (1965) (for example) by a different method. It may be deduced that modal curves are tangential to the boundary of the continuous spectrum at the point of contact, and that the maximum group velocity is less than the sum of the maximum wind speed and the maximum speed of sound in the model. Briefly the proof of this latter statement is:

$$d\omega/dk = \omega/k - v_m/k + (v_m/k) (c_{\max})^2 (k/v_m)^2,$$

where

$$v_m = \int (k^2 p^2 / v^2 + v^2 q^2) / \int (k^2 p^2 / v^3 + v q^2),$$

and

$$v_m^2 = c_{\max}^2 \int (p^2 / c^2 + n^2 q^2) / \int p^2 / v^2.$$

Hence

$$d\omega/dk = U_m + c_{\max} \{ (1 - U_m / (\omega/k)) / (1 - U_m (\omega/k)) \} \\ \{ c_{\max} / (\omega/k - U_m) \},$$

and the result follows if  $\omega/k > c_{\max} + U_{\max}$ . The case for  $\omega/k \leq c_{\max} + U_{\max}$  follows from

$$|d\omega/dk| \leq \{ |\omega/k|, |U_{\max}| \}_{\max}.$$

## THE ENERGY FLUX

Consider the stream surface in the flow given by

$$z = z_0 + \tilde{q}(x, y, t; z_0) \cdot \Xi S(x, y, z, t; z_0) = 0.$$

Then if  $(\tilde{p}(x, y, t; z_0))$  is the total pressure at a point of this surface and  $\underline{v}$  is the velocity of a point of it, the total work done by this surface is exactly

$$\int_0^{\infty} dt \int_{-\infty}^{\infty} dx \int_{-\infty}^{\infty} dy \tilde{p}(x, y, t; z_0) (\underline{N} \cdot \underline{v} / \underline{N} \cdot \underline{\hat{z}}) \quad (4.1)$$

where  $\underline{N}$  is the unit normal to the surface and  $\underline{\hat{z}}$  is a unit vector in the direction of the  $z$  axis.  $\underline{v}$  is not necessarily equal to the velocity of an air particle since there may be tangential slip along the surface. If  $\tilde{q}$  is small, say  $O(\delta)$ , then to the first order  $\tilde{q}(x, y, t, z_0) \approx \underline{v}(x, y, z_0, t) \rho^{-\frac{1}{2}}$  and the vertical velocity of an air particle is approximately  $d\tilde{q}/dt \approx d\underline{v}/dt \cdot \rho^{-\frac{1}{2}}$ . Since  $\underline{N} \cdot \underline{v} / \underline{N} \cdot \underline{\hat{z}} = \underline{v} \cdot \underline{v} / \underline{v} \cdot \underline{S} \cdot \underline{\hat{z}}$ , and  $\partial S / \partial t + \underline{v} \cdot \underline{v} S = 0$ , the expression (4.1) may be written

$$\begin{aligned} \int dt \int dx \int dy \tilde{p} \partial \tilde{q} / \partial t &= \int dt \int dx \int dy \tilde{p}_0(z + \tilde{q}) \partial \tilde{q} / \partial t \\ &+ \int dt \int dx \int dy \tilde{p}_1(z_0 + \tilde{q}) \partial \tilde{q} / \partial t, \end{aligned} \quad (4.2)$$

where  $\tilde{p}_0$  is the hydrostatic pressure and  $\tilde{p}_1$  the exact perturbation pressure at a point. The first integral represents the work done by the basic pressure and in many circumstances vanishes, for example when  $\tilde{q}_{t=\infty} = \tilde{q}_{t=0} = 0$ . Here this work is not relevant since it does not represent energy which is propagated through the medium. The second term in (4.2) is  $O(\delta^2)$  and so the rate of doing work is approximately

$$\mathfrak{U}(z, t) = \int_{-\infty}^{\infty} dx \int_{-\infty}^{\infty} dy p(x, y, z, t) \partial \underline{v}(x, y, z, t) / \partial t, \quad (4.3)$$

with an error  $O(\delta^3)$ .

If the surface  $S = 0$  travels with the mainstream wind velocity, then  $\tilde{q}$  is of the form  $\tilde{q}(x - ut, y - vt, t; z_0)$  and in (4.3),  $\partial / \partial t$  is replaced by  $d / dt$ . In this case energy derived from the mainstream velocity is included in the energy flux. This energy is not of present interest and so is excluded from the calculations. However, if the wind velocity at the surface does not vanish, the relevant operator is  $(d/dt)_{z=d} = \partial / \partial t + u(d) \cdot \partial / \partial x + v(d) \cdot \partial / \partial y$  which for the present case coincides with  $\partial / \partial t$ . The nett flux may now be found by employing an averaging device, namely the limiting process

$$F(z) = \lim_{\epsilon \rightarrow 0} \int_0^{\infty} dt \mathfrak{U}(z, t) e^{-\epsilon t},$$

which was described in Warren and Arora, 1967.

$$\begin{aligned} F(z) &= \lim_{\epsilon \rightarrow 0} \int_{-\infty}^{\infty} dx \int_{-\infty}^{\infty} dy \int dt p(x, y, z, t) \\ &\quad (1/8\pi^3 i) \int_{-\infty}^{\infty} dk \int_{-\infty}^{\infty} d\ell \int_N d\omega \omega q(k, \ell, z, \omega) \\ &\quad e^{i(kx + \ell y - \omega t) - \epsilon t} \\ &= \lim_{\epsilon \rightarrow 0} \text{im}(1/4\pi^3) \int_{-\infty}^{\infty} dk \int_{-\infty}^{\infty} d\ell \int_{-\infty}^{\infty} d\omega \int_{-\infty}^{\infty} d\zeta_1 \int_{-\infty}^{\infty} d\zeta_2 \end{aligned}$$

$$\begin{aligned} & \omega(\overline{p_1(\zeta_1)} \overline{S_2(\zeta_1)} + \overline{p_2(\zeta_1)} \overline{S_1(\zeta)}) \\ & (q_1(\zeta_2) S_2(\zeta_2) + q_2(\zeta_2) S_1(\zeta)) \\ & / |W(k, \ell, \omega)|^2 |q_+(k, \ell, d, \omega)|^2 \end{aligned}$$

which follows on setting  $\epsilon = 2 \operatorname{im}(\omega)$ . The path of integration in the  $\omega$  plane is a straight line. The energy density is given by  $dF/dz$ .

#### DISTURBANCE AT THE LOWEST LEVEL

For simplicity it is now assumed that the model is two dimensional  $(x, z)$  with a wind profile  $U(z)$  and that the disturbance which occurs at the lowest level, may be represented by a fluctuation of the lower boundary given by

$$z(x, d, t) = f(x) g(t) ,$$

where  $f(x)$  is defined for  $-\infty \leq x \leq \infty$  and  $g(t)$  for  $t \geq 0$ . Initially the atmosphere is unperturbed. If the Fourier-Laplace transform of  $f(x) g(t)$  is  $f(k) g(\omega)$  then the solution is

$$\begin{aligned} R(x, z, t) &= R\ell(1/2 \pi^2) \int_{-\infty}^{\infty} dk \int_{L_{\frac{1}{2}}}^{\infty} d\omega R_+(k, z, \omega) \\ & f(k) g(\omega) e^{i(kx - \omega t)} / q_+(k, d, \omega) \end{aligned}$$

The expression for the energy flux reduces to

$$\begin{aligned} \lim_{\epsilon \rightarrow 0} \operatorname{im}(1/4\pi^3) \int_{-\infty}^{\infty} dk \int_{i\epsilon}^{i\epsilon+\infty} d\omega \omega \overline{p_+(k, z, \omega)} q_+(k, z, \omega) \\ |f(k)|^2 |g(\omega)|^2 / |q_+(k, d, \omega)|^2 \end{aligned}$$

Consider segments of the  $\omega$ -path for which  $r\ell(\omega)$  lies in the discrete spectrum. Then as in Warren and Arora, 1967, if  $\omega_n(k)$  denotes a modal frequency

$$\lim_{\epsilon \rightarrow 0} \int_{\omega_n - \omega + i\epsilon}^{\omega_n + \omega + i\epsilon} d\omega (\omega |g|^2 \overline{p} q / |q(d)|^2) = r\ell[\pi \{ \partial / \partial \omega i(\omega |g|^2 \overline{p} q) / |\partial q(d) / \partial \omega|^2 \}]_{\omega=\omega_n}$$

where  $\partial / \partial \omega_1$  denotes differentiation in the direction of the imaginary  $\omega$  axis. (Here and henceforth the suffix + is dropped). Thus

$$\begin{aligned} F(z) &= \operatorname{im}(1/4\pi^3) \int_{-\infty}^{\infty} dk \int_{\zeta}^{\infty} d\omega \omega p q |f|^2 |g|^2 / |q(d)|^2 \\ &+ r(1/4\pi^2) \int_{-\infty}^{\infty} dk |f(k)|^2 \sum_n \{ |g(\omega)|^2 |\partial q(d) / \partial \omega|^{-2} \\ &\partial / \partial \omega_1 (\omega \overline{p} q) \}_{\omega=\omega_n} , \end{aligned}$$



since  $\partial/\partial\omega_1(|g|^2)$  is imaginary.  $\zeta$  denotes the continuous spectrum.  $\Sigma_n$  denotes the sum over the discrete modes (which, for fixed  $k$ , is not necessarily a finite sum). This formula may be thrown into a more familiar form. If equation (3.3) is multiplied by  $\omega$ , partial differentiation with respect to  $\omega$  in the direction of the imaginary  $\omega$  axis gives on selection of the real part

$$\text{rl}\{\partial/\partial\omega_1(\omega pq)\}_{-\infty}^z = \int_{-\infty}^z dz \{ (k^2/\nu_n^2 + 1/c^2 + 2k^3 U/\nu_n^3) p_n^2 + (n^2 + \nu_n^2 + 2kU\nu_n) q_n^2 \},$$

where  $\nu(k, \omega, z) = \omega - k U(z)$ . Hence the expression for the ducted energy flux may be written

$$F_T(z) = (1/4\pi^2) \int_{-\infty}^{\infty} dk |f(k)|^2 \sum_n |g(\omega_n)|^2 \omega_n^2 p_n^2(d) \cdot I_n(z)/\{I_n(d)\}^2, \quad (5.1)$$

where

$$I_n(z) = \int_{-\infty}^z dz \{ (1/c^2 + k^2/\nu_n^2) p_n^2 + (n^2 + \nu_n^2) q_n^2 \} + 2 \int_{-\infty}^z dz (k U(z)/\nu_n) \{ (k^2/\nu_n^2) p_n^2 + \nu_n^2 q_n^2 \}. \quad (5.2)$$

Since

$$\int_{-\infty}^d dz \{ (1/c^2 - k^2/\nu_n^2) p_n^2 + (n^2 - \nu_n^2) q_n^2 \} = 0, \\ I_n(d) = 2\omega \int_{-\infty}^d \{ (k^2/\nu_n^3) p_n^2 + \nu_n q_n^2 \} dz. \quad (5.3)$$

In the case where the flux is defined by use of the full derivative  $d/dt$ , the corresponding factor  $\omega$  of the flux integrand is modified to  $\nu$ . The right hand side of the above expression for the ducted energy flux remains unchanged except that  $I_n(z)$  is replaced by

$$I_n^{(0)}(z) = I_n(z) - 2k U(z) \int_{-\infty}^z \{ (k^2/\nu_n^3) p_n^2 + \nu_n q_n^2 \} dz, \quad (5.4)$$

while  $I_n(d)$  remains unchanged. From equations (5.1) to (5.4), it is seen that the equipartition of energy holds only if the wind speed is everywhere zero. The corresponding expression for the contribution from the continuous spectrum is readily obtained from the free flux formula

$$F_T(z) = (1/4\pi^2) \int_{-\infty}^{\infty} dk \int_{\zeta} d\omega \omega \text{im}(\overline{pq}) |fg|^2 / |q(d)|^2 \quad (5.5)$$

by replacing  $\omega$  by  $\nu$ . The continuous spectrum is lengthened by the wind for larger wave numbers, and the free flux calculations must include this range as well as those of the continuous gravity and acoustic spectra. This increases the flux from the continuous spectra but the extra contribution does not represent energy freely radiated to large altitudes, since it is virtually completely absorbed by the inviscid Reynolds stresses in the critical layer. Thus in the absence of wind and therefore of a critical layer, all the flux from the continuous spectra is independent of  $z$ , and radiates freely to large heights but this no longer holds for a windy

model. This effect also overlaps the continuous gravity spectrum (which is therefore doubly continuous), so that some energy which would radiate to high altitudes is also carried away by the wind. However for this part of the spectrum there is also the possibility that the critical layer radiates some energy ( $\partial/\partial t$ ) derived from the mainstream velocity (see appendix B). Formulae for the discontinuity in the flux integrand factor  $\text{im}(\overline{pq})$  at a critical level may be deduced from (3.2), and have been given by Miles (1961) and Booker and Bretherton (1967).

#### REFERENCES

- Booker, J. R. and Bretherton, F. P., The critical layer for internal gravity waves in a shear flow, *J. Fluid Mech.* 27 (3), 513-539, 1967.
- Eckart, C., *Hydrodynamics of Oceans and Atmospheres*, Pergamon Press, 1960.
- Hazel, P., The effect of viscosity and heat conduction on internal gravity waves at a critical level, *J. Fluid Mech.* 30 (4), 775-783, 1967.
- Miles, J. W., On the stability of heterogeneous shear flows, *J. Fluid Mech.* 10 (4), 496-508, 1961.
- Pierce, A. D., Propagation of acoustic-gravity waves in a temperature- and wind-stratified atmosphere, *J. Acoustic Soc. Amer.* 37 (2), 218-227, 1965.
- Warren, F. W. G. and Arora, M. K., A problem of vertical distribution of mechanical wave energy in the atmosphere, *Quart. J. Mech. App. Math.* 20 (3), 316-333, 1967.
- Yanowitch, M., Effect of viscosity on gravity waves and the upper boundary condition, *J. Fluid Mech.* 29 (2), 209-231, 1967.

#### APPENDIX

(A). The modified form of equation (2.5) of Warren (1968) reads

$$\begin{aligned} \text{im} \int_{-\infty}^z dz \, \rho \left[ V \left( \frac{1 + Vc}{1 - V^2/c^2} \right) |\tilde{Q}'|^2 + \{k^2 V(1 + Vc) \right. \\ \left. + \frac{1}{4} V'^2 (1 - V^2/c^2)/V(1 + Vc) - n^2 (1 + Vc)/V \} |\tilde{Q}|^2 \right] \\ = \text{im} \left[ \rho V^2 \overline{q' q} D / (1 - V^2/c^2) \overline{D} \right]_{-\infty}^z . \\ = \text{im} \left[ \overline{pq} D/D \right]_{-\infty}^z . \end{aligned} \quad (\text{A.1})$$

The imaginary part of the integrand on the left-hand side of this equation is by assumption positive definite. Here

$$\begin{aligned} \tilde{Q}(z) &= q(z)/D(z) , \\ D(z) &= (V^{-1} + \int^z (V'(z)/c^2) dz)^{\frac{1}{2}} , \end{aligned}$$

$$V = \omega/k - U(z) ,$$

and

$$e(z) = c_0 + \int_0^z (V'(z)/c^2) dz. \quad (c_0 = \text{constant}).$$

$U(z)$  is the resolved wind velocity profile.

Since  $q(-\infty) = 0$  if  $\text{im } \omega \neq 0$ , it follows that if the model is stable - in accordance with the criteria of Warren (1968) - then the right-hand side of equation (A.1) is a monotonic increasing function of  $z$  if  $\omega_1 > 0$ . In the neighbourhood of a point  $z_0$  on the real  $z$  axis where  $U'(z_0)$  vanishes, and where  $U''(z_0)$  is bounded away from zero, the WKB approximation shows that  $q$  is dominated by the term

$$\exp \left[ \pm i \int_0^z \{n(z) k^{-1} / (\omega - kU(z))\} dz \right], \quad (\text{A. 2})$$

if  $\sigma_0 = \omega_r + i\omega_1 - kU_0$  is of sufficiently small modulus. Hence the factor  $q'\bar{q}$  of the right-hand side of equation (A.1) is dominated by the factor

$$\exp \left[ \pm 2\omega_1 \int_0^z \{n(z) k^{-1} / ((\omega_r - kU(z))^2 + \omega_1^2)\} dz \right].$$

Here  $U(z) = U_0 + \frac{1}{2} U_0'' (z - z_0)^2 + O(z - z_0)^3$ .

Setting  $\sigma_0 = |\sigma_0| e^{i\theta}$  and  $z - z_0 = |\sigma_0|^{\frac{1}{2}} \zeta$ , this last expression may be written

$$\exp \left[ \pm 2 |\sigma_0|^{-\frac{1}{2}} \sin \theta \int_0^\zeta \{n(z) k^{-1} / (\cos \theta - \frac{1}{2} U_0'' k \zeta^2 + \dots)^2 + \sin^2 \theta\} d\zeta \right], \quad (\text{A. 3})$$

where  $\theta \neq 0$ .

Suppose that  $q$  decays exponentially, corresponding to the minus sign in the exponent. Since the remaining terms of the right-hand side of equation (A.1) are rational functions of  $z$  and therefore of  $\zeta$ , it follows that for sufficiently small  $|\sigma_0|$  these terms are dominated by the exponential decay given by expression (A.3) with the negative exponent. Hence for sufficiently small  $|\sigma_0|$ , the right-hand side of equation (A.1) is a decreasing function of  $z$  in the neighbourhood of  $z_0$ . This contradiction implies the presence of the positive exponent in the form for  $q$ , equation (A.2). If  $\text{im } \omega < 0$ , a similar argument holds.

(B). That no singular modes exist follows from a similar argument (as in (A)). If  $\text{im } \omega > 0$ , then equation (A.1) holds with  $z = d$ . In the neighbourhood of an ordinary critical point  $z_c$ ,  $Q(z)$  has the Frobenius expansion

$$\tilde{Q}(z) \rightarrow \tilde{Q}(V) = V^{\text{ir}_0} S_+(V) + V^{-\text{ir}_0} S_-(V), \quad (\text{B. 1})$$

where

$$V = (\omega/k) - U_0'(z - z_c) + O(z - z_c)^2 \quad (U_0' \neq 0),$$

and where  $S_\pm$  are locally convergent power series in  $V$ . Now let  $\omega_c$  be a frequency for which one or more critical levels occur. Write

$$\omega = \omega_c + i\omega_1,$$

and let  $\omega_1 \rightarrow 0$ . Then the range of integration of the left-hand side of equation (A. 1) passes through neighbourhoods in which the expansion (B. 1) holds. The contribution from such a neighbourhood contains a term

$$\lim_{\omega_1 \rightarrow 0} \operatorname{im} \int_{z_c - \epsilon}^{z_c + \epsilon} dz \left\{ \frac{1}{4} V'^2 (1 - V^2/c^2)/V(1 + Vc) - n^2 (1 + Vc)/V \right\} |\tilde{Q}|^2 ,$$

where  $\epsilon > 0$ . This is of the form

$$\lim_{V_1 \rightarrow 0} V_1 \int_{V_c - \epsilon}^{V_c + \epsilon} \left\{ \frac{f(V)}{(V - V_c)^2 + V_1^2} \right\} dV , \quad (\text{B. 2})$$

where  $f(V)$  is positive definite if the model is stable in accordance with the criteria of (6). Hence the expression (B. 2) has a positive definite limit, and so the sum of all contributions from the neighbourhood of all critical points is positive definite in the limit  $\omega_1 \rightarrow 0$ . It follows that the left-hand side of equation (A. 1) is positive definite in the same limit, and so the left-hand side does not vanish and the non-existence of singular modes follows. If  $\operatorname{im} \omega < 0$ , a similar argument holds.

Finally, since  $D/\bar{D} = \operatorname{sgn} V$  when  $\omega_1 = 0$ , the flux term  $\operatorname{im} (\omega \bar{p}q)$  changes sign at a critical level. This implies a possible (perhaps small) radiation from one critical level to another which absorbs this energy. From the expansion (3. 2) it follows that the attenuation factor at a critical level is  $O(e^{-2\pi r_0})$  if  $r_0$  is large (e. g.  $r_0 > 1$ ). This generalises the result obtained by Booker and Bretherton (1967) who use a different argument.

The total energy flux  $d/dt$  is measured by  $\operatorname{im}(\nu \bar{p}q)$  and so is always positive except at a critical level where it is completely attenuated.

VERTICALLY PROPAGATING WAVES IN AN ATMOSPHERE WITH NEWTONIAN  
COOLING INVERSELY PROPORTIONAL TO DENSITY\*  
(Summary)

Richard S. Lindzen  
University of Chicago

In two recent papers Yanowitch (1967a, 1967b) has investigated the effect of viscosity on vertically propagating waves in a fluid where a) the kinematic viscosity is proportional to  $1/\rho_0$ , where  $\rho_0(z)$  is the basic density distribution, and b) the density approaches zero exponentially with increasing altitude. In both these papers, other dissipative processes, like heat conduction, are ignored. Moreover, in the first of these papers, it was necessary to ignore a) the compressibility of the fluid, and b) the possibility that the fluid is on a rotating sphere. In the second paper compressibility was included; however, the treatment was restricted to purely vertical oscillations of the fluid. Tractability clearly required some such restrictions. However, the question remains as to whether the results obtained by Yanowitch--in particular, the reflection of waves with very long vertical wavelengths--depended on these restrictions. Moreover, since the problem of linearized, inviscid, adiabatic waves in an infinite, compressible, spherical, rotating atmosphere has been treated relatively exhaustively (Lamb, 1932, Pekeris, 1937, Sibert, 1961, Eckart, 1960, Lindzen, 1967a, and many others), one might hope to investigate the role of dissipation without introducing restrictions which were not previously needed. In the above, rather classical analyses, the following proved to be a convenient dependent variable:

$$y = \rho_0^{\frac{1}{2}} \nabla \cdot \underline{V}', \quad (1)$$

where  $\underline{V}'$  = wave's wind vector, and  $\rho_0(z)$  = basic density distribution. The equations turn out to be separable and solutions of the following form can be obtained.

$$y = y(z) \Theta(\theta) e^{i(\omega t + s\varphi)}, \quad (2)$$

where  $\theta$  = latitude

$t$  = time

$\varphi$  = longitude

$\omega$  = frequency

$s$  = zonal wave number

$\Theta(\theta)$  is a solution of Laplace's Tidal Equation. For an isothermal atmosphere,  $y$  satisfies (assuming hydrostaticity)

$$\frac{d^2 y}{dx^2} + \left\{ \frac{\kappa H}{h} - \frac{1}{4} \right\} y = 0, \quad (3)$$

where  $x = \frac{gz}{RT_0}$

$g$  = acceleration of gravity

$R$  = gas constant for air

$T_0$  = atmosphere's temperature

$\kappa = (\gamma - 1)/\gamma$

$\gamma = c_p / c_v$

and  $h$  = separation constant (known as equivalent depth).

---

\*Full text in Canadian Journal of Physics, 46, 1835 (1968).



The above structure can be preserved in the presence of dissipation, if we are drastic in modelling dissipation. In particular, if we take for our dissipation Newtonian cooling with a cooling rate coefficient  $a(z)$ , all that is changed in the above is eqn (3) which becomes (Lindzen and Mc Kenzie, 1967)

$$\frac{d^2 y}{dx^2} + \left\{ \frac{\kappa H}{h} \left( 1 + \frac{a}{i\omega\gamma} \right)^{-1} - \frac{1}{4} \right\} y = 0. \quad (4)$$

In order to simulate the fact that dissipation is very small near the ground and grows as  $1/\rho_0$ , we take

$$\frac{a}{\omega\gamma} = \epsilon e^x, \quad (5)$$

where  $\epsilon \ll 1$ .

Using (5), (4) can be reduced to the hypergeometric equation. If we let  $\epsilon e^{x_0} = 1$ , then for  $x > x_0$ ,

$$y \sim A_1 e^{-\frac{x}{2}}$$

while for  $x < x_0$ ,

$$y \sim A_2 e^{i\sqrt{\kappa H/h - \frac{1}{4}}x} + B_2 e^{-i\sqrt{\kappa H/h - \frac{1}{4}}x}.$$

$$\left| \frac{B_2}{A_2} \right| = e^{-2\pi^2 H/L}, \quad (6)$$

where  $L/2\pi H = \sqrt{\kappa H/h - \frac{1}{4}}$ ,  $L$  being the vertical wavelength without dissipation. Equation (6) is exactly the result obtained by Yanowitch--which suggests that his result was simply a consequence of the  $1/\rho_0$  dependence of his dissipation. More surprising, was the finding that the vertical distributions of  $y$  found here are close to those obtained by Yanowitch. This suggests that the present calculations might be used as prototypes for studying the role of molecular dissipation.

As an example, we have considered the main propagating diurnal tidal mode for which  $2\pi^2 H/L \approx 2$ , and  $x_0 \approx 110$  km. Above  $x_0$ , phase changes with height disappear. Maximum amplitudes occur about 0.3 scale heights below 110 km, although the amplitudes decrease only 2 percent above this altitude. The maximum amplitude is that which the adiabatic solution would have reached 1.6 scale heights below  $x_0$  (i. e.  $\sim 95$  km). According to Lindzen (1967b), this corresponds to an amplitude of about 100 m/s in horizontal wind. The above general structure corresponds rather well to measurements of ionospheric winds.

#### REFERENCES

- Eckart, C., Hydrodynamics of Atmospheres and Oceans, Pergamon Press, New York, 1960.
- Lamb, H., Hydrodynamics, 6th ed., Cambridge University Press, 1932.
- Lindzen, R. S., Planetary waves on beta-planes, Monthly Weather Rev., **95**, 441-451, 1967a.
- Lindzen, R. S., Thermally driven diurnal tide in the atmosphere, Quart. J. Roy. Meteorol. Soc., **93**, 18-42, 1967b.
- Lindzen, R. S. and D. McKenzie, Tidal theory with Newtonian cooling, Pure Appl. Geophys., **64**, 90-96, 1967.

Pekeris, C. L., Atmospheric oscillations, Proc. Roy. Soc., A, 158, 650-671, 1937.

Siebert, M., Atmospheric tides, Advan. Geophys., 7, 105-182, 1961.

Yanowitch, M., Effect of viscosity on gravity waves and the upper boundary condition, J. Fluid Mech., 29, 209-231, 1967a.

Yanowitch, M., Effect of viscosity on vertical oscillations of an isothermal atmosphere, Can. J. Phys., 45, 2003-2008, 1967b.



FULL WAVE CALCULATIONS OF COUPLED NEUTRAL  
AIR WAVE PROPAGATION THROUGH THE THERMOSPHERE

by

H. E. Volland\*  
Aeronomy Branch  
Goddard Space Flight Center  
Greenbelt, Maryland

The horizontally stratified thermosphere is a multiple refractive medium with respect to obliquely incident plane neutral air waves. Besides the well known acoustic-gravity waves, three other wave modes can exist in this region: heat conduction waves, ordinary viscosity waves and extraordinary viscosity waves. It can be shown that within the frequency range of gravity waves and at altitudes below 500 km the two viscosity modes are nearly decoupled from the gravity and heat conduction waves. Therefore in the treatment of gravity and heat conduction waves the coefficient of viscosity can be neglected and the coefficient of heat conductivity plays the dominant role in the dissipation of energy of these waves.

From numerical full wave calculations of coupled gravity and heat conduction waves, the scattering matrix of the thermosphere at altitudes between 120 and 600 km has been determined. Its elements are reflection, transmission, coupling, and conversion coefficients. The behavior of these elements depending on frequency, thickness of the model atmosphere and angle of incidence is discussed. The energy coupled from upgoing gravity waves into upgoing heat conduction waves described by a coupling coefficient never exceeds 3% of the total gravity wave energy. Gravity waves, therefore, predominate throughout the thermosphere. Comparison between the transmission coefficients of upgoing gravity waves and simple ray approximation shows that ray treatment is an excellent approximation for upgoing gravity waves.

---

\*NAS-NRC Research Associate

## I. Introduction:

The dynamics of the neutral thermosphere is controlled to a large extent by heat conduction and viscosity (Harris and Priester (1962); Pitteway and Hines (1963)). This is due to the fact that the ratios

$$\frac{\kappa}{\bar{p}}; \frac{\eta}{\bar{p}} \quad (1)$$

( $\kappa$  = coefficient of heat conductivity;  $\eta$  = coefficient of viscosity;  $\bar{p}$  = mean pressure) are exponentially increasing with altitude within an isothermal atmosphere.

Under the influence of heat conduction and viscosity four pairs of plane characteristic waves, propagating through a horizontally stratified medium, exist (Volland, 1968a)

- (a) Acoustic-gravity waves
- (b) Heat conduction waves
- (c) Ordinary viscosity waves
- (d) Extraordinary viscosity waves.

They are dissipative waves. Part of their wave energy is converted into internal energy of the surrounding gas. This is described by a complex eigenvalue of the  $i$ -th characteristic wave:

$$q_i = \alpha_i - j \beta_i \quad (2)$$

in which

$$\beta_i \neq 0$$



is responsible for the dissipation of energy while  $\alpha_i$  is a measure of the phase velocity of the wave.

$$\beta_i \geq 0 \quad (3)$$

corresponds to ascending waves (transporting energy upwards),

$$\beta_i \leq 0 \quad (4)$$

corresponds to descending waves (transporting energy downwards). The equal signs in (3) and (4) are valid only for nondissipative waves

$$(\kappa = \eta = 0).$$

Ion drag and Coriolis force make the atmosphere anisotropic with respect to the characteristic waves. Their propagation behavior for east to west and north to south propagation differ from each other. Moreover, ion drag contribute to dissipation of wave energy.

The eigenvalues  $q_i$  (equation (2)) are functions of the ratios  $\kappa/\bar{p}$  and  $\eta/\bar{p}$  (equation (1)). Therefore, the real atmosphere behaves like an inhomogeneous medium with respect to the characteristic waves. Characteristic waves are well defined only within a homogeneous medium. We have to discuss their eigenvalues therefore within a homogeneous slab in which the ratios  $\kappa/\bar{p}$  and  $\eta/\bar{p}$  are kept constant. This has been done in Section II.

The real atmosphere can be approximated by a number of thin homogeneous slabs. In each of these slabs the eight characteristic waves propagate uncoupled. Coupling occurs only at the boundary between adjacent slabs with different parameters. Full wave calculations taking advantage of such model have been performed. The results in form of reflection, conversion, transmission and coupling coefficients of the characteristic waves within thermospheric heights are presented in Section III.

## II. The eigenvalues of the characteristic waves

Plane harmonic characteristic waves propagating through a homogeneous isothermal atmosphere have the space and time dependence

$$c_i = c_{0i} e^{j\omega t - jk_x x - jk_0 q_i z + z/2H} \quad (5)$$

where  $x, z$  are horizontal and vertical coordinates,  $t$  is the time,  $\omega$  the angular frequency,  $k_x$  the horizontal wave number,  $q_i$  the eigenvalue of the  $i$ -th characteristic wave,

$$k_0 = \frac{\omega}{C}$$

a normalizing wave number,  $C$  the velocity of sound and  $H$  the scale height. The exponential term  $z/2H$  in equation (5) takes into account the constancy of the energy of a nondissipative wave within an atmosphere with exponentially decreasing pressure.

At vertical incidence ( $k_x = 0$ ) and negligible Coriolis force and ion drag the eigenvalues are (Volland, 1968a)

for acoustic-gravity

$$q_{1,2} = \begin{cases} \mp j \sqrt{A^2 + \frac{3}{4} j R} & R \ll 1 \\ \pm \sqrt{1 - A^2} & R \gg 1 \end{cases} \quad \text{for} \quad , \quad (6)$$

for heat conduction waves

$$q_{3,4} = \begin{cases} \mp j \sqrt{A^2 + \frac{2jG}{\gamma}} & R \ll 1 \\ \mp j \sqrt{A^2 + 2jG} & R \gg 1 \end{cases} \quad \text{for} \quad , \quad (7)$$

for ordinary and extraordinary viscosity waves

$$\left. \begin{matrix} q_5 \\ 6 \\ q_7 \\ 8 \end{matrix} \right\} = \mp \sqrt{A^2 + j R} \quad (8)$$

with

$$A = \frac{\omega_a}{\omega}$$

$$G = \frac{\omega_h}{\omega}$$

$$R = \frac{2f}{\gamma} \quad G \text{ Reynolds number}$$

$$\omega_a = \frac{\gamma g}{2C}$$

$$\omega_h = \frac{\gamma g}{2V}$$

$C$  = velocity of sound

$$V = \frac{\kappa g}{c_p \bar{p}} \quad \text{heat conduction velocity}$$

$$f = \frac{c_p}{\eta c_v}$$

$$\gamma = \frac{c_p}{c_v} \quad \text{ratio between specific heats at constant pressure and constant volume}$$

$g$  = gravitational acceleration

$\kappa$  = coefficient of heat conductivity

$\eta$  = coefficient of viscosity

$\omega$  = angular frequency

$\bar{p}$  = mean pressure

The plus and minus signs before the square roots in equations (6) to (8) stand for ascending and descending waves, respectively.

Equations (6) to (8) show that heat conduction waves as well as viscosity waves are evanescent waves for small Reynolds numbers, and are heavily attenuated waves for large Reynolds numbers. They contribute not very much to any wave energy transport through the thermosphere. Acoustic waves ( $A < 1$ ) become also evanescent wave for  $R \ll 1$  but are propagation waves for  $R \gg 1$ . Gravity waves ( $A > 1$ ) are evanescent waves at vertical incidence but become propagation waves at oblique incidence (see figure 1).

It can be shown (Volland 1968a, see also figure 1), that as long as the condition

$$G \gtrsim A > 1 \quad (9)$$

holds, the viscosity waves are nearly decoupled from the gravity waves and from the heat conduction waves. Wave propagation of the two last mentioned waves can be treated as if the coefficient of viscosity  $\eta$  is zero. The eigenvalues of gravity waves and heat conduction waves at the equator for east to west propagation are then

$$\left. \begin{matrix} q_1 \\ 2 \\ q_3 \\ 4 \end{matrix} \right\} = \mp j \sqrt{A^2 + S_0^2 - \frac{\bar{\gamma}}{2} + j G} \pm \sqrt{\left(\frac{\bar{\gamma}}{2} - j G\right)^2 + 2 j G (1 + \bar{B}^2 S_0^2)} \quad (10)$$

( $\eta = 0$ )

with

$$A = \frac{\omega_a}{\omega}; \quad B = \frac{2A}{\gamma} \sqrt{\gamma - 1}; \quad Z_1 = \frac{2\Omega}{\omega}$$

$$G = \frac{\omega_h}{\omega}; \quad S_0 = \frac{k_x}{k_0}; \quad Z_2 = \frac{\nu}{\omega}$$

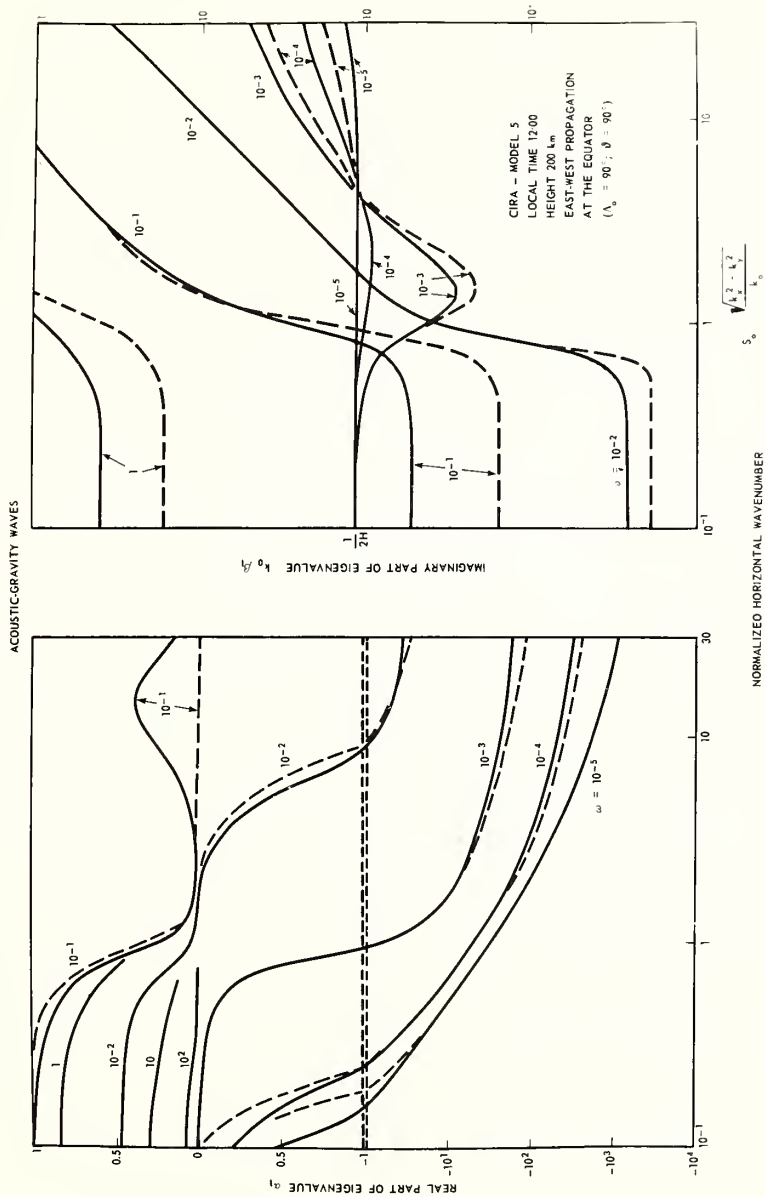


Figure 1—Real part  $\alpha_1$  (left) and negative imaginary part  $k_0 \beta_1$  (right) of eigenvalues of ascending acoustic-gravity waves versus normalized horizontal wave number  $S_0$ . Parameter is the angular frequency  $\omega$  (in  $\text{sec}^{-1}$ ). Full lines are calculated taking into account viscosity, dashed lines are calculated from Equation (10) neglecting viscosity ( $\eta = 0$ ). Propagation conditions — east and west propagation at the equator in 200 km height.



$$\bar{\gamma} = \gamma \left( \Delta - \frac{Z_1^2}{\Delta} \right) + \frac{2S_0 A Z_1}{\Delta}$$

$$\bar{B}^2 = \frac{1}{\Delta S_0^2} \left\{ B^2 S_0^2 - j Z_2 \Delta - Z_1^2 + 2 A S_0 Z_1 \frac{(2-\gamma)}{\gamma} \right\}$$

$$\Delta = 1 - j Z_2$$

The plus sign inside the square root is related to gravity waves, the minus sign is related to heat conduction waves. The signs outside the square root are related to ascending and descending waves, respectively. Equation (10) reduces to Pitteway and Hines (1963) formula (36) if  $\nu = \Omega = 0$ .

Figure 1 shows the real part ( $\alpha_1$ ) and the negative imaginary part of ascending acoustic-gravity waves versus normalized horizontal wave number. Parameter is the angular frequency  $\omega$ . As atmospheric model the CIRA-model 5 at 12:00 local time in 200 km height has been used (CIRA, 1965). Its parameters are  $\omega_a = 8.93 \times 10^{-3} \text{ sec}^{-1}$ ;  $\omega_h = 1.09 \text{ sec}^{-1}$ . Furthermore we used  $\nu = 1 \times 10^{-4} \text{ sec}^{-1}$ ;  $\gamma = 1.5$ . Propagation conditions are east to west propagation at the equator. Full lines have been calculated from the exact eigenvalue equation (Equation 17 in Volland, 1968a). Dashed lines have been calculated from equation (10) showing the degree of approximation of this equation within the range of gravity waves ( $\omega < \omega_a$ ).

In Figure 1a we observe the well known downward directed phase velocity of the ascending gravity waves ( $\alpha_1$  negative). Acoustic waves ( $\omega > \omega_a$ ) show a normal behavior at Reynolds numbers  $R > 1$ , but become evanescent waves at  $R < 1$  ( $\omega_h < \omega$ ) as expected from equation (6). The intermittent frequency ( $\omega_a \sim \omega \sim 10^{-2} \text{ sec}^{-1}$ ) has acoustic wave features at  $S_0 < 1$  and gravity wave features at  $S_0 > 1$  with a continuous transition region. From Figure 1b (attenuation factors  $k_0 \beta_1$ ) it follows however that the gravity wave range at this frequency is heavily attenuated.

From the definition of the attenuation factor (equation (5)) we can deduce that the wave amplitude of an ascending wave remains constant if

$$k_0 \beta_1 = \frac{1}{2H}. \quad (11)$$

This is the general behavior of gravity waves at  $S_0 < 10$  in figure 1b. The frequency  $\omega = 10^{-3} \text{ sec}^{-1}$ , has minimum attenuation at  $S_0 = 1.5$ . At these values of frequency and horizontal wave number we expect therefore especially good propagation conditions in this altitude range. The atmosphere behaves like a frequency and height depending selective filter with respect to gravity waves. (See Section III). It can be shown (Volland, 1968a) that the attenuation factors of heat conduction waves are of the same order of magnitude as the attenuation factors of gravity waves in thermospheric heights. Therefore it is not self evident that gravity waves are the predominant waves within the thermosphere. This must be proved by full wave calculations as follows in the next section.

### III. Calculations of the Scattering Matrix of the Thermosphere

As outlined in Section II, acoustic-gravity waves and heat conduction waves are nearly decoupled from viscosity waves in the range of gravity waves ( $\omega_a > \omega$ ). Their eigenvalues can be determined to a rather high degree of approximation by neglecting the coefficient of viscosity ( $\eta = 0$ ). Otherwise the attenuation rates of gravity waves and of heat conduction waves are of the same order of magnitude within thermospheric heights. In order to determine the relative importance of these two characteristic waves a full wave treatment has been performed to calculate the elements of the scattering matrix of a realistic thermospheric modes extended from 120 km to 600 km. As parameters of the thermosphere CIRA model 5 at 1200 local time has been used.

Since we limit ourselves to the frequency range of gravity waves ( $10^{-4} < \omega < 10^{-2} \text{ sec}^{-1}$ ) we neglect Coriolis force and ion drag. The mathematical background of these calculations as well as additional numerical results can be found in Volland (1968b).

The elements of the scattering matrix connect the characteristic waves going into the layer (region II in figure 2) with waves coming out of the layer:

$$\begin{aligned} \mathbf{b}^I &= \mathbf{R}^I \mathbf{a}^I + \mathbf{T}^{II} \mathbf{b}^{II} \\ \mathbf{a}^{II} &= \mathbf{T}^I \mathbf{a}^I + \mathbf{R}^{II} \mathbf{b}^{II} \end{aligned} \tag{12}$$

Here we introduced column matrices of ascending and descending waves

$$\mathbf{a} = \begin{pmatrix} a_G \\ a_H \end{pmatrix}; \quad \mathbf{b} = \begin{pmatrix} b_G \\ b_H \end{pmatrix} \tag{13}$$

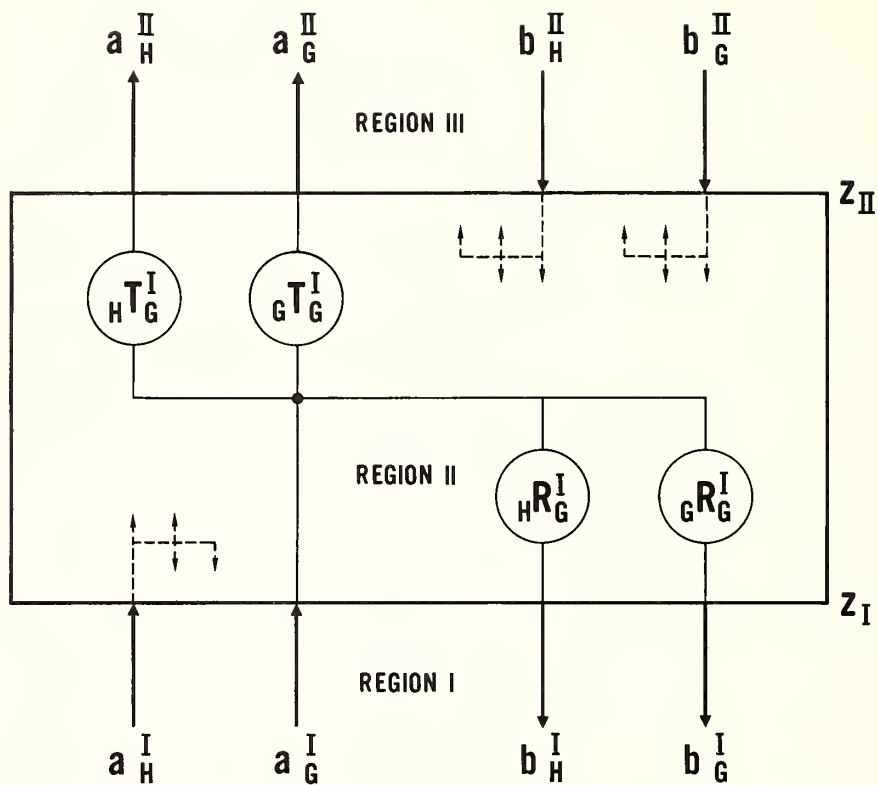


Figure 2—Elements of the scattering matrix. Reflection coefficients (R) and transmission coefficients (T) of upward (a) and downward (b) propagating gravity waves (G) and heat conduction waves (H) within the thermosphere.

Index "G" represents gravity waves, index "H" represents heat conduction waves.  $R^I$  and  $R^{II}$  are  $(2 \times 2)$  - reflection matrices,  $T^I$  and  $T^{II}$  are  $(2 + 2)$  - transmission matrices. It is e.g.

$$R^I = \begin{pmatrix} R_G^I & R_H^I \\ R_G^I & R_H^I \end{pmatrix} \quad (14)$$

where

$${}_G R_G^I = \frac{\tilde{b}_G^I}{a_G^I} ; \quad {}_H R_H^I = \frac{\tilde{b}_H^I}{a_H^I}$$

are related to reflection of gravity waves and heat conduction waves, respectively, coming from below (region I in Figure 2).

$${}_H R_G^I = \frac{\tilde{b}_H^I}{a_G^I} ; \quad {}_G R_H^I = \frac{\tilde{b}_G^I}{a_H^I}$$

are conversion coefficients transferring part of the incoming wave energy of one wave type into reflected wave energy of the other type. Equivalent relations hold for the other three submatrices. We name the elements like

$${}_G T_G ; \quad {}_H T_H$$

transmission coefficients because they describe the amount of wave energy propagating through the layer.

$${}_H T_G ; \quad {}_G T_H$$

are named coupling coefficients because they are related to the energy coupled from one wave type into the other one during the transit through the layer.

Figure 2 shows the four elements of the scattering matrix which give the response of the layer to an ascending gravity wave from below. Twelve equivalent elements for the three other incoming waves exist but are only outlined in Figure 3.

The elements  $a_i$  and  $b_i$  are normalized in such a manner that the products

$$a_i a_i^* \quad \text{and} \quad b_i b_i^*$$

( $a^*$  conjugate complex value of  $a$ ) are a measure of wave energy flux.

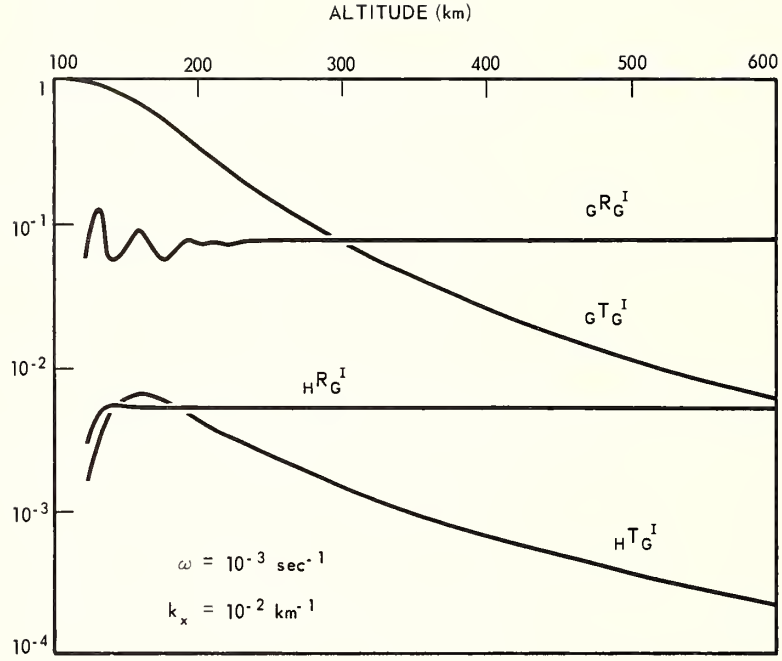


Figure 3—Magnitude of coefficients of reflection ( $G_R^I$ ), transmission ( $G_T^I$ ), conversion ( $H_R^I$ ) and coupling ( $H_T^I$ ) into heat conduction waves of upward propagating gravity waves versus  $Z_{II}$ .

Ray approximation is valid if reflection, conversion and coupling is negligibly small and the transmission coefficients can be approximated by

$$\left. \begin{array}{l} G_T^I \\ H_T^I \end{array} \right\} = e^{-j \int_{Z_I}^{Z_{II}} k_0 q_1(\xi) d\xi} \quad (15)$$

Figure 3 gives the magnitude of the four elements  $G_R^I$ ,  $H_R^I$ ,  $G_T^I$  and  $H_T^I$  which describe reflection, conversion, transmission and coupling into heat conduction waves of incoming gravity from below. The frequency used is  $\omega = 10^{-3} \text{ sec}^{-1}$  (equivalent to a period of  $T = 2\pi/\omega = 105 \text{ min}$ ), the horizontal wave number used is  $k_x = 10^{-2} \text{ km}^{-1}$  (equivalent to a horizontal wavelength of  $\lambda_x = 2\pi/k_x = 628 \text{ km}$ ).



The transmission coefficient  ${}_G T_G^I$  decreases in this altitude range by a factor of 170. The mean pressure decreases in the same height interval by a factor of 420. Therefore the amplitude ratio of the gravity wave between 120 and 600 km is of the order

$$\sqrt{420} \cdot |{}_G T_G^I| = 0.25$$

large enough to be detectable.

The reflection coefficient  ${}_G R_G^I$  remains constant at altitudes above 250 km. Its value of  $8 \times 10^{-2}$  is equivalent to a reflected energy of  $6.4 \times 10^{-3}$  for the incoming energy. The conversion coefficient  ${}_H R_G^I$  which converts part of the incoming gravity wave energy into reflected heat conduction wave energy, has the value  $5 \times 10^{-3}$  and remains constant above an altitude of 200 km. The constancy of the reflection factors indicates that the region above 250 km has no influence on the reflection characteristics of the atmosphere below 120 km.

The coupling coefficient  ${}_H T_G^I$  which is responsible for the transfer of energy from the gravity mode into heat conduction mode never exceeds 3% of the magnitude of the transmission coefficient  ${}_G T_G^I$ . Therefore not more than 1% of the gravity wave energy is coupled into heat conduction wave energy.

In Figure 4 the transmission coefficient  ${}_G T_G^I \hat{=} T_W$  has been compared with the transmission coefficient  $T_R$  derived from a simple ray approximation Equation 15. Here magnitude (Figure 4a) and phase (Figure 4b) are plotted versus height using the same frequency as in Figure 3 and two different values of  $k_x$ . As seen in Figure 4 ray calculation (dashed lines) is an excellent approximation in this range of frequency and horizontal number in heights above 200 km. The discrepancy between full wave and ray calculations at  $k_x = 2.15 \times 10^{-3}$  km arises mainly in the height region below 200 km where the temperature gradient of the atmospheric model is largest.

In order to test the range of validity of the ray approximation the ratio between the magnitudes of both transmission coefficients

$$\left| \frac{T_W}{T_R} \right|$$

and the difference of their phase values in 600 km height have been plotted versus horizontal wave number  $k_x$  in Figure 5a again for  $\omega = 10^{-3} \text{ sec}^{-1}$ . Small horizontal wave numbers mean steep incidence of the waves.

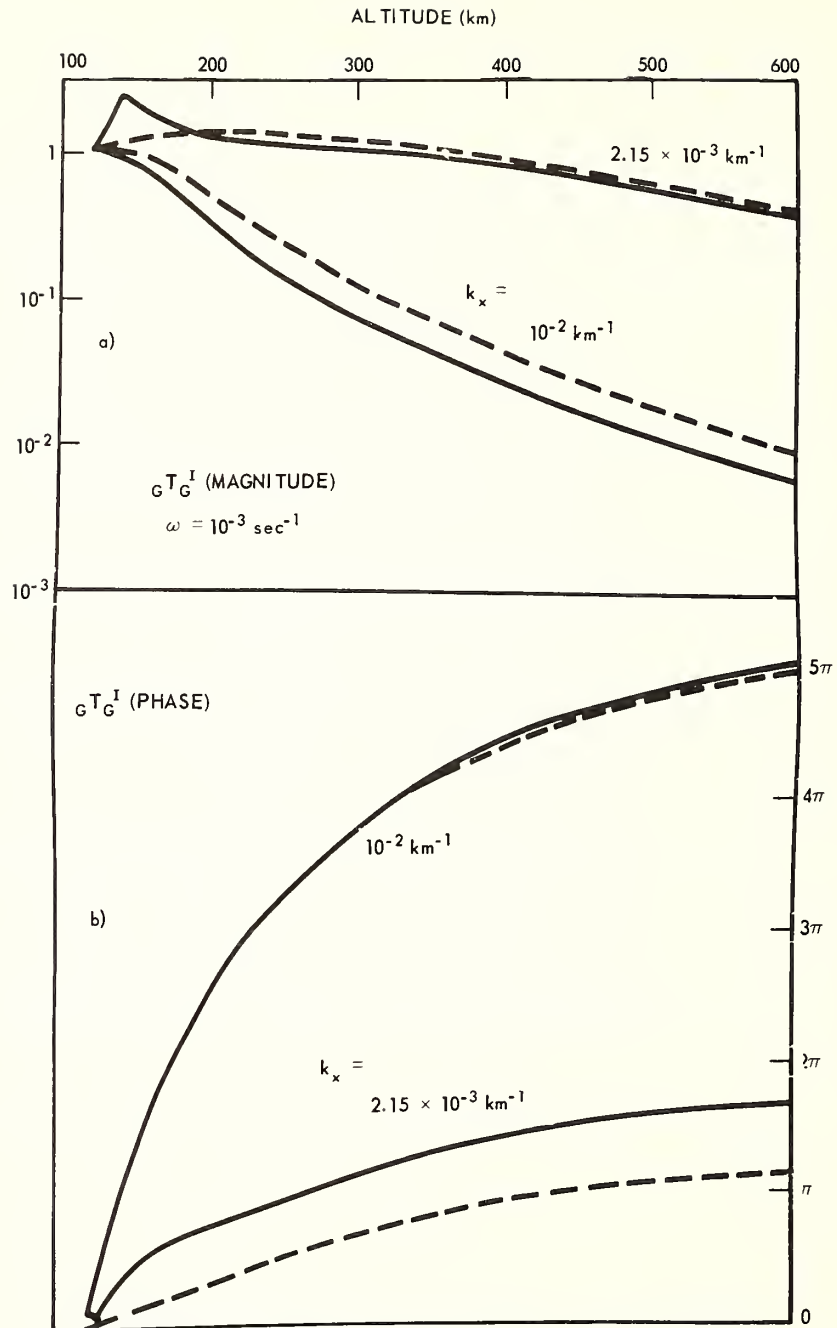


Figure 4—Magnitude (Figure 4a) and phase (Figure 4b) of transmission coefficients of upward propagating gravity waves calculated by full wave theory (full lines) and by ray approximation (dashed lines).

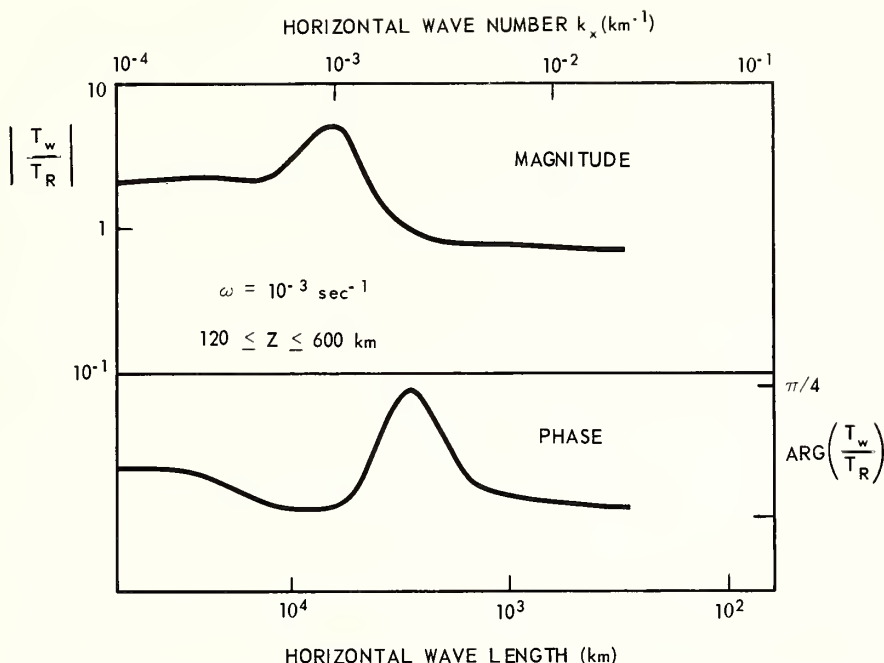


Figure 5a--Ratio between transmission coefficients of upword propagating gravity waves calculated by full wave theory (W) and ray theory (R) versus horizontal wave number  $k_x$ . Range of thermospheric model: 120 to 600 km; angular frequency:  $\omega = 10^{-3} \text{ sec}^{-1}$ .

In the range  $k_x \lesssim 10^{-3} \text{ km}^{-1}$  the ray approximation breaks down. This is the range of horizontal wavelengths where gravity waves are totally reflected within the lower atmosphere (see Figure 5b). In the range  $k_x > 10^{-3} \text{ km}^{-1}$  maximum discrepancy occurs in the phase at  $k_x = 2.15 \times 10^{-3} \text{ km}^{-1}$ . But from Figure 4b we observe that this discrepancy already is generated within the height region  $Z < 200 \text{ km}$ . Therefore a ray approximation is valid at this value of  $k_x$  in heights  $Z \gtrsim 200 \text{ km}$ .

In Figure 5b the magnitudes of the four elements  ${}_G R_G^I$ ,  ${}_H R_G^I$ ,  ${}_G T_G^I$  and  ${}_H T_G^I$  discussed in Figure 3 have been calculated for a region II ranging from 120 to 600 km and are plotted versus horizontal wave number  $k_x$ . We observe a maximum in magnitude of the transmission coefficient  ${}_G T_G^I$  near  $k_x = 2 \times 10^{-3} \text{ km}^{-1}$  which indicates that the atmosphere behaves like a selective transformer depending on frequency and horizontal wave number.

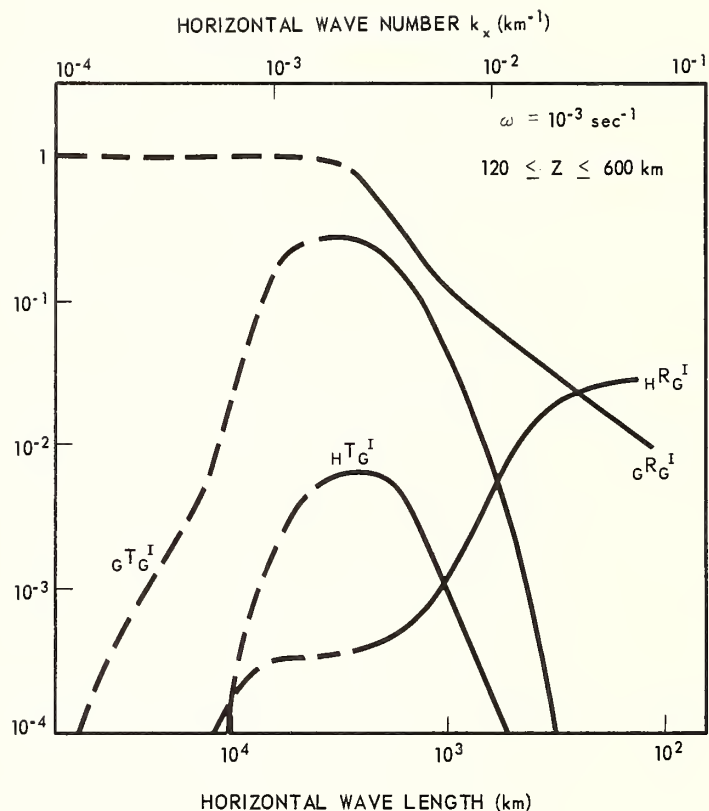


Figure 5b—Magnitude of coefficients of reflection, transmission, conversion and coupling into heat conduction waves of upward propagating gravity waves versus horizontal wave number  $k_x$ . Range of thermospheric model: 120 to 600 km. Angular frequency:  $\omega = 10^{-3} \text{ sec}^{-1}$ . Dashed lines give upper limits.

In the whole range of  $k_x$  the coupling coefficient  $H^T_G^I$  is negligibly small compared with  $G^T_G^I$ . The conversion coefficient  $H^R_G^I$  is also small. Gravity waves therefore predominate throughout the entire thermosphere, and heat conduction waves are unimportant for the transport of wave energy within the thermosphere.

Literature:

CIRA, 1965, "COSPAR international reference atmosphere," North Holland Publishing Company, Amsterdam, 1965.

Harris, I. and W. Priester, "Time dependent structure of the upper atmosphere," Journ. Atmospheric Sci., 19, 286-301, 1962.

Pitteway, M. L. V. and C. O. Hines, "The viscosity damping of atmospheric gravity waves" Can. Journ. Phys., 41, 1935-1948, 1963.

Volland, H., "The upper atmosphere as a multiple refractive medium for neutral air motions," NASA - Goddard Space Flight Center Document X-621-68-160, May 1968, submitted to publication to Journ. Atm. Terr. Phys.

Volland, H., "Full wave calculations of thermospheric neutral air motions" NASA - Goddard Space Flight Center Document X-621-68-176 Greenbelt, Md., May 1968, submitted to publication to Journ. Geophy. Res.





## THE EXCITATION AND DISPERSION

### OF THE ATMOSPHERE SURFACE WAVE

David G. Harkrider and Frederick J. Wells

*Department of Geological Sciences  
Brown University, Providence, Rhode Island 02912*

Atmospheric models terminated at altitude with a half-space, free surface or rigid surface all show a mode characterized by a long period velocity asymptote without a long period cut-off. This mode corresponds to the ocean surface wave mode with a long period velocity limit of  $\sqrt{gH}$ . Kinetic energy density profiles show that this early arriving wave travels in the upper atmosphere. Synthetic barograms indicate that it is most efficiently excited by sources higher than 130 km.

## INTRODUCTION

While calculating the spectra for the theoretical acoustic gravity modes of an atmosphere over ocean model, it was noted that the dispersion of the fundamental mode was remarkably similar in shape to the curves for the "Tsunami" or surface wave in the ocean [Harkrider and Press, 1967]. The ocean mode is characterized by a long period velocity limit of  $\sqrt{gH}$  where  $g$  is the gravitational acceleration and  $H$  is the water depth. In that model the  $GW_0$  mode yielded an  $H$  of 5 km. and the fundamental,  $S_0$ , mode asymptote corresponded to an  $H$  of from 30-35 km. Since the atmospheric model was terminated by a free surface, we felt that in our coupled system we had curves representing two surface waves, one for the ocean and one for the atmosphere.

Previously Press and Harkrider [1962] had calculated dispersion curves for an atmosphere bounded by a rigid surface at the bottom and a free surface at an altitude of 220 km. If the fundamental is indeed an atmosphere surface wave it should have shown the same character in their model. But in their curves the  $S_0$  has a long period cutoff. The model was recalculated and it was found that  $S_0$  had been incorrectly plotted and that to within four significant figures the two models yield the same result. This is what one should expect if the long period segment of  $S_0$  is the surface wave associated with the upper atmosphere.

## SPECTRAL INVESTIGATION

As pointed out by Tolstoy [1967], the characteristics of the atmosphere surface wave are dependent on the altitudes at which the atmosphere is terminated by a free surface. With this in mind, we calculated the spectra of this mode and the first gravity mode,  $GR_0$ , for various free surface altitudes. These theoretical models neglect the effects of wind, viscosity, the earth's rotation, and non-linearity. The results are shown in Figures 1 and 2. Since the acoustic velocity increases monotonically above 220 km, one would expect the phase velocity at a given period to increase with termination altitude as seen in Figure 1.

At altitudes greater than 290 km we have kept the temperature or acoustic velocity constant. In order to determine the extent of the effect on the phase velocity of increasing the free surface altitude, we evaluated theoretically the limit of the dispersion relation as the thickness of the top layer became infinite. As one might suspect, the resulting period equation was for a model terminated by a half-space

with this layer's physical constants. This is true for a system terminated by either a free surface or a rigid surface at altitude. Dispersion results for half-spaces commencing at 220, 310, and 490 km are also shown in Figure 1. The  $S_0$  phase velocities for the 310 and 490 half-space models are essentially equal or greater than the free surface values.

The group velocities for the 220, 310 and 490 km free surface terminations are shown in Figure 2. As with the phase velocities, the long period asymptotes of the  $S_0$  mode increase with free surface termination altitude. The only other remarkable feature of the group velocity curves is in the manner that the  $GR_0$  curves approach a half-space character as the termination altitude increases.

The kinetic energy density profiles for these modes are shown in Figure 3. These profiles are useful in determining the regions of atmospheric influence on each mode. For the 220 km free surface model the  $S_0$  mode is seen to be a mode trapped at the free surface, while  $GR_0$  is trapped at the bottom of the atmosphere.

For the 310 km free surface, the long period segment of  $S_0$  is also trapped at high altitude but the character of  $GR_0$  is seen to vary over the frequency range. At a period of 10 minutes which is a region of constant phase velocity similar to the entire range of the 220 km,  $GR_0$ , the wave is ducted at the earth's surface. At a 30 minute period the trap for  $GR_0$  is in the thermosphere of the upper atmosphere and at the intermediate period of 14 minutes, the mode is ducted in both regions.

Since the  $S_0$  mode for a half-space has similar dispersion properties to the free surface models terminated at large altitudes, one would expect the thermosphere to play a more important role in ducting the surface wave than the presence of a free surface. This is indeed true as can be seen in a comparison of the long period  $S_0$  profiles for a 490 km free surface with the profiles of a 490 km half-space.

The mixed propagation characteristics between various segments of a continuous mode is demonstrated in Figures 4 and 5. In Figure 4, the phase velocity for the  $S_0$ ,  $GR_0$ ,  $GR_1$ , and  $GR_2$  modes are shown for the 490 km free surface model. If we are interested in arrivals which have been trapped in the same part of the atmosphere, we should discuss the pseudo-modes indicated by stippling in Figure 4 and formed by the segments of several modes. From the kinetic energy density profiles in Figure 5, we see that the pseudo-modes, A-A' and C-C' are waves "traveling" in the thermosphere similar to the long period segment of  $S_0$ . Pseudo mode B-B' is a coupled wave "traveling" in the two Brunt frequency minimums in the lower atmosphere. The unstippled flat D-D' pseudo-mode is the acoustic-gravity or Lamb wave "traveling" at the earth's surface which is most frequently observed for near surface explosions at great distance.

Now that we have demonstrated the existence of a "fast" upper-atmosphere surface wave for half-space and free surface terminated models, the question arises as to whether it can be detected at the earth's surface. This is best answered by the inclusion of a source in the time domain.

#### TIME DOMAIN

Barograms and associated displacements were synthesized for various source and receiver altitudes using the far-field relations in Harkrider [1964]. A correction for the earth's curvature is included in the synthesis. The 490 km free surface model was used to obtain time series for four modes  $S_0$ ,  $GR_0$ ,  $GR_1$ , and  $GR_2$  at a distance of 10,000 km from the source. Two sources were used: a pressure source proportional to the eigen pressure profile and a displacement source proportional to the

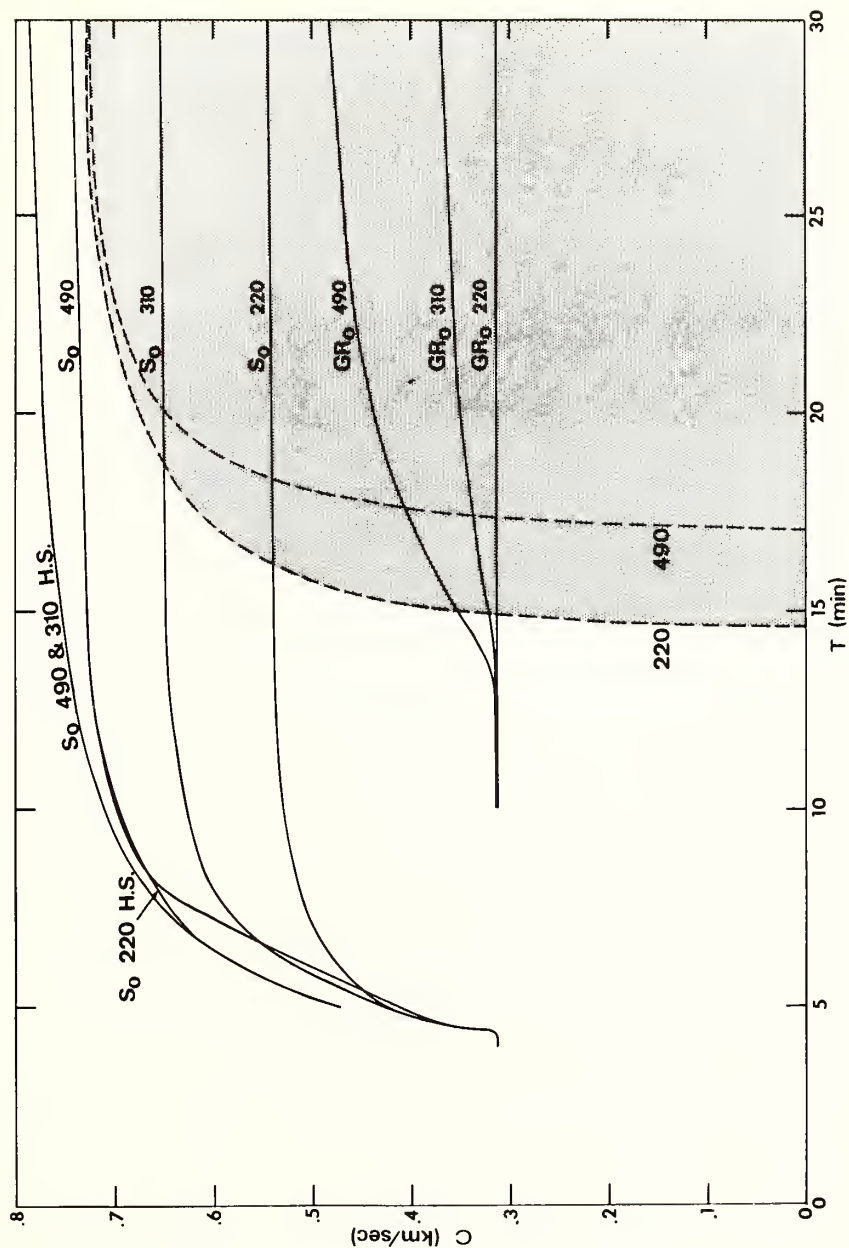


Fig. 1. Phase velocity dispersion curves for  $S_0$  and  $GR_0$  modes of ARDC standard atmospheres terminated by a free surface or a half space at 220, 310, and 490 kms.

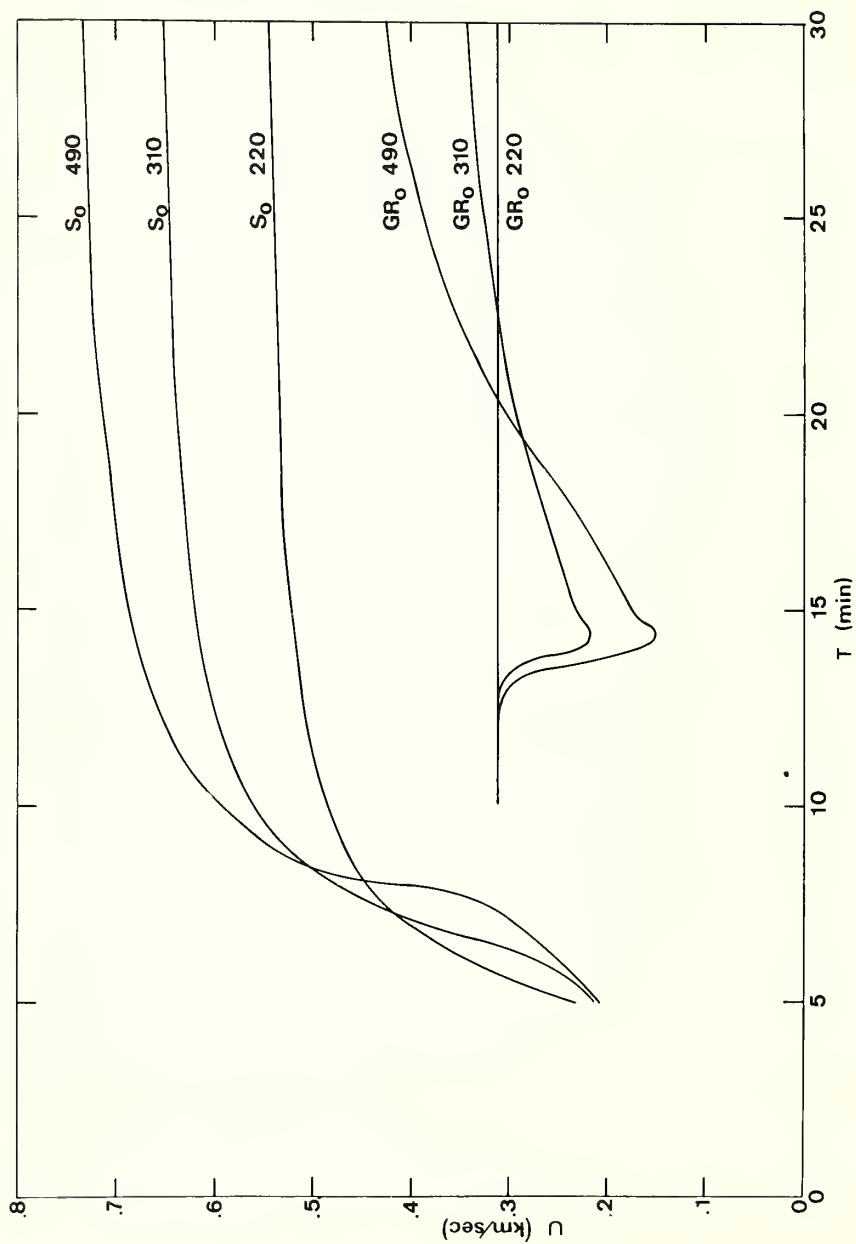


Fig. 2. Group velocity dispersion curves for  $S_0$  and  $GR_0$  modes of ARDC standard atmospheres terminated by a free surface at 220, 310, and 490 kms.



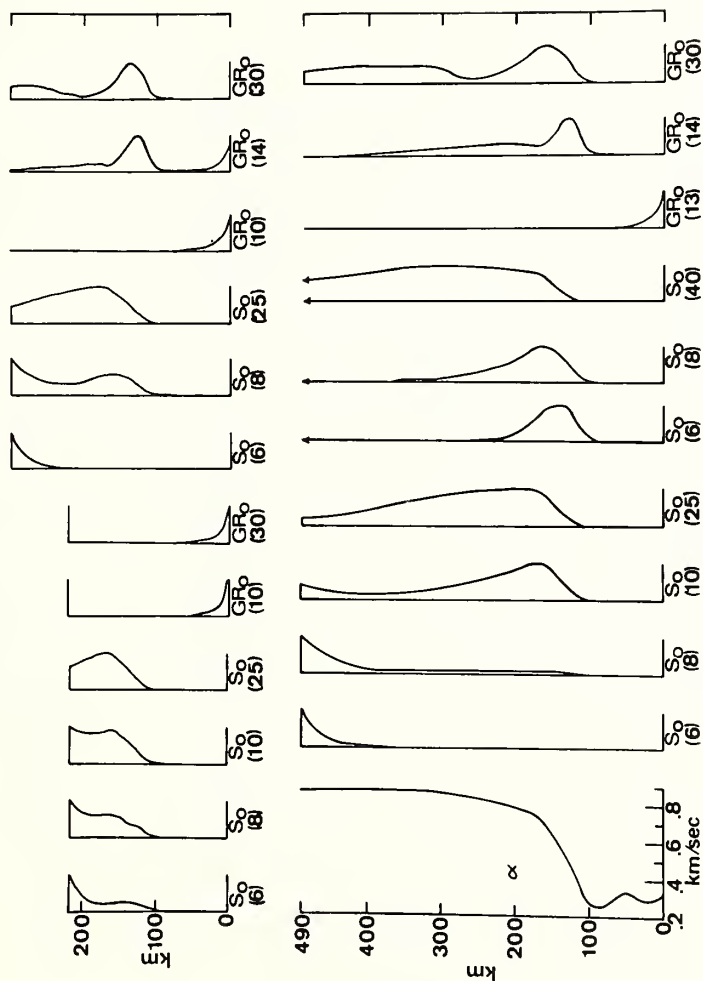


Fig. 3. Acoustic velocity and kinetic energy density versus altitude for  $S_0$  and  $GR_0$  modes. The arrows on the ordinate axes indicate a half space termination. The periods in minutes at which the profiles were measured are given in parenthesis.

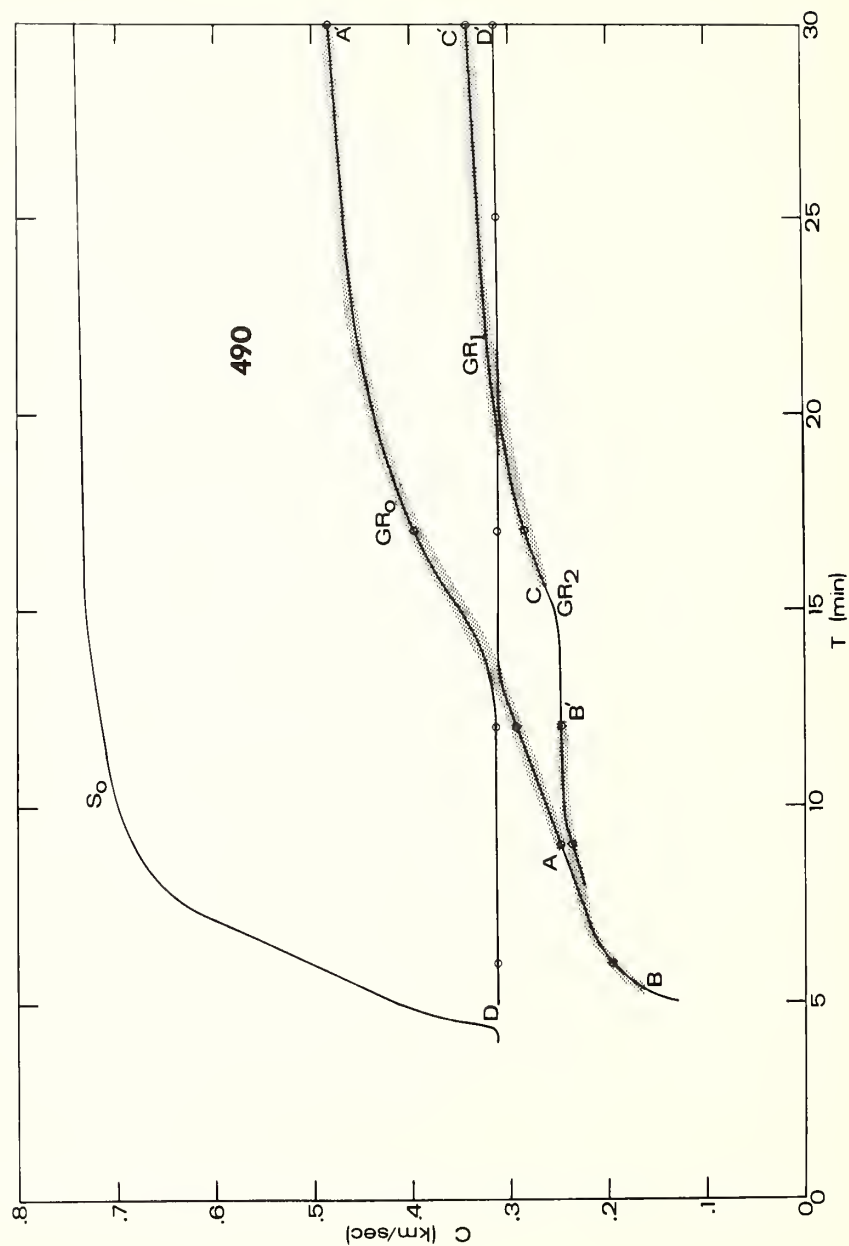


Fig. 4. Phase velocity dispersion curves for  $S_0$  and  $GR_{0,1,2}$  modes of the ARDC standard atmosphere terminated by a free surface at 490 km.

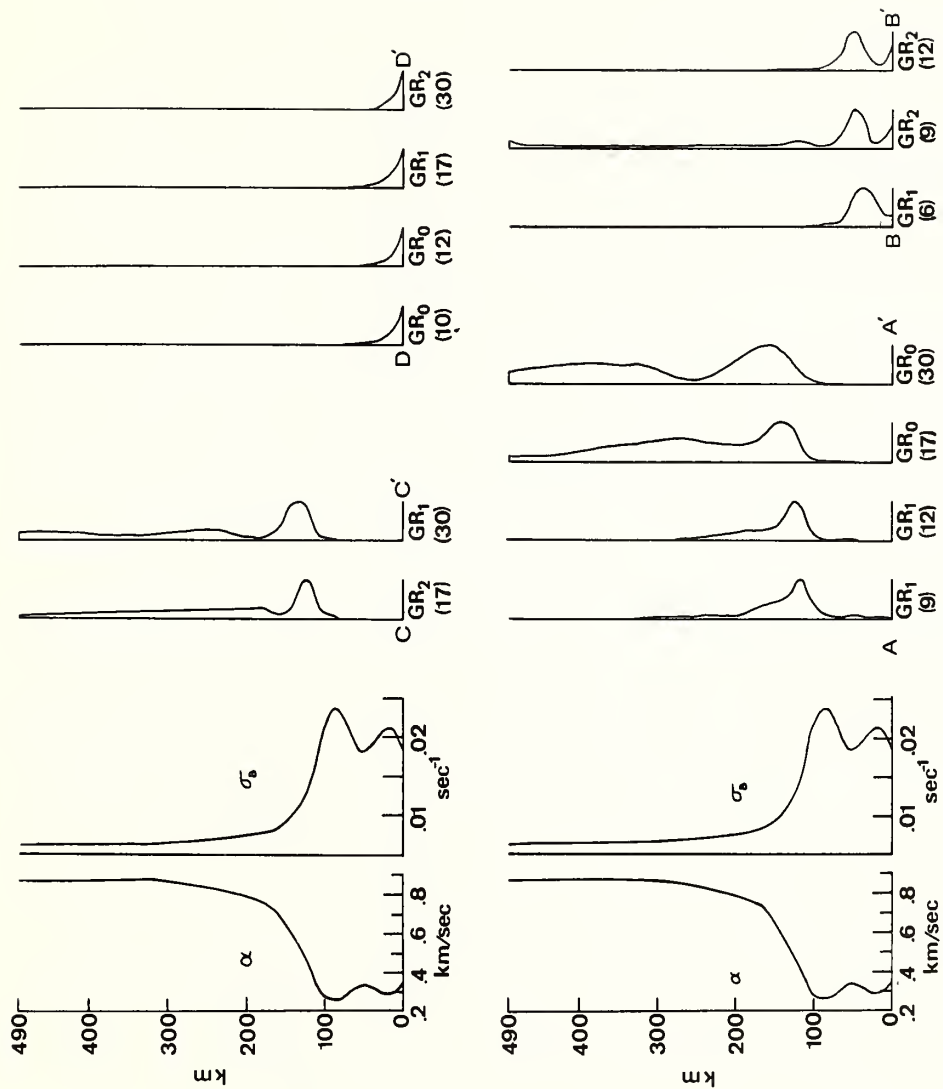


Fig. 5. Acoustic velocity, isothermal Brunt-Väisälä frequency, and kinetic energy density versus altitude for  $GR_{0,1,2}$  modes of the ARDC standard atmosphere terminated by a free surface at 490 km.

eigen displacement profile.

The surface barograms for the  $S_0$  mode generated by the two types of sources at altitudes of 130 and 485 km are shown in Figure 6. The source was an impulse with a period band pass of from 5 to 60 minutes. An early arrival at a group velocity between .75 and .60 km/sec was observed for all cases. One of the more obvious effects of the source type is the relative enhancement by the pressure source of the early arrival to the rest of the wave train. This also occurred for the source height of 165 km.

Theoretical  $S_0$  mode pressure variations for the surface pressure source are shown in Figure 7 as a function of distance from the source at altitudes of 120, 130, 140, 150 and 160 kms. The wave trains are calculated at 200 minutes after the impulse. For these wavelengths and altitudes the wave fronts are vertical and the ratio of horizontal to vertical motion ranges from 10 to 100 with increasing wavelength.

In order to obtain a quantitative measure of the effectiveness of different source types and altitudes in generating the surface wave, the maximum pressure and displacement arrivals of the  $S_0$  mode were normalized to the maximum surface pressure arrival for each event. This was the Lamb wave with a group velocity near .312 km/sec in all cases considered.

Table 1 gives the maximum peak to peak over pressures of the  $S_0$  mode at the earth's surface as a function of source height. The results for the pressure source are in the column headed  $P_R(0) P_S(H)$ , and in the column headed  $P_R(0) W_S(H)$ , for a displacement source. Note that a displacement source as we have defined it cannot exist at the earth's surface. For both classes of source the early arriving  $S_0$  mode is most efficiently generated at an altitude between 130 and 485 km, which as we have seen from the kinetic energy profiles is the region in which this wave is ducted. If the source were a pressure source at 165 km and the .312 km/sec group arrival was 1 mbar, we would observe a surface wave arrival of 6.8  $\mu$  bars.

TABLE 1. Maximum Pressure and Vertical Displacement of the  $S_0$  Mode for Source and Receiver Heights (H). The Data is Normalized to the Maximum Surface Pressure of the  $GR_0$  Mode Generated by the Impulse Source.

H(KM)	$P(S_0)_{MAX}/P_0(GR_0)_{MAX}$		$W(S_0)_{MAX}/P_0(GR_0)_{MAX}$		(KM/MB)
	$P_R(0)P_S(H)$	$P_R(0)W_S(H)$	$W_R(H)P_S(H)$	$W_R(H)W_S(H)$	
0	$6.9 \times 10^{-8}$	-----	0	-----	0
130	$1.9 \times 10^{-3}$	$7.1 \times 10^{-4}$	$1.8 \times 10^2$	$6.5 \times 10^1$	$7.5 \times 10^{-3}$
165	$6.8 \times 10^{-3}$	$8.9 \times 10^{-4}$	$1.8 \times 10^3$	$2.6 \times 10^2$	$2.0 \times 10^{-2}$
485	$2.6 \times 10^{-4}$	$6.1 \times 10^{-5}$	$1.9 \times 10^4$	$4.6 \times 10^3$	$6.1 \times 10^{-1}$

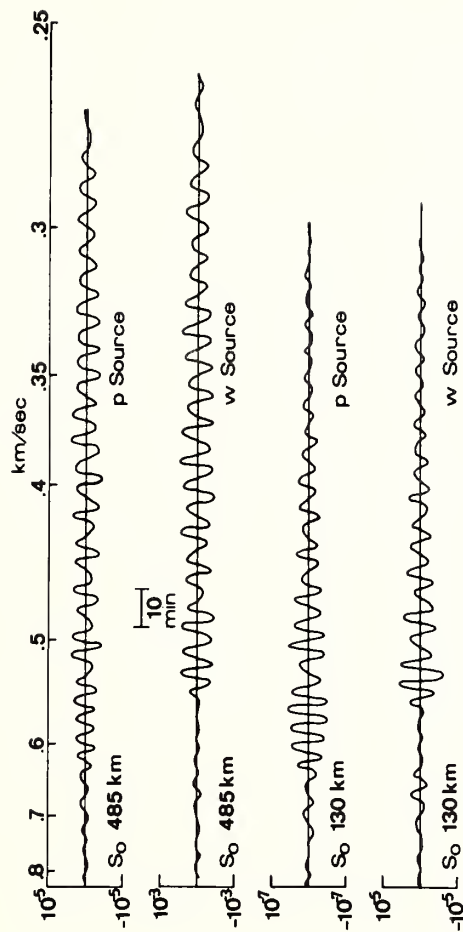


Fig. 6. Theoretical ground level barograms of the  $S_0$  mode generated by pressure and displacement sources at altitudes of 130 and 485 kms. The pressure scales are arbitrary and should not be used for comparison.



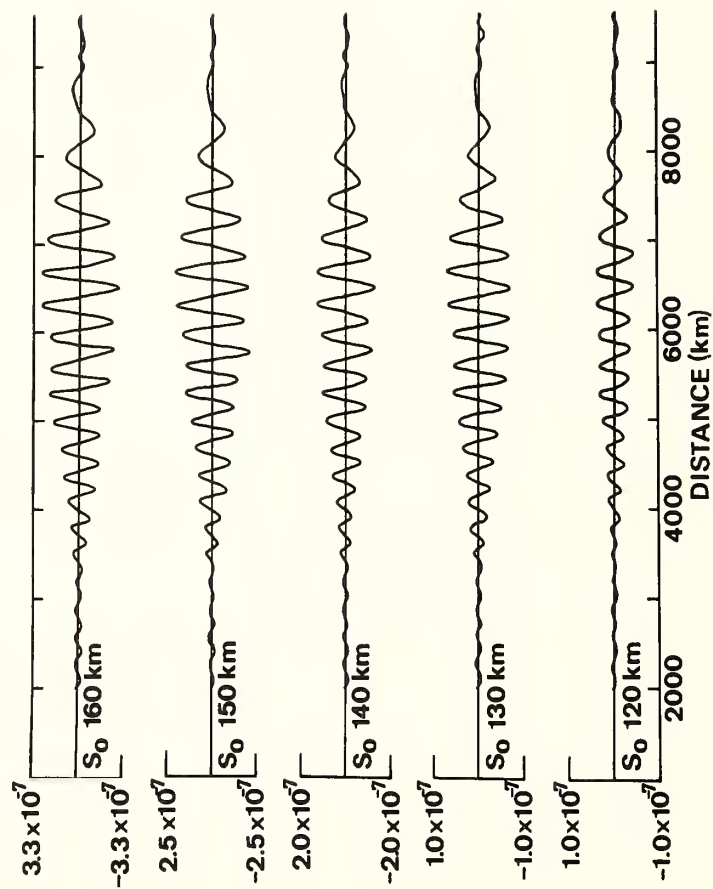


Fig. 7. Theoretical pressure variations versus range and altitude for the  $S_0$  mode generated by a surface pressure sources. The pressure scales are arbitrary and should not be used for comparison.

The vertical displacements of the  $S_0$  mode as a function of altitude are also given in Table 1. The displacement due to a pressure source at the same altitude is given in the column headed,  $w_R(H) P_S(H)$  and for the displacement source in the column headed  $w_R(H) w_S(H)$ . As an example the displacement at an altitude of 130 km due to a displacement source at that altitude is 65 km if the maximum surface pressure is 1 mbar for this event. The unusually large displacements at altitude are in part due to the magnitude of the source needed to excite 1 mbar of pressure on the surface from high altitudes.

This can be seen from the more reasonable displacements at altitude generated by a surface source. These are found in the same table in the column headed  $w_R(H) P_S(0)$ . Even at an altitude of 485 km, the displacement is less than 1 km for the surface event.

Because of the ducting at the rigid surface, it is difficult to numerically obtain eigen functions valid at the 485 km altitude for small periods. For the  $GR_0$  mode, single precision arithmetic on an IBM 360 yields significant results only for periods greater than 10 minutes. Thus the values given in the Table 1 at 485 km must be regarded as a rough estimate even if the assumptions of the theoretical model are valid at that altitude.

The period content of the arrivals was increased by changing the period band pass of the impulse source to 20-130 minutes and by using a one cycle 60 minute sine wave source at this band pass. The results are shown in Tables 2 and 3. The pressures and displacements are normalized to the  $GR_2$  surface pressure which gives the dominant contribution to the Lamb wave at these periods. The quantitative conclusions are similar to the shorter period calculations.

TABLE 2. Maximum Pressure and Vertical Displacement of the  $S_0$  Mode for Source and Receiver Heights (H). The Data is Normalized to the Maximum Surface Pressure of the  $GR_2$  Mode Generated by the Impulse Source.

H(KM)	$P(S_0)_{MAX}/P_0(GR_2)_{MAX}$		$w(S_0)_{MAX}/P_0(GR_2)_{MAX}$ (KM/MB)	
	$P_R(0)P_S(H)$	$P_R(0)w_S(H)$	$w_R(H)P_S(H)$	$w_R(H)w_S(H)$
0	$4.1 \times 10^{-9}$	-----	0	-----
130	$1.6 \times 10^{-4}$	$3.3 \times 10^{-4}$	$4.1 \times 10^1$	$9.3 \times 10^1$
165	$4.6 \times 10^{-3}$	$1.0 \times 10^{-4}$	$4.2 \times 10^3$	$9.7 \times 10^1$
485	$5.3 \times 10^{-4}$	$8.0 \times 10^{-4}$	$9.2 \times 10^3$	$1.4 \times 10^4$

TABLE 3. Maximum Pressure and Vertical Displacement of the  $S_0$  Mode for Source and Receiver Heights (H). The Data is Normalized to the Maximum Surface Pressure of the  $GR_2$  Mode Generated by the 60 Minute Single-Cycle Sine Wave Source.

H(KM)	$P(S_0)_{MAX}/P_0(GR_2)_{MAX}$		$W(S_0)_{MAX}/P_0(GR_2)_{MAX}$ (KM/MB)	
	$P_R(0)P_S(H)$	$P_R(0)W_S(H)$	$W_R(H)P_S(H)$	$W_R(H)W_S(H)$
0	$1.6 \times 10^{-9}$	-----	0	-----
130	$6.0 \times 10^{-4}$	$3.1 \times 10^{-4}$	$1.5 \times 10^2$	$1.1 \times 10^2$
165	$1.7 \times 10^{-3}$	$2.2 \times 10^{-4}$	$1.5 \times 10^3$	$2.7 \times 10^2$
485	$9.2 \times 10^{-4}$	$1.3 \times 10^{-3}$	$1.6 \times 10^4$	$2.9 \times 10^4$

As long as we were at periods in the frequency domain outside of the stippled cutoff region shown in Figure 1, for half-space terminations the time domain results were unaffected by the method of terminating the atmosphere model. For the  $GR_2$  mode which lies in the cutoff region for the half-space "top", this might be important. Therefore we calculated the complex root for the corresponding mode of the 220 half-space model at a period of 30 minutes.

The magnitude of the phase velocity, group velocity, and surface excitation function differed from the values of the 490 free surface model by less than .1%. The height excitation or eigenfunctions differed by less than 10%. The ratio of the imaginary to the real part of the horizontal wave number was  $-.29 \times 10^{-4}$  which is in good agreement with the  $-.27 \times 10^{-4}$  long period limit obtained for atmosphere models in Friedman [1966]. This yields a decay distance for this mode of  $3.14 \times 10^4$  km which is equivalent to nearly eight encirclements of the earth. On the basis of this, we felt justified in using the  $GR_2$  mode of the 490 free surface model at periods greater than 20 minutes in our calculations.

In this study we have restricted our source to two types which are proportional to the "natural" eigenfunctions of a thermally stratified atmosphere. All other types of point sources can be obtained by a linear combination of these two sources. Since the altitude profiles of these eigenfunctions differ according to mode and period, it is possible that another type of source might be more efficient in exciting the atmosphere surface wave. However we felt that it was not worthwhile here to investigate a broader class of sources until more information is available on the non-linear regions associated with explosions.

#### DETECTION

The  $S_0$  height excitation function has no zeros except at the free surface and at ground level for the pressure and displacement sources respectively. The  $GR_2$  mode has two additional nodes at altitude for each type of source. Thus it is possible to enhance the amplitudes of

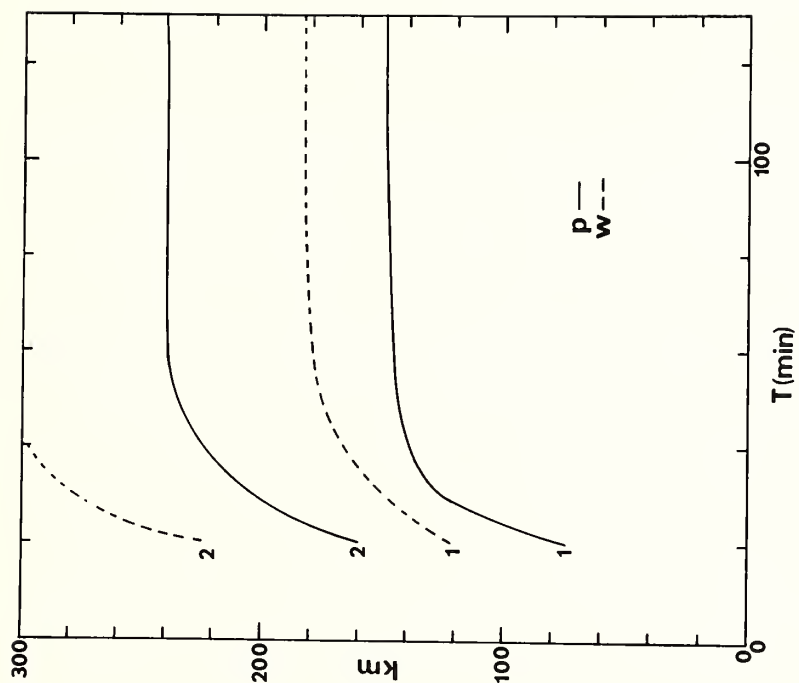


Fig. 8. Pressure and displacement nodes of the source height excitation function versus period for the  $GR_2$  mode of the ARDC standard atmosphere terminated by a free surface at 490 km.

the  $S_0$  mode relative to the  $GR_2$  mode for a source at altitude by limiting the receiver response to frequencies for which this altitude is a  $GR_2$  node. Figure 8 shows the nodes of the  $GR_2$  excitation function for a pressure and displacement source at altitude versus period. For example, a long period receiver with a short period cutoff of around 50 minutes would measure large amplitude  $S_0$  arrivals relative to the  $GR_2$  mode for pressure sources near 150 and 240 kms and for displacement sources near 190 and 310 kms. The degree of enhancement would of course depend on the vertical dimensions of the source region.

Another technique would be to make use of the differences in the long period velocities or horizontal wave lengths of the two arrivals. But this might require instrument arrays on the order of thousands of kilometers. These by no means exhaust the possible techniques for detecting the atmosphere surface wave and may be unimportant compared to existing methods used for detecting high altitude disturbances.

### CONCLUSIONS

Winds and viscosity have been neglected in the calculations presented here. The effects of viscosity are important at altitudes in which the atmospheric surface wave propagates. Since the numerical amplitude results have been normalized to the Lamb wave arrival which travels in the lower atmosphere where viscosity is less important, the amplitudes should be interpreted as upper limits for more realistic atmospheres. The validity of this assertion will be investigated in a later paper.

For the restricted linear theory, an early arriving atmospheric surface wave exists independent of the altitude termination of atmosphere models. This arrival travels in the upper atmosphere with predominantly horizontal motion at long periods. The most efficient source region is above 130 km. At certain source altitudes depending on the source type and thermal structure, it is possible to increase the surface amplitude of the atmosphere surface wave relative to the slower traveling acoustic-gravity or Lamb wave by using long period receivers.

For sources confined near the earth's surface as seen in Tables 1, 2, and 3 it would be nearly impossible to generate a surface expression of the atmosphere surface wave. However these results do not exclude the generation of surface wave by the extension of the source or non-linear region to high altitudes. Recent calculations presented at this symposium by *Whitaker and Greene* indicate that the non-linear region of low altitude explosions extend to altitudes on the order of hundreds of kilometers.

*Acknowledgement.* This research was supported by the Advanced Research Projects Agency and was monitored by the Air Force Office of Scientific Research under contract AF-F44620-67-C-0006.

### REFERENCES

- Friedman, Jack P., "Propagation of Internal Gravity Waves in a Thermally Stratified Atmosphere", *J. Geophys. Res.*, 71, 1033-1054, 1966.
- Harkrider, David G., "Theoretical and Observed Acoustic-Gravity Waves from Explosive Sources in the Atmosphere", *J. Geophys. Res.*, 69, 5295-5321, 1964.
- Harkrider, David and Frank Press, "The Krakatoa Air-Sea Waves: An Example of Pulse Propagation in Coupled Systems", *Geophys. J. of the Roy. Ast. Soc.*, 13, 149-159, 1967



Press, Frank and David Harkrider, "Propagation of Acoustic-Gravity Waves in the Atmosphere", *J. Geophys. Res.*, 67, 3889-3908, 1962.

Tolstoy, Ivan, "Long-Period Gravity Waves in the Atmosphere", *J. Geophys. Res.*, 18, 4605-4622, 1967.



# AN APPROACH TO THE MODE CONVERSION PROBLEM IN NON-UNIFORM ACOUSTIC WAVEGUIDES

James R. Wait  
ESSA Research Laboratories  
Boulder, Colorado 80302

A method is described for treating wave propagation in a waveguide structure whose cross section varies in the direction of propagation. Special attention is given to the conversion of energy between waveguide modes of different order. For simplicity, the waveguide is bounded by impedance-type walls and the lateral height variation is assumed to have circular symmetry. This is considered to be an idealized model of an atmospheric waveguide for acoustic-wave propagation in the case when there is a localized depression.

## Introduction

There has been a great deal of attention paid to acoustic-wave propagation in uniform guiding structures. While the terrestrial environment does tend to be uniformly stratified in its gross characteristics, there are many important instances where the effective cross section of the guide varies significantly in the direction of propagation. A concrete example is the propagation of sound in shallow water where there is a sudden change in depth. An equally striking illustration is when guided acoustic waves in the atmosphere pass over a mountain range.

Previous work in non-uniform waveguides, e. g., [Weston, 1959; Redwood, 1960; Pierce, 1965; Tolstoy and Clay, 1966] has been devoted to situations where the coupling between the modes is sufficiently small to be ignored. In this paper, we present a method, albeit approximate, for handling the more general case where mode coupling is retained. However, to simplify the discussion, we consider a waveguide whose lower boundary is flat but the height of the upper boundary is variable. In order to simulate earth curvature and to allow for the sound speed to vary with altitude, we take the wave number of the medium to be a specified function of height. The lower boundary may be regarded as an idealized smooth earth while the variable upper boundary is some height where there is strong coupling between upgoing and downgoing wave types. As such both walls of the waveguide are assumed to be characterized by impedance-type boundary conditions. The validity of such a description is not investigated here but it has met with considerable success in electromagnetic wave propagation [Wait, 1962, 1968a].

## Formulation

The situation is illustrated in Figure 1. Essentially, we are dealing with a parallel plate waveguide of thickness  $h_1$  except for a depressed region of radius  $a$  where the thickness is  $h_2$ . The respective regions are designated (1) and (2). The field quantity  $\psi$  is assumed to satisfy a scalar wave equation,

$$(\nabla^2 + k^2) \psi = 0 \quad (1)$$

where  $k(z)$ , the wave number, is a function of  $z$  only.

Boundary conditions on the horizontal surfaces are of the type

$$\frac{\partial \psi}{\partial z} + K \psi = 0 \quad (2)$$

where  $K$  is independent of the radial coordinate in either region (1) or (2). For example, in dealing with acoustic waves where  $\psi$  is the velocity potential,  $K$  is zero for a rigid surface or  $\infty$  for a free surface. In general,  $K$  may be regarded as a boundary impedance parameter.

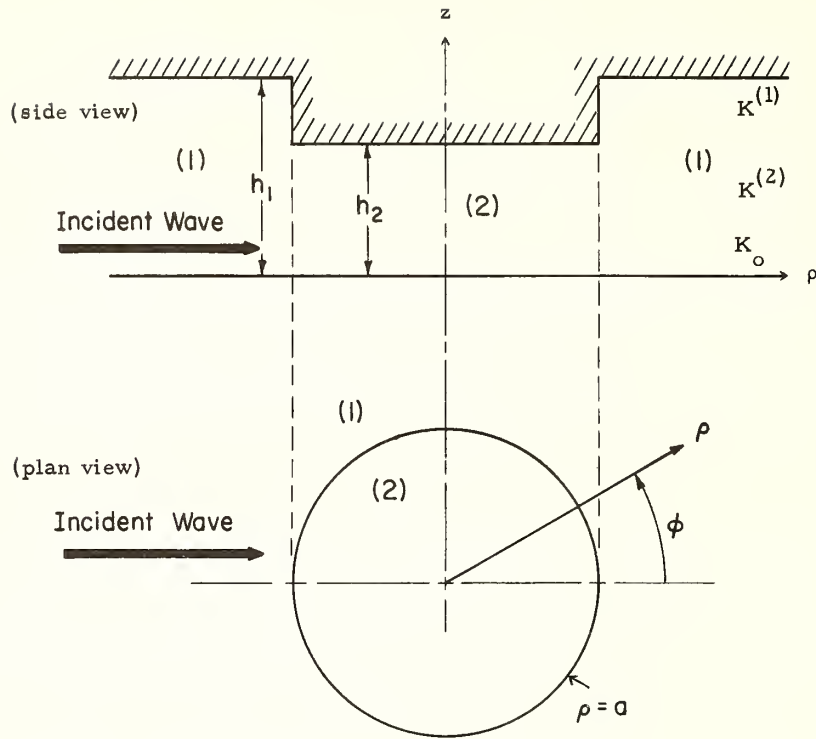


Fig. 1 - The idealized height variation considered in this analysis. (The appropriate boundary impedance parameters  $K_o$ ,  $K^{(1)}$  and  $K^{(2)}$  are indicated.)

Solutions of (1) may be written in the form

$$\psi = Z_p(k_o S \rho) e^{+ip\phi} G(z) \quad (3)$$

where  $Z_p$  is a cylindrical Bessel function of order  $p$ , while  $G(z)$  satisfies

$$\frac{\partial^2 G}{\partial z^2} + [k^2(z) - k_o^2 S^2] G = 0, \quad (4)$$

where  $k_o = k(0)$  and  $S$  is a separation constant.

Some further consideration shows that the general solution is of the form

$$\psi = \sum_{p=-\infty}^{+\infty} e^{ip\phi} \sum_m (A_m)_p Z_p(k_o S_m \rho) G_m(z), \quad (5)$$

where  $(A_m)_p$  is a coefficient to be determined from the boundary conditions. The summation over  $p$  involves integers only, and where the summation index  $m$  indicates that we superimpose all "modes." The latter are exemplified by a discrete set of  $S_m$  obtained as a result of the boundary condition (2) which states that

$$\left. \frac{\partial G_m}{\partial z} + K G_m \right|_{\text{at horizontal surfaces}} = 0 \quad (6)$$

Thus,  $k_o S_m^{(1)}$  is the transverse wave number for a waveguide mode of order  $m$  in region (1), and  $k_o S_m^{(2)}$  is the corresponding wave number in region (2). For convenience, we describe  $G_m(z)$  as a "height gain function" for a mode of order  $m$  and normalize it such that  $G_m(0) = 1$  [e.g., Wait, 1962]. Again, a superscript (1) or (2) is added as appropriate.

We now imagine that a mode of order  $m$  is incident from a distant source in region (1). The problem is to calculate the total field everywhere. The incident field  $\psi_{inc}$ , suitably normalized, is written

$$\psi_{inc} = \frac{\Lambda_m^{(1)}}{h_1} e^{-i k_o S_m^{(1)} \rho \cos \phi} G_m^{(1)}(z_o) G_m^{(1)}(z) \quad (7)$$

where the "excitation factor"  $\Lambda_m^{(1)}$  is a measure of the strength of the incident mode of order  $m$  for a distant point source located at a height  $z_o$ . Summation over  $m$  is implied.

Without difficulty [e.g., Wait, 1962], we may demonstrate that

$$\int_0^{h_1} G_m^{(1)}(z) G_n^{(1)}(z) dz = 0 \quad \text{for } m \neq n \quad (8)$$

while

$$\int_0^{h_1} [G_m^{(1)}(z)]^2 dz = \frac{h_1}{2 \Lambda_m^{(1)}} \quad (9)$$

may be regarded as a definition of the "excitation factor"  $\Lambda_m^{(1)}$  which appears in (7).

#### Construction of the Solution

To deal with the specific problem posed above, we employ an addition theorem and re-write (7) in an equivalent form [Watson, 1944]. Thus,

$$\psi_{inc} = \frac{\Lambda_m^{(1)}}{h_1} G_m^{(1)}(z_o) \sum_{p=-\infty}^{+\infty} e^{-i \pi p/2} J_p(k_o S_m^{(1)} \rho) e^{i p \phi} G_m^{(1)}(z) \quad (10)$$

where  $J_p$  is the Bessel function of the first type. The total field  $\psi^{(1)}$  in region (1) now consists of  $\psi_{inc}$  plus a scattered field  $\psi_{sc}$  which must have the form

$$\psi_{sc} = \frac{\Lambda_m^{(1)}}{h_1} G_m^{(1)}(z_o) \sum_{p=-\infty}^{+\infty} e^{-i \pi p/2} e^{i p \phi} \sum_s (B_{s,m})_p H_p(k_o S_s^{(1)} \rho) G_s^{(1)}(z) \quad (11)$$

where  $H_p = J_p - i Y_p$  is the Hankel function of the second kind. Here,  $(B_{s,m})_p$  may be regarded as a coefficient which describes the scattering from mode of order  $m$  into a mode of order  $s$  for a wave whose azimuthal variation is  $\exp(i p \phi)$ . It may be verified that (11) satisfies the wave equation (1), the appropriate boundary conditions, and it gives rise to outgoing waves as  $\rho \rightarrow \infty$ . The latter statement is a consequence of the asymptotic relation [Watson, 1944]

$$\lim_{Z \rightarrow \infty} H_p(Z) \approx \left(2i/(\pi Z)\right)^{1/2} e^{i \pi p/2} e^{-i Z} \quad (12)$$



Furthermore, when there is any loss in the system, the eigen-value solution for the wave numbers  $k_o S_s^{(1)}$  shows that  $\text{Im } k_o S_s^{(1)} < 0$ , which leads to radial damping of the scattered modes.

The total field  $\psi^{(1)}$  in region (1), i.e., where  $\rho > a$  and  $0 < z < h_1$ , is thus given by  $\psi^{(1)} = \psi_{\text{inc}} + \psi_{\text{sc}}$

We now construct an expression for the field  $\psi^{(2)}$  in region (2), i.e., where  $\rho < a$  and  $0 < z < h_2$ . Without difficulty, we find that

$$\psi^{(2)} = \frac{\Lambda_m^{(1)}}{h_1} G_m^{(1)}(z_o) \sum_{p=-\infty}^{+\infty} e^{-i\pi p/2} e^{ip\phi} \sum_n (A_{n,m})_p J_p(k_o S_n^{(2)} \rho) G_n^{(2)}(z) \quad (13)$$

where the Bessel function  $J_p$  is chosen to be finite at  $\rho = 0$  and  $(A_{n,m})_p$  is a coefficient which describes the modes of order  $n$  transmitted into region (2) for an incident mode of order  $m$  from region (1). We note that the height-gain function  $G_n^{(2)}(z)$ , for region (2), must be employed if  $\psi^{(2)}$  is to satisfy the appropriate boundary conditions.

#### Field Matching

In order to obtain relationships between the unknown coefficients, we impose continuity conditions at the cylindrical interface between regions (1) and (2). Specifically, we require that  $\psi$  and  $\partial\psi/\partial\rho$  be continuous at  $\rho = a$  for  $0 < z < h_2$ , where  $h_2 < h_1$ . Then, on using (10), (11), and (13), we find that

$$J(k_o S_m^{(1)} a) G_m^{(1)}(z) + \sum_s B_{s,m} H(k_o S_s^{(1)} a) G_s^{(1)}(z) = \sum_n A_{n,m} J(k_o S_n^{(2)} a) G_n^{(2)}(z), \quad (14)$$

and

$$S_m^{(1)} J'(k_o S_m^{(1)} a) G_m^{(1)}(z) + \sum_s B_{s,m} S_s^{(1)} H'(k_o S_s^{(1)} a) G_s^{(1)}(z) = \sum_n A_{n,m} S_n^{(2)} J'(k_o S_n^{(2)} a) G_n^{(2)}(z) \quad (15)$$

where the primes indicate differentiation with respect to the argument of the Bessel function. In writing (14) and (15), the subscript  $p$  has been dropped since termwise matching of the  $p$  series is permitted.

We are now faced with the question of what boundary condition to impose on the vertical face  $\rho = a$  when  $h_1 > z > h_2$ . For the moment, we will assume that both  $\psi^{(1)}$  and  $\partial\psi^{(1)}/\partial\rho$  are zero over this surface. An equivalent statement is to say that (14) and (15) apply over the interval  $0 < z < \infty$  but  $G_n^{(1)}(z) = 0$  for  $z > h_1$  and  $G_n^{(2)}(z) = 0$  for  $z > h_2$ . A method to estimate the error of this assumption and a first-order correction has been discussed elsewhere [Wait, 1968b] in connection with electromagnetic waves in the earth-ionosphere waveguide.

#### Reduction of the Solution

To reduce (14) and (15), for the idealizations indicated, we multiply both sides by  $G_q^{(2)}(z)$  and integrate from 0 to  $h_2$ . Thus, we obtain

$$J(k_o S_m^{(1)} a) \hat{\Gamma}_{q,m} + \sum_s B_{s,m} H(k_o S_s^{(1)} a) \hat{\Gamma}_{q,s} = A_{q,m} J(k_o S_q^{(2)} a) \Gamma_{q,q} \quad (16)$$

and

$$S_m^{(1)} J'(k_o S_m^{(1)} a) \hat{\Gamma}_{q,m} + \sum_s B_{s,m} S_s^{(1)} H'(k_o S_s^{(1)} a) \hat{\Gamma}_{q,s} = A_{q,m} S_q^{(2)} J'(k_o S_q^{(2)} a) \Gamma_{q,q} \quad (17)$$

where

$$\Gamma_{q,q} = \frac{h_2}{2 \Lambda_q^{(2)}} = \int_0^h \left[ G_q^{(2)}(z) \right]^2 dz, \quad (18)$$

$$\hat{\Gamma}_{q,m} = \int_0^{h_2} G_m^{(1)}(z) G_q^{(2)}(z) dz, \quad (19)$$

and

$$\hat{\Gamma}_{q,s} = \int_0^{h_2} G_s^{(1)}(z) G_q^{(2)}(z) dz. \quad (20)$$

In getting from (14) and (15) to (16) and (17), we exploit the orthogonality property

$$\int_0^{h_2} G_n^{(2)}(z) G_q^{(2)}(z) dz = 0 \quad \text{for } n \neq q. \quad (21)$$

On eliminating  $A_{q,m}$  from (16) and (17), we obtain the single infinite system

$$\begin{aligned} & \left[ S_q^{(2)} J'(k_o S_q^{(2)} a) J(k_o S_m^{(1)} a) - S_m^{(1)} J'(k_o S_m^{(1)} a) J(k_o S_q^{(2)} a) \right] \hat{\Gamma}_{q,m} \\ & + \sum_s B_{s,m} \left[ S_q^{(2)} J'(k_o S_q^{(2)} a) H(k_o S_s^{(1)} a) - S_s^{(1)} H'(k_o S_s^{(1)} a) J(k_o S_q^{(2)} a) \right] \hat{\Gamma}_{q,s} = 0 \end{aligned} \quad (22)$$

In principle, we may solve for the coefficients  $B_{s,m}$  for each  $p$  by inverting an infinite square matrix. In practice, we truncate the system. In effect, this means we replace the summation over  $s$  by a finite number of terms, say  $N$ . Then, by letting  $q = 1, 2, 3, \dots, N$ , we have a sufficient number of equations to solve for  $B_{s,m}$ . The convergence of solutions of this type as  $N$  becomes large has been discussed previously [Bahar and Wait, 1964; Wexler, 1967]. For the present situation, we will focus our attention on the situation where  $h_1 - h_2 \ll h_1$ . In this instance, we can expect that

$$|S_q^{(1)} - S_q^{(2)}| \ll 1.$$

Furthermore, in such cases, it is found that  $|\hat{\Gamma}_{q,m}| \ll |\Gamma_{q,q}|$  when  $q \neq m$ . Thus, in order to get a zero-order solution for a typical coefficient  $B_{s,m}$ , in (22), we retain only the terms for  $s = q$  and  $s = m$ . First of all, when  $q = m$ , we easily get

$$B_{m,m} \approx B_{m,m}^0 = - \frac{S_m^{(2)} J'(k_o S_m^{(2)} a) J(k_o S_m^{(1)} a) - S_m^{(1)} J'(k_o S_m^{(1)} a) J(k_o S_m^{(2)} a)}{S_m^{(2)} J'(k_o S_m^{(2)} a) H(k_o S_m^{(1)} a) - S_m^{(1)} H'(k_o S_m^{(1)} a) J(k_o S_m^{(2)} a)}, \quad (23)$$

while, if  $q \neq m$ , we must deal with more terms in (22). In most cases, it appears that

$$B_{q,m} \approx B_{q,m}^{(0)} \approx - B_{m,m}^{(0)} P \quad (24)$$

where  $P$  is of the order of 1 or somewhat less.

The zero-order solutions given by (23) and (24) should be applicable for the dominant modes for which  $S_q^{(1)}$  and  $S_q^{(2)}$  are not significantly different from unity.

The final result for the scattered field is given by (11) with the coefficient  $(B_{s,m}^o)_p$  given approximately by (23) and (24) above where we set  $q = s$  and remember that the Bessel functions are of order  $p$ . Of course, if the accuracy is insufficient we should return to (22) and retain additional terms.

#### A Simplification

To provide insight into the behavior of the solution, we will consider a simplification which is valid when the perturbation is small. First of all, we note that, in the zero'th approximation, the scattered field is expressible in the form

$$\psi_{sc} \approx \text{const} \times \sum_q \sum_{p=-\infty}^{+\infty} e^{-i\pi p/2} (B_{q,m}^o)_p H_p(k_o S_q^{(1)} \rho) e^{ip\phi} \quad (25)$$

which amounts to changing the order of the summations indicated in (11). First of all, we shall focus our attention on the terms where  $q = m$ . These are the contribution to the scattered field in mode  $m$  for an incident mode also of order  $m$ . Thus, according to (24), we have

$$(B_{m,m}^o)_p = - \left[ \frac{u \frac{J'_p(u)}{J_p(u)} - \frac{v \frac{J'_p(v)}{J_p(v)}}{\frac{u \frac{J'_p(u)}{J_p(u)} - \frac{v \frac{H'_p(v)}{H_p(v)}}{\frac{J_p(v)}{H_p(v)}}} \right] \quad (26)$$

where  $u = k_o S_m^{(2)} a$  and  $v = k_o S_m^{(1)} a$ . We now set  $\Delta = u - v$  and expand (26) in a series in powers of  $\Delta$ . To within a first order of smallness in  $\Delta$ , we find that

$$(B_{m,m}^o)_p \approx \frac{\pi \Delta}{2i} v \left[ J_p^2(v) - J_{p+1}(v) J_{p-1}(v) \right] \quad (27)$$

In arriving at (27), we have used the following well-known identities for Bessel functions of argument  $v$ :

$$\begin{aligned} J_p H'_p - J'_p H_p &= -2i/(\pi v) \quad , \\ J'_p &= -(p/v) J_p + J_{p-1} = (p/v) J_p - J_{p+1} \quad . \end{aligned}$$

Another simplification in (25) is to replace the Hankel function of argument  $k_o S_s^{(1)} \rho$  by the first term of its asymptotic expansion [e.g., see (12) above]. This will be justified at sufficiently large distances from the scatterer. In other words, we require that both  $k_o a \gg 1$  and  $\rho \gg a$ . Then, on using (27), we find from (25) that the scattered  $m$ 'th mode field is

$$\psi_{sc}]_m \approx \left( \frac{2i}{\pi k_o S_m^{(1)} \rho} \right)^{\frac{1}{2}} e^{-ik_o S_m^{(1)} \rho} \frac{\pi v \Delta}{2i} \sum_{p=-\infty}^{+\infty} \left[ J_p^2(v) - J_{p-1}(v) J_{p+1}(v) \right] e^{-ip\phi} \quad (28)$$

omitting the constant term  $(\Lambda_m^{(1)}/h_1) G_m^{(1)}(z_o)$ . In order to sum these series, we make use of the following identities:

$$J_2\left(v \sin \frac{\phi}{2}\right) = - \sum_{p=-\infty}^{+\infty} J_{p-1}(v) J_{p+1}(v) e^{-ip\phi} \quad (29)$$

and

$$J_0\left(2v \sin \frac{\phi}{2}\right) = \sum_{p=-\infty}^{+\infty} J_p^2(v) e^{-ip\phi}, \quad (30)$$

which follow immediately from formulas given by Erdelyi, et al. [1953]. Then, on using the well-known identity

$$J_2(Z) = (2/Z) J_1(Z) - J_0(Z),$$

we see that (28) is expressible in the closed form

$$\psi_{sc}]_m \approx \left(\frac{\pi}{2 k_o S_m^{(1)} p}\right)^{\frac{1}{2}} e^{-i\pi/4} e^{-ik_o S_m^{(1)} p} \frac{\Delta}{\sin(\phi/2)} J_1\left(2 k_o S_m^{(1)} a \sin \frac{\phi}{2}\right) \quad (31)$$

$$\text{where } \Delta = k_o a (S_m^{(2)} - S_m^{(1)}).$$

We see that the scattered field has a strong maximum in the forward direction. In fact, as  $\phi \rightarrow 0$ ,

$$\frac{J_1\left(2 k_o S_m^{(1)} a \sin \frac{\phi}{2}\right)}{\sin \frac{\phi}{2}} \rightarrow k_o S_m^{(1)} a.$$

Thus, the forward scattered field is proportional to  $a^2$  (i.e., the area of the perturbation) and the contrast between the wave numbers

$$k_o S_m^{(2)} \text{ and } k_o S_m^{(1)}.$$

The development of the coefficients  $(B_{q,m}^o)$  for  $q \neq n$  into a series development in  $\Delta$  follows in a similar fashion to that outlined above. If we restrict attention to modes of order  $q$  such that both

$$|k_o a (S_m^{(2)} - S_m^{(1)})| \ll 1 \quad \text{and} \quad |k_o a (S_q^{(1)} - S_m^{(1)})| \ll 1.$$

Then, (24) reduces to

$$(B_{q,m}^o)_p \approx (B_{m,m}^o)_p \text{ times a factor independent of } p. \quad (32)$$

Thus, for the approximation indicated, it follows that the cross-coupled scattered field in mode  $q$  for an incident mode of order  $m$  is given by

$$\psi_{sc}]_q \approx \psi_{sc}]_m P \quad (33)$$

where  $P$  is more or less proportional to the coupling ratio

$$S_{q,m} = \frac{\hat{r}_{q,m}}{r_{q,q}} = \frac{\int_0^{h_2} G_m^{(1)}(z) G_q^{(2)}(z) dz}{\int_0^{h_2} [G_q^{(2)}(z)]^2 dz}. \quad (34)$$

### Mode Coupling

The coupling parameter given by (20) may be expressed in closed form. We proceed by using a variant of the standard analysis for demonstrating orthogonality of modes in a closed system [e. g., Sommerfeld, 1949].

In region (1), for a mode of order  $m$ , we have

$$\frac{\partial^2 G_m^{(1)}}{\partial z^2} + [k^2(z) - (k_o S_m^{(1)})^2] G_m^{(1)} = 0, \quad (35a)$$

while in region (2), for a mode of order  $n$ ,

$$\frac{\partial^2 G_n^{(2)}}{\partial z^2} + [k^2(z) - (k_o S_n^{(2)})^2] G_n^{(2)} = 0. \quad (35b)$$

Multiplying (35a) by  $G_n^{(2)}$  and (35b) by  $G_m^{(1)}$ , and subtracting the resulting equations, we find that

$$\frac{\partial}{\partial z} \left[ G_n^{(2)} \frac{\partial G_m^{(1)}}{\partial z} - G_m^{(1)} \frac{\partial G_n^{(2)}}{\partial z} \right] = [(k_o S_n^{(2)})^2 - (k_o S_m^{(1)})^2] G_m^{(1)} G_n^{(2)}. \quad (36)$$

Both sides of (36) are now integrated over the interval from 0 to  $h_2$ . Thus, we find that

$$\Gamma_{n,m} = \int_0^{h_2} G_m^{(1)}(z) G_n^{(2)}(z) dz = \frac{[G_m^{(1)'}(h_2) + K^{(2)} G_m^{(1)}(h_2)] G_n^{(2)}(h_2)}{(k_o S_m^{(1)})^2 - (k_o S_n^{(2)})^2} \quad (37)$$

where  $G^{(1)'}(h_2) = \partial G^{(1)}/\partial z$  evaluated at  $z = h_2$ . Also, in obtaining (37), we have used the boundary condition

$$\left[ \frac{\partial G^{(2)}}{\partial z} + K^{(2)} G^{(2)} \right]_{z=h_2} = 0. \quad (38)$$

In a similar manner, we find that, for  $n \neq m$ ,

$$\Gamma_{n,m} = \int_0^{h_2} G_m^{(2)}(z) G_n^{(2)}(z) dz = 0$$

which is a demonstration of the orthogonality property already used. For the case  $m = n$ , we consider the height-gain function  $G^{(2)}(z)$ , in region (2), which satisfies

$$\frac{\partial^2 G^{(2)}}{\partial z^2} + [k^2(z) - (k_o S)^2] G^{(2)} = 0. \quad (39)$$

Combining (35b) and (39), we obtain

$$\frac{\partial}{\partial z} \left[ G^{(2)} \frac{\partial G^{(2)}}{\partial z} - G^{(2)} \frac{\partial G^{(2)}}{\partial z} \right] = [(k_o S)^2 - (k_o S)^2] G^{(2)} G^{(2)}.$$

We again integrate both sides with respect to  $z$  over the range 0 to  $h_2$  and assume that both  $G_n^{(2)}$  and  $G^{(2)}$  satisfy the impedance boundary conditions at  $z = h_2$ , but only  $G_n^{(2)}$  satisfies the impedance boundary condition  $G_n^{(2)} = K_o G_n^{(2)}$  at  $z = 0$ . Thus, we find that



$$\int_0^{h_2} G_n^{(2)}(z) G_n^{(2)}(z) dz = - \frac{G_n^{(2)}(0)}{k_o^2 [S^2 - (S_n^{(2)})^2]} \left[ \frac{\partial}{\partial z} G_n^{(2)}(z) - K_o G_n^{(2)}(z) \right]_{z=0} \quad (40)$$

We now require that  $G_n^{(2)}(z)$  satisfy the same impedance boundary condition as  $G_n^{(2)}(z)$  at  $z = 0$ . Thus,  $S \rightarrow (S_n^{(2)})$ . Then, on applying Cauchy's theorem to the right-hand side of (40), we get

$$\Gamma_{n,n} = \int_0^{h_2} [G_n^{(2)}(z)]^2 dz = - \frac{G_n^{(2)}(0)}{2 k_o^2 S_n^{(2)}} \left\{ \frac{\partial}{\partial S} [G_n^{(2)}(z) - K_o G_n^{(2)}(z)] \right\}_{S=S_n^{(2)}} \quad (41)$$

$z = 0$

An explicit evaluation of this normalizing factor requires that we are able to solve (39) subject to the boundary condition at  $z = h_2$ . For example, if  $k^2(z)$  is a linear function of  $z$  the solutions of (39) are Airy functions and a relatively simple closed form for  $\Gamma_{n,n}$  is available [Wait, 1962]. The important point is that  $\Gamma_{n,n}$  is of the order of  $h_2$  for the propagating modes of low attenuation. On the other hand,  $\Gamma_{n,m}$  (for  $n \neq m$ ) is much less than  $h_2$  when  $h_1 - h_2 \ll h_1$ . Thus, we are justified in our exploiting the condition  $|\Gamma_{n,m}/\Gamma_{n,n}| \ll 1$  in considering first-order perturbation effects.

More work on this subject is obviously needed if we are to obtain useful information about acoustic-wave propagation (with or without gravity) in nonuniform atmospheric ducts.

#### References

- Bahar, E., and J.R. Wait, Microwave model techniques to study VLF propagation in the earth-ionosphere waveguide, Quasi-Optics (ed. J. Fox), 447-464, Polytechnic Institute of Brooklyn Press, Brooklyn, N.Y., 1964.
- Erdelyi, A., et al., Higher Transcendental Functions, vol. 2, 101, McGraw-Hill Book Co., New York, N.Y., 1953.
- Pierce, A.D., Extension of the method of normal modes to sound propagation in an almost stratified medium, J. Acoust. Soc. Amer., 37, No. 1, 19-27, 1965.
- Redwood, M., Mechanical Waveguides, Pergamon Press, Oxford, England, 89-91, 1960.
- Sommerfeld, A.N., Partial Differential Equations, Academic Press, New York, N.Y., 1949.
- Tolstoy, I., and C.S. Clay, Ocean Acoustics, McGraw-Hill Book Co., New York, N.Y. 1966.
- Wait, J.R., Electromagnetic Waves in Stratified Media, Pergamon Press, Oxford, England, 1962.
- Wait, J.R., Recent theoretical advances in the terrestrial propagation of VLF electromagnetic waves, Advances in Electronics and Electron Physics (ed. L. Marton), Academic Press, New York, N.Y., 1968a.
- Wait, J.R., On the theory of VLF propagation for a step model of the non-uniform earth-ionosphere waveguide, Can. J. Phys. 1968b. (in press)
- Watson, G.N., Theory of Bessel Functions, Cambridge University Press, Cambridge, 2nd ed. 1944.
- Weston, D.E., Guided propagation in a slowly varying medium, Proc. Phys. Soc. (London) 73, 365-384, 1959.
- Wexler, A., Solution of waveguide discontinuities by modal analysis, IEEE Trans. MTT-15, No. 9, 508-516, 1967.



THE DIURNAL SOURCE AND NATURE OF GRAVITY WAVES  
DUCTED IN THE LOWER THERMOSPHERE

by A. F. Wickersham, Jr.  
Radio Physics Laboratory  
Stanford Research Institute  
Menlo Park, California

The theory of gravity waves in a thermoclinical atmosphere shows that dispersion decreases as thermal gradient increases. If the thermal gradient is large enough it offsets the increase in amplitude caused by upward propagation into a region of decreasing ambient density, and there is no non-viscous damping of the motion. Thus long distance propagation can occur in the principal duct at 100 to 160 km altitude where the thermal gradient is large enough to eliminate much of the non-viscous damping.

It is shown that thermal perturbation of the principal duct by the long winter-solstice sunrise in the polar regions is a possible source of ducted gravity waves consistent with the seasonal variations in directions of travelling ionospheric disturbances (TIDs) observed in Australia.

The observed tilts of TIDs are compared with theory and can be used to determine the period of a disturbance. The effect of ionospheric charge equilibration is discussed briefly, and a leaky-duct gravity wave model is proposed which reconciles the observations of tilted wave fronts and long distance propagation.

INTRODUCTION

Naturally occurring travelling ionospheric disturbances (TIDs) have been detected for many decades, and several writers have suggested that they are propagating atmospheric gravity waves (for example, Martyn, 1950 and Hines, 1960). For more than 10 years it has been known that TIDs have fronts that are inclined in the direction of travel. Munro and Heisler (1956a) measured the tilt in 430 naturally occurring TIDs and found it to be 65 degrees, measured from the horizontal, for disturbances travelling in the direction of the geomagnetic meridian; however, they found that disturbances travelling at right angles to such direction also have tilted fronts, the tilt being about 54 degrees. This probably means the tilt is in the neutral disturbance itself and is not principally a result of charged particle interaction with the geomagnetic field. Additional work of Munro and Heisler (1956b) shows that such tilted-front TIDs propagate horizontally over large distances, and Munro (1958) has measured the seasonal variation in number and direction of such naturally occurring disturbances.

In the past few years it has been shown that there is quantitative agreement between the observed speed distributions of TIDs and those expected theoretically for ducted gravity waves; also, there is agreement between the theoretical speeds expected for various ducted modes and the observed speeds of disturbances caused by a nuclear detonation at Novaya Zemla (Wickersham 1964, 1965a, 1966). The theoretical speeds used for comparison with observations are the numerical results of Pfeffer and Zarichny (1963) and are based on a realistic atmosphere.

It is our purpose now to further examine the theory of gravity waves in a thermoclinical atmosphere in order to attempt additional comparisons with observations. We shall see, from an approximate form of the equations of motion, that a principal duct exists in the thermosphere where minimal damping occurs because of the large thermal gradient. By analyzing the consequences of a thermal perturbation of the duct in the thermosphere we find that winter sunrise in the polar regions is a possible source of ducted gravity waves consistent with the seasonal changes in direction observed by Munro.

#### DISPERSION EQUATIONS FOR AN ATMOSPHERE WITH A LINEAR THERMOCLINE

For an atmosphere with a linear gradient in scale height,  $H = H_0(1 + \alpha z)$ , the equation satisfied by the hydrodynamical divergence,  $\chi$ , is

$$\chi'' + (H'-1)H^{-1}\chi' + (\omega^2/c^2 - K_x^2 + K_x^2\omega_B^2/\omega^2)\chi = 0 \quad (1)$$

(Lamb, 1945; or more recently, Martyn, *loc.cit*). In this notation  $\omega$  is frequency,  $c$  the local speed of sound,  $K_x$  is the horizontal wave number and may be complex,  $K_x = k_x + i\beta_x$ ,  $K_x^2 \approx k_x^2 + i2k_x\beta_x$ ,  $\omega_B$  is the angular Brunt frequency, and primes denote differentiation with respect to  $z$ , the vertical coordinate. The reciprocal of the Brunt frequency is sometimes called the thermobaric period,

$$\tau_B = 2\pi(H/g)^{1/2}[(\gamma-1)/\gamma + H']^{-1/2} \quad (2)$$

A graph of thermobaric period based on the 1961 CIRA standard atmosphere is shown in Figure 1.

In the present discussion we shall use an approximate form of equation 1 obtained by replacing  $H$  by  $H_0$  in the denominator of the second term. With the understanding that the equation of motion now is approximately valid only in a region  $z_0 \pm \Delta z$ , such that  $\Delta z dH/dz \ll H_0$ , we can seek solutions of the form  $\chi_0 \exp(-iK_z z)$ , where  $K_z$  is complex,  $K_z = k_z + i\beta_z$ . We obtain the dispersion equations

$$\omega^4/c^2 - \omega^2 \left[ k_z^2 - \beta_z^2 \left( \alpha - \frac{1}{H_0} \right) - \beta_z^2 \right] + k_x^2 \omega_B^2 = 0 \quad (3)$$

$$\beta_x = \left[ \tau_B^2 / (\tau^2 - \tau_B^2) \right] \left[ k_z / k_x \right] \left[ \beta_z + \alpha/2 - 1/2H_0 \right] \quad (4)$$

where  $k^2 = k_x^2 + k_z^2$ . Introducing  $\cot\varphi = k_z/k_x$  into the first of the dispersion equations we find a useful expression for the angle  $\varphi$  that a wavefront makes with the horizontal,

$$\cot^2\varphi = \left[ (\tau^2 - \tau_B^2) / \tau_B^2 \right] + \left[ \lambda_x^2 / c^2 \tau^2 \right] \left[ 1 + (\beta_z^2 c^2 \tau^2 / 4\pi^2) \left( \alpha - \frac{1}{H_0} - \beta_z \right) \right] \quad (5)$$

where  $\lambda_x$  is the horizontal wavelength. We also can use equation 3 to compute the direction of energy flow,  $-\partial k_x / \partial k_z$ , and find that it is given by the same angle,  $\varphi$ . In other words, the direction of energy flow is in the plane of the phase front, a result pointed out by

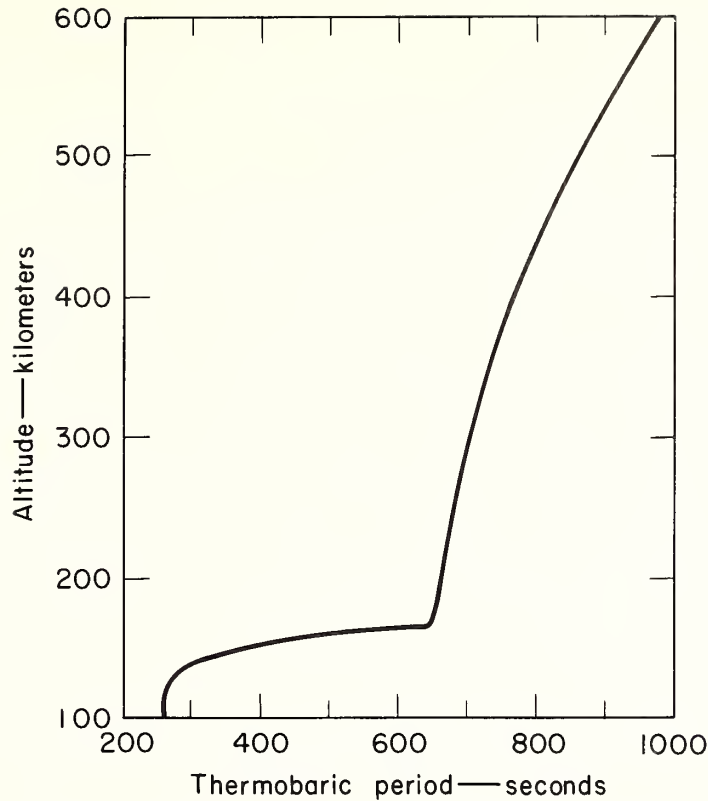


FIG. 1 THERMOBARIC PERIOD FOR A COSPAR MODEL ATMOSPHERE

Hines (loc.cit.) for an isothermal model atmosphere.

We see from equation 4 that if the conditions  $\alpha = 1/H_0$  and  $\beta_z = 0$  prevail, then  $\beta_x$  vanishes and there is no non-viscous damping. From the definition of linear variation of scale height,  $H = H_0(1 + \alpha z)$ , the first condition can be expressed as  $\partial H / \partial z = 1$ . On examining these conditions, we shall find that the first implies the second; further, the first is nearly satisfied in the normal atmosphere at about 150 km altitude.

The energy in a gravity wave is partitioned equally into a kinetic form,  $\frac{1}{2} \rho_0 u^2$ , and a potential form, the latter being further partitioned into elastic energy,  $\frac{1}{2} \rho_0 \xi_e^2 c^2$ , where  $\xi_e$  is the condensation,  $\delta \rho_e / \rho$ , and into thermobaric energy (for example, Eckart, 1960). The thermobaric energy is the product of the average thermobaric force during a quarter-cycle of the motion and the vertical displacement  $W_t = \frac{1}{2} (-\rho \omega_B^2 \delta z) (\delta z)$ , (Eckart, loc.cit.). If we introduce the abbreviation  $\xi_t = -\delta z / H$ , the thermobaric energy can be written as  $\frac{1}{2} \rho_0 \omega_B^2 \xi_t^2$ . With the help of equation 2 and the relation  $c^2 = \gamma g H$ , we obtain

$$W_t = \frac{1}{2} \rho_0 \left( \frac{1}{\gamma} \right) \left( \frac{\gamma - 1}{\gamma} + \frac{\partial H}{\partial z} \right) c^2 \xi_t^2 \quad (6)$$

and the total energy in a gravity wave is

$$E = \frac{1}{2} \rho_0 u^2 + \frac{1}{2} \rho_0 c^2 \xi_e^2 + \frac{1}{2} \rho_0 \left( \frac{1}{\gamma} \right) \left( \frac{\gamma - 1}{\gamma} + \frac{\partial H}{\partial z} \right) c^2 \xi_t^2 \quad (7)$$



Since  $E = \rho_0 u^2$ , we find from equation 7

$$u = c\xi \quad (8)$$

where  $\xi^2 = \gamma^{-1}[(\gamma-1)/\gamma + \partial H/\partial z]\xi_t^2 + \xi_e^2$

The energy carried across a unit area must be conserved; i.e.,  $\rho u_z^2 c$  is constant or, by virtue of equation 8,  $\rho c^2 |u_z| |\xi_z|$  is constant. If now we ask that the product of the kinetic and elastic amplitudes be constant or independent of altitude, then we must have  $(\partial/\partial z)(\rho c^2) = 0$ , or

$$\frac{1}{\rho} \frac{\partial \rho}{\partial z} + \frac{1}{2} \frac{\partial c^2}{\partial z} = 0 \quad (9)$$

From equation 9, the perfect gas law, and the definition of scale height, it follows that  $-1/H + (1/H)(\partial H/\partial z) = 0$ , or  $\partial H/\partial z = 1$ . Thus we see that the motion is undamped when the thermal gradient is large enough to offset the growth in amplitude that results from decrease in ambient density with altitude (equation 9). If amplitude is independent of altitude, then  $\beta_z = 0$  and it follows that  $\beta_x = 0$  and the motion is undamped, neglecting viscosity.

The condition  $\partial H/\partial z = 1$  is almost satisfied ( $\partial H/\partial z \approx 0.7$ ) from about 150 to 160 km altitude in the 1961 CIRA standard atmosphere. This altitude range is the upper boundary of a duct that has a lower boundary at about 100 km (Wickersham, 1965b). Because it is almost free of non-viscous damping, we conclude that this is a major duct for the long distance propagation of gravity waves that perturb the lower ionosphere. This conclusion is supported by the kinetic energy profiles computed numerically by Pfeffer and Zarichny (*loc.cit.*).

#### A SOURCE OF DUCTED GRAVITY WAVES

In Figure 1 we see that in the principal thermospheric duct the thermobaric period varies from 270 sec at the lower boundary near 100 km to 650 sec at the upper boundary near 160 km. In the region of the upper boundary, 150 to 160 km, the period varies from  $\tau_{\min} = 430$  sec to  $\tau_{\max} = 650$  sec and has a mean or central value of about  $\tau_0 = 540$  sec, or 9 minutes. We shall regard this altitude region as an ensemble of thermobaric oscillators having an approximately uniform density in frequencies. Perturbation of this layer of oscillators by any means can be a source of gravity waves, but we shall consider here only thermal perturbations caused by sunlight. Beyond the altitude interval of interest we shall consider the thermobaric period to be constant, as indicated in the idealized distribution shown in Figure 2.

A major thermal perturbation may occur diurnally when dawn, first at 160 km and then down to 150 km, increases the temperature and local scale height, causing an atmospheric heave or vertical displacement. If  $\delta z$  is the vertical displacement within the region, the corresponding thermobaric force is  $-\rho \omega_B^2 \delta z \sim -\rho \omega_B (\partial z/\partial H)(\partial H/\partial t) \delta t$ , which is proportional to the time rate of change in temperature. We shall neglect equilibration time lag and represent this perturbing force in time by a simple square pulse, starting at dawn at 160 km and ending at dawn at 150 km (Figure 3). The width of the pulse varies from about 1.6 minutes in the equatorial regions to 1 hour and 20 minutes for the winter solstice dawn nearest the pole.

The square pulse shown in Figure 3 can be regarded as a superposition of up and down Heaviside step-functions. The second step-function will excite an oscillator with a phase opposite to that of the first; therefore, maximum excitation occurs when the pulse width is equal to half the period of the oscillator. For the central oscillator this would be a pulse width of 4.5 minutes. A time difference of 4.5 minutes corresponds to 1.125 degrees of rotation of the earth. The segment between dawn lines at 160 and 150 km altitude that

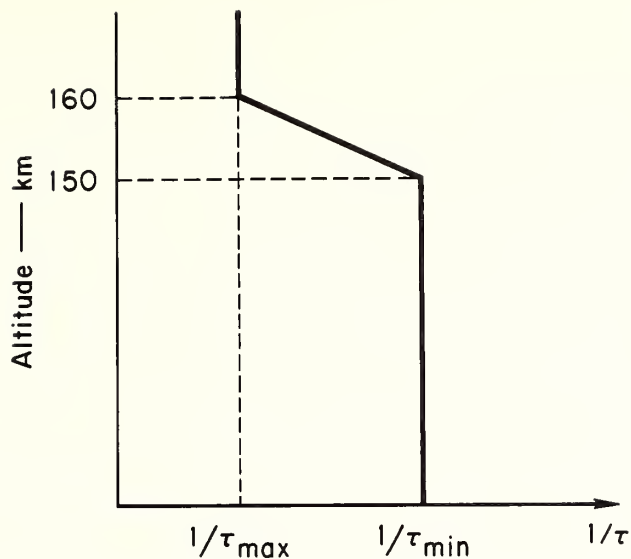


FIG. 2 IDEALIZED DISTRIBUTION OF THERMOBARIC PERIODS ASSUMED FOR ESTIMATING THE RESPONSE OF THE 150-160 km ALTITUDE INTERVAL TO A THERMAL IMPULSE

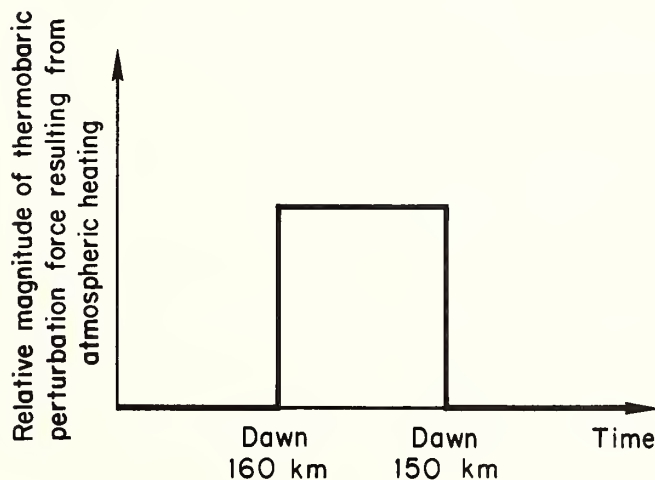


FIG. 3 AN ASSUMED FORM OF THE PERTURBATION CAUSED BY SUNRISE IN THE 150 TO 160 km ALTITUDE REGION

includes 1.125 degrees of polar arc is shown in Figure 4, a projection of the dawn lines onto a plane tangent to the south pole. The segment is about 6 degrees north of the Antarctic Circle. A line drawn from the segment and normal to the dawn line indicates the most probable directions of propagation of disturbances excited in the duct. Extended on a great circle to Sidney, Australia, the line indicates a direction of arrival there of about  $30^\circ$  east of north. The geometry shown in Figure 4 is based on the assumption that dawn at 150-160 km occurs when the sun is no longer shielded by the atmosphere at 40 km altitude. We estimate that

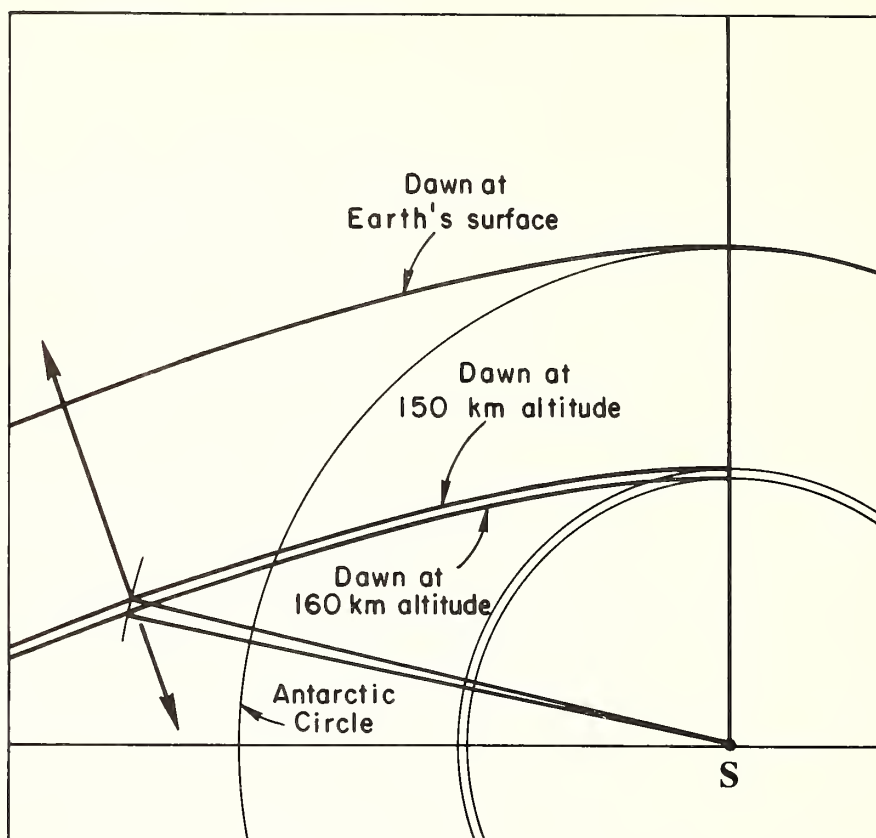


FIG. 4 A PROJECTION OF THE POLAR REGION ONTO A TANGENT PLANE AT THE SOUTH POLE. Three approximately parallel lines indicate dawn at sea level, 150, and 160 km altitude.

most of the solar energy capable of supporting atmospheric photochemical reactions does not penetrate below 40 km; however, changing this estimate by tens of kilometers would change our final result by only a few degrees.

We see that during the Australian winter, when the dawn line near the Antarctic Circle is at its closest approach to Australia, we should expect ducted gravity waves to arrive in Australia from the southeast. Conversely, during the Australian summer, disturbances should arrive from the northwest from the winter dawn line near the Arctic Circle. These indeed are the seasonal characteristics observed by Munro (loc.cit., Figure 11).

To obtain a quantitative prediction of the observed angular spectrum, we note that the amplitude, or response, of a pulse-excited oscillator is proportional to its bandwidth. The bandwidth of the central oscillator is the largest and is approximately  $B_0 \approx \tau_0(\tau_{\max} - \tau_{\min}) / \tau_{\max} \tau_{\min}$ . For an oscillator displaced  $\pm \Delta\tau$  seconds in period from the central period, the relative bandwidth is approximately  $B \approx B_0 - 2\Delta\tau / \tau_0$ , from which we have

$$\Delta B \approx 2\Delta\tau / \tau_0 \quad (10)$$

At points along the dawn line to the left or right of the 4.5 minute dawn interval, there are dawn intervals inferior or superior to 4.5 minutes. These pulses will excite oscillators

that have bandwidths less than that of the central oscillator; thus, their response will be less than that of the central oscillator. According to equation 10, the response decreases linearly as the time interval becomes inferior or superior to  $\tau_0$ .

We assume that excitation of the ensemble of thermobaric oscillators is a source of gravity waves that propagate down into the duct below and that some of the waves are subsequently trapped in the duct. If we further assume that probability of this occurrence is proportional to thermobaric oscillator response, we can associate a relative probability with each directional normal on the dawn line and obtain the relative angular spectrum shown in Figure 5. In the same figure we show a histogram of Munro's five-year average of observations in the month of June. The two spectrums are in agreement. A mirror image of Figure 4 serves for the northern hemisphere and can be used to predict the spectrum observed during the Australian summer; however, the source in this case is now more than twice as far removed from Australia and, as might be expected, the observed spectrum has somewhat more angular spread than predicted. During the equinoxes both spectrums appear to be observed.

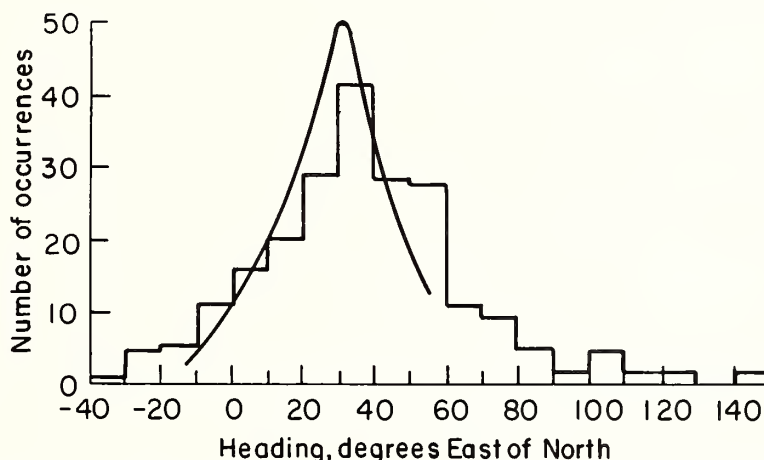


FIG. 5 A COMPARISON OF THE ANGULAR SPECTRUM OF TIDs OBSERVED BY MUNRO WITH A SPECTRUM DERIVED HEURISTICALLY BY POSTULATING A THERMAL SOURCE OF GRAVITY WAVES IN THE ANTARCTIC REGION

#### THE TILT AND PERIOD OF TIDs

The morphology of TIDs as deduced from ionosonde data by Munro and Heisler appears to be confirmed by the incoherent scattering measurements recently presented by Thome (1964). The electron density perturbation caused by a disturbance as measured by Thome is reproduced here in Figure 6. Unfortunately, Thome did not report the speed of the disturbance but gave only a range of 50 to 100 m/s as typical of most disturbances. If we assume a horizontal speed of 57 m/s we obtain the iso-density contours in spatial coordinates, as shown in Figure 7. We shall consider this to be a representative TID since the 45 degree slope near the center is almost as large as the mean values of 51 to 65 degrees observed by Munro and Heisler.

From equation 5 we see, since the last term in the equation is small, that when the wave front is vertical the period of the disturbance must be  $\tau \approx \tau_B$ . From either Figure 6 or 7 we see that the leading edge of the disturbance is vertical just above 300 km altitude, and thus from Figure 1 we conclude that the period of the disturbance is about 705 sec or 11.7 min. This conclusion is independent of the speed assumed for the disturbance.

At the center of the disturbance, near 225 km, the slope of an 11.7 min gravity wave should be, by equation 5, about  $75^\circ$ . This is somewhat greater than the average upper limit of  $65^\circ$  measured by Munro and Heisler and considerably greater than the slope of the TID shown in Figure 7. The slope near the center of the TID shown in Figure 7 is, of course, dependent on the speed assumed

for the disturbance. We can obtain agreement with Munro and Heisler's value of  $65^\circ$  if we assume  $\beta_z$  small and  $\lambda_x = 200$  km. To obtain agreement with the center slope of the TID in Figure 3 we should have to assume  $\lambda_x \geq 445$  km. So large a value of horizontal wavelength would be difficult to reconcile with our first determination of an 11.7 min period and the theoretical and observed propagation speeds of TIDs. The difficulty increases at still lower altitudes. Even with a horizontal wavelength as large as 445 km we cannot reconcile theory and observation at 160 km altitude. From equation 5 we should predict a slope of  $38^\circ$  where the observed slope is zero. It is possible that the observed slope is zero at 160 km because the disturbance does not extend to lower altitudes. But if this were so, then the disturbance would consist of an oblique rising of energy from no apparent source at 160 km altitude to an ultimate dissipation at 300 km altitude, an interpretation difficult to reconcile with long-range horizontal propagation. We find a more satisfactory model by assuming that the neutral disturbance extends to lower levels and that the disagreements between theoretical and observed slopes at the lower edges derive from the effects of ionospheric chemistry.

It is possible that the trailing edge of the disturbance is more a measure of ionospheric chemical equilibration time rather than the duration or width of the neutral wave. We note that above 180 km altitude the ionospheric electron reservoir is controlled by the charge-exchange reaction  $O^+ + N_2 \rightarrow NO^+ + N$ . Using the atmospheric model and reaction-rate compilation of Ferguson et. al. (1965), and assuming a linear, positive temperature dependence for the reaction rate, we find that the effective time constant for the above reaction is about 500 sec at 270 km altitude. This is also the time interval between the 6 percent or half amplitude levels at 270 km altitude for the TID shown in Figures 6 and 7. Just below

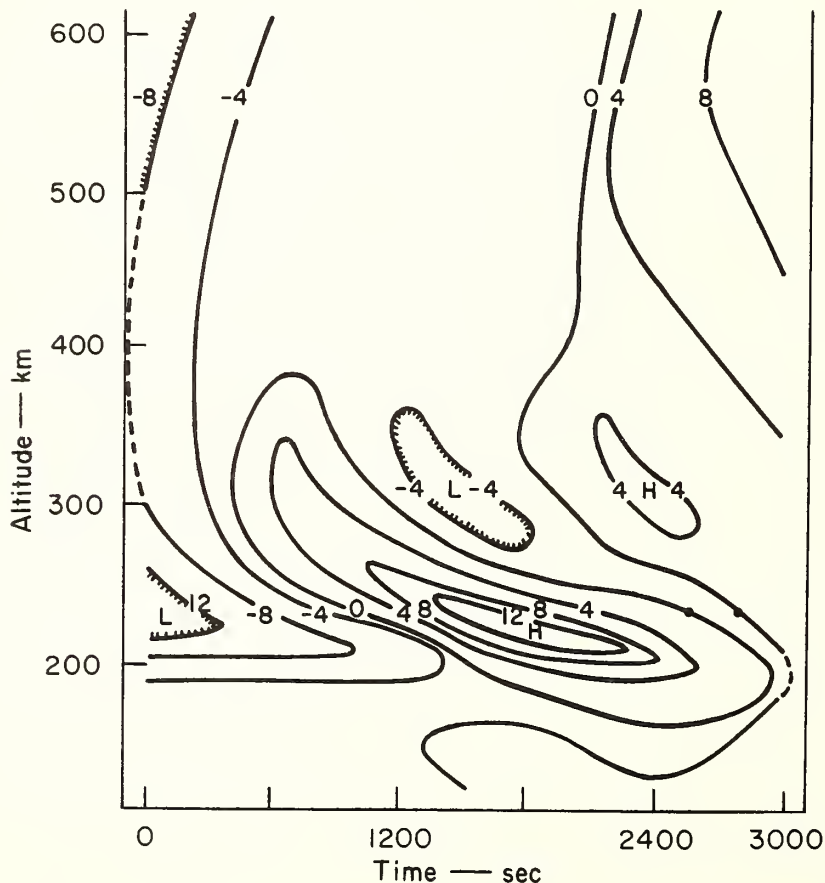


FIG. 6 CHARGE DENSITY CONTOURS ASSOCIATED WITH A TID DETECTED BY THE INCOHERENT SCATTERING TECHNIQUE, FROM THOME



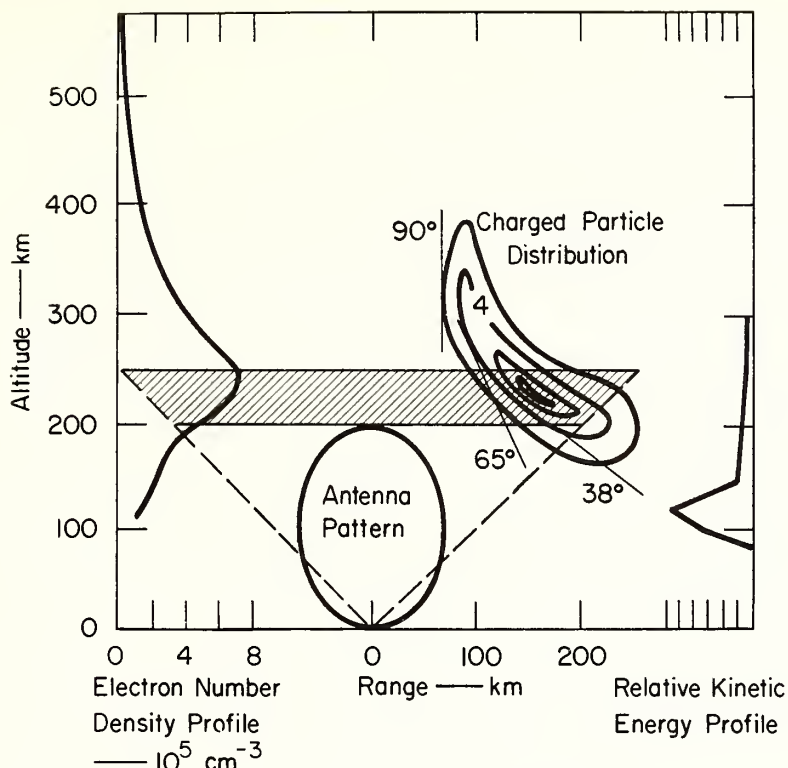


FIG. 7 CHARGE DENSITY CONTOURS, ASSOCIATED WITH THE TID OBSERVED BY THOME, TRANSFORMED TO SPATIAL COORDINATES BY ASSUMING A HORIZONTAL PROPAGATION SPEED OF 57 m/s. Ambient electron density, from Thome, is shown at left; an energy density profile for a ducted gravity wave, from Pfeffer and Zarichny, is shown at right. At bottom left there is an assumed cosine squared antenna radiation pattern.

170 km altitude the reaction  $\text{NO}^+ + e^- \rightarrow \text{N} + \text{O}$  controls the electron reservoir; however, at this altitude both reactions have effective time constants less than 20 sec. Because of the rapid equilibration, the charge density no longer reflects the neutral particle perturbation and the TID is almost unobservable by radio means. This expectation appears to be confirmed by the data shown in Figure 6 as well as by other data shown by Thome. If chemical equilibration time determines the duration of the charge perturbation caused by a TID then the slope of the electron density perturbation will be less than that of the neutral density perturbation, especially at the lower altitudes, and at 170 km the almost zero slope may be a result of fast equilibration.

From the above brief consideration we see a difficulty in determining period from slope; a difficulty, however, that may ultimately prove useful in studying ionospheric chemistry. We also shall see that it is difficult to determine period on the basis of the time during which the charge perturbation interacts with radio equipment.

On the right-hand side of Figure 7 we show the relative kinetic energy profile for a 13-minute period, fully ducted, third order gravity mode computed by Pfeffer and Zarichny. This profile is typical of many of the gravity modes in that some energy appears in the F-region but the centroid is between 100 and 165 km altitude. On the left-hand side of the figure we show the ambient electron density measured by Thome at about the time of the TID. We see that the charge density perturbation can be expected to be considerably higher than the maximum disturbance in the neutral particles; thus, it is possible that an observed F-region charge perturbation is only the wake of a stronger disturbance in a lower region.

In Figure 7 we also show a cosine squared radiation pattern which is typical of many sweep-frequency ionosondes. The half-power points of such radiation pattern are at 45 degrees, and these are shown as broken lines in the figure. With such sounders one can detect disturbances up to the maximum in the electron density profile, about 250 km altitude. The sensitivity of most vertical incidence sounders is greatest in the shaded region shown in the figure. The average charged particle perturbations caused by TIDs, as measured by Munro and Heisler, is 20 percent of equilibrium, with maximum perturbations as large as 30 percent. A TID that causes a 20 percent charge perturbation possibly could affect the edge of the antenna radiation pattern and continue to do so as it moves through the shaded region. A disturbance similar to that shown in Figure 7, moving at a speed of 57 m/s, would interact with the sounder for 130 minutes. It is possible that the first half of such interaction could be observed and a "period" ascribed to the disturbance of about 65 minutes. Some observers, however, would take the time interval between this disturbance and the next one to be the period. We see that interaction times might be longer than the periods we have discussed earlier and should not necessarily be taken as a measure of the period of a TID.

#### A LEAKY-DUCT MODEL OF TIDS

We now have a large number of theoretical and experimental restrictions and can attempt to construct a gravity-wave model of TIDs. A model should be consistent with all of the following information.

1. TIDs have fronts inclined in the direction of travel.
2. The slopes of TIDs are nearly independent of the direction of the geomagnetic field.
3. TIDs propagate large distances with little attenuation.
4. The speed distributions of TIDs agree with those predicted theoretically for ducted acoustic-gravity waves.
5. The effective time constant of the reaction  $O^+ + N_2 \rightarrow NO^+ + N$  corresponds to the observed half-width of a TID observed by Thome.
6. Most of the centroids of the energy profiles of ionospheric, long-period, ducted gravity waves, as computed numerically by Pfeffer and Zarichny, lie in the strong thermoclinical channel between 100 and 165 km altitude.
7. Fast chemical equilibration in the 100 to 165 km altitude region would prevent observation of long-period neutral particle disturbances by means of radio detection of charged-particle perturbations.
8. Fast equilibration in the lower ionosphere appears to be consistent with the fact that observed slopes of TIDs are less than can be predicted by gravity-wave theory.

To obtain a model consistent with the above information we turn to a leaky-duct model somewhat similar to one suggested originally by Hines (loc. cit.). We assume a model in which a wave packet, or pulse, of gravity waves is ducted in the thermoclinical channel between 100 and 165 km altitude. The longer-period components of the wave packet leak through the upper boundary of the channel--the knee in the thermobaric period profile of Figure 1--to provide detectable perturbations of the upper ionospheric charge density.

This model is analogous to the bow wave caused by a ship. To an observer in a nearby rowboat, the bow wave appears to move normal to its wavefront. To an observer in an airplane, the wake of the bow wave has an apparent velocity equal to and in the direction of that of the ship. Thus the horizontal speed of an unseen disturbance, ducted in the channel at 100 to 165 km altitude, can be determined from measurements of the wake detectable in the upper ionosphere; however, the wake itself has neither the morphology nor direction of motion of a ducted disturbance. A principal difference between model and analogy is the forward slope of the energy leaking through the top of the duct, as contrasted with the backward slope of a ship's bow wave. This effect is peculiar to gravity waves. Energy propagates upward in the plane of the downward sloping wavefront.

# REFERENCES

- Eckart, C., Hydrodynamics of oceans and atmospheres, Pergamon Press, 1960.
- Ferguson, E. E., F. C. Fehsenfeld, P. D. Goldan, and A. L. Schmeltekopf, Positive ion-neutral reactions in the ionosphere, J. Geophys. Res. 70, (17), 4323, 1965.
- Hines, C. O., Internal atmospheric gravity waves at ionospheric heights, Can. J. Phys. 38, 1441, 1960.
- Lamb, H., Hydrodynamics, Sec. 312, Dover Publications, New York, 1945.
- Martyn, D. F., Cellular atmospheric waves in the ionosphere and troposphere, Proc. Roy. Soc. 201, 216, 1950.
- Munro, G. H., Travelling ionospheric disturbances in the F-region, Aust. J. Phys., 11, 91, 1958.
- Munro, G. H. and L. H. Heisler, Divergence of radio waves in the ionosphere, Aust. J. Phys. 9, 359, 1956a.
- Munro, G. H., and L. H. Heisler, Cusp type anomalies in variable frequency ionospheric records, Aust. J. Phys. 9, (3), 343, 1956.
- Pfeffer, R. L., and J. Zarichny, Acoustic-gravity wave propagation in an atmosphere with two sound channels, Geofisica Pura E Applicata - Milano 55, 175, 1963.
- Thome, G. D., Incoherent scatter observations of travelling ionospheric disturbances, J. Geophys. Res. 69 (19), 4047, 1964.
- Wickersham, A. F. Jr., Identification of ionospheric motions detected by the high-frequency backscattering technique, J. Geophys. Res. 69, (3), 457, 1964.
- Wickersham, A. F. Jr., Comparison of velocity distributions for acoustic-gravity waves and traveling ionospheric disturbances, J. Geophys. Res. 70 (19) 4875, 1965a.
- Wickersham, A. F. Jr., A ducted gravity wave interpretation of traveling ionospheric disturbances detected by a narrow beam, slewable, backscattering radar, J. Geophys. Res. 70 (7) 1729, 1965b.
- Wickersham, A. F. Jr., Identification of acoustic-gravity wave modes from ionospheric range-time observations, J. Geophys. Res. 71, (19), 4551, 1966.



## SCATTER PROPAGATION OF INFRASOUND

William C. Meecham

University of California, Los Angeles

One of the outstanding characteristics of acoustic signals received from distant nuclear explosions is this: sound energy arrives over an observation time of up to an hour. The extended signal often contains a very great number of (apparent) pulses, 10 to 20 seconds duration. Ordinary dispersion cannot account fully for the multi-pulse appearance. This paper enlarges on a suggestion that the shorter period effects may be partly due to "scatter propagation" involving the upper and lower sound channels. The multi-pulse, 20-second period behavior may be a diffraction effect involving scattering by wind ducts. It has been shown that the very commonly occurring wind ducts, with wind speeds of 10 fps and several thousand feet thickness, can "split" the pulse hundreds of times by diffracting the pulse. Such splitting into a transmitted and a reflected portion occurs for component time-periods less than 20 seconds.

### INTRODUCTION

This report is concerned with the propagation of shorter period infrasonic waves (periods between 1 second and 1 minute) generated by nuclear explosions. Periods longer than this have been extensively investigated by a number of authors [Weston (1961), Pfeffer and Zarichny (1963), Pierce (1963), Harkrider (1964), Meecham (1965)]. For such longer-period waves a normal mode description of the propagation process is most convenient.

We shall be here concerned primarily with the acoustic portion of the signal as suggested. It will be convenient to describe briefly the time characteristic of overpressures at short ranges produced by explosions. Glasstone (1962) has given the expression

$$p(t) = p_0 \left(1 - \frac{t}{t_+}\right) e^{-t/t_+} \quad (1)$$

where  $t_+ = y^{1/3} t_1$ ,  $t_1$  is approximately equal to 1 second and  $Y$  is the yield in kilotons. The overpressure  $p_0$  is also proportional to  $y^{1/3}$  and becomes equal to about 1/10 of atmospheric pressure at sea level at a range of approximately 1 kilometer for a burst yield of 1 kiloton. That is, the overpressure becomes a linearized phenomenon at a range of about 1 kilometer for a burst of approximately 1 kiloton.

One of the outstanding characteristics observed for signals from such explosion is that at ranges of 5,000 kilometers and more, the shorter-period portions of the signals appear to be composed of hundreds of pulses of width about 20 seconds. These pulses appear to be replicas of the shorter-period portions of the initiating signal. The pulses themselves spread out over a time interval of an hour or more. We have previously suggested [Meecham (1968)] that these characteristics of the shorter-period portions of the signal may be caused by diffraction effects produced primarily by wind ducts in the upper atmosphere. (Temperature ducts also contribute diffraction effects but to a lesser extent.) It is our purpose here to further develop these diffraction characteristics. We put particular emphasis upon the more important diffraction effects produced by thicker wind ducts, as revealed by recent work.

### EFFECT OF WIND DUCTS ON INFRASONIC PROPAGATION

In order to examine the effect of wind ducts on infrasound let us begin by considering the following reflection problems. (See Figure 1) A sound wave of unit pressure amplitude change is incident upon a wind duct of thickness  $L$  and wind speed  $\Delta C$ . It is noted from the outset that in general the effect of the wind duct is different for waves proceeding toward the right and waves proceeding toward the left. However, for small effects it will be seen that this particular



difference is not important. Referring to Figure 1, consider a plane wave incident making an angle  $\theta_0$  with the horizontal where the plane wave originates in the region 1 as shown. It will be assumed that the fluid density is constant in this problem and that the incident wave has an angular frequency  $\omega$ . The transmission coefficient into the region 3 is given by

$$A_3 = 2 \left\{ 2 \cos(k_2 L \sin \theta_2) + i \left[ r_{12} + r_{12}^{-1} \right] \sin k_2 L \sin \theta_2 \right\}^{-1} \quad (2)$$

with

$$\begin{aligned} r_{12} &= k_0 \sin \theta_0 / (k_2 \sin \theta_2), \\ k_2 &= \omega / (C_0 + \Delta C), \quad k_0 = \omega / C_0 \end{aligned} \quad (3)$$

and

$$\cos \theta_2 / \cos \theta_0 = k_0 / k_2 \quad (4)$$

Here we can restrict to small effects:  $\theta_0$ ,  $\Delta C / C_0$ ,  $k_0 L \ll 1$ . There is a critical angle for the problem shown in Figure 1. Waves arriving with incident angles less than the critical angle are totally reflected if  $L$  is very large. The critical angle for small angles, is

$$\theta_C \approx (2\Delta C / C_0)^{1/2} \quad (5)$$

For  $\theta_0$  of order the critical angle,  $\theta_C$ , the fraction of incident energy which is reflected is given by

$$\text{Fraction} \sim (2\Delta C / C_0)^2 (k_0 L)^2 \quad (6)$$

provided that all quantities are small as indicated above. Consider a typical case for the reflection infrasound from a wind duct.

$$\text{Frequency} = 0.10 \text{ sec}^{-1}$$

$$C_0 = 300 \text{ m/sec}$$

$$L = 3 \text{ km}$$

$$\Delta C = 5 \text{ m/sec}$$

In this case the formula 9 yields a reflection coefficient of about 4%. The critical angle  $\theta_C$  is approximately 2/10 of a radian, that is, about 10%.

#### COMPARISON WITH EXPERIMENTS

We continue by describing the characteristics of wind ducts as they have been determined by a number of investigators during the past decade. For the reviews of this work, see Webb (1962) and Diamond (1963). These characteristics as related to infrasound have been discussed in an earlier paper, see Meecham (1968). We shall enlarge upon that discussion, emphasizing in particular the weak-wind-duct effects. Wind duct characteristics are reviewed in Figures 2 to 4. Information presented there is taken mainly from Webb (1962). In Figure 2 is shown a plot of the frequency of occurrence of wind subducts of various intensities. We know that in the atmosphere there also exist temperature ducts. These are primarily of weaker intensity than are wind ducts. Their frequency of occurrence is also shown in Figure 2 for comparison. In the remainder of the discussion of this paper we ignore the effects of these weaker ducts upon sound propagation. We see in Figure 2 that the most frequently occurring wind duct has an intensity of 0 to 10 ft. per second. Furthermore, we see that ducts of intensity of 10 to 20 ft. per second are common; they account for about 20% of the observed ducts. Ducts of still stronger intensity occur less commonly. In Figure 3 is shown the relative probability of occurrence of ducts of various thicknesses. It is seen that 80% of all observed ducts have thicknesses less than 10,000 ft., that about 15% have thicknesses of 10,000 - 20,000 ft., etc. In Figure 4 is shown the frequency of occurrence of subducts as a function

of altitude. The two curves show respectively the frequency for ducts less than 10,000 ft. thick and for ducts with thicknesses between 10,000 and 20,000 ft. More data are needed but it would appear from these data that the thinner ducts occur most probably at altitudes something like 70,000 to 90,000 ft. and that the thicker ducts occur most probably at altitudes between 90,000 and 100,000 ft. and that each of them has a peak probability of about 2/10 and that furthermore, they occur with probability 1/10 over large altitude ranges. In particular, the thicker ducts occur with this probability (in a 10,000 ft. interval) for most altitudes up to about 130,000 ft.

From the old (6) we see that the thicker ducts are more effective in diffracting the sound than are thinner ducts, the effect increasing like the square of the thickness of the wind duct. Thus, we shall focus attention on wind ducts between 10,000 and 20,000 ft. thick. From Figure 4 we see that in the range from 60,000 to 130,000 ft. we can expect to meet a duct with thickness between 10,000 and 20,000 ft. with probability about  $0.7 \left( = .1 \times \frac{130-60}{10} \right)$ . For the present purpose we suppose that this probability is unity: that is, that a ray traversing into the upper atmosphere will meet a duct of thickness 10,000 to 20,000 ft. with probability 1. Then the amount of energy lost from a ray due to diffraction in going from ground level into the upper atmosphere is given by (6).

The same amount of energy is lost as the ray returns from the upper sound channel back to earth again, see Figure 5. Let us let  $L_u$  represent the skip distance associated with the upper sound channel. Then the fractional reduction in sound intensity with range,  $r$ , is given by

$$\exp - \left( \frac{2\Delta C}{C_o} \right)^2 (k_o L)^2 \frac{2r}{L_u} \quad (7)$$

There will be a range at which the main signal is reduced in intensity sufficiently so that it is lost in the multiplicity of diffracted signals that are produced. Each time the ray traverses the atmosphere a new diffractive signal is generated of relative intensity given by Equation 6. The range at which the main signal is lost in its reverberation background is given approximately by

$$\exp - 2 \frac{2r}{L_u} \left( \frac{2\Delta C}{C_o} \right)^2 (k_o L)^2 = \left( \frac{2\Delta C}{C_o} \right)^2 (k_o L)^2 \quad (8)$$

This range at which the main signal is lost in the diffraction reverberation, for the example considered in the previous section turns out to be approximately

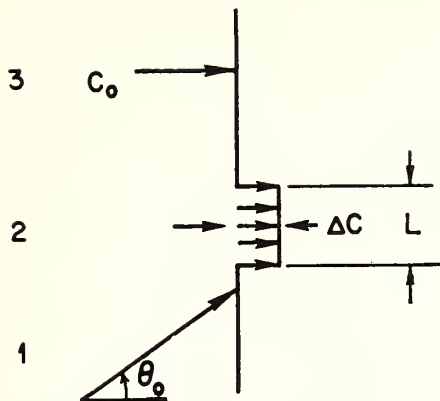
$$\frac{r}{L_u} \cong 50 \quad (9)$$

Where  $L_u$ , the skip distance in the upper duct is approximately 300 kilometers. Equation 9 gives a result a little too large [see Hunt et al. (1960)]. However considering the many uncertainties, this mechanism is believable as the cause of the signal degeneration.

We expect then that when the range is greater than this range just discussed, the signal will be composed of a multiplicity of pulses generated by a diffraction phenomenon caused by the frequently occurring wind ducts. These pulses will arrive at different times depending on the path taken. For ranges less than this range, there should remain one (or a few) main components to the signal partially masked perhaps by the diffraction-generated pulses of the type described. Of course, for very close ranges, the diffraction effects will be quite small and the central pulse will dominate. All of this discussion is meant to apply, of course, to the shorter period components of the infrasound; that is, periods up to perhaps one minute. The longer period components, as already suggested, have been described in numerous references dealing with the normal mode behavior of the acoustic-gravity waves generated by explosions.

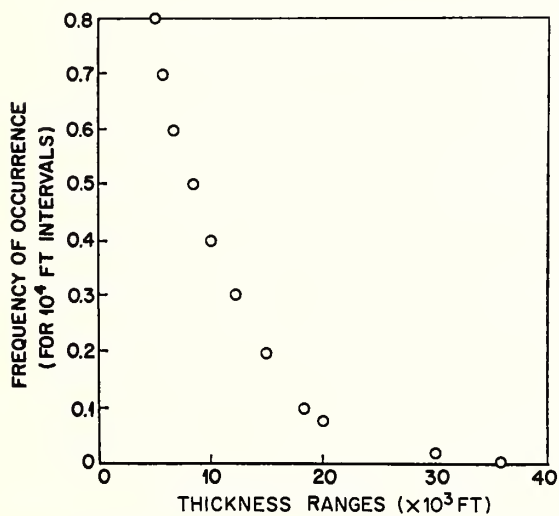
#### REFERENCES

- Diamond, M., Sound Channels in the Atmosphere, J. Geophys. Res., 68, 3459, 1963.
- Glasstone, S., Editor, The Effect of Nuclear Weapons, U.S. Government Printing Office, April 1962.
- Harkrider, D.G., Theoretical and Observed Acoustic-Gravity Waves from Explosive Sources in the Atmosphere, J. Geophys. Res., 69, 5295, 1964.
- Hunt, J.N., R. Palmer, and W. Penney, Atmospheric Waves Caused by Large Explosions, Phil. Trans. Roy. Soc. (London), A252, 275.
- Meecham, W.C., Simplified Normal Mode Treatment of Long-Period Acoustic-Gravity Waves in the Atmosphere, Proc. IEEE, special issue on Nuclear Test Detection, 2079, December 1965.
- Meecham, W.C., Effect of Atmospheric Wind Structure on Shorter-Period, Nuclear-Generated Infrasound, J. Geophys. Res., 73, 377, 1968.
- Pfeffer, R.L., and J. Zarichny, Acoustic-Gravity Wave Propagation in an Atmosphere with Two Sound Channels, Geofis. Pura Appl., 55, 175, 1963.
- Pierce, A.D., Propagation of Acoustic-Gravity Waves from a Small Source Above the Ground in an Isothermal Atmosphere, The RAND Corporation, RM-3596, May 1963.
- Webb, W.L., Detailed Acoustic Structure Above the Tropopause, J. Appl. Meteorol., 1, 229, 1962.
- Weston, V.H., The Pressure Pulse Produced by a Large Explosion in the Atmosphere, Can. J. Phys., 39, 993, 1961.



WIND-DUCT DIFFRACTION PROBLEM

FIGURE 1



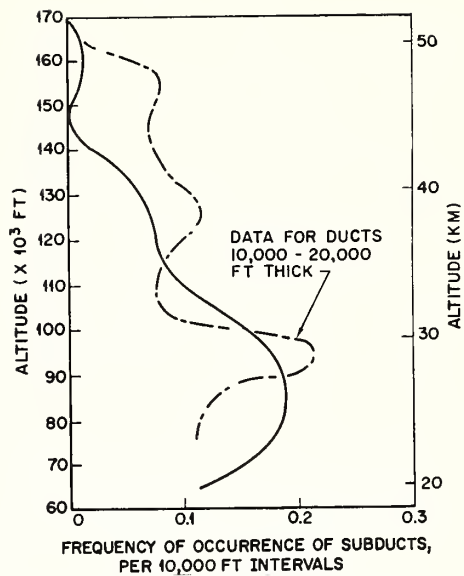
PROBABILITY THAT OBSERVED SUBDUCTS WILL HAVE VARIOUS THICKNESSES

FIGURE 3



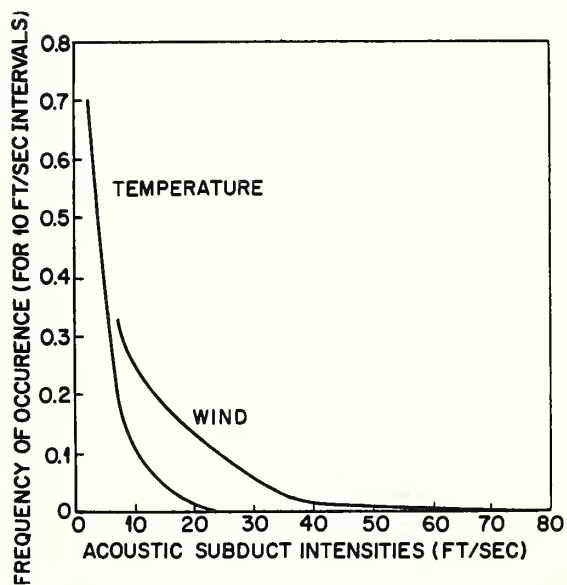
TEMPERATURE PLOT WITH ALTITUDE SHOWING A TYPICAL RAY DIAGRAM

FIGURE 5



FREQUENCY OF OCCURRENCE OF SUBDUCTS OF VARIOUS INTENSITIES

FIGURE 2



FREQUENCY OF OCCURRENCE OF SUBDUCTS WITH HEIGHT

FIGURE 4





## HIGHER ORDER APPROXIMATIONS IN THE THEORY OF ACOUSTIC-GRAVITY WAVES

F. Einaudi

Department of Physics, University of Toronto  
Toronto, Ontario, Canada

A singular perturbation technique of acoustic-gravity waves has been carried out, in which not only the dependent but also the independent variables are expanded in power series of  $\epsilon$ . The series expansion of the independent variables gives us additional freedom which can be used to correct the family of characteristic lines of the equations. The crossing of adjacent characteristic lines is determined and the formation of shocks in the flow is discussed.

### INTRODUCTION

The study of nonlinear effects in several problems of hydrodynamics by a regular perturbation expansion in terms of a small parameter  $\epsilon$  gives at times unsatisfactory results. In such a perturbation expansion for the velocity or density of a propagating plane sound wave, successive terms of the series contain contributions which vary as successively higher powers of the distance variable  $x$ ; in the case of internal acoustic-gravity waves, successive terms contain contributions which vary as successively higher powers of an exponential growth factor, so that in either situation the solutions break down at large distances in the sense that higher order terms become larger than lower ones. In principle one may continue adding new terms, but in practice the determination of higher order terms is lengthy and one wishes to calculate only the first approximation and sometimes the second. In addition, a regular perturbation expansion does not provide satisfactory information concerning the range of validity of the solution itself and the position of a possible shock in the flow.

As an alternative, we use a singular perturbation technique by which not only the dependent but also the independent variables are expanded in series of  $\epsilon$ . The method stems first from the recognition that the system of equations governing the propagation of acoustic-gravity waves is hyperbolic and that in the  $(x, t)$  plane there are special lines, "characteristic directions," which play an important role. [See Courant and Friedrichs, 1948]. Then the fundamental hypothesis is made that linearized theory gives a valid first approximation to the flow everywhere provided that the approximate characteristics in it are replaced by the exact ones, or at least by a sufficiently good approximation of the exact ones. This hypothesis introduced by Whitham [1952] is an extension of Lighthill's idea [1949] that the linearized solution may have the right form, but not quite at the right place. As an example, consider the propagation of an initial wave form  $u = F(x)$  in linear wave motion:

$$u = F(x - c_0 t) ,$$

where  $c_0$ , constant, is the speed of sound. The above equation says that  $u$  is constant along the family of straight lines  $s = x - c_0 t = \text{constant}$ , which are the zero order approximations to one set of characteristic lines of the governing system of equations. In the linear approximation the wave form travels unchanged, whereas in fact it becomes distorted. This is because the velocity  $u$  changes along the line  $s = \text{constant}$  whereas it remains unchanged on some other line which is slightly inclined relative to  $s = \text{constant}$ . This new line is a characteristic one: it may deviate far from the initial line  $s = \text{constant}$  as the wave propagates far from its source.

The method we shall follow will indeed allow a very simple determination of such a new line, by introducing two new independent variables with respect to which the equation of the characteristics has a very simple form. The series expansion of the independent variables gives us additional freedom which we use to correct the family of characteristic lines at each stage of the expansion, i. e. for each successive approximation. By correcting them at each stage of the expansion, one can determine the crossing of adjacent characteristic lines, and thus the

position of a shock, if such a crossing occurs for the chosen boundary conditions. As a boundary condition we impose that at  $x = 0$ ,  $u = u_0 \sin \omega t$ ; since the same condition is satisfied by the usual linear solution we can expect that the two solutions will not be much different close to the section of excitation. The distance at which a crossing first forms can be taken as an upper limit of the distance over which the linear solution applies.

We shall consider only the case of vertical propagation, but the same reasoning can be applied to the three dimensional case.

### SINGULAR PERTURBATION ANALYSIS

Consider the one-dimensional problem of wave propagation in the vertical direction: the governing equations of hydrodynamics are

$$\rho_t + u\rho_x + \rho u_x = 0, \quad \text{conservation of mass} \quad (1a)$$

$$\rho(u_t + uu_x) + p_x + \rho g = 0, \quad \text{conservation of momentum} \quad (1b)$$

$$\rho(p_t + u p_x) = \gamma p(\rho_t + u \rho_x), \quad \text{adiabatic equation of state} \quad (1c)$$

Writing the velocity, pressure and density as series expansions of the form

$$u = \sum_{n=1}^{\infty} u^{(n)}, \quad p = p_0 + \sum_{n=1}^{\infty} p^{(n)}, \quad \rho = \rho_0 + \sum_{n=1}^{\infty} \rho^{(n)}, \quad (2)$$

where  $u^{(n)}$ ,  $p^{(n)}$ , and  $\rho^{(n)}$  are found to be of  $O(\epsilon^n)$ ,  $\epsilon$  being an expansion parameter as yet undefined, substituting (2) into (1) and collecting terms of the same order yields a sequence of linear systems from which quantities of any desired order may be established. Terms of order  $\epsilon$  correspond to the usual linear solution for gravity waves [Hines, 1960]

$$u^{(1)} = u_0 e^{x/2H} \sin(\omega t - kx), \quad p^{(1)} = p_g u_0 e^{-x/2H} [P_1 \sin(\omega t - kx) + P_2 \cos(\omega t - kx)]$$

$$\rho^{(1)} = \rho_g u_0 [(R_1 \sin(\omega t - kx) + R_2 \cos(\omega t - kx)] e^{-x/2H}, \quad (3a)$$

where

$$P_1 = \gamma k/\omega, \quad P_2 = \gamma g(\gamma/2 - 1)/\omega c_0^2, \quad R_1 = k/\omega, \quad R_2 = -1/2H\omega, \quad 1/H = \gamma g/c_0^2, \quad c_0^2 = \gamma p_0/\rho_0. \quad (3b)$$

$\rho_g$  and  $p_g$  being the values of the background density  $\rho_0$  and pressure  $p_0$  at an arbitrary origin  $x = 0$ , and  $H$  being the usual scale height for an atmosphere taken to be isothermal. The wave number  $k$  and the frequency  $\omega/2\pi$  satisfy the dispersion equation

$$\omega^2 = k^2 c_0^2 + \gamma g/4H. \quad (4)$$

For the three equations (1) governing the flow there are three characteristic directions:

$$C_+: dx/dt = u + c, \quad C_-: dx/dt = u - c, \quad C_0: dx/dt = u, \quad (5)$$

where  $c$ , the local speed of sound can be written as

$$c = (\gamma p / \rho)^{\frac{1}{2}} = c_0 + \sum_{n=1}^{\infty} c^{(n)} \quad (6)$$

Since we are only concerned with wave propagating in the positive  $x$  direction (i. e. , vertically upwards), we consider only the family of curves  $C_+$ .

If

$$\bar{\Phi}(t, x, s) = 0, \quad s = \text{constant} \quad (7)$$

is the equation of the family of characteristics  $C_+$ , then  $\bar{\Phi}$  must satisfy the equation

$$\bar{\Phi}_t + \bar{\Phi}_x (u + c) = 0 \quad (8)$$

In the zero order approximation, (8) becomes

$$\bar{\Phi}_t + c_0 \bar{\Phi}_x = 0,$$

which has solution

$$\bar{\Phi}(t, x, s) = c_0 t - x - s \quad (9)$$

Including terms of  $O(\epsilon)$ , (8) becomes

$$\bar{\Phi}_t + (c_0 + c^{(1)} + u^{(1)}) \bar{\Phi}_x = 0,$$

and its solution can be written in the form

$$\bar{\Phi}(t, x, s) = c_0 t - x - s - S^{(1)}(x, s) \quad (10)$$

$S^{(1)}$  satisfying the relation

$$S_x^{(1)} = -(u^{(1)} + c^{(1)})/c_0 \quad (11)$$

We now make the hypothesis that the linear solutions (3) are a valid first approximation everywhere in the flow provided that the zero order characteristics are replaced by the first order ones. Thus, for example,  $u^{(1)}$ ,  $p^{(1)}$ , and  $\rho^{(1)}$ , rather than being time independent along the family of curves  $c_0 t - x - s = \text{constant}$ , are taken to be time independent along the family of curves  $c_0 t - x - s - S^{(1)} = 0$ ,  $s = \text{constant}$ .

Analytically this can be obtained by the following change of variables

$$x = \tau, \quad c_0 t - x = s + \sum_{n=1}^{\infty} S^{(n)}(\tau, s) \quad (12)$$

The quantity  $s$  which so far has played the role of a parameter, becomes the new independent variable. In the new coordinates the velocity, the density and the pressure have the same form as before

$$u^{(1)} = u_0 e^{\tau/2H} \sin \omega/c_0 [s + (1-n)\tau],$$

$$p^{(1)} = u_0 p_g e^{-\tau/2H} \left\{ P_1 \sin \omega/c_0 [s + (1-n)\tau] + P_2 \cos \omega/c_0 [s + (1-n)\tau] \right\} \quad (13)$$

$$\rho^{(1)} = u_0 \rho_g e^{-\tau/2H} \left\{ R_1 \sin \omega/c_0 [s + (1-n)\tau] + R_2 \cos \omega/c_0 [s + (1-n)\tau] \right\}$$

where

$$n = kc_0/\omega$$

By imposing the condition that the equation of the forward revised characteristics has the simple form  $s = \text{constant}$ , and using (10)-(12) we get

$$S^{(1)}(\tau, s) = -u_0/(\omega \sqrt{2} \sqrt{1-n}) e^{\tau/2H} [(\gamma-1)/2 \sin(\alpha-\psi) + \sin(\alpha+\psi)] + f(s), \quad (14)$$

where

$$\alpha = \omega/c_0 [s + (1-n)\tau], \quad \sin \psi = -\sqrt{1-n}/\sqrt{2}, \quad \cos \psi = \sqrt{1+n}/\sqrt{2}.$$

The integration constant  $f(s)$  is as yet undetermined: this indeterminacy is typical of perturbation techniques, and is eliminated by choosing boundary or initial conditions. In order to have a solution that at least initially follows closely the usual linear solution, we require, as for the usual linear solution, that

$$u^{(1)}(x=0, t) = u_0 \sin \omega t, \quad (15)$$

which implies

$$f(s) = u_0 [(\gamma-1)/2 \sin(\omega s/c_0 - \psi) + \sin(\omega s/c_0 + \psi)] / (\sqrt{2} \omega \sqrt{1-n}). \quad (16)$$

The same procedure can be followed to obtain higher order terms:  $S^{(2)}$ ,  $S^{(3)}$ , ... are determined by requiring that the equation  $s = \text{constant}$  represents the forward characteristic to the desired order of approximation.

Equations (12), (13), (14), and (16) represent our new solution in a parametric form. In order to find the velocity, pressure and density as explicit functions of  $x$  and  $t$  it is necessary to solve (12) explicitly for  $s$ . We shall solve (12) for  $s$  as a function of  $t$  and  $x$  numerically.

## SHOCK FORMATION AND NUMERICAL SOLUTIONS

To obtain an analytical expression for the distance at which a shock takes place, we note that a characteristic must intersect with its nearest neighbor before it can cross other characteristics [e.g., Courant and Friedrichs, 1948]. Hence

$$t_s = x_s = 0 \quad (17)$$

can be used as criterion for the crossing of adjacent characteristics. The above relation implies that

$$1 + S_s^{(1)} = 0 \text{ and } S_{ss}^{(1)} = 0. \quad (18)$$

The solution  $x_0$  of (18) represents the distance at which a shock takes place; the corresponding value of  $s$  is  $s_0$ . Upon substitution of  $x_0$  and  $s_0$  into the equation of the characteristics, we obtain the value of the "shock formation time"  $t_0$ , i.e., the time it takes for a wave leaving the plane  $x = 0$  at  $t = 0$  to develop into a shock. The values of  $x_0/\lambda$  versus  $kc_0/\omega$  are plotted in

figure 1a) for given value of  $M = u_0/c_0 = 10^{-1}$ . It is interesting to note that as  $n \rightarrow 1$ , i. e., as  $g \rightarrow 0$ ,  $x_0/\lambda \rightarrow 1/[\pi M(1 + \gamma)]$ , which is a well-known result of sound theory. [See Blackstock, 1962, or Keck and Beyer, 1960.] In figure 1b)  $x_0/\lambda$  is plotted versus  $M = u_0/c_0$ , for  $n = 0.96$ . In figure 2 the solution just obtained and the usual linear solution are plotted versus  $x/x_0$  and for  $t/t_0 = 1$ . Finally in figure 3 the two solutions are plotted versus time for the three values of  $x$ :  $x = \lambda$ ,  $x = 2\lambda$ , and  $x = x_0$ .

## CONCLUSIONS

We have presented a new approximate solution for the propagation of acoustic-gravity waves in the vertical direction. It represents a periodic shock wave satisfying the condition that at the plane of excitation,  $u(x = 0, t) = u_0 \sin \omega t$ . The solution is valid for any value of  $t$  and for  $0 \leq x \leq x_0$ . At  $x = x_0$  the wave form steepens to the point of having a vertical tangent. Where this occurs one would expect that our original equations are not adequate in representing the flow: viscosity and heat conduction may in fact become very important. As expected the present solution and the usual linear solution do not differ very much at sufficiently small values of  $x/\lambda$  and/or of  $t/t_0$ . However, as  $x/x_0$  increases, the harmonic content of the wave increases rather rapidly. The value of  $x_0$  can be taken as a rough estimate of the maximum value of  $x$  over which the usual linear solution is valid.

We would like to mention finally that the expansion parameter implied in the above treatment is

$$\epsilon \equiv u_0/c_0 \exp(x_0/2H)$$

A more refined expression for  $\epsilon$  could be obtained by calculating higher order terms which also give some information about the convergence of the above method.

## ACKNOWLEDGMENTS

I am greatly indebted to Prof. C. O. Hines for invaluable advice and criticism. This work was supported by the National Research Council of Canada under Grant A3940.

## REFERENCES

- Blackstock, D. T., Propagation of plane sound waves of finite amplitude in nondissipative fluids, J. Acoustical Soc. America, 34, 9, 1962.
- Courant R. and Friedrichs, K. O., Supersonic flow and shock waves, Interscience Publishers, Inc., 1948.
- Hines, C. O., Internal atmospheric gravity waves at ionospheric heights, Can. J. Phys., 38, 1441, 1960.
- Keck, W. and Beyer, R. T., Frequency spectrum of finite amplitude ultrasonic waves in liquids, Phys. Fluids, 3, 346, 1960.
- Lighthill, M. J., A technique for rendering approximate solutions to physical problems uniformly valid, The Philosophical Magazine, Ser. 7, 40, 1179, 1949.
- Whitham, G. B., The propagation of spherical blast, Proc. Roy Soc. A203, 571, 1950.



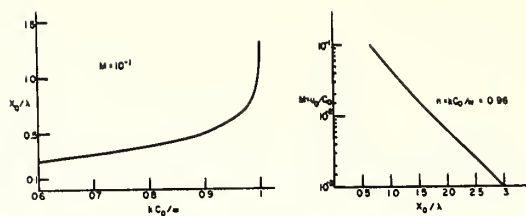


Figure 1. a):  $x_0/\lambda$  versus  $kc_0/\omega$  for  $M = u_0/c_0 = 10^{-1}$ ; b):  $x_0/\lambda$  versus  $M = u_0/c_0$  for  $kc_0/\omega = 0.96$ .

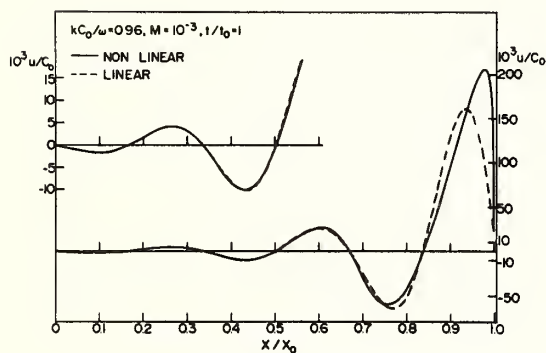


Fig. 2:  $u/c_0$  versus  $x/x_0$  for  $t/t_0 = 1$ ;  $M = 10^{-3}$  and  $kc_0/\omega = 0.96$ .

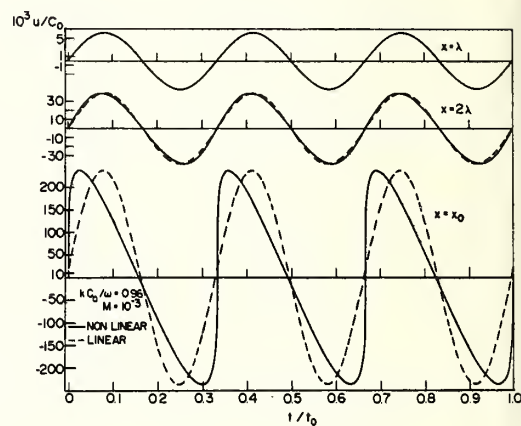


Fig. 3:  $u/c_0$  versus  $t/t_0$  for  $x = \lambda$ ,  $2\lambda$  and  $x_0$ ;  $M = 10^{-3}$  and  $kc_0/\omega = 0.96$ .

# ITERATIVE SERIES METHODS FOR FINDING EXACT NUMERICAL SOLUTIONS FOR A CLASS OF SECOND ORDER DIFFERENTIAL EQUATIONS

Jack P. Friedman and Bruce W. Crawford

KNOLLS ATOMIC POWER LABORATORY  
General Electric Company  
Schenectady, New York

A method for finding exact numerical solutions of the acoustic-gravity wave equation is presented. The technique, known as the iterative series method, is designed to treat arbitrarily complicated temperature and wind profiles in an exact way, in contrast to conventional step-function approximations. Calculations of E-region reflection properties, originating from thermal gradients, provide an illustrative example. The results suggest that the iterative series method is an efficient way of calculating very accurate solutions and that the step-function approach is particularly poor at high wave periods.

## 1. INTRODUCTION

Acoustic-gravity wave propagation in an inhomogeneous atmosphere has been traditionally treated by using step-function representations of temperature and wind profiles and then solving the resulting equations. Although Pierce (1966) has demonstrated the validity of this approach, others (Hines (1965); Friedman (1966)) have pointed out that errors associated with this method have never been investigated for finite layer thicknesses.

The method described here produces numerical solutions based on exact descriptions of temperature and wind distributions. In this formalism, the solution of the exact problem is an iterative series of terms with each term being the solution of an easy-to-solve equation. Analytical solutions of these easy-to-solve equations are given and the computational problem is effectively reduced to numerical quadrature evaluations. Interestingly enough, the step-function approach turns out to be a special case.

Iterative series methods are generally applicable to linear systems. Major successes have been attained, thus far, in their application to the neutron transport equation (Kopp (1963); Crawford (1965); Crawford and Friedman (1966); Crawford and Friedman (1967)) which is an integral equation. This research constitutes a first attempt to derive an iterative series formalism for differential equations.

A first-order coupled form of the acoustic gravity wave equation is reviewed in section 2 and the iterative series solution method is derived in section 3. An application is examined in section 4 where calculations pertinent to E-region reflections are examined under varying numerical conditions.

## 2. ACOUSTIC-GRAVITY WAVE EQUATIONS

Let Cartesian coordinates  $x$  and  $z$  represent horizontal and vertical directions respectively for an atmosphere whose characteristic properties (temperature, horizontal winds, and gravitational field strength) possess spacial variations in the  $z$  direction only. To be neglected in the formulation are: viscous forces, thermal conductivity, non-linear effects, explicit sources, vertical components of background winds, effect of the earth's curvature, and effect of the earth's rotation (i.e., Coriolis forces). The basic fluid-dynamical equations of momentum and mass conservation, together with the adiabatic equation of state of an

ideal gas, are collectively subjected to wave perturbations of the form  $\exp i(\omega t - K_x x)$  relative to an undisturbed atmosphere (with a steady horizontal background wind). This analysis, which may be found in Pitteway and Hines (1965), isolates the  $z$ -dependence and leads to coupled first-order differential equations

$$df(z)/dz = A(z)f(z)$$

where  $f(z) = \begin{bmatrix} \xi(z) \\ \eta(z) \end{bmatrix}$  and  $A(z) = K_x \begin{bmatrix} \gamma/\alpha - 1/\beta & (1/\beta - \beta)/\alpha \\ 1 - \alpha/\beta & 1/\beta \end{bmatrix}$  (1)

for continuous dependent variables  $\xi$  ( $\alpha$  velocity divergence) and  $\eta$  ( $\infty$  vertical velocity) in terms of the independent variable  $z$ . The coupling matrix  $A$  is expressed in terms of dimensionless quantities  $\alpha(z)$  and  $\beta(z)$  which are respectively proportional to the temperature and  $(\omega - K_x V_{ox})^2$ . Note that  $\omega - K_x V_{ox}$  is the Doppler-shifted frequency due to the background wind velocity  $V_{ox}$ . More precise definitions of these quantities may be found in the following list of symbols.

$V_{ox}$  = steady background wind velocity (in the  $x$ -direction)  
 $u$  = wave motion velocity vector  
 $u_z$  = vertical component of  $u$   
 $K_x$  = horizontal wave number  
 $\omega$  = angular frequency  
 $w$  =  $\omega - K_x V_{ox}$  = Doppler-shifted frequency  
 $\xi$  =  $\text{div } u/w$   
 $\eta$  =  $K_x u_z/w$   
 $\alpha$  =  $\gamma H K_x$   
 $\beta$  =  $w^2/(g K_x)$   
 $g$  = gravitational field strength  
 $\gamma$  =  $c_p/c_v$  = specific heat ratio (=1.4)  
 $H$  =  $RT/(gM)$  = scale height  
 $R$  = universal gas constant  
 $T$  = temperature  
 $M$  = molecular weight

Equation (1) will be considered with reference to an atmosphere of thickness  $D$  (i.e.,  $0 \leq z \leq D$ ) with boundary conditions imposed on  $f(0)$  and  $f(D)$ . There are two categories of numerical problems requiring investigation:

1. The general problem. Equation (1) may be solved numerically to yield a matrix  $F$  which relates  $f(0)$  and  $f(D)$  according to  $f(D) = Ff(0)$ . Indeed, the use of an iterative series method for calculating  $F$  is the main subject of this paper. It should be noted that  $F$  depends only on atmospheric properties and wave variables (e.g. period). In particular,  $F$  does not depend on boundary conditions imposed on  $f(0)$  and  $f(D)$ . A unique  $F$ -matrix therefore pertains to all applications characterized by identical temperature and wind distributions and different boundary conditions. An investigation of how accurately  $F$  may be calculated is therefore of general interest.
2. The specific problem. Physical information cannot be obtained from the calculation of  $F$  alone. Boundary conditions in  $f(0)$  and  $f(D)$  must supplement the calculation of  $F$  in specific applications. For example, consider an atmosphere which is bounded by rigid flat surfaces at both ends. The boundary conditions for such a problem would be

$$f(0) = \begin{bmatrix} \xi(0) \\ 0 \end{bmatrix} \text{ and } f(D) = \begin{bmatrix} \xi(D) \\ 0 \end{bmatrix} \quad (2)$$

where either  $\xi(0)$  or  $\xi(D)$  is arbitrary (but nonzero). Solving this problem first

requires the calculation of  $F$  followed by the application of (2) to the relation  $f(D) = Ff(0)$ . The latter procedure will produce dispersion curves relating various wave parameters with each other.

An important problem requiring analysis is one which compares the accuracy of a general problem solution (i.e.,  $F$ ) with that of various specific problems (e.g. dispersion curves). It is desirable to understand how sensitive various computed quantities are to errors in  $F$ .

### 3. ITERATIVE SERIES SOLUTION METHOD

It is desired to solve

$$df(z)/dz = A(z)f(z); \quad 0 \leq z \leq D \quad (3)$$

where  $A$  is an  $2 \times 2$  matrix whose elements may be complex and  $f$  is a 2-component column vector. The method for solving (3) is to find an approximate matrix  $A_0$  which is constant in  $0 \leq z \leq D$ ; i.e.

$$A(z) = A_0 + A_1(z) \quad (4)$$

$$||A_1(z)|| \ll ||A_0|| \quad (\text{in some sense}) \quad (5)$$

There are many possible choices for  $A_0$ , an obvious one being  $A_0 = A(D/2)$ . Next, expand  $f(z)$  as an iterative series

$$f(z) = f_0(z) + f_1(z) + f_2(z) + \dots \quad (6)$$

where  $f_0(z)$  satisfies

$$df_0(z)/dz = A_0 f_0(z)$$

and

$$f_0(0) = f(0); \quad f_n(0) = 0 \quad \text{for } n = 1, 2, \dots \quad (7)$$

The subscripts in this formalism represent orders of accuracy. Hence  $f_0(z)$  is a zeroth order solution,  $f_1(z)$  is a first order correction, etc. If (6) is substituted into (3) and quantities of the same order are separated out, the following differential equations result:

$$df_0(z)/dz = A_0 f_0(z) \quad (8)$$

$$df_n(z)/dz = A_0 f_n(z) + S_n(z); \quad n = 1, 2, \dots \quad (9)$$

$$S_n(z) = A_1(z) f_{n-1}(z) \quad (10)$$

Equations (8) and (9), subject to the conditions of (7), have solutions (Condon and Odishaw (1958))

$$f_0(z) = \exp(A_0 z) f(0) \quad (11)$$

$$f_n(z) = \exp(A_0 z) \int_0^z dz' \exp(-A_0 z') S_n(z'); \quad n = 1, 2, \dots \quad (12)$$

Note that  $\exp(\pm A_0 z)$  may be expressed in the form (Friedman (1961)):

$$\exp(\pm A_0 z) = (a_2 - a_1)^{-1} ((a_2 - A_0) \exp(\pm a_1 z) + (A_0 - a_1) \exp(\pm a_2 z)) \quad (13)$$

where  $a_1$  and  $a_2$  are the eigenvalues of  $A_0$ .

If (11)-(12) is reorganized, the following convenient form for the solution at  $z = D$  may be obtained:

$$f(D) = Ff(0); \quad f_n(D) = \exp(A_0 D) T_n f(0) \quad (14)$$

where

$$F = \exp(A_0 D)(T_0 + T_1 + T_2 + \dots) \quad (15)$$

$$T_0 = \text{unit matrix} \quad (16)$$

$$T_1 = \int_0^D dz_1 H(z_1) \quad (17)$$

$$T_2 = \int_0^D dz_2 H(z_2) \int_0^{z_2} dz_1 H(z_1) \quad (18)$$

$$T_n = \int_0^D dz_n H(z_n) \int_0^{z_n} dz_{n-1} H(z_{n-1}) \dots \int_0^{z_2} dz_1 H(z_1) \quad (19)$$

$$\vdots$$

$$\text{and } H(z) = \exp(-A_0 z) A_1(z) \exp(A_0 z) \quad (20)$$

Observe that the original homogeneous equation (3), characterized by an arbitrarily complicated  $A(z)$ , has been transformed into a series of solutions (6) of much simpler equations (8)-(9) which are all characterized by a constant matrix  $A$  and a "synthetic" source term  $S_n(z)$ . The transformed equations are so simple that their solutions can be formally written down in terms of quadratures ((11)-(12) or (14)-(20)). Note that spacial dependence of  $A(z)$  is manifested in  $S_n(z)$  via the difference matrix  $A_1(z)$ .

Convergence of the iterative series depends on the "smallness" of  $A_1(z)$  which in turn depends on the choice of  $A_0$  relative to the properties of  $A(z)$ . In order to keep  $A_1$  small, it will usually be necessary to partition  $0 \leq z \leq D$  into  $L$  layers and apply the iterative method to each layer separately. Each layer  $m$  defined over  $z_{m-1} \leq z \leq z_m$  ( $m = 1, 2, \dots, L$ ) has its own  $A_{0,m}$  and relational matrix  $F_m$  such that  $f(z_m) = F_m f(z_{m-1})$ . Since  $f(z)$  is continuous at layer boundaries, it follows that  $f(D) = F f(0)$  with  $F = F_N F_{N-1} \dots F_1$ . Since  $F$  is the ordered product of individual layer matrices  $F_m$ , the problem is conceptually reduced to that of calculating  $F_m$  for a single layer.

An interesting way of looking at this method results if  $A_0$  is chosen in each layer to correspond to constant values of temperature, wind velocity, and gravitational field strength. Then  $f_0(z)$  represents the solution for the conventional homogeneous layer formulation. First order deviations from homogeneity in each layer are manifested in  $f_1(z)$  via the quadrature (17) which involves  $A_1(z)$ . Second order deviations from homogeneity are analogously manifested in  $f_2(z)$  via (18) where  $A_1(z)$  appears twice. (Note that the double appearance of  $A_1$  in (18) is consistent with  $f_2(z)$  being a second order quantity).

On the other hand, other choices for  $A_0$  are possible. If  $A_0 = D^{-1} \int_0^D A(z) dz$ , for example, the zeroth order solution  $f_0(z)$  would not be the solution of a properly-posed physical problem. It would seem difficult, if not impossible, to find self-consistent temperature and wind profiles which lead to the differential equations  $df/dz = A_0 f_0$  for  $A_0 = D^{-1} \int_0^D A(z) dz$ . This choice of  $A_0$  may nevertheless be a desirable one in cases where it accelerates the convergence of the iterative series.

#### 4. EXAMPLE: E-REGION REFLECTIONS

The E-region (90-150 km height range) was selected for studying the iterative series method. Figure 1 illustrates the model which was derived from a least squares quadratic fit to CIRA (1961) scale-height data. Isothermal half-spaces are assumed to bound the E-region on both sides and background winds are neglected. A gravity wave, incident from below, undergoes partial reflections (in addition to total reflections at sufficiently high wave speeds), resulting in a leakage of wave energy into the upper half-space.



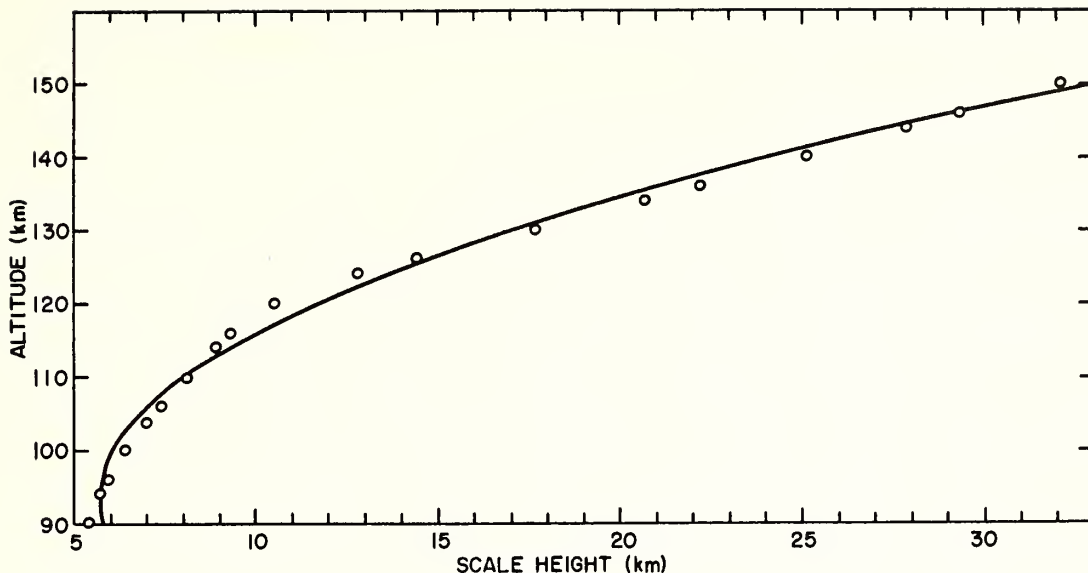


Fig. 1. E-region scale height profile derived from a least-squares quadratic fit to CIRA (1961) data. The data points are denoted by circles.

The formula  $g_0 R_0 / (R_0 + z)^2$  is used for the gravitational field strength, where  $g_0 = 9.81$  m/sec<sup>2</sup> and  $R_0 = 6378$  km are deduced from CIRA (1961) data.

Relational F-matrices and transmission coefficients are calculated for the E-region as functions of wave period at a constant horizontal wave length of 300 km. The F-matrix relates E-region boundary solutions via

$$f(150) = Ff(90), \quad (21)$$

while the transmission coefficient is  $1 - |a/b|^2$  (Hines and Reddy (1967)) where  $a$  and  $b$  are defined by the expression for  $f$  ( $\propto$  vertical velocity) in the lower half-space:

$$f \propto a \exp(-ikz) + b \exp(ikz); \quad k > 0 \quad (22)$$

Once  $F$  is calculated, the upper boundary condition of upward energy flow (which imposes a relationship between components of  $f(150)$ ) is coupled to  $f(90)$  via (21). This information, combined with (22), facilitates the calculation of  $a/b$ .

In order to achieve convergent solutions, the E-region is stratified into layers of equal thickness and the iterative series method is applied to each layer as discussed in section 3. To be varied for the purpose of making comparisons are the number of layers  $L$  and the order of the iterative series  $N$ . (Order  $N$  solutions are of the form  $f_0(z) + f_1(z) + \dots + f_N(z)$ ;  $N = 0, 1, 2, \dots$ ) The constant  $A_0$  matrix for each layer is calculated from (1), using  $N$  layer-midpoint values of the scale height ( $\propto$  temperature) and gravitational field strength. For this choice of  $A_0$ , the  $N = 0$  solutions pertain to the homogeneous layer formulations.

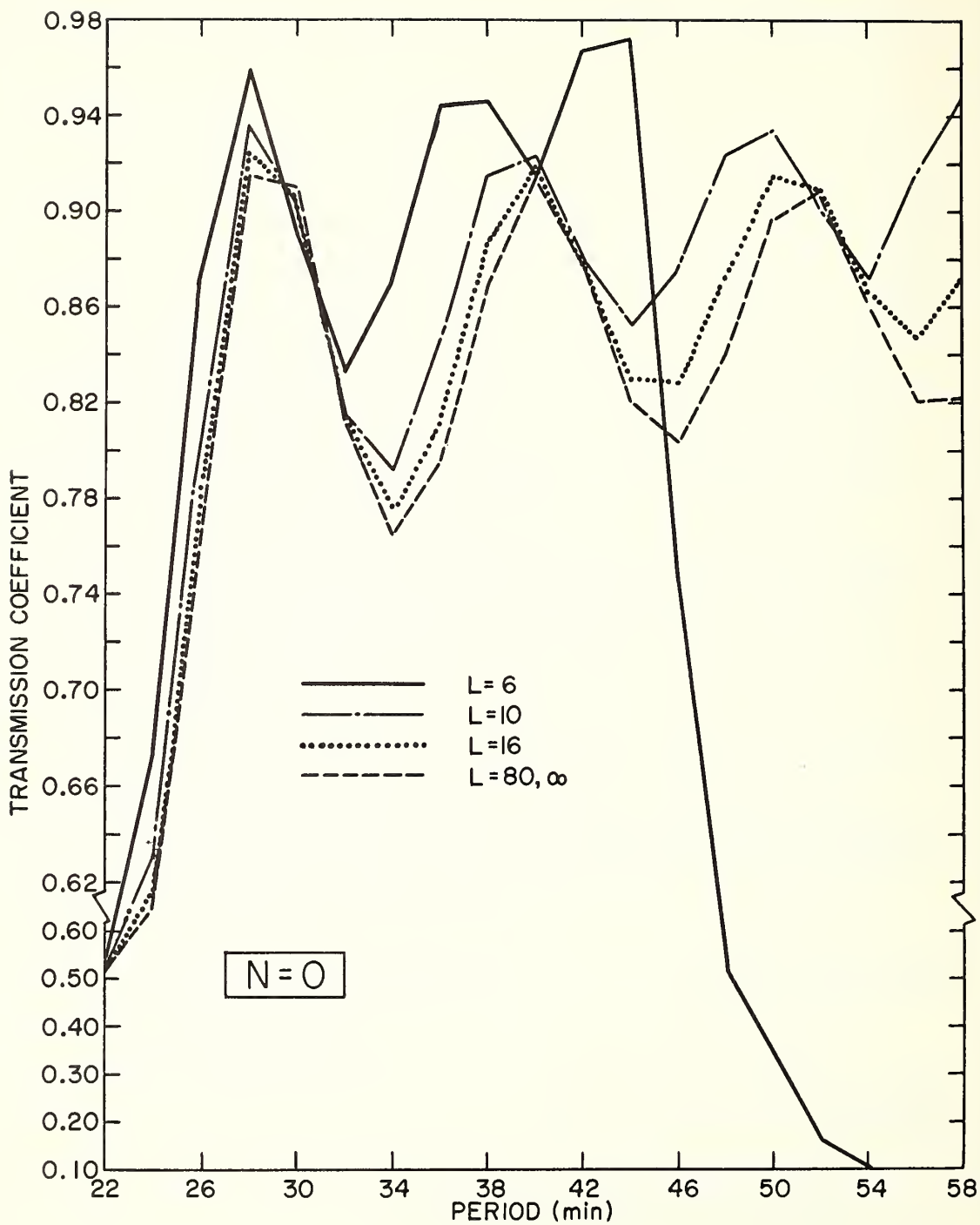


Fig. 2.  $N = 0$  transmission coefficient versus wave period for several values of  $L$ .

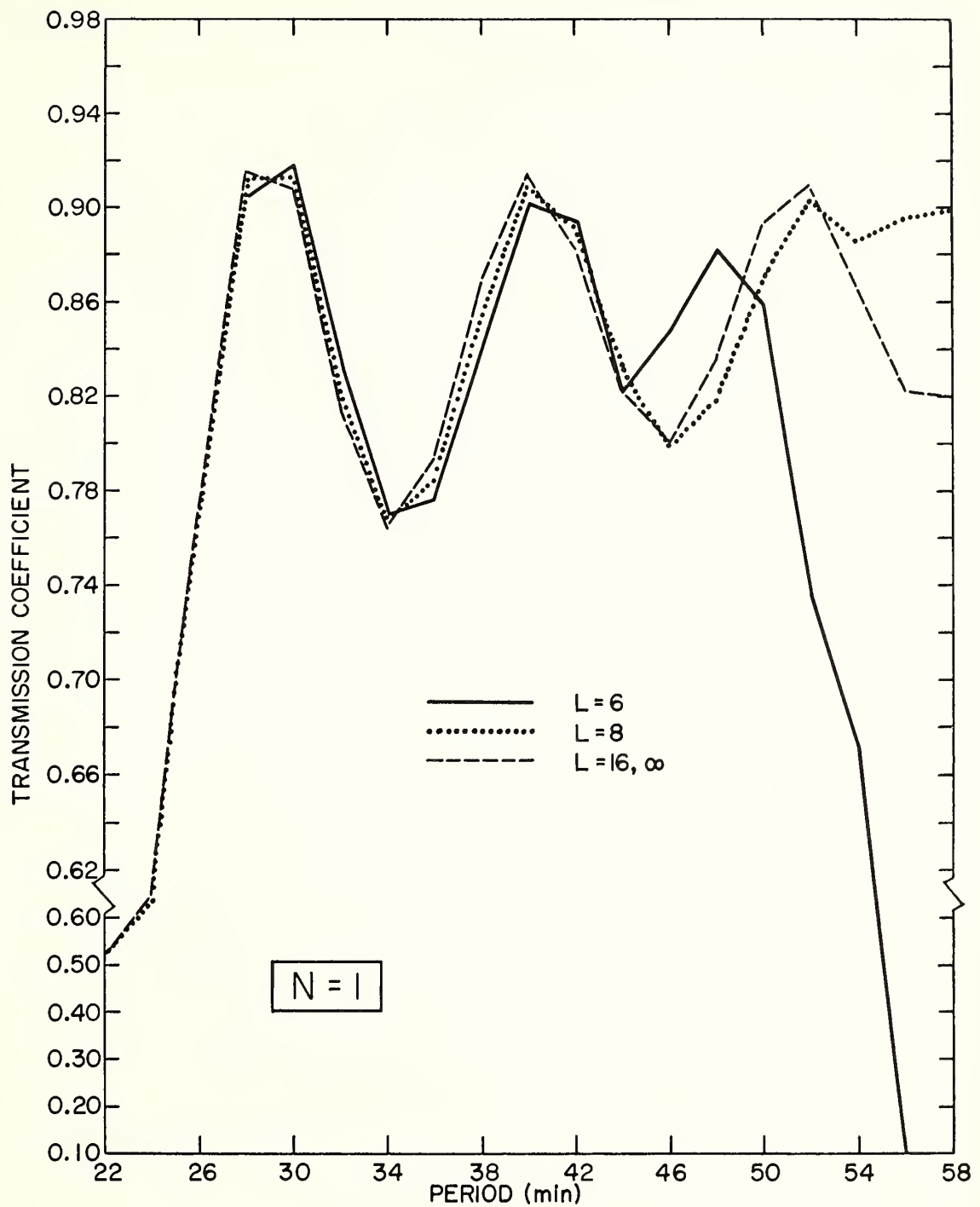


Fig. 3.  $N = 1$  transmission coefficient versus wave period for several values of  $L$ .

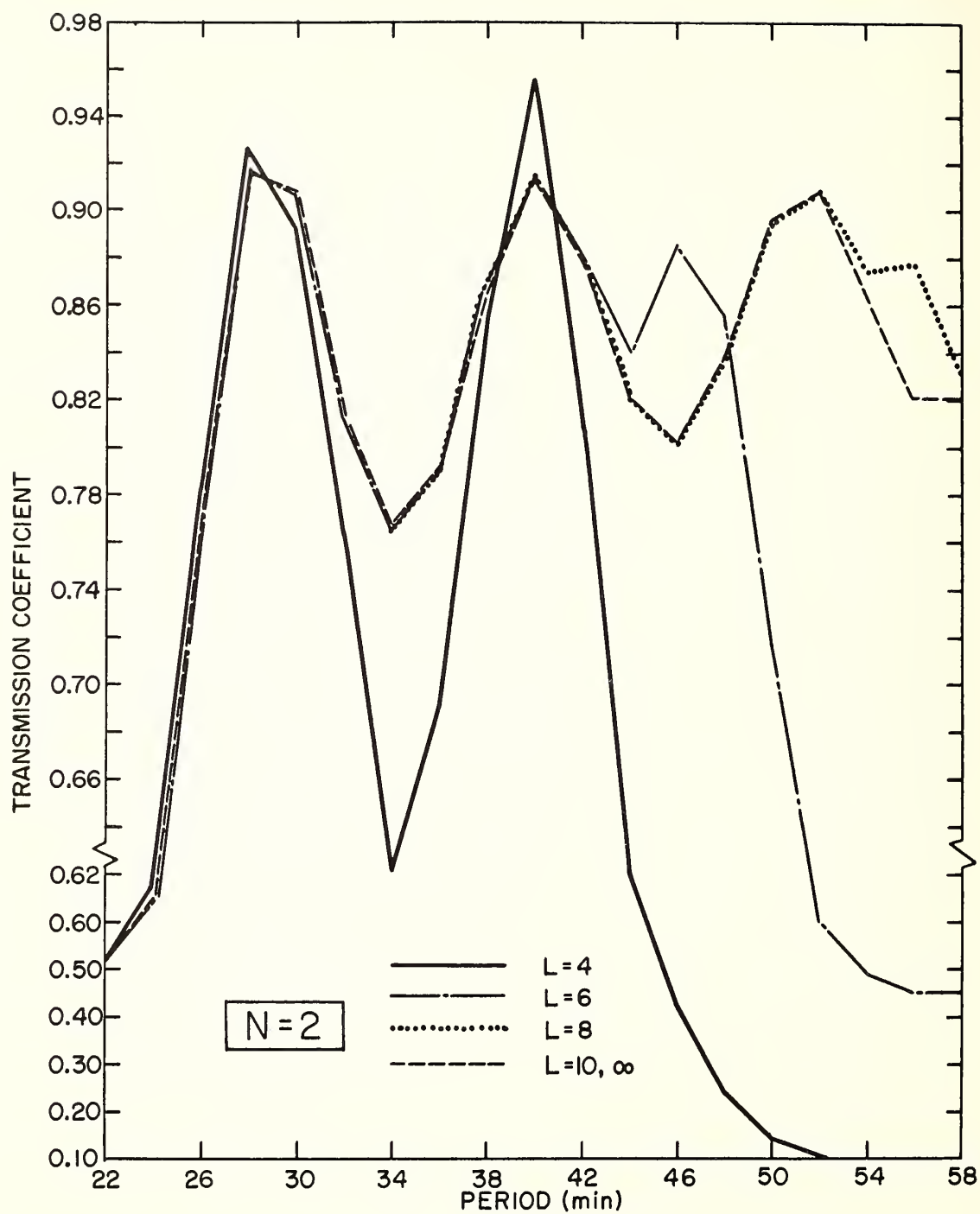


Fig. 4.  $N = 2$  transmission coefficient versus wave period for several values of  $L$ .

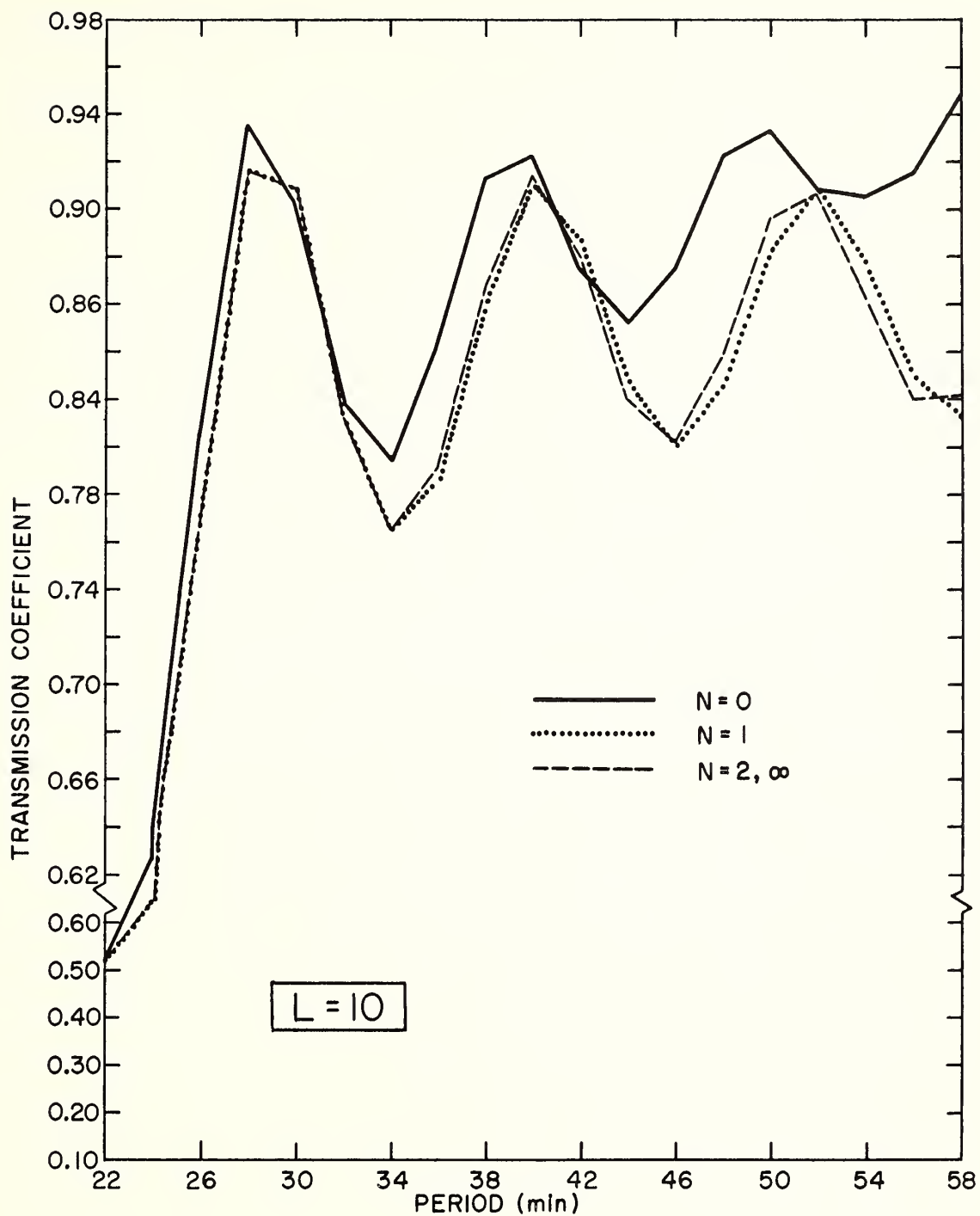


Fig. 5.  $N = 0, 1, 2$  transmission coefficients versus wave period for constant  $L = 10$ .



Figures 2, 3 and 4 illustrate  $N = 0, 1$ , and 2 solutions (i.e., transmission coefficients) respectively. In each case, the calculated solution converges to the exact solution as  $L$  increases. The fact that  $N = 0, 1$ , and 2 calculated solutions all converge to the same exact solution constitutes a check on both the iterative series formalism and the numerical calculations. Note the strong dependence of numerical accuracy on wave period. In particular, the high period solutions converge much more slowly than the lower period solutions.

Figure 5 compares the accuracy of  $N = 0, 1$ , and 2 solutions for a fixed number of layers, namely 10. The  $N = 2$  solution is closest to the exact solution which is to be expected. The discrepancy for different values of  $N$  is greatest at the high periods.

The number of layers required to achieve given accuracies in the reflection coefficient and F-matrix is given in Tables 1, 2, and 3 for wave periods of 22, 40, and 58 minutes respectively. Solutions at  $L = 1, 2, 3, 4, 6, 8, 10, 12, 16, 20, 30, 40, 50, 60, 70, 80, 90, 100, 150, 200, 250, 300, 400$ , and 500 were utilized in this tabulation. An L-mesh error is therefore implicit in the results.

TABLE 1. - Number of Layers  $L_N$  (for Order  $N$  Calculations) Required to Attain Given Accuracies at a 22 Minute Period.

Period (min.)	Computed Quantity	% Accuracy	$L_0$	$L_1$	$L_2$	$L_0/L_1$	$L_0/L_2$
22	Transmission Coefficient	10	6	3	3	2.0	2.0
		1	10	6	4	1.7	2.5
		.1	30	10	4	3.0	7.5
	$F_{11}$	10	6	6	3	1.0	2.0
		1	16	8	4	2.0	4.0
		.1	50	12	6	4.2	8.3
	$F_{21}$	10	4	4	3	1.0	1.3
		1	10	6	3	1.7	3.3
		.1	30	10	6	3.0	5.0
	$F_{12}$	10	6	4	3	1.5	2.0
		1	10	6	4	1.7	2.5
		.1	30	8	4	3.8	7.5
	$F_{22}$	10	6	4	3	1.5	2.0
		1	16	8	4	2.0	4.0
		.1	50	16	6	3.1	8.3

TABLE 2. - Number of Layers  $L_N$  (for Order N Calculations) Required to Attain Given Accuracies at a 40 Minute Period.

Period (min.)	Computed Quantity	% Accuracy	$L_0$	$L_1$	$L_2$	$L_0/L_1$	$L_0/L_2$
40	Transmission Coefficient	10	6	6	4	1.0	1.5
		1	12	8	6	1.5	2.0
		.1	40	12	6	3.3	6.7
	$F_{11}$	10	16	10	6	1.6	2.7
		1	50	20	8	2.5	6.2
		.1	150	30	10	5.0	15.0
	$F_{21}$	10	12	10	6	1.2	2.0
		1	40	20	8	2.0	5.0
		.1	100	30	10	3.3	10.0
	$F_{12}$	10	16	12	6	1.3	2.7
		1	50	20	8	2.5	6.2
		.1	150	30	10	5.0	15.0
	$F_{22}$	10	12	12	6	1.0	2.0
		1	40	20	8	2.0	5.0
		.1	90	30	10	3.0	9.0

TABLE 3. - Number of Layers  $L_N$  (for Order N Calculations) Required to Attain Given Accuracies at a 58 Minute Period.

Period (min.)	Computed Quantity	% Accuracy	$L_0$	$L_1$	$L_2$	$L_0/L_1$	$L_0/L_2$
58	Transmission Coefficient	10	16	8	8	2.0	2.0
		1	40	12	8	3.3	5.0
		.1	150	30	12	5.0	12.5
	$F_{11}$	10	50	20	10	2.5	5.0
		1	200	40	16	5.0	12.5
		.1	500	60	20	8.3	25.0
	$F_{21}$	10	150	40	16	3.8	9.4
		1	400	60	20	6.7	20.0
		.1	>500	100	30	>5.0	>16.7
	$F_{12}$	10	150	40	16	3.8	9.4
		1	400	60	20	6.7	20.0
		.1	>500	100	30	>5.0	>16.7
	$F_{22}$	10	70	30	12	2.3	5.8
		1	250	50	16	5.0	15.6
		.1	>500	80	30	>6.3	>16.7

Results from Table 1 (22 minute period) indicate that the  $N = 0$  solution converges very slowly with increasing  $L$  compared with that of  $N = 1$  and  $N = 2$  solutions. A relatively small increase in computational effort ( $\propto$  number of layers) is required for  $N = 1$  and  $N = 2$  to improve accuracy from 10% to .1%. Also note that all computed quantities (i.e., transmission coefficient and  $F$ ) require approximately the same number of layers in order to achieve comparable accuracies.

Tables 2 and 3 (40 and 58 minute periods respectively) further illustrate substantial improvement in efficiency (for high-accuracy solutions) as  $N$  increases. This effect appears to become more pronounced with increasing period as may be deduced by comparing  $L_1/L_0$  and  $L_2/L_0$  columns in Tables 1, 2, and 3. In contrast with Table 1 results, given accuracies for 40 and 58 minute periods are achieved with fewer layers for the transmission coefficient than for the F-matrix components. There evidently must be a partial insensitivity in the transmission coefficient calculation to numerical errors in  $F$ .

Tables 1, 2, and 3, viewed compositely, again indicate the relatively poor accuracy at high periods and the relative efficiency in using the iterative series method (i.e.,  $N \geq 1$ ) at high periods.

## 5. CONCLUSION

The results not only illustrate the rapid convergence of the iterative series method ( $N \geq 1$ ) but also questions the utility of the conventional homogeneous layer method ( $N = 0$ ), especially for calculations at high wave periods. High-accuracy solutions appear to be in-expensive to calculate with the iterative series method. The number of E-region layers required to achieve given accuracies was significantly less for the transmission coefficient than for the relational F-matrix at all but very low periods.

## 6. ACKNOWLEDGEMENT

We are grateful to Professor Max Goldstein of the AEC Computer Center at New York University for providing computer time for the calculations.

## 7. REFERENCES

- CIRA, Cospar International Reference Atmosphere, Report of the preparatory group for an international reference atmosphere accepted at the Cospar meeting in Florence, April 1961.
- Condon, E. U. and H. Odishaw, Handbook of Physics, p. 1-65, McGraw Hill Book Company, New York, 1958.
- Crawford, B. W., An iterative solution method for the neutron transport equation with anisotropic scattering, Ph.D. thesis, University of California, Berkely, 1965.
- Crawford, B. W. and J. P. Friedman, A two-dimensional application of an iterative transport method for solving the neutron transport equation with anisotropic scattering, Trans. Am. Nucl. Soc., 9, 2, 472-473, 1966.
- Crawford, B. W. and J. P. Friedman, Multigroup two-dimensional neutron transport, Trans. Am. Nucl. Soc., 1, 172, 1967.
- Friedman, B., Principles and Techniques of Applied Mathematics, 3rd printing, chapter 2, John Wiley and Sons, New York, 1961.
- Friedman, J. P., Propagation of internal gravity waves in a thermally stratified atmosphere, J. Geophys. Res., 71, 1033-1054, 1966.
- Hines, C. O., Atmospheric gravity waves: a new toy for the wave theorist, Radio Sci., 69D (3), 375-380, 1965.
- Hines, C. O. and C. A. Reddy, On the propagation of atmospheric gravity waves through regions of wind shear, J. Geophys. Res., 72, 1015-1034, 1967.
- Kopp, H. J., Synthetic method solution of the transport equation, Nucl. Sci.-Eng., 17, 65-74, 1963.

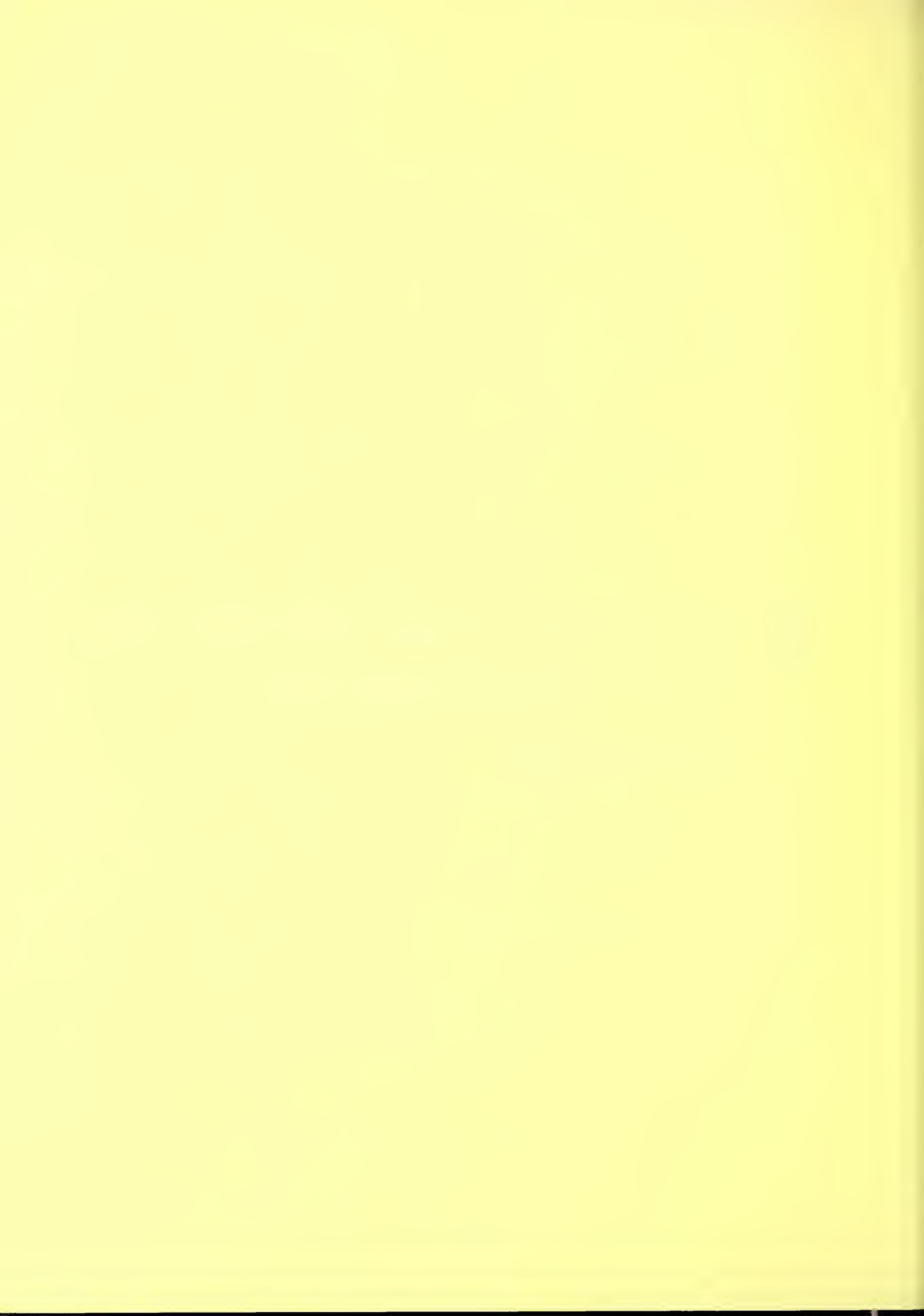
Pierce, A. D., Justification of the use of multiple isothermal layers as an approximation to the real atmosphere for acoustic-gravity wave propagation, Radio Sci., 1 (3), 265-267, 1966.

Pitteway, M. L. V. and C. O. Hines, The reflection and ducting of atmospheric acoustic-gravity waves, Can. J. Phys., 43, 2222-2243, 1965.





## V Atmospheric wave effects in the upper atmosphere and ionosphere



MEASUREMENTS OF GRAVITY WAVES IN THE NEUTRAL  
AIR AT THERMOSPHERIC HEIGHTS BY EXPLORER 32  
(SUMMARY)

by

G. P. Newton, D. T. Pelz, and H. Volland\*  
Aeronomy Branch  
Goddard Space Flight Center  
Greenbelt, Maryland

Density gauge measurements from the Explorer 32 satellite have revealed wave structure in the neutral density distribution in the thermosphere. These observations and their interpretation have been presented elsewhere in detail (Newton, et. al. 1968). The following information is essentially a synopsis of that paper.

The wave structure has been observed at altitudes greater than 290 km (satellite perigee) up to at least 550 km and occurs predominately during the night. The horizontal extent of the structure is greater than 1000 km. The amplitudes of the observed waves vary from the limit of detectability to 50% of the mean value of the density and remain nearly constant with height. The apparent vertical wavelengths are between zero and 200 km increasing systematically with height. The maximum horizontal wavelengths are between 130 and 520 km, and four harmonically related wavelengths have been observed. Observations of the waves appear to be limited to latitudes greater than 20°N (data were not obtained in the southern hemisphere for latitudes greater than 20°) and the phenomena is seen more frequently near the auroral zone. The wave structure occurs both on days indicated as geomagnetically disturbed and undisturbed.

These waves are interpreted as free internal dissipative gravity waves propagating obliquely upward into the thermosphere in a predominant north-south or south-north direction. The altitude dependence of the apparent vertical wavelengths results from a doppler effect due to the satellite which moves with varying vertical velocity through a slowly propagating wave pattern.

The small effective frequency spread observed may result from possible filtering action of the atmosphere in addition to any frequency characteristics of the unknown wave source. It is interesting to note with respect to a wave source however, that in addition to an apparent relationship between the frequency of observations of the wave structure and proximity to the auroral zone, there might also be a relationship with the polar frontal zone cyclogenesis.

The energy transported by the observed waves appears to be very small relative to the EUV energy flux into the thermosphere from the sun. The small energy flux could perhaps account for the waves being observed almost exclusively in the late evening and early morning hours. If the energy flux of the wave is considered to be constant, then the density perturbation of the wave might be larger in a less dense atmosphere. Hence, the diurnal density variation could reduce the density perturbation to a value below the experiment detection threshold during the day. Further, it is possible that energy transmission characteristics of the atmosphere could perhaps change diurnally thus diurnally changing the ability of the waves to propagate upward from lower altitudes.

Reference:

Newton, G. P., D. T. Pelz and H. Volland, Direct, In Situ Measurements of Wave Propagation in the Neutral Thermosphere, submitted for publication in J. Geophys. Res., 1968.

\*NAS-NRC Research Associate on leave from Bonn University, Bonn, West Germany.



# THE RESPONSE OF THE F-REGION IONOSPHERE TO INTERNAL ATMOSPHERIC GRAVITY WAVES

William H. Hooke  
Institute for Telecommunication Sciences  
Environmental Science Services Administration  
Boulder, Colorado 80302

Some results of calculations illustrating the anisotropy of the F-region ionospheric response to internal atmospheric gravity wave motions are presented. The anisotropy of the F2-region response to individual waves and some possible effects of this anisotropy on observed TID propagation statistics are discussed. Diurnal and seasonal variations of the lower F-region response to individual waves are shown.

## INTRODUCTION

It is now generally accepted, thanks mainly to the efforts of Hines (1960 and subsequent work), that internal atmospheric gravity waves propagating at F-region heights create the ionospheric irregularities commonly known as traveling ionospheric disturbances or TID's. It has also been generally known for some time that since the wave-associated motions of the neutral gas act dynamically through collisional interaction with the ionization to produce these irregularities, and since the ionization at F-region heights is nearly perfectly constrained to follow magnetic field lines, there is an anisotropy in the ionospheric response to wave motions of the neutral gas. Two waves alike in all respects except their direction of propagation over the face of the globe will produce ionospheric irregularities of quite different magnitude (for an extensive bibliography of this entire subject, see Georges [1967]).

Recently, Hooke (1968) showed that at the lower F-region heights, wave-associated changes in the rates of photochemical processes are as important as the wave-induced ion motions in producing ionospheric irregularities. He also showed that the magnitude of wave-induced changes in the photoionization rate depends upon the direction of wave propagation relative to the sun and suggested that this effect would result in diurnal and seasonal variations in the response of the lower F-region ionosphere to atmospheric wave passage.

This paper presents results of calculations illustrating these features of the F-region ionospheric response to internal atmospheric gravity wave passage. The author intends to discuss these results and the calculations themselves in more detail in a paper now in preparation; only a list of the assumptions underlying the calculations is given here: It is assumed in all the calculations that

- 1) The atmosphere is isothermal and stationary in the absence of wave motions so that Hines' (1960) description of the wave motions is applicable.
- 2) The relative phase and amplitude of the motions, density perturbations, and temperature perturbations of the neutral gas are given by the full polarization relations of Hines (1960).
- 3) The motions of the ionization are given by (MacLeod, 1966)

$$\underline{u}_1 = \frac{1}{1 + \rho_1^2} [ \rho_1^2 \underline{u} + \rho_1 (\underline{u} \times \underline{\Gamma}) + (\underline{u} \cdot \underline{\Gamma}) \underline{\Gamma} ] ,$$

where  $\underline{u}_1$  is the ion velocity,  $\underline{u}$  is the neutral gas velocity,  $\underline{\Gamma}$  is a unit vector in the direction of the earth's magnetic field, and  $\rho_1 \equiv \nu_1 / \omega_1$  is the ratio of the ion-neutral collision frequency  $\nu_1$  to the ion gyrofrequency  $\omega_1$ .



- 4) Geographic north and geomagnetic north coincide.
- 5) The magnetic dip angle  $I = 57^\circ$ , directed upward (corresponding to Australian locations).
- 6) The waves are all normalized in amplitude to a constant value of energy density per unit mass, chosen so that the wave-associated neutral gas motions are of the order of 6 m/s at the height of interest (see Hines, 1960, eq. (45)).
- 7) All the waves have 100-km vertical wavelengths.

It is assumed in the F2-region calculations that

- 1) The height of the F2 peak is 300 km, and it is at this height that the TID's are observed.
- 2) The scale height  $H = 50$  km.
- 3) The ratio of neutral-gas specific heats  $\gamma = 1.4$ .
- 4) The acceleration of gravity  $g = 8.93 \text{ m/s}^2$ .
- 5)  $\rho_1 = 0.05$ .

It is assumed in the F1-ledge calculations that

- 1)  $H = 28$  km,  $\gamma = 1.4$ ,  $g = 9.35 \text{ m/s}^2$ ,  $\rho_1 = 0.1$ .
- 2) The photoionization rate  $q$  has a height profile that is  $\alpha$ -Chapman-like, and the height of maximum  $q$  at the subsolar point is 150 km. At this point  $q = q_{\text{max}} = 3000 \text{ cm}^{-3} \text{ s}^{-1}$ .
- 3) The height at which the TID's are observed is 160 km.
- 4) Plasma diffusion is an unimportant process; the ionization is motionless in the absence of wave motion.
- 5) The ambient ionosphere is of the type described by Ratcliffe (1956) so that the perturbed ionosphere is of the type described by Hooke (1968), with the effects of plasma diffusion neglected.
- 6) The ionospheric chemical reaction rates are temperature-independent.
- 7) The dissociative recombination rate  $\alpha = 10^{-7} \text{ cm}^3 \text{ s}^{-1}$ .
- 8) At a height of 150 km, the ion-atom interchange rate  $\beta = 6.54 \times 10^{-2} \text{ s}^{-1}$ .
- 9) The geographical location considered is  $35^\circ$  south of the equator (corresponding to Australian locations).

#### ANISOTROPY OF THE F2-REGION RESPONSE TO INDIVIDUAL WAVES

At F2-region heights, ionospheric photochemical processes are slow, and in determining the effects of wave passage on the ionosphere, one may assume in most cases that the ions have infinitely long lifetimes. Furthermore, at these heights the neutral gas imparts to the ions primarily that component of its motion parallel to the earth's magnetic field lines. Finally, at the height of the F2 peak, where there is no ambient gradient of free electron number density,

atmospheric waves must create not only motion of the neutral gas parallel to the field lines, but also variations of this motion along the field lines, if they are to create a perturbation in the free electron number density (see, for example, Hooke, 1968).

Figure 1 shows, for several choices of horizontal wavelength, the fractional perturbation  $\Delta N_e / N_{e0}$  in free electron number density  $N_e$  occurring at the height of the F2 peak during wave passage at the given location ( $I = 57^\circ$ ) as a function of the azimuth of wave propagation. The horizontal wavelengths and the corresponding wave periods, calculated from the full dispersion equation of Hines (1960), are given in this figure. The figure shows that at this location, the wave with 50-km horizontal wavelength causes a relatively large ionospheric disturbance when it is propagating poleward, away from the equator. When it is propagating in directions within  $45^\circ$  of due north (equatorward), it creates a relatively small perturbation. On the other hand, the wave with the 100-km horizontal wavelength creates the largest ionospheric perturbation when it is propagating due east or west. The other waves create the largest ionospheric perturbations when propagating equatorward. Note that the wave-induced perturbations  $\Delta N_e / N_{e0}$  are typically the order of 5 percent, even for waves of the extremely small amplitudes considered here.

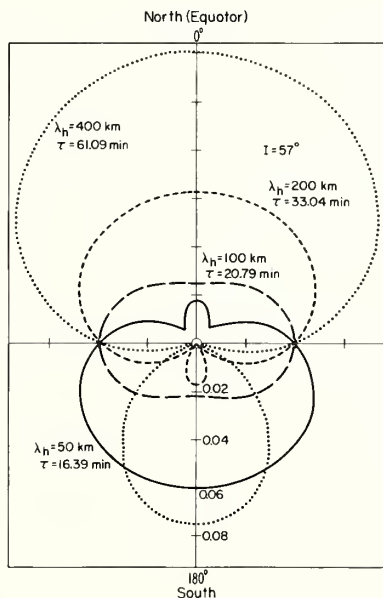


Figure 1.  $N_e / N_{e0}$  perturbations produced at the height of the F2 peak by internal atmospheric gravity waves as a function of the azimuth of wave propagation.

#### STATISTICALLY PREFERRED DIRECTIONS OF TID PROPAGATION

Some statistical studies of TID's indicate the existence of certain preferred directions of TID travel (see, for example, Munro [1958]). It is interesting to examine the role played by the anisotropy of the ionospheric response to the internal atmospheric gravity waves in determining the observed statistical patterns of TID propagation.

Consider the following model: During a hypothetical observing period (a week, a month, etc.), 50 waves of each of the four types shown in figure 1 propagate over the observing site in each  $10^\circ$  azimuth sector. Thus, 1800 waves of 50-km horizontal wavelength propagate over

the site during this period, 50 in each  $10^\circ$  sector. Similarly, 1800 waves of 100-km horizontal wavelength propagate over the site during the same period, etc. All waves are taken to have the energy density per unit mass used in the construction of figure 1. This wave model is of course idealized, but it suffices for present purposes.

Suppose now that the observer can determine directions of travel of TID's having fractional perturbations  $\Delta N_e / N_{e0}$  of 2 percent or more. He finds that during the observing period, the TID's have the occurrence statistics of the curve labeled 0.02 in figure 2, a plot of the number of TID's observed propagating in each  $10^\circ$  sector during the observing period. He sees many TID's, propagating in all directions, but he finds that the largest number are propagating due east and due west. If, instead, he can determine directions of travel only for TID's of amplitude greater than 4 percent, he finds the distribution shown in figure 2 as the curve labeled 0.04. He sees fewer TID's, since his observing instrument is less sensitive, and he finds a smaller spread in the observed directions of propagation. Observers with still less sensitive instruments, having sensitivities of 6 percent and 8 percent respectively, see the distributions shown in figure 3. They see still fewer TID's, and they find still smaller spreads in the observed directions of travel. Furthermore, they find that the largest number of TID's are propagating not east or west but equatorward.

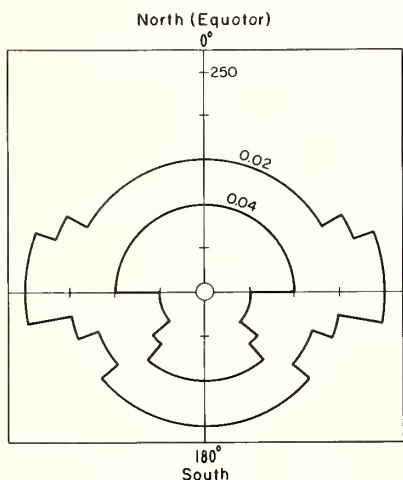


Figure 2. Number of TID's observed propagating in each  $10^\circ$  azimuth sector during the observing period.

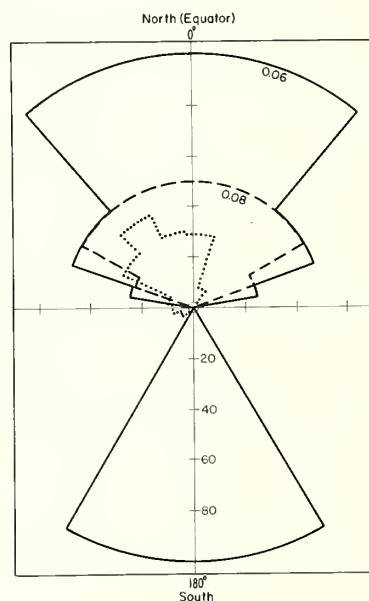


Figure 3. Number of TID's observed propagating in each  $10^\circ$  azimuth sector during the observing period.

There is thus an observational selection in force: observers with sensitive instruments (such as Munro's network of fixed-frequency sounders) should see a relatively large spread in the observed directions of travel (as indeed Munro [1958] did), while those using less sensitive techniques (such as Bowman's [1960a, 1960b] technique for observing the TID-like irregularities responsible for temperate-latitude spread-F) should see a relatively narrow spread of directions (some of Bowman's results are shown as a dotted curve in figure 3). Although the model of the observing instruments having sensitivities independent of TID parameters is undoubtedly an oversimplification, the problem indicated here is a real one.

## THE F1-LEDGE RESPONSE TO INDIVIDUAL WAVES

At the lower F-region heights, wave-associated photochemical effects are important to the production of  $\Delta N_e / N_{e0}$  perturbations. Figure 4 illustrates the azimuthal dependence of the  $\Delta N_e / N_{e0}$  perturbations produced by a wave having the parameters shown, at four different times of day during local summer. ( $v_{ph}$  is the horizontal phase speed of the wave.  $u_h$  is the amplitude of the horizontal wave-induced motions.) The arrows in the figure indicate directions of wave propagation for which the sun's rays lie in surfaces of constant wave phase. The solid curves give the total ionospheric response to the wave passage; the dashed curves indicate that part of the response due solely to the effects of wave-induced motions of the ions. It is clear that the latter effects are still important at these lower heights, but it is also clear that the ionospheric response is in general asymmetric with respect to due north, and that this asymmetry exhibits a considerable diurnal variation.

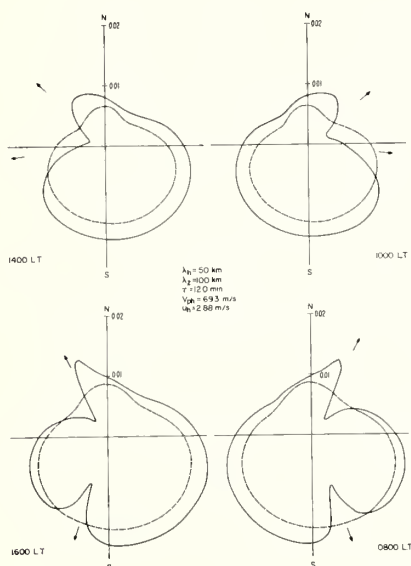


Figure 4. Diurnal variation of the azimuthal dependence of the F1-ledge response to internal atmospheric gravity wave passage during local summer.

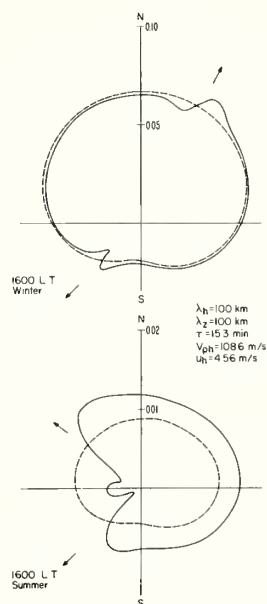


Figure 5. Seasonal variation of the azimuthal dependence of the F1-ledge response to internal atmospheric gravity wave passage.

Figure 5 illustrates the azimuthal and seasonal dependence of the  $\Delta N_e / N_{e0}$  perturbations produced by a wave having the parameters shown. Again the solid curves give the total ionospheric response to wave passage, while the dashed curves indicate the response to the wave-induced motions of the ions. The figure makes it quite clear that seasonal variations in the ionospheric response may be considerable.

In this connection, it is interesting to note that Munro's observations, which do indicate diurnal and seasonal variations in the preferred directions of TID travel, are observations of TID's at heights below 200 km (Heisler, 1958), where wave-associated photochemical effects are important.

## REFERENCES

- Bowman, G. G., Further studies of spread-F at Brisbane. I. Planet. Space Sci. 2, 133-149 (1960a).
- Bowman, G. G., Further studies of spread-F at Brisbane. II. Planet. Space Sci. 2, 150-156 (1960b).
- Georges, T. M., Ionospheric effects of atmospheric waves, ESSA Tech. Report IER-57/ITSA-54, U. S. Govt. Printing Office (1967).
- Heisler, L. H., Anomalies in ionosonde records due to travelling ionospheric disturbances, Aust. J. Phys. 11, 79-90 (1958).
- Hines, C. O., Internal atmospheric gravity waves at ionospheric heights, Can. J. Phys. 38, 1441-1481 (1960).
- Hooke, W. H., Ionospheric irregularities produced by internal atmospheric gravity waves, J. Atmos. Terrest. Phys. 30, 795-823 (1968).
- MacLeod, M. A., Sporadic E theory, 1, collision-geomagnetic equilibrium, J. Atmos. Sci. 23, 96-109 (1966).
- Munro, G. H., Travelling ionospheric disturbances in the F region, Aust. J. Phys. 11, 91-112 (1958).
- Ratcliffe, J. A., The formation of the ionospheric layers F1 and F2, J. Atmos. Terr. Phys. 8, 260-269 (1956).



## ON POSSIBLE METHODS OF DETERMINING THE ORIGIN OF E-REGION WIND SHEAR

William H. Hooke  
Institute for Telecommunication Sciences  
Environmental Science Services Administration  
Boulder, Colorado 80302

Results of calculations indicate that internal gravity wave motions of the neutral gas, which at E-region heights appear as nearly vertical shears in a nearly horizontal flow, produce ionospheric effects significantly different from the effects that would be produced by strictly vertical shears in a strictly horizontal flow, if these in fact exist.

This paper suggests the possibility of distinguishing between internal gravity wave motions and purely horizontal "winds" of the E-region atmosphere by simultaneously measuring height profiles of the neutral gas motions  $u$ , the free electron number density  $N_e$ , and the electron temperature  $T_e$ . Single rocket- and meteor-trail measurements of atmospheric motions do not distinguish between motions of the two types since they do not resolve the small vertical motions of the neutral gas that theory (Hines, 1960) predicts should be associated with the waves. At present, this distinction can only be made by time sequences of such measurements, which reveal a phase progression of the wave-associated motions that is not exhibited by the "winds." On the basis of such measurements, it is possible to estimate the relative importance of the various types of motion present (see, for example, Hines, 1966).

This paper also suggests the possibility of determining the horizontal direction of wave propagation on the basis of  $u$ ,  $N_e$ , and  $T_e$  height profiles determined at a single location. To date, networks of spaced observers have been required for this task.

The theoretical basis for the above is as follows: Internal gravity wave motions of the neutral gas differ from purely horizontal "winds" because the former are accompanied by vertical motions as well as by density and temperature perturbations of the neutral gas at any fixed point (Hines, 1960, 1965), while the latter are not. The wave-associated temperature perturbations should be almost directly reflected in the electron temperature profiles at E-region heights. Furthermore, while both waves and "winds" act dynamically, through the magnetoshear mechanism, to produce ionospheric irregularities (Whitehead, 1961), the waves in addition act photochemically to produce such irregularities, since the rates of ionospheric photochemical processes depend upon neutral gas number density and temperature. (This possibility was first suggested in passing by Hines [1960]; the theory has been developed quantitatively by Hooke [paper in preparation].) Thus, internal gravity waves and horizontal "winds" of the same amplitude produce ionospheric irregularities of dissimilar magnitudes.

The above statements are based on a theoretical analysis that the author intends to describe in more detail elsewhere. Only results of some calculations based on that analysis are presented here. The following assumptions are implicit in the calculations:

- 1) The neutral atmosphere is isothermal and stationary in the absence of internal gravity wave motions, so that the waves can be described by the theory presented by Hines (1960). The wave period is determined from the wave vector by the full dispersion relation given in that work, and the wave motions and density and temperature perturbations are related in amplitude and phase by the full polarization relations given there.
- 2) The daytime E-region is an  $\alpha$ -Chapman-layer ionosphere, consisting of a single constituent that is ionized by monochromatic radiation.
- 3) The motions of the ionization are given by (MacLeod, 1966):

$$\underline{u}_i = \frac{1}{1 + \rho_i^2} [ \rho_i^2 \underline{u} + \rho_i (\underline{u} \times \underline{\Gamma}) + (\underline{u} \cdot \underline{\Gamma}) \underline{\Gamma} ] ,$$

where  $\underline{u}_i$  is the ion velocity,  $\underline{u}$  is the neutral gas velocity,  $\underline{\Gamma}$  is a unit vector in the direction of the earth's magnetic field, and  $\rho_i \equiv \nu_i / \omega_i$  is the ratio of the ion-neutral collision frequency  $\nu_i$  to the ion gyrofrequency  $\omega_i$ .

4) The electron temperature  $T_e$  is approximately related to the neutral gas temperature  $T_n$  by (Cole and Norton, 1966)

$$T_e - T_n = \frac{3}{2} q k T_e^\dagger / (1.55 \times 10^{-18} n(N_2) N_e) ,$$

where  $q$  is the photoionization rate,  $k$  is Boltzmann's constant,  $T_e^\dagger$  is an "injection" temperature of the photoelectrons, and  $n(N_2)$  is the number density of molecular nitrogen.

5) Geographic north and geomagnetic north coincide.

6) The scale height  $H = 8$  km.

The ratio of neutral gas specific heats  $\gamma = 1.4$ .

The acceleration of gravity  $g = 9.5$  m/s.

At the height  $z_0 = 108$  km,  $q = q_{\max} = 5 \times 10^3 \text{ cm}^{-3} \text{ s}^{-1}$ .

The ambient neutral gas temperature  $T_{n0} = 300^\circ\text{K}$ .

At the height  $z_0$ ,  $n(N_2) = 2 \times 10^{12} \text{ cm}^{-3}$ .

The magnetic dip angle  $I = 25^\circ$ .

The solar zenith angle  $\chi = 0^\circ$ .

The recombination rate coefficient  $\alpha = 5 \times 10^{-7} \text{ cm}^3/\text{s}$ , and it is temperature-independent. The effect of temperature-dependence of this reaction rate is discussed further in the more detailed papers now in preparation.

$T_e^\dagger = 1 \text{ ev.} = 8000^\circ\text{K}$ .

$\rho_i (108 \text{ km}) = 3$ .

The model ionosphere described above has the  $N_e$  height profile labeled  $N_{e0}$  in figure 1. Consider a perturbation of this ambient ionosphere by an internal gravity wave of 10-km vertical wavelength and 100-km horizontal wavelength; the direction of wave phase propagation is downward and due east. At a moment when the horizontal wave-associated atmospheric motions have the height profile shown at the right-hand side of the figure, the perturbed  $N_e$  profile theoretically expected is that labeled  $N_e E$ . Consider now a perturbation of the ionosphere by the same wave, propagating due west. At a moment when the horizontal wave-associated atmospheric motions have the profile shown in figure 1, the perturbed  $N_e$  profile is that labeled  $N_e W$ . It is clear that the eastward-propagating wave creates a more perturbed profile than does the westward-propagating wave. The reason is that wave-associated vertical motions and photochemical effects act to enhance the effects of wave-associated horizontal motions when the wave is propagating due east, while the various effects tend to cancel when the wave is propagating due west.

An observer who measures only the horizontal neutral-gas motions and assumes that these motions act only through the magnetoshear mechanism to perturb the ionosphere would expect to see an  $N_e$  profile intermediate between the two shown. Uncertainties in present estimates of the values of atmospheric parameters, such as ion-neutral collision frequencies, reaction rate coefficients, etc., would make it difficult in this case to distinguish between atmospheric motions of wave origin and "winds" on the basis of such discrepancies. The discrepancies can be even greater, however, in cases where the wave-associated photochemical effects are more important than they are here (higher magnetic latitudes, waves of larger wavelength).

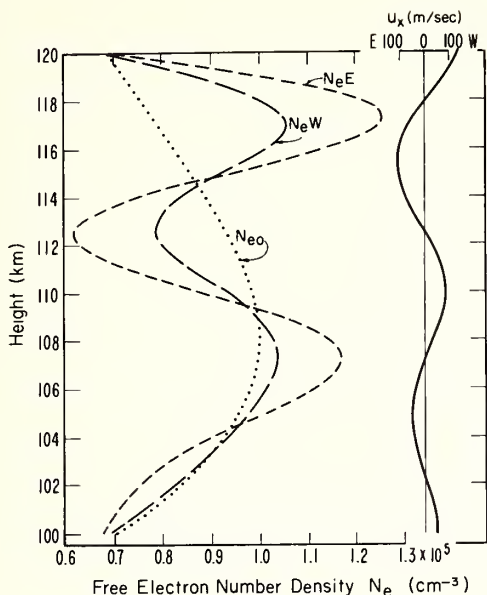


Figure 1. Ambient and perturbed  $N_e$  height profiles for the model ionosphere.

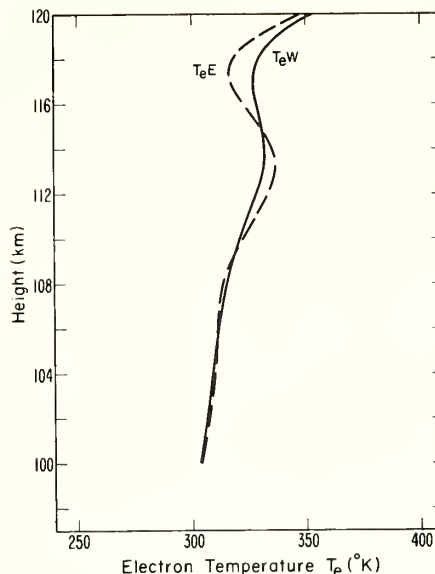


Figure 2. The electron temperature height profiles corresponding to the  $N_e$  E and  $N_e$  W profiles of figure 1, when the latter profiles are produced by strictly horizontal "winds."

A more certain method for distinguishing between motions of the two types lies in simultaneously measuring  $T_e$  height profiles. If a purely horizontal "wind" is assumed responsible for producing either the  $N_e$  E or the  $N_e$  W profile of figure 1, the  $T_e$  profile theoretically expected (Cole and Norton, 1966; Gleeson and Axford, 1967) is that shown in figure 2 as the  $T_e$  E profile or the  $T_e$  W profile respectively. The cooling rate of the electron gas is inversely proportional to  $N_e$  and to the neutral-gas number density  $n$  (Cole and Norton, 1966). Height variations in  $N_e$  then cause corresponding variations in  $T_e$ ; the ambient decrease of  $n$  with increasing height causes the general increase in  $T_e$  with increasing height.

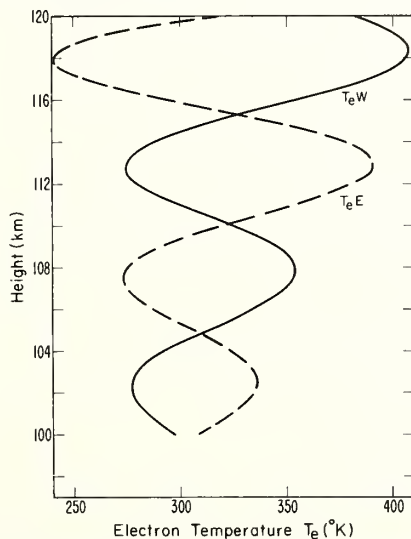


Figure 3. The electron temperature height profiles associated with passage of the eastward- and westward-propagating internal gravity waves.

The eastward- and westward-propagating gravity waves (producing the  $N_e$  E and  $N_e$  W profiles of figure 1) would result in the  $T_e$  E and  $T_e$  W profiles of figure 3 respectively. Unlike the profiles of figure 2, these profiles exhibit large, rapid height variations in  $T_e$  because of the wave associated variations in the neutral-gas temperature  $T_n$ . Furthermore, the variations are opposite in sense in the two cases (a direct consequence of the difference in the horizontal directions of wave phase propagation, for reasons discussed more fully in the papers in preparation). The eastward-propagating wave produces  $T_e$  minima at the heights of  $N_e$  maxima, while the westward-propagating wave produces  $T_e$  maxima at these heights. Thus, in principle, simultaneous measurements of E-region  $T_e$  and  $N_e$  height profiles can be used to determine the horizontal direction of wave propagation.

Wave motions of the neutral gas should produce height variations of the ion temperature  $T_i$  at E-region heights; one observed sinusoidal  $T_i$  profile has already been interpreted on this basis (Knudsen and Sharp, 1965). The relative phase of  $T_i$  and  $N_e$  height variations is also determined by the horizontal direction of wave propagation.

Direct measurements of vertical neutral-gas motions would also distinguish between wave motions and horizontal "winds." At least one such measurement from rocket-trail observations has been reported (Murphy et al, 1967), and a sophisticated radio drift measurement technique holds some promise for making such measurements in the future (Wright, private communication).

#### ACKNOWLEDGMENT

The author is grateful to Mr. J. W. Wright of the Ionospheric Telecommunications Laboratory, ESSA, for many helpful comments.

#### REFERENCES

- Cole, K. D. and R. B. Norton (1966), Some problems associated with midlatitude sporadic E, *Radio Sci.* 1 (New Series), 235-241.
- Gleeson, L. J. and W. I. Axford (1967), Electron and ion temperature variations in temperate zone sporadic-E layers, *Planet. Space Sci.* 15, 123-136.
- Hines, C. O. (1960), Internal atmospheric gravity waves at ionospheric heights, *Can. J. Phys.* 38, 1441-1481.
- Hines, C. O. (1965), Dynamical heating of the upper atmosphere, *J. Geophys. Res.* 70, 177-183.
- Hines, C. O. (1966), Diurnal tide in the upper atmosphere, *J. Geophys. Res.* 71, 1453-1459.
- Knudsen, W. C. and G. W. Sharp (1965), Evidence for temperature stratification in the E region, *J. Geophys. Res.* 70, 143-160.
- MacLeod, M. A. (1966), Sporadic E theory. 1. Collision-geomagnetic equilibrium, *J. Atmos. Sci.* 23, 96-109.
- Murphy, C. H., G. V. Bull, and J. W. Wright (1967), Motions of an electron-ion cloud released at 100 kilometers from a gun-launched vehicle, *J. Geophys. Res.* 72, 3511-3514.
- Whitehead, J. D. (1961), The formation of the sporadic E layer in the temperate zones, *J. Atmos. Terr. Phys.* 20, 49-58.



# COLLISIONAL INTERACTION OF ATMOSPHERIC WAVES WITH THE IONOSPHERIC F REGION

T. M. Georges  
ESSA Research Laboratories  
Boulder, Colorado 80302

Formulas are derived for the distribution of electron density in the F region during the passage of a compressional or a transverse atmospheric wave propagating in any direction with respect to the earth's magnetic field. The only forces acting on the ionization are taken to be momentum transfer by collisions with neutrals and confinement by the magnetic field.

---

Motions imparted to F-region ionization by the neutral air can be considered "field-dominated" because the ionization collision frequencies are much less than the electron or ion gyrofrequencies. If, furthermore, the time scale of neutral-air motions is much longer than the mean time between collisions, the ionization motions can be considered in equilibrium with the neutral gas. Atmospheric waves with periods between about 1 min and 1 h, under conditions that prevail in the F region, thus cause ionospheric electrons to oscillate back and forth "along the field lines" in response to the field-aligned component of neutral-air velocity (Georges, 1967). Such an approximation permits the derivation of relatively simple analytical expressions for the electron-density distribution resulting from the passage of a purely compressional or a purely transverse atmospheric wave.

Our attention is restricted to waves of sufficiently long wavelength that we can neglect diffusion processes, both in the neutral gas and in the ionization (Georges, 1967). Below the F region, ionization motions are not field-dominated, so they are also excluded from consideration. Hydromagnetic reactions on the neutral wave impose the long-period limit on the waves to be considered. Electron-ion interaction can be neglected because the electrons, ions, and neutrals are essentially in equilibrium, the wave period being much longer than either the electron-neutral or ion-neutral collision frequencies. Possibly important effects of the neutral wave on ionization production-loss processes are ignored here, but could presumably be added later in the form of a correction (Hooke, 1968a).

Let the neutral-air motion arise from an atmospheric wave denoted by

$$\underline{U}_n = U(z)E \quad (1)$$

where

$$E = \exp i(k_x x + k_y y + k_z z - \omega t),$$

$\underline{U}_n$  is the air velocity oscillating at an angle  $\Psi$  with the  $z$  axis, and  $U$  is its height-dependent amplitude,  $\omega$  is the angular wave frequency, and  $k_x$ ,  $k_y$ , and  $k_z$  are components of the wave propagation vector  $\underline{k}$ . The electron velocity  $\underline{U}_e$  responds to the wave by oscillating along the magnetic field direction so that

$$\underline{U}_e = \underline{a}_B \underline{U}_n \cos \theta, \quad (2)$$

where  $\underline{a}_B$  is a unit vector directed along the field, and  $\theta$  is the angle between  $\underline{U}_n$  and  $\underline{a}_B$ . The geometry is shown in figure 1. Combining (1) and (2) and expressing  $\underline{a}_B$  as  $x$  and  $z$  components yields

$$\underline{U}_e = (\underline{a}_x \cos I + \underline{a}_z \sin I) U E \cos \theta \quad (3)$$

where  $I$  is the magnetic inclination, positive upward (Southern hemisphere), negative downward (Northern hemisphere). Knowing  $\underline{U}_e$ , we can calculate the electron number density distribution  $n_e$  using the continuity equation for electrons,

$$-\frac{\partial n_e}{\partial t} = \nabla \cdot (n_e \underline{U}_e). \quad (4)$$



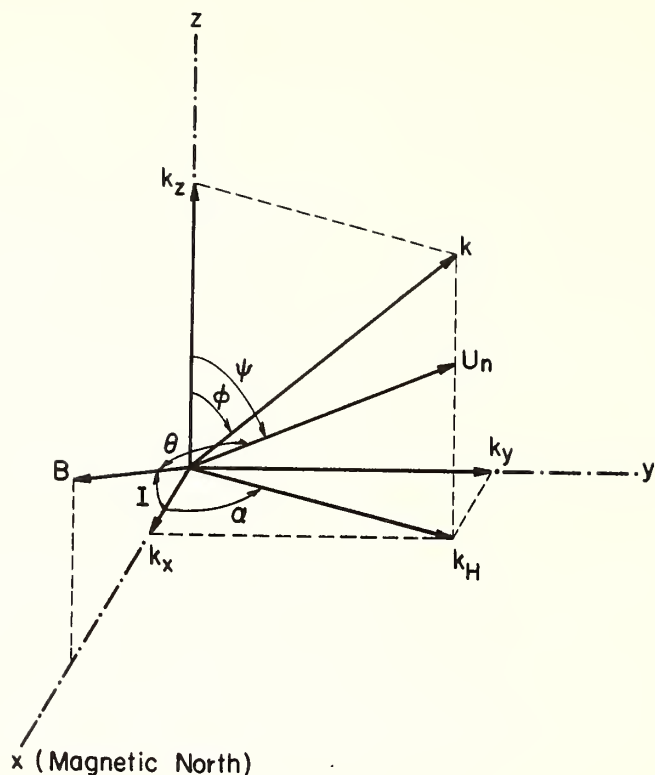


Figure 1. Geometry for atmospheric wave interaction with ionization.

If we let

$$n_e(x, y, z, t) = n_{eo}(z) + n'_e(x, y, z, t) \quad (5)$$

and

$$n'_e \ll n_{eo}, \quad (6)$$

we obtain a linearized continuity equation,

$$-\frac{\partial n'_e}{\partial t} = n_{eo} \left( \frac{\partial u_{ex}}{\partial x} + \frac{\partial u_{ez}}{\partial z} \right) + u_{ez} \frac{\partial n_{eo}}{\partial z} \quad (7)$$

If we assume that  $n'_e$  is of the form

$$n'_e = N'_e(z)E, \quad (8)$$

then

$$\frac{\partial n'_e}{\partial t} = -i\omega n'_e = -i\omega N'_e E. \quad (9)$$

Evaluating the other terms in (7), using (3), we obtain

$$\frac{\partial u_{ex}}{\partial x} = (ik_x U \cos \theta \cos I)E, \quad (10)$$

$$\frac{\partial u_{ez}}{\partial z} = \left( ik_z U \cos \theta \sin I + \frac{\partial U}{\partial z} \cos \theta \sin I \right) E. \quad (11)$$

Equation (7) then becomes

$$\frac{N'_e}{n_{eo}} = \frac{U \cos \theta}{\omega} \left[ k_x \cos I + k_z \sin I - i \sin I \frac{\partial}{\partial z} (\ln n_{eo} U) \right] \quad (12)$$

and

$$n_e(x, y, z, t) = n_{eo}(z) \left( 1 + \frac{N'_e}{n_{eo}} E \right). \quad (13)$$

Notice the possibility of a "phase shift" between the neutral gas motions and the electron density perturbations, arising solely because of the vertical variations in ambient electron density and wave amplitude.

In general the angle  $\theta$  (fig. 1) is given by

$$\cos \theta = \cos I \sin \Psi \cos \alpha + \sin I \cos \Psi, \quad (14)$$

where

$$\begin{aligned} \Psi &= \varphi \text{ for a compression wave} \\ \Psi &= \varphi + \pi/2 \text{ for a transverse wave} \\ (\cos \Psi &= -\sin \varphi; \sin \Psi = \cos \varphi). \end{aligned}$$

Some special cases of particular orientations of  $\underline{k}$  yield simplified versions of (12). In what follows, we neglect the vertical gradients of  $n_{eo}$  and  $U$ .

Transverse wave: Here  $\cos \theta = \cos I \cos \varphi \cos \alpha - \sin I \sin \varphi$ .

(a) Propagation in the magnetic meridian. In this case  $\alpha = 0$  and  $\theta = I + \varphi$ , and (12) becomes

$$\frac{N'_e}{n_{eo}} = \frac{U \cos(I + \varphi)}{\omega} (k_z \sin I + k_x \cos I). \quad (15)$$

(b) Nearly vertical propagation. Here we let  $k_z \gg k_x$  and the air motions are nearly horizontal. Equation (12) then becomes, neglecting terms of order  $(k_h/k_z)^2$  and noting that  $k_x = k_h \cos \alpha$

$$\begin{aligned} \frac{N'_e}{n_{eo}} &= \frac{U k_z}{\omega} \left[ \frac{1}{2} \sin 2I \cos \alpha + \frac{k_h}{k_z} (\cos^2 I \cos^2 \alpha - \sin^2 I) \right] \\ &\approx \frac{U k_z}{2\omega} \sin 2I \cos \alpha \end{aligned} \quad (16)$$

provided  $I \neq 0$ . In the case of exactly vertical propagation,  $\alpha$  becomes indeterminate, but for real transverse (gravity) waves  $k_h$  cannot be zero.

(c) Nearly vertical propagation in the magnetic meridian. Combining the two previous approximations we obtain

$$\frac{N'_e}{n_{eo}} = \frac{U k_z \sin 2I}{2\omega} = \frac{U}{2V_z} \sin 2I \quad (17)$$

where  $V_z$  is the vertical trace velocity of the wave.

Compression wave: Here  $\cos \theta = \cos I \sin \varphi \cos \alpha + \sin I \cos \varphi$

(a)  $\alpha = 0$ :

$$\frac{N'_e}{n_{eo}} = \frac{U \sin(I + \varphi)}{\omega} (k_x \cos I + k_z \sin I) \quad (18)$$

(b)  $k_z \gg k_x$  (nearly vertical propagation; air motions vertical):

Neglecting terms of order  $(k_h/k_z)^2$

$$\frac{N'_e}{n_{eo}} = \frac{U k_z}{\omega} \left( \sin^2 I + \frac{k_h}{k_z} \cos \alpha \sin 2I \right) \quad (19)$$

$$\approx \frac{U k_z}{\omega} \sin^2 I = \frac{U}{V_z} \sin^2 I. \quad (20)$$

With these formulas, numerical calculations of the ionization distribution caused by any transverse or compressional wave in any ambient ionosphere (satisfying the basic assumptions) should be possible. Long-period atmospheric gravity waves can usually be approximated as transverse waves, while acoustic waves are essentially compression waves. The principal unknown is the wave amplitude  $U$  and its height distribution.

Some estimates of the errors involved in the assumption of linear air-parcel orbits were made by comparing the electron density perturbations calculated using (12) with those calculated by Hooke (1968b) using the general "polarization relations" of Hines (1960). The two kinds of calculations were compared by postulating equal wave energies in the two cases and computing the ionosphere response for several hundred combinations of propagation directions and wave parameters. Errors were mostly less than one percent, with the larger errors occurring in cases where the electron density perturbations were quite small.

These calculations also indicate that the effects of the term in (12) containing the gradients of  $n_e$  and  $U$  are not normally negligible.

#### References

Georges, T.M., Ionospheric effects of atmospheric waves, ESSA Technical Report IER 57-ITSA 54, U.S. Gov't. Printing Office, 1967.

Hines, C.O., Internal atmospheric gravity waves at ionospheric heights, Can. J. Phys. 38, 1441-1481, 1960.

Hooke, W.H., Ionospheric irregularities produced by internal atmospheric gravity waves, J. Atmosph. Terr. Phys. 30, 795-823, 1968a.

Hooke, W.H., F-region ionospheric irregularities produced by internal gravity waves, this symposium, 1968b.

The Effect of Velocity Bandwidth on the Cross-Spectra  
of Wave Recordings from Spatially Separated Sites

EARL E. GOSSARD

Naval Electronics Laboratory Center  
San Diego, California 92152

It is argued that the coherence between records from a triangle of stations can be used to deduce not only the effective beamwidths of wave patterns, but can also be used to obtain explicit information about the velocity bandwidth throughout the wave spectrum and its effect on the apparent velocity of propagation. Relationships between apparent velocity of propagation and the velocity bandwidth are derived that are analogous to the cross correlation approach of Briggs, Phillips and Shinn.

INTRODUCTION

A method for separating temporal fluctuations from spatial fluctuations in the diffraction pattern of radio waves reflected from an inhomogeneous ionosphere has been given in terms of convenient measurables by Briggs, Phillips & Shinn (1950). It is fairly general, and its main limitations are:

1. It requires that the same functional form be assumed for the temporal correlation as for the spatial correlation function.

2. It is only applicable to drift analysis. Information on wave motion cannot in general be obtained because the method uses correlation functions, which give no direct information about the movement of individual frequency components in the records.

It is the intent of this paper to try to remove both limitations by deriving functional forms for the temporal and spatial behavior of cross power and thus extend the analysis into the frequency domain to permit the study of wave motions as well as drift.

CROSS CORRELATION ANALYSIS

It is useful to briefly review the method of Briggs Phillips and Shinn. Suppose the correlograms are Gaussian and there is no drift. Then

$$\rho(\tau, \ell) = e^{-\left(\frac{\ell^2}{\ell_o^2} + \frac{\tau^2}{\tau_o^2}\right)} \quad (1)$$

where  $\ell$  is station separation in the x direction and  $\tau$  is time lag between records.

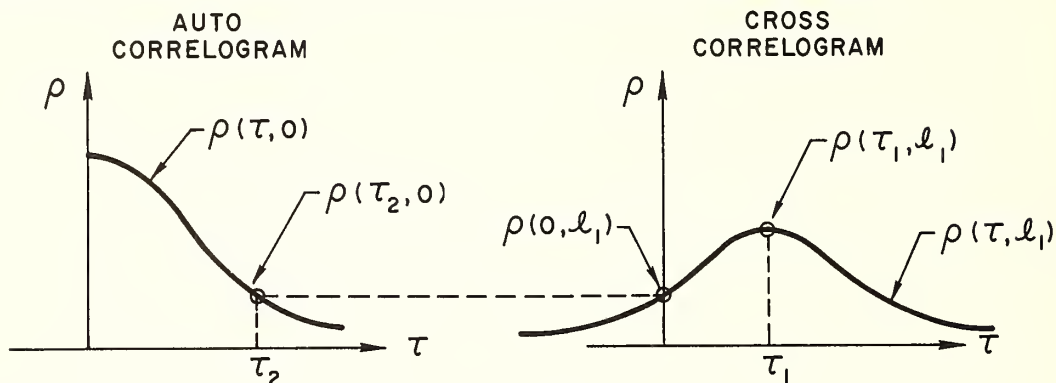
If a drift,  $V$ , in the X direction is superimposed on the turbulent medium the correlation function is unaltered if the coordinate system is given a velocity,  $V$ . So

$$\rho(\tau, \ell) = e^{-\left(\frac{(\ell - V\tau)^2}{\ell_o^2} + \frac{\tau^2}{\tau_o^2}\right)} \quad (2)$$

A contour of constant  $\rho$  is an ellipse in the  $\ell, \tau$  plane and this requires that the exponent be constant, so

$$\ell^2 - 2V\tau\ell + V^2\tau^2 + \frac{\ell_o^2}{\tau_o^2}\tau^2 = K \quad (3)$$

It is desired to find the drift velocity,  $V$ , and the characteristic velocity,  $V_c = \ell_0/\tau_0$  which describes the space and time scales of the turbulence. The convenient measurement points on the ellipse are shown circled in the following sketches.



When  $\ell$  is zero (i.e.  $\rho = \rho(\tau_2, 0)$ ) we see that  $K = (V^2 + V_c^2) \tau_2^2$ . When  $\tau$  is zero (i.e.  $\rho = \rho(0, \ell_1)$ ) we see that  $K = \ell_1^2$ . So, using the notation of Briggs, Phillips and Shinn:

$$V^2 + V_c^2 = \frac{\ell_1^2}{\tau_2^2} = V_c'^2 \quad (4)$$

where  $V_c'$  is easily obtained from two recordings separated by a distance  $\ell_1$  in the  $x$  direction. Since both  $V$  and  $V_c$  are unknown, another equation is required for solution. This may be obtained by using the time lag  $\tau_1$ , for which the cross correlation is maximum at separation  $\ell_1$ . The apparent drift velocity,  $V' = \ell_1/\tau_1$ , is easily measured and can be easily related to  $V$  and  $V_c$  by noting that  $\tau_1$  occurs where  $\partial/\partial\tau(K) = 0$ . This provides the other needed equation in the independent measurable  $V'$  as

$$V^2 + V_c^2 = VV' \quad (5)$$

so that the true drift velocity  $V$  and the velocity characterizing the temporal and spatial scales of the irregularities,  $V_c$  can be calculated. We now proceed to a consideration of the cross spectra.

#### CROSS SPECTRUM ANALYSIS

If  $E_{12}(\omega)$  is the cross power spectrum between records No. 1 and No. 2, it will, in general, be complex. If  $C_{12}(\omega)$  is the real part and  $Q_{12}(\omega)$  the imaginary part, then

$$C_{12}(\omega) = |E_{12}(\omega)| \cos \omega\tau \quad (6)$$

$$Q_{12}(\omega) = |E_{12}(\omega)| \sin \omega\tau \quad (7)$$

where  $\omega\tau$  is the phase lag for the frequency component  $\omega$  between records No. 1 and No. 2 and is found as  $\arctan Q/C$ . Suppose records No. 1 and No. 2 are separated by a distance  $L$ . Then the phase lag,  $\omega\tau$ , will depend on the propagation velocity,  $V$ , of the component,  $\omega$ ; and the station separation in the direction of propagation,  $L \sin \theta$  where  $\theta$  is the angle between the line of station separation and the wave crest-line.



A quantity called coherence is often useful. It is related to the magnitude of the normalized cross power and is usually defined as

$$\text{coh} = \frac{C^2 + Q^2}{E_1 E_2} \quad (8)$$

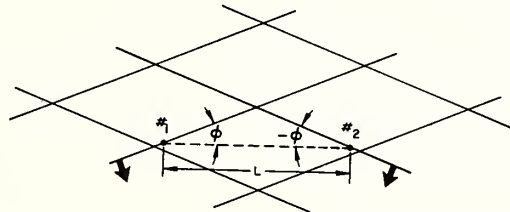
The meaning and application of coherence in geophysical and electromagnetic investigations has been reviewed in detail by Gossard and Noonkester (1967).

Several physical processes can reduce the coherence from unity.

1. The "smear" that results for the same frequency arriving from more than one direction.
2. A variable propagation velocity within the sampling period.
3. Local generation or dissipation within the recording array.
4. Significant phase change within the bandwidth of the analysis.

We will direct our attention in this paper principally to the second process, but shall first briefly discuss number one.

If wave components of the same frequency,  $\omega$ , have different  $\tau$ , the magnitude of  $(C^2 + Q^2)$  will be decreased due to "smearing" of the phase relationship between the records. This "smear" in phase could occur if the same frequency were to arrive at stations No. 1 and No. 2 from different directions,  $\phi$  and  $-\phi$ , as shown in the following sketch where the average propagation angle  $\theta$  is here taken to be zero.



Now  $\omega\tau$  is related to the station separation geometry and propagation velocity as follows:

$$\omega\tau = \frac{\omega L}{V} \sin(\theta + \phi) \quad (9)$$

or

$$\omega\tau = \frac{\omega}{V} (x \cos\phi + y \sin\phi)$$

where  $x$  is defined as the component of  $L$  in the average direction of propagation and  $y$  is the component of  $L$  normal to the direction of propagation. This dependence on geometry has been used (Cox 1962) to study the "beamwidth,"  $2\phi$ , of internal waves in the sea by measuring the normalized magnitude of the cross spectrum (the coherence) from a triangle of spaced wave recorders; and, in fact, a general theory for spatial arrays of recorders has been formulated and applied to ocean wave studies (Munk et al, 1963). In fact, the latter authors demonstrated the power of the technique by successfully measuring the aperture between New Zealand and Australia using storms in the Indian Ocean. The main effect of azimuthal "beamwidth" is to reduce the coherence of stations separated perpendicular to the mean direction of propagation.

We suggest that the velocity "bandwidth" associated with a given frequency in a time series is primarily responsible for reducing the coherence along the direction of propagation by "smearing" the phase difference for the time interval during which the sample was taken. Variations in the ambient wind field due to turbulence or other causes during the sampling interval could cause the necessary velocity changes, but they would have to be interpreted as changes in the average flow of the atmosphere over the whole height range including the wave system. It was suggested to the author by Professor C. O. Hines that the spectrum of untrapped gravity waves provides a more convincing mechanism to account for the required range of velocities associated with a given frequency.

Suppose such velocity deviations,  $v$ , are small compared with the average wave velocity,  $V$ . Then substituting  $k = \omega/V$  we find

$$\omega \tau \approx k \left\{ \left( 1 - \frac{v}{V} \right) x \cos \phi + \left( 1 - \frac{v}{V} \right) y \sin \phi \right\} \quad (10a)$$

or

$$\omega \tau \approx k \left\{ x \cos \phi + y \sin \phi - x \left( \frac{v}{V} \right) \right\} \quad (10b)$$

In writing 10b it has been assumed that the range of  $\phi$  is small so  $(v/V) \sin \phi$  can be neglected, and  $(v/V) \cos \phi$  is nearly  $v/V$ .

Calculation of the cross power requires that an average be taken over the ranges of  $\phi$  and  $v$ . Assuming the spectral density  $E = E_0$  and is independent of both  $\phi$  and  $v$ , the cross power in the wave spectrum is given by

$$C + iQ = \frac{E_0}{4\Phi v_c} \int_{-\Phi}^{\Phi} \int_{-v_c}^{v_c} e^{ik(x \cos \phi + y \sin \phi) - ikx \frac{v}{V}} dv d\phi \quad (11)$$

or

$$C + iQ = \frac{E_0 \sin\left(kx \frac{v_c}{V}\right)}{2\Phi \left(kx \frac{v_c}{V}\right)} \int_{-\Phi}^{\Phi} e^{ik(x \cos \phi + y \sin \phi)} d\phi \quad (12)$$

The integral over the  $\sin(ky \sin \phi)$  function is odd and disappears because  $\phi$  is symmetrical about zero so that

$$C + iQ = \frac{E_0 \sin\left(kx \frac{v_c}{V}\right)}{2\Phi \left(kx \frac{v_c}{V}\right)} \int_{-\Phi}^{\Phi} \cos(ky \sin \phi) e^{ikx \cos \phi} d\phi \quad (13)$$

or for small  $\phi$

$$C + iQ \approx \frac{E_0 \sin\left(kx \frac{v_c}{V}\right)}{2\Phi \left(kx \frac{v_c}{V}\right)} e^{ikx} \int_{-\Phi}^{\Phi} \cos(ky \phi) e^{\frac{-ikx\phi^2}{2}} d\phi \quad (14)$$

The integral can be evaluated by writing it as Fresnel Integrals (see, for example, Cox (1962), Gossard and Noonkester (1967)). For simplicity, consider the special case of  $x = 0$ , i.e., separation of stations normal to the direction of propagation. For this case,

$$C + iQ \approx E_0 \frac{\sin ky\phi}{ky\phi} \quad (15)$$

shows the way the cross power depends on station separation in the y direction.

The magnitude of  $\frac{C + iQ}{E_0}$  was calculated from Equation (14) for various orientations of the line of receiver separation ranging from  $x = 0$  to  $y = 0$  and assuming  $v_c = 0$ . Three values of  $\phi$  were assumed and the resulting curves for magnitude of the cross spectrum are shown plotted in Figure 1(a). It was assumed that  $L/\lambda = \sqrt{2}$  where  $\lambda$  is the wavelength of the frequency component considered. For comparison, the corresponding contours calculated from Equation 15 are shown in Figure 1(b). The agreement is remarkable and suggests that when  $2\phi$  is less than one radian the magnitude of the cross spectrum or  $\sqrt{\text{coherence}}$  is very well approximated by the simple expression (15) which depends only on the component of station separation perpendicular to the direction of propagation. This shows that angular "beamwidth"  $2\phi$ , has virtually no role in reducing the coherency along the direction of propagation while the velocity "bandwidth",  $2v_c$ , can do so effectively.

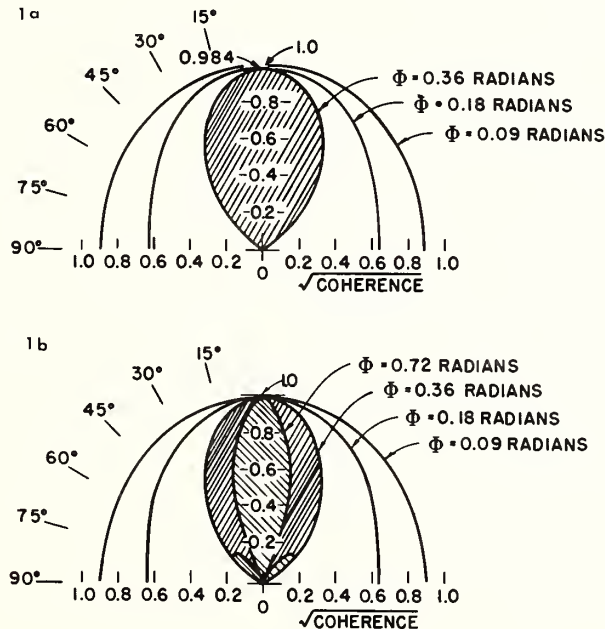


**Figure 1.** Polar diagram of  $\sqrt{\text{coherence}}$  showing dependence of direction of station separation on direction at propagation. Assumed station separation is  $\sqrt{2}$  wavelengths. Magnitude of coherence is given by distance of any point on the curves from the origin. Units of  $\sqrt{\text{coherence}}$  are indicated on both the horizontal and vertical axes. Zero angle on the polar diagram means the stations are separated in the direction of propagation (the x direction). TOP: Rigorous plot from Equation 14 (assuming  $v_c = 0$ ) after writing in terms of Fresnel Integrals. BOTTOM: Corresponding plot from Equation 15 using only y component of station separation. Excellent agreement shows that coherence depends almost exclusively on the component of station separation perpendicular to the direction of propagation.

The phase information in the cross spectrum provides the travel time,  $x/V$  of each frequency component between stations. It is mostly contained in the factor  $e^{ikx}$  which is outside the integral in Equation 14. Therefore, to a good approximation for small beamwidths

$$\frac{C + iQ}{E_0} \approx e^{ik\beta x} \frac{\sin\left(kx \frac{v_c}{V}\right)}{kx \frac{v_c}{V}} \frac{\sin(ky\Phi)}{ky\Phi} \quad (16)$$

where  $\beta$  includes the modification of the phase lag or lead between stations due to the integration over  $\phi$ .  $\beta$  is slightly less than unity because the average velocity in the  $x$  direction of the wave ensemble covering the angular range  $2\phi$  is slightly higher than the phase velocity  $V$  since the wave crests, in general, make a slight angle with respect to the  $x$  direction. For many purposes  $\beta$  can be considered to be unity.

It seems that Equation 16 provides a simple expression for the spatial pattern of the cross spectrum which offers potential for calculating not only the direction and speed of individual frequency components, but also a measure of the velocity bandwidth in the medium and the "long crestedness" or  $y$  scale,  $\lambda_y = \lambda/\Phi$ , of the wave structure.

For no velocity variation ( $v_c = 0$ ) coherence will remain unity in the direction of propagation to the degree of approximation involved in identifying Figure 1(a) with 1(b). This seems a reasonable result by analogy with the corresponding result for cross correlation. The maximum cross correlation of a frozen, (temporally non-varying) but spatially randomly inhomogeneous medium drifting at constant velocity across fixed recording sites remains unity regardless of recorder separation in the direction of movement. The amount of separation merely determines the lag required between the time series for a correlation of unity.

In summary, it is suggested that coherence between records for a triangle of stations can be used to separate the spatial and temporal characteristics of a moving pattern of irregularities in a more effective way than cross-correlation since it provides the information for all the various frequencies comprising the spectrum. In general, the velocity corresponding to the phase,  $\beta kx$ , is analogous to the "apparent drift velocity,"  $V'$ ; and the velocity  $v_c(\omega)$  represents the degradation in coherence due to turbulence and is roughly analogous to  $V_c$ . Finally,  $\lambda_y(\omega)/\lambda(\omega)$  is a measure of the "long crestedness" or anisotropy of the wave pattern at frequency  $\omega$ . The characteristic velocity  $v_c(\omega)$  may be obtained from the coherence between stations separated in the direction of propagation of the particular frequency component and  $\lambda_y(\omega)/\lambda(\omega)$  may be obtained from stations separated normal to the direction of propagation. The direction and magnitude of  $V$  is, in practice, obtained from the time lag in the records between stations which is  $\omega^{-1} \arctan Q/C$ . If  $v_c(\omega)$  is a result of turbulence only, it contains information about the turbulent velocity structure of the propagation medium in which the wave structure is imbedded.

#### APPARENT AND TRUE WAVE VELOCITIES

So far, the power in the wave spectrum has been considered to be independent of wave number and therefore independent of  $v_c$ . We proceed now to consider the case of a wave spectrum of the form  $E = E_0 k^{-n}$ . We will consider the one-dimensional case and will compare the results with the one dimensional correlation analysis in Section 1 to obtain expressions corresponding to those of Briggs, Phillips and Shinn. In the present interpretation, in the one dimensional limit the dimension of the wave perpendicular to the direction of propagation approaches infinity which means the "beamwidth,"  $2\phi$  approaches zero.

Now, as in developing Equations 10(a) and 10(b), we assume that a certain frequency,  $\omega$ , is associated with a varying wavelength due to velocity fluctuations. Therefore

$$k = \frac{2\pi}{\lambda_0 + \delta\lambda} = \frac{2\pi}{\lambda_0} \left( \frac{1}{1 + \frac{v}{V}} \right) = k_0 \frac{1}{1 + \frac{v}{V}} \quad (17)$$

and

$$E(k) = E_0 k^{-n} = E_0 k_0^{-n} \left( 1 + \frac{v}{V} \right)^n \quad (18)$$

Equation 11 now becomes

$$\frac{C + iQ}{E_0 k_0^{-n}} \approx \frac{1}{4\Phi v_c} \int_{-\Phi}^{\Phi} \int_{-v_c}^{v_c} \left( 1 + \frac{v}{V} \right)^n e^{ik_0 \left[ x \left( 1 - \frac{v}{V} \right) \cos \phi + y \left( 1 - \frac{v}{V} \right) \sin \phi \right]} dv d\phi \quad (19)$$

Neglecting terms higher than 2nd order in  $\frac{v}{V}$ ,

$$\begin{aligned} \frac{C + iQ}{E_0 k_0^{-n}} \approx \frac{1}{4\Phi v_c} \int_{-\Phi}^{\Phi} \cos(k_0 y \sin \phi) e^{ik_0 x \cos \phi} & \left[ \int_{-v_c}^{v_c} e^{-ik_0 x \frac{v}{V} \cos \phi} dv \right. \\ & \left. + n \int_{-v_c}^{v_c} \frac{v}{V} e^{-ik_0 x \frac{v}{V} \cos \phi} dv + \frac{n(n-1)}{2} \int_{-v_c}^{v_c} \left( \frac{v}{V} \right)^2 e^{-ik_0 x \frac{v}{V} \cos \phi} dv \right] d\phi \end{aligned} \quad (20)$$

The integrations over  $\sin(k_0 x \frac{v}{V} \cos \phi)$ ,  $\frac{v}{V} \cos(k_0 x \frac{v}{V} \cos \phi)$  and  $\left( \frac{v}{V} \right)^2 \sin(k_0 x \frac{v}{V} \cos \phi)$  are zero because the functions are odd so that

$$\frac{C + iQ}{E_0 k_0^{-n}} \approx \frac{1}{2\Phi} \int_{-\Phi}^{\Phi} \cos(k_0 y \sin \phi) e^{ik_0 x \cos \phi} \frac{\sin(k_0 x \frac{v_c}{V} \cos \phi)}{k_0 x \frac{v_c}{V} \cos \phi} \left[ 1 - i \frac{n}{3} k_0 x \left( \frac{v_c}{V} \right)^2 \cos \phi \right] d\phi \quad (21)$$



So neglecting terms in the product  $\phi \left(\frac{v_c}{V}\right)^2$  and 3rd or higher order terms in  $\frac{v_c}{V}$  we get

$$\frac{C + iQ}{E_0 k_0^{-n}} \cong \frac{\sin\left(k_0 x \frac{v_c}{V}\right)}{k_0 x \frac{v_c}{V}} e^{ik_0 x \left[1 - \frac{n}{3} \left(\frac{v_c}{V}\right)^2\right]} \frac{1}{2\Phi} \int_{-\Phi}^{\Phi} \cos(k_y \sin \varphi) e^{-ik_0 x \frac{\Phi^2}{2}} d\varphi \quad (22)$$

From Equation 22 it is evident that the phase lag between two recorders separated by distance  $x$  in the direction of propagation is  $k_0 x \left[1 - \frac{n}{3} \left(\frac{v_c}{V}\right)^2\right]$  when  $\phi \ll 1.0$  so that the apparent wave number for small  $v_c/V$  is

$$k' = \frac{2\pi}{\lambda'} \cong \frac{2\pi}{\lambda \left[1 + \frac{n}{3} \left(\frac{v_c}{V}\right)^2\right]} \quad (23)$$

and

$$V' = f \lambda' = f \lambda \left[1 + \frac{n}{3} \left(\frac{v_c}{V}\right)^2\right] \quad (24)$$

Finally,

$$VV' = V^2 + \frac{n}{3} v_c^2 \quad (25)$$

Equation 25 is clearly of the same form as Equation 5 and indicates that a correction for the apparent velocity should be made for wave propagation characterized by continuous wave spectra. Equation 25 indicates that the apparent velocity found by cross spectrum analysis will be the true velocity only when the wave spectrum is white ( $n=0$ ) or when the velocity range associated with a given frequency is zero ( $v_c = 0$ ).

The velocity bandwidth parameter,  $\frac{v_c}{V'}$ , can be found from the decrease of coherence in the direction of propagation as described in Section 4. This can be inserted into Equation 25 to obtain the true velocity,  $V$ , if  $n$  is known.  $n$  can be determined from the power spectrum if the form of the power spectrum is dominated by the wave spectrum rather than turbulence.

## RESULTS FOR WAVES IN THE LOWER IONOSPHERE

As an example of the conclusions to be derived from this kind of analysis, radio fading data recorded on 13-14 June 1966 were analysed.

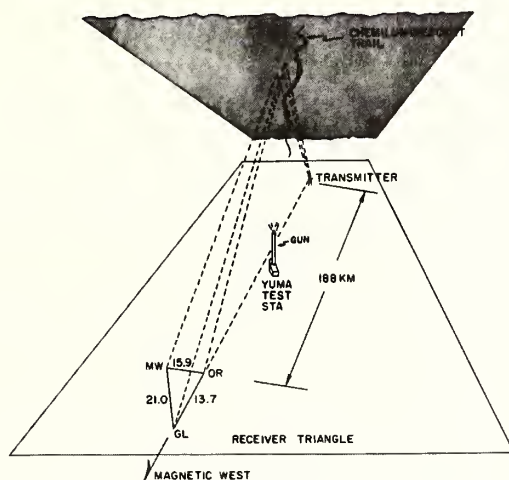


Figure 2. Perspective view of geometry of experiment

The configuration of the experiment is shown in Figure 2 and the movement of the radio diffraction pattern across the receiver triangle was used to deduce the ionospheric structure at a height of about 90 km. Samples of the amplitude and phase records recorded for 8 hours during the night are shown in Figure 3.

A cross spectrum analysis of the records sampled each minute gave the results shown in Table I for the coherence, anisotropy ( $\lambda_y/\lambda$ ) and velocity bandwidth ( $v_c$ ) of the important spectral lines. (The speeds of movement of the patterns at the ground are twice those shown which apply to the irregularities at the ionosphere. Note also that  $\lambda_y/\lambda \approx \phi^{-1}$  for small  $\phi$ ).

The function  $\frac{\sin x}{x}$  is inconvenient to work with when solving for the values of  $v_c$  and  $\lambda_y$  for an actual triangle of recorders, because there will generally be no leg of the triangle aligned in or normal to the direction of propagation. However any two legs in the triangle are, in principal, sufficient to solve for  $v_c$  and  $\lambda_y$  with the third leg providing redundancy and evidence of internal consistency. In the above example the small argument approximation was used for  $\frac{\sin x}{x}$  except for the smaller coherence values. For those legs of the triangle with very small coherence a modification of the small argument approximation was used which provided a better fit to the function at small values of coherence. The values of  $v_c$  and  $\lambda_y/\lambda$  given in Table I represent averages from the three pairs of legs of the triangle.

The average of the product of frequency and the spectral power of the three stations is shown in Figure 4 along with the speed,  $V'$ , and the direction of movement of the component frequencies. The spread shown in the curves of speed and direction is a measure of the reliability or confidence to be given the analysis. It has been discussed in more detail by Gossard (1967). For a triangle of receivers the three combinations of pairs of legs yield an overdetermined solution set and a redundancy of physical information which provides a measure of confidence in the analysis. More than three receivers would increase the redundancy and permit "best fit" procedures as described by Fedor (1967) and Munk et al [loc cit]. More receivers would also permit resolution of the "lead vs lag" ambiguity problem which plagues the 3 receiver analysis. In the three station analysis three velocity vectors are in general obtained instead of one, and the width of the curves is the range of the three values of speed and direction. The minimum possible thickness of the direction curve is three degrees which

TABLE I

T (Min)	MW-OR Coh	MW-GL Coh	OR-GL Coh	$V'$ (mps)	$V$ (mps)	$V_c$ (mps)	$\lambda$ (km)	$\phi^{-1}$ or $\lambda_y/\lambda$	$\lambda_y$ (km)
120	0.66	0.48	0.79						
60	0.61	0.24	0.61						
40	0.68	0.29	0.51						
30	0.57	0.56	0.65						
24	0.70	0.59	0.83	27	27	6.3	38.9	1.23	47.6
20	0.78	0.65	0.85	28	28	8.2	33.6	2.12	71.4
17	0.65	0.67	0.85	33	32.4	11.1	33.7	1.99	66.8
15	0.74	0.72	0.85	40	39.2	14.4	36.0	2.42	87.2
13.3	0.83	0.76	0.84	46	45.4	13.3	36.7	1.86	68.3
12.0	0.69	0.60	0.86	44	43.3	13.9	31.7	2.15	68.3
10.9	0.41	0.14	0.70						
10.0	0.14	0.01	0.72						
9.2	0.09	0.04	0.76	46	45.1	15.5	25.4	1.53	38.8
8.6	0.16	0.24	0.76	39	38.6	9.8	20.1	2.20	44.3
8.0	0.09	0.12	0.62						
7.5	0.22	0.03	0.37						
7.1	0.15	0.04	0.36						
6.7	0.14	0.04	0.50	38	35.3	8.6	15.3	2.05	31.4
6.3	0.25	0.30	0.65	40	36.0	10.3	15.1	3.65	55
6.0	0.34	0.45	0.71	49	45.3	11.9	17.6	3.00	53
5.7	0.34	0.38	0.56	52	48.3	12.5	17.8	2.50	44.2
5.5	0.27	0.13	0.29	43	41.0	8.6	14.2	2.57	36.6
5.2	0.28	0.19	0.09	44	42.1	8.5	13.7	2.50	34.5
5.0	0.03	0.38	0.01						
4.8	0.10	0.69	0.08	27	26.5	3.5	7.8	4.33	33.8
4.6	0.23	0.32	0.29	38	37	6.0	10.5	3.44	36.1
4.4	0.19	0.16	0.59	44	42.3	8.0	11.6	3.75	43.6
4.3	0.09	0.24	0.60	47	44.8	9.6	12.1	4.20	50.05
4.1	0.13	0.15	0.44	52	50	10.7	12.8	3.05	38.8
4.0	0.02	0.15	0.29	52	49	11.1	12.5	2.85	36.6
3.9	0.12	0.46	0.16	48	46.3	8.6	11.2	3.30	37.0
3.75	0.18	0.57	0.08	53	51	9.6	11.9	2.15	25.8
3.64	0.10	0.20	0.10						
3.53	0.04	0.11	0.17						
3.42	0.03	0.12	0.12						
3.33	0.04	0.04	0.09						
3.24	0.04	0.16	0.35						
3.16	0.07	0.30	0.50	45	44	6.4	8.5	5.35	45.6
3.08	0.004	0.09	0.44	47	45.9	7.0	8.7	4.6	40.3
3.00	0.10	0.06	0.11	52	50.7	7.9	9.4	3.6	33.8
2.93	0.34	0.19	0.08	52	51.1	6.6	9.1	3.7	33.1
2.86	0.21	0.28	0.14	48	47.2	5.9	8.2	4.15	34.2
2.79	0.15	0.40	0.21						
2.73	0.28	0.20	0.28						
2.67	0.03	0.04	0.01						
2.61	0.03	0.004	0.19						
2.55	0.16	0.14	0.22						
2.50	0.33	0.07	0.07						
2.45	0.14	0.08	0.30						
2.40	0.006	0.10	0.36						

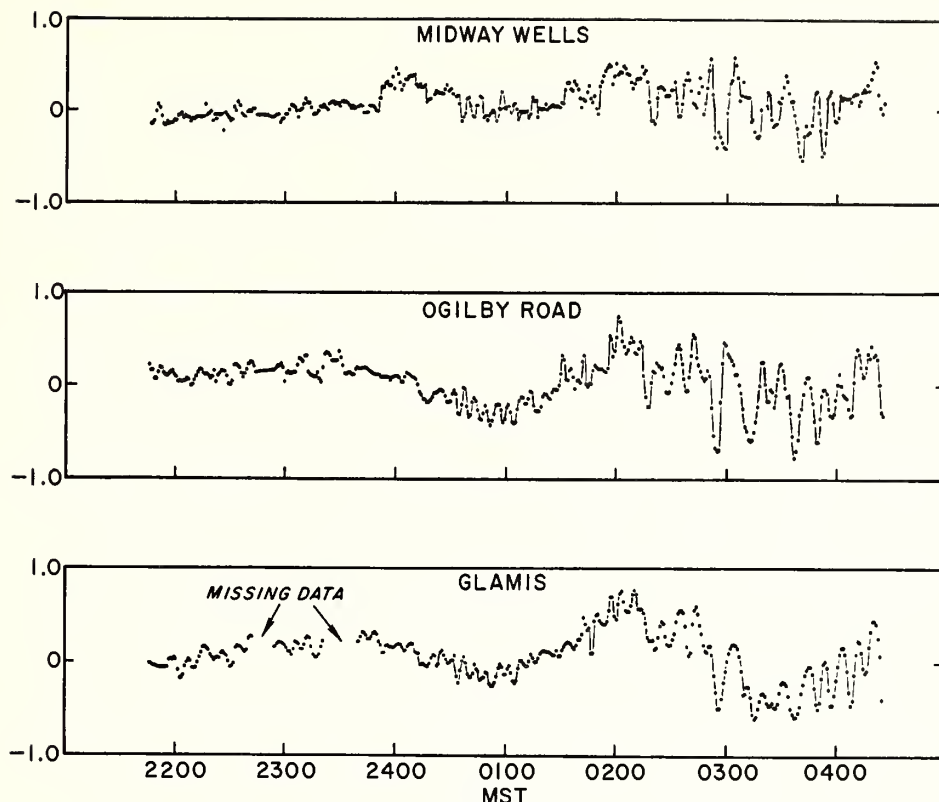


**Figure 3.** Normalized amplitude records from three receiver sites on night of 13-14 June 1966. Radio frequency is 44.3 kHz.

is the resolution of the direction analysis. The resolution in velocity is 4 mps. The curves are not plotted when the spread is greater than 10 degrees in direction or 10 mps in velocity. It is immediately clear that the confidence is best near the center of the spectral lines and falls apart between lines.

It is evident that the magnitude of the velocity range,  $2 v_c$ , required to explain the coherence pattern is not unreasonable. The values of  $v_c/V$  and  $\lambda/\lambda_y$  are not as small as one would like in using the approximations of "narrow beams" and "small bandwidth", which were assumed in the derivation of the elementary functional expressions. However, as pointed out earlier, the calculations are not very sensitive to these assumptions and these results should at least serve as a useful illustrative example of the power of the method. The true velocity,  $V$ , shown in Table I was calculated using values of  $n$  obtained from the average power spectrum of the three recording sites. For the lower frequencies  $n = 0.45$ . For periods less than 8 minutes  $n = 3.3$ . For the relatively small ratios of bandwidth of velocity to wave velocity characterizing this sample the correction to the apparent velocity is small and not very significant compared with other factors. This is especially true at the lower frequencies where the spectrum is fairly flat.

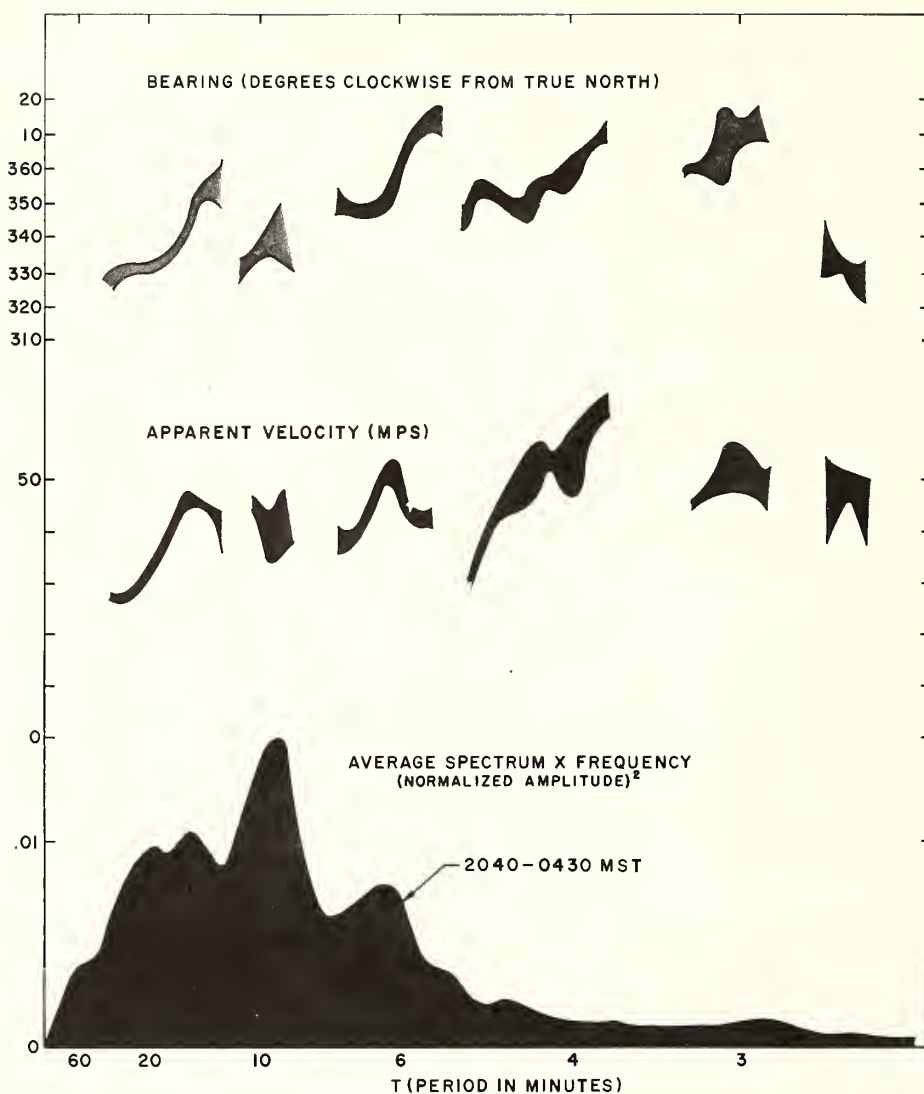


Figure 4. Spectra of amplitude of 44.3 kHz radio records on night of 13-14 June 1966. TOP: Spectra of direction and velocity of movement of irregularities from analysis of cross spectra from a triangle of receivers. BOTTOM: Product of frequency and average power spectrum of records from the three receiver sites.



Since for this case the speed and direction of movement is fairly constant over the whole frequency range we might expect to find good agreement between the results of the cross spectrum analysis and a cross correlation analysis according to the method of Briggs, Phillips and Shinn. This analysis will permit us to test the compatibility of the results of the two interpretations of turbulent characteristic velocity. For this comparison the complete theory for anisotropic irregularities as developed by Phillips and Spencer (1955) and Yerg (1959) was used. The results gave:

$$V' = 45 \text{ mps}, V = 44 \text{ mps}, V_c = 4.5 \text{ mps}, R = 1.67$$

$$\text{True drift direction} = 348^\circ \text{ clockwise from North}, \psi = 260^\circ$$

where  $R$  is the ratio of the major axis of the characteristic ellipse to the minor axis, and  $\psi$  is the direction of the major axis. The estimated reading accuracy in obtaining  $V'$  is  $\pm 2.5$  mps, and  $V_c$  is very sensitive to  $V'$ . Over this range of uncertainty  $V_c$  varies from 0 to 9 mps. Comparing equations 5 and 25 and assuming an average value of  $n = 1.5$  we find  $v_c = \sqrt{2} V_c$ . It seems clear that the two approaches lead to compatible results for the records here considered, with the cross spectrum approach permitting the added capability of examining individual frequencies.

Because of the large slope of the spectrum on each side of the spectral lines, the values near the middle of the lines should most nearly represent the true conditions. Since the "signal-to-noise ratio" is also greatest near the center of the lines it is reasonable to conclude that these values are the most reliable. If these values are studied it is apparent that there is a trend toward larger wave velocity and smaller velocity bandwidth as frequency increases. Since the change is not large ( $V = 40 \rightarrow 50$  mps,  $v_c = 14 \rightarrow 8$  mps) compared with the scatter of individual frequencies, these trends may not be significant. The situation is further obscured by the fact that the data sample is not statistically stationary in time, and some frequencies are more prominent than others at different times during the night. Therefore, different wind and wave conditions may apply to different lines in the spectrum. Figure 5 is chosen to illustrate the temporal variability; 5a is the spectrum at GL for the period 2344-0124 (see record shown in Figure 3) and 5b is the spectrum from 0315-0420. Although the same basic lines are present in both records their strength differs greatly. The line at 9 minute period has increased tremendously between the two time periods. This line is actually very narrow and appears broader in the average spectrum of the three sites because of variations in the frequency of its peak. In spite of the difference in appearance of the power spectra, figure 6 shows that the principal features of the directional spectra show impressive similarities. There is a significant shift in the direction of the line for 9 minute period and some overall changes in direction at the higher frequencies, but considering the relatively great scale expansion the qualitative similarity is encouraging.

It is unlikely that the D-Region is a shallow diffracting screen so that radio fields are a simple picture of ionospheric irregularities. In fact, from analysis of the radio records at 44.3 kHz and 21.6 kHz, and from the cross spectra of phase vs amplitude, it is almost certain that the lower frequencies in the records (15-30 minute periods) are predominantly Doppler in origin. On the other hand, the line of 5.5-6.0 minutes period is almost certainly a direct result of a wave-like structure and probably the line of 3.0-3.2 minutes period is also due to waves. The line at 9 minutes period (prominent during the last 2 hours of the night) and the line at 4-5 minutes period are of doubtful origin. Near the middle of these lines the phase relationship between amplitude and phase is 90 degrees and 270 degrees respectively; but it is changing very rapidly, ranging over a complete cycle. It seems probable that these lines are a mixture in which large wave-like traveling irregularities contribute Doppler frequency components due to off-path reflections. The change in apparent velocity with frequency so noticeable in the lines centered at 20 minutes period and at 4.5 minutes period undoubtedly results from the change in geometry controlling the Doppler phenomenon as the off-path irregularities move (see Gossard and Paulson, 1968a). It is important to note that all the plotted velocities are one-half the indicated velocities of the diffraction pattern at the ground. This correction is based on the assumption that the ionospheric irregularities move at one-half the speed of the ground patterns and is not appropriate if the Doppler mechanism dominates. For the sake of consistency it has been applied to all frequencies in the spectrum. If the Doppler mechanism predominates, the apparent velocity of the interference pattern across the receiver triangle would vary approximately inversely as the fluctuation period,  $T$ . This may partially explain the trend toward higher velocities at higher frequencies noted earlier. However the trend toward smaller velocity bandwidth would be expected from the wave hypothesis if the higher frequencies were the more completely trapped.

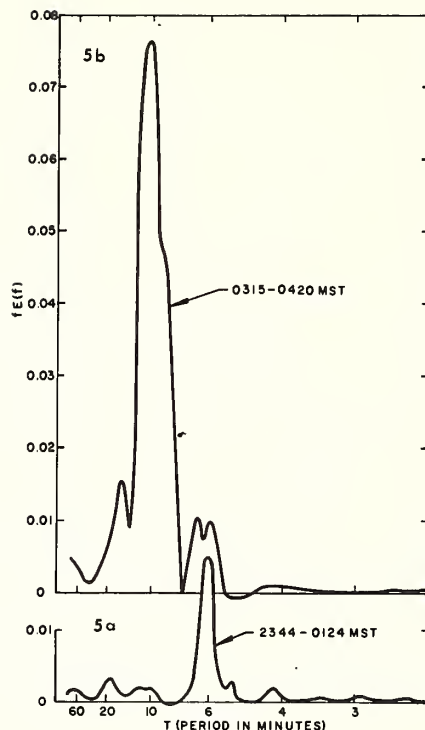


Figure 5. Spectra from two separate periods during the night of 13-14 June showing temporal non-stationarity. From Glamis receiver site.

A potentially important factor which has so far been neglected is the ambient wind stream in which the waves are imbedded. A few wind measurements were obtained from chemiluminescent trails injected by ballistic probe. These measurements have been provided by Murphy and Bull (1967), and have been compared with the portion of the radio records between 2344 and 0130 by Gossard and Paulson (1968b). It was concluded that the wind probably had an important effect on the measured frequency, velocity and direction of movement of the periodic structure. Furthermore, both the speed and direction of the wind change rapidly with height near the height of radio reflection. Although these factors probably do not have a major bearing on the conclusions of the present paper they make it very difficult to deduce the reason for the trends noted in the spectra because the radio reflection occurs over a depth of 2 or 3 kilometers. If the size or speed of either the waves or turbulence varies with height this variation could appear as a trend in the frequency spectrum. The ratios  $v_c/V$  and  $\lambda_y/\lambda$  and the wavelengths  $\lambda$  and  $\lambda_y$  should be little affected, but the magnitudes of  $v_c$  and  $V$  may be considerably influenced by the background wind.

This data sample was chosen because it is the best data recorded to date showing convincing evidence of wave motion in the lower ionosphere. Since the variance and spectrum of the records change through the night, the data does not possess the statistical stationarity desirable if confidence levels are to be calculated for prediction purposes. However prediction is not the purpose of the present analysis and the non-stationarity should not seriously alter the main conclusions about the irregular structure.

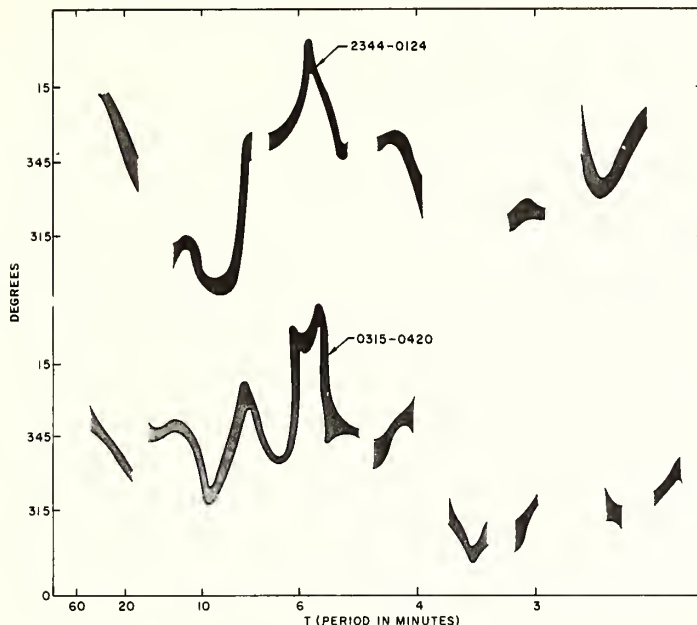


Figure 6. Directional spectra for the same time periods as Figure 5.

In conclusion, some comments concerning the assumption implicit in the foregoing discussion, that the prominent lines in the spectra are a result of wave motion, is appropriate. Only one wind sounding was obtained from a chemiluminescent trail on the night of 13 June 1966 and that sounding was taken at 2214 MST. It showed the wind below 93 km to have a speed of about 40 mps toward 160° clockwise from north. Since this wind is almost opposite to the direction of movement of the ionization irregularities it suggests that the movement of the irregularities is dominated by wave propagation. Gossard and Paulson pointed out that the resulting waves deduced using this wind profile are compatible with the 1st gravity wave mode for a realistic atmosphere. This is probably the correct interpretation; although the fact that the principal "wave" activity occurred during the morning hours makes the appropriateness of the wind sounding questionable. The patterns of movement for the period 2145-2344 are less definite than those of the other two-hourly intervals, but the directional spectrum is sufficiently similar to the others to suggest little change in the wind regime throughout the night.

#### REFERENCES

- Briggs, B.H., G.S. Phillips, and D.H. Shinn, The analysis of observations on spaced receivers of the fading of radio signals, *Proc. Phys. Soc. London*, B, 63, 106-121, 1950.
- Cox, C.S., *The Sea*, Chapt. 22, Editor, M. Hill, Vol. I, Internal waves, Part II, Interscience Publishers, pp. 752-763, 1962.
- Fedor, L.S., A statistical approach to the determination of three-dimensional ionospheric drifts, *J. Geophys. Res.* 72 pp. 5401-5415, 1967.
- Gossard, E.E., and V.R. Noonkester, A guide to digital computation and use of power spectra and cross-power spectra, Technical Document 20, Naval Electronics Laboratory Center, 1967.
- Gossard, E.E., The apparent movement of the spectral components in fading records of ionospherically reflected radio waves, *Jour. Geophys. Res.* V. 72, No. 5, pp. 1563-1569, 1 Mar 1967.
- Gossard, E.E. and M.R. Paulson, Movement of off-path ionospheric irregularities deduced from short-path VLF measurements, *J. Atmos. Terr. Phys.* 1968a, (In press).
- Gossard, E.E. and M.R. Paulson, A case study of periodic structure in the atmosphere near the 90 km level, *Jour. Atmos. Terr. Physics*, Vol. 30, pp. 885-896, 1968b.
- Munk, W.H., G. Miller, F.W. Snodgrass and N.F. Barber, Directional recording of swell from distant storms, *Phil. Trans. Roy. Soc. London*, Vol. 255, pp. 505-584, 1963.
- Murphy, C.H. and G.V. Bull, HARP 5-inch and 16-inch guns at Yuma Proving Ground, Arizona, BRL MR 1825, 1967.
- Phillips, G.J., and M. Spencer, The effects of anisometric amplitude patterns in the measurement of ionospheric drifts, *Proc. Phys. Soc. of London*, Series B, 68, pp. 481-492, 1955.
- Yerg, D.G., An analysis of drifts of the signal pattern associated with ionospheric reflections, *J. Geophys. Res.*, 64, 1, pp. 27-31, 1959.



# A Hydromagnetic Coupling of Acoustic Gravity Waves with the Ionized Atmosphere

S. Kato\*, C. A. Reddy & S. Matsushita

High Altitude Observatory  
Boulder, Colorado 80302

Acoustic gravity waves give rise to disturbances in the ionization density in the ionosphere. These disturbances consist of two components. One is a duplication of the neutral gas perturbation by the gravity waves, but the other is controlled by the electrostatic field  $E_0$  and the geomagnetic field  $B_0$  in the ionosphere. The latter component (the H. M. component) travels with the ion velocity if the wave propagation vector is not orthogonal to  $B_0$  and with the electron velocity if the wave vector is orthogonal to  $B_0$ . In the uniform medium with infinite extension, the H. M. component cannot be generated, but if there is a sudden change in the propagation of gravity wave or in the electric field, a conversion from the G. W. component to the H. M. component may occur. Total reflection or propagation across the equatorial electrojet of gravity wave may induce such a conversion.

## I. Introduction

It is possible that certain irregularities in ionization are produced by acoustic gravity waves (G.W.) in the ionosphere (e.g. Hines 1960). For instance, the traveling ionospheric disturbances (TID) and some types of sporadic E may be the manifestation of ionization irregularities generated by G.W.'s. However, the geomagnetic field ( $B_0$ ) and the electrostatic field ( $E_0$ ) may complicate the situation and raise a question as to how irregularities are produced and move under such circumstances. Answer to this question is essential for interpreting observations by radio wave technique, which can detect only the ionization irregularities.

Movement of ionization irregularities has been studied intensely in recent years (e.g. Kato 1965, Tsedilina 1965, Kato 1967). It is found that field-aligned irregularities behave as a space charge wave which travels approximately with electrons, but non-field aligned irregularities move bodily and approximately along with ions. However, this theory, which may be denoted MCKT theory after Martyn (1953), Clemmow et al. (1955), Cole (1960), Kato (1963) and Tsedilina (1965), can answer only the question as to how irregularities move in the presence of  $E_0$  and  $B_0$  once they exist (Kato 1965). No source producing them is considered (Kato 1968). This may be likened to the free motion of a dynamical system.

In this paper a gravity wave is introduced as a source function which produces ionization irregularities. The air motion accompanying gravity wave drives electric current  $J$  which further produces a hydromagnetic force ( $J \times B_0$ ) causing convergence or divergence of ionization. The photoionization and recombination rates are perturbed by a gravity wave (Hooke 1967). This will also be discussed. The reaction of ionization motion upon neutral gas becomes effective over a time scale  $t_0$ , which equals  $\rho/\sigma_{1,2} B_0^2$  where  $\rho$  = total mass density,  $\sigma_{1,2}$  = Pedersen and Hall conductivity (e.g. Kato 1965). Since  $t_0 > 30$  min through the ionosphere, this means that the produced ionization irregularities cannot modify the behavior of gravity wave with period less than, say 30 minutes. In this paper the effects of gravity waves with periods of about 20 minutes will be considered so that the reaction of ionization on the neutral medium can be neglected.

## 2. Theory

The ambient gas is assumed to be uniform in the absence of perturbations. This simplification is necessary for dealing with the basic questions of the problem. A Cartesian coordinate is chosen so as the  $z$  axis to be along  $k$ , and  $B_0$  is taken to be in the  $x$ - $z$  plane (Fig. 1). The gravity wave perturbation velocity  $U$  is assumed to be strictly transverse to  $k$  and to be in the  $x$ - $y$  plane. This is approximately true except for high frequencies approaching the Brunt-Vaisala frequency. Since  $\text{div } J = 0$ ,  $J_1$  the perturbation in  $J$  is

\* On leave from Kyoto University, Kyoto



orthogonal to  $\underline{k}$  and  $(\underline{j} \times \underline{B}_0)$  has a longitudinal component along  $\underline{k}$  if  $\underline{k}$  is not along  $\underline{B}_0$ . This force tends to converge or diverge ionization, producing irregularities. The absorption of ionizing radiation, the collision frequencies and the electron temperature are also perturbed by G.W. and contribute to the production of ionization irregularities. The equation of continuity is as follows.

$$\frac{\partial n}{\partial t} + \frac{\partial}{\partial z} (n V) = q - L \quad (2.1)$$

where

- $n$  = electron number density
- $V$  = velocity of ionization
- $q$  = production rate of ionization
- $L$  = loss rate

We consider only the case of small amplitude gravity wave. We consider values of  $\psi \ll \arctan (\sigma_0/\sigma_1)^{1/2}$  where  $\psi$  = angle between  $\underline{k}$  and  $\underline{B}_0$  and  $\sigma_0$  = parallel conductivity. This means  $\psi \ll 87^\circ$  at 100 km. Note that  $(\sigma_0/\sigma_1)$  increases with height. Under this condition the polarization field, being along  $\underline{k}$  (Fig. 1), in the presence of irregularity in ionization dissipates along the highly conducting lines of force of geomagnetic field (Kato 1966). As a result

$$|\underline{E}_p| \ll |\underline{U} \times \underline{B}_0| \quad \text{or} \quad |\underline{E}_0| \quad (2.2)$$

where  $\underline{E}_p$  = electric polarization field due to irregularities

$\underline{U}$  = velocity amplitude of gravity waves

The velocity of (neutral) ionization  $\underline{V}$  is given as

$$\underline{V} = \frac{\underline{j} \times \underline{B}_0}{n(m_e \nu_e + m_i \nu_i)} + \underline{U} \quad (2.3)$$

where

$\underline{j}$  = electric current density

$\nu_{e,i}$  = collision frequencies of electrons and ions

$m_{e,i}$  = mass of electrons and ions

Ohm's law is  $\underline{j} = [\sigma] (\underline{E}_0 + \underline{U} \times \underline{B}_0)$  (2.4)

where  $[\sigma]$  = conductivity tensor (e.g. Maeda and Kato 1966). Then, (2.1) becomes

$$\frac{\partial n_1}{\partial t} + V_0 \text{grad } n_1 + \beta n_1 = P \quad (2.5)$$

where

$$P = q_1 - \beta_1 n_0 - n_0 \text{div } \underline{V}_1 \quad (2.6)$$

Subscript 1 denotes perturbation which is assumed as to be small enough to allow the first order perturbation approximation. Assuming  $L = \beta n$ , we have  $q_0 = \beta_0 n_0$  in the background uniform plasma. Putting  $P = A \sin (\omega t - kz)$  where  $\omega$  and  $k$  are the angular frequency and wave vector of a given G.W. travelling along the  $z$  direction, the general solution of (2.5) is as follows:

$$n_1 = \frac{A k V_1}{\sqrt{(\omega - k V_{0z})^2 + \beta^2}} \sin [\omega t - kz + \delta] + \exp \left( -\frac{\beta}{V_0} z \right) f \left( t - \frac{z}{V_{0z}} \right) \quad (2.7)$$

where

$$\tan \delta = -\frac{\omega - k V_{0z}}{\beta}$$

The first term in the right-hand side of (2.7) gives an ionization perturbation moving with the exciting G. W., but the second term gives an ionization perturbation which moves with  $V_0$ , i.e. approximately the ion velocity in the ambient plasma. The first term may be called G. W. component and the second H. M. (hydromagnetic) component. It is the H. M. component which has been discussed in the M. C. K. T. theory (e. g. Kato 1965). This H. M. component is assumed here to be excited at boundary (at  $z = 0$ ) where  $n_1$  is different from the G. W. component proportional to  $\sin(\omega t + \delta)$  at  $z = 0$ . Sudden changes in  $V_0$  or  $k$  may produce such discontinuous boundary and H. M. component in  $n$ .

A conversion of G. W. component to H. M. component may happen around the height at which the gravity wave reflects almost totally. Consider a G. W. which reaches  $z = z_0$  from  $z < 0$  and is reflected totally;  $P = A \sin \omega t \neq 0$  for  $z < 0$  and  $P = 0$  for  $z > 0$ . Note that  $k$  becomes very small near  $z = 0$  and put zero in  $P$  for simplification. Then, if  $V_{0z}$  is uniform for  $z \geq 0$  and positive, for  $z < 0$

$$n_1 = A \frac{\sin(\omega t - \delta)}{\sqrt{\omega^2 + \beta^2}} \quad (2.8)$$

where  $\tan \delta = \omega/\beta$ .

For  $z > 0$

$$n_1 = \exp\left(-\frac{\beta z}{V_0}\right) f(z - V_0 t) \quad (2.9)$$

where

$$f(z - V_0 t) = \frac{A}{\sqrt{\omega^2 + \beta^2}} \sin\left[\omega\left(t - \frac{z}{V_0}\right) - \delta\right] \quad (2.10)$$

which satisfies the condition that  $n_1$  is continuous at  $z = 0$ . We assume  $n_0$  to be continuous at  $z = 0$ .

And if  $V_0 < 0$ , for  $z \leq 0$

$$n_1 = \frac{A}{\sqrt{\beta^2 + \omega^2}} \sin(\omega t - \delta) - \exp\left(-\frac{\beta}{V_0} z\right) \sin\left\{\omega\left(t - \frac{z}{V_0}\right)\right\} \quad (2.11)$$

and for  $z \geq 0$

$$n_1 = 0 \quad (2.12)$$

which shows that the ionization perturbation is totally reflected at  $z = 0$  where the G. W. is reflected.

### 3. Discussion

It is found that the gravity wave perturbs the ionization in the ionosphere, and the resultant perturbation in ionization consists of two components. One, G. W. component, is a replica of the gravity wave perturbation of the neutral medium and the other, H. M. component, is very different, moving in a way as expected by the MCKT theory under the control of the ambient electron and ion movement. If the medium extends infinitely and uniformly, no H. M. component exists as found from the exponentially decreasing factor  $\exp(-\beta/V_0 z)$  in (2.7) where  $z$  is the distance from the boundary where certain sudden change in  $P$  are assumed to exist generating the H. M. component. In the F region,  $\beta$  may be  $10^{-3} - 10^{-4} \text{ sec}^{-1}$  which gives the effective distance  $z_0$  of H. M. component  $z_0 = (V_0/\beta)$  as large as 20-200 km. It seems possible that a conversion from G. W. to H. M. component occurs upon reflection of the original disturbance of G. W. in neutral atmosphere. Then, if  $V_0$  is upwards as caused by an eastwards ambient electric current  $J_0$ , the produced irregularity in ionization can travel far above the reflection height (equation 2.9). If  $V_0$  is downwards, the H. M. component may modulate the G. W. component (equation 2.11).

Another possibility of such conversion may exist at both interfaces of the equatorial electrojet. These interfaces constitute a discontinuity of the horizontal electron drift which is driven mainly by vertical electrostatic field. If a G. W. travels at the equator along east-west direction and (slightly) obliquely traverses the electrojet,  $n_1$  is determined by the equation as

$$\frac{\partial n_1}{\partial t} + v_p \text{grad } n_1 + \beta_0 n_1 = P \quad (3.1)$$

where

$$v_p = \frac{\underline{J}_0 \times \underline{B}_0 - \frac{\sigma_2}{\sigma_1} \underline{B}_0 \underline{J}_0}{n(m_e v_e + m_i v_i)} \quad \text{electron velocity (Kato 1963)}$$

$$P = q_1 - \beta_1 n_0 \quad (3.2)$$

Note that  $V$  in (3.1) replaces  $V$  (2.5), and also in (3.2)  $n \frac{dV}{dz}$  is dropped because of a large  $E_p$  field for  $\underline{k}$  orthogonal to  $\underline{B}_0$  (Kato 1965). Then, (3.1) gives

$$n_1 \propto \frac{1}{\sqrt{(\omega - kv_p)^2 + \beta^2}}$$

Since  $V_p$  can be as large as 600 m/s,  $(kv_p)$  in the electrojet is much larger than in the outside even for  $\underline{k}$  with a small horizontal east-west component. Then, the flux across the interfaces ( $V n_1$ ) is discontinuous. It should be pointed out that the time average over one cycle of  $(n_1 V_z)$  cannot vanish because of phase relation between  $n_1$  and  $V_z$ . Thus, the ionization tends to continuously accumulate at or leave the interfaces of the electrojet. The irregularities produced by this process, however, may move away with  $V_z$  which is nearly equal to the ambient electron velocity; the H. M. component, as a surface  $P$  wave, is strongly excited. This irregularity may explain weak perturbations observed at the interfaces (Bowlsey 1968). It seems likely that the produced irregularities are intensified with  $V_z$ , because the discontinuity in flux across the interface increases with  $V_z$ . We cannot specify any particular process giving  $P$  which now contains perturbations only of  $q$  and loss coefficient, because  $q$  and  $L$  at night are not yet well understood.

#### REFERENCES

- Balsley, B. B., Evidence for plasma turbulence in the equatorial electrojet, (to be published in J. Geoph. Res.).
- Clemmow, P. C., Johnson, M. A. and Weekes, K., A note on the motion of a cylindrical irregularity in an ionized medium, Rep. Conference Phys. Ionosph. Phys. Soc. London P.P. 136-139, 1955.
- Cole, K. D., A dynamo theory of the aurora and magnetic disturbance, Australian J. Phys. 13, 484-497, 1960.
- Hines, C. O., Internal atmospheric gravity waves at ionospheric heights, Can. J. Phys. 38, 1441-1481, 1960.
- Hooke, W. H., Ionospheric irregularities produced by internal atmospheric gravity waves, J. Atm. Terr. Phys. 30, 795-824, 1968.
- Kato, S., Movement of ionized irregularities in the upper atmosphere, Planet. Space Sci. 11, 823-830, 1963.
- Kato, S., Theory of movement of irregularities in the ionosphere, Space Sci. Reviews 4, 223-235, 1965.
- Kato, S., Discussion on theories of movement of ionospheric irregularities, J. Atm. Terr. Phys. (in press).
- Kato, S. and Matsushita, S., Space charge waves and ionospheric irregularities, J. Atm. Terr. Phys. 30, 857-870, 1968.

Martyn, D. F., Electric current in the ionosphere III Ionization drift due to wind and electric fields, Phil. Trans. Roy. Soc. London A246, 306-320, 1953.

Tsedilina, Ye. Ye., Movement of inhomogeneities in plasma (ionosphere), Geomag. Aeronomy 5, 525-530, 1965.

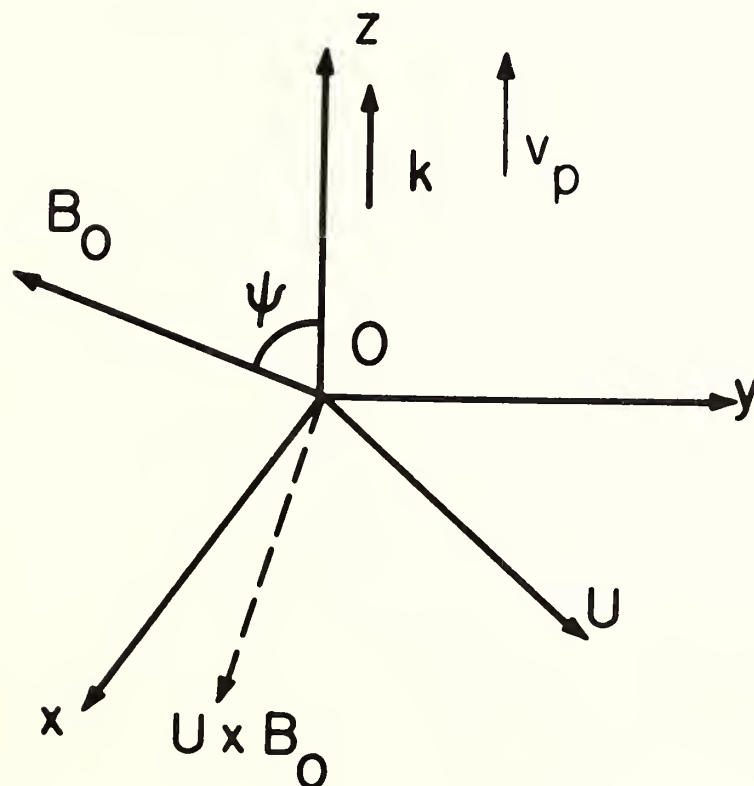


Figure 1. Reference system,  $B_0$  is in the  $x$ - $z$  plane.





## Hydromagnetic Waves With Influence of Gravity

H. Poeverlein  
Air Force Cambridge Research Laboratories  
Bedford, Massachusetts 01730

The gravity force decisively affects hydromagnetic waves at the lowest frequencies, corresponding to periods of some hours or one day. A number of simplifying assumptions had to be made in deriving formulas for modified Alfvén waves and ion-acoustic waves at these frequencies. A joint motion of plasma and neutral gas due to a sufficiently high collision frequency is assumed. Different properties of the waves are obtained, depending on the ratios between  $g/\omega$  (with the gravitational acceleration  $g$  and the angular frequency  $\omega$ ) and the two basic wave velocities (sound velocity and Alfvén velocity). The coupled-wave theory and the generalization of the theory for application to magnetospheric and ionospheric processes are briefly discussed.

### 1. Introduction

Modified Alfvén waves and ion-acoustic waves are coupled in the stratified atmosphere. The theory of coupled hydromagnetic waves was extended to periods or time constants of some hours or one day in a previous paper [Poeverlein, 1968], in the following referred to as [I]. The gravity force had to be introduced at the long periods under consideration. Most of the simplifying assumptions made in [I] will be retained, but two different cases are now considered: the one of the earlier paper, in which only the ion-acoustic waves are modified by gravity, and the second with a modification of both the ion-acoustic waves and the modified Alfvén waves.

The general assumptions are: plane waves, horizontal stratification corresponding to an isothermal atmosphere, rigorous coupling between plasma and neutral gas (i.e., identical motion of these two constituents of the atmosphere), adiabatic change of state in a parcel of material, homogeneous geomagnetic field in an oblique direction. Linearized equations are used; the Coriolis force is neglected. The assumption of a joint (identical) motion of plasma and neutral gas requires that all collision frequencies, including that of neutrals against ions, are large compared to the angular frequency of the oscillation. Formulas will be presented for vertical propagation (vertical propagation vectors of the individual wave modes). More details and references to the literature may be found in the earlier publication [I].

### 2. Wave Modes in Vertical Propagation

The basic equations to be used are the pressure-density relationship of the isothermal atmosphere, the equation of an adiabatic change of state, the hydrodynamic continuity condition, the macroscopic equation of motion, the condition for highly conductive media

$$\vec{E} + \vec{v} \times \vec{B}_0 = 0 \quad (1)$$

and Maxwell's equations (without displacement current density). Subscript 0 is used to denote stationary quantities; no subscript indicates oscillatory quantities. Material velocity, density, and fields are denoted by  $\vec{v}$ ,  $\rho$ ,  $\vec{E}$ , and  $\vec{B}$  respectively;  $\vec{v}$  and  $\rho$  refer to the total medium as does  $\rho_0$ .

Stationary and oscillatory quantities are now supposed to be functions of height (z) only. The geomagnetic field ( $\vec{B}_0$ ) may be in the x, z-plane. Alfvén waves with the field components  $E_x$  and  $B_y$  will not be considered. Dealing with modified Alfvén waves and ion-acoustic waves only, the number of oscillatory quantities in the formulas can be reduced to four:  $v_z$ ,  $\rho$ ,  $E_y$ , and  $B_x$ . Alfvén waves appear decoupled from the other two types of waves in a homogeneous geomagnetic field.

The four oscillatory quantities multiplied by some factors will be combined in the column matrix

$$\vec{F} = \begin{pmatrix} \rho_0 v_z \\ C\rho \\ \epsilon_0 E_y \\ (\epsilon_0/\mu_0)^{1/2} B_x \end{pmatrix}. \quad (2)$$

The constant C is the sound velocity.

From the basic equations one obtains the relationship for  $\vec{F}$

$$\frac{d\vec{F}}{dz} = -ik_0 \vec{P}\vec{F} \quad (3)$$

with  $k_0 = \omega/c$  denoting the vacuum propagation constant and  $\vec{P}$  representing the coefficient matrix

$$\vec{P} = \begin{pmatrix} 0 & \lambda & 0 & 0 \\ \frac{\lambda}{\cos^2 \alpha} & -ih & \lambda \mu^2 B_0 \frac{\sin \alpha}{\cos^2 \alpha} & 0 \\ 0 & 0 & 0 & -1 \\ -\frac{1}{B_0} \frac{\sin \alpha}{\cos^2 \alpha} & 0 & -\frac{\mu^2}{\cos^2 \alpha} & 0 \end{pmatrix} \quad (4)$$

The angle  $\alpha$  gives the direction of  $\vec{B}_0$  toward the vertical. The following dimensionless parameters appear in  $\underline{P}$ :

$$\left. \begin{aligned} \mu &= \frac{(\rho_0/\epsilon_0)^{1/2}}{B_0} \quad (\text{varying with height}) \\ \lambda &= c/C \\ h &= \frac{\gamma g}{k_0 C^2} \end{aligned} \right\} \quad (5)$$

The ratio of specific heats is denoted by  $\gamma$  ; the light velocity in vacuum is  $c$ .

At the considered frequencies there is in general

$$h \gg \lambda \gg \mu \gg 1 \quad (6)$$

The first of the inequalities can be written

$$C \ll \frac{\gamma g}{\omega} \quad (7)$$

With regard to the Alfvén velocity ( $V_A \gg C$ ) two limiting cases may now be considered, the first being

$$\left. \begin{aligned} \lambda^2 &\gg \mu h \\ V_A &\gg \frac{\gamma g}{\omega} \end{aligned} \right\} \quad (8)$$

the second being

$$\left. \begin{aligned} \lambda^2 &\ll \mu h \\ V_A &\ll \frac{\gamma g}{\omega} \end{aligned} \right\} \quad (9)$$

The refractive indices of the modes are derived in the conventional way as the eigenvalues of the matrix  $\vec{F}$ , equation (4). They would correspond to propagation in a homogeneous medium if the matrix were constant. In the present situation, however, a homogeneous medium can hardly be imagined;  $\rho_0$  and the parameter  $\mu$  vary with height, but refractive indices of the wave modes can still be derived and are useful. The refractive indices of the first case were in [I] found to be

$$\left. \begin{aligned} n_1 &= -ih \\ n_2 &= -i \frac{\lambda^2}{h \cos^2 \alpha} \\ n_{3,4} &= \pm \mu \end{aligned} \right\} \quad (10)$$

Subscripts 1 and 2 denote the severely modified ion-acoustic modes, whereas subscripts 3 and 4 refer to modified Alfvén waves of the common form in ascent and descent. In the second case all modes are affected by gravity and the refractive indices (solutions of the dispersion equation, equation (17) in [I]) become

$$\left. \begin{aligned} n_1 &= -ih \\ n_2 &= -i \frac{\lambda^2}{h} \\ n_{3,4} &= \pm \frac{\mu}{|\cos \alpha|} \end{aligned} \right\} \quad (11)$$

The ion-acoustic waves are evanescent in both cases. The modified Alfvén waves are propagated waves even in the second case, in which they are affected by gravity. They may, however, become evanescent and no longer be equal in ascent and descent in the transition between the two cases ( $\lambda^2 \approx \mu h$ ).

The first case, corresponding to equations (10), is expected at higher altitudes (beyond F2 maximum), whereas the second case may be encountered in the ionosphere at the considered frequencies (cf. section 4). It should be kept in mind that the Alfvén velocity in inequalities (8) and (9) is much reduced by insertion of the total gas density in the common expression. Because of the wider altitude range available for the first case, this case may be of greater practical importance.

The material motion in modes 2, 3, 4 behaves differently in the two cases. In the first case it was found that the motion is parallel to the force lines in mode 2 and normal to them in modes 3 and 4 [I]. In the second case equations (25) of [I] yield vertical motion in mode 2 and nearly horizontal motion in modes 3 and 4. The plasma motion in mode 1 is parallel to the force lines in both cases, but the neutral gas may move vertically as a study with use of realistic values of collision frequencies shows.

A matrix  $\vec{T}$  was introduced in [I] to decompose  $\vec{F}$  into the contributions of the four modes according to

$$\vec{F} = \vec{T} \begin{pmatrix} \rho_0 v_{z1} \\ \rho_0 v_{z2} \\ \rho_0 v_{z3} \\ \rho_0 v_{z4} \end{pmatrix} \quad (12)$$

With neglect of insignificant elements the matrix  $\vec{T}$  becomes in the first case [I]

$$\vec{T} = \begin{pmatrix} 1 & 1 & 1 & 1 \\ -\frac{ih}{\lambda} & -\frac{i\lambda}{h \cos^2 \alpha} & 0 & 0 \\ 0 & 0 & -\frac{1}{\mu^2 B_0 \sin \alpha} & -\frac{1}{\mu^2 B_0 \sin \alpha} \\ 0 & 0 & \frac{1}{\mu B_0 \sin \alpha} & -\frac{1}{\mu B_0 \sin \alpha} \end{pmatrix} \quad (13)$$

and in the second case

$$\vec{T} = \begin{pmatrix} 1 & 1 & 1 & 1 \\ -\frac{ih}{\lambda} & -\frac{i\lambda}{h} & \frac{\mu}{\lambda |\cos \alpha|} & -\frac{\mu}{\lambda |\cos \alpha|} \\ 0 & -\frac{\sin \alpha}{\mu^2 B_0} & \frac{ih |\cos \alpha|}{\mu \lambda^2 B_0 \sin \alpha} & -\frac{ih |\cos \alpha|}{\mu \lambda^2 B_0 \sin \alpha} \\ 0 & 0 & -\frac{ih}{\lambda^2 B_0 \sin \alpha} & -\frac{ih}{\lambda^2 B_0 \sin \alpha} \end{pmatrix} \quad (14)$$

In both cases it is mode 1 that entails significant density oscillations ( $\rho$ ). In the second case, with  $|n_2| \ll |n_{3,4}|$ , the modes 3 and 4 may contribute to the density oscillations. Mode 1, in any case, requires a stratification of  $\rho$  along the magnetic force lines that corresponds to the stationary density stratification ( $\rho_0$ ).

Electromagnetic fields should mainly accompany the modified Alfvén waves, modes 3 and 4. In the second case, however, mode 2 may introduce an additional contribution to the electric field. One should, of course, not consider the individual  $\vec{T}$ -elements as measure of the various oscillatory quantities in single modes; each column of  $\vec{T}$  has to be multiplied by an amplitude



factor representing the intensity of the corresponding mode. Mode 2 with its small matrix elements  $T_{22}$ ,  $T_{23}$ ,  $T_{24}$ , may have to carry a higher amplitude factor. Modes 3 and 4 in the second case have to obtain a small amplitude factor if  $v_x$  is to be kept at a reasonable magnitude despite the nearly horizontal direction of the velocity ( $v_z \approx 0$ ).

### 3. Coupled-Wave Theory

Although the wave modes were derived under assumption of an isothermal stratification of the atmosphere, a combination of the four modes with constant amplitudes would not fulfill the basic equations. The density stratification leads to coupling of the modes. A fairly easy method for dealing with the amplitude variations due to coupling was described in the earlier paper [I]. One approximates the function  $\rho_0(z)$  by a step function, letting the steps later shrink to differentials. Continuity of all  $\vec{F}$ -components is postulated at each step. Thus, four relationships for the four mode amplitudes before and after the step are obtained<sup>1</sup>. The continuity condition for the  $\vec{F}$ -components results simply from the appearance of the  $\vec{F}$ -components under the  $d/dz$ -sign in equation (3).

It was seen previously that in case 1 coupling from modified Alfvén waves into ion-acoustic waves is severe whereas the inverse coupling is negligible. However, without inequality (8), which is the limiting condition of case 1, there may be significant coupling either way. In particular, two modes can become identical under some condition, with the consequence of a quite strong coupling between these two modes.

### 4. Application and Generalization

The wave theory in the present form may be of some help in the treatment of slow processes (for example, diurnal variations) in the magnetosphere. One has to be aware, however, of the limitations of plane-wave theory and of the poor validity of some of the assumptions. The small dimensions of the magnetosphere in terms of wavelengths of most of the modes may prevent the wave nature of the modes from showing up. The wave treatment thus may be thought of as somewhat formal and one may tend to speak of oscillations rather than of waves.

Some numerical values indicating the size of the parameters of equations (5) were given previously [I]. With an intermediate density of the atmosphere [Johnson, 1965] one obtains the transition between the two considered cases, corresponding to

$$V_A \approx \frac{\gamma g}{\omega}, \quad (15)$$

at roughly 800 km for  $\omega = 10^{-4} \text{ sec}^{-1}$  and at lower heights for higher frequencies. Above 800 km the conditions are those of the first case in the present description.

<sup>1</sup> The present amplitude consideration is essentially expressed by equation (28) of the earlier paper; but note that the exponential functions of equations (27) in [I] were inadvertently omitted in equation (28). This omission can only be justified by choosing the respective height of the considered step as the lower limit of integration in the exponential functions.

Motions along the force lines and normal to them appeared separated in the modes of case 1. This separation should be very useful also in non-plane wave fields in the magnetosphere. The distinction between Alfvén and modified Alfvén waves is in general not possible in non-plane wave fields, but separate wave equations for Alfvén-type waves and ion-acoustic waves, referring to the two types of motions, can still be given under the conditions of case 1 (cf. [I]). The coupling remains unidirectional under these conditions -- from Alfvén-type waves into ion-acoustic waves, which have the much lower wave velocity.

Co-rotation of the magnetospheric plasma with the earth and simultaneous compression by the solar wind on the dayside lead primarily to a diurnal oscillation corresponding to Alfvén and modified Alfvén waves (largely standing waves). Ion-acoustic oscillations arise as a secondary phenomenon in the density gradient [Poeverlein, 1966]. The magnetosphere is small compared to a wavelength of Alfvén-type waves at a period of one day. In a plane-wave field of this dimension there could be no significant current flow. Non-plane wave fields, however, permit remarkable currents or current densities along geomagnetic force lines even in a small space.

The assumption of a perfectly joint motion of plasma and neutral gas appears to be an oversimplification. The frequency of one cycle per day still is somewhat high for this assumption [Poeverlein, 1967]. Further decrease of the frequency should bring the motions of plasma and neutral gas closer together, at least in modes 2, 3, and 4, which are the modes involving material motion in particular. In mode 1, which is mainly associated with density oscillation and only with smaller material velocities, the two motions may always differ. With partial participation of the neutral gas in the plasma motion one finds energy dissipation in collisions and an increase of the Alfvén velocity toward the value obtained in the plasma alone.

#### References

- Johnson, F.S., Structure of the upper atmosphere, in Satellite Environment Handbook, 2nd edition, edited by F.S. Johnson, pp. 3-20, Stanford University Press, Stanford, 1965.
- Poeverlein, H., Geomagnetic and ionospheric effects of magnetospheric motions, J. Atmospheric Terrest. Phys. 28, 1111-1123, 1966.
- Poeverlein, H., Characteristic heights for hydromagnetic processes in the atmosphere, J. Geophys. Res. 72, 251-256, 1967.
- Poeverlein, H., Ion-acoustic waves modified by gravity, Ann. Géophys. 24(1), 325-332, 1968.



# A RAY-TRACING STUDY OF DIRECTION OF ARRIVAL VARIATIONS THROUGH A TRAVELING IONOSPHERIC DISTURBANCE

W. J. Surtees

Institute for Telecommunication Sciences  
Environmental Science Services Administration  
Boulder, Colorado

Rays have been traced through a representative daytime ionosphere containing a single irregularity, to simulate a long-front traveling ionospheric disturbance. The ESSA/ITS three-dimensional ray-tracing computer program was used for the determination of direction of arrival in both elevation and azimuth. The simple model employed shows the direction of arrivals are both intimately related to the type of irregularity and to its position in the ray path. The frequency dependence shows that the azimuth direction of arrival is expected to increase as the frequency is lowered within the HF band. Computed results of the time dependence of direction of arrival show good qualitative agreement with some experimental observations.

## Introduction

Large-scale traveling ionospheric disturbances (TIDs) in the F-region can be observed by many different HF radio techniques. One technique for detecting the presence and motions of these perturbations is by direction-finding experiments (Bramley and Ross, 1951; Bramley, 1953) in which the direction of arrival (DOA) of ionospherically reflected HF signals is measured in both elevation and azimuth. The purpose of this paper is to examine, using ray-tracing techniques, the relationship between the shape and magnitude of such DOA variations and certain characteristics of the TID model that produces them. The effect of changing the operating frequency is also examined and some inferences drawn. The results are compared with some observations.

## Method

During the study of traveling ionospheric disturbances, Thome (1964) measured overall average electron density profiles and irregularity structures at the Arecibo site in Puerto Rico. The data he presented for the electron density averaged over a 50-minute period on November 11, 1963, have been used to define for our ray-tracing program, a daytime ambient ionospheric profile whose critical frequency of 7.6 MHz occurs at a height of 240 km. He also has shown contours of percentage change from the average profile over the same 50-minute period. These contours, which define the observed ionospheric disturbance, suggest that the longitudinal vertical cross section of an irregularity may be approximated by an ellipse. An analytic expression for such a perturbation has been developed and described in a previous publication (Surtees, 1968). This model, a torus with a tilted elliptic cross section, which is representative of a long-front traveling ionospheric disturbance, has proven useful in the ray-tracing synthesis of HF backscatter records. Use of this model with the ESSA three-dimensional ray-tracing computer program (Jones, 1968) allows us to determine changes in the elevation and azimuth DOAs of signals passing through an ionosphere containing such a long-front TID as will now be described.

Figure 1 illustrates the notation used for the main angles and distances considered. The center of the irregularity in the direction of frontal motion is located at a great circle distance  $d_i$  from the transmitter T. In this work, the irregularity is centered at a height  $H_0 = 202.5$  km, has a tilt of  $\psi = 16^\circ$ , and an elliptic cross section given by semi-major axis = 102.5 km and semi-minor axis = 17.9 km. The azimuth angle of transmission,  $\phi$ , is the angle between the normal to the front (assumed to be the direction of frontal motion) and the direction of



transmission. A ray leaving T with an elevation take-off angle of  $\beta$  after passing through the disturbance will return to the earth with an elevation landing angle  $\chi$  at R, which is located at a great circle ground range of D from T. The irregularity will, in general, cause the rays passing through it to be bent away from the direction of transmission. The azimuth deviation so produced is  $\Delta\varphi$ . It should be noted that positive and negative azimuth deviations correspond, respectively, to increased and decreased apparent azimuth directions of the landing point R as viewed from T, when  $0^\circ < \varphi < 90^\circ$ . The opposite correspondence applies when  $270^\circ < \varphi < 360^\circ$ . By fixing the transmitter position and changing  $\varphi$  it is possible to compute azimuth deviations as a function of  $\beta$  and  $\varphi$ . By moving the transmitter to other distances from the irregularity (i. e., by varying the distance  $d_i$  in steps) and repeating the calculations for fixed azimuth directions of transmission it is possible to simulate the effect of a moving front. The ray-sets so produced by the computer could be used to produce synthetic ground backscatter records by the methods given previously (Surtees, 1968).

To show how the computed raysets may be used to simulate DOA vs. time records, consider the situation shown in plan view in Figure 2. Figure 2a applies to the raysets calculated with the transmitter T at the origin for a fixed azimuth angle of transmission,  $\varphi$ , relative to the long front. As the front was changed from position  $d_{i1}$  to  $d_{i2}$ , the landing point of the rays, at a fixed ground range where  $TR = D$ , changed from the point  $R_1$  to the point  $R_2$ , while the true bearing of the landing points changed from  $\varphi - \Delta\varphi_1$  to  $\varphi - \Delta\varphi_2$ ,  $\Delta\varphi_1$  and  $\Delta\varphi_2$  being the azimuth deviations. The apparent bearings of both landing points, measured from the origin, remain equal to the angle  $\varphi$ .

Figure 2b illustrates the situation for the direction-finding problem, where now the receiving system, which measures the direction of arrival of the signal, is placed at the origin. In this case,  $\varphi$  represents the true bearing of the transmitter relative to the direction of frontal motion. The apparent bearing of the transmitter at a ground distance  $RT = D$ , changes from  $\varphi + \Delta\varphi_1$  to  $\varphi + \Delta\varphi_2$  as the irregularity moves from  $d_{i1}$  to  $d_{i2}$ . Here,  $\Delta\varphi_1$  and  $\Delta\varphi_2$  are the changes of the direction of arrival in azimuth. Since the earth's magnetic field is neglected in this study, the principle of reciprocity allows us to trace rays from the origin R to T and to apply these to actual rays which would travel in the opposite direction. The three-dimensional ray-tracing program, which we used, does not have a homing feature to obtain those ray paths that would arrive at the specified point T as the front is moved. As long as  $\Delta\varphi < \varphi$ , it should be sufficiently accurate for our purposes to assume the ray paths of Figure 2a would be almost unchanged if the azimuth were rotated so that points  $R_1$  and  $R_2$  would fall on R. That is, the azimuth deviation,  $\Delta\varphi$ , in this case would equal the change in the azimuth direction of arrival,  $\Delta\varphi$ , illustrated in Figure 2b. It should be noted that negative values of  $\Delta\varphi$  are drawn in both parts of Figure 2.

As a matter of economy, only three values of  $\varphi$  were selected for computation, namely  $15^\circ$ ,  $30^\circ$ , and  $45^\circ$ . Thus a comparison was not made with the work of Detert (1968) who examined Doppler shifts and only the elevation angle of arrival of rays passing through a similar model disturbance but with the single value of  $\varphi = 90^\circ$ .

#### Azimuth and Elevation Deviations

Figure 3 shows the computed undisturbed ground range, D, versus elevation angle,  $\beta$ , curve (solid line) for the ambient ionosphere. The effect on elevation angle and range of an irregularity of depleted electron density, the maximum value being a 15.4% decrease from the ambient, is shown by the dashed curve, when  $d_i = 1200$  km and  $\varphi = 30^\circ$ . The enhanced focusing characteristic of a hole irregularity is evident for elevation take-off angles between  $6^\circ$  and  $7^\circ$ . The dot-dash curve showing  $\Delta\varphi$ , the azimuth angle deviation, as a function of  $\beta$  indicates that the azimuth deviation is negative when the irregularity is crossed by upgoing rays ( $4^\circ < \beta < 7^\circ$ ) and is positive when traversed by downcoming rays ( $7^\circ < \beta < 12^\circ$ ).

Figure 4 shows the effect of increasing  $\varphi$  to  $45^\circ$ , for  $d_i = 800$  km. It should be noted that  $d_i \sec \varphi$  is about 1200 km for the two cases illustrated by Figures 3 and 4. It may be seen that the maximum magnitude of the azimuthal deviation, which occurs at the take-off angle where



there is maximum focusing, increases rapidly with  $\varphi$ . However, the  $D$  vs.  $\beta$  curve and the amount of focusing caused by the irregularity remain almost constant. Since the group delay,  $P'$  vs.  $\beta$  curves are very similar to the  $D$  vs.  $\beta$  curves, as long as the operating frequency is above the critical frequency of the ionosphere, they also would not be expected to change much as  $\varphi$  is changed. As synthetic range-time ground backscatter records are easily derivable from the  $P' - \beta$  curves (Surtees, 1968), one can conclude that apart from a scale factor, backscatter records (caused by irregularity focusing) are relatively insensitive to the azimuth direction of view of such a long-front TID as considered here. However, the azimuth DOA-time record (as will be synthesized below) would be very sensitive to the aspect angle  $\varphi$ .

Figure 5 shows effects attributable to frequency when comparison is made with Figure 3. For F-region TIDs, and this is borne out by other ray-tracing results not illustrated here, it can be said that the amount of focusing and the magnitude of the maximum azimuth deviation both increase as the frequency decreases. This latter behavior has been observed in measurements (Bramley, 1954) of azimuth DOA-fluctuations for signals reflected from the F-region.

In the cases illustrated, the irregularity was placed closer to the transmitter as the frequency was decreased. In each case it was centered near the reflection height of the skip ray - the position which yielded the greatest azimuthal deviation. Figure 5 also shows that the presence of the irregularity can cause a ducting by decreasing the curvature of the rays passing near the irregularity's center allowing them to escape through the ionosphere. Furthermore, it can be seen that rays with four different elevation take-off angles can reach a fixed ground range, although we are considering only the single-hop F-layer mode of propagation.

#### Direction of Arrival Variations

By using the results exemplified by Figure 5, as well as others calculated for different values of  $d_i$ , it is possible to determine  $\Delta\varphi$  and  $\beta$  as functions of  $d_i$  for a fixed ground range, that is, to simulate the effect of a TID. If the front is assumed to move at a fixed velocity, a plot of  $\Delta\varphi$  and  $\beta$  versus  $d_i$  will represent azimuth and elevation DOA-time records, respectively.

Figure 6 shows the results obtained in this way for the ionosphere (identified as H02) containing an irregularity of depleted electron density. The ducting discussed in connection with Figure 5 is evident by the breaks in the record for values of  $d_i$  between 230 and 270 km. This synthetic record is compatible with observed DOA variations, as illustrated by Figure 7. The observations (Tveten, 1968) were obtained at a time when traveling irregularities were evident on simultaneous ground backscatter records. A transponder was placed at Meridian, Mississippi, which is at a true bearing of  $115.1^\circ$  east of north from Boulder, Colorado. The high-resolution scan ground backscatter system described by Hunsucker and Tveten (1967) was used to obtain these results. The breaks, in Figure 7, around 2230 and 2300 hours occur because at those times the transmitter was shut off. Naturally, there is not an exact correspondence between Figures 6 and 7 as the ionosphere, frequency of operation and ground range between terminals were different for the model and for the observations.

Figure 8 shows another synthetic DOA record which was calculated for the same conditions as those used for Figure 6, except that the ground distance between transmitting and receiving terminals is increased to 1100 km. The ducting is not evident at this range. Both the elevation and azimuth DOA variations are smooth and continuous, although their maximum excursions are less than those occurring in Figure 6.

Similar calculations were carried out for the average ionosphere containing a blob irregularity of enhanced electron density (identified as H01). All the other parameters were unaltered. The resulting synthetic DOA-time record is given by Figure 9. Comparison of Figures 8 and 9, for example, shows the azimuth and elevation DOAs each change together in the same sense, that is, they are in phase, when  $\varphi > 0$ . Such cophasal variations have been observed experimentally by Bramley (1953). When  $\varphi < 0$ , a few moments reflection will show the sense of the elevation DOA is unchanged but the sense of the azimuth DOA is reversed; thus, the

two DOAs are out of phase, in this case. It should be noted that the abscissa of Figures 6, 8 and 9 can be converted to a time scale by assuming the irregularity moves at a given speed. If the front moves away from the origin, time will increase in the direction of increasing  $d_i$ ; if it moves towards the origin, however, time will increase in the direction of decreasing  $d_i$ .

It should thus be possible, when large TIDs are present, to infer from DOA records whether the frontal irregularity under observation behaves as a hole or a blob, provided its approximate direction of motion is known by some other means, such as, perhaps, simultaneous observations of ground backscatter over the same path. A further advantage of simultaneous measurements of DOA and of ground backscatter is the frequency dependence of the signals received. For backscatter, the reflection height of those (low angle) rays having a take-off angle less than that of the skip ray varies in the same sense as  $\beta$ . Also, the reflection height of the rays with fixed  $\beta$  decreases with a decrease of frequency. Thus, when a TID, whose structure and size are not changing, moves further from the backscatter transmitter it is progressively intercepted by rays with lower take-off angles. If it moves at a constant height, less of the irregularity will be "seen" as time progresses. If the observing frequency is lowered, it is possible for the irregularity to be above the height reached by low angle rays, and it will "disappear" from view at a shorter range.

For DOA measurements between fixed terminals, the reflection height of low-angle rays below the MUF also decreases as the frequency is lowered. Thus, the effects of the irregularity on the elevation DOA might be lessened by decreasing the frequency. Such observations, combined with a knowledge of the average ionization distribution with height, should allow for the determination of the approximate height of the maximum change in electron density resulting from a TID.

#### References

- Bramley, E. N., Direction-finding studies of large-scale ionospheric irregularities, *Proc. Roy. Soc.*, A220, 39, 1953.
- Bramley, E. N., Some aspects of the rapid directional fluctuations of short radio waves reflected at the ionosphere, *Proc. IEE*, 101, PtIII, 533, 1954.
- Bramley, E. N., and W. Ross, Measurements of the direction of arrival of short radio waves reflected at the ionosphere, *Proc. Roy. Soc.*, A207, 251, 1951.
- Detert, D. G., Ray-tracing simulation of HF radio measurements of large traveling ionospheric disturbances, *Radio Sci.*, 3 (New Series), 33, 1968.
- Hunsucker, R. D., and L. H. Tveten, Large traveling-ionospheric-disturbances observed at midlatitudes utilizing the high resolution h.f. backscatter technique, *J. Atmosph. Terr. Phys.*, 29, 909, 1967.
- Jones, R. M., A three-dimensional ray-tracing computer program, *Radio Sci.*, 3 (New Series), 93, 1968.
- Surtees, W. J., An approximate synthesis of HF backscatter considering ionospheric motions, *Radio Sci.*, 3 (New Series), 57, 1968.
- Thome, G. D., Incoherent scatter observations of traveling ionospheric disturbances, *J. Geophys. Res.*, 69, 4047, 1964.
- Tveten, L. H., Private communication, 1968.

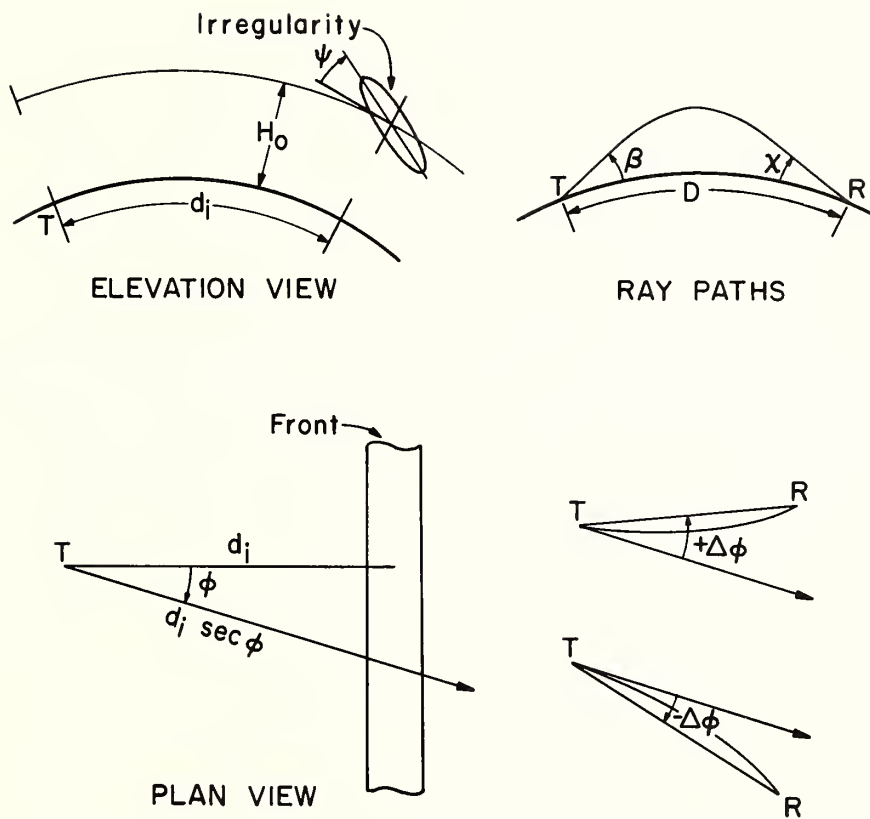


Fig. 1. Notation for principal angles and distances.

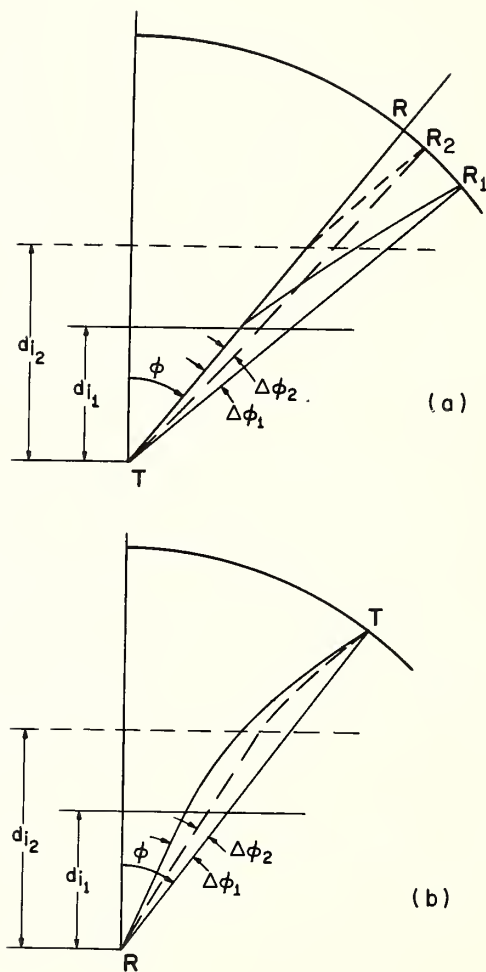


Fig. 2. Ray paths to a fixed ground range through a moving front,  
 (a) backscatter case,  
 (b) direction-finding case.

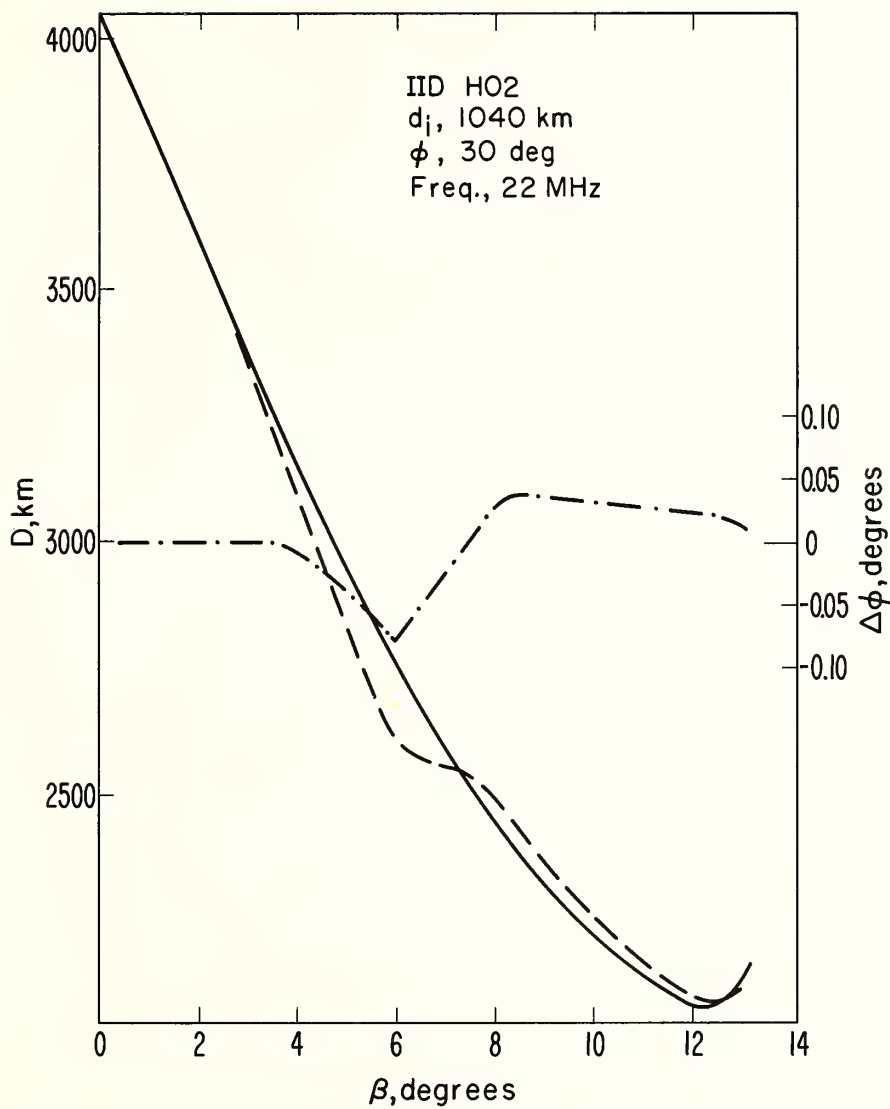


Fig. 3. Ground range  $D$  (dashed curve) and azimuth deviation  $\Delta\phi$  (dot-dash curve) as functions of elevation take-off angle  $\beta$  for rays crossing a long front 1040 km away.



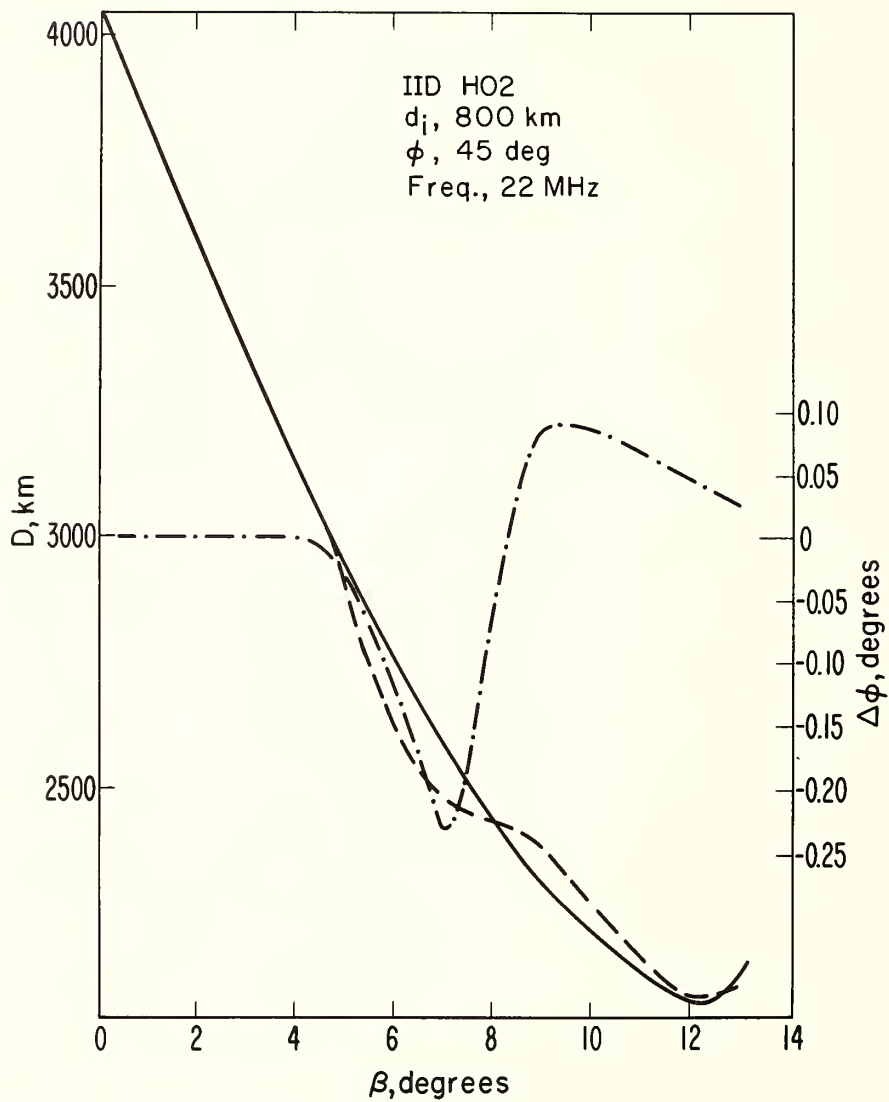


Fig. 4. Ground range  $D$  (dashed curve) and azimuth deviation  $\Delta\phi$  (dot-dash curve) as functions of elevation take-off angle  $\beta$  for rays crossing a long front 800 km away.

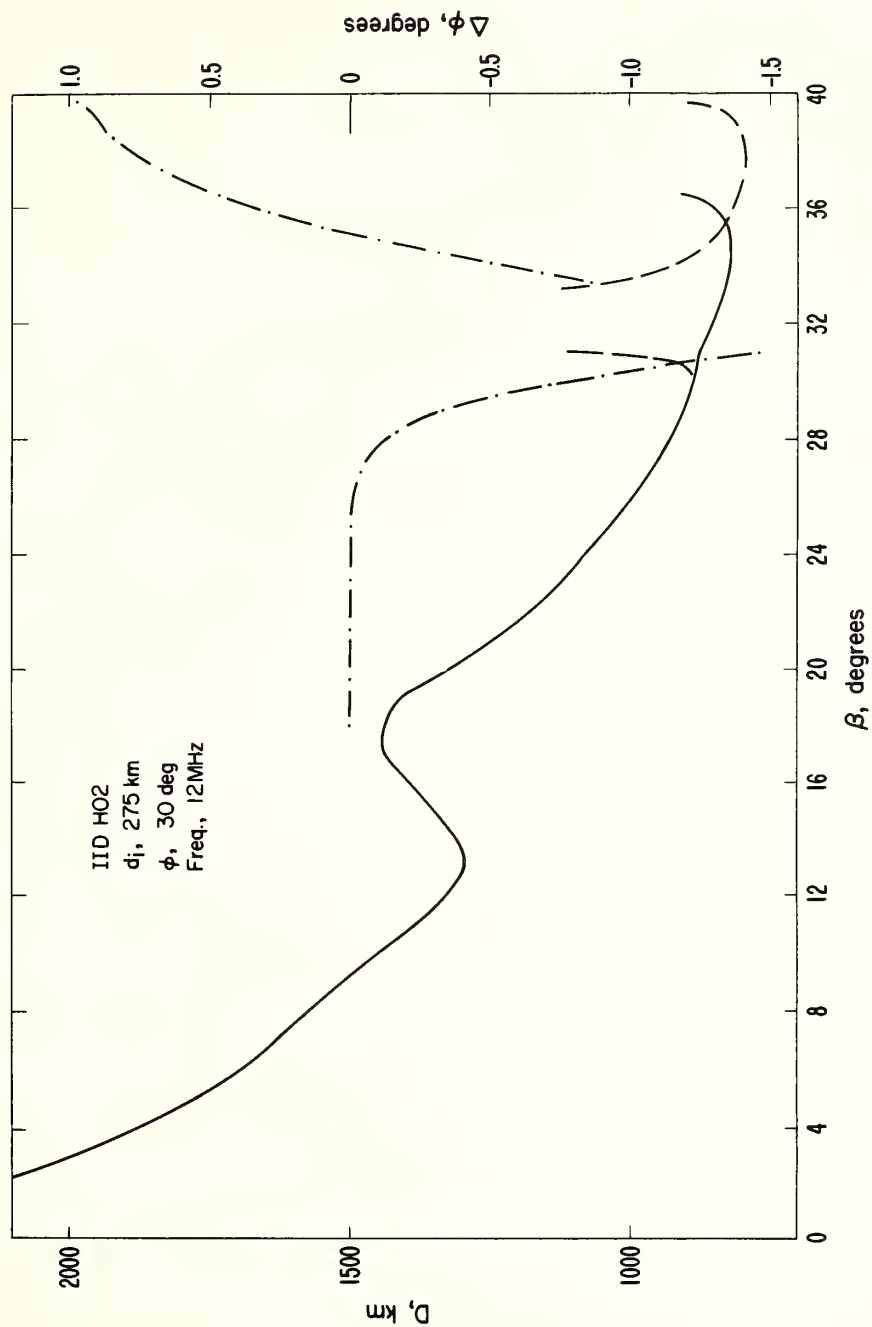


Fig. 5. Ground range  $D$  (dashed curve) and azimuth deviation  $\Delta\phi$  (dot-dash curve) as functions of elevation take-off angle  $\beta$  for rays crossing a long front 275 km away.

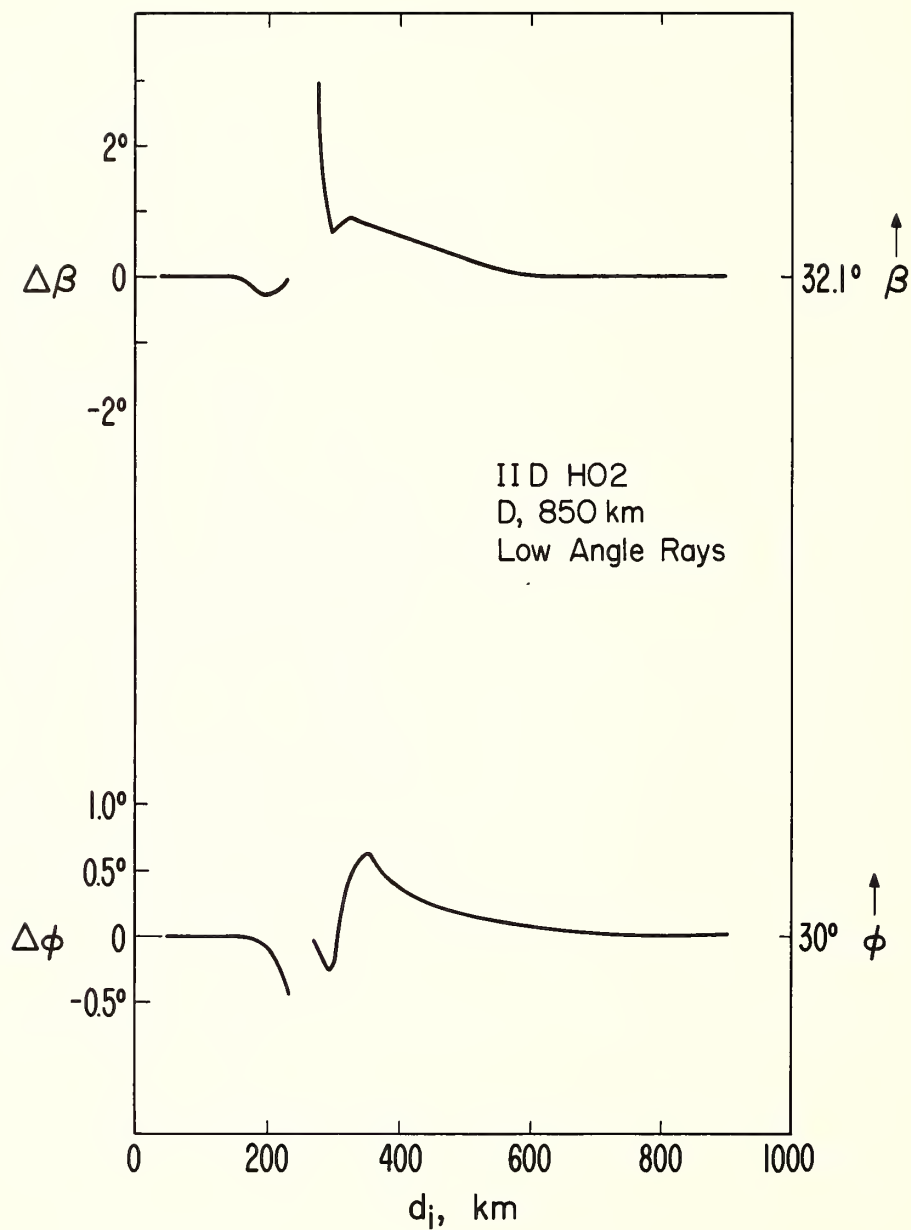


Fig. 6. Elevation and azimuth angles of arrival from a distance of 850 km at a frequency of 12 MHz, through a hole irregularity,  $\phi = 30^\circ$ .

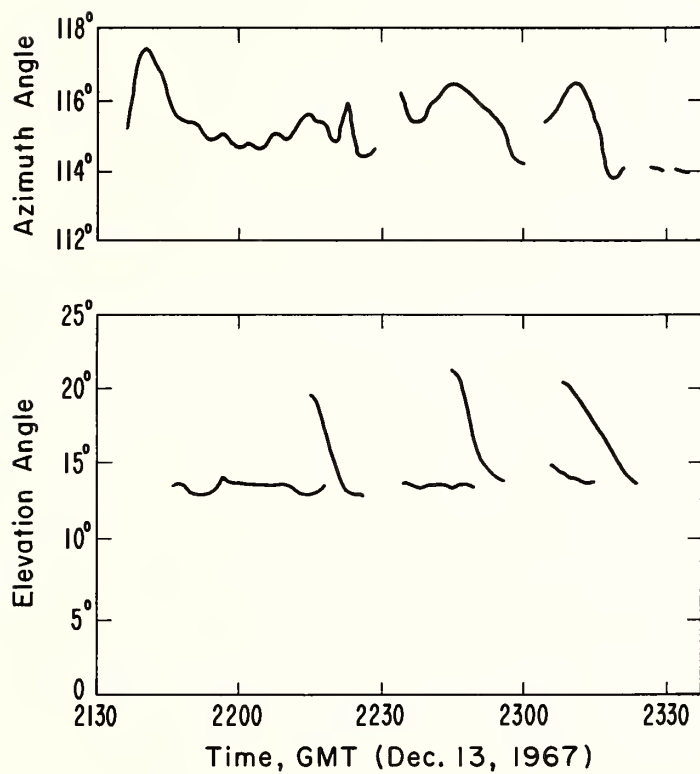


Fig. 7. Azimuth and elevation angles of arrivals of the one-hop F mode transmitted from Meridian, Mississippi and received at Boulder, Colorado, at a frequency of 17.65 MHz.

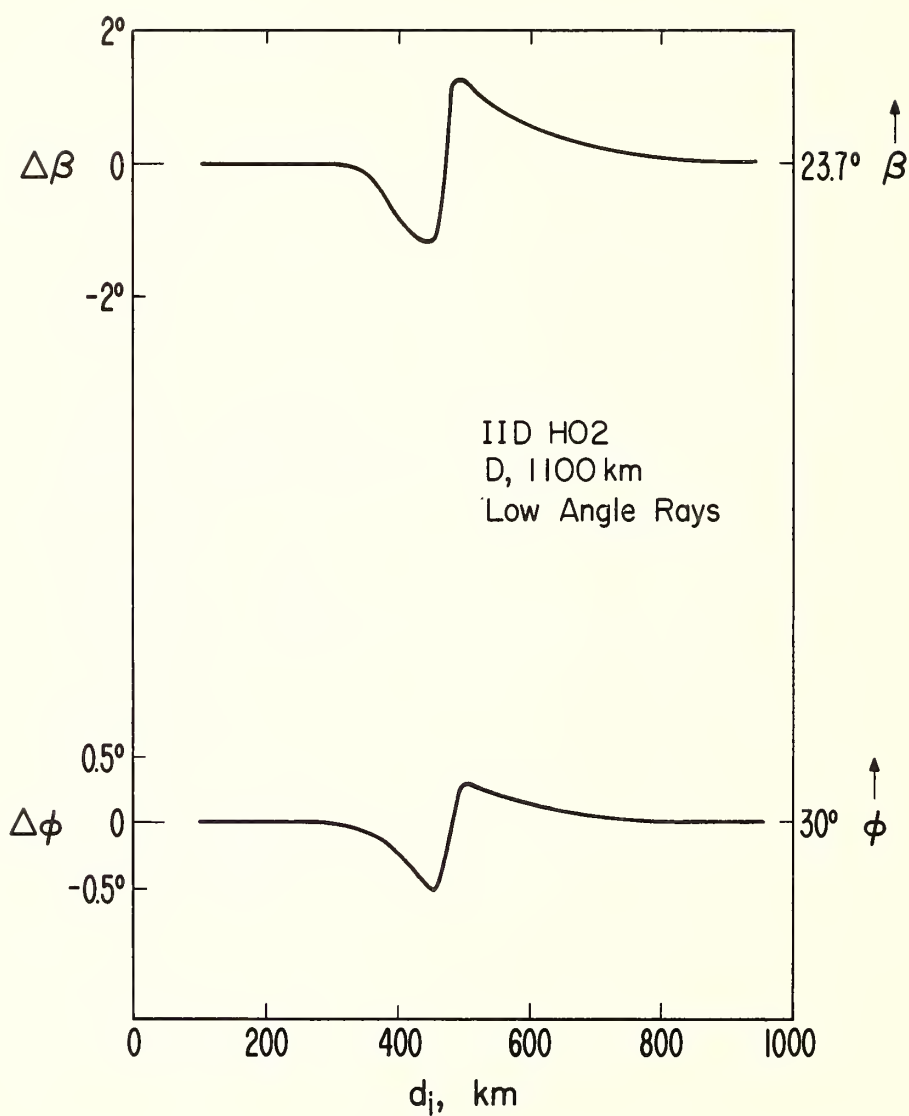


Fig. 8. Elevation and azimuth angles of arrival from a distance of 1100 km at a frequency of 12 MHz, through a hole irregularity,  $\varphi = 30^\circ$ .



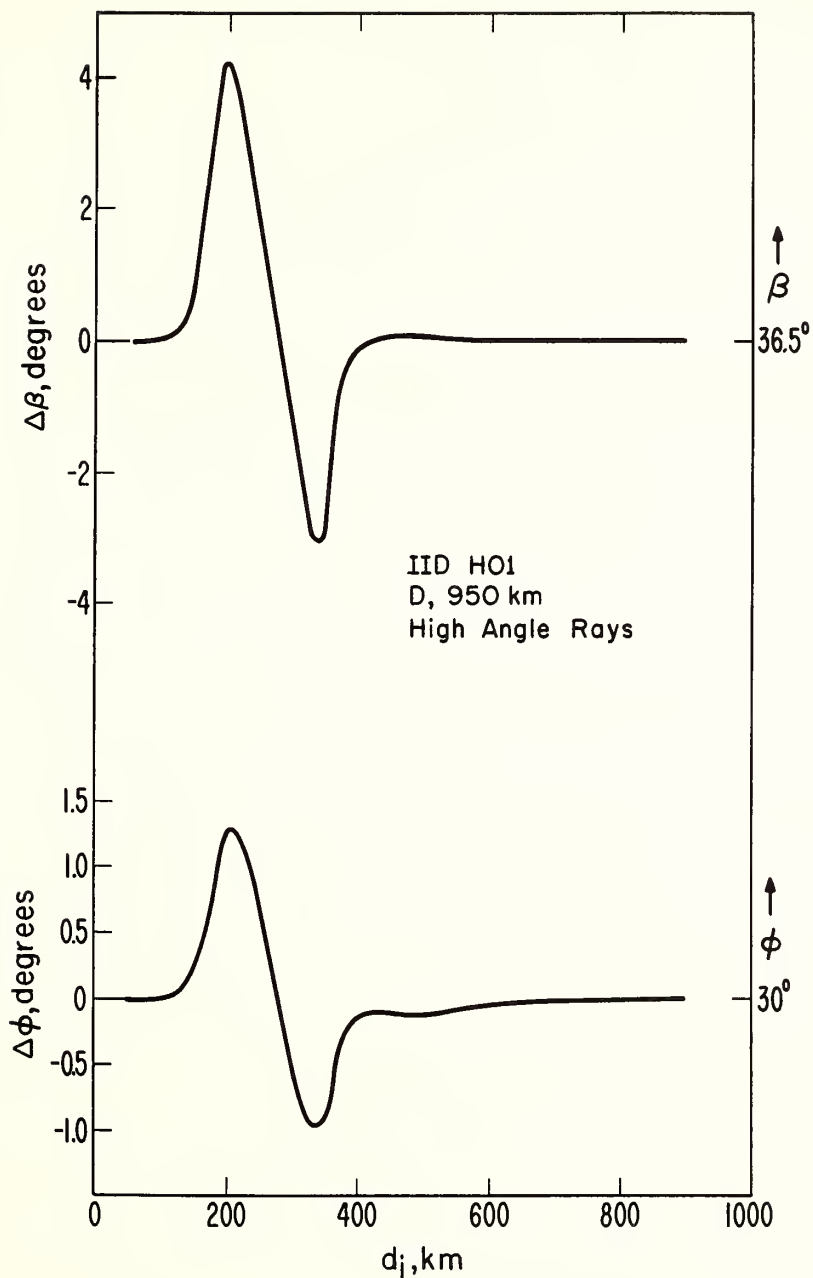


Fig. 9. Elevation and azimuth angles of arrival from a distance of 950 km at a frequency of 12 MHz, through a blob irregularity,  $\varphi = 30^\circ$ .



## CLOSING REMARKS

C. O. Hines  
University of Toronto  
Toronto, Ontario, Canada

In these closing remarks, which I have been asked to make, I believe it will be more useful if I comment on two or three topics that were not dealt with at this symposium, rather than attempting to summarize what was discussed or even picking out highlights.

First I would note that, while generation of waves from well-defined but rather constricted sources was dealt with in a few papers, no treatment was given of generation from the rather ill-defined, almost sloppy sources that normal meteorological processes will tend to provide. In this respect the analysis for the solar atmosphere, with generation in the turbulence of the photosphere, appears to be more advanced than are our accounts for our own atmosphere; the solar work, had it been included here, would have brought a better balance to the discussion of sources. In any event, generation from turbulence and other quasi-random processes, and from extended regions of strong shear, appears to warrant fuller consideration in the future.

Next, we have heard much about the application of mode analyses, but we have had virtually no discussion of the inapplicability of such analyses. This, it seems to me, is a great mistake. The conditions under which mode analyses are valid, let alone useful, are extremely limited; and yet the analyses have often been applied almost wantonly without checking into their value. It is perfectly clear, for example, that waves very close to the source cannot usefully be described in terms of normal modes: too many modes would have to be included, even if the modal description were valid, and the modes would contain information (concerned with reflection conditions at great altitudes, for example) that was as yet unavailable to the energy of the wave and that was therefore irrelevant to the description of the wave. Ray techniques, and even wave analyses for simple homogeneous media, would be far more appropriate to the description in this case. Again, the modal analyses assume a constancy of temperature structure and wind structure, both geographically and in time, that is simply not available in practice; unless some verification is made that the probable variations are unimportant, then the modal results are highly suspect to say the least. This comment is of particular importance in the gravity-wave case when much of the energy reflection occurs, or much of the energy content resides, at E-region altitudes where the wind structure is known to change in times comparable to the "bounce" time of gravity-wave energy between the ground and the E region. Again, any modes that carry substantial energy at these heights should be examined with respect to dissipative processes, which may well be severe even though ignored in the modal analysis. And so on: the rather blind adherence some authors have shown to specific modal computations, without adequate questioning of validity or utility, seems to me quite inappropriate regardless of how convenient it may be.

Finally, I should like to re-emphasize the wealth of research potential that I feel must be associated with critical layers. It may be perfectly true that the physics of these layers can be treated in rather callous fashion for some purposes, such as integration through the layers from infinity to find their effective reflection coefficients; but an understanding of what goes on near and within the layers cannot be gained without a proper treatment, which would include viscosity and thermal conduction in particular. The rich content of the studies that have been undertaken so far, the complications that more realistic physics would introduce, and the probable applicability of the results in such phenomena as clear air turbulence, all suggest that much more effort can be expended profitably in this area. The present symposium has only scratched the surface.



APPENDIX I

ABSTRACTS OF PAPERS PRESENTED AT THE SYMPOSIUM BUT NOT  
INCLUDED IN THESE PROCEEDINGS





## HORIZONTAL WIND-SHEAR ACTION AND ITS RESULTING IRREGULARITIES IN THE IONOSPHERE

D. J. Fang  
Radio Physics Laboratory  
Stanford Research Institute  
Menlo Park, California 94025

The effect of the horizontal shear wind on the generation of the density gradient is examined in this paper. Our approach defines a driving function  $G$  which indicates the gradient of plasma density per unit length produced by unit quantity of wind. We have found that  $G$  is inversely proportional to the coefficient of eddy diffusion of the medium, a well defined quantity in the turbulent theory. A rudimentary analysis based on the observations of meteor trails shows that  $G$  is  $1.67 \times 10^{-5}$  per meter per meter-per-second, indicating that for meteor trails a wind of about 150 m/s is possible to result a 10 percent density gradient within 100 meters. We have found that associated with the density-gradient irregularity there is a general pattern of counter-clockwise eddy wind which spirals in from small magnitude and reaches maximum at the "rim" and then drops to zero at the center of the irregularity. The mechanical energy required to set up the irregularity and its motion have been calculated and compared with existing results. The sustaining factor of the irregularity as well as the physics of plasma gradient as a source of radio noise has also been briefly noted.

## SECOND-ORDER ENERGY FLUX FOR WAVES IN A SHEARING BACKGROUND WIND

C. O. Hines  
Department of Physics, University of Toronto  
Toronto, Ontario, Canada

The perturbation analysis of non-dissipative plane atmospheric acoustic-gravity waves has been carried to second order in the perturbation amplitude. Some of the more important results are given, including those that pertain to the vertical flux of energy in the presence of background wind shears. It is shown that, as measured in a given inertial coordinate system, there is no divergence of this flux (except at critical layers). This conclusion stands in contrast to an earlier one by Eliassen and Palm, in part for semantic reasons. The necessity for a clarification of the physics that underlies the semantics is emphasized.

## A JET-STREAM SOURCE OF WAVES IN NOCTILUCENT CLOUDS

C. O. Hines  
Department of Physics, University of Toronto  
Toronto, Ontario, Canada

It is shown that wave systems observed in noctilucent clouds can, in three cases considered, be attributed plausibly to generation in the tropospheric jet stream at times when that stream is deformed from purely zonal flow. One other case considered, which embraced two wave systems, could not be interpreted similarly unless allowance were made for gross errors of measurement.

## F-REGION TRAVELING IONOSPHERIC DISTURBANCE FROM LOW-ALTITUDE NUCLEAR EXPLOSIONS

Demetri P. Kanellakos  
Radio Physics Laboratory  
Stanford Research Institute  
Menlo Park, California 94025

The response of the ionosphere to the passage of neutral internal atmospheric gravity waves generated by low-altitude nuclear explosions is determined by the study of ionograms taken at various locations about the point of explosion. By means of a theoreticoempirical formula the rearrangement of the F-region electron density is determined taking into account the presence and influence of the geomagnetic field vector. It is found that the shape of the F2 region peak electron-density profiles is changed in a predictable manner which sheds some light in the vast amount of similar data collected after large nuclear explosions conducted by both the USA and USSR. The empirical formalism allows the identification of the traveling ionospheric disturbances at various locations away from and around the point of explosion. The variation of the velocity, period and magnitude of the internal gravity wave are estimated as a function of distance from the point source. The overall shape of the spatial disturbance as a function of distance from the source will be given for times corresponding from about 20 to 120 min. after the explosion of a megaton range low-altitude nuclear explosion. Applications of these findings to naturally occurring traveling ionospheric disturbances will be made.

## ON THE QUESTION OF TSUNAMI HEIGHT PREDICTIONS BASED ON ATMOSPHERIC WAVE DATA

Gaylord R. Miller  
Joint Tsunami Research Effort----ESSA  
University of Hawaii  
Honolulu, Hawaii 96822

Tsunamis are generated by the net vertical sea bed displacements resulting from earthquakes. Transfer of momentum is unimportant in the generation process. The duration of an earthquake is short compared to wave travel times across the generating area. Tsunamis wavelengths are long compared to the depths of the ocean; thus the wave speed  $C$  equals  $\sqrt{gh}$  where  $h$  is the water depth and  $g$  is the acceleration due to gravity. A typical oceanic depth is 5 km, the corresponding speed is 800 km/hr.

Theoretically information about source motion is transmitted by the seismic signal but in practise the complex inhomogeneous transmission path through the earth makes a seismogram difficult to interpret in terms of the vertical ground displacement.

If the characteristics of the atmospheric wave generated by an earthquake are controlled mainly by the same parameters which determine the nature of the tsunami, then it may be possible to make a tsunami prediction based on atmospheric wave observations. The difference in travel time between the atmospheric wave and the tsunami would be from one to a few hours in practical cases. The quality of atmospheric data relating to transmission paths from source to barographs would be limited to average or statistical models of the atmosphere. Platforms to locate the barographs are limited in the Pacific basin if good spatial coverage is required. The signal-to-noise ratio at the recording stations may be unfavorable. The question to be answered is: Will these and many other factors so modify the atmospheric wave that no useful data for tsunami predictions can be extracted from the barographic observations?

## GRAVITY WAVES NEAR AURORAL REGIONS OBSERVED ON RTW HF PROPAGATION

C. A. Moo  
AVCO Corporation, Space Systems Div.  
Lowell, Massachusetts 01851

The presence of gravity waves at ionospheric heights is exhibited in the large Doppler variations in the frequency spectra of around-the-world (RTW) coherent HF transmissions from Manila at 320° azimuth propagating near the southern auroral zone. On many days, frequency displacement of the center of the received energy band by as much as 10 Hz alternately above and below the transmitted frequency occurred for periods of hours. These disturbances appear when the southern propagation path is in night and are most prevalent when the portion of the path nearest the auroral zone is at about 2200 geomagnetic time, corresponding to the time of maximum occurrence of precipitation electrons reported by Hartz and Brice (1967). Samples of spectral records will be presented, and the RTW raypath structure indicated by pulse measurements during these dynamic disturbances will be discussed.

## COMPARISON OF ACOUSTIC GRAVITY WAVE THEORY WITH RECENT EXPERIMENTAL RESULTS

George Thome  
Raytheon Company  
Spencer Laboratory, Wayside Road  
Burlington, Massachusetts 02100

The extent to which existing acoustic gravity wave theory agrees or disagrees with observation is an important factor in determining the direction which further work in the field should take. Since the propagation of such waves is dispersive and anisotropic, it is essential that as many wave variables as possible be observed simultaneously. Towards this end a series of observations were made at Puerto Rico during the summer of 1967 in which the Thomson scatter radar at Arecibo was used in conjunction with a network of HF phase path sounders to study naturally occurring traveling ionospheric disturbances. The HF sounder network was used to measure the horizontal speed and direction of events, while the Arecibo radar was used to make vertical structure measurements. The observations have been combined to give a two-dimensional description (horizontal and vertical distance) of the electron density perturbation caused by these disturbances.

The observations have been compared with theory by applying the equations for acoustic gravity waves in a viscous isothermal gas to a layered model of the neutral atmosphere (10 km slabs). Partial reflections at the slab boundaries have been ignored. The electron and neutral gasses have been coupled by assuming that the electron gas moves only along magnetic field lines and acquires the velocity component of the neutral gas in that direction. Starting from the observed speed and period for particular disturbances, the two-dimensional structure of the perturbation in the electron gas has then been calculated. The predictions are in substantial agreement with the observations.

## AURORAL INFRASONIC WAVES

Charles R. Wilson  
Geophysical Institute, University of Alaska  
College, Alaska 99725

The morphology of infrasonic waves from the auroras has been determined from three seasons of observations at College, Alaska. Supersonic motions of large-scale auroral forms during magnetic sub-storm activity have been identified as the source of the shock-wave-like pressure waves that are generated by the auroras. A model has been developed to explain the highly directional radiation of infrasound by supersonic auroras. Observations relating auroral all-sky photographs to the arrival of infrasonic waves at two auroral zone infrasonic observatories are used to support the model. Transit velocities have been determined for auroral infrasonic waves received from the same source successively at College and Palmer 368 km apart. The geometry of the auroral shock waves, in plan view, has been determined for a few signals by parallax measurements. Two modes of infrasonic energy propagation have been found for signals from distant supersonic auroras.

## EXPERIMENTAL OBSERVATIONS OF TROPOSPHERIC JET STREAM WAVES

Jessie M. Young  
Geoacoustics Group, Environmental Science Services Administration  
Rockville, Maryland 20852

Ground observations from arrays of pressure sensors have revealed a class of traveling pressure waves that are closely associated with the tropospheric jet stream. Distinguishing characteristics are the degree of spatial coherence, velocity, spectral content, and duration. Comparisons with Weather Bureau data indicate that the velocity and direction of travel of these waves are in reasonable agreement with the velocity and direction of the jet stream winds at the tropopause. Characteristic differences between this class of waves and other pressure fluctuations observed in the same 4 to 30 minute spectral region are emphasized.



APPENDIX II

PROGRAM FOR THE SYMPOSIUM



SYMPOSIUM ON ACOUSTIC-GRAVITY WAVES

July 15-17, 1968

Auditorium, Radio Bldg., ESSA/NBS, Boulder, Colorado

Monday, 8:00 a.m. - Introductory Remarks by Dr. G. S. Benton, Director  
ESSA Research Labs. and Col. J. K. Lerohl, Nuclear  
Test Detection Office of ARPA.

8:15 a.m. - Session A: THEORY

Chairman: James R. Wait, ESSA Research Labs.

1. "The excitation and dispersion of the atmosphere surface wave," by D. G. Harkrider, Brown University, Providence.
2. "Ducting of internal gravity waves in a thermally and wind-stratified atmosphere," by C. A. Reddy, High Altitude Observatory of NCAR, Boulder.
3. "Transient energy flux and the initial value problem," by F. W. G. Warren, Imperial College of Science and Technology, London.
4. "Vertical energy flux in a wind and temperature stratified atmosphere," by Robert F. MacKinnon, Imperial College of Science and Technology, London.
5. "Oscillations in atmospheres with tops," by R. S. Lindzen, University of Chicago.
6. "Vertically propagating waves in an atmosphere with Newtonian cooling inversely proportional to density," by R. S. Lindzen, University of Chicago.
7. "Long period pressure fluctuations in the atmosphere," by Ivan Tolstoy, Hudson Labs of Columbia University, Dobbs Ferry.
8. "Full wave calculations of coupled neutral air wave propagation through the thermosphere," by H. E. Volland, Goddard Space Flight Center, Greenbelt.

1:30 p.m. - Session B: GENERATION AND PROPAGATION

Chairman: Colin O. Hines, University of Toronto

1. "Auroral infrasonic waves," by C. R. Wilson, Geophysical Institute, University of Alaska.
2. "The origin and propagation of gravity waves ducted in the thermosphere," by A. F. Wickersham, Stanford Research Institute.
3. "Acoustic-gravity waves produced by energy release," by J. D. Cole and C. Greifinger, The RAND Corporation, Santa Monica.
4. "The generation of traveling ionospheric disturbances by auroral currents," by G. Chimonas, University of Toronto.
5. "Propagating energy in the upper atmosphere and lower ionosphere generated by artificial sources," by U. Fehr, Lamont Geological Observatory, Columbia University.
6. "Ray tracing of internal gravity waves in fluids with spatial and temporal variations in mean flow," by W. L. Jones, National Center for Atmospheric Research, Boulder.
7. "Gravity wave propagation with a time dependent critical level," by D. D. Houghton and W. L. Jones, National Center for Atmospheric Research, Boulder.
8. "Infrasonic air waves from natural and artificial sources," by W. L. Donn and E. Posmentier, Lamont Geological Observatory, Columbia University.

5:00 p.m. - Adjourn.

5:30 p.m. - Reception.

8:00 p.m. - Special Evening Lecture. Prof. Emil Wolf, Department of Physics, University of Rochester. "Some recent developments in physical optics."

Tuesday, 8:00 a.m. - Session C:

Chairman: Ivan Tolstoy, Hudson Labs of Columbia University.

Part I. MORE THEORY

1. "Second order energy flux for waves in a shearing background wind." by C. O. Hines, University of Toronto.
2. "Higher order approximations in the theory of acoustic-gravity waves," by Franco Einaudi, University of Toronto.
3. "High speed solution of ordinary differential wave equations with slowly varying coefficients," by M. L. V. Pitteway, Brunel University, Uxbridge, England.
4. "Iterative series methods for finding exact solutions for a class of second order differential equations," by J. P. Friedman and B. W. Crawford, Knolls Atomic Power Laboratory, General Electric Co., Schenectady.
5. "Mode conversion in non-uniform acoustic waveguides," by J. R. Wait, ESSA Research Labs.

Part II. NEUTRAL-ION COUPLING

6. "On the coupling between acoustic-gravity waves and the ionospheric plasma," by H. Raemer, Northeastern University, Boston.
7. "Vertical propagation of gravity wave disturbances," by J. Claerbout, Stanford University.
8. "Collisional interaction of atmospheric waves with the ionospheric F region," by T. M. Georges, ESSA Research Labs.
9. "A hydromagnetic coupling of acoustic gravity waves with the ionized atmosphere," by S. Kato, C. A. Reddy and S. Matsushita, High Altitude Observatory, Boulder.
10. "Hydromagnetic waves with influence of gravity," by H. Pöeverlein, Air Force Cambridge Research Laboratories, Bedford.

1:30 p.m. - Session D: NUCLEAR EFFECTS

Chairman: A. Glenn Jean, ESSA Research Labs.

Prefatory remarks by Chairman.

1. "Theoretical source models for the generation of acoustic-gravity waves by nuclear explosions," by A. D. Pierce, Massachusetts Institute of Technology, Cambridge.
2. "Generation of gravity-acoustic waves by nuclear detonations," by S. L. Kahalas and W. E. Knabe, Mt. Auburn Research Associates, Inc., Cambridge.
3. "Theoretical calculations of shock arrival times at ionospheric heights for low altitude nuclear bursts," by W. A. Whitaker, and J. S. Greene, Jr., Air Force Weapons Laboratory, Kirtland AFB.
4. "Dispersion of atmospheric waves from nuclear explosions," by W. L. Donn and N. K. Balachandran, Lamont Geological Observatory, Columbia University.
5. "Observations of acoustic waves in the ionosphere following nuclear explosions," by D. M. Baker, ESSA Research Labs.

6. "Ionospheric disturbances caused by nuclear explosions," by K. M. Kotadia, Gujarat University, Ahmedabad, India.
7. "Identification of acoustic-and gravity-wave modes associated with travelling ionospheric disturbances caused by nuclear explosions," by A. F. Wickersham, Jr., Stanford Research Institute.
8. "F-region traveling ionospheric disturbance from low-altitude nuclear explosions," by D. P. Kanellakos, Stanford Research Institute.
9. "Propagation velocity of acoustic gravity wave due to large nuclear explosion," by R. Yamamoto, Kyoto University.

Wednesday, 8:00 a.m. - Session E: TRAVELLING IONOSPHERIC DISTURBANCES

Chairman: Kenneth Davies, ESSA Research Labs.

1. "Comparison of acoustic gravity wave theory with recent experimental results," by G. Thome, Raytheon Company.
2. "F-region ionospheric irregularities produced by internal gravity waves," by W. H. Hooke, ESSA Research Labs.
3. "E-region ionospheric irregularities produced by internal gravity waves," by W. H. Hooke, ESSA Research Labs.
4. "The effect of turbulence on the cross-spectra of wave recordings from spatially separated sites," by E. E. Gossard, Naval Electronics Laboratory Center, San Diego.
5. "Measurements of gravity waves in the neutral air at thermospheric heights by Explorer 32," by G. P. Newton, D. T. Pelz, and H. Volland, Goddard Space Flight Center, Greenbelt.
6. "Gravity waves near auroral regions observed on RTW HF propagation," by C. A. Moo, AVCO Corporation, Lowell, Mass.
7. "The auroral zone as a source of traveling ionospheric disturbances," by W. L. Flock, University of Colorado, Boulder, and R. D. Hunsucker, ESSA Research Labs.
8. "A ray tracing study of direction of arrival variations through a traveling ionospheric disturbance," by W. J. Surtees, ESSA Research Labs.
9. "Horizontal wind-shear action and its resulting irregularities in the ionosphere," by D. J. Fang, Stanford Research Institute.

1:30 p.m. - Session F: WEATHER AND RELATED EFFECTS

Chairman: George S. Benton, ESSA Research Labs.

1. "A jet-stream source of waves in noctilucent clouds," by C. O. Hines, University of Toronto.
2. "Subsonic atmospheric oscillations," by R. K. Cook, ESSA, Rockville.
3. "Experimental observations of tropospheric jet stream waves," by J. M. Young, ESSA, Rockville.
4. "Observations of jet stream gravity waves and their implications concerning jet stream stability," by T. R. Madden, Massachusetts Institute of Technology and J. Claerbout, Stanford University.
5. "Short-period ionospheric oscillations associated with severe weather and geomagnetic activity," by T. M. Georges, ESSA Research Labs.
6. "Subsonic waves and severe weather phenomena," by H. S. Bowman, ESSA, Rockville.
7. "On the question of Tsunami height predictions based on atmospheric wave data," by G. R. Miller, ESSA, University of Hawaii.
8. "Scatter propagation of infrasound," by W. C. Meecham, University of California, Los Angeles.

4:30 p.m. - Final Remarks and Summary Statements, including final comments by C. O. Hines.











PENN STATE UNIVERSITY LIBRARIES



A000072010495